For better or worse

Frank debate is needed about the balance between beneficial and detrimental uses of research. Scientists must be the first to open discussions.

Many bench scientists are just too caught up in their research to consider its ethical possibilities, and very few want to take the time to rigorously explore them.

However, the controversy over the research into the genetic modification of the H5N1 flu virus, finally approved for publication, should offer a reminder of the importance of debate. Conversations about dual-use technology — work that could be used for both humanitarian and unethical ends — should go way beyond mutant flu. On page 432 of this issue, we discuss broader case studies and show the need for reflection and discussion in many areas of science.

'Dual-use technology' is not a synonym for science, of course — a simple knife can be a tool or a weapon, whereas research into turtle navigation will not yield long-range missile technology, for example. But dual-use basic research is a special case because its implications, for good and bad, are often viewed with the greatest clarity by only a small minority of people. The scientists involved (and they are increasingly specialists in very small fields) are often the only ones that can fully understand the risks posed by a line of research.

Some fields have structures in place to ensure scrutiny from outside, yet, too often, scientists are slow to raise their hands with uncomfortable questions. Why? Some may feel that speaking frankly and drawing attention to dangers, real or perceived, will cause trouble for their labs, whereas others feel that they would be wasting time on what they regard as hypothetical conundrums. Optimism is also a factor: most researchers genuinely believe in the benefits of their work, and few want to think about the drawbacks.

There are disadvantages to leaving it up to outsiders to initiate debate about risks, benefits and ethics. The first is that in the early, fertile stages of public debate, some threats are easily underestimated whereas others are overestimated. Everyone can understand the risk posed by a knife, but few are qualified to recognize the dangers of using lasers to enrich nuclear isotopes. And misconceptions are rife: many members of the public believe that neuroscientists have already made mind-reading possible, even though fundamental research into predicting a subject's intent has only just begun.

The second risk is that non-scientists can take control of the debate, especially when concerns about science are expressed as surrogates for concerns about associated values and perceived benefit. For example, environmental groups made a strong public case against the use of genetically modified organisms in food, especially in Europe, even though most scientists who have studied the risk from such food say that it is vanishingly small.

Finally, there is the possibility that decisions about research will end up in the lap of a regulator that lacks either the knowledge or the authority to handle it. The US National Science Advisory Board for Biosecurity found itself effectively refereeing the publication of the controversial H5N1 papers. And in the Netherlands, legal arguments over whether the nation's export-control authorities have jurisdiction over the export of mutant-flu data have caused further problems.

The US government has responded to the H5N1 debate by asking its funding agencies to increase their vigilance when assessing research proposals for the potential for harm. Such problems can also be tackled through greater open discussion of research. That may mean individual researchers raising flags about their own work, but it is more likely to involve scientists taking the time to think about the potential dangers as a community. Whether in conference sessions, peer review or funding decisions, researchers should publicly ask whether the work being done by their colleagues poses any threat — and, if it does, how that weighs against the benefits. Then they should be prepared to discuss potential problems collectively to reach a decision on to how to proceed.

> *"Researchers should publicly ask whether the work being done by their colleagues poses any threat."*

Open discussions carry risks. In the United Kingdom, for example, part of a geoengineering experiment has been delayed indefinitely by its funding council to satisfy the need for a lengthy public debate. But not having these debates carries even greater risks. And although scientists are uniquely qualified to understand what will be possible, they are not always best able to judge the dangers.

More funders should copy the United States and look at introducing early oversight of research. The public must be well forewarned of problems that it might care about, and scientists can make sure that discussions of risk and hazard remain grounded in reality. ∎

Chase the dragon

A planned commercial trip to the space station shows a future direction for NASA.

The US space programme is trapped in a war between financial constraints and costly inertia. For decades, the political talk was that manned space flight would continue as it always had, or become even bolder and more inspiring. Last week's final flight of the space shuttle *Discovery*, piggy-backing on a jumbo jet on its way to a museum, showed the reality — the glory days of NASA, for now at least, are behind it.

Next month, the agency is scheduled to take a small but significant step towards a different future. Supplies for NASA's one remaining flagship piece of manned hardware, the International Space Station, will be packed into a capsule built and sent into orbit by a private firm — SpaceX of Hawthorne, California.

Success is far from assured — a scheduled 30 April launch had been delayed as *Nature* went to press, and the testing schedule of the Falcon 9 launch rocket has been accelerated to accommodate the unmanned supply flight. But if the Dragon capsule does succeed in its mission to dock with the space station and then return to Earth, NASA will be optimistic that the craft could soon carry more than supplies. With the retirement of the shuttle, the agency lost its independent link to its space station, and must now rely on the Russian Soyuz system to launch new crews and bring its astronauts home again. A contract with SpaceX to send people into space in Dragon would restore some national pride, as well as reducing crucial dependence on the production and continued success of a foreign rocket. A Soyuz failure that saw the loss of astronauts would effectively close down the space station.

The impending launch of Dragon has brought conflicting reactions. Enthusiasts see a new frontier opening up for commercial operators at all levels, from suborbital research flights to full-on private hotels in space. In a World View article on page 417, Alan Stern, an unashamed enthusiast, explains how far private firms are determined to boldly go.

Then there are the curmudgeons, those who claim that the new model is a classic case of the emperor's new clothes. NASA has always relied on private companies to build its rockets and capsules, they point out, and is handing a huge subsidy to SpaceX. So this heralded new dawn is merely a reworded contract here and a shift in financial emphasis there. The dragon, they say, has no teeth.

The truth, as so often, is likely to fall somewhere in between. Although aerospace firms such as Lockheed and Boeing have always helped NASA to carry the stars and stripes aloft, they did so on a cost-plus basis, with the agency meeting all costs, however large the eventual bill, and then adding on a substantial and guaranteed profit. If Dragon shows that the private sector can do more on its own terms — from design to sourcing component parts — then the costs will come down. Scientists should welcome the move. The further NASA can get from the cost-plus contracts of the past, and the nearer to buying room on a rocket as a commodity — similar to seats on a commercial airliner — the better. NASA could then spend more of its money on the things to be launched, people and probes, rather than on rocket launches that remain as expensive as they have always been.

> **"The great unknown remains the demand from scientists and wealthy individuals willing to pay to access space."**

And as the News story on page 426 shows, the planned launch of Dragon — and its ability to bring back scientific samples under controlled conditions — is already raising hopes in the space-science community that the space station could finally begin to fulfil its potential for research.

There is strong precedent for the way the US government is trying to nurture the commercial space-flight business. In the early days of aeroplane flight, government officials handed out guaranteed contracts to aviation pioneers for carrying airmail. And in the 1970s, by both funding the developers of microchips and promising to buy the results, the US Department of Defense kick-started the computer industry.

The market for the services provided by SpaceX and its ilk is, of course, smaller. The space station is scheduled to operate — and so will need to be supplied — until only 2020. Contracts to launch satellites are lucrative, but the great unknown on the balance sheet remains the demand from scientists and from wealthy individuals willing to pay big money for tourist flights to space.

A successful SpaceX operation next month will not resolve such questions, but it would make more people ask them more seriously. And that can only be a good thing. ■

Suckers for success

The use of leeches is making a comeback, and not just in medicine.

In the 1807 poem *Resolution and Independence*, William Wordsworth recalls a dawn encounter with a withered old man on a moor: "He told, that to these waters he had come | To gather leeches, being old and poor: | Employment hazardous and wearisome!"

Nineteenth-century gatherers often dunked their legs into leech-filled bogs and ponds until the bloodsuckers began to feast. The motivation was money: medical use of leeches, or hirudotherapy, was at its height in Europe, and surgeons needed every leech they could get. France reportedly imported 42 million medicinal leeches in 1833 alone.

Leech therapy dates to ancient Greece, and perhaps earlier. Hippocrates preached the importance of balancing the four humours (blood, phlegm and black and yellow bile) through bloodletting. Because they secrete a host of enzymes to anaesthetize their victims at the spot of a bite and to keep the blood flowing, leeches were useful when drawing blood from sensitive parts of the body such as the mouth, larynx and anus.

Nicander of Colophon, who lived in the second century BC, described the medical use of leeches, which belong to the same phylum (Annelida) as earthworms, in his poem *Alexipharmaca*. Greek, Roman and Arabic doctors embraced their use, and English doctors in the Middle Ages were often called leeches; the Anglo–Saxon word *læce* means healer.

The leech bubble burst in the second half of the nineteenth century, when people realized that the animals made most patients worse, not better. By 1879, London's leading leech importer was distributing just a tenth of the 30,000 or so it once had, and they "principally go to Scotland", the *British Medical Journal* noted that year.

Still, the leech has never really left the medical mind, and it is starting to be used again. Reconstructive surgery, always a hotbed of innovation, was the first field to re-embrace the medicinal leech (*Hirudo* spp.). A survey of the 62 plastic-surgery units in the United Kingdom and Republic of Ireland in 2002 found that 80% had used leeches in the past five years, with just four centres reporting that a patient had turned down hirudotherapy (I. S. Whitakera *et al. Br. J. Plast. Surg.* **57,** 348–353; 2004). No wonder. Leeches are thought to improve the outcomes of reattached digits, ears and other body parts by preventing veins from becoming clogged .

Leeches also ease the pain caused by osteoarthritis. Among the 30 or so biologically active substances in their saliva are molecules that stop inflammation and blood clotting, both of which are involved in arthritis.

Medical-grade-leech sales haven't returned to their early-nineteenth-century heights, but the animals are once again selling briskly. Britain's largest supplier, Biopharm Leeches in Hendy, Wales (which has the tag line "The biting edge of science"), ships around 50,000 per year, and in 2004, a French firm, Ricarimpex in Eysines, won clearance from the US Food and Drug Administration to market its leeches as medical devices in the United States.

Leech use is not restricted to medicine. As we report on page 424, tropical leeches are being recruited in the search for endangered species. These leeches preserve DNA from the last mammal they fed on, so can offer clues to the mammal's range and location. Conservationists in Vietnam and Laos plan to scour the bellies of leeches in their search for the saola antelope (*Pseudoryx nghetinhensis*), one of the world's rarest animals.

It is a fitting twist for the medical leech, which itself is listed as a 'near threatened' species in the wild and may have been in decline even in Wordsworth's time. "Once I could meet with them on every side," the old leech gatherer tells the young poet. "But they have dwindled long by slow decay; | Yet still I persevere, and find them where I may." ■

↻ NATURE.COM
To comment online, click on Editorials at:
go.nature.com/xhunqv

Commercial space flight is a game-changer

The first private-sector flight to the International Space Station will open up myriad opportunities for science, says **Alan Stern**.

Next month, SpaceX, an aerospace company in Hawthorne, California, is scheduled to launch the first cargo resupply mission by a commercial space company to the International Space Station (ISS). Its Falcon 9 orbital rocket will send to the station a Dragon capsule stocked with food, water and other astronaut provisions.

The flight will be the first of many resupply missions, under contract by NASA to SpaceX in a deal worth around US$1.6 billion. But more importantly, it represents the entry of commercial space companies into the big league. It will place SpaceX at the heart of ISS operations and will open up important capabilities for science by increasing the number of future science experiments aboard the station and providing a way to bring samples produced in microgravity back to Earth.

The flight is a watershed, but it is just the beginning of the potentially game-changing capabilities and economic promise of the emerging commercial space industry for science.

Take the realm of suborbital flight — missions that stay just a short time in space. It has been used effectively by researchers around the world for more than 60 years to test new techniques and technologies, conduct special-purpose observations and train students. But the concept is about to undergo a reboot, thanks to commercial firms such as Virgin Galactic in Las Cruces, New Mexico, and Blue Origin in Seattle, Washington, along with less well known but equally interesting entrants XCOR Aerospace and Masten Space Systems in Mojave, California, and Armadillo Aerospace in Heath, Texas. The companies will revolutionize suborbital access by lowering costs to a tenth of those today by flying reusable rather than throw-away space vehicles.

Together, these firms will vastly increase access to microgravity for scientists, instrument technology testers and educators, in much the same way that personal computers expanded access to computing in the 1980s from the mainframe machines of the 1970s.

And commercial space companies offer science capabilities and options at more than just the low altitudes at which the station and suborbital vehicles fly. The Google Lunar X Prize is spurring companies such as Moon Express in San Francisco, California, backed by deep-pocketed Internet moguls, to offer flights to the Moon for cut-rate prices.

How? Moon Express and its competitors hope to build a twenty-first-century robotic space business niche by amalgamating payloads from various universities, labs and countries, and sharing the costs. They are betting that although few countries and private entities can afford the one to two hundred million dollars to mount a lunar mission, many can afford to share the cost with half a dozen others, thereby reducing the cost

COMMERCIAL SPACE FIRMS WILL VASTLY INCREASE ACCESS TO MICROGRAVITY FOR SCIENTISTS.

of lunar missions to perhaps a few tens of millions of dollars — or even less — for small payloads.

Space firms also have attractive deals for science in Earth orbit. For space experiments needing short stays (weeks to months), SpaceX is offering cut-rate access to orbit aboard Dragon, and the opportunity for later re-flight.

Bigelow Aerospace of Las Vegas, Nevada, intends to take the commercial space concept to a new level — by constructing a fully functional orbiting lab that could rival the available volume and crew complement of the ISS. Bigelow's station will give private companies and the 150 or so smaller countries that are not a part of the ISS consortium the capability to fly experiments and experimenters for stays of three months or longer — perhaps even years. And although pricing is still in flux, Bigelow hopes that mission prices will be less than what small science satellites cost today.

Some of these nascent ventures may be successful, others not. And some are less conventional than others. Perhaps the most conventional, and most game-changing in the long run, is SpaceX's promise of Falcon rocket launches at costs of $55 million that have the same capabilities as rockets now offered almost exclusively at costs of $150 million or more.

Those lower prices have caught the eye, and the purse, of big-name communications-satellite suppliers — such as SES, based in Betzdorf, Luxembourg; Iridium in McLean, Virginia; and Orbcomm in Fort Lee, New Jersey — who have showered SpaceX with contracts for more than a dozen launches.

It is unlikely to be long before science agencies such as NASA and the European Space Agency, which are feeling the simultaneous pinch of cost overruns and budget squeezes, begin to make similar contracts. Over a series of missions, a saving of $100-million per launch could add up to more than a billion extra dollars in the bank — and that, in turn, could result in science missions that might otherwise not have been possible.

Who says that commercial space flight is possible only for wealthy space tourists and communications-satellite operators? Commercial space ventures will provide scientists with much-needed and welcome new ways to advance their research by making space easier and cheaper to access. ■ SEE EDITORIAL P.415 AND NEWS P.426

↻ **NATURE.COM**
Discuss this article online at:
go.nature.com/ad34kw

Alan Stern *is a planetary scientist and aerospace consultant, and former associate administrator in charge of science at NASA. He is also chairman of the Commercial Spaceflight Federation's Suborbital Applications Researchers Group.*
e-mail: astern2010@aol.com

MATERIALS

Could graphene be a laser?

Graphene — sheets of carbon just one atom thick with exceptional mechanical and electrical properties — also has the potential to be used as a laser.

Tianqi Li of the Ames Laboratory at Iowa State University and his colleagues demonstrate that 'pumping' a graphene monolayer with 35-femtosecond pulses of light causes the graphene to reach an excited state called a population-inverted state. It can then be triggered to emit light. With strong pumping, the graphene emits more light across a range of near-infrared frequencies than it absorbs — a sign of the 'optical gain' that is crucial for lasers.

Graphene's unique properties could improve the performance of current laser technology.
Phys. Rev. Lett. **108,** 167401 (2012)

ZOOLOGY

Mammal sings with syntax

Mammalian vocalizations containing complex structure, or syntax — such as those of whales and bats — may be more common than previously thought.

Arik Kershenbaum at the University of Haifa in Israel and his colleagues analysed the calls of the male rock hyrax (*Procavia capensis*; **pictured**), a small mammal common in Africa and the Middle East. Hyrax songs are made up of five types of syllable — wail, chuck, snort, squeak and tweet. The authors found that animals living within a few kilometres of each other produced songs with a similar syllable order. Over larger areas, there was no relationship between syntax and location, suggesting that hyraxes have a limited territorial range and that their songs may be a socially learned behaviour.
Proc. R. Soc. B http://dx.doi.org/ 10.1098/rspb.2012.0322 (2012)

ECOLOGY

Savannah trees resist fires

A fire-sensitive tree species has managed to survive in one of Earth's most fire-prone locales because the trees form closed canopies that support a fire-resistant plant community.

The conifer *Callitris intratropica* can be found in patches of woodland across the savannah of northern Australia. Clay Trauernicht and his colleagues at the University of Tasmania in Australia conducted controlled burns and compared the response of *C. intratropica* conifer groves with either open or closed canopies. Closed-canopy groves (pictured) supported a distinct plant community with lower fuel availability and produced more seedlings and saplings. Compared with the surrounding eucalyptus-dominated savannah, closed-canopy conifer groves were less likely to burn, and experienced milder fires.
J. Ecol. http://dx.doi.org/10.1111/j.1365-2745.2012.01970.x (2012)

MICROBIOLOGY

Gene behind MRSA's menace

A rare gene from a dangerous antibiotic-resistant bacterium is becoming more common by being transferred between strains, and seems to boost virulence in skin and respiratory infections.

Yuan Lu at Fudan University in Shanghai, China, and Michael Otto at the National Institute of Allergy and Infectious Diseases in Bethesda, Maryland, and their colleagues studied the gene — called *sasX* — which was recently discovered in methicillin-resistant *Staphylococcus aureus* (MRSA). They found that *sasX* encodes a cell-surface protein that helps the bacterium to cling to human nasal cells and to evade the immune system. Mice infected with *sasX*-positive bacteria developed larger skin abscesses and more severe lung inflammation and tissue damage than animals infected with bacteria engineered to lack *sasX*.

The SasX protein could be a target for new drugs to combat MRSA, the authors suggest.
Nature Med. http://dx.doi. org/10.1038/nm.2692 (2012)

NEUROSCIENCE

Making morphine work better

Two compounds boost morphine's painkilling effects when injected into mice.

Morphine and other opioids induce inflammation in the central nervous system, which can suppress pain relief and lead to opioid dependence. Hang Yin at the University of Colorado at Boulder and his team show that morphine causes inflammation by binding to the protein MD2, which, in turn, causes the protein to bind to an immune-system receptor called TLR4. In cultured cells, this process activates TLR4 signalling and the release of inflammatory molecules.

Injecting mice with two synthetic compounds known to block MD2 binding to TLR4 enhanced morphine-induced analgesia. Interfering with TLR4 signalling could be a promising strategy for improving painkilling therapies, the authors say.
Proc. Natl Acad. Sci. USA
http://dx.doi.org/10.1073/
pnas.1200130109 (2012)

MARINE MICROBIOLOGY

Microbe alliance with gutless worm

Microbes that help a gutless worm to eat and to process waste have developed unusual metabolic pathways to meet their own needs.

The worm *Olavius algarvensis* — found in marine sea-grass beds off the coast of the Italian island of Elba — harbours five species of bacteria in its body wall. Manuel Kleiner of the Max Planck Institute for Marine Microbiology in Bremen, Germany, and his colleagues identified and analysed 2,819 proteins and 97 metabolites produced by the worm or its associated bacteria. On the basis of their analyses, the authors propose that the bacteria generate energy for themselves using carbon

monoxide and hydrogen from the surrounding sediment, and produce proteins that allow them to recycle waste products from the worm.
Proc. Natl Acad. Sci. USA
http://dx.doi.org/10.1073/
pnas.1121198109 (2012)

GEOSCIENCE

Methane from the Arctic Ocean

The Arctic Ocean seems to be emitting substantial amounts of methane, an important human-influenced greenhouse gas.

Eric Kort, now at NASA's Jet Propulsion Laboratory in Pasadena, California, and his team measured atmospheric methane levels during five flights over the Arctic carried out in 2009 and 2010. They detected high methane levels near the ocean surface that were not accompanied by high carbon monoxide levels, indicating that the methane did not arise from combustion. The researchers estimate that the methane-emission rate is similar to that seen off the coast of Siberia and attributed to melting permafrost.

Because high methane levels were observed over open water near sea ice, the authors say that Arctic Ocean methane emissions may increase as more sea ice melts.
Nature Geosci. http://dx.doi.
org/10.1038/ngeo1452 (2012)

MICROBIOLOGY

How gut flora can turn deadly

Resident gut bacteria can cause disease if the balance of gut microflora is disrupted, for example, by antibiotics. Researchers at the University of California, Berkeley, show that a strain of gut *Escherichia coli* can cause sepsis in antibiotic-treated mice by triggering excessive inflammation.

Janelle Ayres and her colleagues gave mice a cocktail of antibiotics and a gut-injuring chemical. The animals soon showed hypothermia

and multiple organ damage — signs of sepsis. A strain of antibiotic-resistant *E. coli* isolated from these mice caused disease when injected into normal animals.

This *E. coli* strain seems to cause sepsis by activating protein complexes called inflammasomes, which can stimulate excessive inflammation in the presence of pathogens.
Nature Med. http://dx.doi.
org/10.1038/nm.2729 (2012)

STEM CELLS

Patient-specific heart cells

Using skin cells from a family with a cardiac disorder, researchers have generated

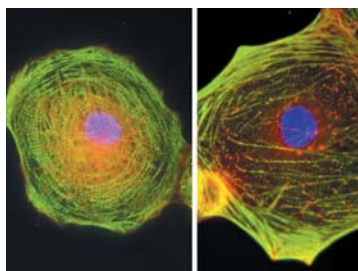heart cells that reveal some of the defects underlying the disease.

Joseph Wu and his colleagues at Stanford University in California took skin cells from family members with and without dilated cardiomyopathy, a common cause of heart failure, and reprogrammed them into stem cells. The authors then used cardiac growth factors to turn the stem cells into heart cells. Compared with cells derived from healthy individuals (**pictured left**), heart cells from patients with dilated cardiomyopathy (**right**) showed a decreased ability to contract and an abnormal distribution of a filament protein called α-actinin (shown in red), which has a key role in cell contraction.

Cells from the patients functioned better after being treated with a drug often given to cardiac patients.
Sci. Transl Med. 4, **130ra47** (2012)

ATMOSPHERIC SCIENCE

Arctic heat link to weather extremes

★ HIGHLY READ
on www.agu.org
17 Mar–16 Apr

The Arctic is warming faster than the rest of the Northern Hemisphere; this could be increasing the likelihood of extreme weather events in mid-latitude regions by altering the circulation of air currents in the upper atmosphere.

Jennifer Francis at Rutgers University in New Brunswick, New Jersey, and Stephen Vavrus at the University of Wisconsin-Madison studied changes in 'Rossby waves' — large north-south meanders in high-altitude winds. The authors detected a slowed eastward movement of Rossby waves in a fast-flowing air current called the jet stream, and identified two contributing factors: weaker west-to-east winds and increased wave amplitude. Both of these seem to be linked to earlier spring snow-melt on high-latitude land and to sea-ice loss in summer — two likely consequences of enhanced Arctic warming.

A slowing of jet-stream waves that influence weather leads to more persistent weather patterns in the mid-latitudes. This could raise the likelihood of drought, flooding, cold snaps and heatwaves.
Geophys. Res. Lett. http://dx.doi.org/10.1029/2012GL051000 (2012)

SCIENCE/AAAS

Space shuttle makes its final flight

Having completed 39 missions in 27 years — more than any other manned spacecraft — NASA's space shuttle *Discovery* had spectators looking up one last time as it flew over Washington DC on 17 April atop a modified Boeing 747 aeroplane. After landing, *Discovery* was transported to the National Air and Space Museum's Steven F. Udvar-Hazy Center in Chantilly, Virginia, part of the Smithsonian Institution. Other retired shuttles are also moving around: *Endeavour* to the California Science Center in Los Angeles and the flight test vehicle *Enterprise* to the Intrepid Sea, Air and Space Museum in New York City.

POLICY

Flu publishing

The US government has agreed that two studies that created ferret-transmissible versions of the H5N1 avian influenza virus should be published. It accepted the recommendation from its National Science Advisory Board for Biosecurity on 20 April. But the fate of one of the studies, by researchers in the Netherlands, remains in limbo, with its publication held up by export control laws. A 23 April meeting to review the controversy, organized by the Dutch government, made no breakthrough; its discussions were kept confidential as *Nature* went to press.

Fracking curbed

The US Environmental Protection Agency announced national standards for emissions from oil and gas drilling on 18 April. Oil and gas companies working in the United States now have until 2015 to introduce technology to capture excess methane and other volatile organic compounds. The long-awaited decision marks the Obama administration's first efforts to tighten regulation of hydraulic fracturing, or 'fracking', which involves pumping fluid into rocks to release natural gas and oil.

US export controls

Space-science researchers have welcomed an 18 April report recommending a relaxation of rules on US export controls. Many in industry and academia believe the rules have stunted satellite research and manufacturing in the country, partly by blocking research collaboration with non-US scientists. In 1998, authority over satellite technology that might have a second military use was shifted from the commerce department to the state department, and export rules were tightened. But the report from the defence and state departments recommends that the shift be reversed for some technologies, such as certain communications satellites. Congress would have to approve any legislative changes. See go.nature.com/c2ckea for more.

Ecosystems panel

Governments have launched a United Nations scientific panel that will independently assess research on the state of the planet's fragile ecosystems — in much the same way as the Intergovernmental Panel for Climate Change summarizes climate research. Representatives of more than 90 countries agreed to establish the Intergovernmental Platform on Biodiversity and Ecosystem Services (IPBES) at a meeting in Panama City last weekend. The panel's secretariat will be hosted in Bonn, Germany, and its budget and assessment themes will be decided in 2013. See go.nature.com/gcfdli for more.

Arctic fishing

More than 2,000 scientists from 67 countries have signed an open letter urging Arctic nations to prevent commercial fishing in waters exposed by melting sea ice. Industrial fishing has not yet begun there, but with more research needed into ecosystem impacts, the letter says that Arctic countries should put a moratorium on it anyway. The letter was released by the Pew Environment Group on 23 April to coincide with the International Polar Year 2012 scientific conference in Montreal. See go.nature.com/fw9cov for more.

Mexico climate law

Mexico passed one of the strongest national climate-change laws so far on 19 April, committing to reduce emissions of carbon dioxide by 30% below business-as-usual levels by 2020 and 50% below 2000 levels by 2050, as well as aspiring to produce 35% of the country's electricity from renewable sources by 2024. See page 430 for more.

PEOPLE

Royal Society intake

Cosmologist and Nobel laureate Brian Schmidt, of the Australian National University in Weston Creek, was one of 44 fellows (42 of them men)

AP

elected to London's Royal Society on 19 April. Others include Steve Jones, a geneticist and public communicator of science at University College London, and Michele Dougherty, a space physicist at Imperial College London and a principal investigator on the Cassini–Huygens mission round Saturn. The Royal Society has around 1,350 fellows.

EVENTS

India missile test

India's nuclear-capable Agni-V missile made a successful maiden flight on 19 April, hitting its designated target in the southern Indian Ocean 20 minutes after launch from Wheeler Island, off India's east coast. With a range of at least 5,000 kilometres, the 50-tonne, 17.5-metre-long missile brings major Chinese cities such as Shanghai and Beijing into India's strike envelope. The missile is not expected to be a part of the Indian army's arsenal for at least two years, after more tests have been done.

Mexican volcano

The volcano Popocatépetl, 60 kilometres from Mexico City, was throwing out ash and chunks of rock last week (**pictured**), putting local officials on the alert for a possible evacuation of nearby

towns. The volcano, which is one of Mexico's most active and is well monitored, could close Mexico City's airport if winds blow ash in that direction. As *Nature* went to press, locals were being asked to stay at least 12 kilometres away. See go.nature.com/czvd3r for more.

BUSINESS

Vioxx endgame

The long-running legal fallout from the marketing of the infamous painkiller Vioxx (rofecoxib) has finally concluded, after a US judge accepted manufacturer Merck's plea of guilty to promoting the drug as an arthritis treatment before it was officially approved. The court settlement on 19 April came with a previously announced US$950-million fine. Merck, which is based in Whitehouse Station, New Jersey, agreed in 2007 to pay $4.85 billion to settle nearly 27,000 other lawsuits that claimed the medicine had caused heart

attacks and strokes. But industry watchdogs say that the legal punishments are unlikely to prevent similar problems from arising with other drugs. See go.nature.com/vcetix for more.

Takeover dropped

Drug giant Roche, based in Basel, Switzerland, has withdrawn its hostile takeover bid for DNA-sequencing company Illumina. The move came after shareholders at Illumina, of San Diego, California, rebuffed Roche's efforts at Illumina's 18 April annual meeting to install board members who favoured the merger. Roche offered US$5.7 billion ($44.50 per share) in January, then raised its offer to $6.7 billion in March before announcing last week that the offer would expire on 20 April. See go.nature.com/d3e7po for more.

Mining asteroids

A venture that aims to mine asteroids made a media splash on 24 April, announcing support from Google's chief executive Larry Page, film-maker James Cameron and other wealthy backers. Mining venture Planetary Resources, in Seattle, Washington, says that it will launch a surveyor into low Earth orbit in two years to identify asteroids rich in metal and water, with the aim of opening up deep-space

prospecting to private firms. See go.nature.com/pmuq8p for more.

Offer rebuffed

Human Genome Sciences (HGS) has rejected a US$2.6-billion takeover bid from its research partner GlaxoSmithKline (GSK), saying that the offer undervalues the company. HGS, a biotechnology firm based in Rockville, Maryland, is best known for the lupus medication Benlysta (belimumab), but it is also working with GSK on phase III trials for the cardiovascular drug darapladib and the type 2 diabetes treatment albiglutide.

Biotech buy

Pharmaceutical giant AstraZeneca of London will spend around US$1.26 billion to buy Ardea Biosciences, it announced on 23 April. Ardea is a biotechnology company based in San Diego, California; its main asset is lesinurad, a potential treatment for gout that is in phase III clinical trials. The deal (worth $1 billion once cash held by Ardea is taken into account) is AstraZeneca's largest acquisition since it bought MedImmune, of Gaithersburg, Maryland, for $15.6 billion in 2007.
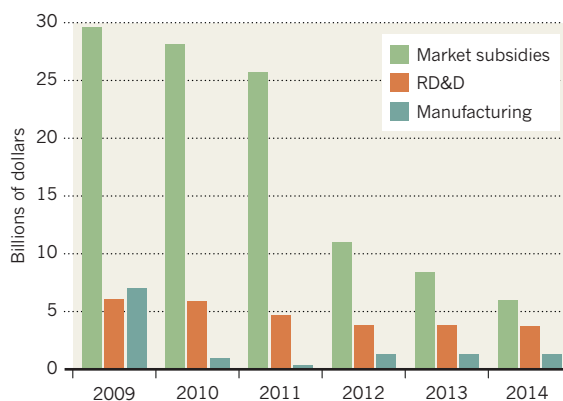
↻ **NATURE.COM**
For daily news updates see:
www.nature.com/news

SOURCE: WRI/BREAKTHROUGH INST./BROOKINGS INST.

TREND WATCH

By 2014, US government investment in clean-energy technologies could be about 75% less than in 2009, owing to the end of stimulus spending and the lapse of subsidies, says a report by bodies including the Brookings Institution in Washington DC. Funding for energy research, development and demonstration (RD&D) has already dropped by 38%. The report argues that subsidies should be reformed to reward innovation, and calls for RD&D funding to be tripled. See go.nature.com/ypnww3 for more.

HARD TIMES AHEAD FOR CLEAN TECH
Government spending on clean-energy technologies is set to decline dramatically in the United States.

Legend: Market subsidies, RD&D, Manufacturing. Y-axis: Billions of dollars, 0–30. X-axis years: 2009, 2010, 2011, 2012, 2013, 2014.

ESA
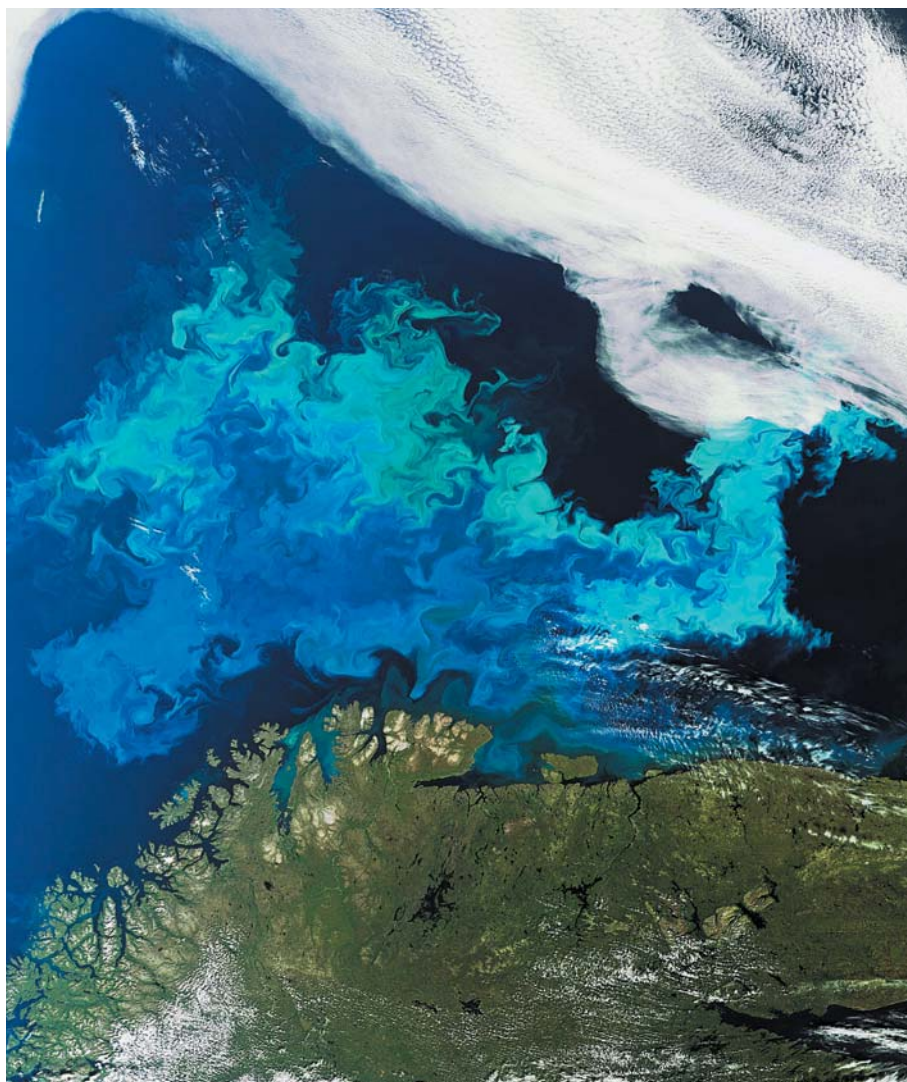
Envisat's MERIS instrument could monitor toxic algal blooms, such as these swirling in the Barents Sea.

ENVIRONMENTAL MONITORING

Europe loses sight of Earth

Envisat crisis rekindles row over funding for its successors.

BY GEOFF BRUMFIEL

With hopes fading fast for the crippled Earth-observing satellite Envisat, researchers are warning that delays to its replacements will leave Europe lacking vital monitoring data for years to come.

Launched in 2002, Envisat is the largest environmental satellite ever built and the mainstay of the Earth-observing programme for the European Space Agency (ESA). The 8.2-tonne satellite has 10 instruments with which to take the planet's pulse, including radars, infrared and optical imagers, and spectrometers.

Controllers at ESA unexpectedly lost contact with the €2.3-billion (US$3-billion) behemoth on 8 April. Failure of either the satellite's main computer or its power system is thought to be to blame, according to Manfred Warhaut, head of ESA's mission operations department in Darmstadt, Germany. "It's not looking promising," he says.

Envisat's data have been used in more than 2,000 scientific publications, according to ESA, and the satellite also supports a plethora of political, commercial and humanitarian efforts. Its altimeter is crucial for ocean-wave forecasts used by the shipping industry, for example, says Erland Källén, director for research at the European Centre for Medium-Range Weather Forecasts in Reading, UK. And the satellite's ozone measurements have been vital in showing the success of the Montreal Protocol in controlling ozone-damaging pollution, says John Burrows, a physicist at the University of Bremen in Germany, and principal investigator on Envisat's SCIAMACHY instrument, which tracks atmospheric pollution. "It's an absolute disaster for all sorts of reasons," Burrows says.

SCIAMACHY also had a limited ability to measure carbon dioxide in the atmosphere, which became crucial after the 2009 launch failure of NASA's Orbiting Carbon Observatory. Envisat's silence leaves only one satellite capable of measuring CO_2 throughout Earth's atmosphere: Japan's Greenhouse Gases Observing Satellite.

The loss of Envisat has also stoked a row about funding for its successors. ESA plans to launch five Sentinel satellites during the coming decade to both improve on and replace Envisat's capabilities, with the first three scheduled to launch over the next two years. Although Envisat had already exceeded its anticipated five-year operational lifetime, researchers had hoped that it would last ▶

long enough to overlap with at least some of the Sentinels, allowing for cross-calibrations of instruments and continuous data-taking. "Continuity for a climate record is extremely important," says Fred Prata, a climate scientist at the Norwegian Institute for Air Research in Kjeller. Given Envisat's troubles, he says, "Europe should really be fast-tracking ESA's Sentinel programme".

But the European Commission does not want to allocate €5.8 billion of its 2014–20 budget to the programme that would operate the satellites, the Global Monitoring for Environment and Security (GMES). Instead, the commission says, member states should make additional contributions to finance the programme — something that is unlikely to happen in the current fiscal climate (see *Nature* **480,** 19–20; 2011). ESA, meanwhile, says that it will not launch the first Sentinel without being certain that its operating costs will be covered.

Volker Liebig, director of ESA's Earth-observing programme, accuses the commission of using GMES as a bargaining chip in broader budget negotiations. "They are taking this as a tactical hostage to get more

money from the member states," he says. Carlo Corazza, a spokesman for the commission, denies this, insisting that his organization is only trying to ensure that the GMES programme receives adequate funding.

With the negotiations dragging on, Liebig says that he is running out of time to make arrangements with the French spaceflight company Ariannespace in Evry-Courcouronnes, which will provide the rocket to launch Sentinel 1. That deal must be in place by June if the satellite is to fly by mid-2013. Corazza says that discussions are continuing fast enough to keep Sentinel on track.

Not everyone believes that the situation poses a significant problem for Earth observation. Other satellites, such as NASA's Aqua and Terra missions, can replace Envisat's capabilities, says Ranga Myneni, an environmental scientist at Boston University in Massachusetts. Indeed, satellites launched by NASA freely provide their data in formats preferred by many scientists, and are thus more widely used than Envisat.

But Envisat had some functions that cannot be replaced. In addition to its ability to measure CO_2, the satellite's Advanced Along

Track Scanning Radiometer was, Prata says, the world's best instrument for measuring sea surface temperatures. It was also part of a €2-million project to improve the forecasting of volcanic ash clouds, such as the one that belched from Eyjafjallajökull in Iceland and disrupted transatlantic air traffic in 2010. The failure — together with the gap in observations — means that the project will have to look to NASA instruments instead.

Michel Verstraete, a climate scientist at the European Commission's Joint Research Centre in Ispra, Italy, points out that Envisat's synthetic aperture radar was particularly good at spotting standing water, even under heavy cloud cover. "If tomorrow there is a flood, people will ask, 'Where are the data?'" he says. Europe needs its own robust capabilities to monitor weather and crops, Prata adds. "If you have control of your own satellites, you don't have to ask your friends or your enemies," he says.

With a financial impasse on one side and a moribund satellite on the other, researchers are left with few options, Burrows says. "We're praying that Envisat might come back. I'm going to church again." ∎

A bloody boon for conservation

Leeches provide traces of DNA from other species.

BY EWEN CALLAWAY

Bloodsucking leeches are offering the best hope of finding one of the world's rarest animals. The saola (*Pseudoryx nghetinhensis*) was first described from skulls found in a Vietnamese forest reserve[1], but the elusive antelope has rarely been seen alive. Little is known about its range or population, which probably numbers in the low hundreds.

Conservationists are now planning to trawl tropical leeches for saola DNA. Prompted by research published this week[2] showing that the bloodsuckers can store DNA from their meals for several months, the saola search is at the vanguard of an approach to gauging biodiversity that could prove much more efficient than conventional methods. Rather than setting out camera traps, the idea is to collect and sequence DNA left in the environment, in everything from soil to leeches' stomachs.

"I am almost sure that in ten years all the research on biodiversity will be done with

DNA, because it will be so easy to get this type of information and the cost is not very high," says Pierre Taberlet, a geneticist at Joseph Fourier University in Grenoble, France, and co-editor of the April issue of *Molecular Ecology*, which is devoted to the emerging field of

Bloodsuckers feast on the forest's rare delicacies.

studying environmental DNA.

The saola is so elusive that it has been dubbed the Asian unicorn. It hadn't been spotted for a decade until 2010, when villagers in the Laotian province of Bolikhamxay caught one alive, only for the animal to die after a few days in captivity.

In 2011, Vietnam established a small saola reserve in the animal's only known habitat, the Annamite mountains that straddle the country's border with Laos. A more precise estimate of the antelope's range would help to target conservation efforts, says Nicholas Wilkinson, a Vietnam-based wildlife ecologist at the University of Cambridge, UK, who is working with the conservation group WWF. Their team failed to find the saola using camera traps and considered bringing in trained dogs to help the hunt, at an estimated cost of US$400,000. "I, to a large extent, had given up on finding a survey method that would be useful in time to save the species," Wilkinson says.

But last year, he received an e-mail from geneticist Thomas Gilbert at the University of Copenhagen, describing his experiments with leeches. Gilbert, his colleague Mads Bertelsen and their team had fed goat blood to medicinal leeches (*Hirudo* spp.) — something that is "a lot harder than it sounds", says Gilbert. The team resorted to tempting the creatures with blood-filled condoms warmed under a heat-lamp, and putting the leeches into syringes attached to blood-filled test tubes sealed by a thin film. After killing the leeches over the course of several months, the team identified goat DNA in every one of them.

▶ long enough to overlap with at least some of the Sentinels, allowing for cross-calibrations of instruments and continuous data-taking. "Continuity for a climate record is extremely important," says Fred Prata, a climate scientist at the Norwegian Institute for Air Research in Kjeller. Given Envisat's troubles, he says, "Europe should really be fast-tracking ESA's Sentinel programme".

But the European Commission does not want to allocate €5.8 billion of its 2014–20 budget to the programme that would operate the satellites, the Global Monitoring for Environment and Security (GMES). Instead, the commission says, member states should make additional contributions to finance the programme — something that is unlikely to happen in the current fiscal climate (see *Nature* **480**, 19–20; 2011). ESA, meanwhile, says that it will not launch the first Sentinel without being certain that its operating costs will be covered.

Volker Liebig, director of ESA's Earth-observing programme, accuses the commission of using GMES as a bargaining chip in broader budget negotiations. "They are taking this as a tactical hostage to get more

money from the member states," he says. Carlo Corazza, a spokesman for the commission, denies this, insisting that his organization is only trying to ensure that the GMES programme receives adequate funding.

With the negotiations dragging on, Liebig says that he is running out of time to make arrangements with the French spaceflight company Ariannespace in Evry-Courcouronnes, which will provide the rocket to launch Sentinel 1. That deal must be in place by June if the satellite is to fly by mid-2013. Corazza says that discussions are continuing fast enough to keep Sentinel on track.

Not everyone believes that the situation poses a significant problem for Earth observation. Other satellites, such as NASA's Aqua and Terra missions, can replace Envisat's capabilities, says Ranga Myneni, an environmental scientist at Boston University in Massachusetts. Indeed, satellites launched by NASA freely provide their data in formats preferred by many scientists, and are thus more widely used than Envisat.

But Envisat had some functions that cannot be replaced. In addition to its ability to measure CO_2, the satellite's Advanced Along

Track Scanning Radiometer was, Prata says, the world's best instrument for measuring sea surface temperatures. It was also part of a €2-million project to improve the forecasting of volcanic ash clouds, such as the one that belched from Eyjafjallajökull in Iceland and disrupted transatlantic air traffic in 2010. The failure — together with the gap in observations — means that the project will have to look to NASA instruments instead.

Michel Verstraete, a climate scientist at the European Commission's Joint Research Centre in Ispra, Italy, points out that Envisat's synthetic aperture radar was particularly good at spotting standing water, even under heavy cloud cover. "If tomorrow there is a flood, people will ask, 'Where are the data?'" he says. Europe needs its own robust capabilities to monitor weather and crops, Prata adds. "If you have control of your own satellites, you don't have to ask your friends or your enemies," he says.

With a financial impasse on one side and a moribund satellite on the other, researchers are left with few options, Burrows says. "We're praying that Envisat might come back. I'm going to church again." ∎

A bloody boon for conservation

Leeches provide traces of DNA from other species.

BY EWEN CALLAWAY

Bloodsucking leeches are offering the best hope of finding one of the world's rarest animals. The saola (*Pseudoryx nghetinhensis*) was first described from skulls found in a Vietnamese forest reserve[1], but the elusive antelope has rarely been seen alive. Little is known about its range or population, which probably numbers in the low hundreds.

Conservationists are now planning to trawl tropical leeches for saola DNA. Prompted by research published this week[2] showing that the bloodsuckers can store DNA from their meals for several months, the saola search is at the vanguard of an approach to gauging biodiversity that could prove much more efficient than conventional methods. Rather than setting out camera traps, the idea is to collect and sequence DNA left in the environment, in everything from soil to leeches' stomachs.

"I am almost sure that in ten years all the research on biodiversity will be done with

DNA, because it will be so easy to get this type of information and the cost is not very high," says Pierre Taberlet, a geneticist at Joseph Fourier University in Grenoble, France, and co-editor of the April issue of *Molecular Ecology*, which is devoted to the emerging field of

Bloodsuckers feast on the forest's rare delicacies.

studying environmental DNA.

The saola is so elusive that it has been dubbed the Asian unicorn. It hadn't been spotted for a decade until 2010, when villagers in the Laotian province of Bolikhamxay caught one alive, only for the animal to die after a few days in captivity.

In 2011, Vietnam established a small saola reserve in the animal's only known habitat, the Annamite mountains that straddle the country's border with Laos. A more precise estimate of the antelope's range would help to target conservation efforts, says Nicholas Wilkinson, a Vietnam-based wildlife ecologist at the University of Cambridge, UK, who is working with the conservation group WWF. Their team failed to find the saola using camera traps and considered bringing in trained dogs to help the hunt, at an estimated cost of US$400,000. "I, to a large extent, had given up on finding a survey method that would be useful in time to save the species," Wilkinson says.

But last year, he received an e-mail from geneticist Thomas Gilbert at the University of Copenhagen, describing his experiments with leeches. Gilbert, his colleague Mads Bertelsen and their team had fed goat blood to medicinal leeches (*Hirudo* spp.) — something that is "a lot harder than it sounds", says Gilbert. The team resorted to tempting the creatures with blood-filled condoms warmed under a heatlamp, and putting the leeches into syringes attached to blood-filled test tubes sealed by a thin film. After killing the leeches over the course of several months, the team identified goat DNA in every one of them.

W. KOLVOORT/NATUREPL.COM

Scientists hope to find DNA from the rare saola in leeches from the antelope's expected range.

To see whether the technique could find mammal DNA in the wild, Gilbert asked Wilkinson to ship him some tropical leeches (*Haemadipsa* spp.). Wilkinson collected them on the Vietnamese side of the Annamite Range and sent them to Copenhagen. Gilbert's team did not find any saola DNA, but 21 of the 25 leeches they tested contained DNA from other mammals, including the Truong Son muntjac deer (*Muntiacus truongsonensis*) and the Annamite striped rabbit (*Nesolagus timinsi*), which was discovered only a decade ago. The International Union for Conservation of Nature (IUCN) lists both species as 'data deficient' because scientists know so little about their populations or habitat.

"It is a very easy way to get a snapshot of what animals are in the area," says Gilbert. Leeches are impossible to avoid in tropical forests, and they can be collected by the dozen by simply peeling them off intrepid researchers' clothes. The plummeting cost of DNA sequencing makes leech surveys cheap, and DNA from hundreds of the animals could be combined and analysed in a single experiment.

The method is unlikely to provide information about an animal's population, but leeches should help to pin down its range. The Vietnam field trial suggests that leeches preserve DNA from only their most recent blood meal, so an animal's range is likely to include the location where the leech was found.

Surveying leech blood is just one of many ways to collect environmental DNA that have emerged in recent years. In the *Molecular Ecology* special issue, various research teams worked out the diet of a leopard by sequencing DNA in its faeces[3]; tracked earthworm communities in soil[4]; and reconstructed ancient Siberian habitats from DNA preserved in permafrost[5]. Meanwhile, Australian scientists have found DNA from critically endangered species and potentially toxic plants in traditional Chinese medicines[6].

Most of these studies are one-offs that show the potential of the techniques but not how to apply them to routine biodiversity surveys, points out Mehrdad Hajibabaei, an evolutionary molecular geneticist at the University of Guelph in Ontario, Canada. Even so, he says, assessments of environmental DNA have matched up well against more conventional surveys.

His team found that DNA surveys of water samples from a Canadian river identified the same invertebrate species as visual surveys[7]. And studies of plant DNA in soil from French Alpine meadows and a tropical rainforest in French Guiana agreed well with ground-based vegetation studies[8].

Researchers refer to environmental DNA studies as 'meta-bar-coding', because they rely on DNA bar codes: short DNA sequences that uniquely identify a species. Bar-coding makes it possible to distinguish between two species of butterfly, for example, by sequencing just a portion of a gene. But much of the DNA recovered from environmental sources such as soil or faeces has been shredded into short strands, and existing bar-coding databases tend to contain the longer stretches that were identified with old DNA sequencing technologies. Many of today's next-generation sequencers can read stretches of DNA that are shorter than the length of a bar code. "It's a shame that we cannot use all that has been developed," says Taberlet.

Hajibabaei, an adviser to the International the Barcode of Life project, which collates bar codes in to a publicly accessible library, responds that shorter, 'mini' bar codes, as well as advances in DNA sequencing technology, will address this problem.

In Vientiane last month, leeches were the talk of the IUCN's Saola Working Group meeting. Wilkinson says that the group hopes to offer rewards to villagers who bring in leeches with saola DNA, and to conduct targeted surveys led by scientists and park rangers. Wilkinson and his colleagues at the WWF plan to gather leeches from the Vietnamese side of the Annamites, and the Wildlife Conservation Society in New York intends to include leeches in its upcoming surveys of Laos.

"Everyone is, unsurprisingly, very excited about the potential," Wilkinson says. "We haven't detected a saola yet, but it's a very promising method for finding it and pretty much any other mammal in the forest." ■ **SEE EDITORIAL P.416**

1. Van Dung, V. *et al. Nature* **363,** 443–445 (1993).
2. Schnell, I. B. *et al. Curr. Biol.* **22,** R262–R263 (2012).
3. Shehzad, W. *et al. Mol. Ecol.* **21,** 1951–1965 (2012).
4. Bienert, F. *et al. Mol. Ecol.* **21,** 2017–2030 (2012).
5. Jørgensen, T. *et al. Mol. Ecol.* **21,** 1989–2003 (2012).
6. Coghlan, M. L. *et al. PLoS Genet.* **8,** e1002657 (2012).
7. Hajibabaei, M., Shokralla, S., Zhou, X., Singer, G. A. S. & Baird, D. J. *PLoS ONE* **6,** e17497 (2011).
8. Yoccoz, N. G. *et al. Mol. Ecol.* advance online publication http://dx.doi.org/10.1111/j.1365-294X.2012.05545.x (2012).

MORE ONLINE

TOP STORY

Satellite system will speed up tsunami warnings go.nature.com/kgganp

MORE NEWS

● Artificial DNA can replicate and 'evolve' go.nature.com/ffevkj
● Virulence-enhancing MRSA gene could be superbug's secret weapon go.nature.com/leqr9c
● Survey finds no hint of dark matter near Solar System go.nature.com/dj4sgd

Q&A

Next-generation DNA sequencers compared go.nature.com/5ra5c7

Samples from experiments performed on the International Space Station may soon have a return route to Earth aboard the Dragon capsule developed by SpaceX.

Space-station rendezvous set to spur research push

Upcoming docking of commercial supply craft heralds easier access to orbiting laboratory.

BY ERIC HAND

When it comes to doing science on the International Space Station (ISS), the laws of gravity have been flipped: what goes up mostly stays up. A case in point are two freezers packed with more than 2,000 *Arabidopsis* seedlings awaiting return to Earth, where they can be analysed for changes in gene expression.

The samples cannot fly home aboard the unmanned European, Japanese and Russian cargo capsules that regularly deliver equipment and experiments to the station, because these capsules burn up on re-entry. Even the Russian Soyuz capsules that are the only route back to

Earth since the space shuttle was retired last year are not ideal, because they lack freezers to store the seedlings during the plunge home, says the experiment's lead investigator Imara Perera, a plant biologist at North Carolina State University in Raleigh. "If they thaw out, then the RNA will be degraded."

Now science is about to get a new way home from the ISS. It marks a first step in what NASA hopes will be the space station's transformation from an orbiting construction site into a thriving research laboratory (see 'Making space for science').

Next month, SpaceX of Hawthorne, California, is scheduled to launch Dragon, a pressurized capsule that can make a round trip

to the station. Lofted by the company's Falcon 9 rocket, it should dock with the space station four days later. As a demonstration mission, it will carry low-priority cargo. But if all goes well, several aluminium-alloy rods, melted and solidified under microgravity in a special furnace, will be returned to Earth, where researchers will study their recrystallization patterns.

Eventually, NASA will pay for four resupply missions a year — which could come from both SpaceX and Orbital Sciences, based in Dulles, Virginia, which is planning to test its Antares rocket and Cygnus capsule later this year (see 'Planned missions').

NASA is betting that scientific interest will match the increased tempo of the upcoming

MAKING SPACE FOR SCIENCE

The viability of the International Space Station (ISS) as a research platform depends on transport to and from it and on having a full (six-person) crew available.

NOVEMBER 1998 First ISS module deployed

NOVEMBER 2000 First station crew dock

FEBRUARY 2003 Loss of *Columbia* grounds shuttle fleet for more than 2 years

MARCH 2008 European Space Agency launches its first resupply vehicle

MAY 2009 First six-person crew arrives at ISS

SEPTEMBER 2009 Japanese space agency JAXA launches its first resupply vehicle

MARCH 2011 ISS completed

JULY 2011 Space-shuttle fleet retired

launches. Last year, NASA picked the non-profit Center for the Advancement of Science in Space (CASIS), based at Cape Canaveral in Florida, to manage half of the US research area on the station, which the US Congress deemed a national laboratory in 2005. CASIS will get US$15 million in annual funding from NASA, and 50% of the cargo space on rides to and from the station, including Dragon. By holding researchers' hands and helping them through the thicket of NASA rules and regulations, the centre aims to reduce bureaucratic hassle. "What sometimes took years, we want to be able to do in months," says CASIS's interim director, Jim Royston.

For months, CASIS staff have been attending scientific conferences and visiting pharmaceutical labs, trying to drum up interest among researchers outside NASA. They have also begun to put together a panel of external scientists to review and prioritize experiments. Solicitations for research, planned for June, will offer $3 million of CASIS's own seed money to researchers, although the centre hopes that the attraction of free flights and free space on the station, along with the free labour of station crew members, will be so enticing that proposers will bring their own grant money to the table. That money could come from other US science agencies, such as the National Institutes of Health in Bethesda, Maryland, or from private sources.

The panel will judge proposals not only on their scientific merit, but also on their potential for commercialization. The emphasis on applied research is motivated in part by the limited lifetime of the space station, which is currently scheduled to operate until 2020, says Timothy Yeatman, who on 5 April was named interim chief scientist for CASIS and head of the review panel. "We know that funding for the ISS can't go on in perpetuity," says Yeatman, a surgical oncologist at the Moffitt Cancer Center in Tampa, Florida.

CASIS also has the challenge of wooing back researchers — particularly those in biomedicine, physics and materials science — who were involved in experiments on the ISS but were sidelined in the mid-2000s when the station's

> *"What sometimes took years, we want to be able to do in months."*

crew was reduced following the loss of the space shuttle *Columbia*. Moreover, ISS-based research shifted towards medical research related to a manned Moon mission — a plan that has since been dropped. "You really have to coax people back now," says Jeffrey Manber, managing director of NanoRacks in Houston, Texas, which built small cubic experimental modules, installed them on the space station and now rents the modules to researchers.

Some of CASIS's first solicitations will be for research in materials science and remote Earth observations. Yeatman says that biomedical research is also ripe for renewal, especially in areas such as osteoporosis and protein crystallography. The osteoporosis-like disorders that develop in mice after just a few months in space may be a more natural model on which to test drugs than mice that acquire osteoporosis through gene experiments, he says. Previous ISS research also suggested that proteins form higher-quality crystals in space than on Earth, Yeatman adds. That may help biologists to deduce currently unknown protein structures — if they can get the specialized crystals back from space to an X-ray light source before they degrade.

Paul Reichert, a structural chemist at Merck Research Laboratories in Kenilworth, New Jersey, is keen to see success. He is a veteran of experiments on six space-shuttle missions, and tried to crystallize one particular kinase, a signalling protein, aboard the ISS. He obtained some crystals, but by the time he brought the samples back three months later, they were so degraded that it was impossible to get a clean X-ray diffraction signal. "I only had one shot," he says. He is eager for another chance to do research in space. "It gets in your blood."

Perera is similarly eager to see her experiment through — but has been waiting since July last year, when her *Arabidopsis* seedlings were taken up on the last shuttle mission. Her plants are currently on the return manifest for the first official Dragon resupply mission, which could launch later this year. "There's some kind of history here," she says. "You go up on the last shuttle and come back on the first SpaceX. It's very exciting, but it's kind of nerve-racking." ∎

> ↻ **NATURE.COM**
> Read about science and commercial space flight at:
> go.nature.com/dqp9qd

PLANNED MISSIONS

SPACEX

Artist's impression of the Dragon capsule.

MAY 2012 First docking of SpaceX's Dragon capsule

AUGUST 2012 First Dragon resupply mission

2012 (4TH QUARTER) Test flight of Orbital Science's Cygnus capsule

2013 First Cygnus resupply mission

GENETICS

RNA studies under fire

High-profile results challenged over statistical analysis of sequence data.

BY ERIKA CHECK HAYDEN

High-throughput RNA sequencing has yielded some unexpected results in the past few years — including some that seem to rewrite conventional wisdom in genetics. But a few of those findings are now being challenged, as computational biologists warn of the statistical pitfalls that can lurk in data-intensive studies.

The latest case centres on imprinted genes. Humans and most other animals inherit two copies of most genes, one from each parent. But in some cases, only one copy is expressed; the other copy is silenced. In such cases, the gene is described as being imprinted. In July 2010, a team led by Catherine Dulac and Christopher Gregg, both then at Harvard University in Cambridge, Massachusetts, published a study[1] in *Science* estimating that 1,300 mouse genes — an order of magnitude more than previously known — were imprinted.

Now, researchers are arguing that a flawed analysis led Dulac and Gregg to vastly overestimate imprinting in their paper. "The reason this paper was published in *Science* is that they made this big claim that they saw an order-of-magnitude more genes that are imprinted, and I don't think that's true," says Tomas Babak, a computational biologist at Stanford University in California, who challenged the study in a paper[2] published on 29 March.
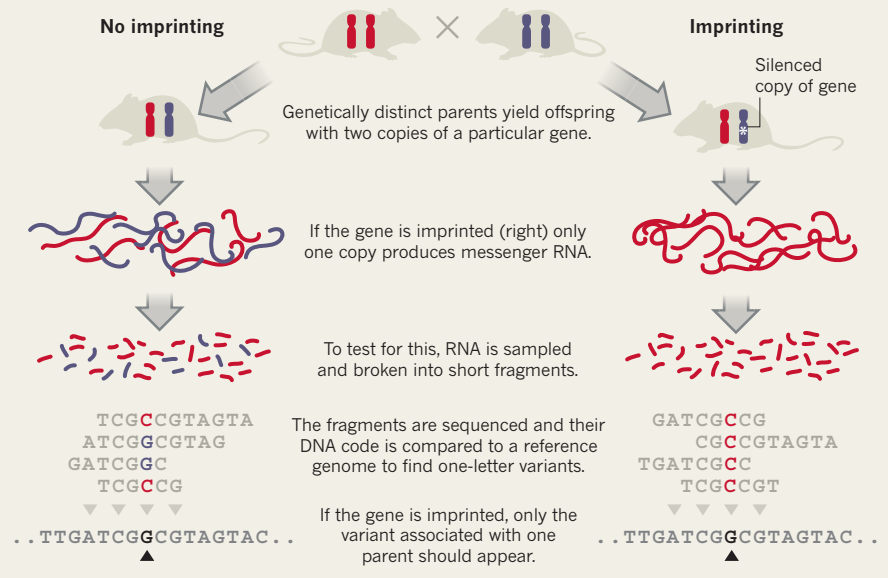
Dulac counters that she and her team "absolutely stand by those data", adding that they have confirmed some of their findings by other means. The situation resembles an ongoing debate over another RNA-sequencing paper[3] published in 2011. In that study, Vivian Cheung of the University of Pennsylvania in Philadelphia and her colleagues reported evidence that RNA editing — which creates differences between a gene's DNA sequence and the RNA sequence it gives rise to — is "widespread" in the human genome. RNA editing had been seen before, but the finding that it was so frequent challenges the central dogma, which holds that an organism's genes are transcribed faithfully.

Other scientists have argued that Cheung's results arose largely from errors in data analysis and that the true extent of RNA editing is probably no greater than previously thought[4]. Cheung did not respond to *Nature*'s request for comment on this story, but she has stood by her results.

For their study, Dulac and Gregg used high-throughput RNA sequencing to search mouse RNA for single nucleotide polymorphisms (SNPs) — one-letter variations in genetic sequence. The researchers then asked whether the SNPs they found for each gene could be traced to one or to both parents. If the SNPs were encoded mainly by one parent's copy of the gene, the team concluded that the gene was imprinted (see 'The silence of the genes').

But Babak says that the statistical methods Dulac and Gregg used were not rigorous enough to rule out false positives. His team used multiple methods to estimate the false discovery rate — for instance, by applying stricter criteria for what could be considered instances of imprinting and by estimating how many spurious examples of imprinting would appear by chance if mice from identical genetic backgrounds were bred together. Babak's team then applied its false discovery rate to Dulac and Gregg's data and concluded that most of the instances of imprinting identified in the original paper were probably false positives. Dulac counters that Babak's analysis may be filtering out legitimate but complex instances of imprinting.

"What's happened in the first few papers on these problems is that the statistics and analysis in general have not been done very carefully," says Lior Pachter, a computational biologist at the University of California, Berkeley. "And that means you may get completely wrong answers." Researchers have had many years to develop standard methods to minimize errors and biases in DNA sequencing, but such methods are still being developed for high-throughput RNA sequencing.

Pachter says that another key problem is that high-profile papers in the field may be well reviewed for their biology but not their computational foundations. "The culture is not the same in biology as it is in statistics or math, where reviewers sit with a paper for months, check the statistics and the math, and run the programs and test them," he says.

The debate has implications for any sequencing-based study that requires statisticians to identify rare genetic phenomena using relatively new methods. "If you don't deal with the analytical details very carefully, you're going to get into trouble because of the low signal-to-noise ratio" in these types of experiments, says Jin Billy Li, a genomicist at Stanford University who was one of the critics of Cheung's RNA-editing paper.

Dulac says that she and her colleagues are now using different statistical methods to reanalyse the imprinting data, but adds, "I am quite confident that we will find things that are likely to be around the same order of magnitude" as originally reported. ■

1. Gregg, C. *et al. Science* **329,** 643–648 (2010).
2. DeVeale, B., van der Kooy, D. & Babak, T. *PLoS Genet.* **8,** e1002600 (2012).
3. Li, M. *et al. Science* **33,** 53–58 (2011).
4. Check Hayden, E. *Nature* http://10.1038/nature.2012.10217 (2012).

THE SILENCE OF THE GENES
Questions have been raised over the interpretation of data from an experiment that used high-throughput RNA sequencing to identify imprinted genes (copies of genes that are silenced).

No imprinting

Imprinting

Silenced copy of gene

Genetically distinct parents yield offspring with two copies of a particular gene.

If the gene is imprinted (right) only one copy produces messenger RNA.

To test for this, RNA is sampled and broken into short fragments.

The fragments are sequenced and their DNA code is compared to a reference genome to find one-letter variants.

If the gene is imprinted, only the variant associated with one parent should appear.

TCGCCGTAGTA
ATCGGCGTAG
GATCGGC
TCGCCG

..TTGATCGGCGTAGTAC..

GATCGCCG
CGCCGTAGTA
TGATCGCC
TCGCCGT

..TTGATCGGCGTAGTAC..

Earth has been struck by as many as 100 impactors as big as those that formed the Moon's giant basins.

PLANETARY SCIENCE

Ancient asteroids kept on coming

Two-billion-year barrage hit Earth when life was beginning.

BY HELEN THOMPSON

The evidence is in the hollow-eyed face of the man in the Moon: a wave of asteroids showered Earth and the Moon in the distant past. They scarred the lunar surface with vast, circular impact basins and wreaked even greater havoc on this planet, which presented a bigger target. Now, a pair of studies published in *Nature*[1,2] suggests that the battering lasted much longer than was thought, spanning nearly the entire first half of Earth's history. The results imply that a prolonged succession of impacts — some of them large enough to vaporize oceans — could have shaped the early evolution of life.

Computer simulations of movements in the early Solar System had suggested that the Late Heavy Bombardment (LHB) that came after the initial accretion of the planets lasted from 4.1 billion to 3.8 billion years ago — a time frame that matches the dates of the lunar basins derived from Moon rocks. The 2005 'Nice model'[3] showed how, after Uranus and Neptune formed, a shift in the orbits of the outer planets could have destabilized the asteroids in their orbits, putting many on a collision course with the Earth–Moon system. But the model also suggested that the unstable asteroids were quickly depleted, causing the LHB to peter out around the time that the last giant circular impact basin on the Moon was created.

Yet the continuing record of large lunar craters being created after the 3.8-billion-year

cut-off, and hints of ancient impacts on Earth, suggested that the story was incomplete. "There had to be something missing," says William Bottke, a planetary dynamicist at the Southwest Research Institute in Boulder, Colorado.

That something, Bottke and his colleagues[1] now hypothesize, was an extension to the asteroid belt. Currently, asteroids orbit between Mars and Jupiter, with the main belt starting 2.1 astronomical units (AU) from the Sun (1 AU is the distance from the Sun to Earth). Bottke and his colleagues suggest that during the LHB, the inner boundary of the asteroid belt lay just 1.7 AU from the Sun. In computer simulations, the researchers discovered that asteroids dislodged from this extension would

have been ten times more likely to have ended up on Earth-crossing orbits than their main-belt counterparts. That would have prolonged the LHB on Earth to around 2 billion years ago (see 'The long tail of bombardment').

On Earth, weathering and geological activity have erased any obvious signs of the LHB, but a second study published this week[2] examined traces of it in the rock record. When an impact splashes molten rock debris into the atmosphere, tiny droplets solidify to form distinctive 'impact spherules'. Impacts as large as the one that may have caused the extinction of the dinosaurs 65 million years ago can scatter spherules around the globe. By looking for similar spherules in layers of rock that formed 2 billion to 3.5 billion years ago, Brandon Johnson and Jay Melosh, geophysicists at Purdue University in West Lafayette, Indiana, found evidence for an extended LHB. They were also able to relate the thickness of each layer and the size of the spherules to the diameter and incoming velocity of the impactor that produced them.

"Our work shows that a lot more big asteroids — meaning dinosaur-killer or larger — were hitting Earth well after the current idea of when it ended," says Johnson.
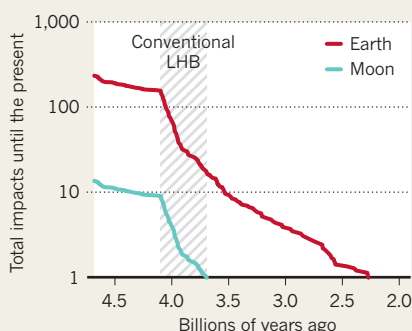
The time frame matches Bottke's model and corresponds to the Archaean aeon. This was a key period in early evolution, which saw the split of the single-celled organisms called archaea from bacteria, and the rise of photosynthesizing cyanobacteria. How life would have responded to a sustained barrage throughout this period is unclear. A giant impact would have come as a severe blow for some forms of early life, but it need not have been all bad news, says Steve Mojzsis, a geologist at the University of Colorado Boulder. That is because the energy deposited by the ongoing impacts could have created hot zones like those found near hydrothermal vents today. "These are great places for microbes," says Mojzsis, who notes that some phylogenetic evidence suggests that the last common ancestors of all present-day life were heat-loving organisms.

The two studies are not in perfect agreement. Johnson and Melosh's work[2] suggests that the impactors came from near-Earth orbits and hit at around 20 kilometres per second, whereas Bottke's model[1] has them arriving directly from the asteroid belt at a wider range of speeds. More work will be needed to resolve those differences, says Barbara Cohen, a planetary scientist at NASA's Marshall Space Flight Center in Huntsville, Alabama.

"Both models do a nice job of building on the evidence that we have but, especially on Earth, that evidence is sparse," says Cohen. "The more evidence we find, the better our constraints are going to be." ■

THE LONG TAIL OF BOMBARDMENT

Simulations hint that the Late Heavy Bombardment (LHB), in which asteroids showered Earth and the Moon, lasted much longer than was thought.

1. Bottke, W. F. *et al. Nature* http://dx.doi.org/10.1038/nature10967 (2012).
2. Johnson, B. C. & Melosh, J. *Nature* http://dx.doi.org/10.1038/nature10982 (2012).
3. Gomes, R., Levison, H. F., Tsiganis, K. & Morbidelli, A. *Nature* **435**, 466–469 (2005).

SOURCE: REF. 1

D. DAVIS

POLICY

Mexico sets climate targets

But a plan to ramp up wind power could spark more conflict with indigenous groups.

BY ERIK VANCE IN MEXICO CITY

Faced with slow progress towards an international agreement to limit greenhouse-gas emissions, governments are taking the initiative by passing their own climate laws. Last week, Mexico — plagued by a persistent drought but optimistic about its prospects for wind power — made one of the boldest commitments of any nation to limit climate change. Although many countries have established domestic climate regulations, Mexico is only the second, after the United Kingdom, to make tough national targets legally binding.

Climate-policy experts say that the move sets an encouraging precedent. As a developing country with rapidly increasing emissions, "Mexico taking the lead is probably more important" than Britain doing so, says Mark Maslin of University College London, who studies climate change and its implications.

"It's at the domestic level that the rubber hits the road," says Elliot Diringer, vice-president of the Center for Climate and Energy Solutions in Arlington, Virginia. "The actions we need to see at this stage are more in the nation's capitals than in the UN negotiations."

The Mexican government has pushed for climate measures in the past, supporting efforts to develop a successor to the Kyoto Protocol, which would lock countries into an international programme of emissions reductions. And Mexico City, where transport accounts for almost half of greenhouse-gas emissions, has developed bus and subway facilities through its 2008 Green Plan to cut carbon dioxide emissions by 7 million tonnes by the end of this year.

The biggest spur to action, however, has been Mexico's current drought — the worst since records began some 70 years ago — which has ramped up public pressure on the government to take the initiative on climate change. The new law, which passed 128 to 10 in the lower house and unanimously in the Senate, mandates that CO_2 emissions be reduced by 30% from business-as-usual levels by 2020, and by 50% from 2000 levels by 2050.

To achieve this, it demands that by 2024, 35% of the country's electricity supply come from renewable sources, up from its current level of about 20% (see 'A mighty wind?').

⭤ NATURE.COM
For more on troubled international climate negotiations, see:
go.nature.com/c3zfk2

Mandatory emissions reporting by the country's largest greenhouse-gas producers will be overseen by a new commission, and a carbon-trading scheme also looks likely.

It will be no easy task to monitor greenhouse-gas-intensive businesses that are thriving in the rapidly developing country. The cement industry, for example, had put up vigorous opposition to the legislation. Juan Bezaury, an expert in Mexican policy with the Nature Conservancy in Arlington, says that Mexico is "very good at making laws. The problem is enforcing them."

As with other countries that are developing national climate plans, including South Korea, Australia and South Africa, Mexico hopes to cash in on green technologies. Almost 14% of the country's electricity comes from hydro-power, but output has been hampered by the drought. Its solar-power capacity is still limited, so Mexico, much like many emerging economies, is focusing on wind power.
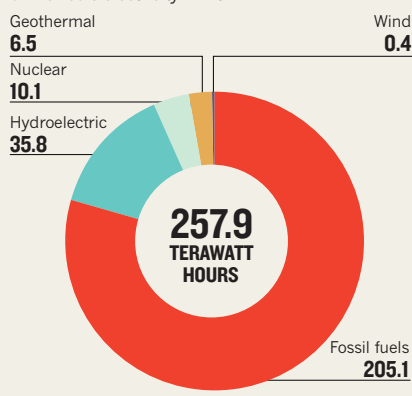
Mexico's government estimates that the country has the potential to generate 71 gigawatts of wind power — 40% more than its generating capacity from all energy sources, including coal and hydropower. One promising site is the Isthmus of Tehuantepec in southern Oaxaca, which is ideally placed to tap the trade winds from the Gulf of Mexico. The conditions have attracted companies to install about 2,500 megawatts of wind-power capacity in the area. But this 'wind rush' has sparked outrage from indigenous groups, who fear that their communal lands are being taken over.

"The money will always disappear, but the land will not. If we rent our land then we will lose it," says Beatriz Gutierrez Luis, a local teacher and activist in San Mateo, which last year rejected entreaties from a company to develop a wind-power station there. Protests in the area have already led to some activists being arrested, and at least one death.

"Our organization generally supports sustainable development and green energy," says Gustavo Esteva, a campaigner for indigenous peoples' rights at the Center for Intercultural Dialogues and Encounters, Oaxaca. "But it's always with the question of 'At the expense of what?'" ∎

Mexico hopes to reduce its greenhouse-gas emissions by developing wind power capacity in Oaxaca.

A MIGHTY WIND?
Wind power generated a tiny fraction of Mexico's electricity in 2011.

Geothermal 6.5	Wind 0.4
Nuclear 10.1	
Hydroelectric 35.8	

257.9 TERAWATT HOURS

Fossil fuels 205.1

CORRECTION
The News story 'Gene hunt is on for mental disability' (*Nature* **484,** 302–303; 2012) incorrectly said that a rare-diseases conference was hosted by the Wellcome Trust Sanger Institute near Cambridge, UK; it was held at the Wellcome Trust Genome Campus in Hinxton.

S. DE PROUW/GETTY

SOURCE: MEXICO MINISTRY OF ENERGY

GOOD SCIENCE

WORK ON MUTANT FLU CAUSED A FURORE, BUT IS FAR FROM THE ONLY SUBJECT IN WHICH RISKS MIGHT OUTWEIGH BENEFITS.

BY GEOFF BRUMFIEL

It sounds like a great idea: experimentally mutate a rare but deadly virus so that scientists can do a better job of recognizing dangerous emerging strains. But it also sounds like a terrible idea — the studies could create a virus that is easier to transmit and produce findings that are useful to bioterrorists.

Last year's news that two research teams had done exactly that with the H5N1 bird flu virus was enough to spread fear around the globe and prompt a temporary moratorium on the work. A US biosecurity panel has since lifted its restrictions on publication of the teams' findings in *Nature* and *Science*, arguing that the work has clear potential benefits, that the modified virus seems to be less lethal than the original and that the data are already circulating in the community. But the episode has highlighted how thin the line can be between research that's a blessing and research that's a threat.

Such fraught lines of enquiry exist in many scientific fields. Some could undermine global security, whereas others could create painful ethical dilemmas for families. The four examples *Nature* profiles here are hardly a definitive list, but they do give a sense of how frequently such conundrums arise — and show that scientists must constantly ask themselves whether the benefits outweigh the risks.

NUCLEAR FUEL ◀ OR ▶ NUCLEAR WEAPONS?

A technology that could quickly and efficiently separate radioisotopes for nuclear power plants and nuclear medicine is one that many physicists might find irresistible. But isotope separation is also key to making nuclear weapons, so such a technology could make it easier both to perform and to conceal illicit work on such weapons.

Naturally occurring uranium ore is mostly uranium-238, which cannot sustain the kind of runaway chain reaction required to produce an explosion. Just 0.7% is fissile uranium-235. Enriching that quantity to 3–5% makes fuel for reactors. To make a bomb, it must be enriched to more than 90%. Because the chemistry of the various isotopes is almost identical, sorting one from another has always been one of the major barriers to the proliferation of nuclear weapons. Today's state-of-the-art technology involves cascades of thousands of centrifuges, and so requires space, a massive amount of electricity, precision-machined parts and time.

Lasers can be more efficient. Tiny differences in the mass of uranium nuclei alter the energy levels of their electron shells. Finely tuned lasers can excite just the levels associated with the desired isotope and, together with other technology, can sort the uranium-235 from the rest. The work can be done quickly and secretly. In 2004, it emerged that scientists in South Korea had used lasers to enrich small quantities of uranium-235 to near weapons purity in a matter of weeks. The work went undetected for years before it was eventually disclosed to international inspectors.

Now, with the advent of cheap and tuneable lasers, laser separation is within relatively easy reach of physicists the world over. A good example is Mark Raizen at the University of Texas at Austin, who is developing lasers to separate medically important isotopes such as calcium-48, used in the diagnosis of bone disorders; and nickel-64, a promising agent for cancer therapy. The world is facing a shortage of medical isotopes[1], Raizen says. "People's lives will depend on finding new sources."

Raizen's technique is straightforward[2]: finely tuned lasers push electrons in the desired isotope into higher energy states, temporarily changing the atoms' magnetic moment. From that point, all that is needed to sort the isotopes is a large, static magnet.

J. KRZYSZTOFIAK

BAD SCIENCE

Raizen says he is aware that working with lasers and isotopes poses a proliferation risk. But he argues that it is unlikely that his technique will work well for heavy elements such as uranium.

Others stress that laser-enrichment technology should be undertaken with caution. "I think the risks are high," says Francis Slakey, co-director of the programme on science in the public interest at Georgetown University in Washington DC. Slakey, who has openly opposed the commercialization of laser isotope separation for creating nuclear fuel[3], would like to see a more open debate in the community — especially given that many physicists in the field of atomic and molecular optics could follow lines of enquiry similar to Raizen's. "I think there's value in taking a pause and reflecting," Slakey says.

Raizen is pushing ahead, driven by the excitement of using physics for the good of society. As for the risks, "you can't stop scientific ideas", he says. If he didn't do it, somebody else would. He expects his first results, on light atoms such as lithium, in a matter of months.

BRAIN SCANNING ◀ OR ▶ BIG BROTHER?

A machine able to accurately read a person's thoughts could be an extraordinary boon — allowing security officials to catch terrorists before they act, for example, or providing a new voice to some brain-damaged patients who cannot move or communicate. But such a device could also be the stuff of science-fiction nightmares, raising the spectre of Big Brother and ever-vigilant thought police.

That may be why the scientists doing such 'mind-reading' research prefer to call it 'brain scanning' or 'brain decoding'. "The whole concept of 'mind' comes with a lot of baggage," says Adrian Owen, a neuroscientist at the University of Western Ontario in London, Canada.

Nevertheless, these researchers have made extraordinary progress in understanding the human mind. The key has been functional magnetic resonance imaging (fMRI), which allows researchers to monitor blood flow throughout the brain. Blood flow is believed to be a reasonable proxy for neural activity, so fMRI gives a picture of the brain in action.

Owen, for example, has worked with patients who have been left in an apparently vegetative state by traumatic injuries. By asking specific questions to stimulate activity in different parts of their brains, he has been able to establish that around 16% of such patients can respond[4], suggesting that they have at least some level of awareness.

Jack Gallant, a neuroscientist at the University of California, Berkeley, has developed algorithms that track patterns of activation in the visual cortex as people watch videos. Reversing those computer codes can create shadowy movies of whatever people are looking at. Gallant thinks that this work could lead to even more advanced methods of communication with locked-in patients, who are paralysed but aware, or brain–machine interfaces that allow people to operate devices with their thoughts.

Going further still, John-Dylan Haynes, a neuroscientist at the Charité Medical University of Berlin, is looking for intent. Haynes scans the brain to see whether he can pick out patterns of activity that correspond to a person's decision to act. It works in simple cases[5]: he can see whether an individual decides to press a button up to seconds before the button is pressed, for example.

Whether this work could be extended to real-world applications such as lie detection or counter-terrorism is another matter. For one thing, says Gallant, each person's brain is different; it's far from clear that scientists will ever come up with a general-purpose 'mind-reading' algorithm applicable to everyone. For another, says Haynes, fMRI machines could not easily be deployed in airports. Even if they were, a simple shake of the head would throw them off. "You can't build a detector that says 'this person is going to blow up a plane now'," Haynes says.

Nevertheless, even the prospect of such a device raises hackles. "The thought that someone could use a machine to gain access to your most secret inner thoughts is not pleasant," says Gallant.

Yet entrepreneurs are already dabbling in this arena. Two US companies have fielded fMRI lie-detection services, and the world of advertising has embraced the concept of 'neuromarketing' — the use of fMRI and other techniques to measure people's subconscious emotional responses to stimuli. So far, concerns raised by such efforts seem hyped. Most courts have listened to scientists' doubts about fMRI lie-detection, and are not admitting them as evidence, says Steven Laken, chief executive of Cephos, an fMRI lie-detection firm in Tyngsboro, Massachusetts. Neuromarketing "is even more dubious", says Haynes. But Gallant thinks that the applications of the technology will come. "It'll go way further than you think," he says.

CLIMATE SAVIOUR ◀ OR ▶ CLIMATE DISASTER?

To hear proponents talk, humanity's best hope to escape the ravages of global warming may be geoengineering: manipulating Earth's environment on a planetary scale. This might involve solar-radiation management — spraying tiny particles high into the stratosphere, for example, where they could cool things down by reflecting some of the incoming sunlight. Or it might involve the removal of carbon dioxide, perhaps by seeding the ocean with iron to create algal blooms that would take up carbon dioxide from the air and then carry it to the ocean floor when they die.

To critics, geoengineering would be reckless in the extreme — and might further inflame the volatile politics of climate change.

Witness the controversy that has swirled around the UK-government-funded Stratospheric Particle Injection for Climate Engineering (SPICE) project, which involves researchers from the universities of Bristol, Cambridge, Edinburgh and Oxford, as well as the UK Met Office and Marshall Aerospace in Cambridge. SPICE is a proof-of-principle project designed to test solar-radiation management. The idea is to pump water up a 1-kilometre-long hose and spray it into the air. The altitude is too low to alter the climate, and there is plenty of water vapour already up there, says David Keith, a geoengineering specialist at the University of Calgary in Canada. "It doesn't pose a risk other than the hose falling on someone's head," he says.

Nevertheless, environmentalists sounded the alarm on SPICE as soon as they caught wind of it last year. Quite aside from geoengineering's potential for unintended consequences — such as accidentally shifting rainfall patterns and triggering droughts — there is a moral hazard to such work, argues Pat Mooney, executive director of the ETC Group, an environmental organization based in Ottawa, Canada. With climate negotiations stalled around the world, the very presence of such an experiment may make politicians think that there's a way to wriggle out of emissions caps. "It will be an easy way for governments to sidestep their obligations," Mooney says.

ETC and other groups petitioned the British government to halt SPICE last autumn, saying it would hurt the country's credibility in this year's climate talks in Rio de Janeiro, Brazil. "It did get a little bit bumpy at the time," says Phil Macnaghten, a geographer at Durham University, UK, who is overseeing an ethical and societal assessment of SPICE. In September 2011, Macnaghten and others recommended that the experiment pause while researchers engage with the public and interest groups — at present, it is still on hold.

Mooney wants to see internationally agreed rules that would include prohibitions on geoengineering experiments with transnational consequences until major questions are answered. For example, will geoengineering even work? And what unintended consequences might it have? But as global temperatures continue to rise, Macnaghten believes that, provided researchers answer public concerns, the science should be allowed to continue. "When you don't know what you don't know, then it's very hard to know how to progress," he says.

BABY BLESSING ◀ OR ▶ BRAVE NEW WORLD?

Within a pregnant mother's blood is her unborn child's full genetic sequence. Soon, say geneticists, the question will no longer be how to get at it, but how to use it to understand the baby's future behaviour and health — and how to cope with the thorny ethical issues that will inevitably ensue.

The key to this new form of prenatal diagnosis lies in the fragments of DNA that float freely through every person's bloodstream. In pregnant women, around 15% of that DNA comes from the fetus, according to

Dennis Lo, a pathologist at the Chinese University of Hong Kong, who is working to develop fetal genetic screening with Sequenom, a biotechnology company based in San Diego, California.

The trick is figuring out which DNA belongs to the fetus and which belongs to the mother. Finding the father's genetic contribution is easiest. Researchers extract DNA from the expectant mother's blood and look for variations in common with the father's genetic code to separate his half of the fetal DNA. The mother's half is tougher to identify because it is identical to the rest of the DNA in her blood. To find it, researchers count the number of times particular versions of genes are sequenced. Those held by the child and mother will appear fractionally more frequently than those held by the mother alone.

Screens for specific diseases based on this method are already nearing the market, says Lo. Scientists can check for Down's syndrome, a disorder that arises when an embryo receives three copies of chromosome 21, instead of the usual two. The test is more than 95% sensitive, making it comparable to more invasive tests such as amniocentesis[6]. Because it carries no risk, Lo believes that it will soon become nearly universal.

It may sound positive that many more parents will be forewarned of Down's syndrome and other genetic diseases such as cystic fibrosis, but it raises some thorny societal questions, says Henry Greely, a bioethicist at Stanford University in California. With universal screening, many more pregnancies might be terminated — and women who choose to carry a child with, say, Down's syndrome to term could face social and legal stigmas, he warns. "There are countries that are very concerned about mental retardation and might be willing to enforce genetic selection to avoid it," he says. Private insurers or public-health services might resist paying for the care of disabled children if their birth could have been avoided. These dystopian developments aside, some patient advocates fear that a sudden drop in the number of children with these diseases could mean less social support and fewer research dollars for their conditions.

Going beyond targeted diseases, full sequencing of the fetal genome is technically possible and will soon be affordable, says Stephen Quake, a researcher at Stanford University who works with Verinata Health, a fetal-screening company in Redwood City, California. And that, says Greely, will raise even more contentious issues. "People who come from a family with Alzheimer's might choose to terminate a pregnancy at high risk of Alzheimer's even though that Alzheimer's might occur 65 years into the future," he says — or might never occur at all, given that it is currently impossible to predict whether this condition or the vast majority of other diseases will occur on the basis of genetic information alone.

At present, there are no guidelines on how to counsel prospective parents about the avalanche of genetic information they may be about to receive. Lo says that he would be wary of telling parents before birth about a disease that could be cured within a child's lifetime. "Who knows where medical science will be in 60 years?"

But that is no reason to stop the research, says Quake, who has a cousin with Down's syndrome. He says he has thought long and hard about the issues raised by early testing, but in the end feels that the benefits greatly outweigh the risks. "The earlier parents find out, the better prepared they are," he says. ■ SEE EDITORIAL, P.415

Geoff Brumfiel *is a senior reporter for* Nature *based in London.*

1. Gould, P. *Nature* **460,** 312–313 (2009).
2. Jerkins, M., Chavez, I., Even, U. & Raizen, M. G. *Phys. Rev. A* **82,** 033414 (2010).
3. Slakey, F. & Cohen, L. R. *Nature* **464,** 32–33 (2010).
4. Monti, M. M. *et al. N. Engl. J. Med.* **362,** 579–589 (2010).
5. Soon, C. S., Brass, M., Heinze, H.-J. & Haynes, J.-D. *Nature Neurosci.* **11,** 543–545 (2008).
6. Chiu, R. W. K. *et al. Br. Med. J.* **342,** c7401 (2011).

RARE SPECIMENS

A handful of plant collectors has shaped the field of botany. Now they are disappearing, and there are no clear successors.

BY JOHN WHITFIELD

John Wood has had malaria twice, and Dengue fever once. He has shaved leeches off his legs with a machete in southeast Asia — "you're supposed to use a lit cigarette, but I don't smoke" — had his car stolen in Bolivia and lain face down in the Yemeni desert while local tribes exchanged gunfire over his head.

He encountered such inconveniences in the process of collecting more than 30,000 plant specimens over 40 years of travelling the globe, mostly as a hobbyist. More than 100 of his finds have become type specimens, from which new species are described. Those numbers elevate him to the ranks of a star collector — the top 2% of botanical gatherers, who have accumulated more than half of the type specimens in some of the world's most important collections[1].

These elite field workers have probably numbered fewer than 500 people throughout history. But they have contributed much of what scientists know about plant diversity, ecology and evolution, and have been crucial in the race to document the world's plants before they are lost to deforestation, development, invasive species and climate change.

Many botanists, however, believe that the era of the superstar collector is drawing to a close, at least in the 200-year-old form of a man (or occasionally woman) setting out from Europe or North America to see what the tropics hold. As botany has moved away from taxonomy and towards molecular studies, few of the jobs available allow researchers to spend long periods in the field gaining an encyclopaedic knowledge of plants. Tropical countries have also imposed restrictions on foreign researchers and are developing their own botanical expertise among home-grown scientists. "It's possible that the days of the non-native plant collector are virtually at an end, and people like myself are the last examples," says Wood.

As the star collectors disappear, botanists are debating how to fill the gap. Some researchers, including Wood, are training botanists in tropical countries, the presumed home of most undiscovered plants. But others think that it might be more efficient to recruit a large group of less-skilled

collectors, aided by technology and crowdsourcing techniques. "The real question is, can we exchange a few elite collectors for an army of enthusiastic less-experienced collectors?" asks Cam Webb, a Harvard University plant scientist based in Indonesian Borneo.

That is a tall order, given the seminal part that top collectors continue to play. "The most interesting results are produced mostly by people who know what the plants look like, and what to expect in a certain area, and that's why they can pick out what's unexpected," says Henk Beentje, a specialist in tropical palms at Kew Gardens in London. "They're worth more than their weight in gold."

BUDDING INTEREST

Like many elite collectors, Wood started early. As a child, he accumulated stamps, rocks, butterflies and as many flowers as he could. As a teenager, he contributed to a project to record all the plant species living in his home county of Essex, UK. When he moved to Saudi Arabia in 1970 to teach English, botany provided him with an excuse to travel to wild and remote places. A contact in the British embassy put him in touch with a researcher at the Natural History Museum in London who was interested in receiving Arabian plants, and Wood sent his first specimens back in the diplomatic pouch.

In 1974, Wood moved to North Yemen, where he spent six years working in educational development, volunteering to inspect remote schools so that he could visit the places with the most interesting plants. Gradually, he began to try to identify and understand plants himself, driven by the thrill of finding something new, or something that had last been collected two centuries ago. He also became interested in broader questions of plant ecology — his first paper, published in 1979, discussed whether Yemen had once been forested[2].

He went on to collect in Colombia, Bhutan and Bolivia. Since 2001,

The iris **Mastigostyla woodii** **is named after its discoverer, John Wood.**

J.R.I.WOOD

John Wood, seen here examining the tree bromeliad *Aechmea bromeliifolia* in Bolivia this month, has collected tens of thousands of plant specimens.

he has been a professional botanist, spending half the year in plant taxonomist Robert Scotland's lab at the University of Oxford, UK, and the other half in Bolivia, doing fieldwork and training local scientists. Together with Scotland and others, Wood is finishing a monograph on *Strobilanthes*, a tropical genus of several hundred species.

It was Scotland who led the study that revealed the influence of the elite collectors. Along with Wood and an international team of botanists and ecologists, he scoured databases to find out who had collected each of 103,000 type specimens in four of the world's largest herbaria — at the Natural History Museum in London, the Royal Botanic Garden Edinburgh, UK, the Missouri Botanical Garden in St Louis and the Royal Botanic Gardens in Melbourne, Australia.

The analysis showed that a small group of what the team calls big hitters has been hugely and disproportionately effective at finding species over the past two centuries. It also showed that most big hitters are wide-ranging, in both where and what they collect — Wood, for example, has combined regular intercontinental relocations with an omnivorous collecting habit that takes in half a dozen plant families, including large groups such as the grasses and daisies. This breadth seems to underpin the ability to find lots of new species.

Broad experience helps a collector to know what to sample, and what to ignore. If a plant looks new, collectors try to get as many parts — flowers, leaves, root and fruit — as possible. (When sampling a tree, this often involves climbing it.) In the tropics, they have to race to get specimens into a press or preserved in alcohol before the plants start to decay. Drying and mounting plants so that they display their diagnostic features, and yield high-quality DNA samples, requires skill and practice.

That craftmanship must be allied to innate gifts in pattern recognition, says Quentin Luke, a botanist affiliated with the East African Herbarium in Nairobi. "People with a natural ability to distinguish plants from each other are few and far between," he says. Identifying plants that aren't in flower — which will be most of them in a tropical forest with no set flowering season — is particularly challenging. It requires knowledge of subtle features of leaf morphology or bark, or even the smell of wood or the taste of leaves.

A prodigious visual memory also helps. Alwyn Gentry of the Missouri Botanical Garden, one of the leading botanists of the twentieth century, claimed to remember every plant he had ever collected, amounting at his death to more than 80,000 specimens[3].

FIELD TESTED

For elite plant collectors, experience and ability reinforce one another: field botanists find the largest number of new species per year at the end of their careers. But they can't get that far without a cast-iron constitution and a certain sangfroid. Tom Croat of the Missouri Botanical Garden — who, with more than 100,000 specimens from 37 countries, is probably the most prolific living plant collector — once had a Costa Rican road collapse beneath him, causing his camper van, containing a custom-built plant drier, his wife and two young children, to roll down a mountain and into a river. And Beentje once had to talk down a lynch mob on Madagascar. "They thought I was abducting virgins and stealing their blood. We got out by the skin of our teeth."

Some botanists die at work. Gentry was killed in 1993, aged 48, when a plane taking him on a collecting trip in the mountain forests of Ecuador crashed. And in 2010, Leonard Co, one of the Philippines' top plant researchers, was shot dead while working in the forest, either in crossfire between government forces and communist insurgents, or because the army mistook him for a guerrilla.

There is no shortage of adventurous and skilful young botanists willing to embrace such a life, say senior collectors. And there is plenty of work left to do: estimates suggest that there are 70,000 plant species left to discover[4], mostly in equatorial Latin America and Indonesia, to add to the 350,000 or so already known. For the

🔿 **NATURE.COM**
For a slideshow on plant collectors, see:
go.nature.com/qndlr7

past few decades, about 2,000 new species have been described each year, with no sign of a slowdown.

There are, however, few places employing plant collectors. The first wave of globe-trotting botanists, in the late eighteenth and early nineteenth centuries, carried out surveys on behalf of the European empires; later, horticultural companies paid top collectors to bring back new products. Now, nearly all the serious collectors work for major botanic gardens and museums.

Yet even there, general botanists are no longer in such demand. The modern botanist tends to focus on one plant group and uses DNA sequences to decode evolutionary history and relationships. "We'll see fewer collections per individual because people are becoming so specialized. Just collecting a lot of specimens isn't something people have much respect for," says Robbin Moran, who studies ferns at the New York Botanical Garden. The shifts in botany have had costs, he says. "The really big collectors have been tremendous generalists, and that's something that's being lost."

Croat especially laments the waning opportunities to practise floristic taxonomy — describing all the plants in a location. He earned his spurs putting a name to every plant species on Barro Colorado Island[5], a research station in the Panama Canal run by the Smithsonian Institution in Washington DC. "Floristic studies give knowledge of all groups of plants," he says. "Without that, the average student has no idea what to work on. Most of the graduate students today wouldn't be able to find the forest, let alone find anything in it."

Plant collectors are also facing a growing number of bureaucratic hurdles. Tropical countries, seeking to protect potentially lucrative sources of drugs and crops, have tightened their regulation of plant collecting. India is among those that ban the export of plant specimens altogether; other countries demand that botanists specify what groups they will collect, hindering broad floristic work.

"Each time I go back to Bolivia there's more paperwork and more restrictions," says Wood. That makes it harder for botanists to gain international experience, he says. "There's a disincentive to start in another country, because it means starting your permits and contacts from scratch." The top collectors of the future are likely to be born in, or migrate to, tropical countries, he says.

This shift is already happening, with local collectors and herbaria compensating for the decline of the big-hitting Westerner, says Gerrit Davidse, of the Missouri Botanical Garden, a co-author of the collector analysis. "In the past, you could mostly ignore local collections in places such as Mexico and Brazil," he says. "Now you ignore them at your peril."

The tight regulations do not spare native collectors. "We have many problems applying for permits," says Alfredo Fuentes, a botanist at the National Herbarium of Bolivia in La Paz. "It is very difficult to explain why we collect, and that the collections are not for commercial purposes. We spend a lot of time on this." In Kenya, says Luke, it is "a huge song and dance" for local botanists to send specimens abroad to be identified, which is usually necessary for the most interesting finds.

And developing-world botany still requires the support of rich nations. "In Bolivia, the government support for botany is almost non-existent," says Fuentes. "This major shortcoming is largely filled by foreign institutions and researchers who strongly support the training of new botanists."

The changing botanical landscape, and the many threats to plant diversity, have led Webb to advocate a different approach to discovery[6]. Western collectors have always employed local naturalists and students, to gather and process specimens. Now, technology could allow this approach to be scaled up, says Webb. In a few years, he predicts, volunteers will be armed with a tablet computer bearing the world's botanical information in one hand and a pocket DNA sequencer that identifies species in the other. His team is working on software that will allow anyone to help identify specimens online, by pairing up images of known and unknown plants. "Perhaps it doesn't matter which is better, the elite few or the excited rabble," says Webb. "But I am optimistic that the latter could actually be made to be highly selective and effective via good training, augmented with the best of tech."

Others are sceptical that this approach will bear fruit. DNA-based identification has so far yielded little for plants, says Scotland. "We're still trying to work out what the markers are, even though it's been talked about for a decade." And although volunteers can collect huge amounts of material — botanists call it hay baling — they often bring back the weedy and introduced, rather than the rare and interesting. Supporting a new generation of experts might be more productive, Scotland says. "Fewer people over a longer period of time might give more rewards than lots of unfocused people collecting lots of the same thing."

Wherever the collectors of the future hail from, they will have to be content with a long wait for recognition. Herbaria are filled with unidentified specimens, and the gap between a species being collected and being described averages about 36 years[4]. This means that any analysis of collectors' achievements will underestimate the contribution of contemporary botanists. It also suggests that at least half of the 70,000 unidentified plant species are already in a cupboard somewhere.

The bottleneck means that star collectors of the past remain a force in present-day botany. Today's researchers spend their days with plants collected by botanists going back to the eighteenth-century days of Joseph Banks, and speak of their forebears with the same familiarity as they do of their contemporaries. As Wood puts it: "Collectors have a sense of their place in history." ■

Old Man Banksia (*Banksia serrata*) is one of the many plants that Joseph Banks collected.

NATURAL HISTORY MUSEUM, LONDON/SPL

> "It's possible that the days of the non-native plant collector are virtually at an end."

John Whitfield *is a London-based science writer. His latest book is* People Will Talk: The Surprising Science of Reputation.

1. Bebber, D. P. *et al. Proc. R. Soc. Lond. B* http://dx.doi.org/10.1098/rspb.2011.2439 (2012).
2. Hepper, F. N. & Wood, J. R. I. *Proc. Semin. Arabian Stud.* **9,** 65–71 (1979).
3. Miller, J. S. *et al. Ann. Mo. Bot. Gard.* **83,** 433–460 (1996).
4. Bebber, D. P. *et al. Proc. Natl Acad. Sci. USA* **107,** 22169–22171 (2010).
5. Croat, T. B. *Flora of Barro Colorado Island* (Stanford Univ. Press, 1978).
6. Webb, C. O., Ferry Silk, J. W. & Triono, T. *Biodivers. Conserv.* **19,** 955–972 (2010).

COMMENT

Scant information on the myriad kits and reagents purchased by labs can lead researchers to do inappropriate experiments inadvertently.

A recipe for disaster

Manufacturers of commercial reagents should follow scientific norms and be open about the ingredients of their products, says **Anna Git**.

Earlier this year, my colleagues and I experienced every scientist's worst nightmare. Twelve months of experiments were deemed useless after we showed that a recommended negative control for chemically synthesized stretches of RNA (microRNA mimics), bought from a biotechnology company, was inappropriate. The sequence was too short, leading to results that were impossible to interpret, if not just wrong. Because the company didn't reveal much information about the product, we only discovered the discrepancy fortuitously after testing many microRNAs of known sequence, and observing a length-dependent activity among them.

This is the worst in a long line of incidents that we have experienced as a result of the sweeping confidentiality imposed by manufacturers of laboratory reagents, who, for the most part, do not provide full details about the contents of their chemicals, enzymes or kits. This lack of transparency forces researchers to waste time chasing information, restricts the types of experiments they can and cannot do and, most troublingly, causes them unknowingly to perform inappropriate experiments and publish misleading results.

To try to decipher the ingredients of commercial products, my colleagues and I have tested pH and conductivity, signed confidentiality agreements to receive extra information not on the label and discarded experiments in which unknown ingredients impeded subsequent reactions. We are on first-name terms with many sympathetic scientists who work in research and development (R&D) for commercial vendors, and who occasionally whisper crucial details off the record.

This secrecy stands in stark contrast to the current practices of scientific publication. No self-respecting referee or journal would accept a research paper in which the authors relied on processes, substances or sequences that they had created themselves but did not describe in detail. Yet this is acceptable ▶

▶ if those tools are purchased from a company. For the sake of science, everyone has to become more transparent.

The commercialization of reagents and kits is not all bad — it has undoubtedly contributed much to modern research, particularly in biological and clinical disciplines. It has enabled faster and higher-throughput experimental protocols, promoted greater uniformity and consistency between independent labs and helped to develop technologies and methodologies that would otherwise be inaccessible to individual labs.

However, the true cost of these advances — besides the price tag — is the inability to adjust confidential methods according to experimental needs, should they exceed scenarios anticipated by the company's R&D department. For instance, molecular and cell biologists often need DNA or RNA sequences that act as negative controls — usually sequences that don't match anything in the cells being tested. Such sequence-based reagents are zealously protected by manufacturers, an understandable precaution for such an easily copied product. But in experiments that combine genomes — such as when human cells are infected with a viral genome, or when a mouse carries human DNA — a strictly human or mouse negative control might not work properly. But how would the researcher know, if they can't find out the actual sequence? Moreover, the dynamics of the industry mean that reagents (and companies) appear, merge, upgrade or disappear at short notice. These changes often take place without leaving an information trail, making it impossible to repeat or reproduce older experiments.

If we are to work towards a more rigorous and productive research community, we must change the way information about materials is disclosed. Such changes require goodwill and open-mindedness, but they are possible. For example, standards for disclosing a minimum level of information about microarray experiments, widely known as the MIAME guidelines[1], have become an accepted default among microarray researchers, replacing jealous guarding of raw data and paving the way to powerful meta-analyses. A call to provide more details in experiments that use the polymerase chain reaction (PCR) in real time has, at the time of writing, been cited by more than 500 other publications[2]. The industry is subject to market forces, so the call for transparency should come from researchers, referees and journals voicing their concerns.

> *"Companies need to rethink their blanket confidentiality policies."*

For companies, obvious and easy changes should start with full disclosure of information on discontinued products, perhaps in a centralized third-party database. This should be followed by disclosure of all non-sensitive, auxiliary information about existing products that does not need to be protected; knowing the composition of the reaction medium does not eliminate the need to purchase the enzyme, for example. On the contrary, this approach enhances products' flexibility, enabling their use in a greater variety of experiments, and thus boosting the company's potential revenue. The sequences of PCR primers are often heavily guarded by manufacturers, but some molecular biologists have suggested[3] that companies could reveal alternative, less-sensitive information that would still allow scientifically rigorous analysis, such as approximate primer positioning and details about *in silico* validation; scientists in other fields could develop similar plans. Likewise, patent law is evolving to protect new application of genetic sequences, both man-made and naturally occurring, so at least partial disclosure of proprietary control sequences should be possible.

Transparency is not just the responsibility of manufacturers — scientists need to demand more information, and disclose everything in their methods sections. Responsible reporting by individuals who use commercial kits should spell out the principles of those kits — such as the kit version, details about the underlying biochemical reactions and all listed reagents. For software, an exact specification of version and parameters should be given. Reviewers of papers should also require this information.

Something has to be done. Because of the too-short sequence my student used as a negative control, one-quarter of her PhD was wasted. I've already seen one published paper that unknowingly reports the same artefact as a valid result. Companies need to rethink their blanket confidentiality policies: patent law safeguards their intellectual advances from financial exploitation by competitors, but it should not confound scientific rigour. ∎

Anna Git *is based at Cancer Research UK, Cambridge Research Institute, Li Ka Shing Centre, Cambridge CB2 0RE, UK.*
e-mail: anna.git@cancer.org.uk

1. Brazma, A. *et al. Nature Genet.* **29,** 365–371 (2001).
2. Bustin, S. A. *et al. Clin. Chem.* **55,** 611–622 (2009).
3. Bustin, S. A. *et al. Clin. Chem.* **57,** 919–921 (2011).

Understand how it works

Over-reliance on automated tools is hurting science, says **David W. Piston**.

As head of Vanderbilt University's core microscopy labs, I recently met a colleague and his student to discuss their confusing results from an experiment studying protein interactions in cells. After applying a treatment that should have disrupted the interaction of two particular proteins inside mitochondria, they still saw the proteins interacting. The student said that to measure the interaction he had used a commercial automated image-analysis system. He didn't understand how it worked, so he just used a colleague's settings from a different experiment. But, without him realizing, this had masked all of the cell except for the mitochondria. If he had modified the settings to leave the entire cell unmasked, he would have seen that the proteins were now present within the mitochondria in relatively small amounts compared with the rest of the cell, and so their interaction had been disrupted — the treatment was, in fact, working.

In this case, it wasn't inspiration that was lacking — it was instruction. The researchers had used a proven and validated tool, but in a way inappropriate for the problem at hand. A hard-working and dedicated student had wasted around two months at the microscope trying to make the treatment 'work'. Between us, we figured out the problem in just a few minutes' discussion.

Unfortunately, this scenario is becoming all too common in many fields of science: researchers, particularly those in training, use commercial or even lab-built automated tools inappropriately because they have never been taught the details about how they work. Twenty years ago, a scientist wanting to computerize a procedure had to write his or her own program, which forced them to understand every detail. If using a microscope, he or she had to know how to make every adjustment. Today, however, biological science is replete with tools that allow young scientists simply to press a button, send off samples or plug in data — and have a result pop out. There are even high-throughput

▶ if those tools are purchased from a company. For the sake of science, everyone has to become more transparent.

The commercialization of reagents and kits is not all bad — it has undoubtedly contributed much to modern research, particularly in biological and clinical disciplines. It has enabled faster and higher-throughput experimental protocols, promoted greater uniformity and consistency between independent labs and helped to develop technologies and methodologies that would otherwise be inaccessible to individual labs.

However, the true cost of these advances — besides the price tag — is the inability to adjust confidential methods according to experimental needs, should they exceed scenarios anticipated by the company's R&D department. For instance, molecular and cell biologists often need DNA or RNA sequences that act as negative controls — usually sequences that don't match anything in the cells being tested. Such sequence-based reagents are zealously protected by manufacturers, an understandable precaution for such an easily copied product. But in experiments that combine genomes — such as when human cells are infected with a viral genome, or when a mouse carries human DNA — a strictly human or mouse negative control might not work properly. But how would the researcher know, if they can't find out the actual sequence? Moreover, the dynamics of the industry mean that reagents (and companies) appear, merge, upgrade or disappear at short notice. These changes often take place without leaving an information trail, making it impossible to repeat or reproduce older experiments.

If we are to work towards a more rigorous and productive research community, we must change the way information about materials is disclosed. Such changes require goodwill and open-mindedness, but they are possible. For example, standards for disclosing a minimum level of information about microarray experiments, widely known as the MIAME guidelines[1], have become an accepted default among microarray researchers, replacing jealous guarding of raw data and paving the way to powerful meta-analyses. A call to provide more details in experiments that use the polymerase chain reaction (PCR) in real time has, at the time of writing, been cited by more than 500 other publications[2]. The industry is subject to market forces, so the call for transparency should come from researchers, referees and journals voicing their concerns.

> "Companies need to rethink their blanket confidentiality policies."

For companies, obvious and easy changes should start with full disclosure of information on discontinued products, perhaps in a centralized third-party database. This should be followed by disclosure of all non-sensitive, auxiliary information about existing products that does not need to be protected; knowing the composition of the reaction medium does not eliminate the need to purchase the enzyme, for example. On the contrary, this approach enhances products' flexibility, enabling their use in a greater variety of experiments, and thus boosting the company's potential revenue. The sequences of PCR primers are often heavily guarded by manufacturers, but some molecular biologists have suggested[3] that companies could reveal alternative, less-sensitive information that would still allow scientifically rigorous analysis, such as approximate primer positioning and details about *in silico* validation; scientists in other fields could develop similar plans. Likewise, patent law is evolving to protect new application of genetic sequences, both man-made and naturally occurring, so at least partial disclosure of proprietary control sequences should be possible.

Transparency is not just the responsibility of manufacturers — scientists need to demand more information, and disclose everything in their methods sections. Responsible reporting by individuals who use commercial kits should spell out the principles of those kits — such as the kit version, details about the underlying biochemical reactions and all listed reagents. For software, an exact specification of version and parameters should be given. Reviewers of papers should also require this information.

Something has to be done. Because of the too-short sequence my student used as a negative control, one-quarter of her PhD was wasted. I've already seen one published paper that unknowingly reports the same artefact as a valid result. Companies need to rethink their blanket confidentiality policies: patent law safeguards their intellectual advances from financial exploitation by competitors, but it should not confound scientific rigour. ∎

Anna Git *is based at Cancer Research UK, Cambridge Research Institute, Li Ka Shing Centre, Cambridge CB2 0RE, UK.*
e-mail: anna.git@cancer.org.uk

1. Brazma, A. *et al. Nature Genet.* **29,** 365–371 (2001).
2. Bustin, S. A. *et al. Clin. Chem.* **55,** 611–622 (2009).
3. Bustin, S. A. *et al. Clin. Chem.* **57,** 919–921 (2011).

Understand how it works

Over-reliance on automated tools is hurting science, says **David W. Piston**.

As head of Vanderbilt University's core microscopy labs, I recently met a colleague and his student to discuss their confusing results from an experiment studying protein interactions in cells. After applying a treatment that should have disrupted the interaction of two particular proteins inside mitochondria, they still saw the proteins interacting. The student said that to measure the interaction he had used a commercial automated image-analysis system. He didn't understand how it worked, so he just used a colleague's settings from a different experiment. But, without him realizing, this had masked all of the cell except for the mitochondria. If he had modified the settings to leave the entire cell unmasked, he would have seen that the proteins were now present within the mitochondria in relatively small amounts compared with the rest of the cell, and so their interaction had been disrupted — the treatment was, in fact, working.

In this case, it wasn't inspiration that was lacking — it was instruction. The researchers had used a proven and validated tool, but in a way inappropriate for the problem at hand. A hard-working and dedicated student had wasted around two months at the microscope trying to make the treatment 'work'. Between us, we figured out the problem in just a few minutes' discussion.

Unfortunately, this scenario is becoming all too common in many fields of science: researchers, particularly those in training, use commercial or even lab-built automated tools inappropriately because they have never been taught the details about how they work. Twenty years ago, a scientist wanting to computerize a procedure had to write his or her own program, which forced them to understand every detail. If using a microscope, he or she had to know how to make every adjustment. Today, however, biological science is replete with tools that allow young scientists simply to press a button, send off samples or plug in data — and have a result pop out. There are even high-throughput

Increasing lab automation means that students need to be given better training on how the techniques and the equipment work.

plate-readers that e-mail the results to the researcher.

Teaching style has not adapted to address this cultural change — we rarely explain to our students how the new automated tools work, how to use them effectively and how to troubleshoot when it seems that things have gone wrong. And young scientists often don't realize that they need to ask questions. As a result, they waste time by using a technique improperly or, equally tragically, miss something exciting when they assume that a strange result means that they did something wrong and they never follow it up.

Of course, the researcher can talk to experts about what might be going wrong, but with 600 scientists (mostly young) using the central microscopy facility at Vanderbilt University, for example, this is not an efficient way to resolve the problem. We need to do a better job of teaching students how techniques work before they start using them.

Automation has its good points, of course. Biomedical discovery has been accelerated by automated computational analysis, expert core facilities and laboratory kits, which give investigators access to technical approaches that go beyond their own training. The interdisciplinarity of modern biomedical research makes it almost impossible for one person to understand the subtleties of all the procedures on which they rely[1].

What is missing are the time and resources for students to learn enough about how their equipment and techniques work

to be able to use them to best advantage[2]. This situation fails both the students and the broader scientific community by leading to uneven training and levels of competence. As educators, it is incumbent on us to teach our students not only the 'hows' of a particular technique, but also the underlying 'whys'. In the past, much of this practical training was conducted by a lab's principal investigator, who is now spending increasing time chasing funding. To fill this gap, many

> *"We need to do a better job of teaching students how techniques work before they start using them."*

students seek out training themselves, for example through summer courses such as those offered by the Marine Biological Laboratory in Woods Hole, Massachusetts. More and more of these intensive short courses are being offered worldwide, but they are always oversubscribed.

We should make this kind of instruction available to all students by refocusing graduate education to emphasize better the fundamental concepts and practice of experimental techniques. This would necessarily include hands-on labs involving state-of-the-art equipment and instruction from experts with proven success in using the techniques. Many labs and institutions (including Vanderbilt) have begun to develop this type of course. The extra instruction will initially slow students'

progress in the lab, but it will better serve them (and their labs and their research fields) in the long run.

The biggest obstacle to hands-on laboratory courses is their cost and the effort required to stage them effectively. Institutional support is therefore crucial, especially given that the appropriate instructors are often well funded researchers who need to be recompensed for their time. In addition, all graduate students should be supported by training grants[3], which fund the needed instruction and also relieve some of the pressure on students to deliver research results in their first years of graduate school. And schools should consider admitting only as many graduate students as they have the resources to give the necessary laboratory instruction.

The research community must take more responsibility for teaching the coming generations not only how to formulate hypotheses, design research approaches and write manuscripts, but also how to build, implement and troubleshoot their experiments at the most basic level. ∎

David W. Piston *is the Louise B. McGavock chair and professor of molecular physiology and biophysics at Vanderbilt University, Nashville, Tennessee 37232, USA.*
e-mail: dave.piston@vanderbilt.edu

1. *Nature Methods* **8,** 983 (2011).
2. Mervis, J. *Science* **328,** 678 (2010).
3. Stephan, P. *Nature* **484,** 29–31 (2012).

Make social sciences relevant

We need to turn the efforts of social scientists towards global challenges, argues **Luk Van Langenhove**.

The social sciences are flourishing. As of 2005, there were almost half a million professional social scientists from all fields in the world, working both inside and outside academia. According to the *World Social Science Report 2010* (ref. 1), the number of social-science students worldwide has swollen by about 11% every year since 2000, up to 22 million in 2006.

Yet this enormous resource is not contributing enough to today's global challenges, including climate change, security, sustainable development and health. These issues all have root causes in human behaviour: all require behavioural change and social innovations, as well as technological development. Stemming climate change, for example, is as much about changing consumption patterns and promoting tax acceptance as it is about developing clean energy. Humanity has the necessary agro-technological tools to eradicate hunger, from genetically engineered crops to artificial fertilizers. Here, too, the problems are social: the organization and distribution of food, wealth and prosperity. And Peter Piot, former head of the Joint United Nations Programme on HIV/AIDS, has argued that the social sciences have great potential for helping policy-makers to combat that disease, by unravelling sexual and addictive behaviours, and more[1].

Despite these factors, many social scientists seem reluctant to tackle such issues. And in Europe, some are up in arms over a proposal to drop a specific funding category for social-science research and to integrate it within cross-cutting topics of sustainable development. This is a shame — the community should be grasping the opportunity to raise its influence in the real world. To paraphrase the great social scientist Joseph Schumpeter: there is no radical innovation without creative destruction.

Today, the social sciences are largely focused on disciplinary problems and internal scholarly debates, rather than on topics with external impact. Bibliometric analyses of the Thomson Reuters Social Sciences Citation Index reveal that the number of papers including the keywords 'environmental change' or 'climate change' have increased exponentially since 2004. However, the numbers are still small: in 2010, about 1,600 of the 100,000 social-sciences papers published globally (just 1.6%) included one of these keywords[2]. A similar trend exists for work on global poverty: even though there was a 500% increase in publications on this topic from 1999 to 2005 (ref. 1), this resulted in only 276 publications during this period.

When social scientists do tackle practical issues, their scope is often local: Belgium is interested mainly in the effects of poverty on Belgium, for example. And whether the community's work contributes much to an overall accumulation of knowledge is doubtful.

Global problems, such as access to clean water, need an integrated approach from social science.

Most peer-reviewed publications in the social sciences have a very short citation half-life; the average article in the social sciences and humanities is cited less than once a year[3].

The problem is not necessarily the amount of available funding. During the late 1990s, national spending on social sciences and the humanities as a percentage of all research and development funds — including government, higher education, non-profit and corporate — varied from around 4% to 25%; in most European nations, it is about 15% (ref. 1). This is an adequate amount so long as it is aimed in the right direction. Social scientists who complain about a lack of funding should not expect more in today's economic climate — the only place where funding might significantly improve is in the BRIC nations (Brazil, Russia, India and China), where economies are expanding fast.

The trick is to direct these funds better. The European Union Framework funding programmes have long had a category specifically targeted at social scientists. This year, it was proposed that the system be changed: Horizon 2020, a new programme to be enacted in 2014, would not have such a category. This has resulted in a flurry of protests from social scientists. But the intention is not to neglect social science; rather, the complete opposite. The idea is to force social scientists to integrate their work with other categories, including health and demographic change; food security; marine research and the bio-economy; clean, efficient energy; and inclusive, innovative and secure societies. That should create more collaborative endeavours and help to develop projects aimed directly at solving global problems.

Another possible solution is to improve the rewards for interdisciplinary work within academia. Several funding streams and centres are now aimed at such research, including the International Human Dimensions Programme on Global Environmental Change in Bonn, Germany (www.ihdp.unu.edu). But most institutions still judge their scholars by achievements in their own disciplines. This hinders the development of such initiatives. It could be that we are evolving two communities of social scientists: one that is discipline-oriented and publishing in highly specialized peer-reviewed journals, and one that is problem-oriented and publishing elsewhere, such as in policy briefs. I am not sure if this is an ideal solution, but it may provide an alternative to the problem of shifting the academic reward system.

The main solution, however, is to change the mindset of the social-science community, and what it considers to be its main goal. If I were a student now, I would throw myself at global challenges and social innovations; I hope to encourage today's young researchers to do the same. ∎

Luk Van Langenhove *is director of the United Nations University Institute on Comparative Regional Integration Studies in Bruges, Belgium. He served as vice-president of the International Social Sciences Council in 2007–10.*
e-mail: lvanlangenhove@cris.unu.edu

1. *World Social Science Report 2010: Knowledge Divides* (UNESCO/International Social Science Council, 2010); available at http://go.nature.com/sqwbzj
2. Jonkers, K. *Bibliometric Report of Social Science Publications on Climate Change and Environmental Change* (International Social Science Council, 2011); available at http://go.nature.com/dto1kr
3. Van Langenhove, L. *Innovating the Social Sciences: Towards More Useable Knowledge for Society* (Passagen, 2007).

G. M. B. AKASH/PANOS

SPRING BOOKS
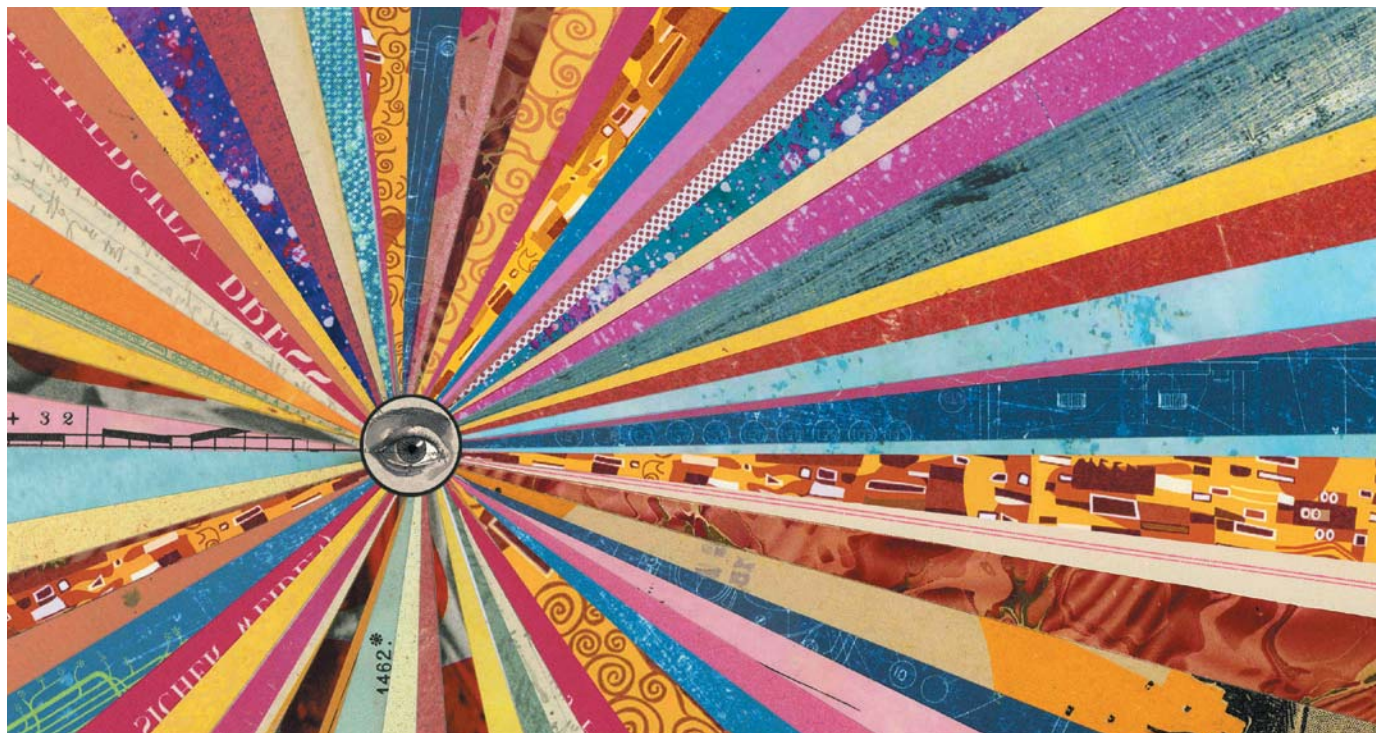
MARTIN O'NEILL

PSYCHOLOGY

The aesthetic brain

Simon Mawer relishes a masterful mix of neuroscience and art that focuses on the early twentieth century.

This is a big book — in size, scope and ambition. Eric Kandel sets out to explore the effect of art not just on the human mind but, in the true spirit of the twenty-first century, on the machinery of the brain itself: the neural mechanisms that give us the phenomena that we describe as feeling and self-awareness. Who better as a guide to this science than Kandel, who won the 2000 Nobel Prize in Physiology or Medicine for his work on the physiological basis of memory?

To bring this vast project into the compass of a single book, Kandel confines his analysis to his native city — the Vienna that he was forced to flee with his family as a child just before the Second World War. (The city has since made overtures to attract him back, if only as an honoured visitor.)

Kandel has further tilted the playing field in his own favour because, although *The Age*

of Insight bills itself as a *Quest to Understand the Unconscious in Art, Mind, and Brain*, it is really an attempt to analyse the psychological effects of figurative art, particularly portraiture. Abstract art gets little or no mention. You may come away from *The Age of Insight* with some idea of why you are moved by the paintings of, say, Lucian Freud; but you will learn little about why you are gripped by a Jackson Pollock.

Nevertheless, this is an impressive work. Kandel considers Gustav Klimt, Egon Schiele and Oskar Kokoschka — three of the great artists of the modern era, at work in Vienna at the start of the twentieth century, when

Sigmund Freud was undertaking his revolutionary investigation of the unconscious. Kandel makes of the

artists a springboard for a comprehensive review of the neurobiology behind perception and art appreciation.

Noting the "remarkable similarity between [Sigmund] Freud's ability to use language to probe the unconscious and the ability of the modernist painters to depict it", Kandel moves from Klimt's highly decorative and often overwrought portraits of society women to the weightier aspects of his art. These resonate with Freud's work — from erotic drawings to memento mori. Here we have the twin pillars of Freudian theory: Eros, the life force, and Thanatos, the death drive.

From Klimt it is a natural step to the art of his protégé Schiele, a wayward genius in the true twentieth-century mould, in whose work Kandel finds "a pictorial version of Freud's *Interpretation of Dreams*". The third of the trio, the expressionist Kokoschka, is perhaps

The Age of Insight: The Quest to Understand the Unconscious in Art, Mind, and Brain, from Vienna 1900 to the Present
ERIC KANDEL
*Random House: 2012.
656 pp. $40, £25.04*

more interesting because he is less obvious. What concerns Kandel is how this artist conveys, and the audience reads, emotion in the human face. Kandel explores what the observer brings to the feast — the "beholder's share" achieved through top-down processing that depends on memory and experience — and how innate processes in the brain filter incoming information from the "bottom up". He suggests how artists may unconsciously exploit these brain functions, for example by using colour to convey emotions in portraiture.

Throughout, Kandel combines a professional knowledge of brain scans with a firm grasp of the ideas of another Viennese exile, the art historian Ernst Gombrich, whose seminal 1960 work *Art and Illusion* examined the mechanics of the artistic response. One might say that Kandel has taken up Gombrich's torch, moving from the psychology of perception to the actual mechanics of it.

Kandel understands, and explains, how the observer brings a lifetime of experience to the simple act of looking at a painting; how "mirror neurons" elicit empathy in the brain; how "we are not only inspired and seduced by art, but also mystified, startled, frightened, and even repulsed by it". And he knows where, in the brain's 1.5 kilograms of fat and water, all these responses are located. It is quite a ride, and a beautifully scenic one with extensive, excellent and apposite illustrations.

Some of his arguments might be seen as contentious. Can our ideal of beauty really be hard-wired so that it has "varied surprisingly little from century to century or one culture to another"? (Has Kandel compared a seventeenth-century Rubens nude with 1960s Twiggy?) And is there really an adaptive advantage in our appreciation of art, or is it nothing more than a quirky by-product of a complex, self-conscious mind? But by and large, you go along with Kandel, because he simply knows so much.

Yet he would be the first to agree that this area of neuroscience is in its infancy. Marrying the sciences and humanities is a worthwhile undertaking, but Kandel admits what any serious observer of art will feel — that even when you have explained every neuron, every synapse, every glimmer in the amygdala or flicker in the prefrontal cortex, you still won't have explained what it is actually like to stand in front of a Klimt or Kokoschka and feel the thrill. That is to do with consciousness, or what Kandel calls introspective experience: "a phenomenon not readily accessible to objective scientific enquiry". I suspect that, even with the best neurobiology in the world, we will never be able to understand that. ∎

Simon Mawer *is a writer based in Rome. His latest book is* The Girl Who Fell From The Sky *(Trapeze in the United States). e-mail: simonmawer@tiscali.it*
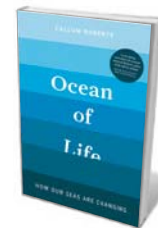
Ultra marine

Stephen R. Palumbi finds both stark warnings and buoyant optimism in an encyclopaedic take on the state of the oceans.

The floating head of Prince Charles, 5 metres tall, chided us about global overfishing. On a February morning in Singapore, at the World Oceans Summit, Charles's video highlighted a sobering fact: in the past decade, marine scientists have uncovered a growing list of serious problems that face the world's oceans. In *Ocean of Life*, Callum Roberts charts these troubled waters.

Roberts, a marine conservation biologist, dives beneath the often deceptively calm surface of our planet's great oceans to discover the agents of change, where they come from and the nature of their impact — as well as a range of pragmatic solutions. It is a story told with both scientific accuracy and narrative skill.

Roberts pulls no punches. In chapter after chapter of this encyclopaedic treatment, he summarizes the current scientific knowledge about crucial troubles facing the seas, almost all driven by humans. Pollution, acidification, shifting species ranges, the 'decapitation' of the marine food chain through over-exploitation of tuna and other predatory fish, invasions of species from other oceans, sedimentation, habitat destruction and more are laid out.

Overfishing is a much-documented issue, on which Roberts has focused his research career. More than one billion people depend on the ocean for food — and some can get animal protein only from the tiny fish left after decades of overfishing. The story of their unmet need is written here. Roberts gives us detailed personal tales, too, about the decline and fall of small fisheries such as the Firth of Clyde in Scotland; bigger-picture accounts look at why the British trawling fleet returns five times

Ocean of Life: How Our Seas Are Changing
CALLUM ROBERTS
Allen Lane/Viking: 2012. 400/416 pp. £25/$30

fewer fish now than it did 75 years ago.

This steady rain of sobering news is neither exaggerated nor minimized, and Roberts's clear, well-written accounts give us access to vast amounts of scientific information about ocean declines. Even in the realm of ocean conservation, scientists tend to specialize, and I know of no other volume that treats such divergent ocean issues as overfishing, decreasing pH, plastic pollution and biogeographic shifts with this much accuracy and acumen.

As a balance to the bad news, each chapter is edged with fascinating details about the life of the sea, such as how currents move through the deep oceans and what problems are caused by invasive marine species. Roberts's exuberance about the ocean bubbles to the surface: he delights in the historical context of how people have used the oceans. Even when he is describing the dire collapse of the tuna catch in the Mediterranean Sea, a historical description of garum (the infamous fermented fish sauce that was crucial to ancient Roman cuisine) creeps in.

Roberts deftly interweaves ocean facts with conversational whimsies, such as the only aphorism that Oscar Wilde got really wrong ("Nothing succeeds like excess"). And he occasionally offers a passage right from the heart; for instance, when he describes a squid's responses to a human encounter as "written on their skin in quick-fire color changes that pulse and

> CRUCIAL TROUBLES FACING THE SEAS ARE **ALMOST ALL DRIVEN BY HUMANS.**

more interesting because he is less obvious. What concerns Kandel is how this artist conveys, and the audience reads, emotion in the human face. Kandel explores what the observer brings to the feast — the "beholder's share" achieved through top-down processing that depends on memory and experience — and how innate processes in the brain filter incoming information from the "bottom up". He suggests how artists may unconsciously exploit these brain functions, for example by using colour to convey emotions in portraiture.

Throughout, Kandel combines a professional knowledge of brain scans with a firm grasp of the ideas of another Viennese exile, the art historian Ernst Gombrich, whose seminal 1960 work *Art and Illusion* examined the mechanics of the artistic response. One might say that Kandel has taken up Gombrich's torch, moving from the psychology of perception to the actual mechanics of it.

Kandel understands, and explains, how the observer brings a lifetime of experience to the simple act of looking at a painting; how "mirror neurons" elicit empathy in the brain; how "we are not only inspired and seduced by art, but also mystified, startled, frightened, and even repulsed by it". And he knows where, in the brain's 1.5 kilograms of fat and water, all these responses are located. It is quite a ride, and a beautifully scenic one with extensive, excellent and apposite illustrations.

Some of his arguments might be seen as contentious. Can our ideal of beauty really be hard-wired so that it has "varied surprisingly little from century to century or one culture to another"? (Has Kandel compared a seventeenth-century Rubens nude with 1960s Twiggy?) And is there really an adaptive advantage in our appreciation of art, or is it nothing more than a quirky by-product of a complex, self-conscious mind? But by and large, you go along with Kandel, because he simply knows so much.

Yet he would be the first to agree that this area of neuroscience is in its infancy. Marrying the sciences and humanities is a worthwhile undertaking, but Kandel admits what any serious observer of art will feel — that even when you have explained every neuron, every synapse, every glimmer in the amygdala or flicker in the prefrontal cortex, you still won't have explained what it is actually like to stand in front of a Klimt or Kokoschka and feel the thrill. That is to do with consciousness, or what Kandel calls introspective experience: "a phenomenon not readily accessible to objective scientific enquiry". I suspect that, even with the best neurobiology in the world, we will never be able to understand that. ∎

Simon Mawer *is a writer based in Rome. His latest book is* The Girl Who Fell From The Sky *(Trapeze in the United States). e-mail: simonmawer@tiscali.it*
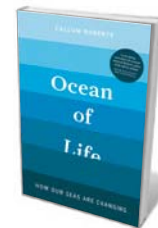
Ultra marine

Stephen R. Palumbi finds both stark warnings and buoyant optimism in an encyclopaedic take on the state of the oceans.

The floating head of Prince Charles, 5 metres tall, chided us about global overfishing. On a February morning in Singapore, at the World Oceans Summit, Charles's video highlighted a sobering fact: in the past decade, marine scientists have uncovered a growing list of serious problems that face the world's oceans. In *Ocean of Life*, Callum Roberts charts these troubled waters.

Roberts, a marine conservation biologist, dives beneath the often deceptively calm surface of our planet's great oceans to discover the agents of change, where they come from and the nature of their impact — as well as a range of pragmatic solutions. It is a story told with both scientific accuracy and narrative skill.

Roberts pulls no punches. In chapter after chapter of this encyclopaedic treatment, he summarizes the current scientific knowledge about crucial troubles facing the seas, almost all driven by humans. Pollution, acidification, shifting species ranges, the 'decapitation' of the marine food chain through over-exploitation of tuna and other predatory fish, invasions of species from other oceans, sedimentation, habitat destruction and more are laid out.

Overfishing is a much-documented issue, on which Roberts has focused his research career. More than one billion people depend on the ocean for food — and some can get animal protein only from the tiny fish left after decades of overfishing. The story of their unmet need is written here. Roberts gives us detailed personal tales, too, about the decline and fall of small fisheries such as the Firth of Clyde in Scotland; bigger-picture accounts look at why the British trawling fleet returns five times

Ocean of Life: How Our Seas Are Changing
CALLUM ROBERTS
Allen Lane/Viking: 2012. 400/416 pp. £25/$30

fewer fish now than it did 75 years ago.

This steady rain of sobering news is neither exaggerated nor minimized, and Roberts's clear, well-written accounts give us access to vast amounts of scientific information about ocean declines. Even in the realm of ocean conservation, scientists tend to specialize, and I know of no other volume that treats such divergent ocean issues as overfishing, decreasing pH, plastic pollution and biogeographic shifts with this much accuracy and acumen.

As a balance to the bad news, each chapter is edged with fascinating details about the life of the sea, such as how currents move through the deep oceans and what problems are caused by invasive marine species. Roberts's exuberance about the ocean bubbles to the surface: he delights in the historical context of how people have used the oceans. Even when he is describing the dire collapse of the tuna catch in the Mediterranean Sea, a historical description of garum (the infamous fermented fish sauce that was crucial to ancient Roman cuisine) creeps in.

Roberts deftly interweaves ocean facts with conversational whimsies, such as the only aphorism that Oscar Wilde got really wrong ("Nothing succeeds like excess"). And he occasionally offers a passage right from the heart; for instance, when he describes a squid's responses to a human encounter as "written on their skin in quick-fire color changes that pulse and

> ## CRUCIAL TROUBLES FACING THE SEAS ARE ALMOST ALL DRIVEN BY HUMANS.

↻ **NATURE.COM**
For more on ocean science and governance, see:
go.nature.com/ukvxur

ripple in incandescent waves".

Roberts's personal anecdotes bring the struggle of one scientist, in service of the sea, into sharp focus. I can just imagine his cheery face as he dressed down the head of the Marine Stewardship Council for sanctioning fisheries with questionable sustainability. I would like to have been there.

About two-thirds of the way through, with the statement "I am an optimist", Roberts starts to introduce solutions to his litany of seemingly intractable problems. In the subsequent chapters, he discusses aquaculture, pollution abatement and his signature research achievement: marine protected areas. These are all fields in which tremendous strides have been made, some by Roberts himself, to help the future oceans and the human communities that rely on them.

Yet Roberts cannot help pointing out that the problems are still huge. This is partly because some of the easiest apparent fixes — such as aquaculture — can do more harm than good in practice. But it may also be partly down to Roberts's need to keep the parlous state of the ocean in the public and governmental eye. Environmental problems can become so polarized in society that any excuse to downplay or deny them is trumpeted by special-interest groups — a reaction that surfaces with greater and greater frequency.

Back at the World Oceans Summit, Steve McCormick, president of the philanthropic Gordon and Betty Moore Foundation, declared that there has never been a time in ocean conservation like now, when the solutions to ocean problems are laid before us and some of the challenges, particularly overfishing, are conquerable. *Ocean of Life*, in detailing sobering facts about the ills that afflict the largest biosphere on Earth, is a call to action. At the heart of this book is a deep love of the ocean and a profound concern for its viability as a resource for us all. ∎

Stephen R. Palumbi *is a marine biologist at Stanford University in Pacific Grove, California. His most recent book, with Carolyn Sotka, is* The Death and Life of Monterey Bay.
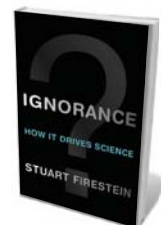*e-mail: spalumbi@stanford.edu*

What we don't know

Michael Shermer enjoys a reminder that cutting-edge research is a step into the unknown.

At a press conference in 2002, Donald Rumsfeld, then US secretary of defence, used epistemology to explain US foreign entanglements and their unintended consequences. "There are known knowns; there are things we know we know. We also know there are known unknowns; that is to say, we know there are some things we do not know. But there are also unknown unknowns, the ones we don't know we don't know," he said.

It is this last category that is the focus of Stuart Firestein's sparkling and innovative look at ignorance, and how it drives the scientific process. Firestein is a neurobiologist at Columbia University in New York, where he teaches a wildly popular course on ignorance, inviting scientists to tell students not what they know, but what they don't. He muses, would you rather earn an A or an F in a class called Ignorance?

Ignorance: How it Drives Science
STUART FIRESTEIN
Oxford University Press: 2012. 256 pp. £14.99, $21.95

Firestein introduces the concept of ignorance by contrasting the public's perception of science — as a systematic process — with a scientists' understanding that it is more haphazard. Most people think of science as a stepwise algorithm, in which researchers grind through experiments that churn out data sets that are analysed statistically and published in peer-reviewed journals: part of an endless cycle of observation, hypothesis testing and adjustment.

In reality, as mathematician Andrew

MARTIN O'NEILL

Changing Planet, Changing Health: How the Climate Crisis Threatens Our Health and What We Can Do About It
Paul R. Epstein and Dan Ferber (University of California Press, 2012; $24.95)
Public-health expert Paul Epstein and science journalist Dan Ferber confront an under-recognized and crucial issue: the effects of climate change on health. Too great a focus on immediate concerns, such as cost, is threatening the planet's basic life-support systems, they argue. Reviewer Tony McMichael called it "an excellent corrective for climate-change myopia" (*Nature* **472,** 292–293; 2011).

ripple in incandescent waves".

Roberts's personal anecdotes bring the struggle of one scientist, in service of the sea, into sharp focus. I can just imagine his cheery face as he dressed down the head of the Marine Stewardship Council for sanctioning fisheries with questionable sustainability. I would like to have been there.

About two-thirds of the way through, with the statement "I am an optimist", Roberts starts to introduce solutions to his litany of seemingly intractable problems. In the subsequent chapters, he discusses aquaculture, pollution abatement and his signature research achievement: marine protected areas. These are all fields in which tremendous strides have been made, some by Roberts himself, to help the future oceans and the human communities that rely on them.

Yet Roberts cannot help pointing out that the problems are still huge. This is partly because some of the easiest apparent fixes — such as aquaculture — can do more harm than good in practice. But it may also be partly down to Roberts's need to keep the parlous state of the ocean in the public and governmental eye. Environmental problems can become so polarized in society that any excuse to downplay or deny them is trumpeted by special-interest groups — a reaction that surfaces with greater and greater frequency.

Back at the World Oceans Summit, Steve McCormick, president of the philanthropic Gordon and Betty Moore Foundation, declared that there has never been a time in ocean conservation like now, when the solutions to ocean problems are laid before us and some of the challenges, particularly overfishing, are conquerable. *Ocean of Life*, in detailing sobering facts about the ills that afflict the largest biosphere on Earth, is a call to action. At the heart of this book is a deep love of the ocean and a profound concern for its viability as a resource for us all. ∎

Stephen R. Palumbi *is a marine biologist at Stanford University in Pacific Grove, California. His most recent book, with Carolyn Sotka, is* The Death and Life of Monterey Bay.
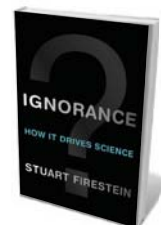*e-mail: spalumbi@stanford.edu*

PHILOSOPHY

What we don't know

Michael Shermer enjoys a reminder that cutting-edge research is a step into the unknown.

At a press conference in 2002, Donald Rumsfeld, then US secretary of defence, used epistemology to explain US foreign entanglements and their unintended consequences. "There are known knowns; there are things we know we know. We also know there are known unknowns; that is to say, we know there are some things we do not know. But there are also unknown unknowns, the ones we don't know we don't know," he said.

It is this last category that is the focus of Stuart Firestein's sparkling and innovative look at ignorance, and how it drives the scientific process. Firestein is a neurobiologist at Columbia University in New York, where he teaches a wildly popular course on ignorance, inviting scientists to tell students not what they know, but what they don't. He muses, would you rather earn an A or an F in a class called Ignorance?

Ignorance: How it Drives Science
STUART FIRESTEIN
Oxford University Press: 2012. 256 pp.
£14.99, $21.95

Firestein introduces the concept of ignorance by contrasting the public's perception of science — as a systematic process — with a scientists' understanding that it is more haphazard. Most people think of science as a stepwise algorithm, in which researchers grind through experiments that churn out data sets that are analysed statistically and published in peer-reviewed journals: part of an endless cycle of observation, hypothesis testing and adjustment.

In reality, as mathematician Andrew

Changing Planet, Changing Health: How the Climate Crisis Threatens Our Health and What We Can Do About It
Paul R. Epstein and Dan Ferber (University of California Press, 2012; $24.95)
Public-health expert Paul Epstein and science journalist Dan Ferber confront an under-recognized and crucial issue: the effects of climate change on health. Too great a focus on immediate concerns, such as cost, is threatening the planet's basic life-support systems, they argue. Reviewer Tony McMichael called it "an excellent corrective for climate-change myopia" (*Nature* **472,** 292–293; 2011).

Wiles says in the book, science consists of "groping and probing and poking, and some bumbling and bungling". A switch is discovered and a light comes on. It is like looking for the proverbial black cat in a dark room.

It is in the dark that cutting-edge science takes place. To make discoveries, researchers need to look beyond the facts — to where they run out, says Firestein. Scientists should "forget the answers, work on the questions". That is good advice, because the mountain of facts is now so vast that we cannot hope to learn, let alone remember, them.

It has been estimated that, from the beginning of civilization — 5,000 years ago or more — until 2003, humanity created a total of five exabytes (billion gigabytes) of information. From 2003 to 2010, we created this amount every two days. By 2013, we will be doing so every ten minutes, exceeding within hours all the information currently contained in all the books ever written.

So it isn't that we need more knowledge; it is that we need to distinguish between what we know and what we don't know, through what Firestein calls "controlled neglect". Researchers must selectively ignore vast quantities of facts and data that block creative solutions, and focus on a narrow range of possibilities.

Ignorance includes an important discussion about scientific errors and their propagation in textbooks. I admit that I passed one on in my last book, *The Believing Brain* (Times Books, 2011): I repeated as gospel the 'fact' that the human brain contains about 100 billion neurons. Firestein reports that it is actually around 80 billion, and that the number of glial cells is an order of magnitude smaller than most textbooks state.

The 'neural spike' recorded by neuroscientists as a fundamental unit of brain activity, Firestein reminds us, is an artefact of our measuring devices and ignores other forms of neural activity. Even the famous and widely printed 'tongue map', which shows sweet flavours sensed on the tip of the tongue, bitter on the back and salt and sour

TO MAKE DISCOVERIES, RESEARCHERS NEED TO LOOK BEYOND THE FACTS.

on the sides, is wrong — the result of a mistranslation of a German physiology paper. These and other errors arise as a result of our lack of scepticism towards the knowledge we have.

To Rumsfeld's categories, Firestein adds one more: unknowable unknowns, or "things that we cannot know due to some inherent and implacable limitation". He puts history in this category, but I would not.

When history is defined as anything that happened before the present, it includes much of astronomy, geology, archaeology, palaeontology and evolutionary biology — fields with hypotheses that can be tested with as much rigour as experiments in the lab.

I worry, too, that too much emphasis on ignorance opens the door to creationists, climate deniers and others with political agendas who wish to challenge mainstream scientists. Acknowledging our ignorance is good, but we should also recognize the well-supported theories that science has confidently given us.

As scientific knowledge grows, so does our awareness of how much we don't know. "Ignorance works as the engine of science because it is virtually unbounded," explains Firestein, "and that makes science much more expansive". We should remember that when a sphere becomes bigger, the surface area grows. Thus, as the sphere of scientific knowledge increases, so does the surface area of the unknown. Firestein's book reminds us that it is at this interface that we can claim true and objective progress. ∎

Michael Shermer *is the publisher of* Skeptic *magazine, a monthly columnist for* Scientific American *and an adjunct professor at Claremont Graduate University in Claremont and Chapman University in Orange, California. e-mail: mshermer@skeptic.com*

Animal Architects
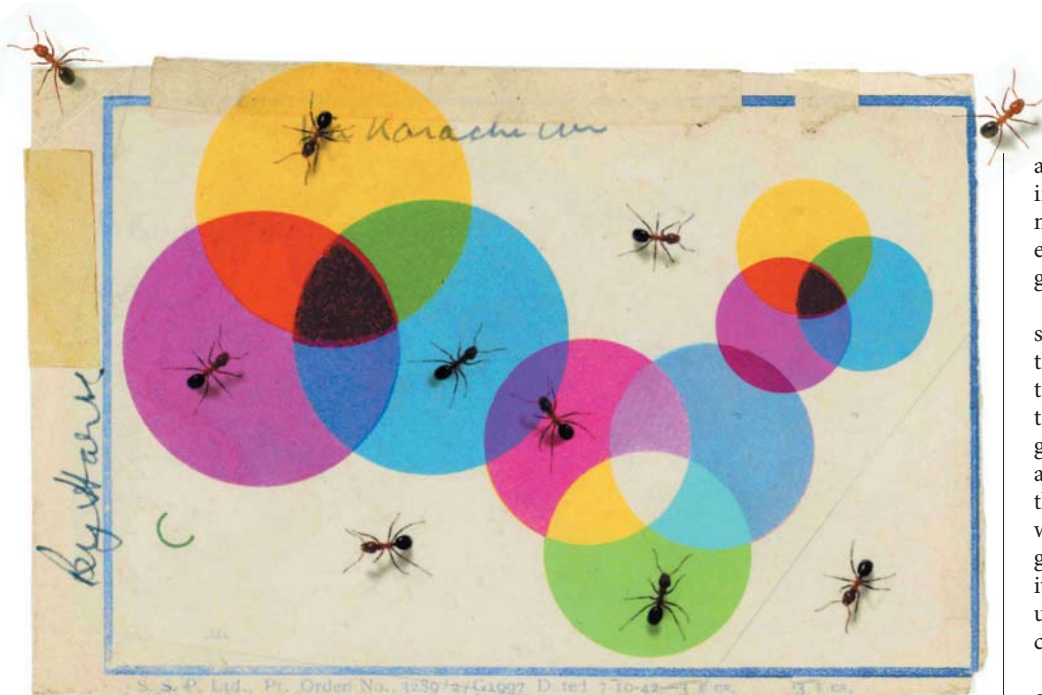*James L. Gould and Carol Grant Gould (Basic Books, 2012; $16.99)*
James and Carol Gould, an ethologist and a science writer, challenge the idea that a good builder needs a human brain. They show how the constructive skills of termites and birds become built in. (See Tore Slagsvold's review: *Nature* **446,** 730; 2007.)

Not Exactly: In Praise of Vagueness
Kees van Deemter (Oxford Univ. Press, 2012; £11.99)
Computer scientist Kees van Deemter makes the case for vagueness, saying that the idea of 'true' and 'false' statements defies classical logic because language is imprecise. (See Andrew Robinson's review: *Nature* **463,** 736; 2010).

BEHAVIOUR

Life interwoven

James H. Fowler applauds a master biologist's model of the evolution of sociality.
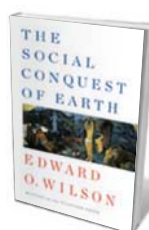
Biologist E. O. Wilson's brilliant new volume, *The Social Conquest of Earth*, could more aptly be entitled 'Biology's Conquest of Science'.

Drawing on his deep understanding of entomology and his extraordinarily broad knowledge of the natural and social sciences, Wilson makes a strong case for the synthesis of knowledge across disciplines. Understanding the biological origin of what makes us human can help us to build better theories of social and psychological interaction; in turn, understanding how other social species have evolved may help us to better understand the origin of our own.

But the main reason that Wilson's book is successful is that he also brings into biology the best of what social science has to offer. He draws on careful work in

linguistics, psychology, economics, religious studies and the arts to elaborate on differences between humans and other species. This give and take, this flow of ideas across disciplines, allows him to study an intriguing set of questions. Why did ants and humans both become social? What is it about being social that helped both species to achieve evolutionary success? And if it worked so well, why aren't all other species like us?

He answers these questions with a general theory about the origin of eusociality, the condition in which a species becomes so socially integrated that natural selection

The Social Conquest of Earth
EDWARD O. WILSON
*Liveright/Norton:*
2012. 352 pp.
$27.95/£18.99

acts on groups as well as individuals. The individual is still the unit of selection, but membership of the group confers such benefit that the individual evolves to act on the group's behalf instead of its own.

Wilson argues that eusociality arises in stages: first the formation of groups, then the development of tightly knit communities built around defensible nests and then the elimination of any desire to leave the group. Dense interactions create intense advantages for group membership, allowing the development of castes in insects (some of which lose the ability to reproduce) and language and culture in humans. At this point, it makes sense to think of the group as the unit of selection — a 'superorganism' — that competes with other groups.

Wilson's theory of eusociality is an elaboration of a paper that he published in *Nature* (M. A. Nowak *et al. Nature* **466**, 1057–1062; 2010). When that paper came out, I was struck by how little the authors discussed one of the key results: that population structure (who interacts with whom) is extremely important in evolution. In this book, Wilson rectifies this oversight, paying particular attention to the fact that humans "are enmeshed in social networks".

For example, Wilson's elegant model of natural selection shows that two populations with an identical set of individuals can favour completely different genetic outcomes with just small changes in their network of interactions. One network may drive the population to be highly cooperative; another may drive it to be highly individualistic. And not only do networks affect genes, but genes also affect networks. In *The Social Conquest of Earth*, Wilson cites work by social scientists Nicholas Christakis, Chris Dawes and myself showing that genetic variation between individuals accounts for a sizeable part of the variation in human social networks. His model suggests that these networks and our capacity to navigate them contribute to the uniqueness of our species.

Wilson contrasts his own model of eusociality with models of inclusive fitness that build on ideas originating in work on kin selection by British evolutionary biologist W. D. Hamilton. Hamilton's key insight was that a gene can survive either by helping an individual to reproduce or by helping

---

The Information: A History, a Theory, a Flood
James Gleick (Vintage, 2012; $15.95)
Science writer James Gleick unpicks our fixation on information as "the driver of just about everything", said reviewer Thomas Misa. Gleick starts with African 'talking' drums, sidesteps into genetics and cryptography, and ends with the modern information overload (*Nature* **471,** 300–301; 2011).
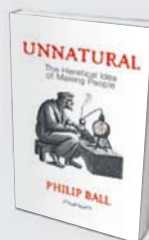
Unnatural: The Heretical Idea of Making People
Philip Ball (Vintage, 2012; £9.99)
Creating artificial people has been a human obsession from medieval ideas of homunculi to lab-created synthetic microbes, says science writer Philip Ball. But our own myths have bred distrust of 'unnatural' forms of life. (See Chris Mason's review: *Nature* **471,** 297–298; 2011.)

other individuals with the same gene to reproduce. So, a gene that promotes an action that is costly to the individual might be able to survive if it provides a benefit for a relative. And because close relatives share more of the same genes than distant ones, interactions between kin increase the likelihood of maintaining such acts of altruism.

Wilson argues that Hamilton's model is based on overly simplistic assumptions about population structure. It does not take into account indirect fitness advantages (all the people who are helped by the people we help, for example). Inclusive fitness is a special case of Wilson's model, but he asks: "Why not simply use the general theory everywhere?"

Many of Wilson's ideas in this book will stand the test of time. However, he is perhaps a bit too assertive in the way he frames his theory. He is excessively critical of inclusive fitness theory, repeatedly claiming that it is "incorrect", and saying that the literature on it has produced "meager" results. Yet inclusive fitness theory has prompted much empirical and theoretical investigation, with more than 1,000 articles published in the past 40 years. Albert Einstein, after all, didn't disparage the numerous physics experiments showing that Isaac Newton's simple formulae work remarkably well under specific conditions.

Wilson would, I am sure, object to this characterization on the grounds that inclusive fitness theory accounts for a much smaller subset of his own theory than Newton's work does for Einstein's. In fact, Wilson continually claims that inclusive fitness theory works only "under stringently narrow conditions". But there is no empirical evidence for this.

One of Wilson's laments is that we have few examples of attempts to specifically measure fitness and interaction networks to test inclusive fitness theory — but the same is true for his own theory. So whether the special case of inclusive fitness is a reasonable simplification remains an open question.

Fortunately, Wilson's provocative and important book gives us a new way to test this theory coherently. ∎

James H. Fowler *is professor of medical genetics and political science at the University of California, San Diego. e-mail: jhfowler@ucsd.edu*
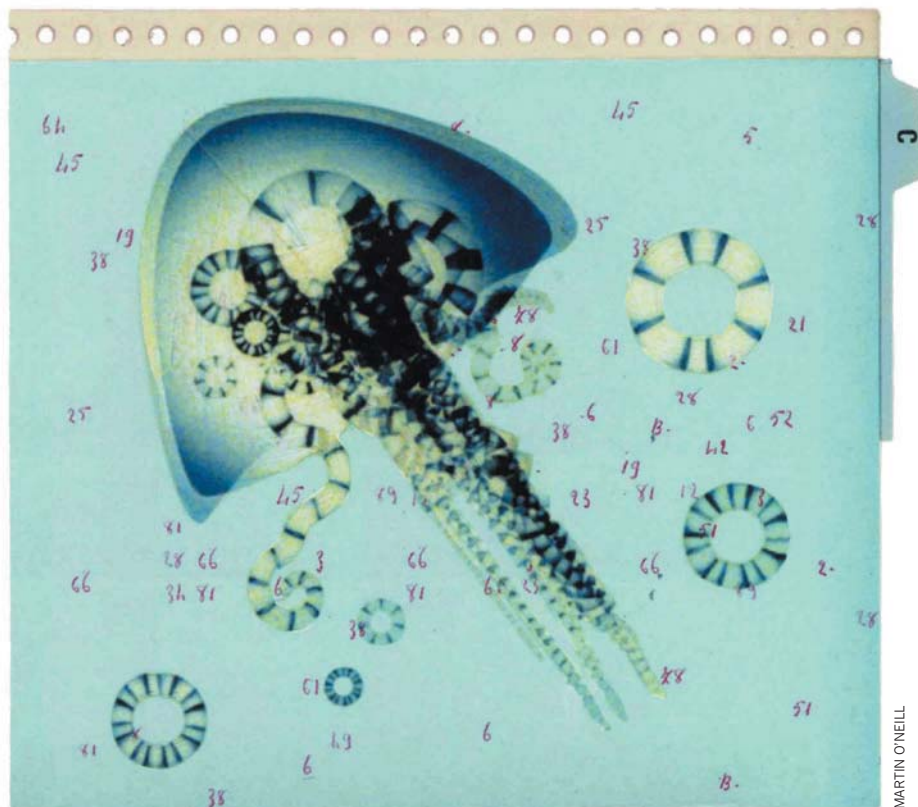
MARTIN O'NEILL

ROBOTICS

Enter the evolvabot

Noel Sharkey is engaged by a take on the intriguing overlap between biology and robotics.

A book on robotics by a marine biologist sounds a bit fishy, but *Darwin's Devices* is anything but. John Long takes us on a journey through the wonderful, oceanic world of research on the evolution of the vertebrae of extinct species.

Long's work is innovative because of his use — and strong defence — of modelling with physically embodied robots, rather than the usual software simulations of computational biology. He is also unusual, as a biologist, for the way that he exploits artificial evolutionary methods called genetic algorithms to test evolutionary hypotheses.
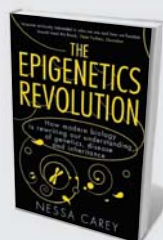

Darwin's Devices: What Evolving Robots Can Teach Us About the History of Life and the Future of Technology
JOHN LONG
Basic Books: 2012. 288 pp. $26.99, £17.99

Long's accounts of justifying his research to sceptical fellow biologists contain both triumphs and difficulties. He relates how, when a colleague asked what robots have to do with biology, he replied that they are

---

The Epigenetics Revolution
Nessa Carey (Icon Books, 2012; £9.99)
Epigeneticist Nessa Carey brings the emergent and controversial field of epigenetics to a wide audience. Carey's lively vision of how DNA works resembles a film script, with "plenty of room for interpretation and retakes", noted reviewer Jonathan Weitzman (*Nature* **477,** 534–535; 2011).

The Big Thirst: The Secret Life and Turbulent Future of Water
Charles Fishman (Free Press, 2012; $16)
In what reviewer Margaret Catley-Carson called a "torrential flow of a book", journalist Charles Fishman argues that we must value water. He shames overusers, praises heroes and sets out policy challenges (*Nature* **473,** 27–28; 2011).

used to model extinct species — and how he realized, "with dread", that the question would haunt his research. This book is his answer.

The opening chapters lay a solid foundation for the use of robots to model biological theories, underlining why testing models in the physical rather than the simulated world is important. In the rest of the book, Long describes a series of his experiments with the robots he dubs evolvabots. Each leads on to the next, adding only what is necessary to get to the next level: a virtue in any scientific model.

Long's chatty style made me laugh out loud at times. But beneath the levity lie robust and sometimes powerful arguments about biomimetics. He moves from his childhood love of fish to his graduate work on the bio-mechanics of marlin vertebral columns. He gives us an accessible run-through of evolution, then moves on to the design issues of engineering his evolvabots, including key decisions about which features of the animal to include. His guiding principle follows Albert Einstein's famous dictum to be as simple as possible, but no simpler.

The brain alone, Long shows, is not sufficient to explain behaviour. As he asks, "Who needs a brain when you have a smart body?" He argues that brainless robot bodies moving through the real world can exhibit seemingly complex cognitive behaviour with little computation. Few have demonstrated this point better than biological cyberneticist Valentino Braitenberg, in his book *Vehicles: Experiments in Synthetic Psychology* (MIT Press, 1984), and Long makes ample use of Braitenberg's core ideas. Robotics researchers such as Rolf Pfeifer, with his morphological computation, have carved out this territory, but Long offers new twists — such as questioning where the brain begins and ends.

By chapter six, sleeves rolled up, we are at the nub of the science. It is time for the test results of Long's key evolutionary hypothesis: "selection for enhanced feeding performance and predator avoidance would increase the number of vertebrae" for robot models of extinct fish. Long is in his stride here and gets down to the technicalities, telling us much about the real evolution of sea creatures.

I was intrigued to see how a biologist might use genetic algorithms to test specific hypotheses about bodily evolution and its impact on behaviour. Such algorithms have

MARTIN O'NEILL
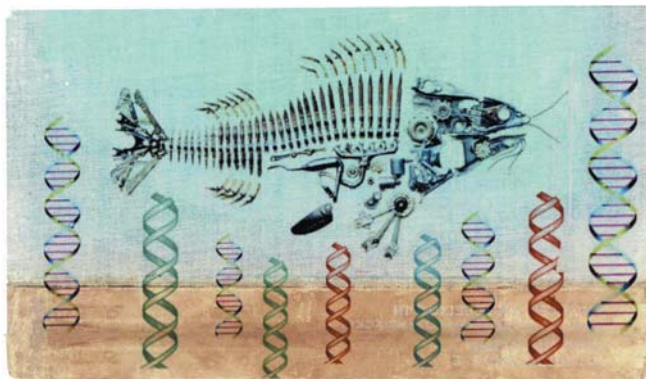
WHO NEEDS A
BRAIN
WHEN YOU HAVE A
SMART BODY?

been used widely in biologically inspired robotics to create artificial gene strings that determine how robots behave; they allow researchers to run through thousands of machine generations in hours. For each generation, the best robots are selected using a mathematical fitness function rather than natural selection, and their genes are incorporated to make the next generation and simulate breeding.

But in Long's experiments, the evolving artificial genes do not directly change the behaviour of the robot fish. Instead, they add vertebrae to the robot bodies, indirectly altering the behaviour of the robots to make them better at feeding and avoiding predators. This drives home Long's point that behaviour is created in the interaction between the physically embodied robot and the world.

There are minor problems with Long's discussion of genetic algorithms. He seems to think that they tell him more about evolution than may be the case. At one point, he writes: "I think Darwin, a keen observer, would have loved watching our robots evolve." But although Darwin would have been intrigued, I doubt he would have gained much scientifically from pure observation of these robots. Unlike natural selection, a genetic algorithm has an experimenter-designed fitness function, which demands a God-like decision about what features are important in choosing the fittest artificial gene strings.

Often, if a genetic-algorithm experiment does not work as hoped, we can make minor modifications to the fitness function and selection procedure until we get the desired results. So refuting a hypothesis is not always meaningful, because results can be dependent on the experimenter's design. A positive outcome, however, has different implications: if a genetic algorithm produces a simple model or mechanism that fits current data from a real creature, we have a scientific hit.

Aside from that, and a final chapter that tries to cram in too much — it includes 20 pages on the military uses of robotic fish, in which the arguments seem rushed and a little naive — this is a sound and hard-hitting work. It is also an insider's view of the scientific world: an honest account of the cut and thrust of academic ambition. Because Long questions his own methods and motivations throughout, his book lacks the pomposity of many texts that motivate through weak appeals to scientific method.

I read this book for the robotics, but I learned more about fish and the evolution of their bodies. *Darwin's Devices* represents a step forward in biomimetics. And, cleverly hidden among the discussions and the humour, gems of scientific philosophy shine. ∎

Noel Sharkey *is professor of artificial intelligence and robotics at the University of Sheffield, UK.*
e-mail: noel@dcs.shef.ac.uk
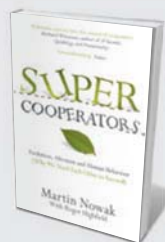
SuperCooperators
Martin Nowak with Roger Highfield (Canongate, 2012; $15)
In a treatment that reviewer Manfred Milinski said was as pacy as a novel, biologist Martin Nowak sets out cooperation as the driving force of evolution, and defends his objections to kin-selection theory (*Nature* **471,** 294–295; 2011).
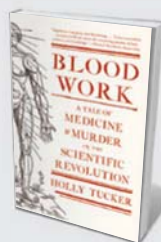
Blood Work: A Tale of Medicine and Murder in the Scientific Revolution
Holly Tucker (Norton, 2012; $15.95)
Medical historian Holly Tucker provides "page-turning insight" into the messy past of blood transfusions, focusing on Anglo-French rivalry during the scientific revolution, found reviewer W. F. Bynum (*Nature* **472,** 164–165; 2011).

FICTION

Wondrous machines

A multilayered tale centred on a nineteenth-century automaton grips **Minsoo Kang**.

Artificial beings throng myth and literature. Science fiction, for instance, has specialized in robots, androids and cyborgs — creatures often associated with a kind of high-tech utility. (The word 'robot', coined by the Czech writer and artist Josef Čapek, stems from the word for 'drudgery' in several Slavic languages.) Literary writers from Herman Melville to Thomas Pynchon, however, have been drawn more to automata, mechanical simulacra of living beings that proliferated in the eighteenth and nineteenth centuries, before electric and digital technology. Designed as devices of wonder and beauty, automata lend themselves to the aesthetic and symbolic.

Now, in his wonderful *The Chemistry of Tears*, Australian writer Peter Carey ponders the automaton through the eyes and thoughts of human characters. This multilayered novel follows the lives of two people separated in time but involved with one mechanical being — based on Jacques de Vaucanson's Defecating Duck, a famous eighteenth-century automaton. The book is dominated by the alternating narratives of the protagonists, a modern museum specialist and a Victorian father on a fraught personal quest, but the cast also includes an inventor with echoes of Charles Babbage — a nineteenth-century mathematician and engineer who restored automata as well as designing a proto-computer, the difference engine.

The Chemistry of Tears follows the Western tradition of using the automaton as a conceptual object for pondering the nature of humanity — a tradition now surfacing in debates about biological determinism and
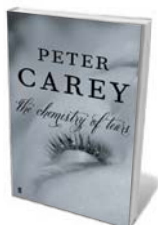
The Chemistry of Tears
PETER CAREY
Faber and Faber/ Knopf: 2012. 288 pp. £17.99/$26

free will, the nature of 'digitized' humans and bioengineered 'DNA robots'. Are we essentially organic automata constructed by some creator? Can we engineer self-aware artificial beings capable of experiencing emotions and making moral decisions? What part of our humanity lies beyond the material world and can never be replicated artificially? Rather than providing easy answers to such questions, Carey presents a narrative that demonstrates their complexity.

First, we meet Catherine Gehrig, a restorer of clocks at a London museum. While mourning the sudden death of her married lover, she is given the task of reassembling an automaton, a nineteenth-century replica of Vaucanson's duck. The parts are presented to her along with the notebooks of Henry Brandling, who commissioned the device. Through Catherine's reading of Brandling's story we follow the second narrative, of his attempt to cheer his ailing son by travelling to Germany and finding a mechanic to recreate Vaucanson's automaton.

The real Defecating Duck was an astonishingly lifelike device with hundreds of moving parts. It could flap its wings, eat and, as its name implies, even produce droppings. Vaucanson first presented it to the Parisian public in 1738, along with two mechanical human figures: the Flute Player and another playing a fife and drum. They were such a financial and intellectual success — praised by luminaries including Voltaire and Denis Diderot — that they set off a century-long automaton craze. The duck itself passed through the hands of multiple owners and toured Europe, until it ended up, dilapidated, in the German town of Helmstadt, where writer and physicist Johann Wolfgang von Goethe saw it in 1805.

Throughout the beautifully told stories of Catherine's grief and Henry's quest, Carey plays with the concept of the automaton metaphorically and symbolically. Catherine, in her distress, describes herself as a "whirring, mad machine", and later remembers how she and her lover had thought of themselves as "intricate chemical machines". The desperation of Henry's search stems from his hope that the recreation of Vaucanson's

DUCK: GETTY; ILLUSTRATION: MARTIN O'NEILL
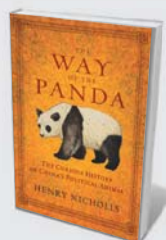
The Way of the Panda: The Curious History of China's Political Animal
Henry Nicholls (Pegasus Books, 2012; $15.95)
The panda's cultural history is interwoven with China's development as a global power. The beast's iconic status is double-edged: it is both conserved and hunted, says journalist Henry Nicholls. (See Jane Qiu's review: *Nature* **468**, 503–504; 2010.)
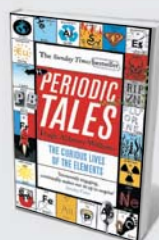
Periodic Tales: The Curious Lives of the Elements
Hugh Aldersey-Williams (Penguin, 2012; £9.99)
Science writer Hugh Aldersey-Williams's cultural history traces chemical elements that have gone in and out of fashion, such as aluminium — once favoured for royal tableware. (See Andrew Robinson's review: *Nature* **470**, 170–171; 2011).

animate duck could somehow heal his beloved son's ill body.

Catherine follows Henry's misadventures in Germany in her increasingly obsessive reading of his notebooks. His story takes a fairy-tale turn as he is led to Furtwagen, a small town in the Black Forest, by a mysterious man named Sumper, who claims to possess the skills to recreate the avian automaton. With a trio of eccentrics — a collector of fairy tales, a preternaturally gifted child and his superstitious mother — Henry listens sceptically to his host's fantastic story of his own travels to England.

In a brilliant narrative turn, Carey uses this third storyline — Sumper's time in England as assistant to Albert Cruickshank, the inventor based on Babbage — to meditate on the automaton as a concept that lies at the heart of modernity. Whereas Enlightenment devices were aesthetic objects demonstrating the wonders of mechanical craft, the technology of the Industrial Revolution was deployed pragmatically to create ever more powerful engines and productive factories, and to expand empires. The process of modernization took what was useful from the beautiful automata and created the world of steam, smoke and industrial machines.

Catherine's efforts to rebuild Sumper's automaton (which turns out to be a swan, in a possible nod to Hans Christian Andersen's *The Ugly Duckling*), and Henry's desire to present a marvel from the previous century to his son, represent a wish to return to untroubled pasts, and to bring the dead and dying back to life, that mirrors the automaton-maker's role in breathing 'life' into inert materials. This deeply moving, intellectually profound novel on the heartbreaking grief of 'living machines' tells the story of the essential human desire to return to the individual Edens that we inhabited before we knew about the unavoidable pain of our mechanical lives. ∎

Minsoo Kang *is associate professor of European history at the University of Missouri–St Louis and the author of* Sublime Dreams of Living Machines. *e-mail: kangmi@umsl.edu*

Trashed world

Sonja Vermeulen ponders two takes on the twinned global issues of consumption and waste.

Consumption drives economies but threatens human existence. Two books deal with this global issue in diametrically opposed ways. Ecologist Rob Hengeveld's *Wasted World* is a monumental *cri de coeur*, echoing ground-breaking 1970s thinking on the issue. But Pulitzer-prizewinning journalist Edward Humes' *Garbology* delivers hard facts and practical solutions.

The United States accounts for one-fifth of global consumption but only one-twentieth of the world's population. Humes focuses on how to reduce the average US citizen's lifetime legacy of 93 tonnes of refuse, using personal stories to draw out the wider social issues around waste management.

The usual approach, Humes observes, has been to make waste "appear to disappear". This is borne out by evocative examples such as the great Pacific garbage patch: not a continent-sized floating island of rubbish, as many imagine, but rather a "swirling sewer" of "barely visible particles circling endlessly". Humes shows how innovative clean-up technologies — such as an artificial 'beach' that collects fine marine debris but not sea life — can be part of the solution. But the more practical answer, he says, is to avoid creating the waste in the first place.

Reducing waste means consuming differently. Humes doesn't believe that profligate consumption is hard to shift. He sees humans as naturally thrifty, and points out that prodigious marketing has gone into creating modern consumer culture, down to the engineered 'preference' for plastic bags over paper

Wasted World: How Our Consumption Challenges the Planet
ROB HENGEVELD
Univ. Chicago Press: 2012. 360 pp. $30, £19.50

Garbology: Our Dirty Love Affair with Trash
EDWARD HUMES
Avery: 2012. 288 pp. £16.90, $27

ones. Not that Humes is anti-business: as in his book *Force of Nature* (HarperBusiness, 2011), he presents a balanced picture of the choices faced by major companies.

Key to Humes's 'can do' message are case studies of commercially successful innovations. Recycling company TerraCycle, for instance, was launched in 2001 by two students at Princeton University in New Jersey, who turned university food waste into organic fertilizer by feeding it to earthworms. Their start-up gained publicity from lawsuits lodged by a larger competitor contesting their advertising claims, even though they lost. TerraCycle is now one of the world's fastest-growing recycling firms.

Humes thinks that individuals can make a difference by simply saying no to unwanted stuff, and focusing on the cost of lifetime ownership rather than the purchase price. The pioneers of new attitudes towards waste, says Humes, are "ordinary people", not moralists or separatists. In this sense, his book is simultaneously reassuring and radical.

In *Wasted World*, Hengeveld's intellectual compass is firmly aligned with the powerful decades-old environmental rhetoric of thinkers such as environmentalist Donella Meadows (co-author of *The Limits to*

MARTIN O'NEILL

The Planet in a Pebble: A Journey into Earth's Deep History
Jan Zalasiewicz (Oxford Univ. Press, 2012; £9.99)
Palaeontologist Jan Zalasiewicz takes a pebble as the protagonist in a story of Earth's geology. He shows that even the most mundane piece of matter has a history that reaches across time and space to the beginning of the Universe.

Neutrino
Frank Close (Oxford Univ. Press, 2012; £7.99)
As you read this, you are being bombarded with neutrinos — the particle about which we know least. Physicist Frank Close recounts the hunt for the "commonest" and "weirdest" of the things that make up the Universe, and explains how following them could lead us to the farthest cosmos.

Growth; Universe Books, 1972) and population biologist Paul Ehrlich. Hengeveld argues that we are depleting resources and polluting the environment faster than human survival can bear — literally "wasting" the planet.

To his credit, Hengeveld squanders no space on using resources more efficiently in support of economic growth. He homes in on how the human population already exceeds Earth's capacity. His basic argument is convincing, but most of the book is a rambling litany on how we waste our world. When Hengeveld finally commits to how much Earth can carry — and gives one paragraph of solutions — he proposes that we reduce the population to less than one billion, through contraception and voluntary sterilization.

Aside from the plan's obvious difficulties, it points the finger at the populations that are growing fastest, not those consuming most. Indeed, Hengeveld says that 75% of Earth-threatening future population growth will be in "poor, non-developing countries". By contrast, the United Nations estimates that the least-developed countries (LDCs) will contribute around 38% of growth up to 2050.

More important is that the LDCs have an annual energy consumption of less than 500 kilograms of oil equivalent per capita, compared with 7,045 kg in the United States. So a Haitian or Ethiopian family of 14 uses less and pollutes less than a single US citizen.

Any serious discussion of planetary capacity must address this. Paul and Anne Ehrlich's most recent analyses give equal weight to population, inequality and power. But Hengeveld does not engage much with these ideas, nor with research that explores how a steady-state society might live, work, eat and govern.

One of Humes's interviewees suggests that the liberty at the heart of the American dream is a call to the financial freedom of reduced consumption, rather than bondage to belongings. Messages such as these — which Humes dubs "the new normal" — strike a chord in these times of recession, resource scarcity and uncertain futures. ∎

Sonja Vermeulen *is head of research at the Consortium of International Agricultural Research Centers' Program on Climate Change, Agriculture and Food Security, based in Copenhagen.*
*e-mail: s.vermeulen@cgiar.org*
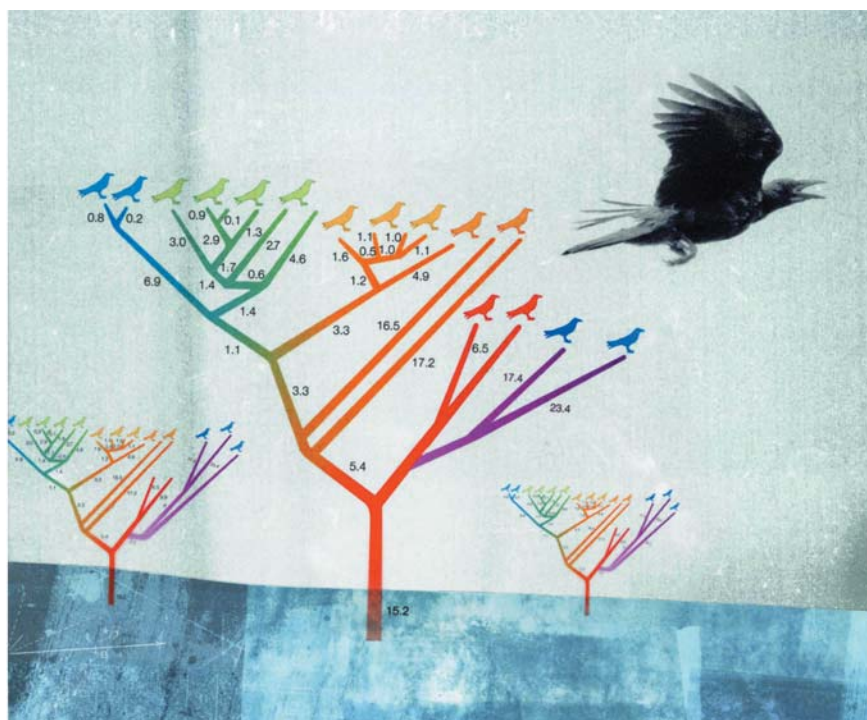
CORVID COGNITION

Feathered apes

Nicola Clayton is fascinated by the mind of the crow, and the bird's ancient links with humankind.

I have often wondered whether it is an evolutionary accident that our planet ended up being ruled by apes. What would it have been like to live on a planet of the crows, with humans serving as mere intellectual curiosities for our avian masters — those big-brained, beady-eyed, feathered apes?

The idea that these birds could be as intelligent as our primate cousins triggers mixed reactions. Dismissed by some as 'birdbrained', the corvids have an alien intelligence that disturbs others, who are reminded of Alfred Hitchcock's 1963 thriller *The Birds*. Yet a select few of us respect them. These few include John Marzluff and Tony Angell, whose delightful
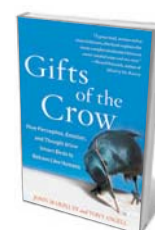
Gifts of the Crow: How Perception, Emotion and Thought Allow Smart Birds to Behave Like Humans
JOHN MARZLUFF AND TONY ANGELL
Free Press: 2012. 304 pp. $25, £15.97

Gifts of the Crow is their second book together on this *rara avis*, following *In the Company of Crows* (Yale University Press, 2005).

The authors argue that crows share seven striking similarities with humans: language, delinquency, frolic, passion, wrath, risk-taking and awareness including

---
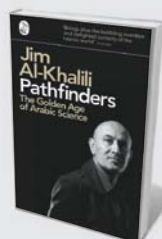
Pathfinders: The Golden Age of Arabic Science
Jim Al-Khalili (Penguin, 2012; £9.99)
Medieval Islam helped to shape science, and physicist Jim Al-Khalili describes the life and work of some of its great thinkers. These polymaths pioneered the study of refraction, were first to use inhalant anaesthetics and calculated the height of the atmosphere.
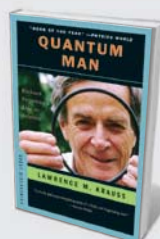
Quantum Man: Richard Feynman's Life in Science
Lawrence M. Krauss (Norton, 2012; $15.95)
An account of Feynman's science, this book documents the effort and insight informing work that fundamentally defined how we look at quantum theory. (See Leonard Mlodinow's review: *Nature* **471,** 296–297; 2011.)

insight such as gift-giving — hence the book's name. Might these similarities be behind corvids' strong associations with humans, and our endless curiosity about these ominous-looking creatures?

Marzluff, an avid ornithologist and wildlife scientist, and Angell, author and illustrator of award-winning natural history books, give us a series of intriguing stories and stunning illustrations that together reveal the sophisticated cognitive abilities of crows and their relationship with humans, which have inspired art, poetry, legend and myth. Anecdotes abound, interspersed with the science on crow behaviour and brains.

The authors persuasively describe the high intelligence of members of the crow family. They detail how corvids use and manufacture tools and show forethought, for instance by planning where to stash their food for tomorrow's breakfast. They have remarkable memories for where they have hidden their caches. The star of this show is surely the Clark's nutcracker (*Nucifraga columbiana*): this bird hides around 33,000 seeds in 6,000–7,000 locations in the autumn each year, and relies on its stunning spatial memory to recover them over the following winter and spring. Corvids devote much of their time to play — important, say Marzluff and Angell, because we "build better brains through play".

The authors relate many examples of corvid ingenuity. Renowned as devious tricksters, the birds can also be creative; for example, rooks have been observed using smouldering cigarette ends to smoke parasites out from under their wings. And thanks to a series of scientific experiments on the performance of rooks, jays and crows, we now know that Aesop's fable *The Crow and the Pitcher*, in which a bird used stones to raise the water level in a jug to quench its thirst, is fact rather than fiction.

This avian family is

also socially sophisticated, and its members go to great lengths to outsmart the competition in finding and protecting food. Jays, for example, keep track of which particular bird was watching when they hid their food, and take protective action to minimize the chance of these potential thieves stealing it. But they only do so if they themselves have been thieves. This reveals a complex

MIGHT CORVIDS' SIMILARITY WITH HUMANS BE BEHIND OUR ENDLESS CURIOSITY ABOUT THESE OMINOUS-LOOKING CREATURES?

form of social cognition called experience projection — in essence, putting yourself in someone else's shoes. Crows can even recognize individual humans and determine which are dangerous and which are not.

The intellectual capabilities of crows challenge assumptions about the uniqueness of the intelligence of humans and other apes. Cognition must have arisen independently in corvids and primates, because not all birds and mammals share their brainpower.

Furthermore, the architecture of the avian brain is distinct from that of the mammalian brain: it lacks the layered structure of the mammals' prefrontal cortex, which had long been thought to provide the unique machinery for intelligence. Bird brains have a nucleated structure, more like a fruitcake than the mammalian gateau. Crows, like apes, have

huge brains for their body size, with a massive expansion of the avian prefrontal cortex, as Marzluff and Angell eloquently describe.

Some corvids have formed a close association with humans, and they have featured in myths from around the world — to take just one example, the Nordic god Odin had wise raven companions, Huginn (thought) and Muninn (memory). In real life, the Tower of London is 'protected' by raven guardians. The birds' interactions with us can seem mischievous. At Paradise Lodge in Banff National Park, Canada, a raven named Herman is well known for his thievery, snatching bars of soap and packets of porridge from the hotel staff.

But in saying that crows share seven key characteristics with humans, Marzluff and Angell go a step too far, I would argue. Their argument seems informed by a leap of faith rather than fact. The evidence provided for these abilities is anecdotal and observational, rather than the result of a critical analysis and the scientific evaluation of alternative accounts. Although this is a popular book, I would welcome more emphasis on the scientific process, rather than a simple description of the most cognitive interpretation of the end result.

Yet the authors do provide intriguing examples that warrant further empirical, scientific evaluation. By alerting readers to these remarkable instances, they heighten our appreciation of the world of crows and argue that corvids have become something of an essential part of our lives — which "may be their greatest survival tool".

I hope this is so. In the United Kingdom, crows are classed as vermin — fair game that can be shot from the sky. If they are as intelligent as apes at physical and social problem-solving, then surely their status should be changed. ∎

Nicola Clayton *is the professor of comparative cognition in the Department of Experimental Psychology at the University of Cambridge, UK.*
e-mail: nsc22@cam.ac.uk

⟳ NATURE.COM
To read more about corvids:
go.nature.com/eikv7c

RAVEN: D. SCHAEFER/GETTY; ILLUSTRATION: MARTIN O'NEILL

Incoming! Or, Why We Should Stop Worrying and Learn to Love the Meteorite
Ted Nield (Granta, 2012; £9.99)
Geologist Ted Nield charts the history of rocks falling from the sky: from a meteorite worshipped by a Roman emperor to a shower 470 million years ago that coincided with a rise in biodiversity. (See Birger Schmitz's review: *Nature* **471,** 573–574; 2011.)
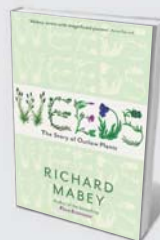
Weeds: The Story of Outlaw Plants
Richard Mabey (Profile, 2012; £8.99)
The concept of weeds is man-made, says naturalist Richard Mabey. By interweaving history, psychology, literature, art and plant biology, he has created a book of wide scope, wrote reviewer Sandra Knapp (*Nature* **467,** 1037; 2010).

Correspondence

Reaping the benefits of no–tillage farming

As president of the Howard G. Buffett Foundation, I am disappointed with the suggestion by Ken Giller, our partner in the nitrogen-fixation research programme N2 Africa, that the teaching of conservation agriculture in sub-Saharan Africa is "wholly misplaced" (*Nature* **483,** 525–527; 2012).

Millions of growers, large and small, are reaping the benefits of no-tillage farming. It is one of the most cost-effective ways to protect and improve soil — a farmer's most precious asset. It builds soil fertility by increasing biological activity, reducing the need for fertilizers and minimizing their effects on the environment. It also reduces soil erosion, improves water quality, increases crop yields, helps to sequester carbon and reduces labour.

No-tillage farmers are growing crops on roughly 111 million hectares worldwide, including 70% of farmland in Brazil and Argentina. At Brazil's agricultural-research organization Embrapa, no-tillage farming is helping to unlock the agricultural potential of the vast Cerrado savannah, fuelling economic growth.

There are challenges in teaching new practices to smallholder farmers, and much work is needed to adapt no-tillage farming to Africa's diverse agroecological and socioeconomic environments. But with the proper research, training and capacity, it will be one of many tools African farmers need to increase productivity sustainably.

Howard G. Buffett *Howard G. Buffett Foundation, Decatur, Illinois, USA.*
amk@hgbfoundation.org

Protect the DNA of museum specimens

We support Henry Nicholls' plea to unite museum exhibitions with behind-the-scenes research (*Nature* **484,** 36; 2012). But to avoid jeopardizing the scientific worth of collections, caution is needed if that research is done in molecular-biology laboratories under the same roof.

Museums store important, often irreplaceable, biological specimens. To protect the authenticity of their DNA, contamination must be prevented. Extraneous DNA amplified in a museum lab by the polymerase chain reaction can easily be transferred to collection storage areas unless strict safeguards are in place.

Protocols similar to those used for studying ancient DNA should be applied to the development and operation of molecular-biology labs within museums. For example, the labs should be in a separate building, with a one-way flow of people and consumables from the collection area to the lab.

Lara Shepherd, Leon Perrie *Museum of New Zealand Te Papa Tongarewa, Wellington, New Zealand.*
lara.shepherd@tepapa.govt.nz

China's bear farms prompt public outcry

Some 10,000 bears are farmed in China to procure their bile for traditional Chinese medicine. This cruel practice has stimulated a wave of condemnation across the country.

Bile is repeatedly collected from live bears through a surgically introduced opening into the bile duct, a procedure that is painful and distressing to the animals (see www.animalsasia.org). Some pharmaceutical companies use a variation of this technique that they say does not hurt the bears.

Even though the ursodeoxycholic acid found in bear bile has been available in synthetic form for decades, many wealthy patients prefer the natural product. Despite the disputed health benefits of bear bile, this has been an incentive for companies to promote bear farming.

The animal-welfare organization Animals Asia Foundation, headquartered in Hong Kong, has been a pioneer in challenging the bear-farming industry. It was recently accused of undermining traditional medical practices by the Chinese Association of Traditional Chinese Medicine. After 10 years of fighting alone, the foundation's work now has strong public backing. Many delegates at the National People's Congress last month declared that the industry should not be tolerated in a modern civilized society (see go.nature.com/vg96sd; in Chinese).

China needs to promote substitutes for bear bile through further campaigning and public education. Legislation should be introduced for an animal welfare bill, which might eventually lead to a ban on bear farming.

Xia Sheng, Haolin Zhang, Qiang Weng *College of Biological Sciences and Biotechnology, Beijing Forestry University, China.*
qiangweng@bjfu.edu.cn

Validate gene findings before telling donors

You report on recommendations that US biobanks should make participants in genome studies aware of incidental findings about their own DNA that might be medically relevant (*Nature* **483,** 373 and 387; 2012). But assigning participants access rights to research that is not validated could be putting the cart before the horse.

Incidental findings about an individual's gene variants need to be verified analytically before being returned to the DNA donor (S. M. Wolf *et al. Genet. Med.* **14,** 361–384; 2012). Even if a variant is accurately defined, further evidence of both clinical validity and utility are needed if its discovery is to be meaningful.

It would be irresponsible to follow the recommendation of Wolf *et al.* to communicate to the research subject the finding of one genotype variant when there may be hundreds of others related to the same phenotype, or when the phenotype varies with ethnic or environmental differences.

Investigations would be needed into whether evidence-based prevention or treatment is available for the particular gene finding, as well as into the reliability of genetic counselling based on complex, often ambiguous, risk information.

DNA donors should be informed that incidental findings must first be confirmed and translated into clinical application before information is communicated to them. We cannot side-step the process of proving clinical utility.

Mats G. Hansson *Centre for Research Ethics & Bioethics, Uppsala University, Sweden.*
mats.hansson@crb.uu.se

Enhance visibility of India's academies

Policy-makers must take bold measures to improve the standing of Indian science (*Nature* **484,** 159–160; 2012), but it is important that the country's scientists own up to their responsibility for the current state of affairs.

Take India's science academies. Because they wield little apparent influence on science, policy or society, they are largely invisible to scientists and to the public. Their relevance seems to be limited to making annual awards to a few scientists who publish their work in journals with high impact factors. It is time for these academies to wake up to the challenge and become scientifically and socially important.

Abhay Sharma *CSIR-Institute of Genomics and Integrative Biology, Council of Scientific and Industrial Research, Delhi, India.*
abhaysharma@igib.res.in

NEWS & VIEWS

FORUM: Immunology

Allergy challenged

An article suggesting that allergic responses may not be an accident of an off-target immune system, but rather a deliberate defence against potential harm, provokes the question of whether our understanding of allergy needs an overhaul. Immunologists provide their opinions. SEE PERSPECTIVE P.465

THE PAPER IN BRIEF

● Allergic responses replicate the immune reaction to parasites such as worms, and are therefore thought to arise from misdirected immune responses.

● Palm *et al.*[1] (page 465) propose instead that a range of allergic-type immune responses evolved as protection against environmental toxins, such as venom and irritants.

● The authors argue that allergies represent a subset of these responses that have been activated to excess.

● The idea of 'intentional' allergic reactions contradicts long-standing immunological dogma.

A multitasking defence

DAVID ARTIS & RICK M. MAIZELS

The prevalence of allergic diseases has reached pandemic proportions in industrialized countries. Although our understanding of the pathways that promote allergy is growing, we still lack good answers to two central conundrums. First, why did allergic responses evolve when they are so damaging to the human body? And second, what do such unlikely triggers as pollen, shellfish and snake venom have in common that provokes similar allergic responses? Palm and colleagues[1] suggest that allergic reactions have evolved both as a defence against foreign toxins and to promote hazard-avoidance behaviour in animals. These challenging ideas should provoke new thinking in this critical area of research.

Conventional wisdom holds that allergic responses, which are mobilized by an arm of the immune system referred to as T_H2 immunity, are the body's first line of defence against macroparasites such as helminth worms and biting arthropods, and that these stimuli have provided the evolutionary driving force to maintain allergy (Fig. 1). However, a small but consistent body of literature has also highlighted the role of T_H2-associated immune cells in neutralizing venom from biting animals[2]. Palm *et al.* have developed this concept to suggest that allergic responses neutralize not only toxins but also other small-molecule chemicals and irritants that damage host tissues. Indeed,

tissue damage might be the unifying trigger for allergy to diverse stimuli. In this context, both environmental toxins and helminth-derived products may share the capacity to elicit the positive effects of T_H2-associated responses — those of wound-healing and tissue repair.

One argument for the appropriateness of allergy in dealing with a multitude of chemical challenges is the speed of the severe allergic response known as anaphylaxis — if a paralysing venom is introduced, time is of the essence. However, the immune system must also race against the clock when parasites first penetrate the body's surface barriers, to prevent them from spreading through the bloodstream.

It is interesting to consider when and how allergic mechanisms evolved. Notably, mammals developed certain immune characteristics that promote allergic reactions, such as IgE antibodies and some granulocyte cells, whereas birds and reptiles lack this allergic 'machinery'. Furthermore, the triggers of allergy almost exclusively originate from eukaryotic organisms (such as plants, animals and fungi): only 1% of known allergens are derived from bacterial organisms. If allergy had evolved primarily to neutralize broad classes of toxins, one might expect these groups of organisms to elicit allergic responses in equal measure. Thus, although a multitude of stimuli provoke allergic responses, it is hard to abandon the hypothesis that allergy is, at least in part, a misdirected anti-macroparasite response.

These considerations bring us no closer to answering the second, and more perplexing, question: what do the several thousand diverse proteins that are known to be allergenic have in common? Palm and colleagues[1] suggest that

Figure 1 | The serpent or the worm? Historians have debated whether the Rod of Asclepius, a commonly used symbol of medicine, represents a venomous snake coiled around the Greek god of healing's staff, or the ancient tradition of using a stick to wind long parasitic guinea worms (*Dracunculus medinensis*) out of infected people's bodies. In a related debate, Palm *et al.*[1] propose that the immune pathways that now manifest themselves in allergy evolved not only to protect the host against parasites such as worms, as has long been thought, but also to combat a broad range of toxins, including venom.

this shared feature is their capacity to cause tissue damage. An alternative consideration is that all of the allergen families (such as plant storage proteins and pet dander) are also represented in macroparasites[3], such that our contemporary allergies to harmless proteins may have their roots in recognition of macroparasite-associated molecules. Consistent with this hypothesis, shared protein families can be found in venom, parasite secretions and the saliva of biting arthropods[4].

Collectively, these findings support a scenario in which the evolutionary pressure to maintain allergic mechanisms is their capacity to forestall tissue damage from either biological or chemical agents. Palm and colleagues have clearly advanced our thinking in this shadowy area of immunology, and their ideas should provoke studies to delineate how diverse stimuli, through common or distinct mechanisms, promote allergic responses.

David Artis *is in the Department of Microbiology and the Institute for Immunology, Perelman School of Medicine, University of Pennsylvania, Philadelphia, Pennsylvania 19104, USA.* Rick M. Maizels *is at the Institute of Immunology and Infection Research, University of Edinburgh, Edinburgh EH9 3JT, UK.*
e-mails: dartis@mail.med.upenn.edu; rick.maizels@ed.ac.uk

The price we pay

FRED D. FINKELMAN

Palm and colleagues[1] propose that allergic responses are important for host defence against noxious environmental substances and that they evolved to promote avoidance of suboptimal environments. They suggest that the sensitivity and rapidity of the allergic response, together with the great diversity of known allergens, argue against the possibility that host protection against worm and insect macroparasites can fully explain the evolution of allergy. However, I believe that protection against macroparasites can explain all the characteristics of allergic responses, including those[2] that protect against toxins.

Allergic responses involve components of both the innate immune system, which generates inflammatory responses against certain classes of pathogen, and the adaptive immune system, which targets specific pathogens following infection. Immunologically naive animals already have the allergy-associated cells of the innate system, which include eosinophils, mast cells and basophils. By contrast, exposure to an allergen or pathogen is required to activate the adaptive allergic response, which includes the production of antibodies of the IgE class and cytokine proteins that enhance antiparasite activity[2]. Host protection against toxins and other inanimate stressors, however, is accomplished by innate immunity only[5]. In fact, IgE antibodies to these molecules increase the risk of inducing deleterious allergy[6]. If adaptive allergic-type responses had evolved to clear toxins also, advantageous involvement of IgE antibodies in these responses would be expected.

Contrary to the argument presented by Palm and colleagues[1], the great sensitivity and rapidity of the allergic response can promote host protection against multicellular parasites, particularly during a repeat infection with a specific parasite. For example, an animal that has previously been infested with a tick may generate tick-specific IgE antibodies that can trigger an allergic response if it is again infected by a tick of the same species. This response includes rapid activation of mast cells and basophils, which secrete products that cause swelling and

fluid accumulation under the skin, making it difficult for the tick to invade[7]. Additionally, IgE-dependent rapid expulsion of some worms can inhibit parasite migration and accumulation that could severely injure the host's brain, lungs and other essential organs[8].

Although these allergic-type responses can cause 'bystander' damage to the host, they have a net protective effect. The cytokines produced by parasite-activated immune cells not only promote parasite expulsion, but also neutralize parasite toxins and promote healing of affected cells and tissues[9,10]. It is not surprising that some of these same mechanisms can also protect against other chemical hazards, but this does not mean that they evolved to do so.

This leaves the issue of how so many substances of diverse structure and function can act as allergens. The simplest answer is that an IgE response can be induced by any foreign protein that induces inflammation without stimulating production of large amounts of cytokines that suppress allergy, such as IL-12. Worms, insects and potent allergens are particularly good inducers of such inflammatory responses, and indeed often actively suppress IL-12 production.

This evidence that the adaptive immune system is required and uses the same mechanisms to protect against macroparasites and to induce allergy, but is not required to protect against noxious environmental agents, suggests that immunity against macroparasites and allergic disorders co-evolved, without the influence of other toxins. Worm infections in vertebrates, which actually suppress allergic responses, were common during the hundreds of millions of years of evolution and should

have provided a selective pressure in favour of the evolution of allergic-type adaptive immunity to macroparasites. Now, however, the low prevalence of worm infections in humans in developed societies is revealing the deleterious potential of these co-evolved allergic responses.

Finally, I am aware of no evidence that the non-allergic majority of individuals are less protected against toxins and other inanimate stressors than allergic individuals, as would be expected if adaptive allergic responses protected against such agents. Taken together, these observations suggest that allergy is indeed the price we pay for the evolution of protection against multicellular parasites. ∎

Fred D. Finkelman *is in the Department of Medicine, Cincinnati Veterans Affairs Medical Center, Cincinnati, Ohio 45220, USA, and in the Department of Internal Medicine, University of Cincinnati College of Medicine, and the Division of Cellular and Molecular Immunology, Cincinnati Children's Hospital Medical Center.*
e-mail: ffinkelman@pol.net

1. Palm, N. W., Rosenstein, R. K. & Medzhitov, R. *Nature* **484**, 465–472 (2012).
2. Akahoshi, M. *et al. J. Clin. Invest.* **121**, 4180–4191 (2011).
3. Fitzsimmons, C. M. & Dunne, D. W. *Trends Parasitol.* **25**, 447–451 (2009).
4. Valenzuela, J. G. *et al. J. Exp. Biol.* **205**, 2843–2864 (2002).
5. Finkelman, F. D. *et al. Annu. Rev. Immunol.* **15**, 505–533 (1997).
6. Hoffman, D. R., Wood, C. L. & Hudson, P. *J. Allergy Clin. Immunol.* **71**, 193–196 (1983).
7. Matsuda, H. *et al. J. Immunol.* **144**, 259–262 (1990).
8. Owor, R. & Wamukota, W. M. *Trans. R. Soc. Trop. Med. Hyg.* **70**, 497–499 (1976).
9. Herbert, D. R. *et al. J. Immunol.* **184**, 6438–6446 (2010).
10. Chen, F. *et al. Nature Med.* **18**, 260–266 (2012).

DEVELOPMENTAL BIOLOGY

Heart under construction

Developing organs adapt dynamically to meet the changing needs of a growing organism. A study in zebrafish reveals surprising patterns of muscle growth that reshape the heart as it matures. SEE ARTICLE P.479

DEBORAH YELON

Remodelling a developing organ without halting its functions must be as challenging as renovating a building without evacuating its occupants. How does the simple structure of an embryonic heart change into the complex architecture of the powerful adult organ? It is easy to imagine a simple model in which the heart grows through steady, gradual expansion, with many cells proliferating and contributing equally. However, the reality

seems to be more complex, with considerable delegation of labour to small subpopulations of cells. On page 479 of this issue, Gupta and Poss[1] apply a sophisticated technique to track patterns of heart growth in zebrafish, and highlight that even a handful of cells can drive substantial changes in the shape of the organ.

Heart function depends on the specific dimensions of the heart chambers — the ventricles and atria that work in series to pump blood through the circulatory system. During organ development, the chambers must

David Artis *is in the Department of Microbiology and the Institute for Immunology, Perelman School of Medicine, University of Pennsylvania, Philadelphia, Pennsylvania 19104, USA.* **Rick M. Maizels** *is at the Institute of Immunology and Infection Research, University of Edinburgh, Edinburgh EH9 3JT, UK.*
e-mails: dartis@mail.med.upenn.edu; rick.maizels@ed.ac.uk

The price we pay

FRED D. FINKELMAN

Palm and colleagues[1] propose that allergic responses are important for host defence against noxious environmental substances and that they evolved to promote avoidance of suboptimal environments. They suggest that the sensitivity and rapidity of the allergic response, together with the great diversity of known allergens, argue against the possibility that host protection against worm and insect macroparasites can fully explain the evolution of allergy. However, I believe that protection against macroparasites can explain all the characteristics of allergic responses, including those[2] that protect against toxins.

Allergic responses involve components of both the innate immune system, which generates inflammatory responses against certain classes of pathogen, and the adaptive immune system, which targets specific pathogens following infection. Immunologically naive animals already have the allergy-associated cells of the innate system, which include eosinophils, mast cells and basophils. By contrast, exposure to an allergen or pathogen is required to activate the adaptive allergic response, which includes the production of antibodies of the IgE class and cytokine proteins that enhance antiparasite activity[2]. Host protection against toxins and other inanimate stressors, however, is accomplished by innate immunity only[5]. In fact, IgE antibodies to these molecules increase the risk of inducing deleterious allergy[6]. If adaptive allergic-type responses had evolved to clear toxins also, advantageous involvement of IgE antibodies in these responses would be expected.

Contrary to the argument presented by Palm and colleagues[1], the great sensitivity and rapidity of the allergic response can promote host protection against multicellular parasites, particularly during a repeat infection with a specific parasite. For example, an animal that has previously been infested with a tick may generate tick-specific IgE antibodies that can trigger an allergic response if it is again infected by a tick of the same species. This response includes rapid activation of mast cells and basophils, which secrete products that cause swelling and fluid accumulation under the skin, making it difficult for the tick to invade[7]. Additionally, IgE-dependent rapid expulsion of some worms can inhibit parasite migration and accumulation that could severely injure the host's brain, lungs and other essential organs[8].

Although these allergic-type responses can cause 'bystander' damage to the host, they have a net protective effect. The cytokines produced by parasite-activated immune cells not only promote parasite expulsion, but also neutralize parasite toxins and promote healing of affected cells and tissues[9,10]. It is not surprising that some of these same mechanisms can also protect against other chemical hazards, but this does not mean that they evolved to do so.

This leaves the issue of how so many substances of diverse structure and function can act as allergens. The simplest answer is that an IgE response can be induced by any foreign protein that induces inflammation without stimulating production of large amounts of cytokines that suppress allergy, such as IL-12. Worms, insects and potent allergens are particularly good inducers of such inflammatory responses, and indeed often actively suppress IL-12 production.

This evidence that the adaptive immune system is required and uses the same mechanisms to protect against macroparasites and to induce allergy, but is not required to protect against noxious environmental agents, suggests that immunity against macroparasites and allergic disorders co-evolved, without the influence of other toxins. Worm infections in vertebrates, which actually suppress allergic responses, were common during the hundreds of millions of years of evolution and should have provided a selective pressure in favour of the evolution of allergic-type adaptive immunity to macroparasites. Now, however, the low prevalence of worm infections in humans in developed societies is revealing the deleterious potential of these co-evolved allergic responses.

Finally, I am aware of no evidence that the non-allergic majority of individuals are less protected against toxins and other inanimate stressors than allergic individuals, as would be expected if adaptive allergic responses protected against such agents. Taken together, these observations suggest that allergy is indeed the price we pay for the evolution of protection against multicellular parasites. ∎

Fred D. Finkelman *is in the Department of Medicine, Cincinnati Veterans Affairs Medical Center, Cincinnati, Ohio 45220, USA, and in the Department of Internal Medicine, University of Cincinnati College of Medicine, and the Division of Cellular and Molecular Immunology, Cincinnati Children's Hospital Medical Center.*
e-mail: ffinkelman@pol.net

1. Palm, N. W., Rosenstein, R. K. & Medzhitov, R. *Nature* **484**, 465–472 (2012).
2. Akahoshi, M. *et al. J. Clin. Invest.* **121**, 4180–4191 (2011).
3. Fitzsimmons, C. M. & Dunne, D. W. *Trends Parasitol.* **25**, 447–451 (2009).
4. Valenzuela, J. G. *et al. J. Exp. Biol.* **205**, 2843–2864 (2002).
5. Finkelman, F. D. *et al. Annu. Rev. Immunol.* **15**, 505–533 (1997).
6. Hoffman, D. R., Wood, C. L. & Hudson, P. *J. Allergy Clin. Immunol.* **71**, 193–196 (1983).
7. Matsuda, H. *et al. J. Immunol.* **144**, 259–262 (1990).
8. Owor, R. & Wamukota, W. M. *Trans. R. Soc. Trop. Med. Hyg.* **70**, 497–499 (1976).
9. Herbert, D. R. *et al. J. Immunol.* **184**, 6438–6446 (2010).
10. Chen, F. *et al. Nature Med.* **18**, 260–266 (2012).

Heart under construction

Developing organs adapt dynamically to meet the changing needs of a growing organism. A study in zebrafish reveals surprising patterns of muscle growth that reshape the heart as it matures. SEE ARTICLE P.479

DEBORAH YELON

Remodelling a developing organ without halting its functions must be as challenging as renovating a building without evacuating its occupants. How does the simple structure of an embryonic heart change into the complex architecture of the powerful adult organ? It is easy to imagine a simple model in which the heart grows through steady, gradual expansion, with many cells proliferating and contributing equally. However, the reality seems to be more complex, with considerable delegation of labour to small subpopulations of cells. On page 479 of this issue, Gupta and Poss[1] apply a sophisticated technique to track patterns of heart growth in zebrafish, and highlight that even a handful of cells can drive substantial changes in the shape of the organ.

Heart function depends on the specific dimensions of the heart chambers — the ventricles and atria that work in series to pump blood through the circulatory system. During organ development, the chambers must
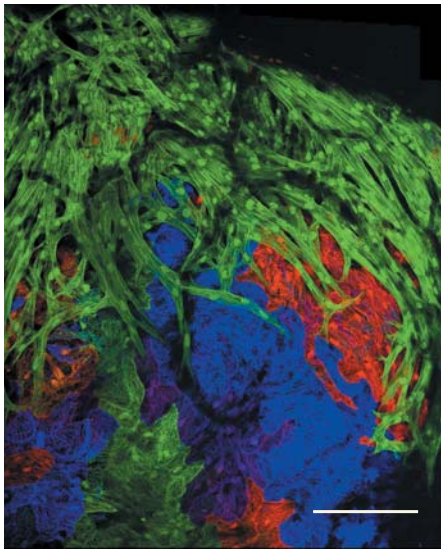
Figure 1 | A rainbow of cells. Gupta and Poss[1] monitored the descendants of individual cells during the development of the zebrafish heart by labelling them with fluorescent proteins of different colours. A high-magnification view of the heart shows how a cell lineage (green, top), derived from a single initial cell, expands over the surface of other cell lineages. Scale bar, 100 micrometres.

accommodate the increases in workload that accompany the increasing size of the organism and its circulatory system. Over time, the chambers enhance their functional capacity by expanding their volume and increasing their muscle mass[2].

Gupta and Poss[1] followed the growth of many individual cardiac cells during the development of the zebrafish heart. This could have been done by conventional clonal analysis[3], an approach that involves labelling a single cell at an early stage and assessing the number and distribution of its labelled progeny at a later stage. Reiteration of these experiments for many individual cells would ultimately reveal how the cells in the early heart contribute to the organ's enlargement over time. Although effective, this one-cell-at-a-time approach is inherently inefficient.

To circumvent the tedious nature of conventional clonal analysis, Gupta and Poss[1] took advantage of a recently developed technique, known as 'Brainbow', for the concurrent labelling of multiple cells. This method was first used[4] to analyse the interconnections of specific neurons in the complex networks of the brain. The Brainbow system marks individual cells with a broad palette of distinct colours that result from combinations of fluorescent proteins generated by gene recombination (Fig. 1). The authors[1] adapted this protocol to create vibrantly coloured mosaic hearts that facilitated simultaneous tracking of more than 20 individual cells within the zebrafish ventricle.

Initially, the embryonic zebrafish ventricle is simply a small, thin-walled balloon of muscle. It begins to add mass through a process called trabeculation[5,6], in which the peeling off of individual cells from the chamber wall seeds the growth of an internal meshwork of muscle (Fig. 2a). Next, as the embryo undergoes the transition into juvenile stages, the ventricle expands its surface area. Gupta and Poss[1] demonstrate that such surface-area expansion is driven by proliferation of a subset of cells from the embryonic wall, each of which creates a patch of tissue within the still-thin juvenile wall (Fig. 2b). Rather than having relatively uniform dimensions, these patches appear in an unexpectedly motley array of shapes and sizes, suggesting an element of competition between the cells that participate in wall expansion.

As juveniles mature into adult fish, the ventricular wall thickens substantially. The authors found, to their surprise, that this thickening does not result from proliferation of the juvenile wall but instead from a new layer of muscle generated by a small number of aggressively proliferating founder cells. These founder cells seem to arise from internal trabecular muscle and then break through the ventricular wall before instigating growth of large, thick blankets of muscle that encase the entire chamber (Fig. 2c). Both layers of the ventricular wall — the new outer layer, dubbed 'cortical muscle', and the original inner layer — persist in the adult heart. Moreover, the researchers report that both layers can participate in ventricular regeneration after an injury: the cortical portion contributes first to the injured area, and reconstructs the outer wall before the inner portion catches up and rebuilds the inner wall.

These unexpected findings — the mode of ventricular wall thickening, the small number of 'clonally dominant' founder cells, and the inside-out origin of the cortical muscle — encourage new ways of thinking about organ remodelling, even beyond the heart. The idea that just a few cells (with the right proliferative proclivities) can drive the construction of new organ features, whereas the remaining cells presumably focus on maintaining organ function, is an appealing one. It will be exciting to determine whether clonally dominant cells act to modify the architecture of other organs.

Notably, the current study[1] stops short of explaining the precise mechanisms that control cortical muscle formation in the zebrafish ventricle. What provokes particular trabecular cells to become the founders of the cortical layer? Is this triggered by the sensing of mechanical cues that result from changes in cardiac workload? How do founder cells manage to breach the ventricular wall, and what drives them to rapidly coat the chamber's exterior?

Studies of cortical muscle will undoubtedly provide fresh perspectives on heart growth, with potential significance for regenerative medicine. Previous research[7,8] has highlighted the possibility that heart regeneration may be triggered through manipulation of the cell cycle. So, it will be particularly interesting to determine which cell-cycle features confer the proliferative behaviour of the cortical layer and whether these properties are conserved among vertebrate species. The discovery of an unpredicted mechanism for chamber growth provides an eye-opening view on the complexities underlying organ architecture. ∎

Deborah Yelon *is in the Division of Biological Sciences, University of California, San Diego, La Jolla, California 92093-0347, USA.*
e-mail: dyelon@ucsd.edu

1. Gupta, V. & Poss, K. D. *Nature* **484,** 479–484 (2012).
2. Christoffels, V. M., Burch, J. B. & Moorman, A. F. *Trends Cardiovasc. Med.* **14,** 301–307 (2004).
3. Buckingham, M. E. & Meilhac, S. M. *Dev. Cell* **21,** 394–409 (2011).
4. Livet, J. *et al. Nature* **450,** 56–62 (2007).
5. Liu, J. *et al. Development* **137,** 3867–3875 (2010).
6. Peshkovsky, C., Totong, R. & Yelon, D. *Dev. Dyn.* **240,** 446–456 (2011).
7. Kikuchi, K. *et al. Nature* **464,** 601–605 (2010).
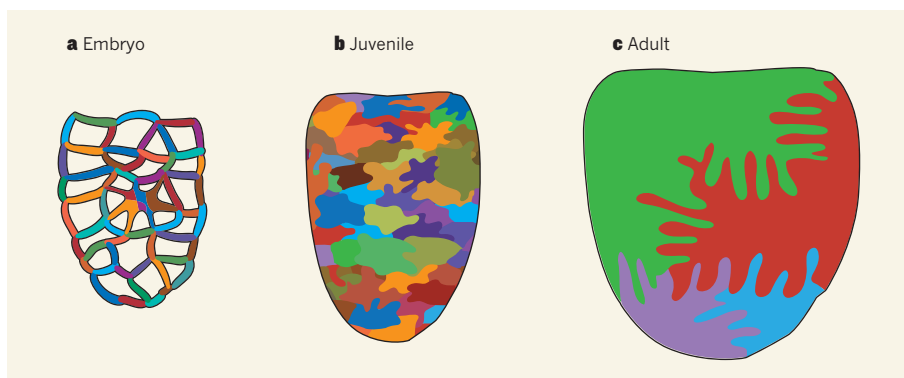8. Jopling, C. *et al. Nature* **464,** 606–609 (2010).

Figure 2 | Tracking cell lineages in the growing heart. Using a multicolour strategy for following the progeny of numerous individual cells simultaneously, Gupta and Poss[1] show the patterns of cell growth in the zebrafish heart. **a**, A section through the ventricle — one of the heart's chambers — of a zebrafish embryo reveals a thin outer wall and an internal meshwork of muscle. Different colours represent different cell lineages. **b**, The surface of the juvenile ventricle is an irregular patchwork of multiple lineages. **c**, The surface of the adult ventricle is encased by a thick cortical layer that is built by the proliferation of a few founder cells derived from the muscle meshwork.

QUANTUM PHYSICS

Simulating magnetism

Laser-excited oscillations of ion crystals can be used to make ions interact like magnetic quantum particles. This mechanism has now been demonstrated in a large, two-dimensional ion lattice. SEE LETTER P.489

CHRISTIAN ROOS

Studies of the oscillation of vibrating plates date back centuries. In the eighteenth century, the German physicist Ernst Chladni used small amounts of sand to visualize the vibrational modes of metallic plates that he excited with a violin bow[1]. Like Chladni's plates, a two-dimensional lattice of trapped ions exhibits a characteristic set of vibrational modes. In an experiment reported on page 489 of this issue, Britton et al.[2] excite vibrations in one such ion lattice and show that the vibrations generate forces between the ions that could be used to perform quantum simulations of magnetism.

What is the link between such lattice vibrations and quantum magnetism? Physical theories can provide a general framework for describing the essential interactions between the particles of a system in terms of simple equations. But it can be difficult to use the equations of a particular physical model to predict the phenomena that will emerge. Faced with this problem, researchers resort to computer simulations to explore the consequences of a model. In quantum physics, however, the computational run time needed to solve the equations grows exponentially with the number of particles in the system. So the simulation approach often fails, even for small systems comprising only a few dozen particles.

One way around this problem is to build a simulator made of quantum-mechanical elements, as pointed out by the American physicist Richard Feynman 30 years ago[3]. The challenge is to engineer a well-controlled quantum system in such a way that the interactions between its particles match the quantum-physical model to be simulated as closely as possible. Then, by manipulating and measuring the quantum system, insight could be gained into the physics of particular models. With the excellent quantum control that is now available for systems such as ultracold neutral atoms, trapped ions, photons and superconducting circuits, this idea has developed into an active research field over the past decade.

Quantum magnetism is an important example of models that present challenges to computer simulation. Particles that have a magnetic moment (spin) minimize their energy by either aligning or anti-aligning their spin orientation relative to each other, depending on the types of interaction between them.

Sometimes, not all of the interaction energies between pairs of particles can be minimized at the same time for any spin configuration. Predicting the properties of these 'spin-frustrated' systems is challenging for numerical simulations.

Proof-of-principle experiments for simulating quantum magnetism have been carried out using strings of ions trapped by means of radio-frequency fields[4–6]. In these studies, laser pulses are used to make the ions behave like interacting spins, where each ion encodes a spin and the spin orientation is stored as a superposition of two electronic states. Such experiments have taken a 'bottom-up' approach aimed at extending the quantum control demonstrated in two-ion experiments to larger numbers of ions, and they are currently run using up to 16 ions.

Britton et al.[2] take a different tack, one that opens up an avenue to performing simulations using hundreds of spins in a two-dimensional geometry. They use a Penning trap, a device that confines ions by means of a combination of magnetic and electric fields, to store about 300 beryllium ions. At low temperatures, the ions form a planar crystal in the shape of a triangular lattice that has inter-ion distances of about 20 micrometres.

To simulate magnetic interactions between the ions, Britton and colleagues make use of a technique developed in the radio-frequency electric-trap experiments, in which laser-induced vibrations of the ion crystal mediate ion–ion interactions. Because of the Coulomb repulsion between any two ions, the ions' motion around their positions at equilibrium is described by a set of vibrational modes (Fig. 1). By using a pair of precisely tuned laser beams that couples all of the ions, subtle vibrations of the crystal can be induced, with the magnitude of the vibrations being governed by the combined electronic states of the ions. Depending on the frequency of the lasers and the distance between the ions, the simulated ion spins either align or do not, thereby generating an effective magnetic interaction between the particles. In their study, Britton et al. demonstrate spin-dependent forces between the ions in this large ion array and control over the distance over which the forces act.

What is particularly exciting about the authors' work is the prospect of being able to couple many more ions than is currently possible using other techniques. Moreover, the two-dimensional crystal geometry available
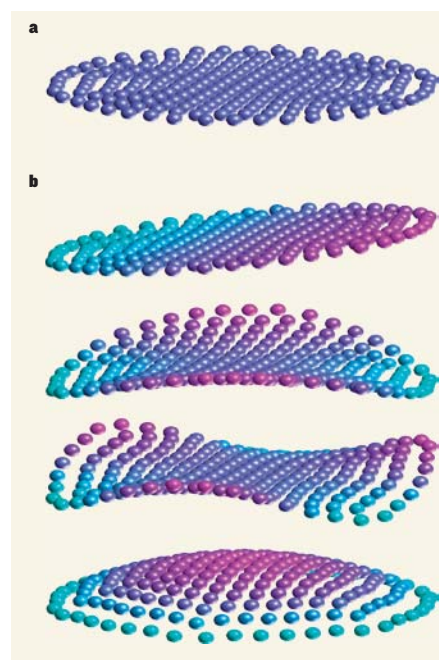
Figure 1 | Vibrational modes of a two-dimensional ion crystal. a, Equilibrium positions of the ions in a two-dimensional crystal after laser cooling. **b**, Four of the many vibrational modes of the crystal. Colours indicate whether an ion is above or below its equilibrium position at the particular time that is represented. Britton et al.[2] used laser pulses to induce such oscillations (although with much smaller amplitudes) and to simulate magnetic interactions between the ions.

in Penning traps provides a richer playground than the one-dimensional strings of ions that have been demonstrated in radio-frequency traps so far. But to bring the experiments into a regime in which numerical simulations cannot efficiently predict the outcome will require greater coupling strength between the ions, which at present is rather low. However, modifications to the current laser set-up should significantly enhance the coupling strength, and allow studies in the more interesting regime in which the coupling has a shorter range than in Britton and colleagues' experiments. Also, by installing a detection system that can measure the correlations between the ions, more insight may be gained into the interactions that are being generated during the experiment.

Future experiments using improved apparatus will provide a clearer picture of whether this is a viable approach for simulating quantum magnetism. Britton and colleagues' work is an encouraging first step towards many-particle quantum simulations that complements existing experiments based on other technologies[7–9]. ∎

Christian Roos is at the Institut für Quantenoptik und Quanteninformation, Österreichische Akademie der Wissenschaften, A-6020 Innsbruck, Austria.
e-mail: christian.roos@uibk.ac.at

1. Chladni, E. F. F. *Entdeckungen über die Theorie des Klanges* (1787).
2. Britton, J. W. *et al. Nature* **484**, 489–492 (2012).
3. Feynman, R. P. *Int. J. Theor. Phys.* **21**, 467–488 (1982).
4. Kim, K. *et al. Nature* **465**, 590–593 (2010).
5. Schneider, C., Porras, D. & Schaetz, T. *Rep. Prog. Phys.* **75,** 024401 (2012).
6. Blatt, R. & Roos, C. F. *Nature Phys.* **8**, 277–284 (2012).
7. Simon, J. *et al. Nature* **472**, 307–312 (2011).
8. Struck, J. *et al. Science* **333**, 996–999 (2011).
9. Ma, X., Dakic, B., Naylor, W., Zeilinger, A. & Walther, P. *Nature Phys.* **7**, 399–405 (2011).

ASTROPHYSICS

Stars throw their weight in old galaxies

The observation that old, massive galaxies have a larger fraction of low-mass stars than their younger, lower-mass counterparts adds to mounting evidence that star formation may have been different in the early Universe. SEE LETTER P.485

NATE BASTIAN

When a star is born, it can have a mass 0.1 to 100 times that of the Sun. This property controls a star's influence on its environment, its lifetime and even its ability to host habitable planets. The relative distribution of low- to high-mass stars in a newly formed population, known as the initial mass function (IMF), is crucial to determining the evolution of any cosmic structure made up of stars, from stellar clusters to galaxies. In the local Universe, where individual stars can simply be counted, the form of the IMF does not seem to vary from one environment to another[1]. But it is possible that in the early Universe the IMF had a different shape. On page 485 of this issue, Cappellari *et al.*[2] present evidence for a different IMF in some

of the oldest known objects — elliptical and lenticular galaxies. If true, this finding would have a drastic effect on our understanding of the Universe, from the formation and evolution of entire galaxies to the complex processes that shape the way that individual stars form.

Although we cannot normally observe individual stars in distant galaxies, the form of the IMF influences nearly every observable property of a galaxy. In most studies, the IMF is assumed to be universal — that is, the same as seen locally[3,4] — so that observable properties can be translated into physical ones. However, one can turn the problem around and ask what the properties of galaxies can tell us about the shape of the IMF. The light emitted by a galaxy is dominated by its high-mass stars, whereas the galaxy's mass is dominated by the much more numerous low-mass stars. Hence, if the mass and light can

be measured independently, this can provide a strong constraint on the form of the IMF.

This is precisely what Cappellari and colleagues have done. They used advanced instrumentation — specifically, integral-field spectroscopy — to measure the rotational and random motions of stars in elliptical and lenticular galaxies, as a function of their position in the galaxy (a lenticular galaxy is intermediate between an elliptical and a spiral one). The stars' motion is controlled by the galaxy's gravitational potential, which is related to the galaxy's mass. By comparing the derived mass with the total light emitted by the galaxy — the mass-to-light ratio — and accounting for the gravitational effects of dark matter, the authors showed that this ratio deviates systematically from that which would be expected if the IMF were universal.

The authors' results suggest that old, massive elliptical galaxies (Fig. 1a) have a larger fraction of low-mass stars than do younger, less-massive lenticular or spiral galaxies such as the Milky Way. Low-mass stars, although faint, account for the majority of stars within galaxies, and are the most likely potential hosts of habitable planets. Although this deviation had already been observed using independent techniques[5], it took the power of integral-field spectroscopy to eliminate the possibility that the deviations were caused by dark matter.

This is a surprising result, in part because a study[6] that used a similar technique on a sample of equally massive galaxies in the young Universe found that they had the same IMF as seen locally. However, Cappellari and colleagues' results[2] agree with a variety of other observations[5,7], adding to a growing chorus of claims that star formation may have been different in the early Universe.

The cause of this over-abundance of low-mass stars is unknown, especially given that studies of nearby stellar populations, in which stars can be easily identified, have not detected variations in the IMF (Fig. 1b). It is also difficult to understand why the IMF would be dependent on global galactic properties such as galaxy mass, as the authors suggest, when it does not seem to depend strongly on local ones[1], including stellar density and metal content.

If confirmed, these results would have far-reaching implications. Using the observed light of galaxies, and adopting some form of the IMF, researchers can estimate the rate at which stars are being born in distant galaxies, along with the total mass of all the stars in the galaxies. If the IMF is varying systematically as a function of environment, the conversion of observable properties to physical ones becomes much more complex. Uncertainty in the IMF is one of the main obstacles limiting our understanding of the evolution of galaxies and of the time during which most of the Universe's stars were formed.

However, a systematic variation in the IMF may provide us with our best chance to

Figure 1 | Viewing galaxies as collections of stars. a, Cappellari and colleagues' results[2] suggest that giant elliptical galaxies, such as NGC 1132, seen here, have a much higher fraction of low-mass stars than that seen in the local Universe. **b**, Peering into nearby stellar clusters such as 47 Tuc, shown here, reveals stars of different masses; low-mass stars are faint whereas higher-mass stars are bright red or yellow. If 47 Tuc had the same relative distribution of low- to high-mass stars as that suspected for NGC 1132, almost the entire background would be filled with stars.

1. Chladni, E. F. F. *Entdeckungen über die Theorie des Klanges* (1787).
2. Britton, J. W. *et al. Nature* **484,** 489–492 (2012).
3. Feynman, R. P. *Int. J. Theor. Phys.* **21,** 467–488 (1982).
4. Kim, K. *et al. Nature* **465,** 590–593 (2010).
5. Schneider, C., Porras, D. & Schaetz, T. *Rep. Prog.*
6. Blatt, R. & Roos, C. F. *Nature Phys.* **8,** 277–284 (2012).
7. Simon, J. *et al. Nature* **472,** 307–312 (2011).
8. Struck, J. *et al. Science* **333,** 996–999 (2011).
9. Ma, X., Dakic, B., Naylor, W., Zeilinger, A. & Walther, P. *Nature Phys.* **7,** 399–405 (2011).

Phys. **75,** 024401 (2012).

ASTROPHYSICS

Stars throw their weight in old galaxies

The observation that old, massive galaxies have a larger fraction of low-mass stars than their younger, lower-mass counterparts adds to mounting evidence that star formation may have been different in the early Universe. SEE LETTER P.485

NATE BASTIAN

When a star is born, it can have a mass 0.1 to 100 times that of the Sun. This property controls a star's influence on its environment, its lifetime and even its ability to host habitable planets. The relative distribution of low- to high-mass stars in a newly formed population, known as the initial mass function (IMF), is crucial to determining the evolution of any cosmic structure made up of stars, from stellar clusters to galaxies. In the local Universe, where individual stars can simply be counted, the form of the IMF does not seem to vary from one environment to another[1]. But it is possible that in the early Universe the IMF had a different shape. On page 485 of this issue, Cappellari *et al.*[2] present evidence for a different IMF in some

of the oldest known objects — elliptical and lenticular galaxies. If true, this finding would have a drastic effect on our understanding of the Universe, from the formation and evolution of entire galaxies to the complex processes that shape the way that individual stars form.

Although we cannot normally observe individual stars in distant galaxies, the form of the IMF influences nearly every observable property of a galaxy. In most studies, the IMF is assumed to be universal — that is, the same as seen locally[3,4] — so that observable properties can be translated into physical ones. However, one can turn the problem around and ask what the properties of galaxies can tell us about the shape of the IMF. The light emitted by a galaxy is dominated by its high-mass stars, whereas the galaxy's mass is dominated by the much more numerous low-mass stars. Hence, if the mass and light can

be measured independently, this can provide a strong constraint on the form of the IMF.

This is precisely what Cappellari and colleagues have done. They used advanced instrumentation — specifically, integral-field spectroscopy — to measure the rotational and random motions of stars in elliptical and lenticular galaxies, as a function of their position in the galaxy (a lenticular galaxy is intermediate between an elliptical and a spiral one). The stars' motion is controlled by the galaxy's gravitational potential, which is related to the galaxy's mass. By comparing the derived mass with the total light emitted by the galaxy — the mass-to-light ratio — and accounting for the gravitational effects of dark matter, the authors showed that this ratio deviates systematically from that which would be expected if the IMF were universal.

The authors' results suggest that old, massive elliptical galaxies (Fig. 1a) have a larger fraction of low-mass stars than do younger, less-massive lenticular or spiral galaxies such as the Milky Way. Low-mass stars, although faint, account for the majority of stars within galaxies, and are the most likely potential hosts of habitable planets. Although this deviation had already been observed using independent techniques[5], it took the power of integral-field spectroscopy to eliminate the possibility that the deviations were caused by dark matter.

This is a surprising result, in part because a study[6] that used a similar technique on a sample of equally massive galaxies in the young Universe found that they had the same IMF as seen locally. However, Cappellari and colleagues' results[2] agree with a variety of other observations[5,7], adding to a growing chorus of claims that star formation may have been different in the early Universe.

The cause of this over-abundance of low-mass stars is unknown, especially given that studies of nearby stellar populations, in which stars can be easily identified, have not detected variations in the IMF (Fig. 1b). It is also difficult to understand why the IMF would be dependent on global galactic properties such as galaxy mass, as the authors suggest, when it does not seem to depend strongly on local ones[1], including stellar density and metal content.

If confirmed, these results would have far-reaching implications. Using the observed light of galaxies, and adopting some form of the IMF, researchers can estimate the rate at which stars are being born in distant galaxies, along with the total mass of all the stars in the galaxies. If the IMF is varying systematically as a function of environment, the conversion of observable properties to physical ones becomes much more complex. Uncertainty in the IMF is one of the main obstacles limiting our understanding of the evolution of galaxies and of the time during which most of the Universe's stars were formed.

However, a systematic variation in the IMF may provide us with our best chance to

Figure 1 | Viewing galaxies as collections of stars. **a**, Cappellari and colleagues' results[2] suggest that giant elliptical galaxies, such as NGC 1132, seen here, have a much higher fraction of low-mass stars than that seen in the local Universe. **b**, Peering into nearby stellar clusters such as 47 Tuc, shown here, reveals stars of different masses; low-mass stars are faint whereas higher-mass stars are bright red or yellow. If 47 Tuc had the same relative distribution of low- to high-mass stars as that suspected for NGC 1132, almost the entire background would be filled with stars.

understand the details of the complex process of star formation[8]. Current numerical and theoretical models of star formation can reproduce the form of the IMF observed locally. One way to distinguish between this myriad of models is to see whether any can reproduce the types of variation reported by Cappellari and colleagues.

There is a long tradition of studies claiming that the IMF varies as a function of environment, especially in distant galaxies where individual stars cannot be identified directly and secondary tracers must be used. Most of these claims have fallen by the wayside when newer and better data became available, or as our understanding of the intricacies of the tracers has improved. However, the observations and analysis of Cappellari and colleagues[2] present a promising avenue that may

lead to fundamental changes in the way that we understand how stars form and galaxies evolve. ∎

Nate Bastian *is at the Excellence Cluster 'Universe', Technische Universität München, Garching 85748, Germany.*
e-mail: bastian@usm.lmu.de

1. Bastian, N., Covey, K. R. & Meyer, M. R. *Annu. Rev. Astron. Astrophys.* **48,** 339–389 (2010).
2. Cappellari, M. *et al. Nature* **484,** 485–488 (2012).
3. Kroupa, P. *Science* **295,** 82–91 (2002).
4. Chabrier, G. *Publ. Astron. Soc. Pacif.* **115,** 763–795 (2003).
5. Auger, M. *et al. Astrophys. J.* **721,** L163–L167 (2010).
6. Cappellari, M. *et al. Astrophys. J.* **704,** L34–L39 (2009).
7. Van Dokkum, P. G. & Conroy, C. *Nature* **468,** 940–942 (2010).
8. McKee, C. F. & Ostriker, E. C. *Annu. Rev. Astron. Astrophys.* **45,** 565–687 (2007).

PROTEIN ENGINEERING

Tighter ties that bind

A stepwise process of mutation and structural analysis has modulated a flexible binding interface of an immune–cell signalling protein, interleukin-2, and generated mutant proteins with enhanced anticancer activity. SEE ARTICLE P.529

ERIC T. BODER

Interleukin-2 is a cytokine protein that signals to cells of the immune system, such as T cells and natural killer cells, to regulate their growth, activation and differentiation. This multifaceted role means that interleukin-2 (IL-2) is the subject of intense investigation as a potential therapeutic agent to boost immune responses in the treatment of diseases such as cancer. On page 529 of this issue, Levin *et al.*[1] describe the engineering of enhanced versions of IL-2 that more potently stimulate T-cell proliferation and antitumour immune responses. The authors also provide a compelling structural explanation for the mutated proteins' superior activity.

The cell-surface receptor for IL-2 comprises three protein subunits: the IL-2 receptor α-chain (IL-2Rα, usually called CD25), the IL-2 receptor β-chain, and the common γ-chain (γ$_c$), which is shared by numerous cytokine receptors. IL-2 binding bridges the β-chain with the γ-chain; this is sufficient to form an active signalling complex and thus yield a cellular response[2]. Complicating this picture is the CD25 chain, which is variably expressed on IL-2 target cells. CD25 binds at a site on the IL-2 molecule distinct from that bound by the β-chain and γ$_c$-chain[3], generating a tripartite receptor (CD25–IL-2Rβ–γ$_c$) that binds more tightly to IL-2 than does the IL-2Rβ–γ$_c$ complex alone (Fig. 1a).

The story, however, does not end there. In addition to helping to capture IL-2 on the

cell surface, IL-2 binding by CD25 increases the strength of binding between IL-2 and the β-chain[4]. Structural comparison of IL-2 and the IL-2–receptor complexes[3] using X-ray crystallography provides an explanation for this behaviour: the β-chain binding site on IL-2 is structurally flexible, and CD25 binding causes this site to become less mobile and to adopt a conformation more favourable to β-chain binding. Thus, although CD25 has no direct role in signalling, it greatly enhances the effect of IL-2 signalling on those cells that express high levels of CD25; these include T cells in the early stages of an immune response against, for example, a tumour.

However, a class of cell called regulatory T cells, which suppress T-cell-mediated immune responses[2], routinely express high levels of CD25, whereas the precursors to one of the cell types that is largely responsible for antitumour immunity — cytotoxic T cells — normally express little or no CD25 prior to stimulation. Although IL-2 is already approved for the treatment of melanoma and renal cancer, a version of the cytokine that can bind tightly to the β-chain, without requiring CD25 enhancement, could be a highly potent and useful therapeutic immune stimulator.

Levin and colleagues[1] applied a two-step strategy to generate such a protein. The researchers used yeast cells to express a library of randomly mutated IL-2 proteins, from which they identified one variant protein that showed enhanced binding to the isolated β–γ$_c$ receptor. A single amino-acid change in this variant, at a

understand the details of the complex process of star formation[8]. Current numerical and theoretical models of star formation can reproduce the form of the IMF observed locally. One way to distinguish between this myriad of models is to see whether any can reproduce the types of variation reported by Cappellari and colleagues.

There is a long tradition of studies claiming that the IMF varies as a function of environment, especially in distant galaxies where individual stars cannot be identified directly and secondary tracers must be used. Most of these claims have fallen by the wayside when newer and better data became available, or as our understanding of the intricacies of the tracers has improved. However, the observations and analysis of Cappellari and colleagues[2] present a promising avenue that may

lead to fundamental changes in the way that we understand how stars form and galaxies evolve. ■

Nate Bastian *is at the Excellence Cluster 'Universe', Technische Universität München, Garching 85748, Germany.*
e-mail: bastian@usm.lmu.de

1. Bastian, N., Covey, K. R. & Meyer, M. R. *Annu. Rev. Astron. Astrophys.* **48,** 339–389 (2010).
2. Cappellari, M. *et al. Nature* **484,** 485–488 (2012).
3. Kroupa, P. *Science* **295,** 82–91 (2002).
4. Chabrier, G. *Publ. Astron. Soc. Pacif.* **115,** 763–795 (2003).
5. Auger, M. *et al. Astrophys. J.* **721,** L163–L167 (2010).
6. Cappellari, M. *et al. Astrophys. J.* **704,** L34–L39 (2009).
7. Van Dokkum, P. G. & Conroy, C. *Nature* **468,** 940–942 (2010).
8. McKee, C. F. & Ostriker, E. C. *Annu. Rev. Astron. Astrophys.* **45,** 565–687 (2007).

Tighter ties that bind

A stepwise process of mutation and structural analysis has modulated a flexible binding interface of an immune–cell signalling protein, interleukin-2, and generated mutant proteins with enhanced anticancer activity. SEE ARTICLE P.529

ERIC T. BODER

Interleukin-2 is a cytokine protein that signals to cells of the immune system, such as T cells and natural killer cells, to regulate their growth, activation and differentiation. This multifaceted role means that interleukin-2 (IL-2) is the subject of intense investigation as a potential therapeutic agent to boost immune responses in the treatment of diseases such as cancer. On page 529 of this issue, Levin *et al.*[1] describe the engineering of enhanced versions of IL-2 that more potently stimulate T-cell proliferation and antitumour immune responses. The authors also provide a compelling structural explanation for the mutated proteins' superior activity.

The cell-surface receptor for IL-2 comprises three protein subunits: the IL-2 receptor α-chain (IL-2Rα, usually called CD25), the IL-2 receptor β-chain, and the common γ-chain (γc), which is shared by numerous cytokine receptors. IL-2 binding bridges the β-chain with the γ-chain; this is sufficient to form an active signalling complex and thus yield a cellular response[2]. Complicating this picture is the CD25 chain, which is variably expressed on IL-2 target cells. CD25 binds at a site on the IL-2 molecule distinct from that bound by the β-chain and γc-chain[3], generating a tripartite receptor (CD25–IL-2Rβ–γc) that binds more tightly to IL-2 than does the IL-2Rβ–γc complex alone (Fig. 1a).

The story, however, does not end there. In addition to helping to capture IL-2 on the

cell surface, IL-2 binding by CD25 increases the strength of binding between IL-2 and the β-chain[4]. Structural comparison of IL-2 and the IL-2–receptor complexes[3] using X-ray crystallography provides an explanation for this behaviour: the β-chain binding site on IL-2 is structurally flexible, and CD25 binding causes this site to become less mobile and to adopt a conformation more favourable to β-chain binding. Thus, although CD25 has no direct role in signalling, it greatly enhances the effect of IL-2 signalling on those cells that express high levels of CD25; these include T cells in the early stages of an immune response against, for example, a tumour.

However, a class of cell called regulatory T cells, which suppress T-cell-mediated immune responses[2], routinely express high levels of CD25, whereas the precursors to one of the cell types that is largely responsible for antitumour immunity — cytotoxic T cells — normally express little or no CD25 prior to stimulation. Although IL-2 is already approved for the treatment of melanoma and renal cancer, a version of the cytokine that can bind tightly to the β-chain, without requiring CD25 enhancement, could be a highly potent and useful therapeutic immune stimulator.

Levin and colleagues[1] applied a two-step strategy to generate such a protein. The researchers used yeast cells to express a library of randomly mutated IL-2 proteins, from which they identified one variant protein that showed enhanced binding to the isolated β–γc receptor. A single amino-acid change in this variant, at a

50 Years Ago

We have obtained what we believe to be a unique photograph of a pinched lightning discharge … Over the years we have taken hundreds of photographs of lightning discharges, and this is our first photographic evidence of a pinched lightning. We estimate the distance of the lightning to the camera at

between 200 to 1,000 metres, and thus, the transverse dimension of the lightning between 1 and 5 m. Somewhat puzzling is the apparent much larger intensity of the integrated luminosity of the pinched lightning when compared with the luminosity of the aforementioned standard lightning stroke.
From *Nature* 28 April 1962

100 Years Ago

Prof. Milne … has now further increased the debt of seismologists to him by compiling, at the cost of several years' labour, a "Catalogue of Destructive Earthquakes from A.D. 7 to A.D. 1899," … Though containing only half as many entries as the earlier version, its value, it may be anticipated, will be even greater. Being confined to shocks of an intensity sufficient to damage buildings, it deals with those movements which are of chief consequence in the moulding of the earth's crust. An analysis of the catalogue for different epochs should reveal to us some of the laws which govern the distribution of seismic energy within extensive regions, such, for instance, as the Pacific coast of the America continent.
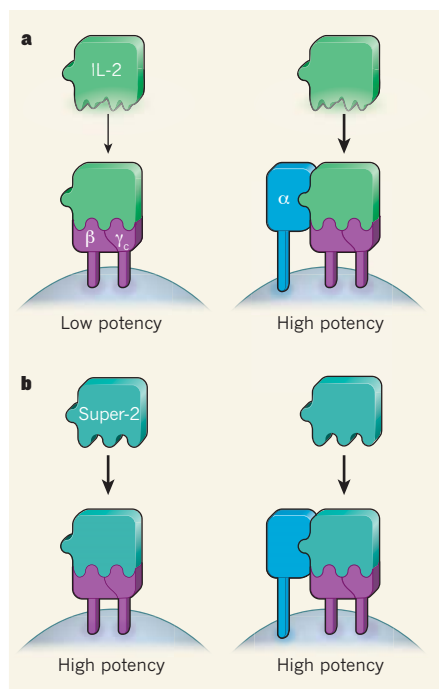**From *Nature* 25 April 1912**

Figure 1 | Signalling superpowers. a, The cell-signalling protein interleukin-2 (IL-2) binds to two versions of its receptor (IL-2R), both of which include the β- and γ_c-chains, and one that also includes the α-chain (also called CD25). These receptors are variably expressed on the surface of target cells, including T cells of the immune system. The IL-2 surface that makes contact with IL-2Rβ undergoes structural changes upon the binding of IL-2 to CD25, which leads to tighter IL-2Rβ–γ_c binding. Thus, IL-2 stimulates cells that have high levels of CD25 more potently than cells with low CD25 levels. **b**, Levin et al.[1] engineered IL-2 proteins, mutated to create a β-receptor-binding interface that allows tight binding to β–γ_c in the absence of CD25. These "super-2" proteins stimulate enhanced antitumour responses owing to their increased potency towards cells lacking CD25.

location in the protein remote from the β-chain binding site and within the protein's hydrophobic core, pointed to the importance of this core region in modulating β-chain recognition by IL-2. The investigators therefore designed and screened a second, smaller library that was biased towards mutations in the hydrophobic core. In this manner they identified several IL-2 variants, called "super-2s", that demonstrate superior potency in stimulating cellular activation in the absence of CD25.

Several of these super-2 variants bind tightly to the β-chain. Using a combination of X-ray crystallography and computer simulation of protein structure, the researchers verified that the mutations in one representative super-2 altered the structure and dynamics of key elements of the IL-2 surface that contacts the receptor β-chain. In effect, these mutations cause 'pre-organization' of the normally flexible binding site, in a manner that mimics the effect of CD25 binding. The authors show that, in contrast to normal IL-2, the super-2s activate

T cells and natural killer cells with or without CD25 with almost equal potency (Fig. 1b). This potency is roughly equivalent to that of normal IL-2 on cells with CD25. The approach used to identify the super-2s thus represents a powerful demonstration of the use of 'directed evolution' to elucidate structure–function relationships to such an extent as to allow highly effective, rationally guided molecular engineering — an approach that is particularly challenging in a system with such complex structural regulation as that of IL-2 receptor binding.

Levin et al.[1] then evaluated their super-2s' ability to inhibit tumour growth, and found the mutant proteins to be superior agents in treating mice bearing any of three different types of human tumour. In comparison with normal IL-2, the super-2s also promoted greater proliferation of cytotoxic T-cell precursors in normal mice, but equivalent expansion of regulatory T cells, which suggests that an increase in cytotoxic T-cell number may be the mechanism for the improved antitumour responses. Another advantage of Levin and colleagues' super-2s is that they cause, somewhat paradoxically, significantly less fluid accumulation (oedema) than normal IL-2 — pulmonary oedema related to activation of CD25-lacking natural killer cells arises in patients treated with IL-2 and limits the dose that can be used[5]. Further investigation of this result might help us to better understand the biological basis of this side effect.

In addition to regulating the activity of T cells and natural killer cells, IL-2 contributes to the development of regulatory T cells in the thymus[2]; the multiple roles of this cytokine mean that further studies are required to fully understand the basis of super-2 activity *in vivo*.

Promising behaviour of anticancer agents in mouse experiments is not always predictive of success in human patients. Nonetheless, these IL-2 variants have exciting potential as investigational therapeutic agents for cancer and other diseases, such as HIV. Furthermore, the protein-engineering approach taken by Levin and colleagues, which iteratively combined structural analysis with directed evolution, might point the way to tailored versions of other proteins that have their activity regulated by the structural effects of complex binding interactions. Structural knowledge of the super-2 molecules might even aid the design of small-molecule drugs that modulate IL-2 behaviour in a similar manner. ■

Eric T. Boder *is in the Department of Chemical and Biomolecular Engineering, University of Tennessee, Knoxville, Tennessee 37996-2200, USA.*
e-mail: boder@utk.edu

1. Levin, A. M. et al. Nature **484**, 529–533 (2012).
2. Malek, T. R. & Castro, I. Immunity **33**, 153–165 (2010).
3. Wang, X., Rickert, M. & Garcia, K. C. Science **310**, 1159–1163 (2005).
4. Arima, N. et al. J. Exp. Med. **176**, 1265–1272 (1992).
5. Eklund, J. W. & Kuzel, T. M. Curr. Opin. Oncol. **16**, 542–546 (2004).

50 Years Ago

We have obtained what we believe to be a unique photograph of a pinched lightning discharge … Over the years we have taken hundreds of photographs of lightning discharges, and this is our first photographic evidence of a pinched lightning. We estimate the distance of the lightning to the camera at

between 200 to 1,000 metres, and thus, the transverse dimension of the lightning between 1 and 5 m. Somewhat puzzling is the apparent much larger intensity of the integrated luminosity of the pinched lightning when compared with the luminosity of the aforementioned standard lightning stroke.
From *Nature* 28 April 1962

100 Years Ago

Prof. Milne … has now further increased the debt of seismologists to him by compiling, at the cost of several years' labour, a "Catalogue of Destructive Earthquakes from A.D. 7 to A.D. 1899," … Though containing only half as many entries as the earlier version, its value, it may be anticipated, will be even greater. Being confined to shocks of an intensity sufficient to damage buildings, it deals with those movements which are of chief consequence in the moulding of the earth's crust. An analysis of the catalogue for different epochs should reveal to us some of the laws which govern the distribution of seismic energy within extensive regions, such, for instance, as the Pacific coast of the America continent.
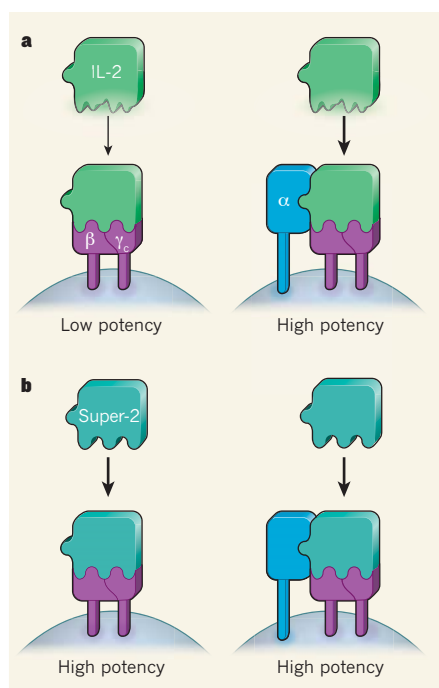**From *Nature* 25 April 1912**

Figure 1 | Signalling superpowers. a, The cell-signalling protein interleukin-2 (IL-2) binds to two versions of its receptor (IL-2R), both of which include the β- and γ_c-chains, and one that also includes the α-chain (also called CD25). These receptors are variably expressed on the surface of target cells, including T cells of the immune system. The IL-2 surface that makes contact with IL-2Rβ undergoes structural changes upon the binding of IL-2 to CD25, which leads to tighter IL-2Rβ–γ_c binding. Thus, IL-2 stimulates cells that have high levels of CD25 more potently than cells with low CD25 levels. **b**, Levin *et al.*[1] engineered IL-2 proteins, mutated to create a β-receptor-binding interface that allows tight binding to β–γ_c in the absence of CD25. These "super-2" proteins stimulate enhanced antitumour responses owing to their increased potency towards cells lacking CD25.

location in the protein remote from the β-chain binding site and within the protein's hydrophobic core, pointed to the importance of this core region in modulating β-chain recognition by IL-2. The investigators therefore designed and screened a second, smaller library that was biased towards mutations in the hydrophobic core. In this manner they identified several IL-2 variants, called "super-2s", that demonstrate superior potency in stimulating cellular activation in the absence of CD25.

Several of these super-2 variants bind tightly to the β-chain. Using a combination of X-ray crystallography and computer simulation of protein structure, the researchers verified that the mutations in one representative super-2 altered the structure and dynamics of key elements of the IL-2 surface that contacts the receptor β-chain. In effect, these mutations cause 'pre-organization' of the normally flexible binding site, in a manner that mimics the effect of CD25 binding. The authors show that, in contrast to normal IL-2, the super-2s activate

T cells and natural killer cells with or without CD25 with almost equal potency (Fig. 1b). This potency is roughly equivalent to that of normal IL-2 on cells with CD25. The approach used to identify the super-2s thus represents a powerful demonstration of the use of 'directed evolution' to elucidate structure–function relationships to such an extent as to allow highly effective, rationally guided molecular engineering — an approach that is particularly challenging in a system with such complex structural regulation as that of IL-2 receptor binding.

Levin *et al.*[1] then evaluated their super-2s' ability to inhibit tumour growth, and found the mutant proteins to be superior agents in treating mice bearing any of three different types of human tumour. In comparison with normal IL-2, the super-2s also promoted greater proliferation of cytotoxic T-cell precursors in normal mice, but equivalent expansion of regulatory T cells, which suggests that an increase in cytotoxic T-cell number may be the mechanism for the improved antitumour responses. Another advantage of Levin and colleagues' super-2s is that they cause, somewhat paradoxically, significantly less fluid accumulation (oedema) than normal IL-2 — pulmonary oedema related to activation of CD25-lacking natural killer cells arises in patients treated with IL-2 and limits the dose that can be used[5]. Further investigation of this result might help us to better understand the biological basis of this side effect.

In addition to regulating the activity of T cells and natural killer cells, IL-2 contributes to the development of regulatory T cells in the thymus[2]; the multiple roles of this cytokine mean that further studies are required to fully understand the basis of super-2 activity *in vivo*.

Promising behaviour of anticancer agents in mouse experiments is not always predictive of success in human patients. Nonetheless, these IL-2 variants have exciting potential as investigational therapeutic agents for cancer and other diseases, such as HIV. Furthermore, the protein-engineering approach taken by Levin and colleagues, which iteratively combined structural analysis with directed evolution, might point the way to tailored versions of other proteins that have their activity regulated by the structural effects of complex binding interactions. Structural knowledge of the super-2 molecules might even aid the design of small-molecule drugs that modulate IL-2 behaviour in a similar manner. ∎

Eric T. Boder *is in the Department of Chemical and Biomolecular Engineering, University of Tennessee, Knoxville, Tennessee 37996-2200, USA.*
e-mail: boder@utk.edu

1. Levin, A. M. *et al. Nature* **484,** 529–533 (2012).
2. Malek, T. R. & Castro, I. *Immunity* **33,** 153–165 (2010).
3. Wang, X., Rickert, M. & Garcia, K. C. *Science* **310,** 1159–1163 (2005).
4. Arima, N. *et al. J. Exp. Med.* **176,** 1265–1272 (1992).
5. Eklund, J. W. & Kuzel, T. M. *Curr. Opin. Oncol.* **16,** 542–546 (2004).

PERSPECTIVE

Allergic host defences

Noah W. Palm[1]*, Rachel K. Rosenstein[1]* & Ruslan Medzhitov[1]

Allergies are generally thought to be a detrimental outcome of a mistargeted immune response that evolved to provide immunity to macroparasites. Here we present arguments to suggest that allergic immunity has an important role in host defence against noxious environmental substances, including venoms, haematophagous fluids, environmental xenobiotics and irritants. We argue that appropriately targeted allergic reactions are beneficial, although they can become detrimental when excessive. Furthermore, we suggest that allergic hypersensitivity evolved to elicit anticipatory responses and to promote avoidance of suboptimal environments.

The immune system protects the host from a variety of infectious agents, ranging from microscopic RNA viruses to 40-foot-long tapeworms. Mammalian hosts can use several defence strategies to deal with different classes of pathogens. Immune defence against microorganisms (viruses, bacteria, fungi and protozoa), referred to as type 1 immunity, relies primarily on direct killing of pathogens or infected host cells. The adaptive arm of type 1 immunity is mediated by T helper type 1 (T_H1) and T_H17 cells, cytotoxic T cells, and immunoglobulin M (IgM), IgA and several IgG antibody classes. In contrast, type 2 immunity protects against macroparasites (helminthes and ectoparasites, such as ticks) and relies primarily on barrier defences and parasite expulsion. Type 2 immune responses are mediated by T_H2 cells and IgE and IgG1 antibodies, as well as several components of the innate immune system, including epithelial barriers, innate lymphoid cells (ILCs), eosinophils, mast cells, basophils and alternatively activated macrophages[1–3]. Although their role in host defence against macroparasites is well appreciated, type 2 immune responses can notoriously be activated in response to a broad variety of environmental challenges. Non-infectious environmental stimuli that can trigger type 2 immune responses are referred to as allergens, and the allergic reactions they elicit are thought to be a purely detrimental consequence of a mistargeted response that normally operates to protect from parasitic worms.

Here we will argue that defence against macroparasites is only one of several functions of type 2 immunity. Specifically, we propose that type 2 immune responses evolved to protect from at least four different classes of environmental challenges, including: (1) helminthes; (2) noxious xenobiotics; (3) venoms and haematophagous fluids; and (4) environmental irritants. Accordingly, there may be multiple pathways that lead to activation of T_H2 immune responses that are specialized to protect against these environmental challenges. All of these responses, however, share a common defence strategy and their effector functions converge on the surface epithelia (skin and mucosa), smooth muscles and vasculature to promote barrier defences and expulsion. Although activation of these target tissues is intended to protect from the four types of environmental challenges, exacerbation of these defences leads to overlapping immunopathologies commonly known as allergies. These include rhinorrhoea (runny nose), hay fever, hives, itch and allergic dermatitis. At the extreme, allergic hypersensitivity can result in life-threatening anaphylaxis. Notably, unlike other immunopathologies, allergic disorders exclusively affect tissues that interface with the environment.

Allergic immunity

Allergic reactivity remains one of the biggest mysteries of the immune system. The prevailing paradigm holds that T_H2- and IgE-mediated immune responses evolved to provide protection against multicellular parasites; however, these responses can also lead to allergy when inadvertently activated by non-infectious environmental antigens[4]. The allergic response is thus considered a misdirected and unintended type 2 immune response. There are several problems with this view. First, although some allergens (for example, chitin and cysteine proteases) can indeed mimic the immunogenic activities of macroparasites[5], most allergens do not have any obvious relationship with parasitic worms. Second, anaphylactic responses to allergens are extremely rapid, occurring within minutes of exposure. However, there is no obvious reason to respond with such extreme urgency when dealing with slowly replicating macroparasites—even immune responses to bacteria and viruses, which have replication rates that are orders of magnitude faster than helminthes, occur on the time scale of hours to days[6]. Third, allergic hypersensitivity is largely dependent on IgE-mediated activation of mast cells and basophils[7]. In contrast, whereas IgE levels are elevated in mice and people with helminth infections, IgE itself is dispensable for immunity to most helminthes for which its role has been tested[8]. Last, allergic hypersensitivity can develop against a huge variety of allergens that have little in common in terms of their structure or origin. Pollen, shellfish, peanuts, bee venom, latex, penicillin and nickel (Ni^+) are all common allergens, yet they do not share any chemical characteristics and there is no unifying framework to explain their allergenicity[9].

An alternative, but largely ignored, explanation for the existence of the allergic reactivity is that it can provide protection against environmental toxins[6,10,11]. According to this view, the allergic response can be intended and beneficial, and not simply a pathological consequence of immunity to parasites. We present arguments to support the view that allergic immunity is an important component of host defence against non-infectious noxious environmental factors, including venoms and haematophagous fluids, noxious xenobiotics and irritants (Fig. 1). The diversity and prevalence of allergens may in turn reflect an important role of allergic reactivity in defence against these three classes of non-infectious stimuli.

Allergens as noxious environmental stimuli

The most enigmatic feature of type 2 immunity is its propensity to be activated in response to a wide variety of environmental substances known as allergens. Allergens have defied all attempts at a comprehensive and rational classification, and they do not share any one property that would universally define them as allergens[9]. Consequently, allergens can only be defined operationally as substances that elicit an allergic response. We believe that the difficulty in establishing a rational framework for understanding allergens may stem from the fact that there are several

[1]Howard Hughes Medical Institute, Department of Immunobiology, Yale University School of Medicine, New Haven, Connecticut 06510, USA.
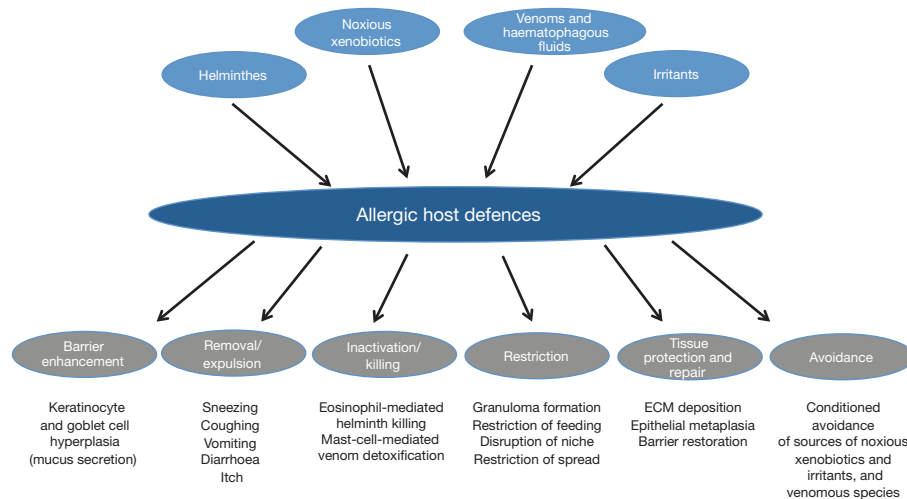*These authors contributed equally to this work.

Figure 1 | Diverse stimuli activate allergic host defences. Four main classes of stimuli activate the allergic host defence response: helminthes, noxious xenobiotics (for example, urushiol from poison ivy), venoms (for example, venom from the honey bee *Apis meliffera*) and irritants (for example, diesel exhaust particles). A variety of effector modules constitute the allergic host defence response. Keratinocye and goblet cell hyperplasia (mucus secretion) enhance barrier functions to reduce exposure to noxious environmental allergens and to restrict helminth entry, feeding and growth. Sneezing, coughing, vomiting, diarrhoea and itch serve to remove or expel noxious xenobiotics, irritants, helminths and ectoparasites. Eosinophils can mediate direct helminth killing, while heparin and proteases from mast cells can inactivate venoms through neutralization and detoxification. Granuloma formation and alternatively activated macrophages can restrict helminth spread, lead to disruption of niches and restrict feeding. Granuloma formation also restricts the damage caused by irritants. Additional allergic defence mechanisms, such as mast-cell-induced hypotension and vasodilation, may restrict the spread of noxious xenobiotics and venoms. Fibroblasts and alternatively activated macrophages coordinate tissue protection and tissue repair through epithelial metaplasia, extracellular matrix (ECM) deposition and barrier restoration. Various allergic host defences may also condition future avoidance of sources of noxious xenobiotics, irritants and venoms. For example, cutaneous hypersensitivity responses (for example, itch and dermatitis) to noxious phytochemicals, such as urushiol, may condition future avoidance of poison ivy. Furthermore, anaphylactic responses to bee venom may condition avoidance of honey bees, and sneezing, coughing, vomiting, diarrhoea, tearing and mucus production may condition avoidance of various irritants and other noxious environmental substances.

distinct classes of allergens, including venoms and haematophagous fluids, xenobiotics and irritants. The common feature of these allergens is that they are noxious to the host, and therefore specific mechanisms have probably evolved for their detection and to provide protection from their noxious effects.

Venoms are complex mixtures of enzymes, peptides and small chemicals that are produced by various species of arthropods, Cnidaria, amphibians and reptiles for predation and defence, and are usually delivered to their victims through bites or stings[12]. Envenomation can cause severe and life-threatening tissue damage. In addition, venoms can induce T_H2 and IgE responses and can cause systemic anaphylaxis, which can be deadly in its own right[13,14]. However, allergic responses triggered by venoms may have evolved to protect the host from the direct damage caused by venoms, and anaphylaxis may be an unfortunate result of overreaction, particularly when the response is triggered systemically[10,11,15]. In this sense, allergic anaphylaxis is analogous to septic shock, which can be elicited by systemic stimulation of Toll-like receptor 4 (TLR4) by bacterial lipopolysaccharide (LPS). Just as the response to LPS evolved to protect from bacterial infections but can result in sepsis, the anaphylactic response may have evolved to protect from venoms and noxious xenobiotics but can result in potentially lethal systemic anaphylaxis. This would explain the apparent urgency of the anaphylactic reaction, which operates within minutes or even seconds—a timescale that is appropriate when dealing with deadly substances[6].

Haematophagous fluids are used by a variety of ectoparasites, including ticks and mosquitoes, to enable feeding on the blood of target species. Venoms and haematophagous fluids are evolutionarily related as both are produced by modified salivary glands and share many molecular components and properties[13]. Haematophagous species also act as vectors for many pathogens; for example, deer ticks harbour *Borrelia burgdorferi*, the causative agent of Lyme disease, and mosquitoes harbour *Plasmodium falciparum*, the causative agent of malaria[16]. Notably, haematophagous fluids can also induce a T_H2 response[17], and IgE-, mast-cell- and basophil-dependent immune responses can prevent tick

feeding[18]. Therefore, the immune system can sense haematophagous fluids and induce an allergic immune response that can prevent blood feeding (and transmission of vector-borne pathogens)[19]. To be effective, this response must be very rapid, thus providing a clear rationale for the urgency of IgE-mediated responses. Importantly, helminthes also use salivary excretions to feed on host tissues[20]. Recognition of salivary components from macroparasites may therefore contribute to defence against both haematophagous ectoparasites and helminthes, as well as from transmission of vector-borne microbes. Thus, defensive immune response to venoms and haematophagous fluids can explain allergies to arthropod bites and stings.

Noxious xenobiotics and toxins, including phytochemicals like urushiol from poison ivy and ricin, can also cause tissue and organ damage[6,21]. For the purpose of this discussion there are two classes of xenobiotics that differ in their site and mode of action. Hydrophobic xenobiotics can enter and accumulate inside cells where they can cause various toxic effects. This class of xenobiotics is detected by various intracellular sensors, including the aryl hydrocarbon receptor (AHR), and the nuclear receptors CAR and FXR, which operate primarily in the liver[22]. These xenobiotics are primarily inactivated by the cytochrome P450 system and ultimately are excreted in the urine[22]; however, at least in some cases they may cause allergic responses if the cytochrome P450 detoxification system is insufficient to prevent their noxious effects. The second class of noxious xenobiotics are haptens—reactive chemicals that have the propensity to form adducts with proteins. These xenobiotics are noxious because adduct formation can alter protein conformation and functions, leading to various toxic effects[23]. Interestingly, haptenation makes otherwise inert proteins immunogenic, leading to IgG1 antibody production, which may promote their clearance[24]. Exposure to reactive haptens can also stimulate inflammasome activation[25] and induction of contact hypersensitivity reactions in the skin, which are mediated primarily by T_H1 and CD8 T cells[26]. However, if the skin barrier is breached, reactive haptens induce a largely T_H2-based response[27], which may provide allergic immune protection from reactive chemicals. Allergic

responses may protect from xenobiotics via increased mucus production, keratinocyte hyperplasia, itch and bronchoconstriction (to reduce entry), vomiting and diarrhoea (to promote expulsion), complement activation (to promote clearance) and vascular leakage (to dilute the noxious substance). When excessive, these defensive reactions can result in allergic disease.

Reactivity to noxious xenobiotics presumably explains the existence of drug allergies. For example, penicillin allergy can develop in some people because penicillin can undergo metabolic transformation, resulting in a reactive product that can form protein adducts[23]. This property of the reactive form of penicillin is shared with noxious xenobiotics, except that penicillin transformation is very inefficient in most individuals. Free (non-conjugated) penicillin is immunologically inert in non-sensitized people and it is the hapten (conjugated) form of penicillin that seems to be immunogenic. However, once the response to the haptenated form is elicited, a hypersensitivity to free (non-conjugated) penicillin may develop, resulting in penicillin allergy[23]. Many idiosyncratic drug reactions of allergic aetiology presumably develop by the same mechanism and, more generally, small molecule allergens may elicit allergic reactions because they either have noxious xenobiotic activity (even if that activity is very low), or because they mimic something that has noxious activity. Therefore, although the xenobiotic-elicited response can be intended and protective, unintended allergic responses can develop to xenobiotics that are not intrinsically noxious.

Environmental irritants are chemicals (for example, mild detergents) and particulates (for example, dust and diesel exhaust particles) that can cause damage to the mucosal epithelium and skin[28]. Airway reflexes (bronchoconstriction, sneezing and coughing) and itch have an obvious protective effect against environmental irritants. When excessively and persistently engaged these responses can cause allergic diseases, including asthma and dermatitis, in susceptible individuals.

Environmental irritants are presumably sensed primarily as a result of their damaging effects on respiratory or gastrointestinal mucosa and skin. Because diverse substances can cause mild tissue damage to surface epithelia, this class of allergens can be extremely heterogeneous. For example, it is estimated that more than half of all major characterized allergens have lipid binding activity[29,30]. One reason for their immunogenicity could be that lipids associated with these proteins may have mild detergent (irritant) properties and therefore may be sensed as noxious. Some lipid binding allergens can also associate with LPS and stimulate TLR4, as is the case with the house dust mite allergen Der p 2 (ref. 31), and in experimental settings, ovalbumin (OVA)[32].

Importantly, host defence against venoms, xenobiotics and irritants relies on the same basic strategies used for the defence against helminthes: barrier enhancement, expulsion, inactivation, restriction and repair (Fig. 1). These defence strategies are well appreciated in the case of helminth infections[1,2], but they are equally well suited to protect from other noxious environmental stimuli.

Allergic defences

Immune protection from helminthes and noxious environmental factors relies on overlapping sets of defensive mechanisms. Activation of these defences is accompanied by a common set of immunopathologies that correspond to different symptoms of allergic diseases.

Barrier defences

Skin and mucosal epithelial barriers prevent or minimize parasite settlement at the mucosal surfaces and entry into internal compartments[2]. Epithelial barriers are also critical in protecting from noxious xenobiotics and environmental irritants and these defences can be enhanced through multiple mechanisms. Goblet cell hyperplasia leads to production of mucus and other defence molecules at mucosal surfaces; keratinocyte hyperplasia leads to a thickening of the epidermis; and metaplasia of columnar epithelium into squamous epithelium results in improved resistance to damage. All of these barrier-enhancing effects occur at the expense of normal epithelial functions, such as nutrient absorption and

gas exchange, and therefore are only activated transiently upon exposure to noxious stimuli. Prolonged or excessive mucus production is a common component of allergies and asthma, for example rhinitis, sinusitis and airway obstruction. Interleukin 13 (IL-13) is the best characterized inducer of goblet cell hyperplasia and mucus production[33]. The source of IL-13 is either type 2 ILCs, also known as nuocytes and natural helper cells[34–37], or T_H2 cells. ILCs secrete IL-13 in response to stimulation by IL-33 and IL-25, which are produced by epithelial cells[3]. The mechanism responsible for induction of these cytokines in epithelial cells is incompletely understood, except that cell damage appears to be an important stimulus for IL-33 release[38]. Mast cells can also be a source of IL-33 for ILC activation[39]. In addition, production of thymic stromal lymphopoetin (TSLP) by epithelial cells can also contribute to barrier defenses[40] and has been linked to allergic dermatitis and induction of T_H2 differentiation in humans[41,42].

Expulsion

Removal or expulsion is a preferred host defence strategy when dealing with helminthes and noxious substances. Their expulsion can be enforced by various means, such as sneezing, coughing, vomiting and diarrhoea. Regulation of these defensive reactions can occur locally through the effect of mast-cell-derived histamine on the smooth muscles in airways and the intestine, as well as by neuronal mechanisms. Expulsion of noxious particulates is also achieved through the effect of the 'ciliary elevator' of the airway epithelia, which functions cooperatively with the mucus layer to promote expulsion of unwanted materials[43,44]. Itch sensation is another important mechanism of barrier defence and a common symptom of allergic diseases. Itch can be caused by the activation of C-fibres by histamine produced by mast cells[45]. The intended effect of itch is to induce mechanical removal of ectoparasites (for example, ticks) and harmful environmental substances (for example, noxious xenobiotics) through scratching[46]. This intended effect, however, when prolonged or excessive is a common manifestation of allergic dermatitis. Likewise, sneezing, coughing, tearing and diarrhoea, although intended to provide host defence by expulsion, are also common symptoms of many allergies.

Inactivation and destruction

Inactivation of noxious substances, including reactive xenobiotics, toxins and venoms can occur through detoxification, neutralization and degradation. Notably, heparin and proteases produced by mast cells can neutralize and destroy various venom components[10,11,15]. IgG1 antibodies have a well-defined protective effect against venoms, presumably because they can neutralize and clear toxic venom proteins. Xenobiotics that trigger allergic reactions are presumably also detoxified. The mechanism of detoxification of this class of xenobiotics is not known, but may involve phagocytosis and degradation of damaged proteins and cells, which may be aided by IgG antibodies and complement.

Direct destruction of helminthes is problematic owing to their large size and the potential for excessive collateral tissue damage. Nevertheless, eosinophils can kill parasite larvae and eggs, and in some cases even adult worms, during tissue-dwelling phases of their life cycle[1].

Restriction

When barrier defences are breached and direct elimination or expulsion is insufficient, restriction provides the next layer of defence. Restriction mechanisms help to prevent the spread of parasites, venoms and noxious chemicals through the body. Vascular restriction mechanisms including endothelial leakage, exudate formation and coagulation can be induced by mast-cell-derived histamine and chymase[4]. Another restriction mechanism involves sequestration through granuloma formation. Collagen deposition by fibroblasts can also help restrict the spread of parasites and noxious substances. Finally, in the case of macroparasites, macrophage-, mast-cell- and eosinophil-derived mediators can act on host tissues to make them less desirable habitats for helminthes[1], or restrict tick feeding on the host blood[18]. At the extreme, restriction processes may also contribute to the pathogenesis of allergic diseases.

Repair

Repair mechanisms help to mend the damage caused by macroparasites, venoms and noxious substances. Alternatively activated macrophages and fibroblasts have a critical role in orchestrating repair responses through the production of growth factors and extracellular matrix deposition, respectively[47]. In addition, ILCs in the lung can produce amphiregulin, which promotes repair of lung epithelium[48]. It has been suggested that much of T_H2-mediated immunity is devoted to promoting tissue tolerance to damage and repair of parasite-inflicted tissue injury[49], and the same argument can be applied to any other noxious stimuli that induce allergic responses. Thus, the physiological rationale for the induction of tissue repair as part of allergic defences is obvious. However, when excessive, these reparative processes can lead to pathological sequelae, such as airway remodelling with epithelial metaplasia and fibrosis in asthma.

In summary, common defence mechanisms provide protection from helminthes, venoms, xenobiotics and irritants, even though the adaptive value of these defences is only appreciated in the case of helminth infections. In the case of allergens, these same defences are primarily known or perceived as pathological. The type of allergic pathology that develops (for example, dermatitis versus rhinitis) depends on which specific defence mechanism is overreacting. All allergic defences, however, can be grouped into two major host defence modules.

Two modules of allergic immunity

Common defence mechanisms that protect from macroparasites, venoms, xenobiotics and irritants are activated by two major functional modules of type 2 immunity (Fig. 2).

The first module centres around type 2 ILCs and their adaptive counterpart, T_H2 cells. These cells produce IL-13 to activate barrier defences by inducing goblet cell hyperplasia and increased mucus production. ILCs also produce growth factors that repair mucosal epithelium[48], and possibly keratinocyte growth factors (KGFs) to induce keratinocyte hyperplasia. The latter can also be achieved by IL-22 produced by ILCs or skin-resident T_H22 cells[50], although this is not generally classified as part of allergic immunity. ILCs and T_H2 cells can also produce IL-5 to induce eosinophil activation and recruitment to the site of infection[51,52]. T_H2- and ILC-derived IL-4 and IL-13 probably also promote alternative activation of macrophages, which in turn contributes to defence against helminthes[47,53] and possibly
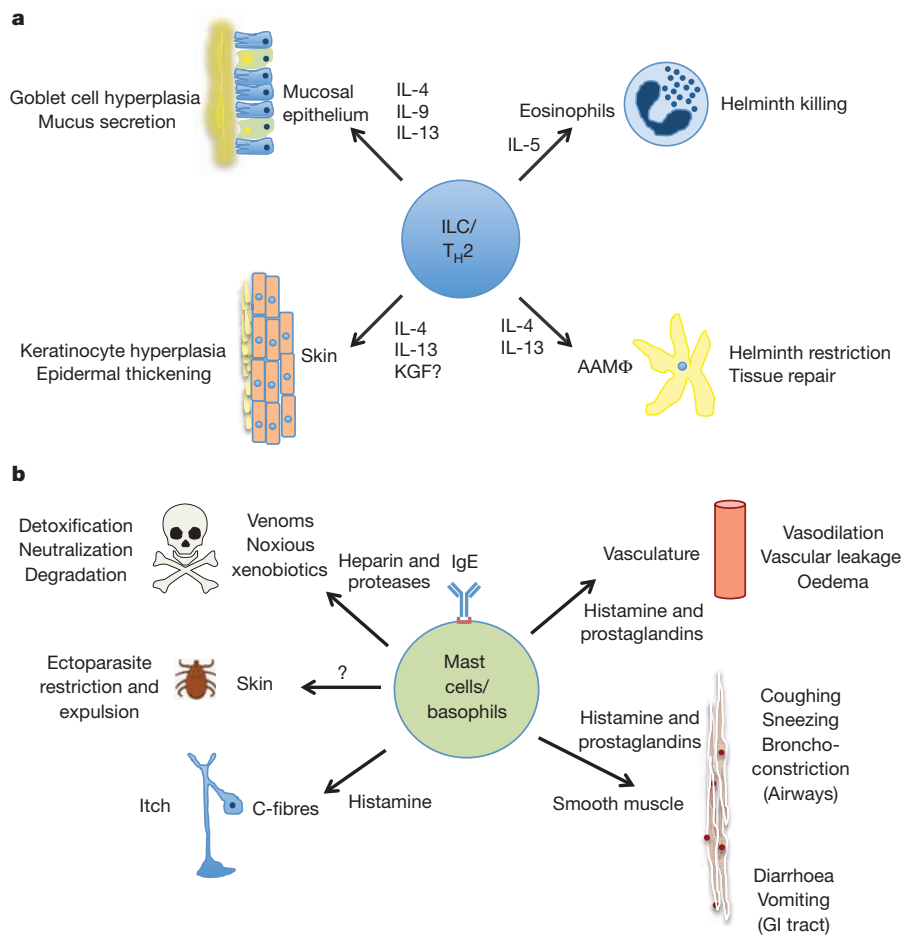

Figure 2 | Functional modules of type 2 immunity. **a**, ILCs and T_H2 cells secrete the canonical type 2 cytokines IL-4, IL-5, IL-9 and IL-13. The IL-4Rα-activating cytokines IL-4 and IL-13 induce epithelial barrier enhancement by promoting goblet cell hyperplasia and mucus secretion at mucosal surfaces, while contributing to epidermal thickening and keratinocyte hyperplasia in the skin. These cytokines also induce alternative activation of macrophages, which have an instrumental role in helminth restriction and tissue repair. IL-5 secretion induces eosinophil recruitment to tissues where they contribute to helminth killing. **b**, Mast cell secretion of proteases and heparin aids in detoxification, degradation and clearance of venoms and noxious xenobiotics, increasing resistance to these toxins. Mast cells mediate many responses by producing histamine and lipid mediators, such as prostaglandins. Histamine and prostaglandins contribute to activation of endothelial cells, inducing vasodilation and vascular leakage, and smooth muscle cells, inducing bronchoconstriction and various mechanisms that contribute to expulsion (coughing, sneezing, vomiting, diarrhoea). Basophils also contribute to antibody-mediated tick resistance. Histamine release from mast cells also can activate C-fibres to induce itch. Notably, crosstalk between these two modules is also common. For example, T_H2 cells produce IL-3, which leads to increased basophil and mast cell production, and IL-9, which leads to recruitment of mast cells. Furthermore, basophils can produce T_H2-inducing cytokines such as IL-4, and mast cells can produce ILC-activating cytokines, such as IL-33.

venoms, irritants and xenobiotics. ILC activation is induced by the epithelial-derived cytokines, including IL-33 and IL-25 (ref. 3), whereas T_H2 production of cytokines must be triggered by antigen recognition, although the relevant antigen-presenting cell in the affected tissues is not well defined.

The second module centres on mast cells and basophils and can be activated by IgE, which is deposited on high-affinity Fcε receptors (FcεR). Mast cells and basophils can also be activated directly, for example, by protease allergens and venoms[10,11,15,54]. However, it is the IgE-mediated activation of mast cells and basophils that makes this module extremely sensitive to allergens. Cross-linking of cell-surface IgE by antigens leads to mast cell degranulation and release of pre-formed mediators, including histamine, leukotrienes, prostaglandins, substance P and various proteases[4]. An important feature of mast cell and basophil degranulation is that it can occur in an all-or-none fashion and is extremely rapid because it does not require new protein synthesis. The rapid kinetics of the mast cell response underlies many features of allergic inflammation and, as argued above, presumably evolved for defence against venoms and noxious chemicals[6]. Mast-cell-derived histamine and prostaglandins act on endothelium to cause vasodilation and exudation; on airway smooth muscles to cause bronchoconstriction; and on intestinal smooth muscles to promote peristalsis and diarrhoea. Mast-cell-derived histamine also acts on C-fibres to cause itching[45]. Finally, mast-cell-derived proteases can contribute to venom degradation[15], while basophils and mast cells can restrict tick feeding[18].

The two modules of allergic immunity can function independently in some settings, but are not functionally isolated. For example, T_H2 cells produce IL-3 and IL-9, which lead to basophil and mast cell expansion. Furthermore, basophils can produce T_H2-inducing cytokines such as IL-4, and mast cells can produce ILC-activating cytokines, such as IL-33 (ref. 39).

Sensing pathways for type 2 immune responses

Given the diversity of stimuli that can elicit type 2 immune responses, it is likely that there are multiple mechanisms used for their detection. These mechanisms can be divided into three categories: pattern recognition, sensing noxious activities, and sensing molecular proxies of noxious activities. In addition, the somatosensory system cooperates with immune recognition in sensing noxious substances.

Pattern recognition

Unlike innate sensing for the type 1 immune response, pattern recognition is of limited use for the initiation of type 2 immunity. The premise of microbial pattern recognition is based on the existence of conserved biochemical products unique to microorganisms. Because multicellular parasites are much more closely related to their hosts on an evolutionary scale (compared to microorganisms), biochemical distinctions in core metabolic processes are limited to only a few examples, such as chitin[55]. Although helminthes have many unique glycoproteins, they are not conserved across species and may not be essential for parasite survival. Nevertheless, there are a few cases of pattern recognition of helminthes and noxious substances. The house dust mite allergen Der p 2 (bound to LPS) and contact allergen Ni^+ can activate TLR4 (refs 31, 56), Schistosome egg antigen (SEA) can be sensed by dectin-2 (also known as CLEC6A)[57], and Ara h 1 from peanuts can be detected by DC-SIGN (also known as CD209)[58]. In addition, sensing of LPS in the respiratory tract by TLR4 can elicit T_H2 responses in the lungs[32]. In this case, LPS is presumably detected as an environmental irritant, rather than as a sign of bacterial infection. Alternatively, commensal-derived LPS may be sensed as a sign of a breach in epithelial barrier. Not all of these examples represent true, intentional pattern recognition: activation of TLR4 by Ni^+ is likely to be purely accidental, as its recognition is not conserved across mammalian species[56], and it is unlikely that TLR4 evolved to recognize Ni^+.

Sensing noxious activities

The more common mechanism of sensing helminthes and allergens is probably based on detection of their unique activities or their effects on

host tissues. For example, many T_H2-inducing stimuli are sensed via their enzymatic activities. These include proteases (for example, Der p 1 from dust mites[59] and papain from papaya[54]), phospholipases (for example, phospholipase A2 from bee venom[60]), and the RNase omega-1 from SEA[61]. Additional classes of allergens, including noxious xenobiotics, non-enzymatic venom components, poisons and irritants are also likely to be sensed via their effects on host tissues. Notably, tissue damage itself has been associated with the induction of type 2 immune responses: IL-33 can be produced by epithelial cells upon damage[38] and ATP released from dying cells promotes allergic inflammation and a T_H2 response in the lung[62]. Mechanical injury induces TSLP expression in the skin[63], and surgery induces a transient rise in total IgE (but not other immunoglobulins) in humans[64]. Additionally, epithelial stress signals mediated by RAE1–NKG2D interactions on keratinocytes and intraepidermal γδT cells, respectively, can induce T_H2 differentiation[65]. At least some toxins, such as the ribosome inactivating proteins from plants (including the famously potent ricin), also induce IgE responses when given at sublethal doses[21]. The NLRP3 inflammasome can be activated by membrane-damaging haptens and produces IL-1 that regulates contact hypersensitivity responses[66]. Tissue damage can also be sensed by nociceptors.

Sensing by proxy

The immune system may be able to detect molecular proxies of at least some noxious stimuli to elicit anticipatory responses, and in some cases, to promote their avoidance. Sensing 'by proxy' is used in a variety of systems as it provides the clear benefit of a pre-emptive response. Pathogen presence in the environment can be detected through molecular proxies of high bacterial density, such as bacteria-specific metabolites (for example, cadaverin and putrescine). When these molecular proxies are volatile, they can be detected by the olfactory system to induce avoidance[67]; if they are not volatile, they trigger the gustatory system to prevent ingestion of contaminated substances or to promote their expulsion (vomiting)[68,69]. We propose that sensing by proxy may also be used to elicit type 2 immune responses to some noxious environmental substances. Thus, innocuous allergens might be sensed because they function as a proxy for a noxious stimulus. Alternatively, innocuous allergens may be mistakenly recognized as a proxy for a noxious stimulus, because sensing by proxy is more error prone than direct sensing. Sensing by proxy is probably used primarily to promote avoidance of noxious substances.

Somatosensory detection of noxious substances

An interesting and perhaps unique aspect of recognition of the stimuli that induce allergic defences is the involvement of somatosensory pathways (Fig. 3). Chemosensory C-fibres may be particularly relevant in the context of allergic inflammation as they can be activated by endogenous mediators of tissue damage, including bradykinin and extracellular ATP[70], and by reactive chemical allergens, including chemical irritants, chlorine, environmental pollutants and reactive oxygen species, through the triggering of TRPA1 and TRPV1 ion channels[71]. Substance P and calcitonin-gene-related peptide (CGRP) produced by C-fibres have direct inflammatory activities and can induce mast cell degranulation[45], thus connecting sensing of tissue damage with allergic inflammation. It is likely that C-fibres are also activated in tissues infected with helminthes. In addition, irritants and other noxious substances can be sensed by epithelial chromaffin cells. Serotonin produced by enteric and pulmonary chromaffin cells in turn activates afferent neurons of the vagus nerve, triggering expulsion and aversion reactions, including vomiting, sneezing and diarrhoea[72]. Importantly, in addition to direct stimulation by noxious substances, C-fibre neurons can also be activated by histamine and other mediators produced by mast cells upon degranulation[45]. The outcome of this stimulation is itch sensation and other defensive reactions. Thus, the IgE–mast-cell module can provide an antigen-dependent entry point into the somatosensory pathways, thus allowing the activation of somatosensory pathways by any allergen
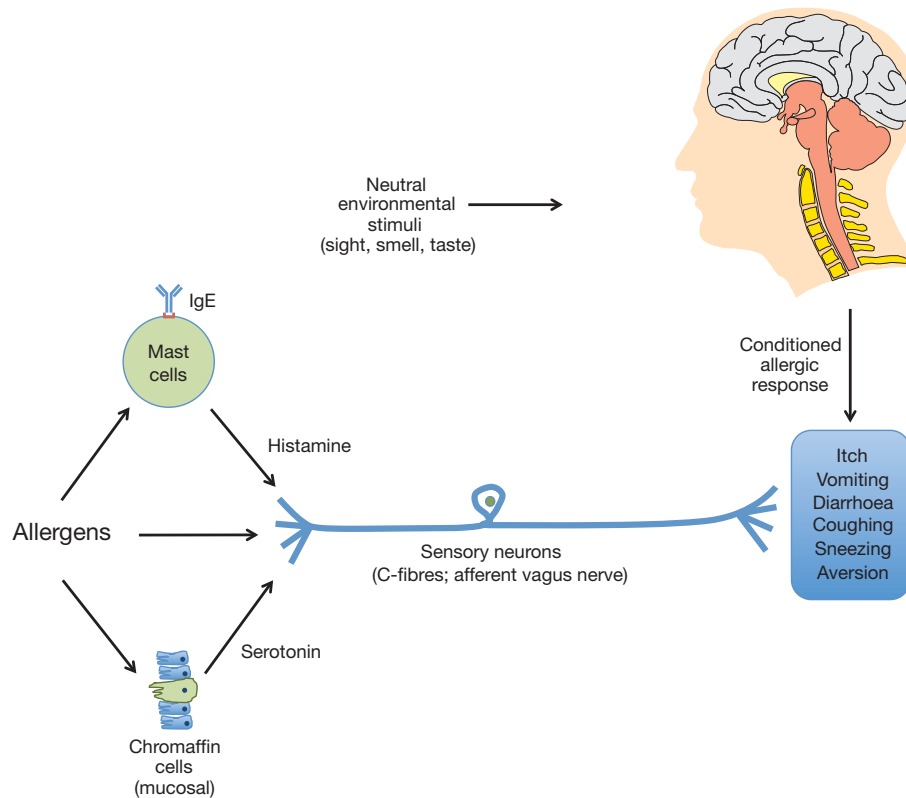
Figure 3 | Somatosensory pathways in allergic immunity. Noxious substances, including allergens, can be detected by somatosensory neurons to elicit protective reflexes, including itch, coughing, sneezing, vomiting and diarrhoea. These pathways can also elicit aversive behaviours that enforce avoidance of exposure to noxious allergens. Somatosensory neurons can sense the noxious effects of allergens directly, for example through TRP channels expressed on C-fibre neurons. Afferent neurons of the vagus nerve can be activated by serotonin produced by chromaffin cells in mucosal epithelia upon exposure to irritants and other noxious substances. Finally, C-fibre neurons can be activated in response to histamine produced by mast cells upon allergen recognition by IgE. The latter mechanism couples immune recognition of allergens with somatosensory pathways. Allergens recognized by IgE can be intrinsically noxious, they can serve as proxies for noxious allergens, or they can be innocuous and accidental. Neutral environmental stimuli perceived through olfactory, gustatory and visual systems can be temporally associated with the stimulation of somatosensory pathways, resulting in Pavlovian conditioning of neutral cues with the antigen-specific response to allergens.

detectable by IgE deposited on mast cells. This, in turn, may provide the basis for an association between allergen recognition by IgE and sensory stimuli detected by the olfactory, gustatory and visual systems, resulting in the phenomenon of conditional allergic reactions[73]. Conditional allergic reactions are elicited by neutral stimuli when they are temporally associated with an allergen. The famous, albeit anecdotal, example of such a response is an allergic reaction elicited by a painting of a flower in individuals that have allergy to the flower. Although this phenomenon was first described over one hundred years ago[74,75], and is well documented in the literature[73,76,77], the mechanistic basis and physiological rationale for conditional allergic reactions remain poorly understood. The coupling between IgE–mast-cell–somatosensory pathways and visual, olfactory and gustatory stimuli may conceivably result in classical (Pavlovian) conditioning with subsequent conditional allergic reactions to otherwise neutral stimuli present in the environment. The biological rationale for such learned allergic reactions might have to do with the assessment of the environment for the presence of noxious substances.

The allergic response as an avoidance strategy

If the allergic response indeed evolved for defence purposes, what might be the reason for the extraordinary level of sensitivity of allergen recognition? What is the purpose of sensing miniscule amounts of allergen when the level of exposure is clearly far too low to cause any harm? We suggest that allergic hypersensitivity evolved to survey the environment (including the air, water and food) for the presence of noxious substances. Once exposure to noxious environmental substances has taken place and allergen-specific IgE is generated, memory of allergen exposure can develop. After such sensitization, subsequent exposure

to even minute amounts of allergen in a given environment will result in an allergic reaction, which has two purposes. First, it will induce anticipatory allergic responses that will help minimize the potentially harmful effects of the allergen by restricting entry and spread, enhancing detoxification, and encouraging expulsion. Second, allergic responses will encourage avoidance of the environment that contains the allergen (which is typically a noxious substance). According to this view, hypersensitivity to allergens triggers avoidance of what is perceived as a suboptimal environment. Repeated exposure may also condition future avoidance of suboptimal environments as well as the specific sources of noxious substances, such as specific foods and plants.

There are several lines of evidence that support the view that allergic sensitization has a role in aversive behaviour. Mice made allergic to OVA avoid drinking an otherwise preferred sweetened solution containing OVA[78]. This aversion is allergen specific and dependent on the immune system[79]. Furthermore, available evidence suggests that allergen-containing food aversion is dependent on functional C-fibre innervation[80,81]. Interestingly, allergen-sensitized mice exhibited an increased level of anxiety upon exposure to the allergen, which is consistent with avoidance of allergen-containing environments. Finally, OVA-sensitized mice avoided entering environments containing traces of OVA. Strikingly, this aversive behaviour was IgE and mast cell dependent[82,83]. Together, these studies strongly support the notion that allergic sensitization promotes avoidance of allergen-containing environments, as well as allergen-containing food and water sources[84].

In should be noted here that allergy is a unique disease in that it only manifests itself when the allergen is present in the environment. As any allergy sufferer would know, the best way to deal with allergy is to avoid

exposure to the allergen. As soon as exposure to allergen is eliminated, which in a natural setting would entail moving to a different environment, allergic symptoms disappear. This is consistent with the view that allergic hyper-reactivity evolved to screen the quality of the environment, to elicit an anticipatory response, and to enforce a change of environment whenever allergens are encountered.

Conclusions and perspectives

The existence of allergic hypersensitivity remains largely unexplained. The commonly held assumption is that allergies are misguided reactions that are intended to protect the host from macroparasites. However, it is not clear from this perspective why allergens would induce the same type 2 immune responses as helminth infections. Moreover, the sensitivity and urgency of the allergic response, as well as the enormous diversity of allergens that can trigger this response, are hard to explain if we are to assume that the only function of these responses is defence against helminthes.

We presented here the argument that allergic immunity evolved to protect the host not only from parasitic infections, but also from noxious xenobiotics, environmental irritants, envenomation and haematophageous ectoparasites. Each of these stimuli also defines a different class of allergens. We propose that allergic responses to noxious allergens are intended and protective, although they can become detrimental when excessive. It is possible, however, that responses to allergens that are truly innocuous (if such allergens indeed exist) are indeed purely detrimental and are due to mistargeting of the immune response. It should be noted that it is difficult to determine with certainty which, if any, allergens are truly innocuous because the noxious effects of allergens may not be immediately obvious. It will be important to evaluate specific allergens from this perspective in the future.

Another unexplained feature of allergic hypersensitivity is its idiosyncrasy. Why are some people hypersensitive to peanuts and pollen whereas others are not? Although genetic factors certainly contribute to differential predispositions to allergic diseases, genetics alone cannot explain the idiosyncrasy of allergic sensitization. Indeed, the dramatic rise in allergic diseases over the past few decades cannot be accounted for by genetic factors alone. Moreover, hypersensitivity can develop or be lost at almost any stage of an individual's life. We propose that the idiosyncrasy of the allergic response may be due to at least two factors. First, allergic sensitization may occur owing to accidental temporal association of a noxious stimulus and a neutral antigen whereby allergic sensitivity develops towards the latter. The noxious stimulus in this case will function as an 'adjuvant' and may or may not be an allergen itself. Thus, the details of an individual's life history may account for the acquisition of hypersensitivity to certain allergens. The second reason for idiosyncrasy may have to do with differential sensitivity among individuals to the noxious effects of allergens. For example, if protection from a noxious xenobiotic can be afforded by both barrier defences and detoxification, the individual that has reduced detoxification capacity (due to genetic variation or physiological status) would have to rely excessively, or even exclusively, on barrier defences. Exaggerated barrier defences will compensate for reduced detoxification and may afford sufficient protection from noxious offences. This protection, however, will come at a cost that may manifest itself as allergic disease. Mutations in filaggrin may provide an example of such compensatory allergic reactivity. Filaggrin encodes a structural epidermal protein and genetic deficiencies in filaggrin are associated with atopic dermatitis[85]. One could argue that development of dermatitis in this case is an attempt to compensate for defects in barrier functions caused by the filaggrin mutation.

Importantly, although hypersensitivity itself is idiosyncratic, subclinical allergic defences presumably operate in all healthy individuals. It would be interesting to investigate in future studies the long-term consequences of deficient allergic defences. Interestingly in this regard, some of the noxious environmental factors that elicit allergic defence responses are likely to be carcinogenic, and some studies suggest that allergies are inversely correlated with incidence of several types of cancer[86].

In conclusion, allergic reactivity may provide an important defence mechanism that protects the host from noxious environmental factors. The very nature of allergic reactions (mucus overproduction, sneezing, itching, and so on) suggests that they are engaged to reduce exposure and promote expulsion of unwanted environmental substances. Furthermore, the extraordinary sensitivity of IgE-based recognition of allergens may have evolved to induce anticipatory responses to noxious substances and to ensure avoidance of unfavourable environments.

1. Allen, J. E. & Maizels, R. M. Diversity and dialogue in immunity to helminths. *Nature Rev. Immunol.* **11**, 375–388 (2011).
2. Anthony, R. M., Rutitzky, L. I., Urban, J. F. Jr, Stadecker, M. J. & Gause, W. C. Protective immune mechanisms in helminth infection. *Nature Rev. Immunol.* **7**, 975–987 (2007).
3. Spits, H. & Di Santo, J. P. The expanding family of innate lymphoid cells: regulators and effectors of immunity and tissue remodeling. *Nature Immunol.* **12**, 21–27 (2011).
4. Galli, S. J., Tsai, M. & Piliponsky, A. M. The development of allergic inflammation. *Nature* **454**, 445–454 (2008).
5. McKerrow, J. H., Caffrey, C., Kelly, B., Loke, P. & Sajid, M. Proteases in parasitic diseases. *Annu. Rev. Pathol.* **1**, 497–536 (2006).
6. Profet, M. The function of allergy: immunological defense against toxins. *Q. Rev. Biol.* **66**, 23–62 (1991).
   This review outlines the 'toxin hypothesis', which proposes that allergic responses provide a defence against environmental toxins and carcinogens.
7. Burton, O. T. & Oettgen, H. C. Beyond immediate hypersensitivity: evolving roles for IgE antibodies in immune homeostasis and allergic diseases. *Immunol. Rev.* **242**, 128–143 (2011).
8. Harris, N. & Gause, W. C. To B or not to B: B cells and the Th2-type immune response to helminths. *Trends Immunol.* **32**, 80–88 (2011).
9. Aalberse, R. C. Structural biology of allergens. *J. Allergy Clin. Immunol.* **106**, 228–238 (2000).
10. Higginbotham, R. D. Mast cells and local resistance to Russell's viper venom. *J. Immunol.* **95**, 867–875 (1965).
    This is the first demonstration of a beneficial role for mast cells in the detoxification of venoms and protection from the noxious effects of envenomation.
11. Higginbotham, R. D. & Karnella, S. The significance of the mast cell response to bee venom. *J. Immunol.* **106**, 233–240 (1971).
12. Fry, B. G. *et al.* Early evolution of the venom system in lizards and snakes. *Nature* **439**, 584–588 (2006).
13. Fry, B. G. *et al.* The toxicogenomic multiverse: convergent recruitment of proteins into animal venoms. *Annu. Rev. Genomics Hum. Genet.* **10**, 483–511 (2009).
14. Müller, U. R. Insect venoms. *Chem. Immunol. Allergy* **95**, 141–156 (2010).
15. Metz, M. *et al.* Mast cells can enhance resistance to snake and honeybee venoms. *Science* **313**, 526–530 (2006).
    This paper provides definitive evidence that mast cells enhance resistance to envenomation by detoxifying venom components.
16. Matthews, K. R. Controlling and coordinating development in vector-transmitted parasites. *Science* **331**, 1149–1153 (2011).
17. Müller-Doblies, U. U. *et al.* Feeding by the tick, *Ixodes scapularis*, causes CD4+ T cells responding to cognate antigen to develop the capacity to express IL-4. *Parasite Immunol.* **29**, 485–499 (2007).
18. Wada, T. *et al.* Selective ablation of basophils in mice reveals their nonredundant role in acquired immunity against ticks. *J. Clin. Invest.* **120**, 2867–2875 (2010).
    This paper demonstrates that basophils are critical for IgE-dependent acquired resistance to tick feeding.
19. Schuijt, T. J., Hovius, J. W., van der Poll, T., van Dam, A. P. & Fikrig, E. Lyme borreliosis vaccination: the facts, the challenge, the future. *Trends Parasitol.* **27**, 40–47 (2011).
20. Loukas, A. *et al.* Vaccinomics for the major blood feeding helminths of humans. *OMICS* **15**, 567–577 (2011).
21. Thorpe, S. C., Murdoch, R. D. & Kemeny, D. M. The effect of the castor bean toxin, ricin, on rat IgE and IgG responses. *Immunology* **68**, 307–311 (1989).
22. Chawla, A., Repa, J. J., Evans, R. M. & Mangelsdorf, D. J. Nuclear receptors and lipid physiology: opening the X-files. *Science* **294**, 1866–1870 (2001).
23. Li, J. & Uetrecht, J. P. The danger hypothesis applied to idiosyncratic drug reactions. *Handb. Exp. Pharmacol.* **196**, 493–509 (2010).
24. Palm, N. W. & Medzhitov, R. Immunostimulatory activity of haptenated proteins. *Proc. Natl Acad. Sci. USA* **106**, 4782–4787 (2009).
25. Sutterwala, F. S. *et al.* Critical role for NALP3/CIAS1/Cryopyrin in innate and adaptive immunity through its regulation of caspase-1. *Immunity* **24**, 317–327 (2006).
26. Kalish, R. S. & Askenase, P. W. Molecular mechanisms of CD8+ T cell-mediated delayed hypersensitivity: implications for allergies, asthma, and autoimmunity. *J. Allergy Clin. Immunol.* **103**, 192–199 (1999).
27. Kondo, H., Ichikawa, Y. & Imokawa, G. Percutaneous sensitization with allergens through barrier-disrupted skin elicits a Th2-dominant cytokine response. *Eur. J. Immunol.* **28**, 769–779 (1998).
28. Bernstein, J. A. *et al.* Health effects of air pollution. *J. Allergy Clin. Immunol.* **114**, 1116–1123 (2004).
29. Thomas, W. R., Hales, B. J. & Smith, W. A. Structural biology of allergens. *Curr. Allergy Asthma Rep.* **5**, 388–393 (2005).
30. Karp, C. L. Guilt by intimate association: what makes an allergen an allergen? *J. Allergy Clin. Immunol.* **125**, 955–960 (2010).

31. Trompette, A. et al. Allergenicity resulting from functional mimicry of a Toll-like receptor complex protein. Nature 457, 585–588 (2009).
32. Eisenbarth, S. C. et al. Lipopolysaccharide-enhanced, toll-like receptor 4-dependent T helper cell type 2 responses to inhaled antigen. J. Exp. Med. 196, 1645–1651 (2002).
33. Finkelman, F. D. et al. Interleukin-4- and interleukin-13-mediated host protection against intestinal nematode parasites. Immunol. Rev. 201, 139–155 (2004).
34. Moro, K. et al. Innate production of T_H2 cytokines by adipose tissue-associated c-Kit$^+$Sca-1$^+$ lymphoid cells. Nature 463, 540–544 (2010).
   References 34–37 describe the discovery of novel classes of ILCs that produce type 2 cytokines in response to IL-25 and IL-33.
35. Neill, D. R. et al. Nuocytes represent a new innate effector leukocyte that mediates type-2 immunity. Nature 464, 1367–1370 (2010).
36. Price, A. E. et al. Systemically dispersed innate IL-13-expressing cells in type 2 immunity. Proc. Natl Acad. Sci. USA 107, 11489–11494 (2010).
37. Saenz, S. A. et al. IL25 elicits a multipotent progenitor cell population that promotes T_H2 cytokine responses. Nature 464, 1362–1366 (2010).
38. Zhao, W. & Hu, Z. The enigmatic processing and secretion of interleukin-33. Cell. Mol. Immunol. 7, 260–262 (2010).
39. Hsu, C. L., Neilsen, C. V. & Bryce, P. J. IL-33 is produced by mast cells and regulates IgE-dependent inflammation. PLoS ONE 5, e11944 (2010).
40. Ziegler, S. F. & Artis, D. Sensing the outside world: TSLP regulates barrier immunity. Nature Immunol. 11, 289–293 (2010).
41. Soumelis, V. et al. Human epithelial cells trigger dendritic cell mediated allergic inflammation by producing TSLP. Nature Immunol. 3, 673–680 (2002).
42. Liu, Y. J. Thymic stromal lymphopoietin: master switch for allergic inflammation. J. Exp. Med. 203, 269–273 (2006).
43. Fahy, J. V. & Dickey, B. F. Airway mucus function and dysfunction. N. Engl. J. Med. 363, 2233–2247 (2010).
44. Knowles, M. R. & Boucher, R. C. Mucus clearance as a primary innate defense mechanism for mammalian airways. J. Clin. Invest. 109, 571–577 (2002).
45. Jeffry, J., Kim, S. & Chen, Z. F. Itch signaling in the nervous system. Physiology (Bethesda) 26, 286–292 (2011).
46. Raap, U., Stander, S. & Metz, M. Pathophysiology of itch and new treatments. Curr. Opin. Allergy Clin. Immunol. 11, 420–427 (2011).
47. Murray, P. J. & Wynn, T. A. Protective and pathogenic functions of macrophage subsets. Nature Rev. Immunol. 11, 723–737 (2011).
48. Monticelli, L. A. et al. Innate lymphoid cells promote lung-tissue homeostasis after infection with influenza virus. Nature Immunol. 12, 1045–1054 (2011).
49. Allen, J. E. & Wynn, T. A. Evolution of Th2 immunity: a rapid repair response to tissue destructive pathogens. PLoS Pathog. 7, e1002003 (2011).
   In this review, the authors propose that the T_H2 response evolved to function as a tissue repair response to damage caused by helminths.
50. Zenewicz, L. A. & Flavell, R. A. Recent advances in IL-22 biology. Int. Immunol. 23, 159–163 (2011).
51. Ikutani, M. et al. Identification of innate IL-5-producing cells and their role in lung eosinophil regulation and antitumor immunity. J. Immunol. 188, 703–713 (2012).
52. Bartemes, K. R. e. t. a. l. IL-33-responsive Lineage$^-$CD25$^+$CD44^{hi} lymphoid cells mediate innate type 2 immunity and allergic inflammation in the lungs. J. Immunol. 188, 1503–1513 (2011).
53. Martinez, F. O., Helming, L. & Gordon, S. Alternative activation of macrophages: an immunologic functional perspective. Annu. Rev. Immunol. 27, 451–483 (2009).
54. Sokol, C. L., Barton, G. M., Farr, A. G. & Medzhitov, R. A mechanism for the initiation of allergen-induced T helper type 2 responses. Nature Immunol. 9, 310–318 (2008).
55. Reese, T. A. et al. Chitin induces accumulation in tissue of innate immune cells associated with allergy. Nature 447, 92–96 (2007).
56. Schmidt, M. et al. Crucial role for human Toll-like receptor 4 in the development of contact allergy to nickel. Nature Immunol. 11, 814–819 (2010).
57. Ritter, M. et al. Schistosoma mansoni triggers Dectin-2, which activates the Nlrp3 inflammasome and alters adaptive immune responses. Proc. Natl Acad. Sci. USA 107, 20459–20464 (2010).
58. Shreffler, W. G. et al. The major glycoprotein allergen from Arachis hypogaea, Ara h 1, is a ligand of dendritic cell-specific ICAM-grabbing nonintegrin and acts as a Th2 adjuvant in vitro. J. Immunol. 177, 3677–3685 (2006).
59. Phillips, C., Coward, W. R., Pritchard, D. I. & Hewitt, C. R. Basophils express a type 2 cytokine profile on exposure to proteases from helminths and house dust mites. J. Leukoc. Biol. 73, 165–171 (2003).
60. Dudler, T. et al. A link between catalytic activity, IgE-independent mast cell activation, and allergenicity of bee venom phospholipase A2. J. Immunol. 155, 2605–2613 (1995).
61. Steinfelder, S. et al. The major component in schistosome eggs responsible for conditioning dendritic cells for Th2 polarization is a T2 ribonuclease (omega-1). J. Exp. Med. 206, 1681–1690 (2009).
62. Idzko, M. et al. Extracellular ATP triggers and maintains asthmatic airway inflammation by activating dendritic cells. Nature Med. 13, 913–919 (2007).
63. Oyoshi, M. K., Larson, R. P., Ziegler, S. F. & Geha, R. S. Mechanical injury polarizes skin dendritic cells to elicit a T_H2 response by inducing cutaneous thymic stromal lymphopoietin expression. J. Allergy Clin. Immunol. 126, 976–984 (2010).
64. Navarro-Zorraquino, M. et al. Determination of the immunoglobulin E postoperative variation as a measure of surgical injury. World J. Surg. 25, 585–591 (2001).
65. Strid, J., Sobolev, O., Zafirova, B., Polic, B. & Hayday, A. The intraepithelial T cell response to NKG2D-ligands links lymphoid stress surveillance to atopy. Science 334, 1293–1297 (2011).
66. Strowig, T., Henao-Mejia, J., Elinav, E. & Flavell, R. Inflammasomes in health and disease. Nature 481, 278–286 (2012).
67. Kavaliers, M., Choleris, E., Agmo, A. & Pfaff, D. W. Olfactory-mediated parasite recognition and avoidance: linking genes to behavior. Horm. Behav. 46, 272–283 (2004).
68. Tizzano, M. et al. Nasal chemosensory cells use bitter taste signaling to detect irritants and bacterial signals. Proc. Natl Acad. Sci. USA 107, 3210–3215 (2010).
69. Rivière, S., Challet, L., Fluegge, D., Spehr, M. & Rodriguez, I. Formyl peptide receptor-like proteins are a novel family of vomeronasal chemosensors. Nature 459, 574–577 (2009).
70. Basbaum, A. I., Bautista, D. M., Scherrer, G. & Julius, D. Cellular and molecular mechanisms of pain. Cell 139, 267–284 (2009).
71. Bessac, B. F. & Jordt, S. E. Breathtaking TRP channels: TRPA1 and TRPV1 in airway chemosensation and reflex control. Physiology (Bethesda) 23, 360–370 (2008).
72. Bertrand, P. P. & Bertrand, R. L. Serotonin release and uptake in the gastrointestinal tract. Auton. Neurosci. 153, 47–57 (2010).
73. Siegel, S. & Kreutzer, R. Pavlovian conditioning and multiple chemical sensitivity. Environ. Health Perspect. 105 (suppl. 2), 521–526 (1997).
74. Mackenzie, M. Rose cold. Historical document. Ann. Allergy 19, 298–304 (1961).
75. MacKenzie, J. N. The production of the so-called "rose cold" by means of an artificial rose. Am. J. Med. Sci. 91, 45–47 (1896).
76. Justesen, D. R., Braun, E. W., Garrison, R. G. & Pendleton, R. B. Pharmacological differentiation of allergic and classically conditioned asthma in the guinea pig. Science 170, 864–866 (1970).
77. MacQueen, G., Marshall, J., Perdue, M., Siegel, S. & Bienenstock, J. Pavlovian conditioning of rat mucosal mast cells to secrete rat mast cell protease II. Science 243, 83–85 (1989).
   This article reports classical conditioning of an allergic response to a neutral stimulus.
78. Cara, D. C., Conde, A. A. & Vaz, N. M. Immunological induction of flavor aversion in mice. Braz. J. Med. Biol. Res. 27, 1331–1341 (1994).
79. Cara, D. C., Conde, A. A. & Vaz, N. M. Immunological induction of flavour aversion in mice. II. Passive/adoptive transfer and pharmacological inhibition. Scand. J. Immunol. 45, 16–20 (1997).
80. Zarzana, E. C., Basso, A. S., Costa-Pinto, F. A. & Palermo-Neto, J. Pharmacological manipulation of immune-induced food aversion in rats. Neuroimmunomodulation 16, 19–27 (2009).
81. Lang, P. M., Moalem-Taylor, G., Tracey, D. J., Bostock, H. & Grafe, P. Activity-dependent modulation of axonal excitability in unmyelinated peripheral rat nerve fibers by the 5-HT(3) serotonin receptor. J. Neurophysiol. 96, 2963–2971 (2006).
82. Costa-Pinto, F. A., Basso, A. S. & Russo, M. Role of mast cell degranulation in the neural correlates of the immediate allergic reaction in a murine model of asthma. Brain Behav. Immun. 21, 783–790 (2007).
83. Costa-Pinto, F. A., Basso, A. S., Britto, L. R., Malucelli, B. E. & Russo, M. Avoidance behavior and neural correlates of allergen exposure in a murine model of asthma. Brain Behav. Immun. 19, 52–60 (2005).
84. Mirotti, L., Castro, J., Costa-Pinto, F. A. & Russo, M. Neural pathways in allergic inflammation. J. Allergy (Cairo) 2010, 491928 (2010).
   This review covers the literature describing allergy-mediated avoidance behaviours.
85. Irvine, A. D., McLean, W. H. & Leung, D. Y. Filaggrin mutations associated with skin and allergic diseases. N. Engl. J. Med. 365, 1315–1327 (2011).
86. Zacharia, B. E. & Sherman, P. Atopy, helminths, and cancer. Med. Hypotheses 60, 1–5 (2003).

ARTICLE

Multiple dynamic representations in the motor cortex during sensorimotor learning

D. Huber[1]†*, D. A. Gutnisky[1]*, S. Peron[1], D. H. O'Connor[1], J. S. Wiegert[2], L. Tian[1], T. G. Oertner[2], L. L. Looger[1] & K. Svoboda[1]

The mechanisms linking sensation and action during learning are poorly understood. Layer 2/3 neurons in the motor cortex might participate in sensorimotor integration and learning; they receive input from sensory cortex and excite deep layer neurons, which control movement. Here we imaged activity in the same set of layer 2/3 neurons in the motor cortex over weeks, while mice learned to detect objects with their whiskers and report detection with licking. Spatially intermingled neurons represented sensory (touch) and motor behaviours (whisker movements and licking). With learning, the population–level representation of task–related licking strengthened. In trained mice, population–level representations were redundant and stable, despite dynamism of single–neuron representations. The activity of a subpopulation of neurons was consistent with touch driving licking behaviour. Our results suggest that ensembles of motor cortex neurons couple sensory input to multiple, related motor programs during learning.

Animals move their sensors to collect information, and these movements are guided by sensory input. When action sequences are required to achieve success in novel tasks, interactions between movement and sensation underlie motor control[1] and complex learned behaviours[2]. The motor cortex has important roles in learning motor skills[3–6], but its function in learning sensorimotor associations is unknown.

The neural circuits underlying sensorimotor integration are beginning to be mapped. Different motor cortex layers harbour excitatory neurons with distinct inputs and projections[7–10]. Outputs to motor centres in the brain stem and spinal cord arise from pyramidal-tract-type neurons in layer 5B (L5B). Within motor cortex, excitation descends from L2/3 to L5 (refs 9–11). Input from somatosensory cortex impinges preferentially onto L2/3 neurons[8,12]. L2/3 neurons therefore directly link somatosensation and control of movements.

L2/3 neurons also participate in learning-related plasticity. Synapses from the somatosensory cortex to L2/3 neurons are critical for learning new motor skills[13] and support long-term potentiation[14]. Learning causes plasticity in networks of L2/3 cells[5,15]. L2/3 neurons are thus poised to organize learned movements and the underlying sensorimotor associations.

To define their roles in learning we imaged large L2/3 neuron populations in the vibrissal motor cortex (vM1) while mice learned a sensorimotor task involving whisking and object detection, followed by licking for a water reward. The vM1 is a subdivision of the primary motor cortex in which low-intensity stimulation evokes whisker movements[8,16–18]. Pyramidal-tract-type neurons in vM1 project to the brainstem to control whisking[19,20] and rhythmic licking[5,21]. Activity in the vibrissal somatosensory cortex (vS1; also known as the barrel cortex), activated by touch, propagates to vM1 (refs 18, 22, 23) to excite L2/3 neurons[8,12]. Thus, L2/3 cells in vM1 may directly mediate the stimulus–response (touch–lick) association learned in the object-detection task.

Tracking neuronal populations during learning is challenging because only a small fraction of neurons can be recorded stably over days using electrophysiological methods[24]. Instead, we imaged activity in large populations of neurons[5,25,26] over weeks while monitoring multiple sensory and motor variables[27,28], enabling us to relate population activity to behaviour during learning. Activity in L2/3 cells correlated with licking, whisker movements (whisking) and touch-related forces. Representations of individual neurons changed with learning, but in a restricted manner so that licking neurons rarely changed into whisking neurons and vice versa. This indicates that motor cortex neurons default to represent specific behavioural features. As mice became expert at the sensorimotor task, representations at the level of neuronal populations stabilized, despite continuing changes at the level of individual neurons. A subpopulation of neurons seemed to trigger licking in response to whisker touch, suggesting that L2/3 cells in the motor cortex learn to link task-related sensory inputs and actions.

Learning under the microscope

We trained head-fixed mice in a vibrissa-based object-detection task[27] while imaging populations of neurons (Fig. 1a)[28]. Following a sound, a pole was moved to one of several target positions within reach of the whiskers (the 'go' stimulus) or to an out-of-reach position (the 'no-go' stimulus) (Fig. 1b). Target and out-of-reach locations were arranged along the anterior–posterior axis; the out-of reach position was most anterior (Fig. 1a). Mice searched for the pole with one whisker row (the C row) and reported the pole as 'present' by licking, or 'not present' by withholding licking. Licking on go trials (hit) was rewarded with water, whereas licking on no-go trials (false alarm) was punished with a time-out during which the trial was stopped for 2 seconds. Trials without licking (no-go, correct rejection, go, and miss) were not rewarded or punished. All mice showed learning within the first two or three sessions ($d' > 0.8$, one-tailed bootstrap test, $P < 0.001$) (Fig. 1c). Performance reached expert levels after three to six training sessions ($d' > 1.75$, approximately 80% correct trials, $P < 0.001$).

We used videography and automated whisker tracking (Fig. 1a)[27] to determine the whisker movements and somatosensory input. Rhythmic whisking (10–20 Hz) was superposed on slower changes
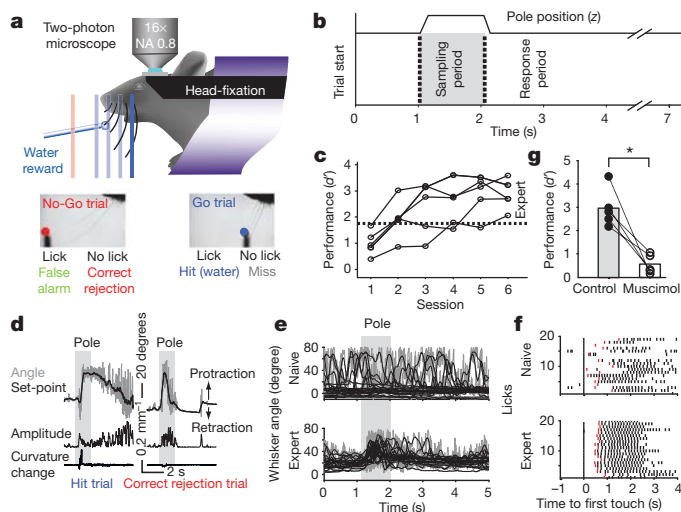
Figure 1 | Learning a whisker-based object-detection task under the microscope. a, A head-fixed mouse under a two-photon microscope. Whisker movements were tracked with high-speed videography. For each trial, a metal pole was presented either within reach of the whiskers (in one of several target locations, corresponding to different hues of blue; go trial) or out of reach (red, no-go trial). **b**, Onset of pole movement produced an auditory cue (vertical dotted lines). The pole was within reach in the sampling period. Answer licks were scored in the response period. **c**, Learning curves. The sensitivity index d' measures behavioural performance ($d' = 0$, chance performance; $d' = 1.75$, expert level (above the dashed line) approximately 80% correct trials). **d**, Whisker movement and forces. Top traces, trial showing whisker angle (grey) and set point (black). Middle traces, whisking amplitude (see Methods). Bottom traces, change in whisker curvature, which is proportional to force acting on the follicle. Left, hit trial; right, correct rejection trial. **e**, Learning-related changes in whisking. Whisker angle (measured at the base of the whisker, grey) and set point (low-pass filtered angle, black) for 20 consecutive correct rejection trials in the first (top; $d' = 0.83$, first session) and fifth session (bottom; $d' = 3.52$). **f**, Learning-related changes in licking. Licks (ticks; answer licks in red) aligned to first touch, for 20 consecutive hit trials of a naive mouse (top; $d' = 0.83$) and of the same animal but in the fourth session (bottom; $d' = 3.59$). **g**, Behavioural performance drops after inactivation of vM1 ($n = 5$ mice; control, solid circles; muscimol, open circles; asterisks, $P < 0.001$).

in the average whisker position, the set point (Fig. 1d, e). Whisking was thus split into set point (<6 Hz) and amplitude (6–60 Hz; Methods)[29] (Fig. 1d). As a measure of sensory input, we extracted touch-induced changes in whisker curvature, which are proportional to the pressure activating mechanoreceptors in the follicle[30,31].

Improved performance in the object-detection task correlated with changes in motor behaviour. Naive mice whisked occasionally, in a manner that was unrelated to the trial structure (Fig. 1e), probably reflecting their uncertainty about the stimulus–response relationship. In contrast, expert mice protracted their whiskers through a large angle to search for the pole soon after it became available (within approximately 350 ms) (auditory cue, Fig. 1d, e)[27]. The repeatability of whisking across trials (Pearson's correlation coefficient; $\rho = 0.57$, $P < 0.001$) (Supplementary Fig. 1a and Methods) and the amplitude of whisker protraction during the sampling period increased with performance ($\rho = 0.54$, $P < 0.001$) (Supplementary Fig. 1b). Licking consisted of rhythmic bouts of 7.2 ± 0.45 Hz[5,21] (Fig. 1f). The timing of lick bouts with respect to touch became stereotyped with learning. Naive mice licked with variable latencies (on hit trials), and licking sometimes even preceded touch, indicating that the mice were guessing. Expert mice licked shortly after first touch, and the temporal jitter of the first lick in a bout decreased with performance ($\rho = -0.50$, $P < 0.001$) (Supplementary Fig. 1c).

Thus, object detection relies on a sequence of actions, linked by sensory cues. An auditory cue triggers whisking during the sampling period. Contact between whisker and object causes licking for a water

reward during a response period. Silencing vM1 indicates that this task requires the motor cortex. With vM1 silenced, task-dependent whisking persisted, but was reduced in amplitude and repeatability (Supplementary Figs 1 and 2), and task performance dropped (permutation test; $P < 0.001$) (Fig. 1g and Supplementary Fig. 1e). Similar experiments revealed that vS1 is also crucial for the object-detection task (Supplementary Fig. 1f)[27,32]. These observations suggest that vM1 and vS1 have critical roles in linking sensation and movement.

Chronic imaging of population activity

L2/3 cells in vM1 may directly mediate the learned association between whisking, touch and licking. We therefore imaged the activity of L2/3 neurons during learning (Fig. 2). To target vM1 for imaging we injected adeno-associated virus (AAV) expressing tdTomato[33]
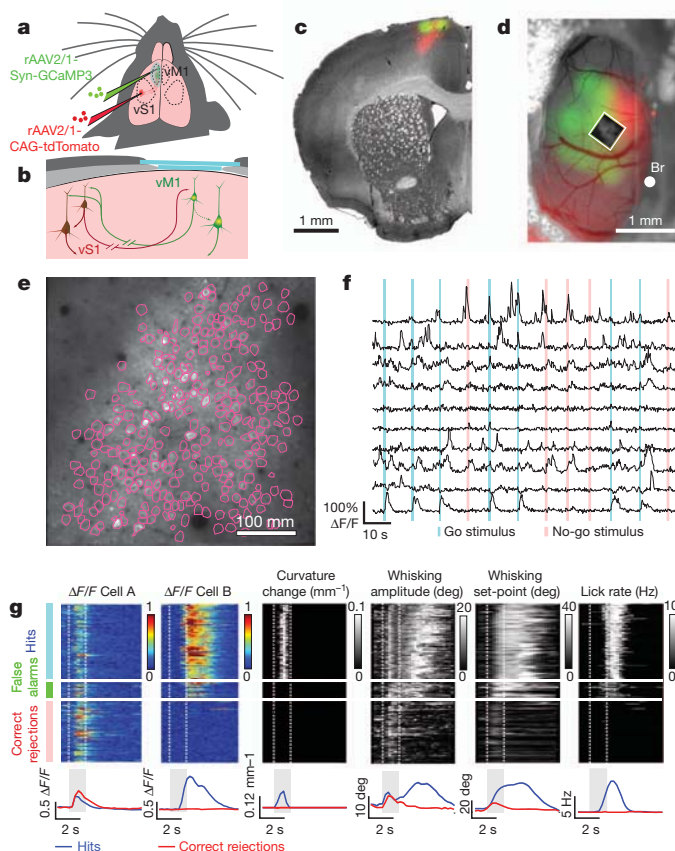

Figure 2 | Imaging population activity across trials. a, Injection sites for GCaMP3 virus in vM1 and tdTomato virus in vS1. rAAV2/1-CAG-tdTomato, recombinant AAV serotype 2/1 (rAAV2/1) virus expressing tdTomato under the *CAG* promoter; rAAV2/1-Syn-GCaMP3, rAAV2/1 virus expressing GCaMP3 under the human synapsin 1 promoter. **b**, L2/3 neurons in vM1 receive strong input from vS1 and excite deep layer neurons in vM1. Light blue, glass imaging window; light grey, bone; dark grey, dental cement. **c, d**, GCaMP3 (green) and tdTomato (red) fluorescence image overlaid on a bright-field image (grey), in coronal section (**c**) and through the imaging window (**d**). Box, field of view in **e**. Br, Bregma. **e**, L2/3 neurons expressing GCaMP3 (depth, 210 μm). Individual regions (individual neurons) are outlined in pink. **f**, Example fluorescence traces (fractional change in fluorescence, $\Delta F/F$; ten neurons in twelve trials). Vertical bars, sampling period (blue, go trials; red, no-go trials). **g**, Example neurons (cells A and B) across one session (329 trials; expert mouse, $d' = 3.13$) and simultaneously recorded behaviours. Consecutive hit, false alarm and correct rejection trials are arrayed from top to bottom (misses were rare in this session). Fluorescence intensity was normalized. Curvature changes due to touch only occur during the sampling period in hit trials, because otherwise the pole was out of reach. Whisking occurred in all trials. Licking occurred in hit and false alarm trials. Lower panel, session averages for correct trial types (blue, hits; red, correct rejections). Deg, degrees.

into the C2 column of vS1 and visualized red axonal fluorescence in vM1 (Fig. 2a–d; see Methods). We infected vM1 with the genetically encoded calcium indicator GCaMP3 (ref. 34). Long-term expression of GCaMP3 did not cause detectable damage *in vivo*, and it did not inhibit long-term potentiation in brain slices (Supplementary Figs 3 and 4).

We imaged GCaMP3-expressing neurons through an imaging window[35] in fields of view overlapping with the red axons (Fig. 2c–e). Images (approximately 250 neurons; Supplementary Table 1) were acquired continuously (4 Hz) over sessions lasting 1 h (280 trials; range of 141–424 trials). Regions of interest were drawn around individual cells to extract fluorescence dynamics caused by neural activity (Fig. 2e and Supplementary Fig. 5). A deconvolution algorithm was used to detect fluorescence events[36] corresponding to small bursts of action potentials (>2 action potentials)[34] (Supplementary Fig. 5 and Methods). Events were detected in 10.6% of neurons per session (Methods and Supplementary Table 1) (Fig. 2f). Of all neurons, 43% showed activity in at least one session. All subsequent analyses were based on these 'events' (286 unique neurons; >10 events per session; 5 animals; 6 sessions per animal). Time series of events were aligned with recordings of behaviour, such as whisking, licking and touch, and grouped by trial type (hit, correct rejection, miss and false alarm) (Fig. 2g).

Intermingled representations in the motor cortex

L2/3 cells in vM1 receive strong input from vS1. To investigate which behaviours are represented by L2/3 cells during active somatosensation, we quantified how well specific behavioural variables could be decoded from neural activity[37]. We used random forests[38], a generalized form of regression (Methods), to decode behaviour based on all neurons (Fig. 3). Each behavioural session was treated separately. The behavioural features measured touch (whisker curvature changes; Fig. 1d) and movements (whisking set-point, whisking amplitude and licking; Methods and Fig. 1d, f). The algorithm used the activity of populations of neurons to fit individual behavioural features (the 'model'), taking into account dynamics within and across trials (Fig. 3). The explained variance (R_i^2, for the *i*th behavioural feature) was used to measure the quality of decoding.

Population activity typically accounted for the recorded behavioural features with high fidelity. The model captured the timing of contact between whisker and object (Fig. 3a) (range of R^2 values was 0.03–0.55 for individual mice and sessions). Coding of touch in the motor cortex[18,22] is consistent with direct input from vS1 to the imaged neurons[8]. The model also predicted motor behaviours (Fig. 3b–e) (whisking amplitude, range of R^2, 0.22–0.60; whisker set-point, range of R^2, 0.22–0.66; lick rate, range of R^2, 0.13–0.75). Accurate decoding of whisking amplitude, whisking set-point and lick rate suggests that vM1 controls these slowly varying motor parameters, as expected from previous motor cortex mapping[5,8,16,18,29,39] and neurophysiological experiments[5,29,39]. The low sampling rate of imaging may have missed rapid modulation in neural activity[29].

We also quantified decoding accurancy as a function of the number of neurons (Supplementary Fig. 6). Each behavioural feature required only a very low number of neurons (1.5–5.5) to reach saturating decoding performance. This suggests that the representations underlying object localization are redundant.

We next asked how individual neurons contribute to the population representation. Correlations between activity of individual neurons and specific behaviours were apparent in the raw traces. For example, some neurons were active at the same time as whisking during the sampling period, independent of trial type (cell A, Fig. 2g), whereas other neurons were active only during licking (cell B, Fig. 2g) or during other phases of the task (Supplementary Figs 7–13).

To quantify neuronal representations we used random forests again, but this time behavioural features were fit using single neurons. The explained variance (R_i^2, for the *i*th behavioural feature) was used
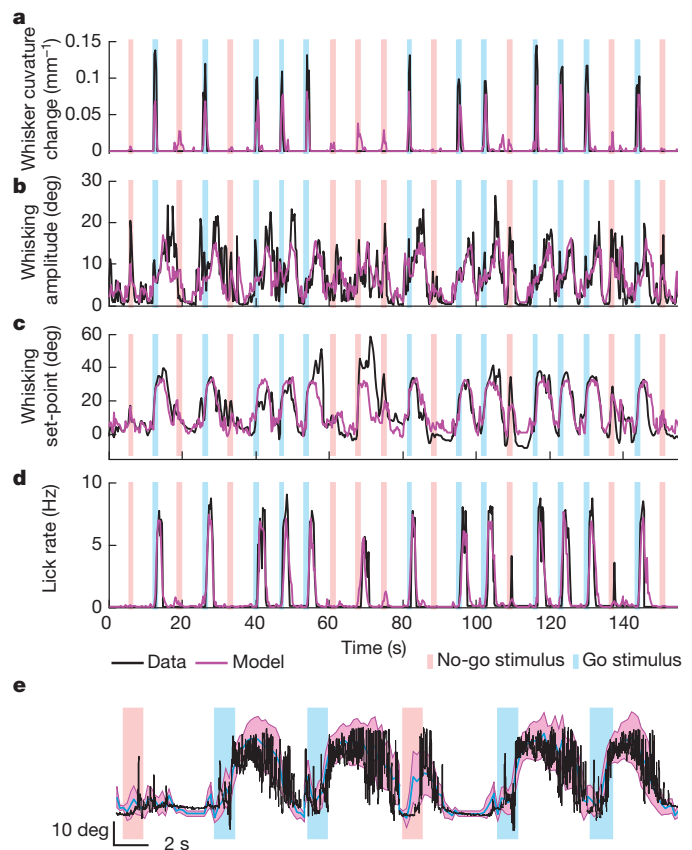

Figure 3 | Population decoding of behavioural features. a–d, Time series of behavioural features (black; down-sampled to the imaging rate, 4 Hz) and a model based on the activity of all active neurons in one session (magenta) (same session as in Fig. 2g). Vertical bars, sampling period (blue, go trials; red, no-go trials). The behavioural features measured are whisker curvature change (**a**), whisking amplitude (**b**), whisking set-point (**c**) and lick rate (**d**). Shuffling trial labels dropped the quality of the fit for all behavioural features. $R_i^2 > R_{i\ shuffled}^2$, $P < 0.001$ for all sessions and animals except for three sessions in which coding of touch was weak (mean *z* scores (1,000 shuffles): whisking amplitude, 73; whisking set-point, 28; licking, 23; touch, 10; see Supplementary Fig. 14l, m for an explanation of *z* scores). **e**, Overlay of whisking at full bandwidth (black) and the model (thick blue trace, whisking set-point; magenta band, whisking set-point ± whisking amplitude). Deg, degrees.

to measure the quality of decoding by single neurons. Almost one-half of the active neurons (42%) decoded one or more of the measured behavioural features (mean R_i^2 for the feature that was decoded best, 0.22) (Supplementary Fig. 7), with varying degrees of reliability (Supplementary Fig. 14a–k). Shuffling the trial labels caused the quality of the fit to decrease ($R_i^2 > R_{i,\ shuffled}^2$, $P < 0.05$ for 351 out of 358 neurons; 1,000 shuffles; average *z* score, 31; Supplementary Fig. 14l, m), indicating that the random forest algorithm captured the covariance of activity and behaviour within trials as well as across trials.

We classified neurons into categories (touch, whisking and licking), mainly based on the largest correlation coefficient (maximum R_i^2) (Supplementary Fig. 7). However, one of the trial types was sometimes more informative than other trial types and caused the largest overall correlation coefficient to be overruled (Methods) (Supplementary Figs 7–13). For example, the relationship between neuronal activity and whisking was only evaluated in trials without touch and licking (correct rejections). In addition, we considered correlations between activity and sensory variables (object location or forces acting on the whisker, Supplementary Figs 10, 13 and 15). For example, in hit trials some licking neurons showed activity levels that varied with object location, a signature of sensory input (Supplementary Figs 8, 11, 13
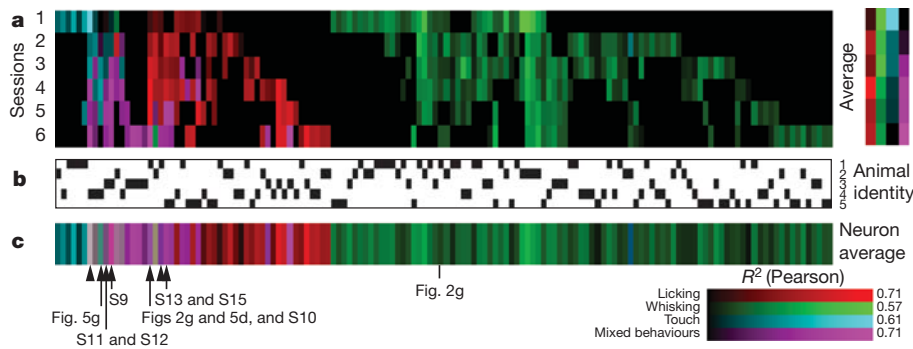
Figure 4 | Single neuron representations across learning. a, Dynamics of classified neurons during learning (cyan, touch; magenta, mixed; red, licking; green, whisking). Each column corresponds to one neuron. The intensity of the colour indicates the correlation (R^2) between data and the model (Methods). Session 1, naive mice; session 6, expert mice. **b**, Animal identity. Each row corresponds to one animal. Black ticks indicate the animal corresponding to the classified cell. **c**, Classification of individual neurons averaged across sessions. Arrowheads, neurons with object location-dependent activity. Tagged neurons, data shown in other figures. S, Supplementary Information figure.

and 15). Such neurons, which correlated with multiple behavioural features, were classified as 'mixed' neurons (see Supplementary Fig. 7 and Methods for a full explanation of the classification rules).

The other active neurons remained unclassified on the basis of the measured behavioural features (mean R_i^2 for best feature, 0.03). However, these neurons still showed interpretable task-related activity (Supplementary Fig. 7). Some neurons became active during errors and others while withholding licking[5]. Together, the unclassified neurons might have roles in cognitive processes; alternatively, they might relate to motor or sensory variables that were not tracked in our study. Overall, only a small fraction of active vM1 neurons expressed any one representation (3% touch, 26% whisking, 9% licking and 4% mixed), suggesting sparse coding of multiple behavioural features in vM1.

Dynamics of representations with learning

We next investigated how individual neurons change with learning. We used the classification of individual neurons to track changes in representations over learning (6 sessions, corresponding to 6–14 days; Methods and Supplementary Fig. 5). Single neurons were dynamic (Fig. 4 and Supplementary Fig. 16): cells that decoded a given feature during one session often did not contribute during other sessions, and vice versa. However, when a neuron was classified in different sessions it decoded similar behavioural features (Supplementary Table 2) so that most neurons were classified as part of no more than one representation throughout learning (Fig. 4a, c). In particular, whisking neurons rarely became licking neurons and vice versa.

All response categories were detected in all animals (Fig. 4a, b and Supplementary Fig. 7) and the representations were spatially intermingled (Supplementary Fig. 16); nearby neurons were equally likely to be part of any of the representations (spatial clustering index (SCI), ~1.0). These data suggest that motor cortex contains intermingled representations of different movements, and that individual neurons are primed to participate in controlling specific movements.

Learning also altered the timing of neuronal activity. In naive mice, activity was distributed uniformly across the trial (Fig. 5a). With learning, activity of the classified neurons (but not the unclassified neurons) shifted towards the sampling period (Fig. 5b, c and Supplementary Fig. 17). The fraction of neurons that were most active in the sampling period increased by a factor of three, with little change in overall activity levels (Supplementary Fig. 17). These shifts in activity were explained in part by changes in whisking, which became more concentrated in the sampling period with learning (Fig. 1e), and a shorter touch–lick latency (Supplementary Fig. 1). With learning, licking neurons became active earlier within the trial and also began to fire earlier with respect to licking. In naive mice, activity in licking
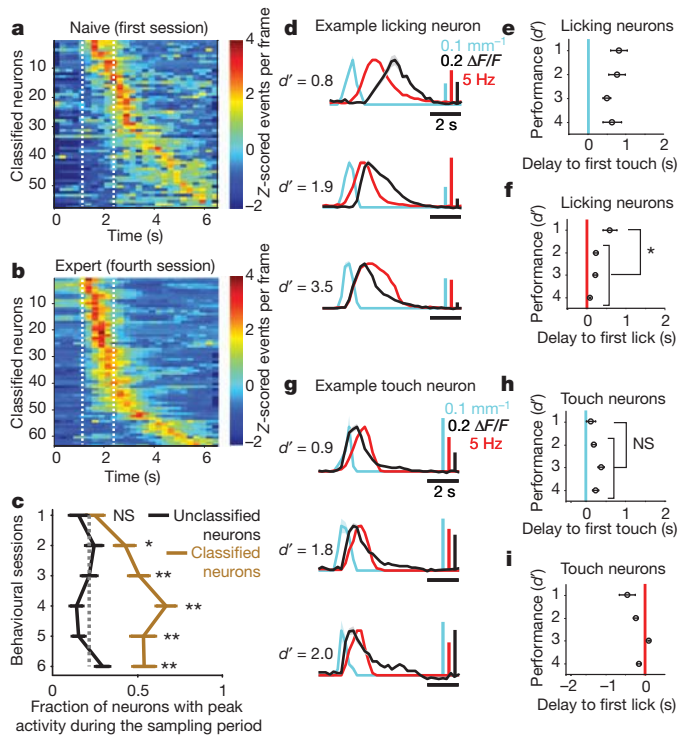

Figure 5 | Plasticity in task-related neuronal dynamics. a, b, Trial averages of all classified neurons, ordered by the timing of their peak activity. **a**, Naive mice (first session). **b**, Expert mice (fourth session). **c**, Fraction of neurons with peak activity during the sampling period of classified (brown) and unclassified neurons (black) as a function of learning (mean ± s.e.m., $n = 5$ mice). The grey dotted line indicates the expected fraction of neurons if the timing of peak activity was uniformly distributed across the trial (*$P < 0.05$; **$P < 0.005$; χ^2 test for each session). **d–i**, Temporal parameters of licking and touch neurons as a function of task performance. Performance (d') was binned as follows: 1, <1.75; 2, 1.75–2.5; 3, 2.5–3.5; 4, >3.5. **d**, Peristimulus time histograms (PSTHs) of touch (cyan, change in whisker curvature), lick rate (red) and fluorescent traces of a representative licking neuron (black) in a naive mouse (top trace), a mouse during learning (middle trace) and an expert mouse (bottom trace). **e**, Delay from first contact to activity onset in licking neurons (12 neurons, decoding licking for at least 4 days; mean ± s.e.m.). **f**, Delay from first lick to activity onset in licking neurons. The delay shortened after learning (*$P < 0.005$, Wilcoxon rank sum test). **g**, PSTHs of touch (cyan, change in whisker curvature), lick rate (red) and fluorescent traces of a representative touch neuron (black) in a naive mouse (top trace), a mouse during learning (middle trace) and an expert mouse (bottom trace). **h**, Delay from first contact to activity onset in touch neurons (12 neurons from 4 animals). **i**, Delay from first lick to activity onset in touch neurons.

neurons trailed licking (Fig. 5d–f); in expert mice, activity anticipated licking (when the slow kinetics of GCaMP3 fluorescence were taken into account[34]). Licking neurons always lagged the first touch (Fig. 5e), as did touch neurons (Fig. 5g, h). These learning-related changes in temporal relationships between activity and motor behaviour suggest roles of these neurons in controlling movement. Furthermore, nearby neurons can participate in highly specific forms of circuit plasticity during learning.

We next analysed the dynamics of population-level representations during learning (Fig. 6a–c). We decoded the behavioural features over all experimental sessions and evaluated the quality of the fit as a function of behavioural performance (Fig. 6a). Overall, the representation of licking strengthened, even though the number of licks per trial remained stable during learning (Supplementary Fig. 17e). In contrast, the representation of whisking remained stable, even though whisking during the sampling period became more vigorous and purposeful (Fig. 1e and Supplementary Fig. 1).

We assessed the stability of population representations by using the model derived in one session to predict the behavioural features of another session (Fig. 6b). For the first two or three sessions the models derived on one day failed to predict movements on subsequent days, implying labile population representations. However, as the behaviour reached a plateau level the representations stabilized, particularly for whisking and licking. More than 44% of the variance in the change in behavioural performance between any two sessions could be explained on the basis of changes in the representations of the different behavioural features (multiple linear regression; $P < 10^{-17}$; $F_{4,145} = 29$). Changes in the representation of licking were more predictive of the behavioural performance changes than whisking or touch (Fig. 6c). The dynamics of the different representations suggest that vM1 innately controls whisking but participates in the control of licking only in the context of specific sensorimotor contingencies, such as licking triggered by touch.

Discussion

The precise roles of motor cortex in shaping movement and motor learning have been debated for more than a century (reviewed in refs 1, 40). Classic recordings from identified pyramidal-tract-type neurons, which carry cortical output to motor centres, revealed activity related to muscle forces and movements[41]. However, pyramidal-tract-type neurons constitute only a tiny fraction of motor cortex neurons[7]. Simultaneous recordings from diverse neuron types indicate that neuronal ensembles define trajectories of multi-joint movements[26,42]. Conversely, stimulating groups of motor cortex neurons on behavioural timescales evokes complex, ethologically relevant movements[43]. vM1 projects to brainstem nuclei that control facial motor programs such as whisking[19,20] and licking[5]. Our imaging experiments in vM1 show spatially intermingled representations of various facial movements (Supplementary Fig. 16), all of which are related to performing the object-detection task (Figs 1 and 3). Together, these observations suggest that small regions of motor cortex help to orchestrate goal-directed movements involving multiple body parts.

Motor cortex activity changes with learning[3–5]. Goal-directed movements might therefore be established or fine-tuned in the motor cortex. Consistent with this view, representations in L2/3 of motor cortex changed during learning of the object detection task. However, individual L2/3 neurons seem to be pre-wired to represent particular motor variables: whisking neurons rarely became licking neurons and vice versa (Fig. 4). In expert animals, population-level representations were stable (Fig. 6), even with unstable representations of single neurons (Fig. 4 and Supplementary Fig. 16). Theoretical work has shown that drifting representations at the level of individual neurons may be crucial for motor learning[4].

The representation of whisking was strong in L2/3 neurons of naive animals and remained strong throughout learning (Fig. 6). In contrast, the representation of licking increased with improvements in behavioural performance. Control of voluntary whisking might therefore be innate to vM1, whereas vM1 assumes control of licking as the animal learns to initiate licking in response to a specific sensory stimulus (for example, touch (Fig. 1) or olfaction[5]). Enabling flexible associations between sensation and action could be a core function of the superficial layers of the motor cortex.

To investigate the cellular mechanisms driving changes in vM1 activity, we used an object-location task. Learning this task requires chaining a set of sensory-modulated actions into a specific order. Behaviourally, we observed that stereotypic whisking and latency between touch and licking were highly correlated with task proficiency (Fig. 1). Early during learning, activity of L2/3 neurons was distributed uniformly across time, and this might provide a basis from which[2,44] appropriate sequences of movements can be selected, depending on task demands (Fig. 5 and Supplementary Fig. 17). After learning, neurons fired mostly during the sampling period, coincident with whisking, touch and onset of licking. This change of timing suggests a role for a dopaminergic reward prediction error signal[45], probably arising in the ventral tegmental area[6], which could implement temporal credit assignment in synaptic plasticity[2].

METHODS SUMMARY

We used adult male PV-IRES-cre mice (over 2 months old) (B6;129P2-Pvalbtm1(cre)Arbr/J, The Jackson Laboratory). Details of surgery, imaging and data analysis are provided in Methods.
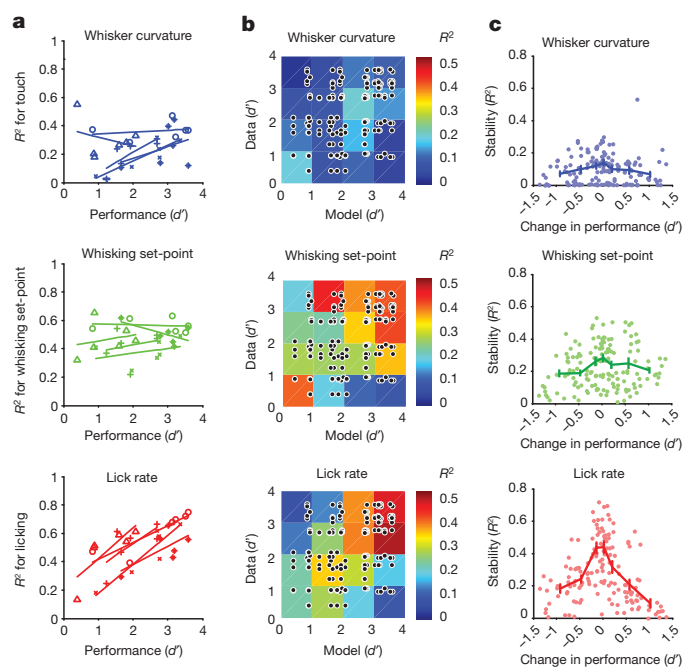

Figure 6 | Stability in population decoding. a, Decoding of behavioural features as a function of behavioural performance. Individual animals correspond to different symbols; lines are linear fits. Top, whisker curvature; middle, whisking set-point; bottom, lick rate. Whisking amplitude was similar to whisking set-point and is not shown. **b**, Matrix of correlation coefficients for all mice, binned and averaged by behavioural performance (d'). Each point corresponds to a model derived at one value of d' applied to a session with another value of d'. The points corresponding to models and data from the same session (diagonal) were excluded. **c**, Stability of population decoding of behavioural features (change in R^2) as a function of change in behavioural performance. Points are derived as in **b**. Changes in the representation of licking were more predictive with respect to changes in behavioural performance than whisking or touch: licking, $R^2 = 0.39$, $F_{1,148} = 94$, $P < 10^{-17}$; whisking set-point, $R^2 = 0.21$; $F_{1,148} = 40$, $P < 10^{-17}$; touch $R^2 = 0.07$; $F_{1,148} = 11$, $P < 0.001$; licking versus set point, $P < 0.001$, Ansari–Bradley test.

1. Scott, S. H. Inconvenient truths about neural processing in primary motor cortex. *J. Physiol. (Lond.)* **586,** 1217–1224 (2008).
2. Wolpert, D. M., Diedrichsen, J. & Flanagan, J. R. Principles of sensorimotor learning. *Nature Rev. Neurosci.* **12,** 739–751 (2011).
3. Wise, S. P., Moody, S. L., Blomstrom, K. J. & Mitz, A. R. Changes in motor cortical activity during visuomotor adaptation. *Exp. Brain Res.* **121,** 285–299 (1998).
4. Rokni, U., Richardson, A. G., Bizzi, E. & Seung, H. S. Motor learning with unstable neural representations. *Neuron* **54,** 653–666 (2007).
5. Komiyama, T. *et al.* Learning-related fine-scale specificity imaged in motor cortex circuits of behaving mice. *Nature* **464,** 1182–1186 (2010).
6. Hosp, J. A., Pekanovic, A., Rioult-Pedotti, M. S. & Luft, A. R. Dopaminergic projections from midbrain to primary motor cortex mediate motor skill learning. *J. Neurosci.* **31,** 2481–2487 (2011).
7. Keller, A. Intrinsic synaptic organization of the motor cortex. *Cereb. Cortex* **3,** 430–441 (1993).
8. Mao, T. *et al.* Long-range neuronal circuits underlying the interaction between sensory and motor cortex. *Neuron* **72,** 111–123 (2011).
9. Hooks, B. M. *et al.* Laminar analysis of excitatory local circuits in vibrissal motor and sensory cortical areas. *PLoS Biol.* **9,** e1000572 (2011).
10. Anderson, C. T., Sheets, P. L., Kiritani, T. & Shepherd, G. M. Sublayer-specific microcircuits of corticospinal and corticostriatal neurons in motor cortex. *Nature Neurosci.* **13,** 739–744 (2010).
11. Kaneko, T., Cho, R., Li, Y., Nomura, S. & Mizuno, N. Predominant information transfer from layer III pyramidal neurons to corticospinal neurons. *J. Comp. Neurol.* **423,** 52–65 (2000).
12. Kaneko, T., Caria, M. A. & Asanuma, H. Information processing within the motor cortex. II. Intracortical connections between neurons receiving somatosensory cortical input and motor output neurons of the cortex. *J. Comp. Neurol.* **345,** 172–184 (1994).
13. Pavlides, C., Miyashita, E. & Asanuma, H. Projection from the sensory to the motor cortex is important in learning motor skills in the monkey. *J. Neurophysiol.* **70,** 733–741 (1993).
14. Iriki, A., Pavlides, C., Keller, A. & Asanuma, H. Long-term potentiation in the motor cortex. *Science* **245,** 1385–1387 (1989).
15. Rioult-Pedotti, M. S., Friedman, D., Hess, G. & Donoghue, J. P. Strengthening of horizontal cortical connections following skill learning. *Nature Neurosci.* **1,** 230–234 (1998).
16. Li, C. X. & Waters, R. S. Organization of the mouse motor cortex studied by retrograde tracing and intracortical microstimulation (ICMS) mapping. *Can. J. Neurol. Sci.* **18,** 28–38 (1991).
17. Brecht, M. *et al.* Organization of rat vibrissa motor cortex and adjacent areas according to cytoarchitectonics, microstimulation, and intracellular stimulation of identified cells. *J. Comp. Neurol.* **479,** 360–373 (2004).
18. Ferezou, I. *et al.* Spatiotemporal dynamics of cortical sensorimotor integration in behaving mice. *Neuron* **56,** 907–923 (2007).
19. Hattox, A. M., Priest, C. A. & Keller, A. Functional circuitry involved in the regulation of whisker movements. *J. Comp. Neurol.* **442,** 266–276 (2002).
20. Grinevich, V., Brecht, M. & Osten, P. Monosynaptic pathway from rat vibrissa motor cortex to facial motor neurons revealed by lentivirus-based axonal tracing. *J. Neurosci.* **25,** 8250–8258 (2005).
21. Travers, J. B., Dinardo, L. A. & Karimnamazi, H. Motor and premotor mechanisms of licking. *Neurosci. Biobehav. Rev.* **21,** 631–647 (1997).
22. Kleinfeld, D., Sachdev, R. N., Merchant, L. M., Jarvis, M. R. & Ebner, F. F. Adaptive filtering of vibrissa input in motor cortex of rat. *Neuron* **34,** 1021–1034 (2002).
23. Sato, T. R. & Svoboda, K. The functional properties of barrel cortex neurons projecting to the primary motor cortex. *J. Neurosci.* **30,** 4256–4260 (2010).
24. Ganguly, K. & Carmena, J. M. Emergence of a stable cortical map for neuroprosthetic control. *PLoS Biol.* **7,** e1000153 (2009).
25. Stosiek, C., Garaschuk, O., Holthoff, K. & Konnerth, A. *In vivo* two-photon calcium imaging of neuronal networks. *Proc. Natl Acad. Sci. USA* **100,** 7319–7324 (2003).
26. Dombeck, D. A., Graziano, M. S. & Tank, D. W. Functional clustering of neurons in motor cortex determined by cellular resolution imaging in awake behaving mice. *J. Neurosci.* **29,** 13751–13760 (2009).
27. O'Connor, D. H. *et al.* Vibrissa-based object localization in head-fixed mice. *J. Neurosci.* **30,** 1947–1967 (2010).
28. O'Connor, D. H., Peron, S. P., Huber, D. & Svoboda, K. Neural activity in barrel cortex underlying vibrissa-based object localization in mice. *Neuron* **67,** 1048–1061 (2010).
29. Hill, D. N., Curtis, J. C., Moore, J. D. & Kleinfeld, D. Primary motor cortex reports efferent control of vibrissa motion on multiple timescales. *Neuron* **72,** 344–356 (2011).
30. Birdwell, J. A. *et al.* Biomechanical models for radial distance determination by the rat vibrissal system. *J. Neurophysiol.* **98,** 2439–2455 (2007).
31. Knutsen, P. M. & Ahissar, E. Orthogonal coding of object location. *Trends Neurosci.* **32,** 101–109 (2009).
32. Hutson, K. A. & Masterton, R. B. The sensory contribution of a single vibrissa's cortical barrel. *J. Neurophysiol.* **56,** 1196–1223 (1986).
33. Shaner, N. C. *et al.* Improved monomeric red, orange and yellow fluorescent proteins derived from Discosoma sp. red fluorescent protein. *Nature Biotechnol.* **22,** 1567–1572 (2004).
34. Tian, L. *et al.* Imaging neural activity in worms, flies and mice with improved GCaMP calcium indicators. *Nature Methods* **6,** 875–881 (2009).
35. Trachtenberg, J. T. *et al.* Long-term *in vivo* imaging of experience-dependent synaptic plasticity in adult cortex. *Nature* **420,** 788–794 (2002).
36. Vogelstein, J. T. *et al.* Fast nonnegative deconvolution for spike train inference from population calcium imaging. *J. Neurophysiol.* **104,** 3691–3704 (2010).
37. Graf, A. B., Kohn, A., Jazayeri, M. & Movshon, J. A. Decoding the activity of neuronal populations in macaque primary visual cortex. *Nature Neurosci.* **14,** 239–245 (2011).
38. Hastie, T., Tibshirani, R. & Friedman, J. *The Elements of Statistical Learning* 2nd edn (Springer, 2009).
39. Carvell, G. E., Miller, S. A. & Simons, D. J. The relationship of vibrissal motor cortex unit activity to whisking in the awake rat. *Somatosens. Mot. Res.* **13,** 115–127 (1996).
40. Graziano, M. S. A. *The Intelligent Movement Machine* 1st edn (Oxford, 2009).
41. Evarts, E. V. Relation of pyramidal tract activity to force exerted during voluntary movement. *J. Neurophysiol.* **31,** 14–27 (1968).
42. Afshar, A. *et al.* Single-trial neural correlates of arm movement preparation. *Neuron* **71,** 555–564 (2011).
43. Graziano, M. S. & Aflalo, T. N. Mapping behavioral repertoire onto the cortex. *Neuron* **56,** 239–251 (2007).
44. Salinas, E. Rank-order-selective neurons form a temporal basis set for the generation of motor sequences. *J. Neurosci.* **29,** 4369–4380 (2009).
45. Schultz, W., Dayan, P. & Montague, P. R. A neural substrate of prediction and reward. *Science* **275,** 1593–1599 (1997).

METHODS

Chronic window preparation. All procedures were approved by the Janelia Farm Research Campus Institutional Animal Care and Use Committee. We used adult (older than postnatal day 60) male PV-IRES–Cre (parvalbumin internal ribosomal entry site (IRES) Cre recombinase) mice (B6;129P2-Pvalbtm1(cre)Arbr/J, The Jackson Laboratory). All surgeries were conducted under isoflurane anaesthesia (1.5–2%). Additional drugs reduced potential inflammation (subcutaneous injection of 5 mg kg^{-1} ketoprofen) and provided local (0.5% Marcaine solution injected under the scalp) and general analgesia (intraperitoneal injection of 0.1 mg kg^{-1} buprenorphine). A circular piece of scalp was removed and the underlying bone was cleaned and dried. The periostium was removed with a dental drill and the exposed skull was covered with a thin layer of cyano-acrylic primer (Crazy glue). A custom-machined titanium frame was cemented to the skull with dental acrylic (Lang Dental).

Afferents from the somatosensory cortex were labelled with virus expressing tdTomato[33] (rAAV2/1-CAG-tdTomato; 20 nl at 300- and 550-μm depths). The C2 barrel was targeted based on intrinsic signal imaging[28]. The virus was injected with a custom, piston-based, volumetric injection system (based on a Narishige, MO-10 manipulator)[46]. Glass pipettes (Drummond) were pulled and bevelled to a sharp tip (outer diameter of 30 μm). Pipettes were back-filled with mineral oil and front-loaded with viral suspension immediately before injection.

A craniotomy was made over the vM1 of the left hemisphere (size, 3 × 2 mm; centre relative to Bregma: lateral, 0.8 mm; anterior, 1 mm) (Fig. 2a–d). These coordinates were previously determined using intracortical microstimulation[8,16,18], by mapping axonal projections from vS1 in vM1 (refs 8, 47), and by trans-cellular labelling with pseudorabies virus (data not shown). Neurons underlying the craniotomy were labelled by injecting rAAV2/1-Syn-GCaMP3 (produced by the University of Pennsylvania Gene Therapy Program Vector Core). The brain was covered with agar (2%). Between four and eight sites (10–15 nl per site; depth, 150–210 μm; rate, 10 nl per minute) were injected per craniotomy.

The imaging window was constructed from two layers of standard microscope coverglass (Fisher; number 2 thickness, 170–210 μm), joined with an ultraviolet curable optical glue (NOR-61, Norland). A larger piece was attached to the bone and a smaller insert was fitted snugly into the craniotomy (Fig. 2b, d). The bone surrounding the craniotomy was thinned to allow for a flush fit between the insert and the underlying dura.

After virus injection, the glass window was lowered into the craniotomy. The space between the glass and the bone was sealed off with a thin layer of agar (2%), and the window was cemented in place using dental acrylic (Lang Dental). At the end of the surgery, all whiskers on the right side of the snout except row C were trimmed. The mice recovered for 3 days before starting water restriction. Imaging sessions started 14–21 days after the surgery.

Behaviour. We designed an object-detection task, with three goals in mind: first, animals should be able to learn the task quickly, in a few days; second, the sensory (whisker contacts and forces) and motor (whisking, licking) behaviours needed to be tracked at high spatial and temporal resolutions throughout learning; third, we wanted to detect neurons in the motor cortex whose activity patterns might be shaped by sensory input. Because different object locations produce different somatosensory stimuli, we presented the object in several locations. Neural activity levels that depend on object location then indicate the coding of sensory variables.

Behavioural training began after the mice had restricted access to water for at least 7 days (1 ml per day)[5,28]. The behavioural apparatus was designed to fit under a custom-built two-photon microscope (https://openwiki.janelia.org/wiki/display/shareddesigns/). All behavioural training was performed under the microscope while imaging neural activity. In a pre-training session mice learned to lick for water rewards from a lick port (~100 rewards). At the same time the brain was inspected for suitable imaging areas. Fields of view were restricted to zones where expression of GCaMP3 and tdTomato (axons from vS1) overlapped (Fig. 2a–d). To escape the vasculature near the midline, imaging was typically performed towards the lateral edge of vM1. Mice with excessive brain movement, limited virus infection or impaired optical access (bone growth or large blood vessels in the vS1 axon projection zone) were excluded from the study.

During the first behavioural session (session 1) the pole was positioned within the range of the whiskers' resting position, thereby increasing the chance of a whisker–pole collision. As soon as performance reached $d' > 1$ the pole was advanced to a more anterior position (~0.5 mm from whisker resting position), forcing the mouse to sample actively for the pole. The target position was adjusted for every session. In expert mice, multiple target positions, all within reach of the whiskers, were introduced to study the effects of object location (Supplementary Figs 8–11, 13 and 15, and Supplementary Table 1).

Reversible inactivation. To inactivate vM1 the GABA (γ-aminobutyric acid) agonist muscimol was injected into the imaging area in expert mice. A small hole was drilled through the imaging window to allow access for a glass injection pipette. Muscimol hydrobromide (Sigma-Aldrich) was dissolved in saline (5 μg μl^{-1}) and 50 nl were injected slowly (10 nl per min) at depths of 500 and 900 μm under the pia[27]. The animals were left to recover for 2 hours before the behavioural session. Inactivation caused a complete absence of fluorescence transients in the imaged field of view (data not shown). Similar methods were used to inactivate vS1 (Supplementary Fig. 1)[27].

Imaging. GCaMP3 was excited using a Ti-Sapphire laser (Chameleon, Coherent) tuned to $\lambda = 1,000$ nm. We used GaAsP photomultiplier tubes (10770PB-40, Hamamatsu) and a 16× 0.8 NA microscope objective (Nikon). The field of view was 450 × 450 μm (512 × 256 pixels; pixel size, 0.88 × 1.76 μm), imaged at 4 Hz. The microscope was controlled with *ScanImage*[48] (http://www.scanimage.org). The average power for imaging was <70 mW, measured at the entrance pupil of the objective. For each mouse the optical axis was adjusted to be perpendicular to the imaging window. Imaging was continuous over behavioural sessions lasting approximately 1 h (average, 53 min; range, 24–72 min). Bleaching of GCaMP3 was negligible. Slow drifts of the field of view were corrected manually approximately every 50 trials using a reference image.

Image analysis. To correct for brain motion we used a line-by-line correction algorithm (similar to a method used previously[49], but based on a correlation-based error metric). First, we averaged five consecutive images showing the smallest luminance changes (chosen from the approximately 40 images comprising a behavioural trial). Each line of each frame was then fit to this reference image using a piecewise rigid gradient-descent method.

To align all trials within one session, the average of the trial showing the smallest luminance changes was used as the session reference and all other trials were aligned using normalized cross-correlation-based translation.

To extract fluorescence signals from individual cells, regions of interest (ROIs) were drawn based on neuronal shape (individual neurons appeared as fluorescent rings; Supplementary Fig. 5). Mean, maximum intensity and standard deviation values of all frames of a session were used to determine the boundaries of the neurons. An automated method was used to align the ROIs across sessions. For each ROI, a small square (50 × 50 pixels) around the ROI was selected. Displacements across sessions were calculated by computing the point at which the normalized cross-correlation for this square and the average image of the day peaked. For each ROI, its displacement vector was compared to that of its five nearest neighbours. In cases in which the displacement exceeded seven times the median of the neighbours' displacements, it was set to the median and flagged for manual inspection. The displacements of all ROIs defined a warp field for the entire image.

The pixels in each ROI were averaged to estimate the fluorescence of a single cell. The cell's baseline fluorescence, F_o, was determined in an iterative manner. First, we estimated the probability distribution function (PDF) of raw fluorescence for each ROI and centred it at its peak (that is, the peak was assigned a value of 0). A 'cutoff value' was calculated by choosing the points below the PDF's peak and determining the value above which 90% of these values lay (which was negative owing to our centring procedure). Cells were 'moderately active' if at least 1% of their fluorescence was above twice the absolute value of this cutoff value (that is, the PDF had a long positive tail). Cells were 'highly active' if the density at this cutoff value relative peak density exceeded 0.1 (that is, the PDF's positive tail was not only long but also fat). All other cells were 'sparsely active'. The initial F_o estimate was generated by taking a 60-s sliding window over raw fluorescence and using the 50th, 20th or 5th percentile as F_o for sparsely, moderately and highly active cells, respectively. Using this first F_o estimate, we computed a preliminary $\Delta F/F$ (defined as $(F - F_o)/F_o$) and extracted events based on a threshold (three times the median absolute deviation (MAD)). An event period was defined as starting 2 s before the peak during a cross of threshold and ending 5 s after the peak. In the subsequent F_o estimation procedure, F_o was only estimated for periods without events, and determined using linear interpolation for periods during events. The final $\Delta F/F$ trace used for all subsequent analysis was computed using this F_o trace. To produce an event vector from the $\Delta F/F$ trace and thereby minimize the temporal distortions caused by GCaMP3 dynamics[34], we used a non-negative deconvolution method (Supplementary Fig. 5)[36].

Calcium imaging with genetically encoded indicators was crucial for tracking the same neurons across multiple sessions. Furthermore, using imaging it is possible to sample neural activity densely within a region. However, current calcium indicators, including GCamP3, are not sufficiently sensitive to detect single action potentials *in vivo* and, as a consequence, activity in neurons with very low firing rates was probably missed[28,34]. Our analysis therefore focuses on relatively active neurons. In addition, the slow dynamics (on the order of 100 ms) of the calcium indicator limits the conclusions that can be drawn about connectivity and causality from imaging data.

Approximately 80% of cortical neurons are pyramidal[50]. GABAergic interneurons produce much smaller activity-dependent fluorescence changes than

pyramidal neurons, presumably because of their short action potentials and high concentrations of endogenous calcium buffer[51], and their activity was not likely to be detected using GCaMP3[28]. For these reasons, the vast majority of active neurons detected with our methods were probably excitatory pyramidal neurons.

Long-term expression of GCaMP3. AAV-mediated expression of GCaMP3 provides the high expression levels that are necessary for *in vivo* cellular imaging. However, expression continues to increase over months, which can lead to compromised cell health[34,52], and this correlates with breakdown of nuclear exclusion. Over the time course of our experiments (up to 4 weeks of expression), no more than 2% of the cells in the imaged field of view showed nuclear GCaMP3. These neurons were excluded from analysis. In addition, overall event rates were stable across time (Supplementary Fig. 17).

Several observations indicate that imaging did not damage the brain. First, because of the brightness and photostability of GCaMP3 we were able to use low average power. Second, there was no evidence for tissue damage (Supplementary Fig. 3). Third, task-related activity increased with learning in a specific manner, so that some representations (for example, licking) increased, whereas other representations did not change (whisking) (Fig. 6). These learning-related changes are inconsistent with nonspecific rundown.

Changes in intracellular calcium are necessary to trigger a variety of forms of cellular plasticity. Could GCaMP3 expression interfere with synaptic plasticity? The strength of calcium buffering (buffer capacity) can be estimated as buffer concentration divided by its dissociation constant (K_d)[53]. High concentrations (>200 μM) of strong (K_d, 170 nM) calcium buffer (for example, BAPTA) are required to block synaptic plasticity[54,55]. We estimated the concentration of GCaMP3 (K_d, 660 nM)[34] under our experimental conditions. We collected acute brain slices from mice that had been used in long-term imaging experiments. We then compared cellular fluorescence at saturating calcium levels, induced by high external K^+ (20–30 mM) to calibrated GCaMP3 solutions (in standard K^+-based internal solution normally used for whole-cell recording). Four weeks of expression in L2/3 pyramidal neurons of the visual cortex yielded 76 μM of GCaMP3 (ref. 52). Seven weeks of expression in vM1 gave 130 μM of GCaMP. These results suggest that GCaMP3 produces lower buffer capacity than BAPTA concentrations that are known not to perturb synaptic plasticity (buffer capacities, <200 versus >1200). Consistent with this, expression of GCaMP3 did not perturb induction of long-term potentiation in hippocampal brain slices (Supplementary Fig. 4) (GCaMP3 concentration was 15 μM, determined as above).

We further tested whether GCaMP3 expression level influenced the plasticity of neuronal responses. The relative baseline fluorescence measured in individual neurons was constant across days and it was therefore a good indicator of GCaMP3 expression. We calculated the probability that a classified cell remained active and retained its classification (that is, was stable). We compared stability in the 25% brightest and dimmest neurons. Dim and bright cells were similarly stable (dim cells, 65% stable; bright cells, 60% stable; $\chi^2 = 0.39$; $P > 0.5$). This analysis suggests that under our conditions GCaMP3 does not obviously perturb cellular plasticity *in vivo*.

Other measurements also suggest that plasticity was not obviously impaired by long-term expression of GCaMP3. Circuit function is shaped by ongoing plasticity, integrated over the recent past. Neurons with long-term expression of GCaMP3 generally show normal circuit properties. Orientation and direction selectivity are normal in GCaMP3-expressing L2/3 neurons in mouse V1 (ref. 52) and hippocampal place cells are normal in CA1 neurons in the hippocampus[56]. The sparseness and response types of L2/3 neurons in vS1 are indistinguishable when measured with electrophysiological methods or GCaMP3 (ref. 28). Finally, in our experiments L2/3 neurons showed specific learning-related changes in activity *in vivo* (Figs 4–6).

Whisker tracking. Whiskers were illuminated with a high-power light-emitting diode (LED) (940 nm, Roithner) and condenser optics (Thorlabs). Images were acquired through a telecentric lens (0.36×, Edmund Optics) by a high-speed CMOS camera (EoSense CL, Mikrotron, Germany) running at 500 frames per s (640 × 352 pixels; resolution, 42 pixels per mm). Image acquisition was controlled by Streampix 3 (Norpix). The whisker position and shape were tracked using automated procedures[27]. Whiskers are cantilevers beams, with one end embedded in the follicle in the whisker pad. The mechanical forces acting on the follicles can be extracted from the shape changes after contact between whisker and object. For example, a change in curvature at point p along the whisker is proportional to the force applied by the pole on the whisker[30]: $F \sim \Delta\kappa_p y_p$, where y_p is the bending stiffness at p (approximately 3 mm from the follicle). We thus present forces on the whiskers as the change in curvature, $\Delta\kappa$. These forces underlie object localization[27,31]. $\Delta\kappa$ was determined using a parametric curve comprising second-order polynomial fits to the whisker backbone. Periods of contact between whisker and object (touch) were detected based on the nearest distance between whisker and object, and $\Delta\kappa$. A total of ~13,000,000 whisker

video images, comprising ~7,500 behavioural trials, were analysed for this project.

Expert mice contacted the pole multiple times with one or several whiskers (average number of contacts for the dominant whisker, 8; range 0–19) before their decision (signalled by an answer lick on correct go trials).

Behavioural features. We analysed neural activity with respect to several behavioural features. Licks were detected with a lickometer[27] and lick rate (Hz) was defined as the inverse of the inter-lick interval. Our imaging rate (4 Hz) was slower than the rapid components of rhythmic whisking (10–20 Hz). In addition, motor cortex neurons primarily code for the slowly varying whisking variables, set-point and amplitude[29,39]. Whisker set-point was the low-pass filtered (6-Hz) whisker angle. Whisker amplitude was defined as the Hilbert transform[29] of the absolute value of the band-pass filtered (6–60-Hz) whisker angle (Fig. 1d). Because whiskers move mostly together[27], set point and amplitude were averaged across all whiskers. The time derivatives of whisker set-point and amplitude were used as independent features. $\Delta\kappa$ was measured during the sampling period. Protraction touch (positive curvature changes), retraction touch (negative curvature changes) and absolute values were treated separately. All behavioural features were down-sampled to match the image acquisition rate (4 Hz). Mean and maximum values were calculated for each feature in a 250-ms window centred on the middle of the new sampling point.

Decoding behavioural variables. The relationship between the calcium activity x_i of the ith neuron and the jth behavioural variable y_j can be characterized as an encoding description $P(x_i| y_j)$ or a decoding description $P(y_j|x_i)$. The encoding description specifies how much of neuronal activity can be accounted for by behavioural variables. The decoding description specifies how behavioural variables can be derived from the activity of one neuron or neuronal populations. Here, we focused on the decoding description.

We used machine learning algorithms to decode behavioural features based on activity. The input to the algorithm was the event rate (that is, deconvoluted $\Delta F/F$). To predict sensory input we also used time-shifted future activity. For motor variables we used both past and future activity, as neural activity could reflect motor commands, corollary discharges or reafferent input.

The goal of the decoder algorithm was to find a mapping $\hat{y}_j(t_k) = f\left[x_i(t_{k-l}), \ldots, x_i(t_k), \ldots, x_i(t_{k+p})\right]$ that best approximates $y_j(t_k)$ for all t_k (discretized time in units of 0.25 s, corresponding to the imaging rate); l and p represent the maximum negative and positive shifts of the activity respectively. We concatenated trials to generate a vector $\bar{t}$ of time-binned data. We used $l = 2$ and $p = 0$ for sensory variables, and $l = 2$ and $p = 2$ for sensory-motor variables (corresponding to time-shifts up to 0.5 s). The dimensionality of the input variables is $l + p + 1$. To simplify the notation, we define the vector $\bar{x}_{i,n}$ as the activity of cell i at all times shifted n frames to the future. The algorithm was trained on a subset of trials (the training set; 80%) and evaluated on a separate set of test trials (20%). We repeated this procedure five times to obtain a prediction for all trials[38].

The accuracy of decoding was evaluated using the Pearson correlation coefficient (ρ) between the model estimate and the data. The explained variance is $R^2 = \rho^2$ (range 0–1). R^2 was calculated separately for each trial type (that is, hit, correct rejection, miss and false alarm). Treating trial types separately was critical to disambiguate the relationship between different behavioural variables and activity. For example, we observed large-amplitude whisking during licking, which complicates the classification of neuronal responses. However, during correct rejection trials, licking was absent and whisking present, allowing classification. Similarly, in trained animals, touch and licking occurred with short latencies in hit trials (Figs 1 and 5). In contrast, touch was absent in false alarm trials.

Decoding was carried out using the random forests algorithm[38,57], a multivariate, non-parametric machine learning algorithm based on bootstrap aggregation (that is, bagging) of regression trees. We used the TreeBagger class implemented in Matlab. TreeBagger requires only a few parameters: the number of trees ($N_{trees} = 128$), the minimum leaf size (minleaf = 5), the number of features chosen randomly at each split ($N_{split} = N_{features}/3$; the typical value used by default). These parameters were chosen as a trade-off between decoder accuracy and computation time. We did not observe much improvement in decoding accuracy for $N_{trees} > 32$ and minleaf <10 (data not shown).

Classification of response types. We measured the R^2 between each measured behavioural variable (for example, whisking speed, lick rate and whisking set-point) and each cell's decoder prediction for all the trials and for each trial type. We considered only cells with more than one event in a session. In addition, for sessions with multiple-pole positions we used an analysis of variance (ANOVA) to determine whether the contact-evoked calcium response was different for the different pole position (Supplementary Figs 8–11, 13 and 15). We grouped the behavioural variables in larger categories such as whisking (for example, whisking

amplitude, set-point and speed), lick rate and touch (for example, touch per whisker, rate of change of forces and absolute magnitude). We considered the best R^2 set for each of the three behavioural categories. Alternatively, all cells were manually classified based on trial-to-trial calcium transients and behavioural prediction for each trial type. For most cells (>82%) classification was unambiguous based on the decoder R^2 values. The remaining cells were more accurately classified based on a rarer trial type (typically false alarm trials). Three of the authors independently arrived at consistent classifications.

Population decoding. For decoding neural populations (Figs 3 and 6) we considered all neurons showing at least one event and created an input vector of size $N_{neurons} \times (l + p + 1)$. We trained the random forest algorithm to decode each of the behavioural variables and evaluated the quality of the fit as before.

With the model based on data from one day we tested decoding of behavioural variables on another day. To compare data between two different days, we normalized the neural activity and the behavioural variables using a z-score transformation (by subtracting the mean and dividing by the standard deviation). In addition, some cells were active on one day but not on other days. We labelled these neurons as missing data.

Measurement of synaptic plasticity in brain slices. Rat hippocampal slice cultures were prepared at postnatal days 4 and 5 (ref. 58). Plasmids encoding GCaMP3 and cerulean under the control of a human synapsin 1 promoter were electroporated into single CA1 pyramidal neurons after 18 days *in vitro* (1:1 ratio; 50 ng μl^{-1} each) (modified from ref. 59). Recordings were taken 3–7 days after transfection. GCaMP3 was mainly excluded from the nucleus and cell morphology was indistinguishable from neurons expressing cerulean alone. Paired whole-cell recordings from CA1 and CA3 pyramidal cells were made at room temperature (21–23 °C), using 3–4 MOhm pipettes containing (in mM): 135 K-gluconate, 4 MgCl$_2$, 4 Na$_2$-ATP, 0.4 Na-GTP, 10 Na$_2$-phosphocreatine, 3 ascorbate and 10 HEPES (pH 7.2). ACSF consisted of (in mM): 135 NaCl, 2.5 KCl, 4 CaCl$_2$, 4 MgCl$_2$, 10 Na-HEPES, 12.5 D-glucose and 1.25 NaH$_2$PO$_4$

(pH 7.4). Excitatory postsynaptic currents were measured at −65-mV holding potential.

46. Petreanu, L., Mao, T., Sternson, S. M. & Svoboda, K. The subcellular organization of neocortical excitatory connections. *Nature* **457,** 1142–1145 (2009).
47. Porter, L. L. & White, E. L. Afferent and efferent pathways of the vibrissal region of primary motor cortex in the mouse. *J. Comp. Neurol.* **214,** 279–289 (1983).
48. Pologruto, T. A., Sabatini, B. L. & Svoboda, K. ScanImage: flexible software for operating laser-scanning microscopes. *Biomed. Eng. Online* **2,** 13 (2003).
49. Greenberg, D. S. & Kerr, J. N. Automated correction of fast motion artifacts for two-photon imaging of awake animals. *J. Neurosci. Methods* **176,** 1–15 (2008).
50. Gonchar, Y., Wang, Q. & Burkhalter, A. Multiple distinct subtypes of GABAergic neurons in mouse visual cortex identified by triple immunostaining. *Front. Neuroanat.* **1,** 3 (2007).
51. Kerlin, A. M., Andermann, M. L., Berezovskii, V. K. & Reid, R. C. Broadly tuned response properties of diverse inhibitory neuron subtypes in mouse visual cortex. *Neuron* **67,** 858–871 (2010).
52. Zariwala, H. A. *et al.* A cre-dependent GCaMP3 reporter mouse for neuronal imaging *in vivo*. *J. Neurosci.* **32,** 3131–3141 (2012).
53. Maravall, M., Mainen, Z. M., Sabatini, B. L. & Svoboda, K. Estimating intracellular calcium concentrations and buffering without wavelength ratioing. *Biophys. J.* **78,** 2655–2667 (2000).
54. Nevian, T. & Sakmann, B. Spine Ca^{2+} signaling in spike-timing-dependent plasticity. *J. Neurosci.* **26,** 11001–11013 (2006).
55. Gordon, U., Polsky, A. & Schiller, J. Plasticity compartments in basal dendrites of neocortical pyramidal neurons. *J. Neurosci.* **26,** 12717–12726 (2006).
56. Dombeck, D. A., Harvey, C. D., Tian, L., Looger, L. L. & Tank, D. W. Functional imaging of hippocampal place cells at cellular resolution during virtual navigation. *Nature Neurosci.* **13,** 1433–1440 (2010).
57. Breiman, L. Random forests. *Mach. Learn.* **45,** 5–32 (2001).
58. Stoppini, L., Buchs, P. A. & Muller, D. A. A simple method for organotypic cultures of nervous tissue. *J. Neurosci. Methods* **37,** 173–182 (1991).
59. Rathenberg, J., Nevian, T. & Witzemann, V. High-efficiency transfection of individual neurons using modified electrophysiology techniques. *J. Neurosci. Methods* **126,** 91–98 (2003).

ARTICLE

Clonally dominant cardiomyocytes direct heart morphogenesis

Vikas Gupta[1] & Kenneth D. Poss[1]

As vertebrate embryos develop to adulthood, their organs undergo marked changes in size and tissue architecture. The heart acquires muscle mass and matures structurally to fulfil increasing circulatory needs, a process that is incompletely understood. Here we used multicolour clonal analysis to define the contributions of individual cardiomyocytes as the zebrafish heart undergoes morphogenesis from a primitive embryonic structure into its complex adult form. We find that the single-cardiomyocyte-thick wall of the juvenile ventricle forms by lateral expansion of several dozen cardiomyocytes into muscle patches of variable sizes and shapes. As juvenile zebrafish mature into adults, this structure becomes fully enveloped by a new lineage of cortical muscle. Adult cortical muscle originates from a small number of cardiomyocytes—an average of approximately eight per animal—that display clonal dominance reminiscent of stem cell populations. Cortical cardiomyocytes initially emerge from internal myofibres that in rare events breach the juvenile ventricular wall, and then expand over the surface. Our results illuminate the dynamic proliferative behaviours that generate adult cardiac structure, revealing clonal dominance as a key mechanism that shapes a vertebrate organ.

Vertebrate organ development is an intricate process that begins in the early embryo and continues until the functional capacity of the organ meets adult requirements. Relatively little is known about the cellular mechanisms of organ morphogenesis after birth or hatching. This can be explained in part by the challenges of analysing dynamic cellular behaviours in complex tissues.

New technologies can shed light on the cellular mechanisms that drive organ morphogenesis. Recently, a system was developed that allowed the designation of ~90 colour labels to murine neurons[1]. With this technology, termed Brainbow, it was possible to visualize adjacent neurons and their connections in the brain with high resolution. The ability to assign many colours to different cells in a population can also be applied to investigating cell proliferation and lineage decisions.

The heart is a set of chambers comprised predominantly of the contractile units, cardiomyocytes. Genetic fate mapping has been performed to determine how separate lineages contribute to developing cardiac structures in mice and zebrafish[2–6]. Additionally, single-marker clonal analysis has traced the activity of individual cells during embryonic heart patterning[7–10]. These studies have enhanced our understanding of cardiogenic mechanisms in early embryos. Nevertheless, a large gap in our knowledge remains in comprehending how the size, shape and structure of an adult heart are finalized through the individual and population behaviours of many cardiac cells.

In this study, we used multicolour clonal analysis to map the proliferative histories of many individual cardiomyocytes as the zebrafish cardiac ventricle transitions from a simple tube of single-cardiomyocyte thickness into a complex adult structure. Our experiments yielded several unexpected discoveries relevant to the number, nature and mechanisms of cardiomyocyte contributions during heart morphogenesis.

Multicolour labelling of cardiomyocytes

To study cell clones in zebrafish, we adapted the Brainbow 1.0L construct for combinatorial expression of three spectrally different fluorescent reporter proteins[1]. Multiple copy integration of this transgene at a single genetic locus is a common outcome of transgenesis. Thus, combinatorial Cre-recombinase-mediated excision events at paired *lox* recognition sites can generate many possible permanent colours (Fig. 1a, b). We generated several transgenic lines containing a *β-actin-2*-promoter-driven multicolour construct, and assessed them in combination with a strain harbouring a tamoxifen-inducible, cardiomyocyte-restricted Cre recombinase, *cmlc2:CreER*[11]. We identified one line, *Tg(β-act2:Brainbow1.0L)*[pd49] (referred to subsequently as *priZm*), showing limited mosaic recombination only in the presence of 4-hydroxytamoxifen (4-HT; Supplementary Fig. 1).

The size and structure of the zebrafish heart is conducive to clonal analysis of cardiomyocytes. The 2–3 days post-fertilization (dpf) zebrafish heart is looped, has a wall of single-cardiomyocyte thickness, and consists of 250–300 muscle cells; by our measurements ~115 of these are contained within the ventricular wall (Supplementary Fig. 2). Cardiomyocyte proliferation is detectable at 2 dpf and is thought to account for most or all subsequent cardiogenesis[2,12–15]. To trace the fates of individual embryonic cardiomyocytes, we briefly incubated 2 dpf *cmlc2:CreER*; *priZm* embryos in 4-HT and raised them to different ages (Fig. 1c).

We first assessed cardiac fluorescence at 10 dpf, a stage comparable in organismal size to 2 dpf. Our optimized 4-HT regimen generated >20 unique colours in cardiomyocytes, as viewed at 10 dpf and subsequent stages. Red fluorescent protein (RFP) is the initial reporter cassette and default expression marker, and 4-HT treatment induced recombination (non-red colours) in ~50% of ventricular cardiomyocytes. Importantly, different colours were consistently assigned to adjacent cardiomyocytes on the surface of the 10 dpf ventricular wall (Fig. 1d–f and Supplementary Fig. 3), a prerequisite for multicolour clonal analysis.

The zebrafish ventricle is recognized to contain two types of cardiac muscle[16]. These include a peripheral wall of compact muscle, and inner myofibres organized into trabeculae that initiate formation at 3 dpf (ref. 17). Histological examination of 10 dpf hearts revealed three notable observations. First, the ventricular wall remained at single-cardiomyocyte thickness, as at 2 dpf. Second, trabecular myocytes

[1]Department of Cell Biology and Howard Hughes Medical Institute, Duke University Medical Center, Durham, North Carolina 27710, USA.
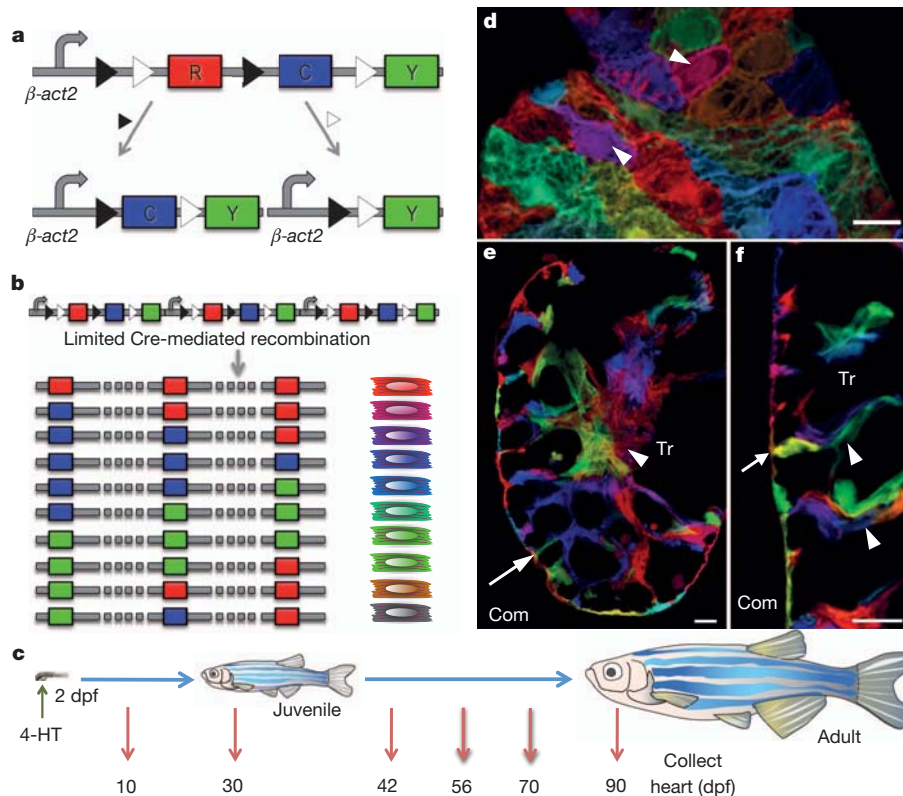
Figure 1 | Multicolour clonal labelling of embryonic zebrafish cardiomyocytes. a, Recombination at paired *lox2272* (black triangles) or *loxP* (white triangles) sites leads to expression of cyan fluorescent protein (CFP) or yellow fluorescent protein (YFP), respectively. **b**, Limited Cre-mediated recombination of tandem cassette insertions results in combinatorial expression of fluorescent proteins. **c**, Cartoon of lineage-tracing experiments.

d, 10 dpf ventricular surface myocardium. Single cardiomyocytes are predominantly labelled with unique colours (arrowheads). **e, f**, 10 dpf ventricular confocal slice, indicating trabecular cardiomyocytes connected with clonally unrelated cardiomyocytes at the wall (**e, f**, arrow) and within trabeculae (**f**, arrowheads). Com, compact muscle; Tr, trabecular muscle. Scale bars, 10 μm.

connected to the wall were most often clonally unrelated to adjoining wall myocytes (58 of 63 observations, *n* = 5 ventricles; Fig. 1e, f). This observation supported a mechanism for trabecularization proposed recently based on different lines of evidence, in which myocytes delaminate from the ventricular wall, seed elsewhere in the chamber, and initiate trabecular growth from a second site[17]. Third, we saw that the trabecular myofibres themselves were comprised of cardiomyocytes arising from different clonal origins within the 2 dpf wall (Fig. 1f).

Juvenile ventricular wall formation

We next examined the ventricles of juvenile zebrafish at 30 dpf, at which time major organismal and cardiac growth have occurred since cardiomyocyte labelling with 4-HT. By whole-mount imaging of surface myocardium, we readily identified multicellular, single-colour regions of myocardium, indicating that progeny of embryonic cardiomyocytes generally remained connected with one another after division (Fig. 2a–c and Supplementary Fig. 4a–c). Although less common (9.8% of clones), we also observed instances suggesting complete separation of a cardiomyocyte from its clonal partners (Supplementary Fig. 4d).

We expected some uniformity to the clonal patches comprising the ventricular wall, with cardiomyocyte clones of similar shape and size. By contrast, ventricles from different animals displayed unique patterns of surface colour clones, and the shapes of clones within each ventricle were highly diverse (Fig. 2a and Supplementary Fig. 5). Clone size also varied. Some clones showed evidence of many cell divisions, whereas others contained a single cardiomyocyte (Fig. 2d). Histological analysis showed retention of a wall of single-cardiomyocyte thickness, indicating that the expansion of wall clones was limited to lateral directions along the surface. They also revealed that substantial expansion of trabecular myocardium had occurred since 10 dpf (Fig. 2e).

To estimate the number of embryonic cardiomyocytes that create the juvenile ventricular wall, we calculated the surface areas occupied by individual clones and divided each by the total ventricular surface area. Most clones (99/146; *n* = 5) each occupied less than 2% of the ventricular surface area, whereas a small number (15/146) of larger clones each represented ~4–8% of the surface (Fig. 2f). Extrapolating for unrecombined myocardium, we determined that the 30 dpf ventricular surface was represented by 55.4 ± 1.9 colour clones (*n* = 10; mean ± standard error of the mean (s.e.m.); Fig. 2g). Thus, our data indicate that the juvenile zebrafish ventricular wall is built by lateral expansion of ~55 embryonic cardiomyocytes. These cardiogenic events create a patchwork of diverse clonal shapes and sizes that varies from animal to animal, indicating that the juvenile cardiac form can be acquired with considerable developmental plasticity.

Emergence of a new adult muscle lineage

Zebrafish are typically recognized as adults at 3 months post-fertilization. We examined ventricles of 6-, 8- and 10-week-old animals that had undergone cardiomyocyte labelling at 2 dpf. At 6 weeks post-fertilization (wpf), most clonal patches comprising the surface myocardium appeared similar to those of 30 dpf ventricles. Additionally, we detected a population of clonally related cardiomyocytes layered upon these patches near the chamber base (Fig. 3a, b). By 8 wpf, large single-colour swaths containing several hundreds of such cardiomyocytes extended from the ventricular base, wrapping around both sides of the chamber and often reaching its midpoint (Fig. 3d–f). At 10 wpf, we began to see evidence of these surface clones converging with each other. These external cardiomyocytes were typically more rod-shaped with more distinct striation than underlying cardiomyocytes (Supplementary Fig. 6).

We examined histological sections and confocal slices through ventricles from 6–10 wpf animals, which confirmed that a new layer
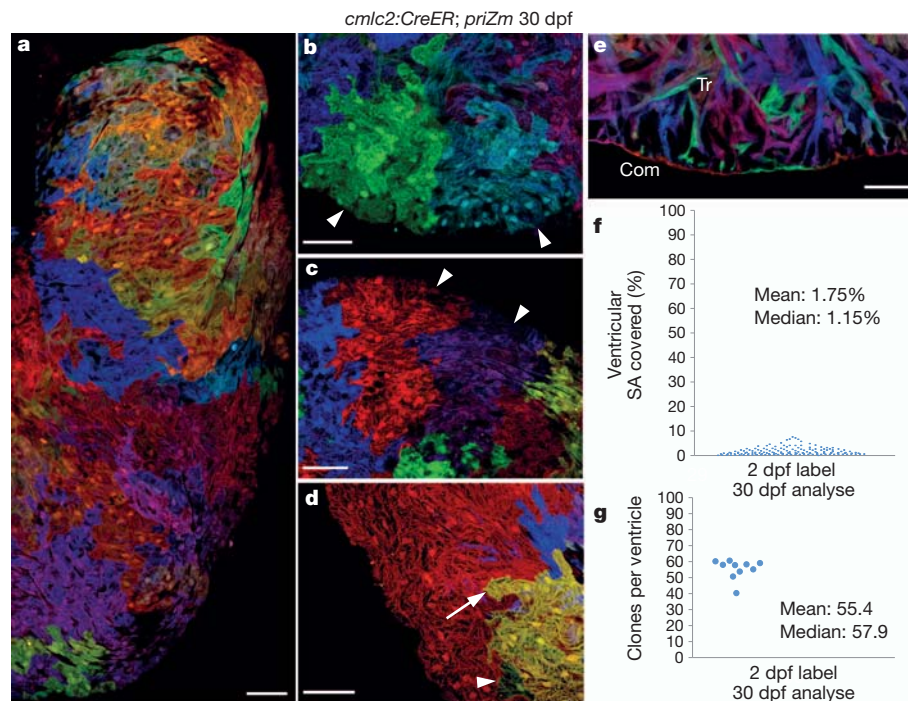
cmlc2:CreER; priZm 30 dpf

Figure 2 | Several dozen embryonic cardiomyocytes build the juvenile ventricular wall. a, Surface myocardium of half of a 30 dpf ventricular side, displaying clonal patches of varied shapes and sizes. **b, c**, Cardiomyocyte clones near the apex or chamber midpoint forming wedge/stripe shapes (arrowheads). **d**, Single-cell clone (green, arrowhead) positioned near a large clone (yellow,

arrow). **e**, 30 dpf ventricular confocal slice, depicting a wall of single-cardiomyocyte thickness (Com) surrounding trabecular muscle (Tr). **f**, Percentage surface area (SA) occupied by 30 dpf clones (146 clones, 5 ventricles). **g**, Surface clones per ventricle (*n* = 10). Scale bars, 50 μm.

of ventricular muscle had emerged externally to the wall of single-cardiomyocyte thickness present at earlier stages (Fig. 3c, g). As indicated by whole-mount imaging, this external layer typically displayed substantial regions of clonally related cardiomyocytes. We will refer subsequently to the inner wall muscle as the 'primordial layer', as it retains the same single-cardiomyocyte thickness and characteristics
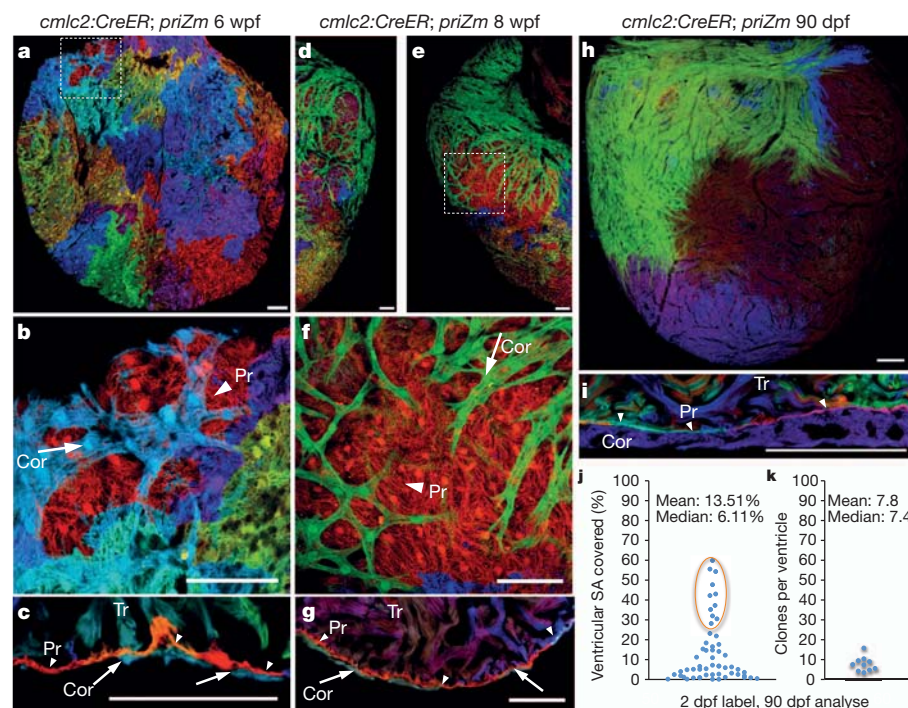

cmlc2:CreER; priZm 6 wpf   *cmlc2:CreER; priZm* 8 wpf   *cmlc2:CreER; priZm* 90 dpf

Figure 3 | Clonally dominant cortical cardiomyocytes. a–c, 6 wpf ventricular surface (**a, b**) and confocal slice (**c**), indicating cortical (Cor; arrow), primordial (Pr; arrowhead) and trabecular (Tr) muscle. **d–g**, 8 wpf ventricular surface indicating a large green basal clone (**d–f**), and section indicating 3 muscle types (**g**). Dashed boxes in **a** and **e** are shown in higher magnification in **b** and **f**,

respectively. **h**, 90 dpf ventricular surface, showing only a few large cortical clones. **i**, 90 dpf ventricular section. **j**, Percentage surface area (SA) occupied by 90 dpf clones (56 clones, 10 ventricles); basal clones representing each ventricle are circled. **k**, Surface clones per ventricle (*n* = 10). Scale bars, 50 μm (**a–g**); 100 μm (**h, i**).

of the embryonic ventricle throughout subsequent life stages. We will refer to the late-emerging, outermost muscle of the ventricular wall as the 'cortical layer'. Thus, by multicolour clonal analysis, we revealed two developmentally distinct and previously unrecognized forms of ventricular wall myocardium.

Dominant clones build adult wall muscle

We next examined ventricles from mature, 90 dpf zebrafish that had undergone cardiomyocyte labelling at 2 dpf. At this stage, the entire surface of the ventricle in each animal was covered by cortical cardiomyocytes (Fig. 3h and Supplementary Fig. 7). Similar to the clonal representation of the primordial layer at earlier stages, cortical clone patterns appeared different in each animal. However, a common theme for each ventricle was the presence of one or two large cortical clones at the base of the heart extending across the ventricular surface towards the apex. We infer from our time-point analysis that these areas of cortex formed by a base-to-apex wave of expansion over the primordial layer. A number of smaller surface clones were apparent at other locations. Clones converged by weaving or fitting with some overlay into each other, and were penetrated by coronary vessels (Supplementary Fig. 8).

Histological analysis of adult ventricular tissue indicated that the primordial layer remained at single-cardiomyocyte thickness and was comprised of multiple colour clones. This appearance contrasted with the overlying cortical myocardium, which was predominantly single colour and could be several cells thick (Fig. 3i). We calculated the areas of surface clones from whole-mount images of ventricles that displayed basal clones of a recombined colour. Ten of twenty ventricles met this criterion, each of which had a large cortical clone covering 30–60% of the total ventricular surface (Fig. 3j). An average of 7.8 ± 1.2 clones contributed the entire cortical muscle of each ventricle ($n = 10$; Fig. 3k), a number several times lower than the clonal surface representation of the much smaller juvenile ventricle. Thus, a rare group of approximately eight clonally dominant cardiomyocytes in the embryonic ventricle ultimately contribute to building the adult cortical myocardium.

Muscle lineage regeneration after injury

Zebrafish possess a robust capacity for heart regeneration throughout life[18], based on the ability to activate the proliferation of spared cardiomyocytes after injury[11,19,20]. We examined the regenerative potentials of primordial and cortical muscle by amputating ventricular apices from 90 dpf *cmlc2:CreER*; *priZm* animals that had been labelled at 2 dpf. At 14 days post-amputation (dpa), we detected growth of adjacent cortical muscle clones in lateral and radial directions into the wound area (Fig. 4a, b), but the primordial layer lagged behind the amputation site. By 30 dpa, as the wall was reconstructed with clonal patches of cortical cardiomyocytes, clones of single-cardiomyocyte thickness contiguous with the primordial layer first became detectable in the regenerate (Fig. 4c). By 60 dpa, the primordial layer was largely restored as a complete structure positioned between cortical and trabecular muscle (Fig. 4d). Thus, regenerating primordial muscle undergoes restricted lateral expansion as during morphogenesis, whereas cortical muscle regeneration is less constrained and assumes the primary component of the new wall. Interestingly, these events occur in a temporally reversed manner compared to initial morphogenesis, with cortical muscle regenerating before the underlying primordial layer.

Origins of dominant cardiomyocyte clones

To determine when cortical cardiomyocytes originate during heart morphogenesis, we initiated colour labelling at 30 dpf, after formation of the juvenile structure but 1–2 weeks before the emergence of cortical muscle. Notably, large clonal patches were present on the surface of 90 dpf ventricles that had been incubated briefly with 4-HT at 30 dpf (Fig. 5a and Supplementary Fig. 9), with the largest clones
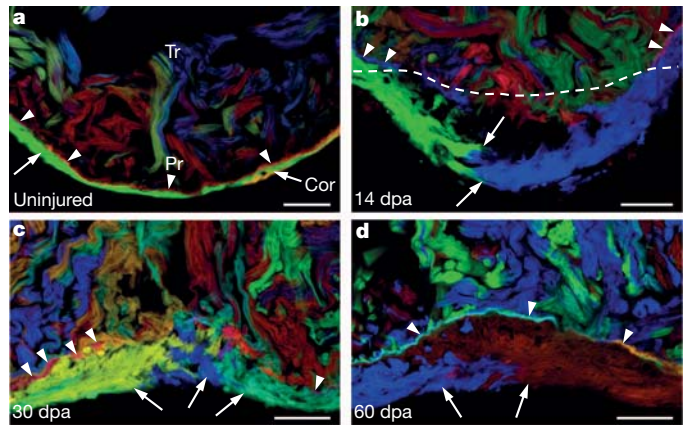

Figure 4 | Regeneration of cortical and primordial muscle after injury.
a, Section of an uninjured ventricular apex, indicating the primordial (Pr; arrowheads) and cortical (Cor; arrows) layers. Tr, trabecular muscle.
b, Regenerating ventricular apex at 14 days after resection (dpa). Cortical muscle clones converge within the injury site, whereas the primordial layer lags behind. Dashed line indicates amputation plane. **c**, 30 dpa ventricular apex, indicating multiple cortical clones and an incomplete primordial layer.
d, Regenerated ventricular apex at 60 dpa, containing cortical muscle overlying a mostly contiguous layer of primordial muscle. $n = 6$ animals for each time point. Scale bars, 50 μm.

present at the chamber base. We quantified the size and number of clones in ventricles with basal clones of recombined colours (11 of 20 animals). Our data indicated that adult cortical myocardium arises in patches of diverse sizes from an average of 8.6 ± 0.7 labelled 30 dpf cardiomyocytes (Fig. 5b, c), a number similar to that observed after labelling at 2 dpf.

In some ventricles assessed 4 weeks after labelling (8 wpf), we observed trabecular muscle of the same colour near the emergent cortical clone (Fig. 5e, g). To confirm this association, we examined sections of 6–7 wpf ventricles (labelled at 2 dpf), and consistently found nearby trabecular muscle of the same colour as the small, basal cortical clone (13 of 13 ventricles; see cyan clone in Fig. 3c). We also could identify cases from these examples in which trabecular and cortical muscle of one colour connected through an apparent breach in the primordial layer (Supplementary Fig. 10). These observations suggested a clonal relationship between trabecular and cortical cardiomyocytes in the maturing zebrafish ventricle.

We noticed lower colour recombination in the primordial layer ($\sim$15%) than in the trabecular and cortical muscle lineages ($\sim$61%) at 8 wpf (Fig. 5d–g). Taking advantage of this differential labelling efficiency, we titrated 4-HT and identified a low dose that induced sparse recombination at 30 dpf in trabeculae and no obvious recombination in primordial muscle. Importantly, even with very limited labelling, cortical clones of a recombined colour were still discernable in 3 of 24 ventricles at 8 wpf (Fig. 5h, i), a finding that reaffirmed a trabecular source for the cortical lineage. As with other samples mentioned above, images of confocal slices from these ventricles could identify single-colour clones containing both cortical and trabecular muscle, connecting through an apparent breach in primordial muscle of unrecombined colour (Fig. 5i–k).

Together, our findings indicate a dynamic mechanism that generates a final ventricular muscle lineage and completes adult cardiac morphogenesis. Trabecular cardiomyocytes penetrate the primordial layer in rare, spatially segregated events at the juvenile stage, seed the ventricular surface, and undergo expansion to create the cortical myocardium.

Discussion

Multicolour clonal analysis enables the simultaneous fate mapping of many similar cells within a developing organ. We used this technology to reveal unsuspected cellular mechanisms guiding heart morphogenesis
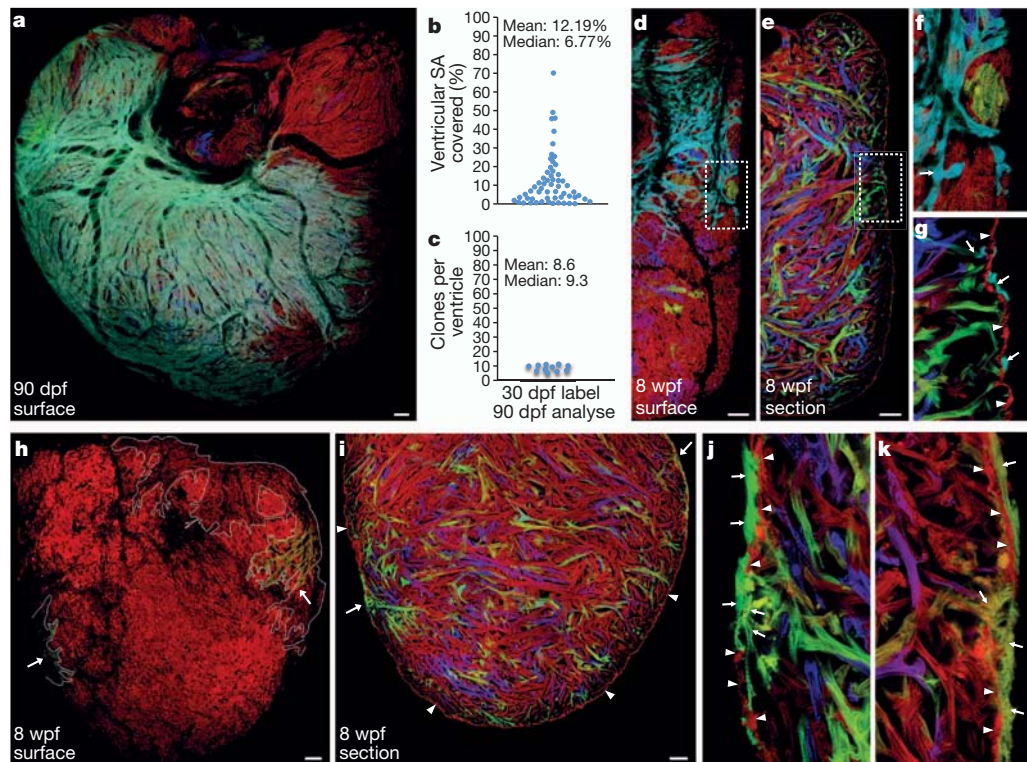
Figure 5 | Origins of clonally dominant cardiomyocytes. a, 90 dpf ventricular surface, after 30 dpf 4-HT labelling. **b**, Percentage surface area (SA) occupied by 90 dpf clones (58 clones, 11 ventricles). **c**, Surface clones per ventricle (n = 11). **d–g**, 8 wpf ventricular surface (**d**, **f**) and confocal slice (**e**, **g**), after 30 dpf 4-HT labelling. Cyan cortical muscle (arrows; **f**, **g**) overlies primordial muscle (arrowheads) that is largely red/unlabelled, and cyan trabeculae (arrow; **g**). Dashed boxes in **d** and **e** are shown at higher magnification in **f** and **g**, respectively. **h–k**, 8 wpf ventricular surface (**h**) and confocal slices (**i–k**) after limited 4-HT labelling, showing no obvious primordial muscle labelling (arrowheads; **i–k**). Arrows indicate green (**h**, **i** (left); **j**) and hazel (**h**, **i** (right); **k**) cortical/trabecular clones. All cortical muscle in **h** is outlined in white. Scale bars, 50 μm.

in zebrafish. We found that three ventricular myocardial lineages are present in the adult form: primordial, trabecular and cortical muscle, created in this order from each other. Our data indicate that the innermost trabecular lineage is initiated predominantly by delamination from the embryonic primordial layer and migration, as proposed in an earlier study[17]. Next, the outermost cortical layer is created as juveniles mature to adults, emerging wholly or in part via an 'inside-out' mechanism from trabeculae. Here, one or more particularly expansive juvenile cardiomyocytes access the ventricular surface at each of only approximately eight sites per animal.

Zebrafish share several aspects of cardiac development with higher vertebrates, and the multicolour clonal analysis results we report here indicate some basic commonalities with results of single-marker clonal analysis performed previously in early mouse and chick embryos. For instance, cardiomyocytes were also observed in coherent clonal populations during cardiac growth in these systems, after an early phase of dispersion[9,10]. Most unexpected is that the zebrafish ventricle maintains a primordial layer of single-cardiomyocyte thickness without noticeable cell division in the z-plane, and that wall thickening instead occurs after seeding of a separate cortical lineage by dominant clones. It will be interesting to determine the evolutionary distribution of aspects of this uncovered morphogenetic mechanism within other bony fish and among other classes of vertebrates like mammals.

The origins and diversity of clonal patterns of cortical muscle we report are more consistent with a stochastic model of source cell selection than a hierarchical or predetermined model. Additionally, the observation of clonal dominance in cardiomyocytes is reminiscent of stem cell compartments that drift towards clonality during homeostatic tissue maintenance, events that have been explained by stochastic models[21–24]. We suspect that molecular and/or physiological cues enable the emergence and proliferative capacity of cortical cardiomyocytes, ostensibly with a preferential influence at the ventricular base. It is likely that clonal dominance behaviour is a recurring mechanistic strategy to help shape vertebrate organs.

METHODS SUMMARY

Wild-type or transgenic zebrafish of the EK/AB background were used for all experiments. Ventricular resection surgeries were performed as described previously[18]. All published transgenic strains used here are listed in Methods and were analysed as hemizygotes. $Tg(\beta\text{-}act2\text{:}Brainbow1.0L)^{pd49}$ was generated and 4-HT labelling experiments were performed as described in Methods. Hearts were extracted at the indicated time points and fixed in 4% paraformaldehyde. After rinsing, the atrium was removed and the ventricle was placed on a coverslip in Fluoromount G. Another coverslip was used to gently compress the ventricle, allowing imaging of both ventricular surfaces. For surface images of whole-mounted ventricles, the z-position was adjusted until only surface muscle was visible. For confocal slices through whole-mounted hearts, the z-position was adjusted through the ventricle until trabecular muscle could be visualized. For histological analysis, 50 μm cryosections were mounted with Fluoromount G. Images from all multicolour samples were acquired using a Leica SP5 AOBS microscope equipped with ×20 (0.7 NA) and ×40 (1.25 NA) objectives. Antibodies were not used to enhance fluorescence. 458 nm, 515 nm and 561 nm lasers were used to excite CFP, YFP and RFP, respectively. Each channel was acquired sequentially and imported into ImageJ, where channels were over-laid. Uniform contrast and brightness adjustments were made using Adobe Photoshop. To visualize the entire outer surface area, images were joined using Photoshop. To quantify the clone area, the size of a given clone in μm² was traced using ImageJ software. The percentage area occupied by a clone was calculated by dividing its measured area by the total surface area of both sides of the ventricle.

1. Livet, J. *et al.* Transgenic strategies for combinatorial expression of fluorescent proteins in the nervous system. *Nature* **450,** 56–62 (2007).

2. Zhou, Y. *et al.* Latent TGF-β binding protein 3 identifies a second heart field in zebrafish. *Nature* **474,** 645–648 (2011).
3. Kikuchi, K. *et al.* tcf21^{+} epicardial cells adopt non-myocardial fates during zebrafish heart development and regeneration. *Development* **138,** 2895–2902 (2011).
4. Cai, C. L. *et al.* Isl1 identifies a cardiac progenitor population that proliferates prior to differentiation and contributes a majority of cells to the heart. *Dev. Cell* **5,** 877–889 (2003).
5. Zhou, B. *et al.* Epicardial progenitors contribute to the cardiomyocyte lineage in the developing heart. *Nature* **454,** 109–113 (2008).
6. Meilhac, S. M., Esner, M., Kelly, R. G., Nicolas, J. F. & Buckingham, M. E. The clonal origin of myocardial cells in different regions of the embryonic mouse heart. *Dev. Cell* **6,** 685–698 (2004).
7. Keegan, B. R., Meyer, D. & Yelon, D. Organization of cardiac chamber progenitors in the zebrafish blastula. *Development* **131,** 3081–3091 (2004).
8. Stainier, D. Y., Lee, R. K. & Fishman, M. C. Cardiovascular development in the zebrafish. I. Myocardial fate map and heart tube formation. *Development* **119,** 31–40 (1993).
9. Mikawa, T., Borisov, A., Brown, A. M. & Fischman, D. A. Clonal analysis of cardiac morphogenesis in the chicken embryo using a replication-defective retrovirus. I. Formation of the ventricular myocardium. *Dev. Dyn.* **193,** 11–23 (1992).
10. Meilhac, S. M. *et al.* A retrospective clonal analysis of the myocardium reveals two phases of clonal growth in the developing mouse heart. *Development* **130,** 3877–3889 (2003).
11. Kikuchi, K. *et al.* Primary contribution to zebrafish heart regeneration by gata4[+] cardiomyocytes. *Nature* **464,** 601–605 (2010).
12. de Pater, E. *et al.* Distinct phases of cardiomyocyte differentiation regulate growth of the zebrafish heart. *Development* **136,** 1633–1641 (2009).
13. Auman, H. J. *et al.* Functional modulation of cardiac form through regionally confined cell shape changes. *PLoS Biol.* **5,** e53 (2007).
14. Hami, D., Grimes, A. C., Tsai, H. J. & Kirby, M. L. Zebrafish cardiac development requires a conserved secondary heart field. *Development* **138,** 2389–2398 (2011).
15. Lazic, S. & Scott, I. C. Mef2cb regulates late myocardial cell addition from a second heart field-like population of progenitors in zebrafish. *Dev. Biol.* **354,** 123–133 (2011).
16. Hu, N., Yost, H. J. & Clark, E. B. Cardiac morphology and blood pressure in the adult zebrafish. *Anat. Rec.* **264,** 1–12 (2001).
17. Liu, J. *et al.* A dual role for ErbB2 signaling in cardiac trabeculation. *Development* **137,** 3867–3875 (2010).
18. Poss, K. D., Wilson, L. G. & Keating, M. T. Heart regeneration in zebrafish. *Science* **298,** 2188–2190 (2002).
19. Wang, J. *et al.* The regenerative capacity of zebrafish reverses cardiac failure caused by genetic cardiomyocyte depletion. *Development* **138,** 3421–3430 (2011).
20. Jopling, C. *et al.* Zebrafish heart regeneration occurs by cardiomyocyte dedifferentiation and proliferation. *Nature* **464,** 606–609 (2010).
21. Snippert, H. J. *et al.* Intestinal crypt homeostasis results from neutral competition between symmetrically dividing Lgr5 stem cells. *Cell* **143,** 134–144 (2010).
22. Klein, A. M., Nakagawa, T., Ichikawa, R., Yoshida, S. & Simons, B. D. Mouse germ line stem cells undergo rapid and stochastic turnover. *Cell Stem Cell* **7,** 214–224 (2010).
23. Lopez-Garcia, C., Klein, A. M., Simons, B. D. & Winton, D. J. Intestinal stem cell replacement follows a pattern of neutral drift. *Science* **330,** 822–825 (2010).
24. Doupé, D. P., Klein, A. M., Simons, B. D. & Jones, P. H. The ordered architecture of murine ear epidermis is maintained by progenitor cells with random fate. *Dev. Cell* **18,** 317–323 (2010).

Author Contributions V.G. and K.D.P. designed experimental strategy, analysed data, and prepared the manuscript. V.G. performed all of the experiments.

Author Information Reprints and permissions information is available at www.nature.com/reprints. The authors declare no competing financial interests. Readers are welcome to comment on the online version of this article at www.nature.com/nature. Correspondence and requests for materials should be addressed to K.D.P. (kenneth.poss@duke.edu).

METHODS

Zebrafish and transgenic lines. Wild-type or transgenic zebrafish of the EK/AB background were used for all experiments and maintained at 3 fish per litre starting at 28 dpf. Water temperature was maintained at 26 °C for animals after 1 wpf. Ventricular resection surgeries were performed as described previously[18], removing approximately 20% of the ventricle at the apex. Published transgenic strains used in this study were (*Tg(cmlc2:CreER)*[pd10])[11], (*Tg(gata5:loxP-mCherry-STOP-loxP-nucEGFP)*[pd40])[11], (*Tg(cmlc2:EGFP)*[f1])[25], (*Tg(cmlc2:nucDsRed2)*[f2])[25] and *(Tg(β-actin:HRAS-EGFP)*[vu119])[26]. Experiments with zebrafish were approved by the Institutional Animal Care and Use Committee at Duke University.

Construction of *priZm*. The Brainbow 1.0L plasmid was digested with NheI and partially digested with NotI to obtain the entire cassette, and subcloned downstream of the 9.8 kb zebrafish *β-actin 2* promoter from the *β-act2:RSG* construct[11]. The resulting plasmid was linearized by I-SceI digestion and injected into one-cell zebrafish embryos. RFP is the initial reporter cassette and default expression state from this construct. Two paired sites, *lox2272* and *loxP*, exist in the construct, which enable Cre-recombinase-mediated switching to expression of either CFP or YFP.

Thirty founder lines were isolated, and *Tg(β-act2:Brainbow1.0L)*[pd49] was used for this study. The zebrafish *β-actin 2* promoter does not drive expression in epicardial or endocardial cells[11], facilitating clear visualization of *priZm* cardiomyocytes.

4-HT labelling. For 4-HT labelling of *cmlc2:CreER*; *priZm* embryos, 2 dpf embryos were placed in egg water with 4-HT added to a final concentration of 4 μM, from a 1 mM stock made in 100% ethanol. Embryos were treated for 6 h, rinsed once, and placed in fresh egg water. This labelling protocol was highly reproducible and induced recombination and appearance of diverse, non-red colours on half of the ventricular surface, calculated by digital quantification of red and non-red surface areas from whole-mount images of 30 dpf ventricles (50.0%; *n* = 10). By contrast, increased or reduced presence of 4-HT led to higher and lower recombination frequencies, respectively, which each reduced colour diversity.

For labelling of *cmlc2:CreER*; *priZm* juveniles at 30 dpf, animals were incubated in 1 μM 4-HT in aquarium water for 3 h. To specifically label trabecular muscle at 30 dpf, animals were incubated in 0.25 μM 4-HT for 1 h.

Imaging. Hearts were extracted at the indicated time points and fixed in 4% paraformaldehyde. After rinsing, the atrium was removed and the ventricle was placed on a coverslip in Fluoromount G. Another coverslip was used to compress the ventricle, allowing imaging of both ventricular surfaces. For surface images of whole-mounted ventricles, the z-position was adjusted until only surface muscle was visible. For confocal slices through whole-mounted hearts, the z-position was adjusted through the ventricle until trabecular muscle could be visualized. For histological analysis, 50 μm cryosections were mounted with Fluoromount G. Images from all multicolour samples were acquired using a Leica SP5 AOBS microscope equipped with ×20 (0.7 NA) and ×40 (1.25 NA) objectives. Antibodies were not used to enhance fluorescence. 458 nm, 515 nm and 561 nm lasers were used to excite CFP, YFP and RFP, respectively. Each channel was acquired sequentially and imported into ImageJ, where channels were overlaid. Uniform contrast and brightness adjustments were made using Adobe Photoshop. To visualize the entire outer surface area, images were joined using Photoshop. To quantify the clone area, the size of a given clone in μm² was traced using ImageJ software. The percentage area occupied by a clone was calculated by dividing its measured area by the total surface area of both sides of the ventricle.

Embryonic cardiomyocyte assays. *cmlc2:nucDsRed2*; *cmlc2:EGFP* double transgenic animals were raised to 3 dpf, fixed, sectioned at 30 μm, and stained with an antibody to DsRed2. Confocal stacks of the entire heart from each embryo were taken, and the number of myocytes within the ventricular wall was determined from three-dimensional projections generated using Imaris. To determine effects of 4-HT on cardiomyocyte proliferation, we treated 2 dpf embryos with 4 μM 4-HT for 6 h and fixed at 3 dpf. Ten-micrometre sections were stained with Mef2 and PCNA as described[27], and cardiomyocyte proliferation indices for each group were calculated from three ventricular sections. The numbers of Mef2⁺ and Mef2⁺/PCNA⁺ cells were manually counted with the aid of ImageJ software.

Colour combinations and clone size. To examine the possibility that recombined colour combinations had differential effects on cardiomyocyte proliferation, we examined colour diversity in the largest and smallest cortical clones of 90 dpf ventricles that were labelled at 2 or 30 dpf. From 21 ventricles, 16 unique colours were represented in the 21 large basal clones. Seventeen unique colours were represented in 21 of the smallest clones. Individual colours were observed in both small and large clone groups, including two shades of grey (in which the clone is expressing all three fluorescent proteins). This distribution was consistent with the idea that colour combinations do not have adverse effects on proliferative ability.

25. Burns, C. G. *et al.* High-throughput assay for small molecules that modulate zebrafish embryonic heart rate. *Nature Chem. Biol.* **1,** 263–264 (2005).
26. Cooper, M. S. *et al.* Visualizing morphogenesis in transgenic zebrafish embryos using BODIPY TR methyl ester dye as a vital counterstain for GFP. *Dev. Dyn.* **232,** 359–368 (2005).
27. Kikuchi, K. *et al.* Retinoic acid production by endocardium and epicardium is an injury response essential for zebrafish heart regeneration. *Dev. Cell* **20,** 397–404 (2011).

LETTER

Systematic variation of the stellar initial mass function in early-type galaxies

Michele Cappellari[1], Richard M. McDermid[2], Katherine Alatalo[3], Leo Blitz[3], Maxime Bois[4], Frédéric Bournaud[5], M. Bureau[1], Alison F. Crocker[6], Roger L. Davies[1], Timothy A. Davis[1,7], P. T. de Zeeuw[7,8], Pierre-Alain Duc[5], Eric Emsellem[7,9], Sadegh Khochfar[10], Davor Krajnović[7], Harald Kuntschner[7], Pierre-Yves Lablanche[7,9], Raffaella Morganti[11,12], Thorsten Naab[13], Tom Oosterloo[11,12], Marc Sarzi[14], Nicholas Scott[1,15], Paolo Serra[11], Anne-Marie Weijmans[16] & Lisa M. Young[17]

Much of our knowledge of galaxies comes from analysing the radiation emitted by their stars, which depends on the present number of each type of star in the galaxy. The present number depends on the stellar initial mass function (IMF), which describes the distribution of stellar masses when the population formed, and knowledge of it is critical to almost every aspect of galaxy evolution. More than 50 years after the first IMF determination[1], no consensus has emerged on whether it is universal among different types of galaxies[2]. Previous studies indicated that the IMF and the dark matter fraction in galaxy centres cannot both be universal[3–7], but they could not convincingly discriminate between the two possibilities. Only recently were indications found that massive elliptical galaxies may not have the same IMF as the Milky Way[8]. Here we report a study of the two-dimensional stellar kinematics for the large representative ATLAS[3D] sample[9] of nearby early-type galaxies spanning two orders of magnitude in stellar mass, using detailed dynamical models. We find a strong systematic variation in IMF in early-type galaxies as a function of their stellar mass-to-light ratios, producing differences of a factor of up to three in galactic stellar mass. This implies that a galaxy's IMF depends intimately on the galaxy's formation history.

As part of the ATLAS[3D] project[9], we obtained integral-field maps of stellar kinematics for a volume-limited sample of 260 early-type (elliptical and lenticular) galaxies. They were selected to be closer than 42 Mpc to Earth and to have K_s-band total magnitudes of $M_K < -21.5$ mag (corresponding to galaxy stellar masses of $M \gtrsim 6 \times 10^9 M_\odot$, where $M_\odot$ is the solar mass), as determined from the Two Micron All Sky Survey at our adopted distances. Homogeneous imaging for all the galaxies in the r band was obtained in major part from data release 8 of the Sloan Digital Sky Survey and completed with our own photometry.

For all galaxies, we constructed six sets of dynamical models[10], which include an axisymmetric stellar component and a spherical dark halo, and fit the details of both the projected stellar distribution[11] and the two-dimensional stellar kinematics[9] (Fig. 1). Although the shape of the stellar component can be inferred directly from the galaxy images, the dark halo shape must be a free parameter of the models. Using the models, we explored a variety of plausible assumptions for the halo to test how these can affect our result. Our halo models include as limiting cases a maximum-ignorance model, where the halo parameters are directly fitted to the stellar kinematics, and some completely fixed models, where the halo follows the predictions of numerical simulations[12–14]. A detailed description of the model parameters is provided in Table 1. The key parameter we extract from all the models is the ratio, $(M/L)_{stars}$, between the mass of the stellar component and the luminosity (in the r band). As illustrated in Fig. 1, the availability of integral-field data is the key to separating the stellar mass accurately from the possible dark matter using dynamical models and hence determining $(M/L)_{stars}$. In fact, changes in $(M/L)_{stars}$ at the level expected to result from IMF variations cause drastic changes to the quality of the model fits.

We also measured the $(M/L)_{pop}$ ratio (in the r band) of the stellar population by fitting[15] the observed spectra using a linear combination of single stellar population synthetic spectra[16] of different ages (t) and metallicities ($[M/H]$), adopting for reference a Salpeter[1] IMF ($\xi(m) \propto m^x = m^{-2.3}$, where m is the stellar mass). The models use standard lower and upper mass cut-offs for the IMF of $0.1M_\odot$ and $100M_\odot$, respectively. We used linear regularization to reduce noise and produce smooth $M(t, [M/H])$ solutions consistent with the observations. The resulting $(M/L)_{pop}$ ratio is that of the composite stellar population, and excludes the gas lost during stellar evolution. If all this gas were retained in the galaxies in gaseous form, it would systematically increase $(M/L)_{pop}$ by about 30% (ref. 17). However, most of it is probably recycled into stars or expelled to larger radii. Although the measured trends have smaller scatter when using our full-spectrum fitting approach[15], similar conclusions are reached when the galaxies are approximated as one single stellar population, or when $(M/L)_{pop}$ is computed using different population codes[16–18] and with a more traditional approach, which only focuses on the strength of a few stellar absorption spectral lines. Systematic offsets of about 10% in $(M/L)_{pop}$ exist between the predictions of different population models for an identical set of assumed population parameters. The model that we use lies in the middle of this range. This sets the uncertainty in the absolute normalization of our plots. The random errors resulting from our population code[16] were estimated by applying the same spectral fitting approach to our integral-field spectroscopy data and to independent spectra obtained for a subset of 57 of our galaxies by the Sloan Digital Sky Survey. We inferred a root mean squared scatter of 12% in each individual $(M/L)_{pop}$ determination.

The ratio between the dynamically derived $(M/L)_{stars}$ values and the population-derived $(M/L)_{Salp}$ values, calculated using a fixed Salpeter IMF, is shown in Fig. 2 as a function of $(M/L)_{stars}$. We compare the observed ratio with the expected one if the galaxy had the 'light'

[1]Sub-department of Astrophysics, Department of Physics, University of Oxford, Denys Wilkinson Building, Keble Road, Oxford OX1 3RH, UK. [2]Gemini Observatory, Northern Operations Centre, 670 North A'ohoku Place, Hilo, Hawaii 96720, USA. [3]Department of Astronomy, Campbell Hall, University of California, Berkeley, California 94720, USA. [4]Observatoire de Paris, LERMA and CNRS, 61 Avenue de l'Observatoire, F-75014 Paris, France. [5]Laboratoire AIM Paris-Saclay, CEA/IRFU/SAp CNRS Université Paris Diderot, 91191 Gif-sur-Yvette Cedex, France. [6]Department of Astrophysics, University of Massachusetts, 710 North Pleasant Street, Amherst, Massachusetts 01003, USA. [7]European Southern Observatory, Karl-Schwarzschild-Strasse 2, 85748 Garching, Germany. [8]Sterrewacht Leiden, Leiden University, Postbus 9513, 2300 RA Leiden, The Netherlands. [9]Université Lyon 1, Observatoire de Lyon, Centre de Recherche Astrophysique de Lyon and Ecole Normale Supérieure de Lyon, 9 avenue Charles André, F-69230 Saint-Genis Laval, France. [10]Max-Planck Institut für extraterrestrische Physik, PO Box 1312, D-85478 Garching, Germany. [11]Netherlands Institute for Radio Astronomy, Postbus 2, 7990 AA Dwingeloo, The Netherlands. [12]Kapteyn Astronomical Institute, University of Groningen, Postbus 800, 9700 AV Groningen, The Netherlands. [13]Max-Planck Institut für Astrophysik, Karl-Schwarzschild-Strasse 1, 85741 Garching, Germany. [14]Centre for Astrophysics Research, University of Hertfordshire, Hatfield AL1 9AB, UK. [15]Centre for Astrophysics & Supercomputing, Swinburne University of Technology, PO Box 218, Hawthorn, Victoria 3122, Australia. [16]Dunlap Institute for Astronomy & Astrophysics, University of Toronto, 50 St George Street, Toronto, Ontario M5S 3H4, Canada. [17]Physics Department, New Mexico Institute of Mining and Technology, Socorro, New Mexico 87801, USA.
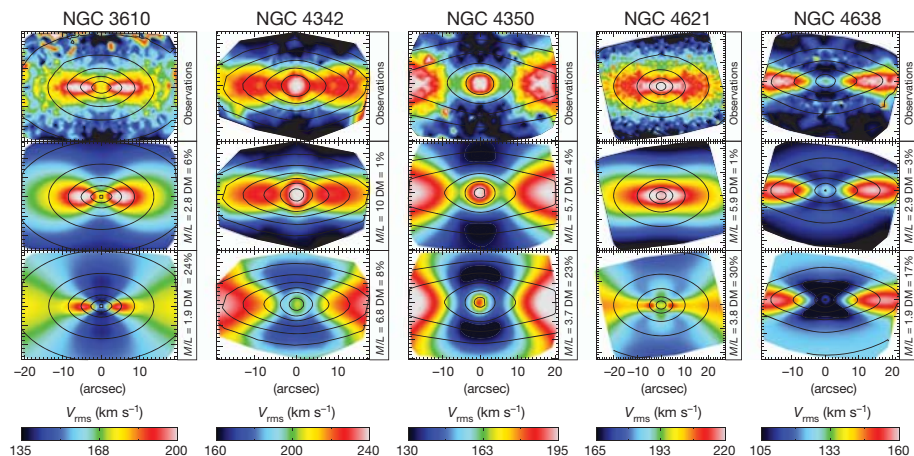
Figure 1 | Differentiating between the stellar and dark matter with integral-field stellar kinematics. The top row shows the symmetrized SAURON stellar kinematics ($V_{rms} = \sqrt{V^2 + \sigma^2}$) as a function of spatial position on the sky for the five named galaxies, which represent a variety of shapes of the kinematics field and span a range of $(M/L)_{stars}$ values. Here V is the mean stellar velocity and σ is the stellar velocity dispersion. The middle row shows the results of the best-fitting dynamical model[10] with a standard[12] dark halo (model B in Table 1). The bottom row shows the results of a dynamical model where the $(M/L)_{stars}$ ratio was fixed to be 0.65 times the best-fitting one. This decrease in $(M/L)_{stars}$ represents the change in stellar mass between a Salpeter IMF and a Kroupa IMF.

The other three model parameters, the galaxy inclination (i), the orbital anisotropy (β_z) and the halo total mass (M_{200}), were optimized to fit the data, but cannot provide an acceptable description of the observations. The plots show that, for a standard halo profile, the data tightly constrain both the dark matter fraction and $(M/L)_{stars}$. The constraint would be even stronger if we had assumed a more shallow inner-halo profile. The contours show the observed (top row) and modelled (middle and bottom rows) surface brightnesses. The $(M/L)_{stars}$ ratio (M/L) and the fraction of dark matter (DM) within a sphere with radius equal to the projected half-light radius are printed next to each panel.

Kroupa[19] or Chabrier[20] IMFs, which are similarly deficient in low-mass stars; with the 'standard' Salpeter IMF, which is described by a simple power law in stellar mass (m) with exponent $x = -2.3$; and with two additional 'heavy' power-law IMFs with $x = -2.8$ and $x = -1.5$, respectively. The last two IMFs predict the same $(M/L)_{pop}$ ratio. However, whereas for $x = -2.8$ the stellar population is dominated by dwarf stars, for $x = -1.5$ the large $(M/L)_{pop}$ ratio is due to stellar remnants: black holes, neutron stars and white dwarfs. The dynamical mass measurements do not constrain the shape of the IMF directly, but only the overall mass normalization, and for this reason do not distinguish between the two cases.

The results from all sets of dynamical models are consistent with a similar systematic variation in the IMF normalization, by a factor of up to three in galaxy stellar mass. A clear trend is visible in particular for the most general of our set of models (Fig. 2d), which makes virtually no assumptions about halo shape but fits it directly to the data. However, similar trends are visible for all our plausible assumptions for the dark halo mass and profile as predicted by numerical simulations. This shows that, although the relative amplitude of the IMF variation does not depend on the correctness of the assumed halo model, it is entirely consistent with standard model predictions for the halo. As $(M/L)_{stars}$ increases, the normalization of the inferred IMF varies from that of Kroupa and Chabrier to one more massive than the Salpeter IMF. The trend in IMF is still clearly visible in the subset of the 60 galaxies outside the Virgo galaxy cluster that have the most accurate

distances and the best models fits. This shows that the trend cannot be due to biases in the models or distances, or to effects related to the cluster environment. The knee in the relation at $(M/L)_{stars} \approx 6$ (r band) shows that the lowest $(M/L)_{stars}$ values mainly reflect the age and metallicity of the population (with younger ages or lower metallicities decreasing $(M/L)_{pop}$), and that the largest $(M/L)_{stars}$ values mainly reflect the population's dwarf- or remnants-dominated IMF. The models with contracted halos show the same IMF trend and relative amplitude as the other models. However, contracted halos predict too little stellar mass for many of the galaxies with low $(M/L)_{stars}$ ratios, even for the lightest Kroupa–Chabrier IMF. This suggests that contraction may not happen in most real galaxies, in agreement with recent numerical simulations that include a realistic treatment of baryon physics[21].

The trend in IMF reported here reconciles a number of apparently contradictory results on the normalization of the IMF that have accumulated in the past decade. The Kroupa–Chabrier-like normalization at low values of $(M/L)_{stars}$ agrees with the one inferred for spiral galaxies[22]. The ATLAS[3D] project discovered that early-type galaxies with the lowest $(M/L)_{pop}$ ratios resemble spiral galaxies with their gas removed[23], implying that these galaxies should have similar IMFs. The Kroupa–Chabrier normalization is also consistent with previous findings that this normalization is required if the stellar mass of early-type galaxies as a class is not to be overpredicted[3,24,25]. A Salpeter normalization at larger $(M/L)_{stars}$ ratios is consistent on average

Table 1 | The axisymmetric dynamical models

Model	Description of the model	Fitted model parameters
A (Fig. 2a)	Galaxy model in which the total mass traces the observed galaxy light distribution. Any dark matter, if present, follows the stellar distribution.	$i, \beta_z, (M/L)_{total}$
B (Fig. 2b)	Galaxy stellar component embedded in a spherical standard dark matter halo[12] with inner density $\rho(r) \propto r^{-1}$ for radii $r \ll r_s$ and outer density $\rho(r) \propto r^{-3}$ for $r \gg r_s$. The halo total mass, M_{200}, is fitted, and r_s is uniquely specified[13] by M_{200}.	$i, \beta_z, (M/L)_{stars}, M_{200}$
C (Fig. 2c)	Model with a standard[12] halo contracted[14] according to the observed galaxy stellar density. The halo mass is fitted, and r_s is specified[13] by M_{200}.	$i, \beta_z, (M/L)_{stars}, M_{200}$
D (Fig. 2d)	Model with a general halo inner density $\rho(r) \propto r^{\gamma}$ with fitted slope ($-1.6 < \gamma < 0$) and fitted total mass. The outer density becomes $\rho(r) \propto r^{-3}$, as in the standard halo[12], at radii $r \gg r_s = 20$ kpc.	$i, \beta_z, (M/L)_{stars}, \gamma, M_{200}$
E (Fig. 2e)	Model with a fixed standard halo[12]. M_{200} is specified[30] by the measured galaxy stellar mass and r_s is specified[13] by M_{200}.	$i, \beta_z, (M/L)_{stars}$
F (Fig. 2f)	Model with a fixed standard halo[12] contracted[14] according to the observed galaxy stellar density. M_{200} is specified[30] by the measured galaxy stellar mass and r_s is specified[13] by M_{200}.	$i, \beta_z, (M/L)_{stars}$

$(M/L)_{total}$ is the ratio between the galaxy total mass and the corresponding luminosity in the r band and r_s is the break radius of the halo, between the two power-law regimes. In model D, the steepest slope, $\gamma = -1.6$, is the extreme measured value for any of the contracted models C. The adopted break radius, $r_s = 20$ kpc, is the median value for all models E. However, this choice is unimportant because the fits are almost insensitive to the shape of the dark halo profile outside the much smaller radii where kinematics is available. The same values of $(M/L)_{stars}$ are obtained with a pure power-law halo.

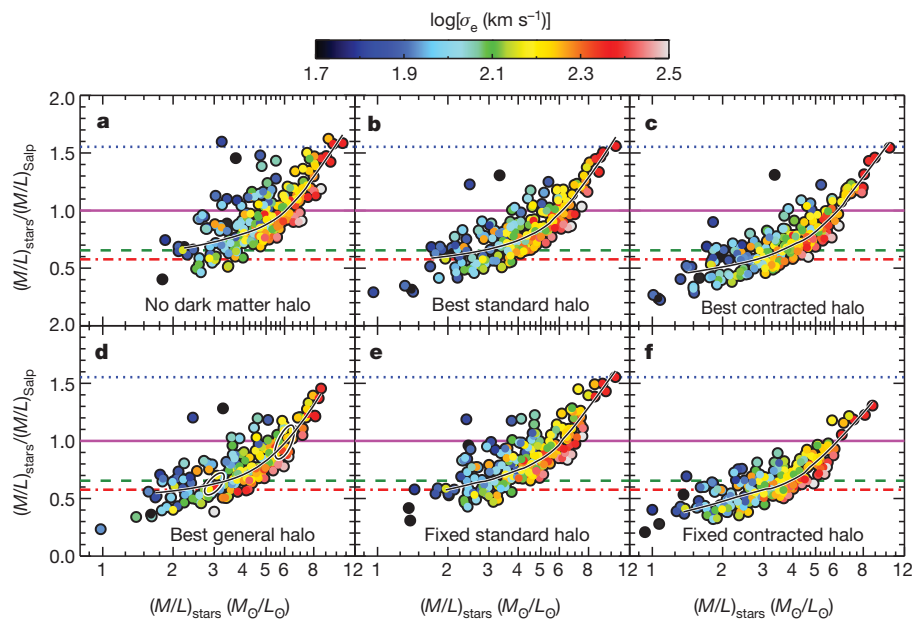**Figure 2 | Systematic variation of the IMF in early-type galaxies.** Ratio between the $(M/L)_{stars}$ values of the stellar component, determined using dynamical models, and the $(M/L)_{Salp}$ values of the stellar population, measured using stellar population models with a Salpeter IMF, as a function of $(M/L)_{stars}$. The black solid line is a locally weighted scatterplot smoothed version of the data. Colours indicate the galaxies' stellar velocity dispersion (σ_e), which is related to galaxy mass. The horizontal lines indicate the expected values for the ratio if the galaxy had (i) a Chabrier IMF (red dash–dot line); (ii) a Kroupa IMF (green dashed line); (iii) a Salpeter IMF ($x = -2.3$, solid magenta line) or one of two additional power-law IMFs with (iv) $x = -2.8$ and (v) $x = -1.5$ (blue dotted line). The different panels correspond to different assumptions for the dark matter halos used in the dynamical models: details are given in Table 1. A clear curved relation

is visible in all panels. Panels **a**, **b** and **e** look quite similar, as for all of them the dark matter contributes only a small fraction (zero in **a** and a median of 12% in **b** and **e**) of the total mass inside a sphere with the projected size of the region where we have kinematics (about one projected half-light radius). Panel **f**, with a fixed contracted halo, still shows the same IMF variation, but is almost systematically lower in $(M/L)_{stars}$ by 35%, reflecting the increase in dark matter fraction. The two ellipses plotted over the smooth relation in **d** show the representative 1σ errors for one measurement at the given locations. We excluded from the plot the galaxies with a very young stellar population (selected as having an Hβ absorption line strength >2.3 Å). These galaxies have strong radial gradients in their populations, which violates our assumption that all our various M/L values are spatially constant and makes both $(M/L)_{Salp}$ and $(M/L)_{stars}$ inaccurate.

with results from strong gravitational lensing[5], which are restricted to the galaxies with the largest velocity dispersions ($\sigma \gtrsim 200\,\mathrm{km\,s}^{-1}$). Finally, that some large-$(M/L)_{stars}$ galaxies have IMF normalizations more massive than the Salpeter normalization is broadly consistent with the finding from the depths of spectral features of eight massive galaxies[8] which indicate that they must be dominated by a population of dwarf stars.

If instead the largest $(M/L)_{pop}$ ratios were due to stellar remnants, our results would be consistent with indirect arguments based on the relation between the colour of a stellar population and its fraction of ionizing photons, suggesting an IMF slope that becomes flatter for more massive, star-forming galaxies[26,27]. However, our result is difficult to compare with this result directly, owing to the large difference in the sample selections. Moreover, these studies[26,27] measure the instantaneous IMF, when the stars are forming, whereas all previous studies we mentioned, and the one in this Letter, measure the 'integrated' galaxy IMF resulting from the cumulative history of star formation[28] and evolutionary mechanisms that the galaxy has experienced.

The discovered trend in IMF is also consistent with previous findings that the total M/L ratio in the centre of galaxies varies by a factor of at least two more than would be expected for a stellar population with constant dark matter fraction and a universal IMF[3]. Various previous attempts could not distinguish whether the mass discrepancy was due to non-universality of dark matter or that of IMF[4–7,29]. The studies were limited either by small samples or non-optimal data[3,6], or used simplified galaxy models that could bias the quantitative interpretation of the results[4,5,7,29]. We resolve both of these issues in this Letter.

Our study demonstrates that the assumption of a universal IMF, which is made in nearly every aspect of galactic astrophysics, stellar populations and cosmology, is inconsistent with real galaxies. Our results pose a challenge to galaxy formation models, which will have

to explain how stars 'know' what kind of galaxy they will end up inside. A possible explanation would be for the IMF to depend on the prevailing physical conditions when the galaxy formed the bulk of its stars. Although galaxies merge hierarchically, there is growing evidence that present-day, massive, early-type galaxies formed most of their stars in more-intense starbursts and at higher redshifts than spiral galaxies. This could lead to the observed difference in IMF. Unfortunately, there is no consensus among the theoretical models for how the IMF should vary with physical conditions. A new generation of theoretical and observational studies will have to provide insight into which physical mechanisms are responsible for the systematic IMF variation we find.

1. Salpeter, E. E. The luminosity function and stellar evolution. *Astrophys. J.* **121,** 161–167 (1955).
2. Bastian, N. Covey, K. R. & Meyer, M. R. A universal stellar initial mass function? A critical look at variations. *Annu. Rev. Astron. Astrophys.* **48,** 339–389 (2010).
3. Cappellari, M. *et al.* The SAURON project – IV. The mass-to-light ratio, the virial mass estimator and the fundamental plane of elliptical and lenticular galaxies. *Mon. Not. R. Astron. Soc.* **366,** 1126–1150 (2006).
4. Tortora, C., Napolitano, N. R., Romanowsky, A. J., Capaccioli, M. & Covone, G. Central mass-to-light ratios and dark matter fractions in early-type galaxies. *Mon. Not. R. Astron. Soc.* **396,** 1132–1150 (2009).
5. Treu, T. *et al.* The initial mass function of early-type galaxies. *Astrophys. J.* **709,** 1195–1202 (2010).
6. Thomas, J. *et al.* Dynamical masses of early-type galaxies: a comparison to lensing results and implications for the stellar initial mass function and the distribution of dark matter. *Mon. Not. R. Astron. Soc.* **415,** 545–562 (2011).
7. Dutton, A. A. *et al.* Dark halo response and the stellar initial mass function in early-type and late-type galaxies. *Mon. Not. R. Astron. Soc.* **416,** 322–345 (2011).
8. van Dokkum, P. G. & Conroy, C. A substantial population of low-mass stars in luminous elliptical galaxies. *Nature* **468,** 940–942 (2010).
9. Cappellari, M. *et al.* The ATLAS[3D] project – I. A volume-limited sample of 260 nearby early-type galaxies: science goals and selection criteria. *Mon. Not. R. Astron. Soc.* **413,** 813–836 (2011).

10. Cappellari, M. Measuring the inclination and mass-to-light ratio of axisymmetric galaxies via anisotropic Jeans models of stellar kinematics. *Mon. Not. R. Astron. Soc.* **390,** 71–86 (2008).
11. Emsellem, E., Monnet, G. & Bacon, R. The multi-gaussian expansion method: a tool for building realistic photometric and kinematical models of stellar systems l. The formalism. *Astron. Astrophys.* **285,** 723–738 (1994).
12. Navarro, J. F., Frenk, C. S. & White, S. D. M. The structure of cold dark matter halos. *Astrophys. J.* **462,** 563–575 (1996).
13. Klypin, A. A., Trujillo-Gomez, S. & Primack, J. Dark matter halos in the standard cosmological model: results from the Bolshoi simulation. *Astrophys. J.* **740,** 102 (2011).
14. Gnedin, O. Y. *et al.* Halo contraction effect in hydrodynamic simulations of galaxy formation. Preprint at 〈http://arxiv.org/abs/1108.5736〉 (2011).
15. Cappellari, M. & Emsellem, E. Parametric recovery of line-of-sight velocity distributions from absorption-line spectra of galaxies via penalized likelihood. *Publ. Astron. Soc. Pacif.* **116,** 138–147 (2004).
16. Vazdekis, A. *et al.* Evolutionary stellar population synthesis with MILES - I. The base models and a new line index system. *Mon. Not. R. Astron. Soc.* **404,** 1639–1671 (2010).
17. Maraston, C. Evolutionary population synthesis: models, analysis of the ingredients and application to high-*z* galaxies. *Mon. Not. R. Astron. Soc.* **362,** 799–825 (2005).
18. Bruzual, G. & Charlot, S. Stellar population synthesis at the resolution of 2003. *Mon. Not. R. Astron. Soc.* **344,** 1000–1028 (2003).
19. Kroupa, P. On the variation of the initial mass function. *Mon. Not. R. Astron. Soc.* **322,** 231–246 (2001).
20. Chabrier, G. Galactic stellar and substellar initial mass function. *Publ. Astron. Soc. Pacif.* **115,** 763–795 (2003).
21. Duffy, A. R. *et al.* Impact of baryon physics on dark matter structures: a detailed simulation study of halo density profiles. *Mon. Not. R. Astron. Soc.* **405,** 2161–2178 (2010).
22. Bell, E. F. & de Jong, R. S. Stellar mass-to-light ratios and the Tully-Fisher relation. *Astrophys. J.* **550,** 212–229 (2001).
23. Cappellari, M. *et al.* The ATLAS³D project – VII. A new look at the morphology of nearby galaxies: the kinematic morphology-density relation. *Mon. Not. R. Astron. Soc.* **416,** 1680–1696 (2011).
24. Renzini, A. in *The Initial Mass Function 50 Years Later* (ed. Corbelli, E., Palla, F. and Zinnecker, H.) 221 (Springer, 2005).
25. Ferreras, I., Saha, P. & Burles, S. Unveiling dark haloes in lensing galaxies. *Mon. Not. R. Astron. Soc.* **383,** 857–863 (2008).
26. Hoversten, E. A. & Glazebrook, K. Evidence for a nonuniversal stellar initial mass function from the integrated properties of SDSS galaxies. *Astrophys. J.* **675,** 163–187 (2008).
27. Gunawardhana, M. L. P. *et al.* Galaxy and mass assembly (GAMA): the star formation rate dependence of the stellar initial mass function. *Mon. Not. R. Astron. Soc.* **415,** 1647–1662 (2011).
28. Kroupa, P. & Weidner, C. Galactic-field initial mass functions of massive stars. *Astrophys. J.* **598,** 1076–1078 (2003).
29. Deason, A. J., Belokurov, V., Evans, N. W. & McCarthy, I. G. Elliptical galaxy masses out to five effective radii: the realm of dark matter. *Astrophys. J.* **748,** 2 (2012).
30. Moster, B. P. *et al.* Constraints on the relationship between stellar mass and halo mass at low and high redshift. *Astrophys. J.* **710,** 903–923 (2010).

Author Contributions All authors contributed extensively to the work presented in this paper.

LETTER

Engineered two-dimensional Ising interactions in a trapped-ion quantum simulator with hundreds of spins

Joseph W. Britton[1], Brian C. Sawyer[1], Adam C. Keith[2,3], C.-C. Joseph Wang[2], James K. Freericks[2], Hermann Uys[4], Michael J. Biercuk[5] & John J. Bollinger[1]

The presence of long-range quantum spin correlations underlies a variety of physical phenomena in condensed-matter systems, potentially including high-temperature superconductivity[1,2]. However, many properties of exotic, strongly correlated spin systems, such as spin liquids, have proved difficult to study, in part because calculations involving N-body entanglement become intractable for as few as $N \approx 30$ particles[3]. Feynman predicted that a quantum simulator—a special-purpose 'analogue' processor built using quantum bits (qubits)—would be inherently suited to solving such problems[4,5]. In the context of quantum magnetism, a number of experiments have demonstrated the feasibility of this approach[6–14], but simulations allowing controlled, tunable interactions between spins localized on two- or three-dimensional lattices of more than a few tens of qubits have yet to be demonstrated, in part because of the technical challenge of realizing large-scale qubit arrays. Here we demonstrate a variable-range Ising-type spin–spin interaction, $J_{i,j}$, on a naturally occurring, two-dimensional triangular crystal lattice of hundreds of spin-half particles (beryllium ions stored in a Penning trap). This is a computationally relevant scale more than an order of magnitude larger than previous experiments. We show that a spin-dependent optical dipole force can produce an antiferromagnetic interaction $J_{i,j} \propto d_{i,j}^{-a}$, where $0 \le a \le 3$ and $d_{i,j}$ is the distance between spin pairs. These power laws correspond physically to infinite-range ($a = 0$), Coulomb–like ($a = 1$), monopole–dipole ($a = 2$) and dipole–dipole ($a = 3$) couplings. Experimentally, we demonstrate excellent agreement with a theory for $0.05 \lesssim a \lesssim 1.4$. This demonstration, coupled with the high spin count, excellent quantum control and low technical complexity of the Penning trap, brings within reach the simulation of otherwise computationally intractable problems in quantum magnetism.

A challenge in condensed-matter physics is the fact that many quantum magnetic interactions cannot currently be modelled in a meaningful way. A canonical example is the spin liquid, an exotic state postulated[1] to arise in a collection of spin-1/2 particles residing on a triangular lattice and coupled to each other by a nearest-neighbour antiferromagnetic Heisenberg interaction. The spin liquid's ground state is highly degenerate, owing to spin frustration, and is expected to have unusual behaviours including phase transitions at zero temperature driven by quantum fluctuations[15]. However, despite recent advances[16,17] a detailed understanding of large-scale frustration in solids remains elusive[2,18–20].

Atomic physicists have recently provided a bottom-up approach to the problem by engineering the relevant spin interactions in quantum simulators[5,21,22]. The necessary experimental capabilities—laser cooling, deterministic spin localization, precise spin-state quantum control, high-fidelity read-out and engineered spin–spin coupling—were first demonstrated in the context of atomic clocks (see, for example, ref. 23). In the domain of quantum magnetism, this tool set permits

control of parameters commonly viewed as immutable in natural solids, for example lattice spacing and geometry, and spin–spin interaction strength and range.

Initial simulations of quantum Ising and Heisenberg interactions with localized spins were done with neutral atoms in optical lattices[6,11], atomic ions in Paul traps[9,10,13,14] and photons[12]. This work involved simulations readily calculable on a classical computer: interactions between $N \approx 10$ qubits localized in one-dimensional (1D) chains. The move to quantum magnetic interactions on two-dimensional (2D) lattices and between larger, computationally relevant numbers of particles is the crucial next step but at present requires more technological development[24].

In our Penning trap apparatus, laser-cooled $^9Be^+$ ions naturally form a stable 2D Coulomb crystal on a triangular lattice with ~300 spins (Fig. 1). Each ion is a spin-1/2 system (qubit) over which we exert high-fidelity quantum control[25]. In this paper, we demonstrate the use of a spin-dependent optical dipole force (ODF) to engineer a continuously tunable Ising-type spin–spin coupling $J_{i,j} \propto d_{i,j}^{-a}$. This capability, in tandem with a modified measurement routine (for example by more sophisticated processing of images such as that in Fig. 1), is a key advance towards useful simulations of quantum magnetism.

A Penning trap confines ions in a static quadrupolar electric potential (Methods) and a strong, homogeneous magnetic field $\mathbf{B} = B_0\hat{\mathbf{z}}$ ($B_0 = 4.46$ T). Axial trapping (along z) is due to the electric field. Ion rotation at frequency ω_r (about z) produces a radial restoring potential due to the velocity-dependent Lorentz force ($q\mathbf{v} \times \mathbf{B}$, where q and $\mathbf{v}$ are respectively the ion's charge and velocity). Tuning the ratio of the axial to radial confinement allows controlled formation of a planar geometry and, after Doppler laser cooling, the formation of a 2D Coulomb crystal on a triangular lattice[26] (Methods). We routinely generate crystals with N ions ($100 \lesssim N \lesssim 350$), where the valence-electron spin state of each ion serves as a qubit[25]. Following techniques developed in linear (1D) Paul traps[27], spins confined in the same trapping potential are coupled through their shared motional degrees of freedom.

Using well-controlled external fields, we engineer spin interactions of the form

$$\hat{H}_B = \sum_i \mathbf{B}_\mu \cdot \hat{\boldsymbol{\sigma}}_i$$
$$\hat{H}_I = \frac{1}{N} \sum_{i<j} J_{i,j} \hat{\sigma}_i^z \hat{\sigma}_j^z \qquad (1)$$

where $\hat{\boldsymbol{\sigma}}_i = (\hat{\sigma}_i^x, \hat{\sigma}_i^y, \hat{\sigma}_i^z)$ is the vector of Pauli matrices for ion i. We label the qubit spin states $|\uparrow\rangle \equiv |m_s = +1/2\rangle$ and $|\downarrow\rangle \equiv |m_s = -1/2\rangle$, where m_s is the spin's projection along the quantizing field $B_0\hat{\mathbf{z}}$, such that $\hat{\sigma}_i^z|\uparrow_i\rangle = |\uparrow_i\rangle$ and $\hat{\sigma}_i^z|\downarrow_i\rangle = |\downarrow_i\rangle$. The Hamiltonian $\hat{H}_B$ encodes an interaction due to an effective magnetic field, $\mathbf{B}_\mu$ (generated by externally applied microwaves at 124 GHz), that couples equally to all spins and permits global rotations (Fig. 1). The interaction $\hat{H}_I$ describes a general coupling, $J_{i,j}$, between spins i and j a distance $d_{i,j}$ apart[28,29]. For $J_{i,j} > 0$
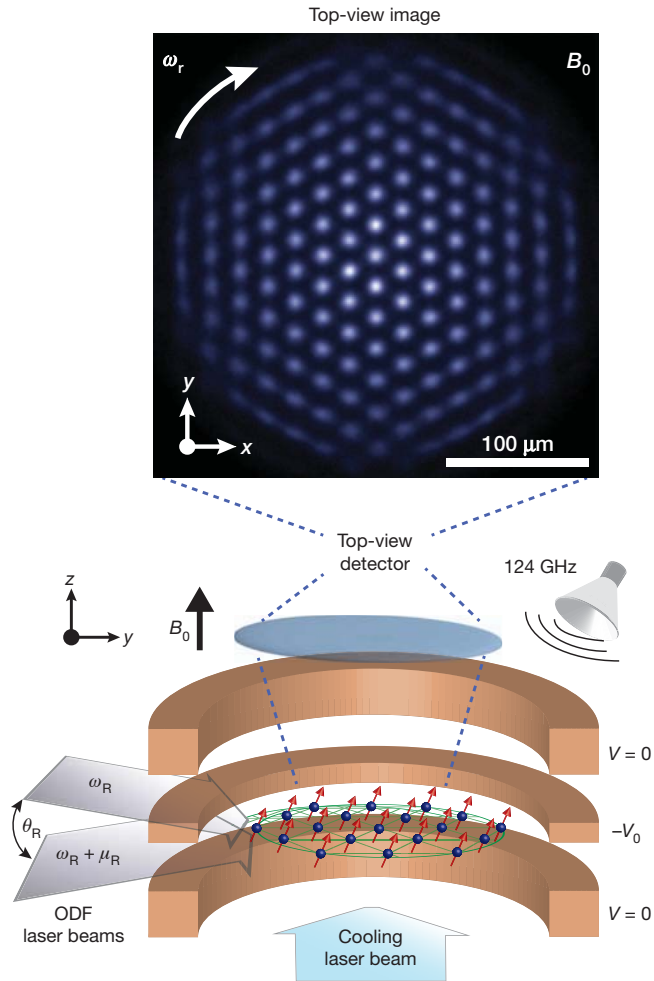
Top-view image

Figure 1 | **The Penning trap confines hundreds of spin-1/2 qubits on a 2D triangular lattice.** Each qubit is the valence-electron spin of a $^9Be^+$ ion. Bottom: a Penning trap confines ions using a combination of static electric and magnetic fields. The trap parameters are configured such that laser-cooled ions form a triangular 2D crystal. A general spin–spin interaction, $\hat{H}_I$, is generated by a spin-dependent excitation of the transverse (along z) motional modes of the ion crystal. This coupling is implemented using an optical dipole force (ODF) produced by a pair of off-resonance laser beams (left side) with angular separation θ_R and difference frequency μ_R. Microwaves at 124 GHz permit global spin rotations $\hat{H}_B$. Top: a representative top-view resonance fluorescence image showing the centre region of an ion crystal captured in the ions' rest frame; in the laboratory frame, the ions rotate at $\omega_r = 2\pi \times 43.8$ kHz (ref. 26). Fluorescence is an indication of the qubit spin state ($|\uparrow\rangle$, bright; $|\downarrow\rangle$, dark); here, the ions are in the state $|\uparrow\rangle$. The lattice constant is $d_0 \approx 20\,\mu m$.

the coupling is antiferromagnetic and for $J_{i,j} < 0$ the coupling is ferromagnetic.

We implement $\hat{H}_I$ using a spatially uniform, spin-dependent ODF generated by a pair of off-resonance laser beams with difference frequency μ_R (Fig. 1 and Supplementary Information). The ODF couples each ion's spin to one or more of the N transverse (along z) motional modes of the Coulomb crystal by forcing coherent displacements of the ions that in turn modify the ions' Coulomb potential energy through the interaction

$$\hat{H}_{ODF} = -\sum_{i}^{N} F_z(t)\hat{z}_i \hat{\sigma}_i^z$$

Here $F_z(t) = F_0\cos(\mu_R t)$ is the ODF; $\hat{z}_i = \sum_{m=1}^{N} b_{i,m}\sqrt{\hbar/2M\omega_m}$ $(\hat{a}_m e^{-i\omega_m t} + \hat{a}_m^\dagger e^{i\omega_m t})$ is the axial position operator for ion i; $b_{i,m}$ are elements of the N transverse phonon eigenfunctions, $\mathbf{b}_m$, at frequencies

ω_m, normalized as $\sum_{m=1}^{N}|b_{i,m}|^2 = \sum_{i=1}^{N}|b_{i,m}|^2 = 1$ (refs 28, 29); M is the ion mass; and $\hbar$ is Planck's constant divided by 2π. The modes include the centre-of-mass (COM) mode (ω_1) as well as an array of modes of higher spatial frequencies that may be derived from atomistic calculations (Fig. 2a) and confirmed by experimental measurement[30].

For small, coherent displacements, where residual spin–motion entanglement can be neglected[29] (Methods), $\hat{H}_{ODF}$ is equivalent to $\hat{H}_I$ in equation (1): spins i and j are coupled in proportion to their spin
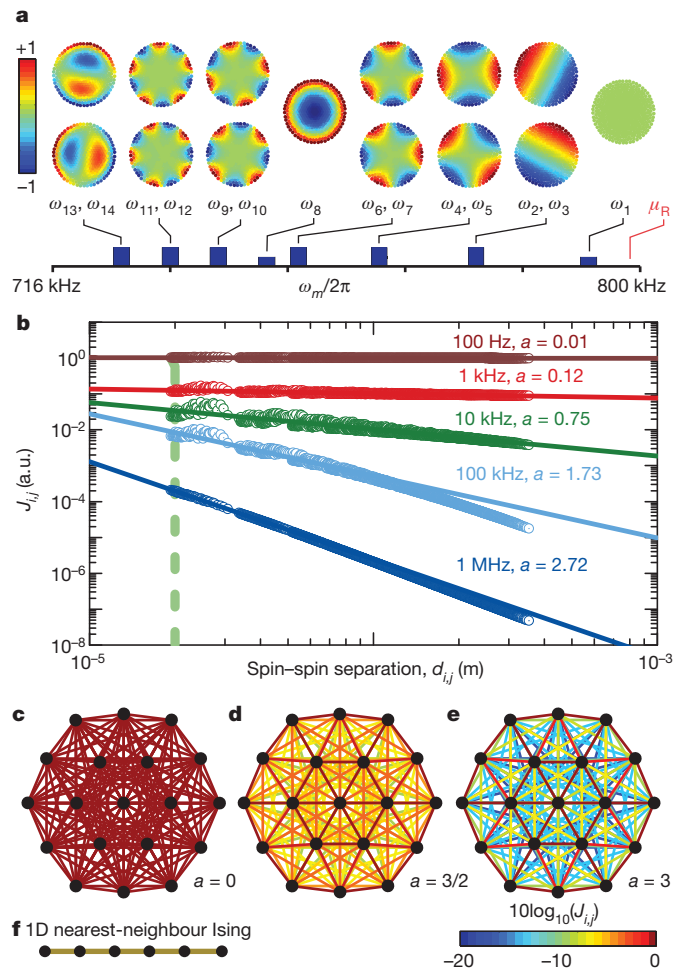

Figure 2 | **Spin–spin interactions are mediated by the ion crystal's transverse motional degrees of freedom. a**, For a 2D crystal with $N = 217$ ions and $\omega_r = 2\pi \times 45.6$ kHz, we calculate the eigenfunctions, $\mathbf{b}_m$, and eigenfrequencies, ω_m, for the N transverse motional modes (Supplementary Information). Plotted here are ω_m and $\mathbf{b}_m$ for the 14 highest-frequency modes. Relative mode amplitude is indicated by colour. The COM motion is the highest in frequency ($\omega_1 \approx 2\pi \times 795$ kHz); $\mathbf{b}_1$ has no spatial variation. The lowest-frequency mode is $\omega_{217} \approx 2\pi \times 200$ kHz; $\mathbf{b}_{217}$ has spatial variation at the lattice-spacing length scale, $d_0 \approx 20\,\mu m$. **b**, Using equation (2), we calculate $J_{i,j}$ explicitly for $N = 217$ spins and plot it as a function of spin–spin separation, $d_{i,j}$. For $\mu_R - \omega_1 < 2\pi \times 1$ kHz, $\hat{H}_{ODF}$ principally excites COM motion in which all ions equally participate: the spin–spin interaction is spatially uniform. As the detuning is increased, modes of higher spatial frequency participate in the interaction and $J_{i,j}$ develops a finite interaction length. We find the scaling of $J_{i,j}$ with $d_{i,j}$ follows the power law $J_{i,j} \propto d_{i,j}^{-a}$. For $\mu_R - \omega_1 \gg 2\pi \times 500$ kHz, all transverse modes participate and the spin–spin coupling power-law exponent, a, approaches 3. The solid lines are power-law fits to the theory points. For comparison with other experiments, the nearest-neighbour coupling ($d_0 = 20\,\mu m$) is marked by the dashed line. **c–e**, The power-law nature of $J_{i,j}$ is qualitatively illustrated for $N = 19$ (for larger N, diagrams of similar size are illegible). Spins (nodes) are joined by lines coloured in proportion to their coupling strength for various values of a. **f**, For context, the graph for a 1D nearest-neighbour Ising interaction, a well-known model in quantum field theory, is plotted.

states, $\hat{\sigma}_i^z$ and $\hat{\sigma}_j^z$, and by their mutual participation in each motional mode m. The coupling coefficient is given by[29]

$$J_{i,j} = \frac{F_0^2 N}{2\hbar M} \sum_{m=1}^{N} \frac{b_{i,m} b_{j,m}}{\mu_R^2 - \omega_m^2} \qquad (2)$$

These pairwise interaction coefficients can be calculated explicitly by use of the ion motional modes. We find that the range of interaction can be modified by detuning away from the COM mode as shown in Fig. 2b. In the limit $\mu_R - \omega_1 \gg 2\pi \times 500$ kHz, all modes participate equally in the interaction and $J_{i,j} \propto d_{i,j}^{-3}$, as discussed in ref. 28. At intermediate detuning, we find a power-law scaling of the interaction range, $J_{i,j} \propto d_{i,j}^{-a}$, where a can be tuned within the range $0 \leq a \leq 3$. That is, by adjusting the single experimental parameter, μ_R, we can mimic a continuum of physical couplings including important special cases: infinite range ($a = 0$); monopole–monopole, or Coulomb-like ($a = 1$); monopole–dipole ($a = 2$); and dipole–dipole ($a = 3$). The choice of $a = 0$ results in the '$\hat{J}_z^2$ interaction', which gives rise to spin squeezing and is used in quantum logic gates[27] (Supplementary Information). In addition, tuning μ_R also gives access to both antiferromagnetic ($\mu_R > \omega_1$) and ferromagnetic ($\omega_2 \ll \mu_R < \omega_1$) couplings[10,13].

Experimentally, we demonstrate a tunable-range Ising interaction by observing a global spin precession under the application of $\hat{H}_I$ (Fig. 3). We compare experimental data with the mean-field prediction that the influence of $\hat{H}_I$ on spin j can be modelled as a magnetic field $\bar{B}_j = (2/N) \sum_{i,i\neq j}^{N} J_{i,j} \langle \hat{\sigma}_i^z \rangle$ in the z direction due to the remaining $N - 1$ spins (Supplementary Information; angle brackets denote expectation value). For a general qubit superposition state, $\bar{B}_j$ gives rise to spin precession about z in excess of that expected to result from simple Larmor precession (Fig. 3b). The experiment sequence shown in Fig. 3a measures this excess precession, averaged over all spins in the crystal. At the outset, each spin is prepared in state $|\uparrow\rangle$ and then rotated about the x axis by angle θ_1. The interaction $\hat{H}_I$ is applied during the arms of a spin echo, each of duration τ_{arm}; precession proportional to $\langle \hat{\sigma}_i^z \rangle$ coherently adds throughout the interaction duration, $2\tau_{arm}$. The final $\pi/2$-pulse maps precession out of the initial plane (y–z) into excursions along z (above or below the equatorial plane of the Bloch sphere) that are resolved by projective spin measurement along z.

We detect global, state-dependent fluorescence ($|\uparrow\rangle$, bright; $|\downarrow\rangle$, dark) as a function of θ_1 using a photomultiplier tube. This measurement permits a systematic study of the mean-field-induced spin precession averaged over all particles

$$\frac{1}{N}\sum_j^N \bar{B}_j = 2\left(\frac{1}{N^2}\sum_j^N \sum_{i,i\neq j}^N J_{i,j}\right)\cos(\theta_1) \equiv 2\bar{J}\cos(\theta_1)$$

The probability of detecting state $|\uparrow\rangle$ at the end of the sequence is

$$P(|\uparrow\rangle) = \frac{1}{2}\left(1 + \exp(-\Gamma \cdot 2\tau_{arm})\sin(\theta_1)\sin(2\bar{J}\cos(\theta_1)\cdot 2\tau_{arm})\right) \qquad (3)$$

and a single-parameter fit to experimental data yields $\bar{J}$. Decoherence due to spontaneous emission is accounted for by Γ and is determined by independent measurement of the ODF laser beam intensities, I_R ($\Gamma \propto I_R$; see Supplementary Information).

In Fig. 3c, d, we show representative measurements of excess precession due to $\hat{H}_I$ for different values of spin coupling strength (determined by $J_{i,j} \propto I_R^2$) and interaction duration ($2\tau_{arm}$). The excess spin precession varies periodically with θ_1 (with period π) and greater interaction strengths result in more precession, manifested in our experiment as a larger amplitude modulation of $P(|\uparrow\rangle)$. Our data agree with equation (3) and allow direct extraction of $\bar{J}$ for given experimental conditions. In Fig. 3e, we plot $\bar{J}$, normalized by I_R^2 (I_R is independently measured), as a function of the detuning $\mu_R - \omega_1$ ($N = 206 \pm 10$ ions). Using no free parameters, we find excellent agreement with the value of $\bar{J}$ obtained by averaging over all $J_{i,j}$, where the $J_{i,j}$ were calculated by including couplings to all N transverse modes (equation (2)).

The mean-field interpretation of our benchmarking measurement applies only for weak spin–spin correlations. Therefore, in the benchmarking regime we apply a weak interaction ($\bar{J} \cdot 2\tau_{arm} \ll \sqrt{N}/4$; see
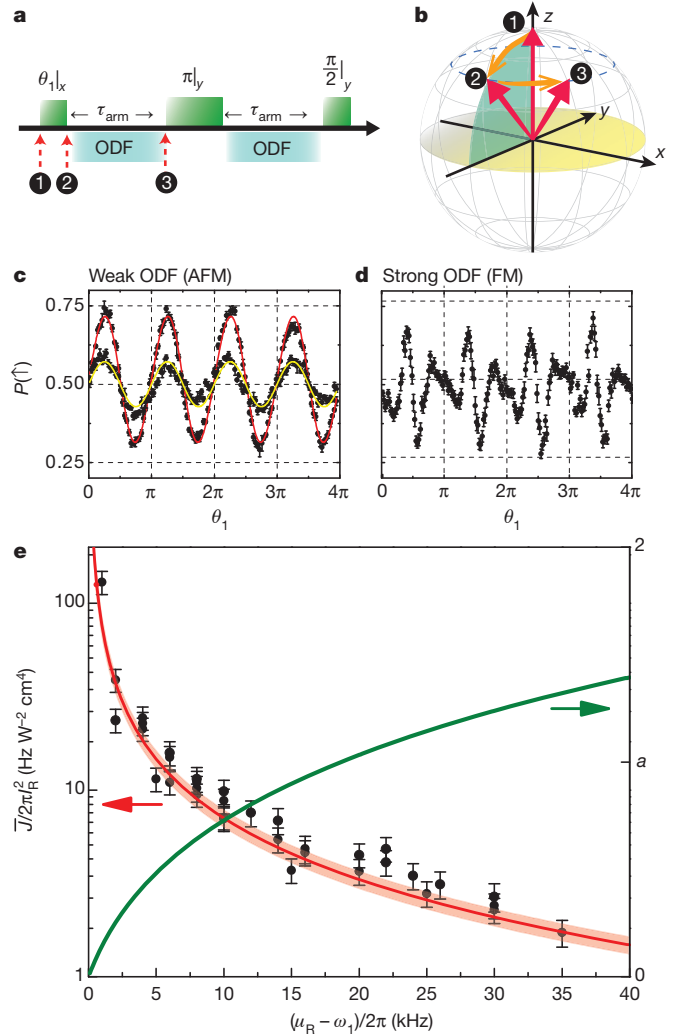

Figure 3 | Benchmarking the 2D Ising interaction. a, Spin-precession benchmarking sequence for $\hat{H}_I$. The spins are prepared at the outset in $|\uparrow\rangle$ (a ferromagnetic state). The spin–spin interaction, $\hat{H}_I$, is present when the ODF laser beams are on. We choose $\mu_R - \omega_1 = n \cdot 2\pi/\tau_{arm}$ so that for small detunings from the COM mode (ω_1), the spins are decoupled from the motion by the end of each period τ_{arm}. **b**, Evolution of a single spin before the application of the spin echo π-pulse. **c, d**, Plots showing spin precession proportional to $\langle \hat{\sigma}_z \rangle$ due to $\hat{H}_I$ as a function of initial 'tipping angle' θ_1. The error bars are statistical (s.d., 200 measurements). The plots show typical experimental data (black) and, in **c**, single-parameter fits to equation (3). For an antiferromagnetic (AFM) coupling, $\tau_{arm} = 250$ μs, $\mu_R - \omega_1 = 2\pi \times 4.0$ kHz and $I_R = 1.4$ W cm^{-2}, we obtain $\bar{J}/I_R^2 = 2\pi \times 25$ Hz W^{-2} cm^4 (yellow fit). Longer drive periods and higher laser intensity, I_R, yield a larger precession. For $\tau_{arm} = 350$ μs, $\mu_R - \omega_1 = 2\pi \times 2.9$ kHz and $I_R = 1.9$ W cm^{-2}, we obtain $\bar{J}/I_R^2 = 2\pi \times 55$ Hz W^{-2} cm^4 (red fit). The data in this plot is typical of the experiments conducted for benchmarking. For a much stronger interaction (**d**), equation (3) cannot be used to obtain $\bar{J}$ because the mean-field assumption is no longer valid (Supplementary Information). Also, here we used a small negative detuning ($\omega_2 \ll \mu_R < \omega_1$), which gives a long-range ferromagnetic (FM) interaction. For these experiments, we set $\omega_r = 2\pi \times 45.6$ kHz. **e**, Benchmarking results for an ion crystal with $N = 206 \pm 10$ ions. Each point is generated by measuring $\bar{J}$ as in **c**) and measuring the laser beam intensity, I_R, at the ions. The error bars are dominated by uncertainty in I_R (Supplementary Information). The solid line (red) is the prediction of mean-field theory that accounts for couplings to all N transverse modes; there are no free parameters. The line's breadth reflects experimental uncertainty in the angle $\theta_R = 4.8 \pm 0.25°$. The mean-field prediction for the average value of the power-law exponent, a, is drawn in green (right axis, linear scale).

Supplementary Information). In a quantum simulation, the same interaction is applied at greater power, producing quantum spin–spin correlations. In the present configuration of our apparatus, spontaneous emission due to the ODF laser beams (parameterized by Γ in equation (3)) is the dominant source of decoherence. With modest laser powers of 4 mW per laser beam and a detuning of $\mu_R - \omega_1 = 2\pi \times 2$ kHz, we obtain $\bar{J} \approx 2\pi \times 0.5$ kHz and $\Gamma/\bar{J} \approx 0.06$. The expected spin squeezing $\langle \hat{J}_z^2 \rangle$ due to this interaction is 5 dB (limited by spontaneous emission). The ratio $\Gamma/\bar{J}$ can be reduced by a factor of 50 by increasing the ODF laser beams' angular separation, θ_R, to $35°$ (Fig. 1), which is a likely prerequisite for access to the shortest-range, dipole–dipole, coupling regime ($a \rightarrow 3$). At present, geometric constraints impose the limit $\theta_R < 5°$; we plan upgrades to our apparatus to permit $\theta_R = 35°$. Thus far we operated with ODF magnitudes equal but opposite for $|\uparrow\rangle$ and $|\downarrow\rangle$; relaxation of this constraint can further reduce $\Gamma/\bar{J}$.

Our work establishes the suitability of Penning traps for simulation of quantum magnetism in a regime inaccessible to classical computation. Our approach is based on naturally occurring 2D Coulomb (Wigner) crystals with hundreds of ion qubits, a novel experimental system that does not require demanding trap-engineering efforts. Experimentally, we used an ODF to engineer a tunable-range spin–spin interaction and benchmarked the interaction strength. Excellent agreement was obtained with the predictions of mean-field theory and atomistic calculations that predict a power-law antiferromagnetic spin coupling, $J_{i,j} \propto d_{i,j}^{-a}$, for $0.05 \lesssim a \lesssim 1.4$.

With this work as a foundation, we anticipate a variety of future investigations. For example, simultaneous application of the non-commuting interactions $\hat{H}_B$ and $\hat{H}_I$ is expected to give rise to quantum phase transitions; $\hat{H}_I$ may be antiferromagnetic ($\mu_R > \omega_1$) or ferromagnetic ($\omega_2 \ll \mu_R < \omega_1$). Geometric modifications to our apparatus will permit access to larger values of θ_R and antiferromagnetic dipole–dipole-type couplings ($a \rightarrow 3$). Improved image processing software will permit direct measurement of spin–spin correlation functions using our existing single-spin-resolving imaging system (Fig. 1).

METHODS SUMMARY

In a frame rotating at frequency ω_r, the trap potential is

$$q\varphi(r,z) = \frac{1}{2} M \omega_1^2 (z^2 + \beta r^2)$$

where $\beta = \omega_r \omega_1^{-2}(\Omega_c - \omega_r) - 1/2$. The $^9\text{Be}^+$ cyclotron frequency is $\Omega_c = B_0 q/M = 2\pi \times 7.6$ MHz and the frequency of the ions' harmonic COM motion along z is $\omega_1 = 2\pi \times 795$ kHz. Ion rotation is precisely controlled with an external rotating quadrupole potential[26]. For $100 \lesssim N \lesssim 350$, we set $\omega_r \approx 2\pi \times 45$ kHz so that the radial confinement is weak enough that a cloud of ions relaxes into a single 2D plane ($\beta \ll 1$). When the ions' motional degrees of freedom are Doppler laser cooled[30] ($T_{\text{COM}} \approx 1$ mK), the ions naturally form a 2D Coulomb crystal on a triangular lattice, which is the geometry that minimizes the energy of their mutual Coulomb potential energy. The crystal has N transverse eigenmodes, ω_m, with eigenfunctions $\mathbf{b}_m$; the COM mode, ω_1, is the highest-frequency mode (Fig. 2a).

The spin-dependent ODF is generated by a pair of off-resonance laser beams with angular separation $\theta_R \approx 4.8°$ and difference frequency μ_R (Fig. 1). The result is a travelling 1D optical lattice of wavelength $\lambda_R = 2\pi/\Delta k \approx 3.7$ μm whose wavefronts propagate along z, traversing the ion crystal at frequency $\mu_R/2\pi$. Alignment of the optical lattice is crucial for proper spin–spin coupling (Supplementary Information). The lattice's polarization gradient induces a differential a.c. Stark shift on the qubit states (a spin-dependent force). We choose operating conditions that give $\mathbf{F}_\uparrow \approx -\mathbf{F}_\downarrow$, where $\mathbf{F}_\uparrow = F_0 \cos(\mu_R t)\hat{z}$. For reference, if the single-beam intensity at the ions is $I_R = 1$ W cm^{-2}, we obtain $F_0 \approx 1.4 \times 10^{-23}$ N.

Small, coherent displacements that produce negligible spin–motion entanglement (as required by equation (2)) are obtained for detunings satisfying

$$\hbar|\mu_R - \omega_m| > F_0 \sqrt{\hbar(2\bar{n}_m + 1)/2M\omega_m}$$

This is a more stringent criterion than that used by others[13,29], because it includes an additional factor of $\sqrt{N}$ to account for a typical distribution of composite spin states. Moreover, we also include a correction factor for finite temperature, $\bar{n}_m \approx k_B T/\hbar\omega_m$, where k_B is the Boltzmann constant.

1. Anderson, P. W. The resonating valence bond state in La$_2$CuO$_4$ and superconductivity. *Science* **235,** 1196–1198 (1987).
2. Moessner, R., Sondhi, S. L. & Chandra, P. Two-dimensional periodic frustrated Ising models in a transverse field. *Phys. Rev. Lett.* **84,** 4457–4460 (2000).
3. Sandvik, A. W. Ground states of a frustrated quantum spin chain with long-range interactions. *Phys. Rev. Lett.* **104,** 137204 (2010).
4. Feynman, R. Simulating physics with computers. *Int. J. Theor. Phys.* **21,** 467–488 (1982).
5. Buluta, I. & Nori, F. Quantum simulators. *Science* **326,** 108–111 (2009).
6. Trotzky, S. *et al.* Time-resolved observation and control of superexchange interactions with ultracold atoms in optical lattices. *Science* **319,** 295–299 (2008).
7. Lin, Y.-J., Compton, R. L., Jiménez-García, K., Porto, J. V. & Spielman, I. B. Synthetic magnetic fields for ultracold neutral atoms. *Nature* **462,** 628–632 (2009).
8. Jo, G.-B. *et al.* Itinerant ferromagnetism in a Fermi gas of ultracold atoms. *Science* **325,** 1521–1524 (2009).
9. Friedenauer, A., Schmitz, H., Glueckert, J. T., Porras, D. & Schaetz, T. Simulating a quantum magnet with trapped ions. *Nature Phys.* **4,** 757–761 (2008).
10. Kim, K. *et al.* Quantum simulation of frustrated Ising spins with trapped ions. *Nature* **465,** 590–593 (2010).
11. Simon, J. *et al.* Quantum simulation of antiferromagnetic spin chains in an optical lattice. *Nature* **472,** 307–312 (2011).
12. Ma, X.-s., Dakic, B., Naylor, W., Zeilinger, A. & Walther, P. Quantum simulation of the wavefunction to probe frustrated Heisenberg spin systems. *Nature Phys.* **7,** 399–405 (2011).
13. Islam, R. *et al.* Onset of a quantum phase transition with a trapped ion quantum simulator. *Nature Commun.* **2,** 377 (2011).
14. Lanyon, B. P. *et al.* Universal digital quantum simulation with trapped ions. *Science* **334,** 57–61 (2011).
15. Sachdev, S. *Quantum Phase Transitions* (Cambridge Univ. Press, 2001).
16. Kohno, M., Starykh, O., a. & Balents, L. Spinons and triplons in spatially anisotropic frustrated antiferromagnets. *Nature Phys.* **3,** 790–795 (2007).
17. Varney, C., Sun, K., Galitski, V. & Rigol, M. Kaleidoscope of exotic quantum phases in a frustrated XY model. *Phys. Rev. Lett.* **107,** 077201 (2011).
18. Levi, B. G. New candidate emerges for a quantum spin liquid. *Phys. Today* **60,** 16–19 (2007).
19. Helton, J. S. *et al.* Spin dynamics of the spin-1/2 Kagome lattice antiferromagnet ZnCu$_3$(OH)$_6$Cl$_2$. *Phys. Rev. Lett.* **98,** 107204 (2007).
20. Balents, L. Spin liquids in frustrated magnets. *Nature* **464,** 199–208 (2010).
21. Lewenstein, M. *et al.* Ultracold atomic gases in optical lattices: mimicking condensed matter physics and beyond. *Adv. Phys.* **56,** 243–379 (2007).
22. Bloch, I. & Zwerger, W. Many-body physics with ultracold gases. *Rev. Mod. Phys.* **80,** 885–964 (2008).
23. Rosenband, T. *et al.* Frequency ratio of Al$^+$ and Hg$^+$ single-ion optical clocks; metrology at the 17th decimal place. *Science* **319,** 1808–1812 (2008).
24. Schmied, R., Wesenberg, J. H. & Leibfried, D. Optimal surface-electrode trap lattices for quantum simulation with trapped ions. *Phys. Rev. Lett.* **102,** 233002 (2009).
25. Biercuk, M. J. *et al.* High-fidelity quantum control using ion crystals in a Penning trap. *Quantum Inf. Comput.* **9,** 920–949 (2009).
26. Mitchell, T. *et al.* Direct observations of structural phase transitions in planar crystallized ion plasmas. *Science* **282,** 1290–1293 (1998).
27. Leibfried, D. *et al.* Experimental demonstration of a robust, high-fidelity geometric two ion-qubit phase gate. *Nature* **422,** 412–415 (2003).
28. Porras, D. & Cirac, J. Quantum manipulation of trapped ions in two dimensional coulomb crystals. *Phys. Rev. Lett.* **96,** 250501 (2006).
29. Kim, K. *et al.* Entanglement and tunable spin-spin couplings between trapped ions using multiple transverse modes. *Phys. Rev. Lett.* **103,** 120502 (2009).
30. Sawyer, B. C. *et al.* Spectroscopy and thermometry of drumhead modes in a mesoscopic trapped-ion crystal using entanglement. *Phys. Rev. Lett.*. (in the press); preprint at ⟨http://arxiv.org/abs/1201.4415⟩ (2012).

Thermal and electrical transport across a magnetic quantum critical point

Heike Pfau[1], Stefanie Hartmann[1]†, Ulrike Stockert[1], Peijie Sun[1]†, Stefan Lausberg[1], Manuel Brando[1], Sven Friedemann[1]†, Cornelius Krellner[1]†, Christoph Geibel[1], Steffen Wirth[1], Stefan Kirchner[1,2], Elihu Abrahams[3], Qimiao Si[4] & Frank Steglich[1]

A quantum critical point (QCP) arises when a continuous transition between competing phases occurs at zero temperature. Collective excitations at magnetic QCPs give rise to metallic properties that strongly deviate from the expectations of Landau's Fermi-liquid description[1], which is the standard theory of electron correlations in metals. Central to this theory is the notion of quasiparticles, electronic excitations that possess the quantum numbers of the non-interacting electrons. Here we report measurements of thermal and electrical transport across the field-induced magnetic QCP in the heavy-fermion compound $YbRh_2Si_2$ (refs 2, 3). We show that the ratio of the thermal to electrical conductivities at the zero-temperature limit obeys the Wiedemann–Franz law for magnetic fields above the critical field at which the QCP is attained. This is also expected for magnetic fields below the critical field, where weak antiferromagnetic order and a Fermi-liquid phase form below 0.07 K (at zero field). At the critical field, however, the low-temperature electrical conductivity exceeds the thermal conductivity by about 10 per cent, suggestive of a non-Fermi-liquid ground state. This apparent violation of the Wiedemann–Franz law provides evidence for an unconventional type of QCP at which the fundamental concept of Landau quasiparticles no longer holds[4–6]. These results imply that Landau quasiparticles break up, and that the origin of this disintegration is inelastic scattering associated with electronic quantum critical fluctuations—these insights could be relevant to understanding other deviations from Fermi-liquid behaviour frequently observed in various classes of correlated materials.

In metallic systems, continuously suppressing magnetic order gives rise to a QCP[7] and leads to non-Fermi-liquid behaviour[2,8–11]. Whether quasiparticles persist near the QCP, however, is a fundamental open issue. An established means to probe the fate of the quasiparticles is to compare the thermal conductivity (κ) and the electrical conductivity (σ). If quasiparticles are well defined, the Wiedemann–Franz law specifies the zero-temperature ($T = 0$) value of the Lorenz number $L \equiv \kappa/T\sigma$ to be $L_0 = (\pi k_B)^2/3e^2$, where k_B is Boltzmann's constant and e is the charge of an electron. Except for superconductors[12], where the Lorenz ratio $L/L_0 = 0$, a violation of the Wiedemann–Franz law would constitute direct evidence for physics beyond the Fermi-liquid theory. L/L_0 becomes larger than one if there are additional carriers which contribute to the heat current but not to the charge current[13]. By contrast, $L/L_0 < 1$ at $T = 0$ implies a breakdown of Landau quasiparticles.

Heavy-fermion metals are prototype systems for antiferromagnetic QCPs. These rare-earth or actinide-based intermetallics contain both f-derived localized magnetic moments and itinerant (spd) conduction electrons, whose entanglement gives rise to the Kondo effect and the concomitant composite quasiparticles with huge effective mass. In these materials, two types of QCPs have been highlighted. The conventional spin-density-wave type relies on the fluctuations of the antiferromagnetic order parameter[14–16]. Here, the main part of the Fermi surface remains unaffected by the critical fluctuations, leaving the quasiparticles intact. In a related picture[17], all states near the Fermi surface are influenced by quantum critical fluctuations. At an unconventional type of QCP, a breakdown of the Kondo entanglement disintegrates all the heavy quasiparticles[4–6]. Neutron scattering and magnetic measurements[18] in $CeCu_{6-x}Au_x$, as well as de Haas-van Alphen[19] and thermodynamic and transport[20] measurements in $CeRhIn_5$, have been interpreted in terms of a local Kondo-breakdown QCP[4,5]. In $YbRh_2Si_2$, the weak antiferromagnetic order is continuously suppressed by a tiny magnetic field[2,3,21]. Electrical transport and thermodynamic measurements have revealed multiple vanishing energy scales[22] and a discontinuity of the Fermi surface across the QCP[23,24]. These materials provide a setting to characterize the quasiparticles near the antiferromagnetic QCP.

We focus on $YbRh_2Si_2$, in order to take advantage of the understanding of its Fermi surface[23,24]. Figure 1 displays the overall temperature–magnetic field (T–B) phase diagram (Fig. 1a) and the thermal conductivity below 12 K (Fig. 1b). At $B = 0$, the compound orders antiferromagnetically at the Néel temperature $T_N = 0.07$ K. Increasing B to its critical value $B_c \approx 0.06$ T (with B perpendicular to the c axis, $\perp c$) continuously suppresses T_N to zero, reaching the QCP. Below T_{FL} the paramagnetic phase at $B > B_c$ is a heavy Fermi liquid[3], in which the Fermi surface is large as a result of the Kondo effect. However, in the antiferromagnetic phase ($B < B_c$), also a mass-enhanced Fermi liquid[3], the Fermi surface is small, without incorporating the f electrons[23,24]. The $T^*(B)$ line defines a crossover of the Fermi surface as a function of the control parameter B, and terminates at $B = B_c$ as $T \to 0$. On cooling, the field range of quantum critical behaviour shrinks to $B = B_c$ in the $T = 0$ limit, whereas a Fermi-liquid ground state exists on either side of the QCP. The QCP is clearly identified by an asymptotic ($T \to 0$) linear temperature dependence of the electrical resistivity, independent of sample quality[21,22]. In addition, the width of the T^* crossover is proportional to T, extrapolating to a sharp jump of the Fermi surface at $T = 0$ (ref. 24). Although these measurements prove the existence of two different states on either side of the QCP, they leave open the nature of not only the electronic excitations in the quantum critical regime but also the dynamical processes underlying the Kondo breakdown.

A previous study of the thermal and electrical transport in the quasi-two-dimensional heavy-fermion metal $CeCoIn_5$ (ref. 25), in which a magnetic QCP is suspected[26] but not identified, found that the Wiedemann–Franz law is violated ($L/L_0 \approx 0.8$ as $T \to 0$) for c-axis transport but obeyed for in-plane transport. These results were discussed in terms of putative strongly anisotropic critical fluctuations, although how spin fluctuations may invalidate the Wiedemann–Franz law was left as an open question. Combined thermal and electrical transport has also been studied near the QCP of $ZrZn_2$, which is considered a canonical ferromagnetic-spin-fluctuation system[27].
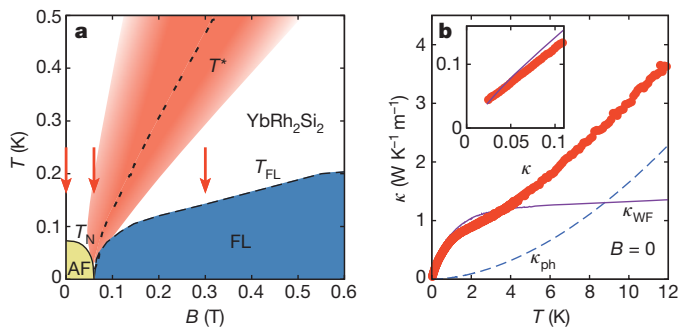
Figure 1 | Phase diagram and thermal conductivity of YbRh$_2$Si$_2$.
a, Temperature–magnetic field (T–B) phase diagram, indicating the
antiferromagnetic phase (AF) boundary (T_N, solid line) and the crossovers
between non-Fermi-liquid and Fermi-liquid (FL) regimes (T_{FL}, dashed line) as
well as between small and large Fermi surfaces (T^*, double-dashed line). The
crossover width at T^* is proportional to temperature (red shaded region) (from
ref. 24). The magnetic field, B, was applied within the basal tetragonal, easy
magnetic plane, $\perp c$. Arrows indicate fields at which combined thermal and
electrical transport measurements were performed (Fig. 2a–c). The
Wiedemann–Franz law is strictly defined only in the $T = 0$ limit and is expected
to describe the electronic transport of a Fermi liquid. This is illustrated in the
low-T transport properties of the field-induced paramagnetic phase, $B > B_c$
(Fig. 2c, d). It is also expected in the antiferromagnetic phase, $B < B_c$: here, at
finite temperature the electronic thermal conductivity, κ_{el}, is masked by a
contribution due to magnons, κ_m (see text). However, as $T \to 0$, κ_m vanishes
such that the heat transport is purely electronic, and the Wiedemann–Franz law
is valid. **b**, Thermal conductivity, κ, as a function of temperature, T, at zero
field (red data points). The solid purple line displaying $\kappa_{WF}(T) = L_0 T/\rho(T)$ was
obtained under the assumption of the Wiedemann–Franz law to hold in the
whole range of temperatures $T \le 12$ K; here, $\rho(T)$ is the electrical resistivity and
$L_0 = (\pi k_B)^2/3e^2$ is Sommerfeld's constant. The dashed blue line shows the
phonon contribution $\kappa_{ph}(T)$, as discussed in the Supplementary Information.
Inset, same data below $T = 0.1$ K.

Although the two transport quantities in ZrZn$_2$ have different tem-
perature dependencies, with $L/L_0 < 1$, their extrapolated $T = 0$ limits
satisfy the Wiedemann–Franz law.

YbRh$_2$Si$_2$ provides a unique opportunity to study the fate of Landau
quasiparticles at QCPs beyond the spin-fluctuation description and,
likewise, the nature of the critical fluctuations associated with the
Kondo breakdown. The compound is also advantageous because
superconductivity is absent down to at least 0.01 K (ref. 21), unlike
the case of CeCoIn$_5$. This not only exposes the properties in the imme-
diate vicinity of the antiferromagnetic QCP but also facilitates the
characterization of the quasiparticles through the Lorenz ratio.
YbRh$_2$Si$_2$ is a magnetically anisotropic metal; the possibility of
quasi-two-dimensional transport necessitates the use of in-plane
transport to probe any quasiparticle breakdown[28]. The present study
therefore focuses on the thermal and electrical transport within the
tetragonal plane.

The thermal conductivity $\kappa(T)$ was measured between 0.025 K and
12 K and is shown in Fig. 1b for $B = 0$. For comparison, the electronic
thermal conductivity calculated from the measured electrical resistivity
$\rho(T)$ through the Wiedemann–Franz law, $\kappa_{WF}(T) \equiv L_0 T/\rho(T)$, is also
presented. Above 4 K, $\kappa(T)$ exceeds $\kappa_{WF}(T)$ due to the contribution of
phonons to the heat transport, $\kappa_{ph}(T)$ (see Supplementary
Information). Below 4 K, $\kappa_{ph}(T)$ is suppressed, and $\kappa(T)$ becomes
smaller than $\kappa_{WF}(T)$ down to about 0.035 K and somewhat larger at
even lower temperatures (inset to Fig. 1b).

In order to investigate the Wiedemann–Franz law, we extrapolate
the Lorenz ratio $L(T)/L_0 \equiv \rho(T)/w(T)$ to $T = 0$ (here $w(T)$ is the ther-
mal resistivity). Because a QCP is a singular point in the phase dia-
gram, and given that there are temperature scales that vary as a
function of the control parameter and vanish at the QCP, the com-
bination of isofield and isothermal scans is crucial for the extrapolation
(Supplementary Information section VI).

Figure 2 depicts the low-temperature behaviour of both the elec-
trical resistivity $\rho(T)$ and thermal resistivity $w(T) = L_0 T/\kappa(T)$ at zero
field, $B = 0.06$ T $\approx B_c$ and $B > B_c$. Here $w(T)$ has the same unit as $\rho(T)$.
Similar results at other magnetic fields are given in Supplementary Fig. 4.
This comparison shows that $w(T)$ exceeds $\rho(T)$ over a wide range of
temperature and field. Figures 3a, b and c, d display, respectively, the
difference $w(T) - \rho(T)$ and the Lorenz ratio for the data shown in
Fig. 2a–d. Corresponding plots for the data shown in Supplementary
Fig. 4 are presented in Supplementary Fig. 5a–d.

Below $T = 0.15$ K, at $B \gtrsim 0.6$ T, $w(T) = \rho(T)$ within the experi-
mental resolution. This is illustrated for $B = 1$ T in Fig. 3b, which
shows that $w(T) - \rho(T)$ approaches zero in this range of T and B,
and in Fig. 3d, which demonstrates that $L(T)/L_0 = 1$ within the experi-
mental error. In this high-field range, both $\Delta\rho(T) = [\rho(T) - \rho_0] \propto T^2$
and $[w(T) - w_0] \propto T^2$ below the Fermi-liquid crossover temperature,
marked by arrows in Fig. 2 and Supplementary Fig. 4. Here, ρ_0 and w_0
are the residual ($T \to 0$) electrical and thermal resistivities, which are
identical within about 1%. These results establish the validity of the
Wiedemann–Franz law in the Fermi-liquid phase for $B \gtrsim 0.6$ T. For
0.2 T $\le B \le 0.6$ T, the results shown in Fig. 2c and Supplementary Fig.
4d–f suggest similar Fermi-liquid behaviour at lower temperatures.

The system is in the quantum critical regime[21] at $B = 0$ and $T \gtrsim$
0.1 K, where $w(T) > \rho(T)$. Both $\rho(T)$ and $w(T)$ decrease linearly with
temperature below about 0.3 K which allows extrapolation of the
quantum critical behaviour of $\rho(T)$ and $w(T)$ to the $T = 0$ limit, giving
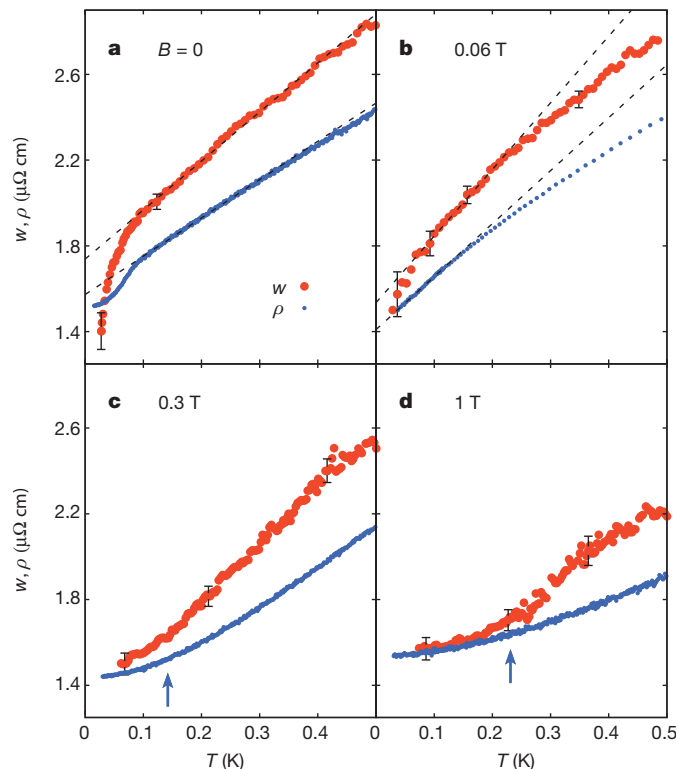
Figure 2 | Thermal and electrical resistivity curves at low temperatures.
a–d, Thermal resistivity $w(T) = L_0 T/\kappa(T)$ (red filled circles) and electrical
resistivity $\rho(T)$ (blue dots) below $T = 0.5$ K for $B = 0$ (**a**), $B = 0.06$ T
(**b**), $B = 0.3$ T (**c**) and $B = 1$ T (**d**), $B \perp c$. Arrows in **c** and **d** indicate the
crossover to Fermi-liquid behaviour (from Fig. 1a). Because T_N is very low
(0.07 K), it is an experimental challenge to elucidate the intrinsic behaviour of
the thermal transport in the antiferromagnetic regime. We have therefore made
special efforts to not only extend the heat-transport measurements at $B = 0$
down to temperatures as low as 0.025 K, but also to reduce the statistical error of
the data by performing substantially more temperature scans than at finite
fields. The extrapolation specified by the dashed lines in **a** and **b** corresponds to
the trajectory C$_1$ and one close to C, respectively (see Supplementary Fig. 8a).
Representative error bars (s.d.) are shown for a few selected temperatures.

Figure 3 | Violation and validity of the Wiedemann–Franz law at $B \approx B_c$ and $B > B_c$, respectively. a, b, Difference $(w - \rho)$ versus T at B values (in T) of 0 and 0.06 (**a**) and 0.3 and 1 (**b**). **c, d,** Lorenz ratio $L/L_0 = \rho/w$ versus T for the same fields as in **a**, **b**. Within the experimental uncertainty, validity of the Wiedemann–Franz law is found below $T \approx 0.15$ K for $B = 1$ T and is anticipated at lower temperature for $B \gtrsim 0.3$ T (**b**, **d**). Dashed lines in **a**, **c** indicate T-linear behaviour of both $w(T)$ and $\rho(T)$ in the paramagnetic non-Fermi-liquid regime. For $B = 0$, the onset of the deviation from quantum critical behaviour (dashed lines in **a** and **c**) seems to occur at about 0.07 K, almost exactly where the corresponding feature becomes visible at $B = 0.06$ T, too. This is in striking contrast to Fig. 2a, showing that the deviation in the $w(T)$ data for $B = 0$ has set in already at $T \approx 0.1$ K. The reason for this seeming discrepancy lies in the pronounced drop of the electrical resistivity at $T_N = 0.07$ K (Fig. 2a). The extrapolation of the dashed lines in **a** and **c** to $T = 0$ demonstrates a violation of the Wiedemann–Franz law in a putative paramagnetic, non-Fermi-liquid ground state. This ground state is realized[22] exactly at the critical magnetic field B_c, compare Fig. 1a. Error bars are derived from the standard deviation of the data in Fig. 2. **e,** Evolution of a shallow minimum in the isothermal (0.1 K $\leq T \leq$ 0.4 K) $L(B)/L_0$ dependence. Data at lower T are not included because of the additional magnon heat transport at $B < B_c$ which will vanish as $T \to 0$. These minima are related to the $T^*(B)$ line of Fig. 1a, as indicated by the crossover fields (arrows) and widths (horizontal bars). Above $B^*(T) = B(T^*)$, L/L_0 values are consistent with L_{el}/L_0 values in Supplementary Fig. 10, implying in the $T = 0$ limit $L/L_0 = 1$ at $B \neq B_c$ and an abrupt dip at $B = B_c$. Error bars as in **c** and **d**.

Supplementary Information we demonstrate that the additional thermal conductivity is due to antiferromagnetic magnons; this magnon contribution will vanish in the $T = 0$ limit, as is inferred from the specific-heat data[21] measured down to 0.018 K (Supplementary Information). Therefore, at $B = 0$ the Wiedemann–Franz law is expected to hold in the $T = 0$ limit.

At $B = 0.06$ T $\approx B_c$, $\rho(T)$ is linear below 0.12 K down to the lowest measured temperature, as is $w(T)$ below about 0.2 K (Fig. 2b). At $T \approx 0.07$ K, $w(T)$ shows a downturn which is similar to, though considerably weaker than, that at $B = 0$ which sets in at higher temperature (Fig. 2a). We interpret this feature as the contribution of overdamped magnons in the paramagnetic regime close to the QCP (Supplementary Information); as in the case of $B = 0$, this magnetic contribution is expected to vanish in the $T = 0$ limit. Extrapolating the linear-in-T electrical resistivity and the electronic thermal resistivity, which is also linear in T between 0.07 and 0.2 K, to $T = 0$ we find $(w_0 - \rho_0) > 0$ and $L(T \to 0)/L_0 < 1$, similar to the behaviour at $B = 0$ (Fig. 3a, c). Here, our extrapolation is taken near path C (Supplementary Fig. 8a).

These results provide an overall picture that can be placed in the context of the phase diagram of Fig. 1a. For fields sufficiently above the critical field B_c, the Wiedemann–Franz law is obeyed at low temperatures. At the same time, the data at $B = 0$ can be interpreted as validating the Wiedemann–Franz law in the $T = 0$ limit, that is, in the antiferromagnetic ground state. The validity of the Wiedemann–Franz law at magnetic fields away from B_c and for sufficiently low temperatures is consistent with a field-induced continuous quantum phase transition between two Fermi liquids with, respectively, small and large Fermi surfaces, which has been inferred from magnetotransport and thermodynamic measurements[22–24]. In contrast, the data in the paramagnetic quantum critical regime are extrapolated to a $T = 0$ limit that violates the Wiedemann–Franz law.

The isothermal field dependence, $L(B)/L_0$, further clarifies these results. This is given in Fig. 3e, which shows a shallow minimum near a field that tracks the $T^*(B)$ line in Fig. 1a. The minimum narrows as temperature is reduced and extrapolates, as $T \to 0$, to an abrupt dip at $B = B_c$ (Supplementary Information); the extrapolated $T = 0$ value at that point is about 0.9 (compare Fig. 3c). The systematic evolution of L/L_0 versus B and T provides evidence for the intrinsic nature of the apparent violation of the Wiedemann–Franz law in YbRh$_2$Si$_2$.

Our findings shed considerable new light on the dynamical electronic processes occurring at the QCP. Quasiparticles disintegrate at a

$w_0 > \rho_0$. This is shown in Fig. 3a (upper dashed line) for $w(T) - \rho(T)$, which is about 0.17 $\mu\Omega$ cm at $T = 0$, and in Fig. 3c for $L(T)/L_0$, where the corresponding extrapolation (lower dashed line) yields about 0.9. Our extrapolation follows path C_1, shown in Supplementary Fig. 8a.

On cooling in zero field, $\rho(T)$ drops at the Néel transition[3] into the antiferromagnetic phase, reflecting the freezing-out of spin-disorder scattering. Below T_N, $\rho(T)$ exhibits a Fermi-liquid T^2 dependence[3]. We also observe a drop in $w(T)$ starting at $T \approx 0.1$ K (Fig. 2a). Furthermore, we find that $w(T) - \rho(T)$ below $T = 0.033$ K becomes negative (Fig. 3a), and L/L_0 exceeds one (Fig. 3c). An upturn of $L(T)/L_0$ just below T_N was also observed in ref. 29 down to 0.05 K, where $L(T)/L_0$ is still below one but appears to extrapolate to one as $T \to 0$. Our observation of $L(T)/L_0 > 1$ below $T = 0.033$ K clearly shows that the thermal transport is not entirely due to electronic-quasiparticle transport, as concluded in ref. 29. Instead, the Fermi-liquid-type electronic transport is masked by that of an additional heat channel. In the

Kondo-breakdown QCP, as illustrated in Fig. 4. The large Fermi surface incorporates both the conduction electrons and delocalized f electrons, whereas the small Fermi surface involves only the conduction electrons. Because the quantum phase transition is continuous, this change of the Fermi surface must result from inelastic processes that operate near the QCP. Such dynamical processes must be electronic, extending to zero energy when the system is precisely at the QCP. Correspondingly, the quasiparticle residue of the large Fermi surface, Z_L, and that of the small Fermi surface, Z_S, must reach zero as the QCP is approached from the paramagnetic and antiferromagnetic sides, respectively. At the critical value of the control parameter, their values respectively at the large Fermi wavevector ($\mathbf{k}_F^L$) and the small one ($\mathbf{k}_F^S$) satisfy dynamical scaling:

$$Z_L\left(\mathbf{k}_F^L, T, \omega\right) = T^\alpha \varphi_L(\omega/T)$$
$$Z_S\left(\mathbf{k}_F^S, T, \omega\right) = T^\beta \varphi_S(\omega/T)$$

(1)

Here, ω is the frequency, α and β are scaling exponents, and φ_L and φ_S are scaling functions. These scaling forms of Z_L and Z_S capture the physics of the critical Kondo breakdown. This breakdown arises from the dynamical competition between RKKY (Ruderman–Kittel–Kasuya–Yosida) and Kondo interactions which, respectively, promote small and large Fermi surfaces. The resulting critical fluctuations between the small and large Fermi surfaces amount to quantum critical inelastic scatterings for the electronic heat carriers, which lead to $L/L_0 < 1$ in the quantum-critical region. The vanishing quasiparticle weights, Z_L and Z_S, imply that such quantum fluctuations and the concomitant fluctuating Fermi surfaces persist at the QCP, thereby making it natural for $L/L_0 < 1$ even in the $T = 0$ limit. In this way, our observation provides evidence for electronic quantum critical fluctuations which are naturally associated with the abrupt reconstruction of the Fermi surface.

Our study is to be contrasted with those that feature extra charge-neutral fermionic heat carriers. For example, over the intermediate temperature range that corresponds to the quasi-one-dimensional case of the 'purple bronze' $Li_{0.9}Mo_6O_{17}$, one expects spin–charge separation. The chargeless spinons, which contribute to the heat conductivity, should give rise to $L/L_0 > 1$, and this is indeed observed[13]. In our case, the non-Fermi-liquid excitations carry both charge and heat

currents and are subject to inelastic scatterings from quantum critical electronic fluctuations. As discussed in Supplementary Information section VI, this leads to a Lorenz ratio of less than one. Because it reflects the different degrees to which normal (that is, non-Umklapp) processes contribute to the electrical and heat resistivities, the deviation in this case is expected to be more modest; this is consistent with the 10% effect observed here.

Our results indicate that a breakdown of Landau quasiparticles accompanies the vanishing of a quantum critical energy scale, $T^*(B)$, in $YbRh_2Si_2$. This linkage between the emergence of non-Fermi-liquid excitations and vanishing of energy scales provides a tantalizing connection between quantum critical heavy-fermion metals and the high-T_c copper oxides near optimal doping, where the pseudogap energy scale collapses and Fermi-liquid quasiparticles are destroyed over the entire Fermi surface[30].

METHODS SUMMARY

The samples used in this work belong to the same batch and have been well characterized previously[3,21]. Thermal and electrical transport coefficients were obtained from the same rectangular ($4.2 \times 0.5 \times 0.1\,mm^3$) single crystal (sample 1) with the same contact geometry. This allows a reliable determination of the Lorenz ratio $L(T)/L_0 = \rho(T)/w(T)$, since the geometry factor l/A cancels out, where l and A are the length and the cross-section of the sample, respectively (see Supplementary Information). Additional measurements of the electrical resistivity were performed on a second single crystal from the same batch, but with a different geometry factor (sample 2). As described in Supplementary Information, the measured resistivity values could perfectly be rescaled by a factor 1.25 ± 0.03 and corrected by a difference in residual resistivity of $0.22\,\mu\Omega\,cm$. Heat and charge currents as well as the magnetic field were applied within the basal tetragonal plane. However, we did not consider the distinction between the [100] and the [110] directions within the basal plane. The parallel orientation of the magnetic field, supplied by a superconducting solenoid, to the heat and charge flow allows us to neglect the contributions of transverse effects (Nernst and electrical/thermal Hall effects) in all measurements.

1. Landau, L. D. The theory of a Fermi liquid. *Sov. Phys. JETP* **6,** 920–925 (1957).
2. Trovarelli, O. *et al.* YbRh$_2$Si$_2$: pronounced non-Fermi-liquid effects above a low-lying magnetic phase transition. *Phys. Rev. Lett.* **85,** 626–629 (2000).
3. Gegenwart, P. *et al.* Magnetic-field induced quantum critical point in YbRh$_2$Si$_2$. *Phys. Rev. Lett.* **89,** 056402 (2002).
4. Si, Q., Rabello, S., Ingersent, K. & Smith, J. L. Locally critical quantum phase transitions in strongly correlated metals. *Nature* **413,** 804–808 (2001).
5. Coleman, P., Pépin, C., Si, Q. & Ramazashvili, R. How do Fermi liquids get heavy and die? *J. Phys. Condens. Matter* **13,** R723–R738 (2001).
6. Senthil, T., Vojta, M. & Sachdev, S. Weak magnetism and non-Fermi liquids near heavy-fermion critical points. *Phys. Rev. B* **69,** 035111 (2004).
7. Schofield, A. J. Quantum criticality and novel phases: summary and outlook. *Phys. Status Solidi B* **247,** 563–569 (2010).
8. Löhneysen, H. V. *et al.* Non-Fermi-liquid behavior in a heavy-fermion alloy at a magnetic instability. *Phys. Rev. Lett.* **72,** 3262–3265 (1994).
9. Aronson, M. C. *et al.* Non-Fermi-liquid scaling of the magnetic response in UCu$_{5-x}$Pd$_x$ ($x = 1, 1.5$). *Phys. Rev. Lett.* **75,** 725–728 (1995).
10. Mathur, N. D. *et al.* Magnetically mediated superconductivity in heavy fermion compounds. *Nature* **394,** 39–43 (1998).
11. Grigera, S. A. *et al.* Magnetic field-tuned quantum criticality in the metallic ruthenate Sr$_3$Ru$_2$O$_7$. *Science* **294,** 329–332 (2001).
12. Einstein, A. Theoretical remark on the superconductivity of metals. http://arxiv.org/abs/physics/0510251; translated from *Gedenkboek aangeb. aan H. Kamerlingh Onnes* (Leiden, 1922).
13. Wakeham, N. *et al.* Gross violation of the Wiedemann-Franz law in a quasi-one-dimensional conductor. *Nature Commun.* **2,** 396, doi:10.1038/ncomms1406 (2011).
14. Hertz, J. A. Quantum critical phenomena. *Phys. Rev. B* **14,** 1165–1184 (1976).
15. Moriya, T. *Spin Fluctuations in Itinerant Electron Magnetism* (Springer, 1985).
16. Millis, A. J. Effect of a nonzero temperature on quantum critical points in itinerant fermion systems. *Phys. Rev. B* **48,** 7183–7196 (1993).
17. Wölfle, P. & Abrahams, E. Quasiparticles beyond the Fermi liquid and heavy fermion criticality. *Phys. Rev. B* **84,** 041101(R) (2011).
18. Schröder, A. *et al.* Onset of antiferromagnetism in heavy-fermion metals. *Nature* **407,** 351–355 (2000).
19. Shishido, H., Settai, R., Harima, H. & Ōnuki, Y. A change of the Fermi surface at a critical pressure in CeRhIn$_5$: dHvA study under pressure. *J. Phys. Soc. Jpn* **74,** 1103–1106 (2005).
20. Park, T. *et al.* Hidden magnetism and quantum criticality in the heavy fermion superconductor CeRhIn$_5$. *Nature* **440,** 65–68 (2006).
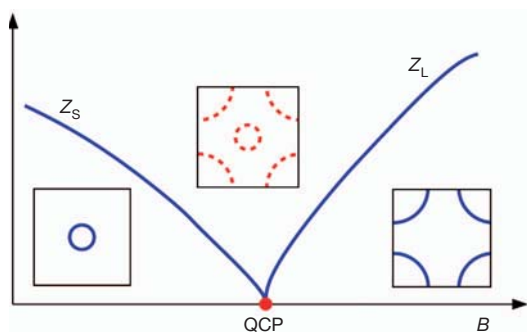
Figure 4 | The evolution of the quasiparticle weights across a Kondo-breakdown quantum critical point. The main panel displays Z_L, the quasiparticle residue at the generic part (away from the 'hot spots', that is, the momenta that are connected by the antiferromagnetic ordering wavevector) of the large Fermi surface and Z_S, the corresponding quasiparticle residue of the small Fermi surface, as a function of the control parameter magnetic field, B. They are non-zero on the two sides of the QCP, but each one approaches zero as the QCP is approached from the respective side. Illustrated in the right and left insets are the large and small Fermi surfaces, which are denoted by the solid blue lines in the Fermi-liquid regimes on the two sides of the QCP. Also illustrated, in the top inset, are the fluctuating small and large Fermi surfaces (dashed red lines) in the quantum critical regime. The actual Fermi surfaces in both cases are multi-sheeted, and can be located in the first Brillouin zone in a more complex way.

21. Custers, J. *et al.* The break-up of heavy electrons at a quantum critical point. *Nature* **424,** 524–527 (2003).
22. Gegenwart, P., Si, Q. & Steglich, F. Quantum criticality in heavy-fermion metals. *Nature Phys.* **4,** 186–197 (2008).
23. Paschen, S. *et al.* Hall effect evolution at a heavy fermion quantum critical point. *Nature* **432,** 881–885 (2004).
24. Friedemann, S. *et al.* Fermi-surface collapse and dynamical scaling near a quantum critical point. *Proc. Natl Acad. Sci. USA* **107,** 14547–14551 (2010).
25. Tanatar, M. A., Paglione, J., Petrovic, C. & Taillefer, L. Anisotropic violation of the Wiedemann-Franz law at a quantum critical point. *Science* **316,** 1320–1322 (2007).
26. Zaum, S. *et al.* Towards the identification of a quantum critical line in the (p, B) phase diagram of $CeCoIn_5$ with thermal-expansion measurements. *Phys. Rev. Lett.* **106,** 087003 (2011).
27. Smith, R. P. *et al.* Marginal breakdown of the Fermi-liquid state on the border of metallic ferromagnetism. *Nature* **455,** 1220–1223 (2008).
28. Smith, M. F. & McKenzie, R. H. Apparent violation of the Wiedemann-Franz law near a magnetic field tuned metal-antiferromagnetic quantum critical point. *Phys. Rev. Lett.* **101,** 266403 (2008).
29. Tomokuni, K. *et al.* Thermal transport properties and quantum criticality of heavy fermion $YbRh_2Si_2$. *J. Phys. Soc. Jpn* **80,** SA096 (2011).
30. Casey, P. A., Koralek, J. D., Plumb, N. C., Dessau, D. S. & Anderson, P. W. Accurate theoretical fits to laser-excited photoemission spectra in the normal phase of high-temperature superconductors. *Nature Phys.* **4,** 210–212 (2008).

LETTER

Deposition of 1.88-billion-year-old iron formations as a consequence of rapid crustal growth

Birger Rasmussen[1], Ian R. Fletcher[1], Andrey Bekker[2], Janet R. Muhling[3], Courtney J. Gregory[1] & Alan M. Thorne[4]

Iron formations are chemical sedimentary rocks comprising layers of iron-rich and silica-rich minerals whose deposition requires anoxic and iron-rich (ferruginous) sea water. Their demise after the rise in atmospheric oxygen by 2.32 billion years (Gyr) ago[1] has been attributed to the removal of dissolved iron through progressive oxidation[2] or sulphidation[3,4] of the deep ocean. Therefore, a sudden return of voluminous iron formations nearly 500 million years later poses an apparent conundrum[3,5]. Most late Palaeoproterozoic iron formations are about 1.88 Gyr old[6–8] and occur in the Superior region of North America[5,9,10]. Major iron formations are also preserved in Australia, but these were apparently deposited[11] after the transition to a sulphidic ocean at 1.84 Gyr ago that should have terminated iron formation deposition[4], implying that they reflect local marine conditions[5,12]. Here we date zircons in tuff layers to show that iron formations in the Frere Formation of Western Australia are about 1.88 Gyr old, indicating that the deposition of iron formations from two disparate cratons was coeval and probably reflects global ocean chemistry. The sudden reappearance of major iron formations at 1.88 Gyr ago—contemporaneous with peaks in global mafic–ultramafic magmatism[13,14], juvenile continental and oceanic crust formation[15,16], mantle depletion[17,18] and volcanogenic massive sulphide formation[5,19]—suggests deposition of iron formations as a consequence of major mantle activity and rapid crustal growth[5,10,15,20]. Our findings support the idea that enhanced submarine volcanism and hydrothermal activity linked to a peak in mantle melting released large volumes of ferrous iron and other reductants that overwhelmed the sulphate and oxygen reservoirs of the ocean, decoupling atmospheric and seawater redox states, and causing the return of widespread ferruginous conditions. Iron formations formed on clastic-starved coastal shelves where dissolved iron upwelled and mixed with oxygenated surface water. The disappearance of iron formations after this event may reflect waning mafic–ultramafic magmatism and a diminished flux of hydrothermal iron relative to seawater oxidants.

Iron formations are chemical sedimentary rocks whose deposition requires an anoxic water column to transport ferrous iron to sites of iron precipitation. Their formation was episodic and broadly coeval with, and in some cases possibly linked to, periods of mantle plume activity as recorded by peaks in mafic and ultramafic igneous activity[5,10]. The largest accumulations of iron formation were deposited between 2.7 and 2.45 Gyr ago[5,10], before the rise of atmospheric oxygen by 2.32 Gyr ago[1]. The decline of iron formations after 2.45 Gyr ago is interpreted to reflect the removal of ferrous iron by progressive oxidation of the deep ocean[2] or, alternatively, by the precipitation of iron sulphides due to enhanced riverine sulphate delivery to the oceans after the rise of atmospheric oxygen[3,4]. Important exceptions are late Palaeoproterozoic iron formations from the Superior craton of North America and the Frere Formation of the Earaheedy Group, Western Australia[5,9,10] (Fig. 1). These late Palaeoproterozoic iron formations comprise very thick and extensive sequences of granular iron formation

that were deposited in shallow coastal environments close to the storm and fair-weather wave base[5]. Banded iron formations are also present and indicate deposition in deeper water settings. The rare-earth element chemistry of these iron formations indicates a significant hydrothermal input[11,21] and the existence of a redox-stratified ocean during their deposition[22].

Iron formations in North America were deposited at 1.88 Gyr ago[6–8] and can be traced for about 3,000 km along the Superior craton (Fig. 1). The age of the granular iron formation of the Frere Formation is poorly constrained, but is considered to be between 1.84–1.65 Gyr ago[11,23], coeval with the development of euxinic conditions in the global ocean linked to the demise of Superior-type iron formations[3,4]. If the deposition of the granular iron formations in Australia, which required ferruginous conditions, was synchronous with sulphidic conditions in North America, then the late Palaeoproterozoic iron formations may reflect the chemistry of local, restricted marine basins and therefore provide no information about the redox state of the global ocean[5,12].

To better constrain the age of the Australian granular iron formations, we sampled tuffaceous and volcaniclastic layers in the basal Frere Formation from a diamond drill-hole (TDH26) drilled on the southwestern margin of the Earaheedy basin, Western Australia (Fig. 1; Supplementary Fig. 1). The Frere Formation is a succession 600–1,200 m thick of granular iron formation, green shale and ferruginous siltstone with minor carbonate, chert and banded iron formation, which is bounded by carbonate units of the lower Earaheedy Group. The occurrence of oolitic and stromatolitic carbonates and the range of sedimentary structures indicate a shallow marine environment[11].

Three samples from the base of the Frere Formation (TDH26, 343.47–343.53 m; 374.45–374.55 m and 386.38–386.46 m) preserve thin tuff beds comprising angular fragments of volcanic quartz, euhedral zircon and monazite in a matrix of chlorite. Zircons extracted from the tuff layers were analysed by sensitive high-resolution ion microprobe (SHRIMP) using established techniques[24]. All zircon U–Pb data are given in Supplementary Tables 1, 2 and 3. Zircon crystals in the lower tuff bed, which occurs about a metre above the base of the Frere Formation, yielded a weighted mean $^{207}Pb/^{206}Pb$ age of $1,891 \pm 8$ million years (Myr) (mean square weighted deviation, MSWD = 1.5; $n = 28$) (see Supplementary Figs 5–8). Zircons in the middle tuff bed gave a $^{207}Pb/^{206}Pb$ age of $1,890 \pm 10$ Myr (MSWD = 1.3; $n = 15$) and zircons in the upper tuff gave $1,885 \pm 18$ Myr (MSWD = 1.1; $n = 9$) (see Supplementary Figs 9 and 10).

The zircons are interpreted to record the age of deposition synchronous with volcanism on the basis of their euhedral shape, igneous growth zoning and uniform size (mostly between 10 and 30 μm), and the presence of pyroclastic debris and angular slivers of quartz in the tuff beds. The 1.89-Gyr depositional age is consistent with the age of the youngest detrital zircons in the lower Earaheedy Group (about 2.0 Gyr ago)[11]. In view of our new age constraints, previous interpretations for the maximum age of the Earaheedy Group (<1.84 Gyr

[1]Department of Applied Geology, Curtin University, Kent Street, Bentley, Western Australia 6102, Australia. [2]Department of Geological Sciences, University of Manitoba, Winnipeg, Manitoba R3T 2N2, Canada. [3]Centre for Microscopy, Characterisation and Analysis, The University of Western Australia, Crawley, Western Australia 6009, Australia. [4]Geological Survey of Western Australia, Department of Mines and Petroleum, Mineral House, 100 Plain Street, East Perth, Western Australia 6004, Australia.
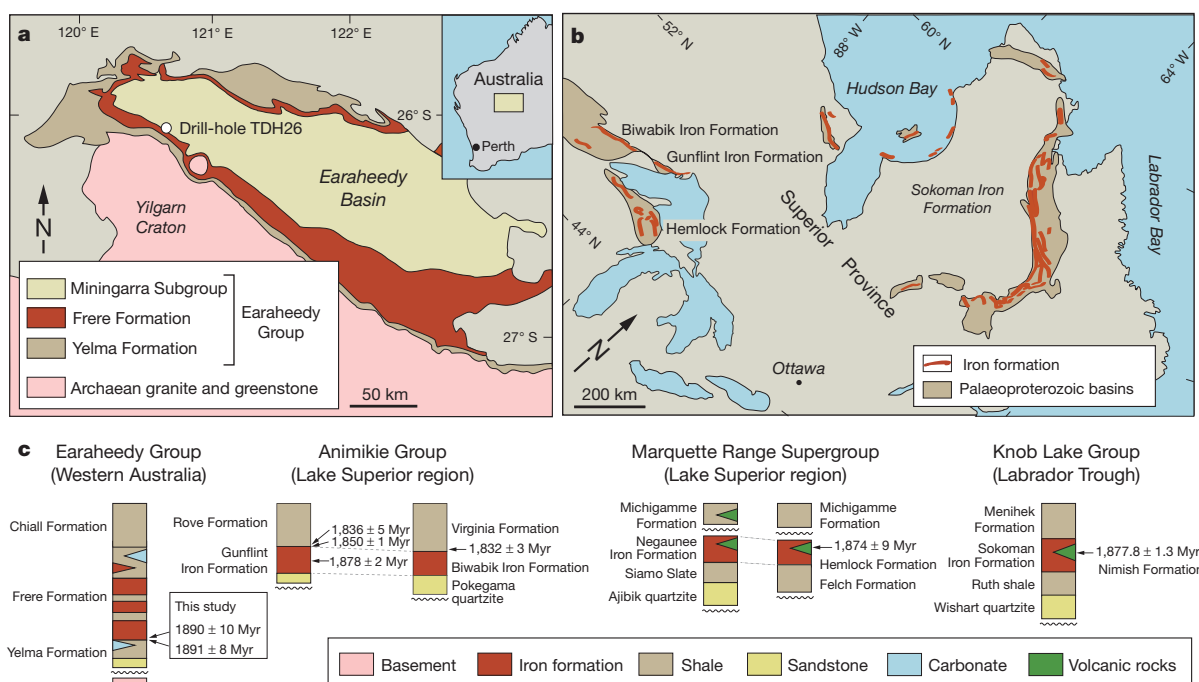
Figure 1 | Location and stratigraphy of late Palaeoproterozoic iron formations. Maps show the distribution of the main Late Palaeoproterozoic iron formations in Western Australia (**a**), and North America (**b**). **c**, Stratigraphic columns of successions containing Late Palaeoproterozoic iron formations and their age constraints (after refs 5–9, 11 and 30).

ago)[11,23] are invalid and the underlying Yerrida Group must be older than 1.89 Gyr ago.

The 1.89 Gyr age of the basal Frere Formation closely corresponds with the age of iron formations in the Superior craton (1.88 Gyr ago)[6–8]. Palaeomagnetic reconstructions suggest that Western Australia and North America were far apart at this time[14], supporting arguments that these iron formations were deposited on the margins of disparate cratons. Therefore, their deposition is likely to reflect the chemistry of the global ocean rather than restricted basin-scale conditions.

The deposition of vast volumes of iron formation on continental shelves indicates that the deep oceans were anoxic, non-sulphidic and rich in dissolved iron 1.88 Gyr ago. The sudden reappearance of these conditions after an interval of over 500 Myr is surprising because iron is inferred to have been progressively removed from the ocean after the rise in atmospheric oxygen between 2.47 and 2.32 Gyr ago[1–3]. After this time, the atmosphere–ocean system shifted to a new redox state where ocean chemistry was increasingly influenced by the high flux of oxygen and sulphate from surface environments and atmosphere. The return to ferruginous, Archaean-like conditions in the ocean was apparently not accompanied by a fall in atmospheric oxygen levels, at least not to levels before the Great Oxidation Event, as indicated by mass-independent fractionation of sulphur isotopes in sedimentary sulphides[1,25] (Fig. 2). This apparent decoupling of the redox state of the atmosphere and the deep ocean at 1.88 Gyr ago is thus problematic.

A possible explanation for the presence of voluminous iron formations at 1.88 Gyr ago is offered by their deposition during a period of intense igneous activity (Fig. 2a, c and d). For example, between 1.89 and 1.87 Gyr ago, extensive mafic and ultramafic magmatism occurred across the world, including the emplacement of dyke swarms and sills with mineralization of Ni, Cu and the platinum group elements, and locally, basaltic flows, in the Superior, Wyoming and Slave cratons in North America, the Dharwar and Bastar cratons in India, the Siberian craton, the Kaapvaal and Zimbabwe cratons in southern Africa, and Baltica[13,14]. The emplacement of numerous large igneous provinces at that time might reflect the activity of multiple mantle plumes (a super-plume event)[10,15,20].

The emplacement of multiple large igneous provinces at 1.88 Gyr ago corresponds with a major episode in continental and oceanic crustal growth recorded by emplacement ages of juvenile igneous rocks[15,20] (Fig. 2c) and the coupled Lu–Hf and O isotope composition of detrital zircons[16] (Fig. 2d). The peak 1.88 Gyr ago in juvenile crust formation is coeval with a major peak in mantle depletion ages, suggesting that new continental crust generation was linked with large-scale mantle melting[17,18]. The peak in crustal growth at that time also corresponds with supercontinent assembly.

The inferred geological consequences of this mantle superplume event include increased rates of seafloor spreading, the generation of seamounts and oceanic plateaus, enhanced ocean anoxia and marine transgressions[5,10,20]. Widespread mafic–ultramafic magmatism and enhanced oceanic crust production is also interpreted to enhance submarine volcanism and hydrothermal activity and the influx of vast volumes of metals and metalloids, including base metals and iron into the deep ocean[10,15,20,26]. There is strong evidence for widespread back-arc magmatism and hydrothermal activity at 1.88 Gyr ago, with a major peak in the formation of volcanogenic massive sulphide (VMS) deposits[5,19] (Fig. 2b). The metals for VMS deposits are released by hydrothermal leaching of volcanic rocks, whereas the sulphur in hydrothermal systems is derived from the reduction of seawater sulphate and leaching of mafic volcanic rocks.

The hydrothermal systems that generate VMS deposits also emit large volumes of dissolved iron into the deep ocean. Under anoxic, sulphidic (euxinic) conditions, as have been inferred to exist in global oceans after and possibly before 1.88 Gyr ago[3,4], hydrothermal iron would rapidly precipitate as iron sulphides. If the flux of sulphate was higher than that of dissolved iron, iron would have been titrated from the ocean[3,4]. However, the presence of vast accumulations of shallow-water granular iron formation at 1.88 Gyr ago indicates that dissolved iron accumulated in the deep ocean and periodically upwelled onto the coastal zones of continental shelves, where it was precipitated as iron-oxyhydroxide particles[22]. The large-scale transport of dissolved iron from the deep ocean to the shallow sea implies that most of the water column was ferruginous 1.88 Gyr ago.

Recent iron speciation data for Proterozoic shales suggest that the deep ocean was at a very low oxidation state with locally developed ferruginous and euxinic conditions, below oxygenated surface water[27] (Fig. 2h). Similarly, iron and sulphur data from the 1.88–1.83-Gyr-old
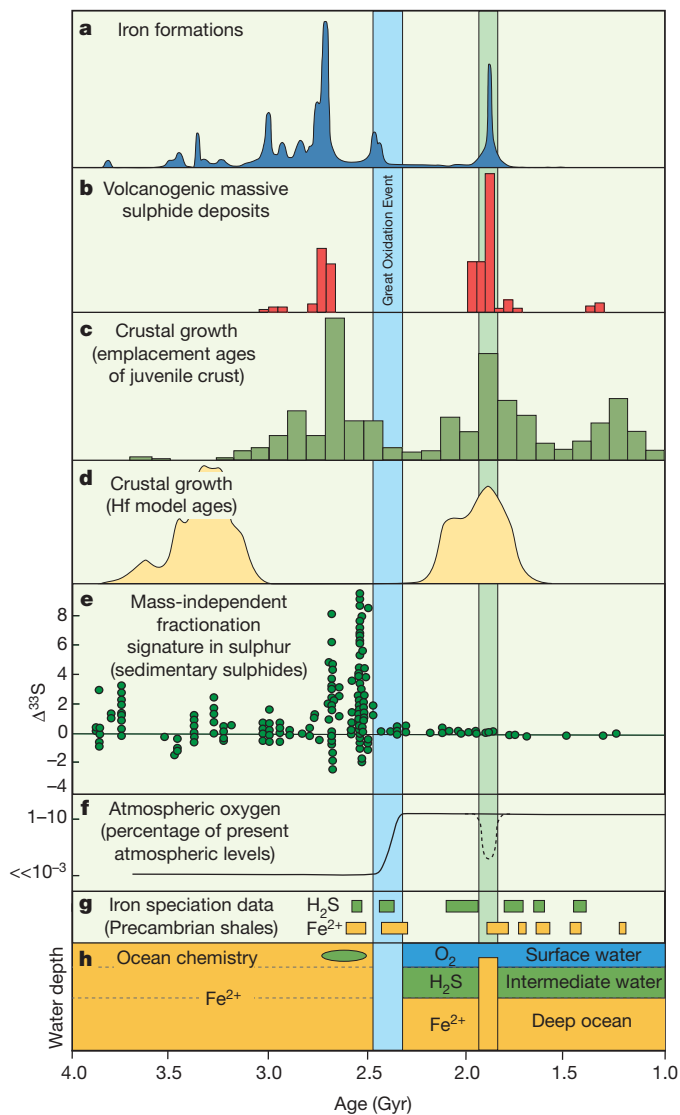
Figure 2 | Summary of the age distribution of iron formations, VMS deposits, juvenile crust and ocean chemistry for the Precambrian. a, Secular trend in the distribution of iron formations (after ref. 10). **b**, The distribution of VMS deposits over time (after ref. 5). **c**, Distribution of U–Pb zircon ages for juvenile crust (after ref. 15). **d**, Gaussian probability distribution of Hf model ages for zircons with low $\delta^{18}O$ values (after ref. 16). **e**, Plot of $\Delta^{33}S$ values versus sample age (after ref. 25). **f**, Summary of the atmospheric oxygen concentrations (after ref. 27). **g**, Iron speciation record of mudrocks indicating ferruginous and sulphidic conditions in the Proterozoic oceans (after ref. 27). **h**, A summary of the inferred ocean chemistry between 4.0 and 1.0 Gyr ago. After the Great Oxidation Event, the chemistry of the oceans shifted to a non-steady redox state controlled by fluctuating fluxes of oxygen, sulphate and iron, where the redox boundaries among oxic, sulphidic and ferruginous conditions were dynamic and moved vertically and laterally in response to variations in submarine hydrothermal fluxes and surface oxygenation.

Animikie basin in the Superior region of North America suggest that ferruginous conditions dominated during deposition of the 1.88-Gyr-old Gunflint Formation and that euxinic conditions subsequently developed at mid-depths along palaeoshorelines, where dissolved iron was removed from the water column, terminating the deposition of iron formations[28]. Although the development of an anoxic water column is required for the mobility of dissolved iron, the coexistence of locally developed euxinic conditions has been inferred to prevent the deposition of iron formations after about 1.88 Gyr ago[28].

We propose that the apparent transition to a ferruginous water column (including mid-depths) at 1.88 Gyr ago was triggered by the

emanation of vast volumes of ferrous iron and other reduced species (such as H_2, CH_4 and Mn^{2+}) during a short-lived period of intense submarine volcanism and hydrothermal activity. A peak in the accumulation of VMS deposits at 1.88 Gyr ago[5,19] shows that large volumes of hydrothermal iron were emitted and subsequently deposited as iron sulphides near vents, removing sulphur compounds from sea water. The concentration of seawater oxygen and sulphate at about 1.88 Gyr ago was significantly lower than that of today[3,4], so that the enhanced influx of reduced species delivered by hydrothermal plumes to the oceans may have overwhelmed both oxidants in sea water[29], greatly reducing the spatial extent of euxinic and oxygenated zones in the oceans.

Our findings provide a simple explanation for the apparent conundrum of the sudden reappearance of iron formations after the first major rise in atmospheric oxygen. Specifically, mantle-driven processes at about 1.88 Gyr ago not only acted as a source of dissolved iron, but also modified ocean chemistry and redox state by releasing a large flux of reductants that temporarily overwhelmed the supply of oxidants to the deep ocean from shallow waters and atmosphere. This led to the development of a largely ferruginous water column beneath an oxygenated surface zone (Fig. 2h). Iron-oxyhydroxides accumulated on the sea floor in shallow marine, coastal environments, where Fe^{2+} was oxidized in clastic-starved settings, forming extensive deposits of granular iron formation.

Although the chemistry of the deep ocean apparently returned to Archaean-like conditions at 1.88 Gyr ago, atmospheric oxygen apparently did not fall to pre-Great Oxidation Event levels (Fig. 2e, f). The decoupling between the redox state of the atmosphere and ocean may be explained by the release of reductants into the bottom of the ocean, where they were buffered by the seawater oxidants, largely restricting anoxia to the ocean. Our findings also provide a mechanism for the cessation of iron formation deposition. Rather than being a consequence of changing surface conditions, we propose that the demise of iron formations corresponds with the termination of this short-lived interval of global mantle-driven magmatism and crustal growth. After 1.88 Gyr ago, the deposition of iron formations was no longer favoured because the flux of oxidants from the atmosphere and surface ocean significantly exceeded the long-term rate of delivery of hydrothermal Fe and reductants to the deeper parts of the oceans. Major iron formations did not reappear until the late Neoproterozoic era, when 'snowball Earth' conditions radically changed the chemistry of the global ocean and once again favoured the deposition of iron formations.

METHODS SUMMARY

Three tuff beds were identified in the basal Frere Formation, Earaheedy Group, Western Australia, from drill-hole TDH26, at depths of 386.38–386.46 m, 374.45–374.55 m and 343.47–343.53 m (see Supplementary Fig. 1). Polished thin sections of the tuffs were examined using transmitted light and reflected light microscopy. Zircon crystals (typically between 10 and 30 μm in size) were identified using their characteristic optical properties: shape, straight extinction, oscillatory zoning, high refractive indices and high birefringence. Zircons that were sufficiently large for analysis by ion microprobe ($\geq$15 μm) were drilled out of polished thin sections in ~3-mm discs and set in conventional 25-mm epoxy resin mounts (see ref. 24). Chips of the zircon Pb/U reference standard (BR266) were cast in separate epoxy resin mounts. *In situ* U–Th–Pb analysis of zircon was carried out using a SHRIMP at the John de Laeter Centre for Isotope Research, Curtin University, Perth, Australia. All data were recorded in two 2-day analytical sessions. In the first session, the primary ion beam was ~0.5 nA on a ~15-μm spot and Pb/U external precision was 1.1% (n = 19). In the second session, the primary ion beam was ~0.3 nA on a ~12-μm spot and Pb/U external precision was 1.3% (n = 34). No corrections were required for instrumental mass fractionation of Pb isotopes. Following SHRIMP geochronology, zircon crystals were examined using a JEOL-6400 scanning electron microscope located in the Centre for Microscopy, Characterisation and Analysis at the University of Western Australia. Details of the sample description, SHRIMP analytical methods, SHRIMP data tables and data assessments are presented in the Supplementary Information.

1. Bekker, A. *et al.* Dating the rise of atmospheric oxygen. *Nature* **427,** 117–120 (2004).
2. Holland, H. D. *The Chemical Evolution of the Atmosphere and Oceans* (Princeton University Press, 1984).
3. Canfield, D. E. A new model for Proterozoic ocean chemistry. *Nature* **396,** 450–453 (1998).
4. Poulton, S. W., Fralick, P. W. & Canfield, D. E. The transition to a sulphidic ocean ~1.84 billion years ago. *Nature* **431,** 173–177 (2004).
5. Bekker, A. *et al.* Iron formation: the sedimentary product of a complex interplay among mantle, tectonic, oceanic, and biospheric processes. *Econ. Geol.* **105,** 467–508 (2010).
6. Findlay, J. M., Parrish, R. R., Birkett, T. C. & Watanabe, D. H. U-Pb ages from the Nimish Formation and Montagnais glomeroporphyritic gabbro of the central New Quebec orogen, Canada. *Can. J. Earth Sci.* **32,** 1208–1220 (1995).
7. Fralick, P., Davis, D. W. & Kissin, S. A. The age of the Gunflint Formation, Ontario, Canada: single zircon U-Pb age determinations from reworked volcanic ash. *Can. J. Earth Sci.* **39,** 1085–1091 (2002).
8. Schneider, D. A., Bickford, M. E., Cannon, W. F., Schultz, K. J. & Hamilton, M. A. Age of volcanic rocks and syndepositional iron formations, Marquette Range Supergroup: implications for the tectonic setting of Paleoproterozoic iron formations of the Lake Superior region. *Can. J. Earth Sci.* **39,** 999–1012 (2002).
9. Gross, G. A. *Iron Formation in Canada, Genesis and Geochemistry* (Geological Survey of Canada, Open File 5987, 2009).
10. Isley, A. E. & Abbott, D. H. Plume-related mafic volcanism and the deposition of banded iron formation. *J. Geophys. Res.* **104,** 15461–15477 (1999).
11. Pirajno, F., Hocking, R. M., Reddy, S. M. & Jones, A. J. A review of the geology and geodynamic evolution of the Palaeoproterozoic Earaheedy Basin, Western Australia. *Earth Sci. Rev.* **94,** 39–77 (2009).
12. Pufahl, P. K., Hiatt, E. E. & Kyser, T. K. Does the Paleoproterozoic Animikie Basin record the sulfidic ocean transition? *Geology* **38,** 659–662 (2010).
13. Heaman, L. M., Peck, D. & Toope, K. Timing and geochemistry of 1.88 Ga Molson Igneous Events, Manitoba: insights into the formation of a craton-scale magmatic and metallogenic province. *Precambr. Res.* **172,** 143–162 (2009).
14. Meert, J. G., Pandit, M. K., Pradhan, V. R. & Kamenov, G. Preliminary report on the paleomagnetism of 1.88 Ga dykes from the Bastar and Dharwar cratons, peninsular India. *Gondwana Res.* **20,** 335–343 (2011).
15. Condie, K. C. Episodic continental growth and supercontinents: a mantle avalanche connection? *Earth Planet. Sci. Lett.* **163,** 97–108 (1998).
16. Kemp, A. I. S., Hawkesworth, C. J., Paterson, B. A. & Kinny, P. D. Episodic growth of the Gondwana supercontinent from hafnium and oxygen isotopes in zircon. *Nature* **439,** 580–583 (2006).
17. Pearson, D. G., Parman, S. W. & Nowell, G. M. A link between large mantle melting events and continent growth seen in osmium isotopes. *Nature* **449,** 202–205 (2007).
18. Parman, S. W. Helium isotopic evidence for episodic mantle melting and crustal growth. *Nature* **446,** 900–903 (2007).
19. Franklin, J. M., Gibson, H. L., Jonasson, I. R. & Galley, A. G. Volcanogenic massive sulfide deposits. *Econ. Geol.* 100th anniversary volume 523–560 (2005).
20. Condie, K. C. Continental growth during a 1.9-Ga superplume event. *J. Geodyn.* **34,** 249–264 (2002).
21. Planavsky, N. *et al.* Rare earth element and yttrium compositions of Archean and Paleoproterozoic Fe formations revisited: new perspectives on the significance and mechanisms of deposition. *Geochim. Cosmochim. Acta* **74,** 6387–6405 (2010).
22. Planavsky, N. *et al.* Iron-oxidizing microbial ecosystems thrived in late Paleoproterozoic redox-stratified oceans. *Earth Planet. Sci. Lett.* **286,** 230–242 (2009).
23. Rasmussen, B. & Fletcher, I. R. Indirect dating of mafic intrusions by SHRIMP U–Pb analysis of monazite in contact metamorphosed shale: an example from the Palaeoproterozoic Capricorn Orogen, Western Australia. *Earth Planet. Sci. Lett.* **197,** 287–299 (2002).
24. Rasmussen, B. & Fletcher, I. R. Dating sedimentary rocks using in situ U–Pb geochronology of syn-eruptive zircon in ashfall tuffs 1 mm thick. *Geology* **38,** 299–302 (2010).
25. Johnston, D. T. Multiple sulfur isotopes and the evolution of Earth's surface sulfur cycle. *Earth Sci. Rev.* **106,** 161–183 (2011).
26. Barley, M. E., Pickard, A. L. & Sylvester, P. J. Emplacement of a large igneous province as a possible cause of banded iron formation 2.45 billion years ago. *Nature* **385,** 55–58 (1997).
27. Planavsky, N. J. *et al.* Widespread iron-rich conditions in the mid-Proterozoic ocean. *Nature* **477,** 448–451 (2011).
28. Poulton, S. W., Fralick, P. W. & Canfield, D. E. Spatial variability in oceanic redox structure 1.8 billion years ago. *Nature Geosci.* **3,** 486–490 (2010).
29. Kump, L. R. & Seyfried, W. E. Jr. Hydrothermal fluxes during the Precambrian: effect of low oceanic sulphate concentrations and low hydrostatic pressure on the composition of black smokers. *Earth Planet. Sci. Lett.* **235,** 654–662 (2005).
30. Addison, W. D. *et al.* Discovery of distal ejecta from the 1850 Ma Sudbury impact event. *Geology* **33,** 193–196 (2005).

LETTER

Antarctic ice–sheet loss driven by basal melting of ice shelves

H. D. Pritchard[1], S. R. M. Ligtenberg[2], H. A. Fricker[3], D. G. Vaughan[1], M. R. van den Broeke[2] & L. Padman[4]

Accurate prediction of global sea-level rise requires that we understand the cause of recent, widespread and intensifying[1,2] glacier acceleration along Antarctic ice-sheet coastal margins[3]. Atmospheric and oceanic forcing have the potential to reduce the thickness and extent of floating ice shelves, potentially limiting their ability to buttress the flow of grounded tributary glaciers[4]. Indeed, recent ice-shelf collapse led to retreat and acceleration of several glaciers on the Antarctic Peninsula[5]. But the extent and magnitude of ice-shelf thickness change, the underlying causes of such change, and its link to glacier flow rate are so poorly understood that its future impact on the ice sheets cannot yet be predicted[3]. Here we use satellite laser altimetry and modelling of the surface firn layer to reveal the circum-Antarctic pattern of ice-shelf thinning through increased basal melt. We deduce that this increased melt is the primary control of Antarctic ice-sheet loss, through a reduction in buttressing of the adjacent ice sheet leading to accelerated glacier flow[2]. The highest thinning rates occur where warm water at depth can access thick ice shelves via submarine troughs crossing the continental shelf. Wind forcing could explain the dominant patterns of both basal melting and the surface melting and collapse of Antarctic ice shelves, through ocean upwelling in the Amundsen[6] and Bellingshausen[7] seas, and atmospheric warming on the Antarctic Peninsula[8]. This implies that climate forcing through changing winds influences Antarctic ice-sheet mass balance, and hence global sea level, on annual to decadal timescales.

Over 80% of Antarctica's grounded ice drains through its fringing ice shelves, and glacier flow is sensitive to changes in ice-shelf extent[5] and thickness[4]. Ice-shelf collapse could lead to abrupt and potentially runaway ice-sheet retreat[9]. At their upper surfaces, ice shelves are vulnerable to changes in atmospheric conditions and at their bases they are exposed to heat transported at depth within the Southern Ocean[10]; they lose mass if basal melting or iceberg calving increase, or glacier influx or the surface mass balance (snow accumulation minus ablation) decrease. Basal melt rates vary considerably with thermal forcing: a function of local ocean temperature and ice thickness as the melting point is depressed with depth[11]. The strongest thermal forcing and highest melt rates (over 40 m yr^{-1}) are found near the deep grounding line of Pine Island Glacier, West Antarctica[11], where recent observations have shown enhanced basal melting in response to modest ocean warming and a local feedback between ice-shelf retreat and greater warm-water ingress[10]. Loss of ice-shelf buttressing there[12] has increased the flow rate of grounded ice by 34% from 1996–2006, contributing a sea level rise of 1.2 mm per decade[2]. Ice shelves are thought to be thinning in other locations[13], but the importance of reduced buttressing for ice-sheet dynamics on the continental scale is not known.

Here, we present thickness changes for all of the major Antarctic ice shelves and neighbouring grounded ice for the period 2003–2008. We measure the rate of surface height change ($\Delta h/\Delta t$) by using a time series of repeat-track satellite laser altimetry[1]. The laser altimeter on NASA's ICESat satellite[14] was primarily designed to detect height change on the ice sheets. It has several advantages over satellite radar altimetry (which is traditionally used for this purpose): an orbit that samples all major Antarctic ice shelves; smaller footprints with well-constrained locations and closer along-track spacing; and negligible surface penetration, regardless of season[14].

Our measurements reveal coherent patterns of ice-shelf elevation change rate ($\Delta h/\Delta t$) at the scale of centimetres per year (Fig. 1). A zone of surface lowering on Ross Ice Shelf corresponds to reduced glacier influx following the shutdown of Kamb Ice Stream, where the grounded ice is thickening by up to 0.65 m yr^{-1} (ref. 1). After converting from elevation to thickness change-rate ($\Delta T/\Delta t$) on the ice shelves (Fig. 2), a comparison with results derived from 15 years of radar altimetry[13] shows a broadly similar pattern. However, our measurements increase sampling (from ~12,000 radar altimeter orbit-crossover measurements[13] to ~4.5 million ICESat along-track measurements), extend coverage southwards, improve on the removal of confounding
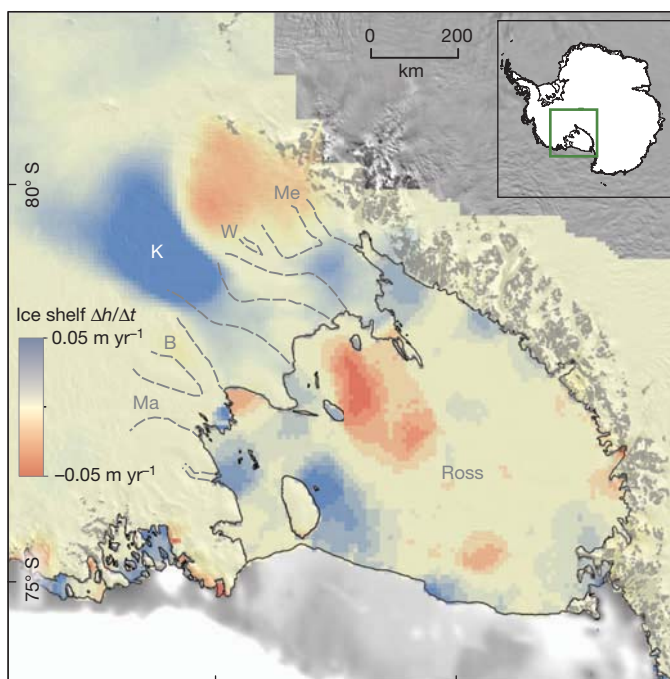
Figure 1 | Surface $\Delta h/\Delta t$ of Ross Ice Shelf, 2003–2008. The colour scale for the grounded ice $\Delta h/\Delta t$ signal is ±30 cm yr^{-1}. The continental shelf is shown in grey, landward of the continental-shelf break[30]. Labels Me, W, K, B and Ma denote the ice streams Mercer, Whillans, Kamb, Bindschadler and MacAyeal. Dashed grey lines show the lateral ice stream margins. Black lines show ice-shelf boundaries (mapped between 1993 and 2003)[31]. The inset shows the location of the figure (green box) overlaid on the outline of Antarctica.

[1]British Antarctic Survey, Natural Environment Research Council, Madingley Road, Cambridge CB3 0ET, UK. [2]Utrecht University, Institute for Marine and Atmospheric Research, 3508 TA Utrecht, The Netherlands. [3]Scripps Institution of Oceanography, University of California San Diego, La Jolla, California 92093, USA. [4]Earth & Space Research, 3350 Southwest Cascade Avenue, Corvallis, Oregon 97333-1536, USA.
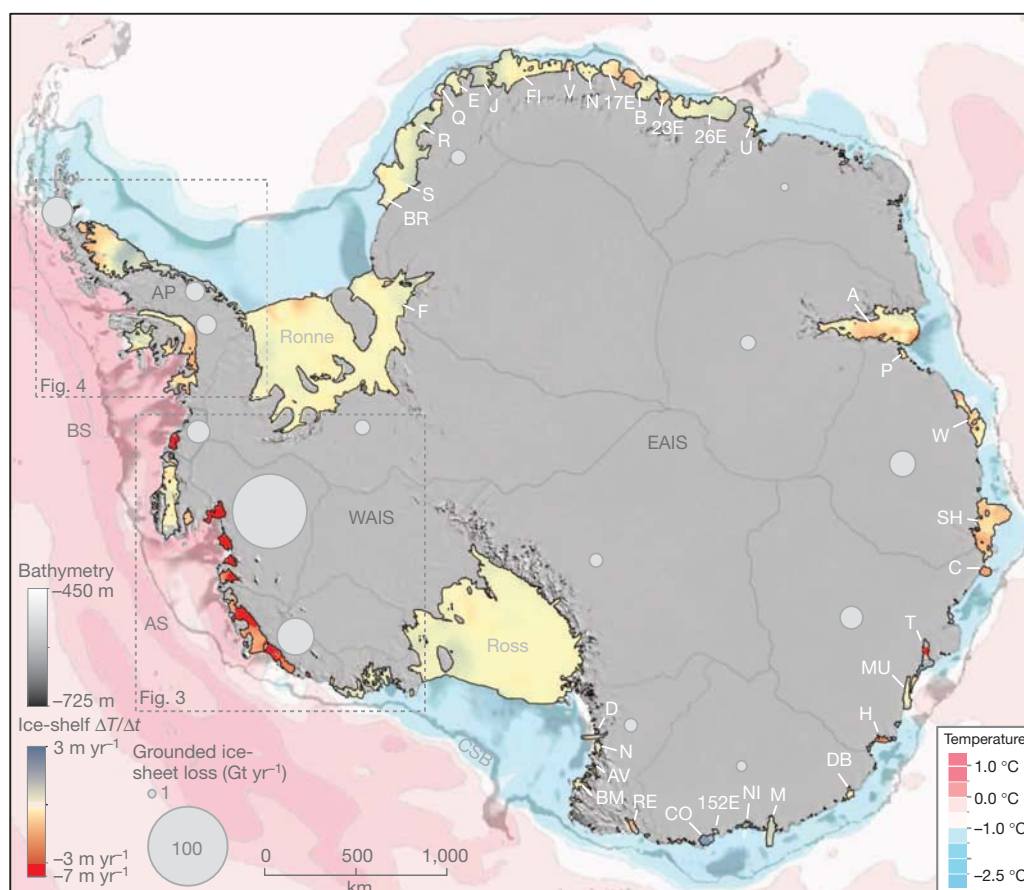
Figure 2 | Antarctic ice-shelf ice-thickness change rate ΔT/Δt, 2003–2008. Seaward of the ice shelves, estimated average sea-floor potential temperatures (in °C) from the World Ocean Circulation Experiment Southern Ocean Atlas (pink to blue) are overlaid on continental-shelf bathymetry (in metres)[30] (greyscale, landward of the continental-shelf break, CSB). Grey labels indicate Antarctic Peninsula (AP), West and East Antarctic Ice Sheets (WAIS and EAIS), Bellingshausen Sea (BS), Amundsen Sea (AS) and the Ross and Ronne ice shelves. White labels indicate the ice shelves (clockwise from top) Vigridisen (V), Nivlisen (N), 17 East (17E), Borchgrevinkisen (B), 23 East (23E), 26 East (26E), Unnamed (U), Amery (A), Publications (P), West (W), Shackleton (SH), Conger (C), Totten (T), Moscow University (MU), Holmes (H), Dibble (DB), Mertz (M), Ninnis (NI), 152 East (152E), Cook (CO), Rennick (RE), Borchgrevink-Mariner (BM), Aviator (AV), Nansen (N), Drygalski (D), Filchner (F), Brunt (BR), Stancombe-Wills (S), Riiser-Larsen (R), Quar (Q), Ekstrom (E), Jelbart (J) and Fimble (FI). Grey circles show relative ice losses for ice-sheet drainage basins (outlined in grey) that lost mass between 1992 and 2006 (after ref. 2) (Supplementary Table 1).

signals and separation of surface and basal processes, and show in detail the relationship between thinning of ice shelves and grounded tributary glaciers. These improvements allow us to identify the major cause of grounded Antarctic ice-sheet mass loss.

The distribution of Antarctic ice-shelf thinning ($\Delta T/\Delta t$) is strongly regional (Fig. 2), being most rapid (up to $6.8\,\mathrm{m\,yr^{-1}}$) along the Amundsen and Bellingshausen Sea coasts. The relatively thick Land, DeVicq, Getz, Dotson, Crosson, Thwaites, Pine Island, Cosgrove and Venable ice shelves thinned during 2003–2008, in marked contrast to the adjacent, thinner Abbott, Nickerson and Sulzberger ice shelves where there was no significant thinning (Fig. 3) (Supplementary Fig. 1, Supplementary Table 1). Firn modelling on the ice shelves (Supplementary Fig. 2) indicates that the firn layer actually thickened throughout this region, mostly through increased accumulation, consistent with ICESat measurements on nearby slow-moving grounded ice (Fig. 3). These neighbouring ice shelves with similar atmospheric forcing but contrasting elevation change signals must therefore be subject to some regional forcing other than local climate. Furthermore, all of the thinning ice shelves maintained their frontal positions or advanced (Supplementary Fig. 3) while simultaneously receiving increased influx from their tributary glaciers[2]. Hence, this regional thinning is not explained by negative surface mass balance, firn compaction, retreating ice-shelf fronts or by reduced glacier influx. We deduce that it is caused by increased basal melt driven by ocean interaction.

Our analysis reveals that there is also evidence of net thinning through enhanced basal melt on the East Antarctic ice shelves Vigridisen, 17E, West, Shackleton, Holmes Glacier, Dibble, Rennick Glacier and the thicker part of Totten. The Nivlisen, Moscow University and 152E ice-shelf surfaces appear to have lowered as a result of firn processes (Fig. 2, Supplementary Figs 4–6, Supplementary Table 1). On the western Antarctic Peninsula, the Stange Ice Shelf and the thicker sections of the George VI Ice Shelf also lowered at a rate greater than the modelled firn-lowering signal in this region, indicating ocean-driven basal melt (Fig. 4, Supplementary Fig. 7). However, the thinning of the retreating Wilkins Ice Shelf during 2003–2008 may combine components of basal melt, surface processes and dynamics (Supplementary Discussion).

An exception to this pattern is the Larsen C ice shelf, where firn processes are an important part of the elevation change signal. Measured $\Delta h/\Delta t$ on the ice shelf increases northwards from $-0.06\,\mathrm{m\,yr^{-1}}$ to $-0.21\,\mathrm{m\,yr^{-1}}$, with similar values on adjacent, slow-flowing grounded ice ($-0.20\,\mathrm{m\,yr^{-1}}$ in the south to $-0.35\,\mathrm{m\,yr^{-1}}$ in the north, on grounded ice at an average 230 m above the ice-shelf altitude; Fig. 4 inset). Our firn modelling independently predicts lowering due to surface processes of $-0.10\,\mathrm{m\,yr^{-1}}$ (south) to $-0.16\,\mathrm{m\,yr^{-1}}$ (north) for the same period (Fig. 4, Supplementary Table 1). This south–north gradient is echoed in the mapped firn-air content (lesser northwards)[15] and melt days (greater northward), and a temporal trend of $+0.5$ melt

Figure 3 | Surface $\Delta h/\Delta t$ on the ice shelves and grounded ice of the Amundsen/Bellingshausen Sea coasts, 2003–2008. Ice shelves labelled are Venable (V), Abbott (A), Cosgrove (C), Pine Island (PI), Thwaites (TH), Crosson (CR), Dotson (D), Getz (G), De Vicq (DV), Land (L), Nickerson (N) and Sulzberger (SZ). Arrows highlight areas of slow-fl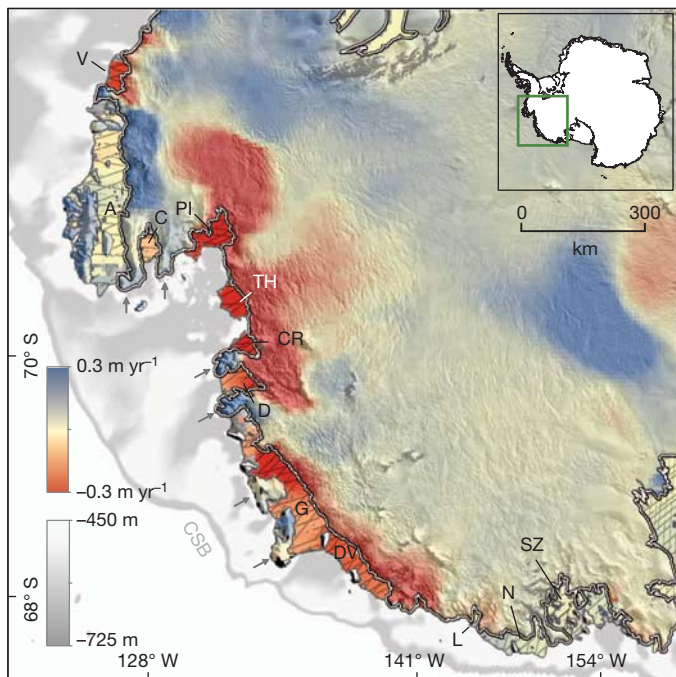owing, grounded ice. Bathymetry[30] landward of the continental-shelf break is in greyscale. Locations of ICESat $\Delta h/\Delta t$ measurements are shown as grey tracks on the ice shelves. The grounding line is in white[31]. The inset shows the location of the figure (green box) overlaid on the outline of Antarctica.

Figure 4 | Ice-shelf $\Delta T/\Delta t$ on the Antarctic Peninsula, 2003–2008. Labelled ice shelves are the former Larsen A and B (LA, LB), Larsen C (LC), George VI (G6), Wilkins (W) and Stange (ST). DI indicates Dolleman Island. Bathymetry[30] landward of the continental-shelf break is in greyscale. Locations of ICESat $\Delta h/\Delta t$ measurements are shown as grey tracks. The upper inset shows $\Delta h/\Delta t$ on Larsen C and adjacent slow-flowing, grounded low-altitude margins, with modelled firn contribution to ice-shelf $\Delta h/\Delta t$ (cm yr^{-1}, at black dots) for 2003–2008. The cross shows the location of the automated weather station used to calibrate the firn model, reducing modelled melt rates by 33%. The grounding line is in white[31]. The lower inset shows the location of the main panel and the inset (bigger and smaller green boxes) overlaid on the outline of Antarctica.

days per year[2] over most of Larsen C from 1979–2009 was reported[16]. We infer that the lowering on the ice shelf and slow-flowing grounded margins is dominated by surface firn processes instead of basal melting, though acceleration of ice-shelf flow in the north may also have contributed to the thinning signal and the modelled firn depth in this area is uncertain (Supplementary Material and Discussion).

Every case of ocean-driven ice-shelf thinning that we identify is linked with previously documented dynamic thinning of grounded, fast-flowing tributary glaciers (Supplementary Table 1)[1,2]. In the absence of significant surface-mass-balance trends (Supplementary Methods 1.2), dynamic thinning accounts for almost all current mass loss from the Antarctic ice sheets and results from glacier acceleration owing to decreased net downstream resistance[1,2]; we attribute this to a reduction in buttressing from the thinning ice shelves[17]. The alternative scenario of dynamic thinning driven by reduced friction at the glacier bed would imply ice-shelf thickening and advance, which is contrary to our observations. A similar attribution of dynamic thinning to ocean-driven melt of marine margins has been made for some Greenland glaciers[18].

Ice-shelf thinning by basal melt implies an increased oceanic heat supply into the sub-ice-shelf cavities. This has been explained by fluctuating incursions of Circumpolar Deep Water (CDW) across the continental shelf of the Amundsen and Bellingshausen seas that sometimes come into contact with the ice-shelf bases, increasing the melt rate[6,7,10]. Originating in the wind-driven Antarctic Circumpolar Current, CDW is relatively warm (over 1 °C), saline and dense. In places, CDW approaches the Antarctic coast (Fig. 2) and is channelled at depth (typically deeper than ~300 m) along bathymetric troughs in the sea floor beneath the ice shelves[19]. At these depths, CDW is up to 4 °C above freezing and so can drive vigorous basal melt[10]. Many major Antarctic glaciers lie in retreated positions within glacially eroded

troughs that span the continental shelf and deepen towards the ice sheet (Fig. 2), and so are well positioned to respond to CDW incursions.

Our observations support this explanation: the most rapid thinning occurs on thick ice shelves with relatively high sea-floor temperatures and deep bathymetric troughs spanning the continental shelf (Fig. 2). This is most apparent on the Amundsen Sea coast, where the only ice shelves not thinning (Abbott, Nickerson and Sulzberger) are those not exposed to deep-lying warm water because they have shallow drafts, lack deep bathymetric troughs or are remote from CDW (Figs 2 and 3). On the Antarctic Peninsula, thinning of the George VI Ice Shelf is also concentrated on the thickest area that is most likely to be exposed to shoaling CDW[7,20] (Figs 2 and 4).

Incursions of CDW can be driven by wind forcing, through upwelling along the continental shelf break[6,21] and vertical mixing. Mixing of CDW with colder, shallower layers over the continental shelf has been inferred following a wind-driven landward shift of the sea-ice formation zone[7]. The link between changing wind fields and heat redistribution in coastal Antarctica is poorly understood, but wind forcing has changed markedly over recent decades[22]. Increased circumpolar winds have caused strong warming of the Southern Ocean since the 1950s through a poleward shift in the Antarctic Circumpolar Current[23] and increased eddy heat flux[24]. Increased atmospheric flow over the Antarctic Peninsula since the 1960s has increased surface melt and initiated the collapse of the Larsen A and B ice shelves[8]. Changing cyclonic winds over the Amundsen Sea have brought a significant sea-ice decline and significant West Antarctic spring climate warming since the late 1970s[25]. These changes in wind forcing have been attributed to a combination of changing tropical Pacific sea surface temperatures[26,27], and stratospheric ozone loss and increased greenhouse

gases[28]. Less is known about CDW incursions and the role of wind forcing along the East Antarctic coast, where typically cooler waters bathe the continental shelf, but warm waters lie close offshore (Fig. 2).

To summarize, we find thinning attributed to ocean-driven basal melt on 20 of 54 ice shelves, with the most widespread and rapid losses (up to $\sim$7 m yr^{-1}) on the coast of West Antarctica, where warm waters at depth have access to thick ice shelves via deep bathymetric troughs. There is evidence that changes in wind forcing explain both the increased oceanic supply of warm water to thinning West Antarctic ice shelves, and the atmospheric warming on the Antarctic Peninsula that caused the loss of Larsen A and B and now dominates the thinning of Larsen C. That is to say, both processes are ultimately linked to the atmosphere. Both mechanisms imply that Antarctic ice shelves can respond rapidly to Southern Hemisphere wind patterns that vary on timescales of years to decades.

We find that ocean-driven ice-shelf thinning is in all cases coupled with dynamic thinning of grounded tributary glaciers that together account for about 40% of Antarctic discharge and the majority of Antarctic ice-sheet mass loss[2]. In agreement with recent model predictions[17], we conclude that it is reduced buttressing from the thinning ice shelves that is driving glacier acceleration and dynamic thinning. This implies that the most profound contemporary changes to the ice sheets and their contribution to sea level rise can be attributed to ocean thermal forcing that is sustained over decades[12] and may already have triggered a period of unstable glacier retreat[9].

METHODS SUMMARY

Measuring change in ice-shelf thickness from altimetry is challenging because of confounding signals from tides, atmospheric pressure fluctuations, near-surface firn processes and sea-level rise. Furthermore, elevation change of the floating surface can represent anything from about 10% of total thickness change (for loss of relatively dense basal ice) to 100% (for loss of air trapped in near-surface firn). We use ICESat GLA12 Release-428 altimetry data from October 2003 to November 2008 (http://icesat.gsfc.nasa.gov/icesat) to measure height change[1]. We correct for confounding signals, subtracting the elevation change modelled for near-surface firn processes (surface mass balance and firn compaction). We use CATS2008A (http://www.esr.org/polar_tide_models/Model_CATS2008a.html) to model tides, RACMOv2.2/ANT27 to model climate and UUFIRNMODELv2.1/ANT to model firn height change (Supplementary Methods). Supplementary corrected ICESat and firn modelling data are available[29]. Where hydrostatic equilibrium applies, we calculate the underlying changes in ice thickness (ΔT) of the ice shelves from the corrected change in freeboard. Our error budget accounts for uncertainty in ICESat measurements, in the correction of each of the confounding signals and in our height change calculations. We find that the uncertainty in spatially averaged ICESat $\Delta h/\Delta t$ averages 0.007 m yr^{-1} but uncertainty in $\Delta T/\Delta t$ is dominated by uncertainties in the firn correction (averaging 0.09 m yr^{-1} and 0.02 m yr^{-1} respectively on ice shelves with and without melt) (Supplementary Methods).

We test for changes in volume due to changing glacier influx or ice-shelf geometry[4] using published measurements[2,13] and recent satellite images of ice-shelf extent (http://www.polarview.aq) (Supplementary Discussion). We then relate the pattern of our calculated ice shelf $\Delta T/\Delta t$ to bathymetry[30] (http://www.earth-syst-sci-data.net/2/261/2010/essd-2-261-2010.pdf) and sea-floor potential temperatures from the World Ocean Circulation Experiment Southern Ocean Atlas (http://woce.nodc.noaa.gov/wdiu/).

1. Pritchard, H. D., Arthern, R. J., Vaughan, D. G. & Edwards, L. A. Extensive dynamic thinning on the margins of the Greenland and Antarctic ice sheets. *Nature* **461**, 971–975 (2009).
2. Rignot, E. B. et al. Antarctic ice mass loss from radar interferometry and regional climate modelling. *Nature Geosci.* **1**, 106–110 (2008).
3. Solomon, S. et al. *Contribution of Working Group I to the Fourth Assessment Report of the Intergovernmental Panel on Climate Change* 2007 (Cambridge University Press, 2007).
4. Dupont, T. K. & Alley, R. B. Assessment of the importance of ice-shelf buttressing to ice-sheet flow. *Geophys. Res. Lett.* **32** (2005).
5. Rott, H., Rack, W., Skvarca, P. & de Angelis, H. Northern Larsen Ice Shelf, Antarctica: further retreat after collapse. *Ann. Glaciol.* **34**, 277–282 (2002).
6. Thoma, M., Jenkins, A., Holland, D. & Jacobs, S. Modelling Circumpolar Deep Water intrusions on the Amundsen Sea continental shelf, Antarctica. *Geophys. Res. Lett.* **35**, L18602 (2008).
7. Holland, P. R., Jenkins, A. & Holland, D. M. Ice and ocean processes in the Bellingshausen Sea, Antarctica. *J. Geophys. Res.* **115**, C05020 (2010).
8. Marshall, G. J., Orr, A., van Lipzig, N. P. M. & King, J. C. The impact of a changing Southern Hemisphere Annular Mode on Antarctic Peninsula summer temperatures. *J. Clim.* **19**, 5388–5404 (2006).
9. Schoof, C. Ice sheet grounding line dynamics: steady states, stability and hysteresis. *J. Geophys. Res.* **112**, F03S28 (2007).
10. Jacobs, S. S., Jenkins, A., Giulivi, C. F. & Dutrieux, P. Stronger ocean circulation and increased melting under Pine Island Glacier ice shelf. *Nature Geosci.* **4**, 519–523 (2011).
11. Rignot, E. & Jacobs, S. S. Rapid bottom melting widespread near Antarctic Ice Sheet grounding lines. *Science* **296**, 2020–2023 (2002).
12. Joughin, I., Smith, B. E. & Holland, D. M. Sensitivity of 21st century sea level to ocean-induced thinning of Pine Island Glacier, Antarctica. *Geophys. Res. Lett.* **37**, L20502 (2010).
13. Shepherd, A. W., Wallis, D., Giles, D., Laxon, K. & Sundal, S. A. V. Recent loss of floating ice and the consequent sea level contribution. *Geophys. Res. Lett.* **37**, L13503 (2010).
14. Shuman, C. A. et al. ICESat Antarctic elevation data: preliminary precision and accuracy assessment. *Geophys. Res. Lett.* **33**, L07501 (2006).
15. Holland, P. R. et al. The air content of Larsen Ice Shelf. *Geophys. Res. Lett.* **38**, L10503 (2011).
16. Tedesco, M. Assessment and development of snowmelt retrieval algorithms over Antarctica from K-band spaceborne brightness temperature (1979–2008). *Remote Sens. Environ.* **113**, 979–997 (2009).
17. Gagliardini, O., Durand, G., Zwinger, T., Hindmarsh, R. C. A. & Le Meur, E. Coupling of ice-shelf melting and buttressing is a key process in ice-sheets dynamics. *Geophys. Res. Lett.* **37**, L14501 (2010).
18. Murray, T. et al. Ocean regulation hypothesis for glacier dynamics in southeast Greenland and implications for ice sheet mass changes. *J. Geophys. Res.* **115**, F03026 (2010).
19. Wåhlin, A. K., Yuan, X., Bjork, G. & Nohr, C. Inflow of Warm Circumpolar Deep Water in the Central Amundsen Shelf. *J. Phys. Oceanogr.* **40**, 1427–1434 (2010).
20. Jenkins, A. & Jacobs, S. Circulation and melting beneath George VI Ice Shelf, Antarctica. *J. Geophys. Res.* **113**, C04013 (2008).
21. Martinson, D. G., Stammerjohn, S. E., Iannuzzi, R. A., Smith, R. C. & Vernet, M. Western Antarctic Peninsula physical oceanography and spatio-temporal variability. *Deep Sea Res. II* **55**, 1964–1987 (2008).
22. Young, I. R., Zieger, S. & Babanin, A. V. Global trends in wind speed and wave height. *Science* **332**, 451–455 (2011).
23. Gille, S. T. Decadal-scale temperature trends in the Southern Hemisphere Ocean. *J. Clim.* **21**, 4749–4765 (2008).
24. Hogg, A. M. C., Meredith, M. P., Blundell, J. R. & Wilson, C. Eddy heat flux in the Southern Ocean: response to variable wind forcing. *J. Clim.* **21**, 608–620 (2008).
25. Schneider, D., Deser, C. & Okumura, Y. An assessment and interpretation of the observed warming of West Antarctica in the austral spring. *Clim. Dyn.* **38** (1–2), 323–347 (2011).
26. Meredith, M. P. et al. Changes in the freshwater composition of the upper ocean west of the Antarctic Peninsula during the first decade of the 21st century. *Prog. Oceanogr.* **87**, 127–143 (2010).
27. Steig, E. J. Ding, Q. Battisti, D. S. & Jenkins, A. Tropical forcing of Circumpolar Deep Water Inflow and outlet glacier thinning in the Amundsen Sea Embayment, West Antarctica. *Ann. Glaciol.* **53**, 19–28 (2012).
28. Fyfe, J. C. & Saenko, O. A. Human-induced change in the Antarctic Circumpolar Current. *J. Clim.* **18**, 3068–3073 (2005).
29. Pritchard, H. D. et al. Corrected ICESat altimetry data, surface mass balance, and firn elevation change on Antarctic ice shelves. http://dx.doi.org/10.1594/PANGAEA.775984 (PANGAEA Data Publisher for Earth & Environmental Science, 2012).
30. Timmermann, R. et al. A consistent dataset of Antarctic ice sheet topography, cavity geometry, and global bathymetry. *Earth Syst. Sci. Data Discuss.* **3**, 231–257 (2010).
31. Bindschadler, R. C. et al. Getting around Antarctica: new high-resolution mappings of the grounded and freely-floating boundaries of the Antarctic ice sheet created for the International Polar Year. *The Cryosphere* **5**, 569–588 (2011).

Author Contributions H.D.P. designed and led the research. H.D.P., H.A.F. and L.P. analysed the altimetry data. S.R.M.L. and M.R.v.d.B. modelled the firn signals. All authors wrote and discussed the paper.

Author Information Reprints and permissions information is available at www.nature.com/reprints. The authors declare no competing financial interests. Readers are welcome to comment on the online version of this article at www.nature.com/nature. Correspondence and requests for materials should be addressed to H.D.P. (h.pritchard@bas.ac.uk).

LETTER

Sexual selection enables long-term coexistence despite ecological equivalence

Leithen K. M'Gonigle[1]†, Rupert Mazzucco[2], Sarah P. Otto[1] & Ulf Dieckmann[2]

Empirical data indicate that sexual preferences are critical for maintaining species boundaries[1–4], yet theoretical work has suggested that, on their own, they can have only a minimal role in maintaining biodiversity[5–9]. This is because long-term coexistence within overlapping ranges is thought to be unlikely in the absence of ecological differentiation[9]. Here we challenge this widely held view by generalizing a standard model of sexual selection to include two ubiquitous features of populations with sexual selection: spatial variation in local carrying capacity, and mate-search costs in females. We show that, when these two features are combined, sexual preferences can single-handedly maintain coexistence, even when spatial variation in local carrying capacity is so slight that it might go unnoticed empirically. This theoretical study demonstrates that sexual selection alone can promote the long-term coexistence of ecologically equivalent species with overlapping ranges, and it thus provides a novel explanation for the maintenance of species diversity.

A central objective of evolutionary ecology is to understand the mechanisms that allow species to coexist. One such mechanism is ecological differentiation. By occupying different niches, species in overlapping ranges are able to reduce direct competition[10]. While there are numerous examples of closely related species occupying different ecological niches, many recently diverged and coexisting taxa are known to differ most markedly in their secondary sexual characters, showing few, if any, ecological differences[1–4]. It therefore seems that sexual selection is an important mechanism for maintaining coexistence. Indeed, models of sexual selection have shown that populations of choosy females and their preferred males can arise and, under various conditions, form reproductively isolated mating groups[11–15]. However, because sexual selection does not lead to ecological differentiation, species differing only in their mating preferences compete for the same ecological niche. This has traditionally led to the conclusion that, if their ranges overlap, one of these species will eventually displace the other[5–9].

Coexistence is facilitated by mechanisms that reduce range overlap between species. Sexual selection provides one such mechanism. Any process that creates spatial variation in female preferences indirectly also creates selection on male display traits, locally favouring those males that are most preferred by the local females. As a consequence, spatially segregated mating domains, characterized by the co-occurrence of matching display and preference traits, can emerge from populations with an initially random spatial distribution. Once segregated, interactions between different mating types are limited to individuals at the peripheries of these domains. In finite populations, however, the mating domains may shrink or grow, and the interface between them may drift randomly in space. Such fluctuations eventually lead to one mating domain replacing all others (Fig. 1a, c). In a pioneering study[16], it was argued that lower dispersal in males with better mating prospects facilitates spatial segregation and maintains coexistence. In finite populations, however, such mating-dependent dispersal fails to stabilize long-term coexistence (Supplementary Fig. 3). Given these difficulties

associated with sexual selection, a recent review concluded that sexually divergent, but ecologically equivalent, species cannot coexist for significant lengths of time[9].

Here we report model results that suggest the contrary and demonstrate that sexual selection can promote long-term coexistence, even without any ecological differentiation. Building on a standard model of sexual selection[14], we develop an individual-based model to examine the long-term fate of species differing only in their secondary sexual characters in an ecologically neutral context with finite population sizes (details are given in Supplementary Information). Except where noted, we assume a simple genetic structure with two unlinked haploid
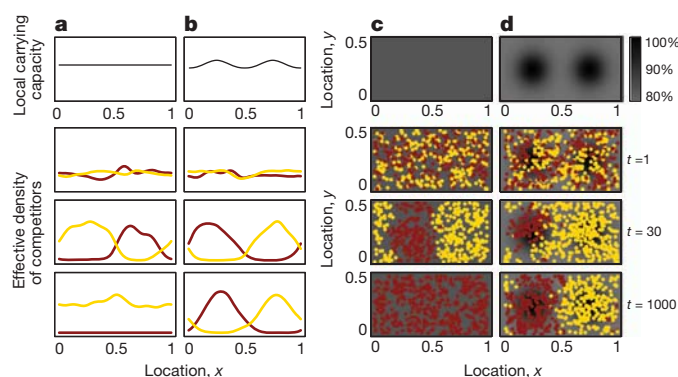
Figure 1 | Sexual selection enables long-term coexistence of ecologically equivalent species. We consider a population distributed across a continuous habitat in one dimension (**a**, **b**) or two dimensions (**c**, **d**) with a local carrying capacity that is either spatially uniform (top panels in **a** and **c**) or that has two peaks (top panels in **b** and **d**). Each peak is of Gaussian shape with standard deviation σ_k. The level v of spatial variation may be altered by changing the height of these peaks relative to the troughs between them. A value of $v = 0.25$, as in **b** and **d**, means that local carrying capacity at the peaks is elevated by 25%. The three lower rows show model runs through time. In each generation, individuals survive after a round of local competition and reproduce after a round of local mating, followed by offspring movement and the death of all parents. Competition between individuals decreases with their distance according to a Gaussian function with standard deviation σ_s. Coloured curves in **a** and **b** show the effective local density of competitors of each type (weighted by their competitive effect; Supplementary Information, equation (4)), and dots in **c** and **d** show surviving adults. Individuals are coloured according to their display locus genotype (similar patterns are observed at the preference locus; Supplementary Fig. 2). Females are α times more likely to mate with a preferred male, when encountered. Males are encountered with a probability that decreases with the distance between them and the female according to a Gaussian function with standard deviation σ_f. Female fecundity declines with the strength of mate-search costs m. Movement distances are drawn from a Gaussian function with standard deviation σ_m, centred at 0, with wrap-around boundaries. The total carrying capacity is $K = 500$, supporting the survival of approximately half of the $N = 1,000$ offspring produced each generation; other parameters: $\sigma_k = 0.1$, $\sigma_s = 0.05$, $\alpha = 5$, $\sigma_f = 0.05$, $\sigma_m = 0.05$, and $m/K = 1$ (roughly halving fecundity, Supplementary Fig. 1).

[1]Department of Zoology, University of British Columbia, 6270 University Boulevard, Vancouver, British Columbia, Canada, V6T 1Z4. [2]Evolution and Ecology Program, International Institute for Applied Systems Analysis, A-2361 Laxenburg, Austria. †Present address: Department of Environmental Science, Policy, and Management, University of California, Berkeley, 130 Mulford Hall, Berkeley, California 94720, USA.

loci: the first locus (with alleles Q and q) governs a display trait that is expressed only in males, and the second (with alleles P and p) governs a preference trait that is expressed only in females (below we allow for more than two alleles; quantitative mating traits are investigated in the Supplementary Information). Because we are interested in coexistence rather than speciation, we assume that the genetic variation at both loci is already present, for example as a result of recent migration from allopatric ranges. All else being equal, females bearing a P (p) allele prefer[14–16] to mate with males carrying a Q (q) allele by a factor α, and a female's preference for a given male attenuates with increasing distance between them. Similarly, competition decreases as the spatial distance between individuals increases. Competition is assumed to reduce an individual's probability of surviving until reproductive maturity (similar results are obtained if competition reduces fecundity; Supplementary Fig. 4). Other than potentially carrying mismatched preference and trait alleles, hybrids suffer no intrinsic fitness costs.

Mating domains can be lost either through movement of the interface between them or when individuals of one mating type colonize the domain of another mating type. In particular, because selection at the preference locus disappears when there is no variation at the display

locus, foreign preference alleles may drift into regions with low variation in male display alleles, eventually causing displacement. Loss of mating domains can, however, be prevented by including two features ubiquitous in populations experiencing sexual selection: spatial variation in local carrying capacity and mate-search costs in females. Spatial variation in carrying capacity is present in most, if not all, biological systems (see Fig. 1 and Supplementary Information for model details). Mate-search costs occur if a female spends time and energy looking for a suitable mate and rejecting non-preferred males, thereby reducing her ability to invest in offspring. To account for such costs we assume that the fecundity of a particular female increases from 0 to a maximum level with the local density of available males, weighted according to her preference (Supplementary Information).

Our model confirms the long-standing view that sexual selection in homogeneous spatial models, without mate-search costs, does not facilitate coexistence and can, in fact, hasten the loss of diversity (compare Fig. 2a with Fig. 2b). Spatial variation in local carrying capacity, on its own, also has little, if any, effect in stabilizing populations (compare Fig. 2b with Fig. 2c). Sexual selection with mate-search costs slightly prolongs coexistence in a spatially uniform environment by helping to prevent mixing of the mating domains, but this effect is weak (compare Fig. 2b with Fig. 2d). However, in an environment with spatial variation in local carrying capacity, sexual selection with mate-search costs dramatically increases coexistence times (compare Fig. 2b with Fig. 2e and also Fig. 1a, c with Fig. 1b, d). In this case, mate-search costs curb the neutral drift of preference alleles, thus preventing the dilution of mating domains, and areas of high local carrying capacity provide spatial 'anchors', stabilizing the location and size of these domains (Fig. 1b, d).

Although neither spatial variation in local carrying capacity nor mate-search costs suffice on their own to stabilize populations, surprisingly little of both can be enough to ensure the long-term persistence of divergent mating types (Fig. 3). When mate-search costs in females are high, long-term coexistence can be maintained with less than 20% spatial variation in local carrying capacity. When mate-search costs are low, 50% spatial variation in local carrying capacity is sufficient to stabilize mating domains. Throughout this study, we have kept population sizes relatively small, to exacerbate the challenge of coexistence
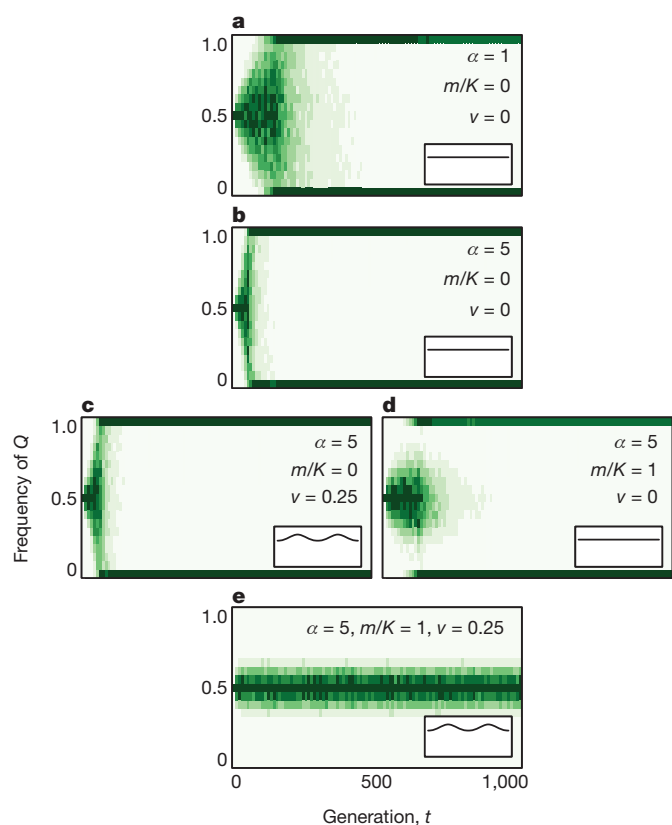
Figure 2 | Loss and maintenance of coexistence. Panels show distributions of allele frequencies at the display locus through time across 1,000 model runs in a two-dimensional landscape; coexistence occurs only while these frequencies remain intermediate. Inset panels depict the spatial variation in local carrying capacity as viewed along transects at $y = 0.25$. a, Homogeneous environment with no sexual selection ($\alpha = 1$). b, As in a, except that females are choosy ($\alpha = 5$). c, As in b, except with variation in local carrying capacity ($v = 0.25$). d, As in b, except with mate-search costs in females ($m/K = 1$). e, As in b, except with spatial variation in local carrying capacity ($v = 0.25$) and mate-search costs in females ($m/K = 1$); only when both features are combined is long-term coexistence observed. To focus on the maintenance of coexistence, we begin with two equally sized and spatially segregated populations of PQ and pq genotypes (all individuals on the left half of the arena initially have the PQ genotype, whereas all individuals on the right initially have the pq genotype). This mimics a situation in which types that previously arose in allopatry come back into contact, revealing the conditions under which they can persist in sympatry. All other parameters are as in Fig. 1.
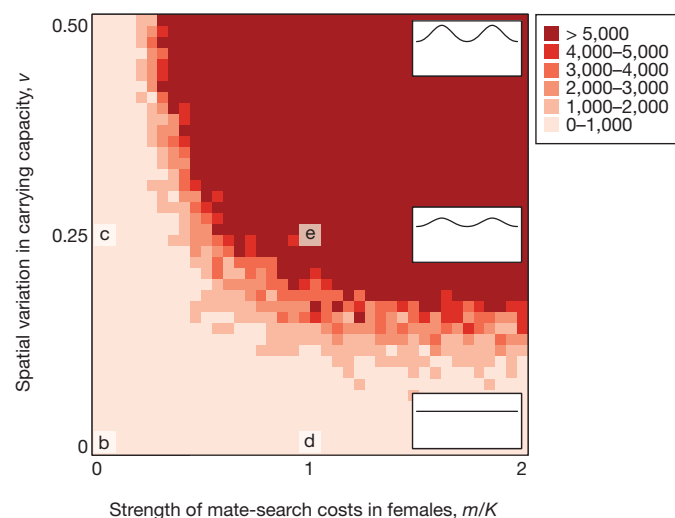
Figure 3 | Conditions for long-term coexistence. Shading indicates the number of generations that polymorphism at the display locus persists when females are choosy ($\alpha = 5$) in a two-dimensional landscape (darker = longer). Each cell represents the mean time to loss of polymorphism for 10 replicate model runs. Letters indicate parameter combinations used to generate the corresponding panels in Fig. 2. Inset panels illustrate the extent of spatial variation in local carrying capacity for the three parameter values shown along the vertical axis. Model runs are initialized as in Fig. 2. All other parameters are as in Fig. 1.

in finite populations. When population sizes are larger, we find that as little as 10% variation in local carrying capacity suffices to stabilize mating domains (Supplementary Fig. 5d). Levels of variation in this range may be difficult to detect in nature, especially if they are to be inferred from observing the stochastic spatial distribution of individuals.

The stabilizing effect of spatial variation in local carrying capacity and mate-search costs readily extends to more realistic and natural landscapes (Fig. 4) and also to three or more genotypes (Fig. 4c–d). As long as spatial variation in local carrying capacity does not become so insignificant that it hardly affects the landscape, or so asymmetric that a single local population dominates, different mating domains can be maintained in mosaic sympatry[17,18] (Supplementary Fig. 7). Our findings are also robust to changes in female-preference strength, mate-search distance, movement distance and competition distance (Supplementary Figs 5a and 6), to changes in the relative importance of ecological competition versus sexual selection (Supplementary Fig. 5b, c), to changes in the genetic architecture of the display and preference traits (Supplementary Fig. 8), and to the inclusion of selective differences between male display traits (Supplementary Fig. 9). Generally, long-term coexistence occurs if female preferences are sufficiently strong to prevent extensive interbreeding, and if individuals move and interact on a spatial scale such that they are affected by spatial variation in local carrying capacity. This phenomenon can be interpreted more generally: whenever positive frequency dependence creates multiple stable states, global coexistence of these states becomes possible in a spatially structured environment if this structure allows the domains in which those states are realized to become anchored in space. In this vein, our results in Fig. 4 extend a previous finding from theoretical work on hybrid zones, predicting that the spatial interface between species moves in space until settling in a region of low population density[19,20]. Similarly, previous theoretical work[21] using habitat boundaries for anchoring mating domains has shown that ecologically equivalent types can coexist when fecundity decreases, or mortality or mobility increase, in the company of heterospecifics.

Because both spatial variation in local carrying capacity and costs associated with mate search are ubiquitous in nature, our model may provide an explanation for the coexistence of many species whose reproductive barriers primarily involve mating preferences. For example, local habitat availability and quality vary around the shoreline of Lake Victoria[22]. The mechanism reported here could help explain how ecologically similar cichlid species can coexist in such vast diversity. That sexual differences have been a primary force maintaining cichlid species' boundaries is supported by the increasing frequency of hybridization that is occurring as a consequence of high turbidity levels, which reduce a female's ability to discern male phenotypes[22]. Similar explanations could plausibly be applied to other species that seem to be largely maintained by sexual selection (for example, species of fruitflies[23], weakly electric fish[24], frogs[25], crickets[3] and grasshoppers[26]). To test this hypothesis, one could analyse spatial associations between mating domains and local carrying capacity: Fig. 4 suggests that boundaries of mating domains often align with troughs of low local carrying capacity.

Our work demonstrates that, with variation in local carrying capacity over space and costs to females that encounter few preferred mates, sexual selection can maintain species that are not ecologically differentiated. This is in stark contrast to the widespread opinion that sexual selection, on its own, is unable to maintain ecologically equivalent species that overlap in space. Throughout this study, we have deliberately avoided making any claims about the emergence of diversity or speciation, choosing instead to focus on the coexistence of mating types. Further theoretical work is therefore needed to determine which conditions are most conducive to the initial appearance of multiple mating types, and further empirical work is needed to show how the mechanism presented here helps to explain natural patterns of coexistence and diversity.

METHODS SUMMARY

We develop an individual-based model of sexual selection[14] in a spatially explicit ecological framework. Individuals are distributed across a continuous habitat in one or two dimensions with wrap-around boundaries. All individuals compete for resources, whose density at any location is gi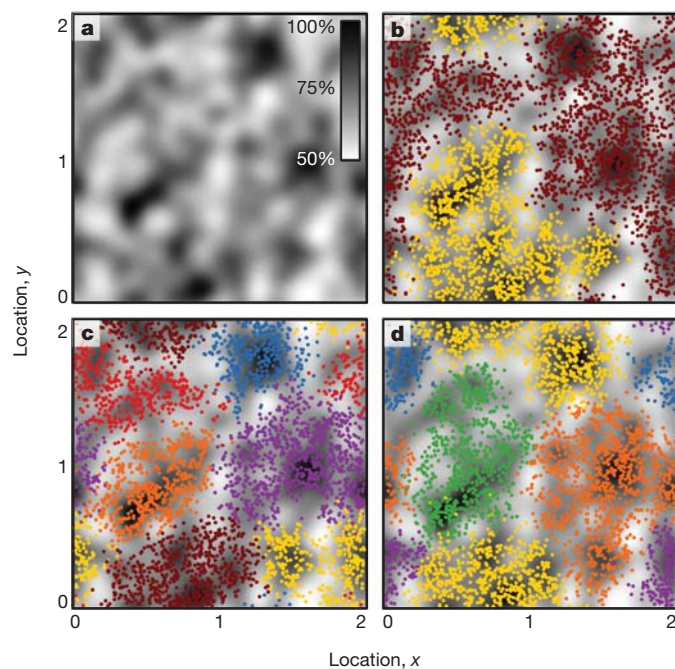ven by a local carrying capacity. Except where noted, the local carrying capacity exhibits two peaks, each of the same Gaussian shape. Competition reduces an individual's resource share, and thereby its survival probability, with the competitive impact of other individuals decreasing with distance according to a Gaussian function. Surviving females encounter surviving males with a probability decreasing with distance according to a Gaussian function, and females choose mates on the basis of their preferences for the males' displays. After mating, females produce offspring in proportion to their fecundities, which are lower for females who experienced higher mate-search costs. After producing offspring, the parents die and the offspring move a distance drawn from a Gaussian function in a direction chosen at random. Although the female preference trait and the male display trait are genetically based (each being determined by a diallelic locus, except where noted), there are no genetic differences in ecological function or competitive ability between individuals, which are therefore all ecologically equivalent. See Supplementary Information for complete model details and for information about alternative models explored to examine the robustness of our results.

Figure 4 | Mosaic sympatry. Four representative model runs in a patchy two-dimensional landscape with random variation in local carrying capacity. a, Underlying spatial variation in local carrying capacity. b–d, Results from independent model runs after 10,000 generations overlaid on the local carrying capacity; b is initialized with two types, whereas c and d are initialized with ten display alleles and ten corresponding preference alleles, all at equal frequencies and distributed randomly across the arena (Supplementary Information). Some of these alleles are then lost during the colonization phase. As in Fig. 1, individuals are coloured according to their genotype at the display locus. The spatial arena is eight times larger than in Fig. 1 and the total carrying capacity is $K = 4,000$, supporting the survival of approximately half of the $N = 8,000$ offspring produced each generation. All other parameters are as in Fig. 1 (except ν, which is defined specifically for bimodal landscapes); for comparison, the coefficient of variation in local carrying capacity is 0.125 here and 0.066 in Fig. 1d.

1. Eberhard, W. G. Sexual Selection and Animal Genitalia (Harvard Univ. Press, 1985).
2. Seehausen, O. & van Alphen, J. J. M. Can sympatric speciation by disruptive sexual selection explain rapid evolution of cichlid diversity in Lake Victoria? Ecol. Lett. 2, 262–271 (1999).

3. Gray, D. A. & Cade, W. H. Sexual selection and speciation in field crickets. *Proc. Natl Acad. Sci. USA* **97,** 14449–14454 (2000).
4. Wilson, A. B., Noack-Kunnmann, K. & Meyer, A. Incipient speciation in sympatric Nicaraguan crater lake cichlid fishes: sexual selection versus ecological diversification. *Proc. R. Soc. Lond. B* **267,** 2133–2141 (2000).
5. Turner, G. F. & Burrows, M. T. A model of sympatric speciation by sexual selection. *Proc. R. Soc. Lond. B* **260,** 287–292 (1995).
6. Panhuis, T. M., Butlin, R., Zuk, M. & Tregenza, T. Sexual selection and speciation. *Trends Ecol. Evol.* **16,** 364–371 (2001).
7. van Doorn, G. S., Dieckmann, U. & Weissing, F. J. Sympatric speciation by sexual selection: a critical reevaluation. *Am. Nat.* **163,** 709–725 (2004).
8. Johansson, J. & Ripa, J. Will sympatric speciation fail due to stochastic competitive exclusion? *Am. Nat.* **168,** 572–578 (2006).
9. Weissing, F. J., Edelaar, P. & van Doorn, G. S. Adaptive speciation theory: a conceptual review. *Behav. Ecol. Sociobiol.* **65,** 461–480 (2011).
10. Schluter, D. *The Ecology of Adaptive Radiation* (Oxford Univ. Press, 2000).
11. Fisher, R. A. *The Genetical Theory of Natural Selection* (Clarendon Press, 1930).
12. Lande, R. Models of speciation by sexual selection on polygenic traits. *Proc. Natl Acad. Sci. USA* **78,** 3721–3725 (1981).
13. Lande, R. Rapid origin of sexual isolation and character divergence in a cline. *Evolution* **36,** 213–223 (1982).
14. Kirkpatrick, M. Sexual selection and the evolution of female choice. *Evolution* **36,** 1–12 (1982).
15. Seger, J. Unifying genetic models for the evolution of female choice. *Evolution* **39,** 1185–1193 (1985).
16. Payne, R. J. H. & Krakauer, D. C. Sexual selection, space, and speciation. *Evolution* **51,** 1–9 (1997).
17. Mallet, J. Hybridization, ecological races and the nature of species: empirical evidence for the ease of speciation. *Phil. Trans. R. Soc. B* **363,** 2971–2986 (2008).
18. Mallet, J., Meyer, A., Nosil, P. & Feder, J. L. Space, sympatry and speciation. *J. Evol. Biol.* **22,** 2332–2341 (2009).
19. Barton, N. H. & Hewitt, G. M. Analysis of hybrid zones. *Annu. Rev. Ecol. Syst.* **16,** 113–148 (1985).
20. Barton, N. H. & Hewitt, G. M. Adaptation, speciation and hybrid zones. *Nature* **341,** 497–503 (1989).
21. Dieckmann, U. in *Adaptive Speciation* (eds Dieckmann, U., Metz, J. A. J., Doebeli, M. & Tautz, D.) 306–307 (Cambridge Univ. Press, 2004).
22. Seehausen, O., van Alphen, J. J. M. & Witte, F. Cichlid fish diversity threatened by eutrophication that curbs sexual selection. *Science* **277,** 1808–1811 (1997).
23. Hollocher, H., Ting, C., Pollack, F. & Wu, C. Incipient speciation by sexual isolation in *Drosophila melanogaster*: variation in mating preference and correlation between sexes. *Evolution* **51,** 1175–1181 (1997).
24. Feulner, P. G. D., Kirschbaum, F. & Tiedemann, R. Adaptive radiation in the Congo River: an ecological speciation scenario for African weakly electric fish (Teleostei; Mormyridae; *Campylomormyrus*). *J. Physiol. (Paris)* **102,** 340–346 (2008).
25. Ryan, M. J. & Wilczynski, W. Coevolution of sender and receiver: effect on local mate preference in cricket frogs. *Science* **240,** 1786–1788 (1988).
26. Tregenza, T., Pritchard, V. L. & Butlin, R. K. The origins of premating reproductive isolation: testing hypotheses in the grasshopper *Chorthippus parallelus*. *Evolution* **54,** 1687–1698 (2000).

Author Contributions U.D. and L.K.M. conceived this project. L.K.M., R.M., S.P.O. and U.D. discussed and designed the model. L.K.M. implemented the model with input from R.M., analysed the results together with R.M., S.P.O. and U.D. and prepared the manuscript. L.K.M., R.M., S.P.O. and U.D. jointly edited the manuscript.

Author Information Program code is available at www.zoology.ubc.ca/prog/coexist. Reprints and permissions information is available at www.nature.com/reprints. The authors declare no competing financial interests. Readers are welcome to comment on the online version of this article at www.nature.com/nature. Correspondence and requests for materials should be addressed to L.K.M. (mgonigle@zoology.ubc.ca).

LETTER

NLRP10 is a NOD–like receptor essential to initiate adaptive immunity by dendritic cells

Stephanie C. Eisenbarth[1]*, Adam Williams[2]*, Oscar R. Colegio[3], Hailong Meng[4], Till Strowig[2], Anthony Rongvaux[2], Jorge Henao-Mejia[2], Christoph A. Thaiss[2], Sophie Joly[5], David G. Gonzalez[1], Lan Xu[1,3], Lauren A. Zenewicz[2], Ann M. Haberman[1], Eran Elinav[2], Steven H. Kleinstein[4,6], Fayyaz S. Sutterwala[5,8] & Richard A. Flavell[2,7]

NLRs (nucleotide-binding domain leucine-rich-repeat-containing receptors; NOD-like receptors) are a class of pattern recognition receptor (PRR) that respond to host perturbation from either infectious agents or cellular stress[1,2]. The function of most NLR family members has not been characterized and their role in instructing adaptive immune responses remains unclear[2,3]. NLRP10 (also known as PYNOD, NALP10, PAN5 and NOD8) is the only NLR lacking the putative ligand-binding leucine-rich-repeat domain, and has been postulated to be a negative regulator of other NLR members, including NLRP3 (refs 4–6). We did not find evidence that NLRP10 functions through an inflammasome to regulate caspase-1 activity nor that it regulates other inflammasomes. Instead, $Nlrp10^{-/-}$ mice had a profound defect in helper T-cell-driven immune responses to a diverse array of adjuvants, including lipopolysaccharide, aluminium hydroxide and complete Freund's adjuvant. Adaptive immunity was impaired in the absence of NLRP10 because of a dendritic cell (DC) intrinsic defect in emigration from inflamed tissues, whereas upregulation of DC costimulatory molecules and chemotaxis to CCR7-dependent and -independent ligands remained intact. The loss of antigen transport to the draining lymph nodes by a subset of migratory DCs resulted in an almost absolute loss in naive $CD4^+$ T-cell priming, highlighting the critical link between diverse innate immune stimulation, NLRP10 activity and the immune function of mature DCs.

To elucidate the *in vivo* biological role of NLRP10, we generated mice deficient in NLRP10 (Supplementary Fig. 1a–c). $Nlrp10^{-/-}$ mice seemed healthy without evidence of autoimmunity or tumour formation, and had a normal composition and activation profile of immune cells including T and B lymphocytes in the periphery, bone marrow and thymus (data not shown). Peritoneal macrophages or bone-marrow-derived dendritic cells (BMDCs) from $Nlrp10^{-/-}$ mice stimulated with Toll-like receptor (TLR) agonists or NLRP3 inflammasome activators secreted normal levels of IL-1β, TNF-α and IL-6 (Supplementary Fig. 2a–c), indicating that loss of NLRP10 does not affect caspase-1 or NLRP3 inflammasome function. To test *in vivo* whether NLRP10 acts as a negative regulator of NLRs, we tested the ability of $Nlrp10^{-/-}$ mice to mount antigen-specific immune responses to ovalbumin (OVA) and aluminium hydroxide (alum) in a T-helper type 2 (T_H2)-driven asthma model[7,8] or complete Freund's adjuvant (CFA; mycobacteria-based) with myelin oligodendrocyte glycoprotein (MOG) peptide in the IL-17-producing T-helper cell (T_H17)-driven model of experimental autoimmune encephalomyelitis (EAE)[9]. Surprisingly, $Nlrp10^{-/-}$ mice had a profound defect in adaptive immunity in both models. T_H2 responses in the lung, lymph nodes (LN) and systemic antibody production were significantly reduced in $Nlrp10^{-/-}$ mice (Fig. 1a–c and Supplementary Fig. 3a). Similarly, most

$Nlrp10^{-/-}$ mice completely failed to develop signs of EAE and showed a marked reduction in MOG-specific IL-17 and IFN-γ production from the spleen, LNs and spinal cord (Fig. 1d–f and Supplementary Fig. 3b). Most surprisingly, immunization using only lipopolysaccharide (LPS) as an adjuvant in an intranasal T_H1/neutrophil airway inflammation model[10] was also defective in $Nlrp10^{-/-}$ mice (Fig. 1g). Together, these findings suggest that $Nlrp10^{-/-}$ mice have a global defect in adaptive immunity upon immunization with multiple adjuvants. Bone marrow chimaeric mice in which NLRP10 deficiency was limited to the haematopoietic compartment failed to respond to OVA/alum immunization, demonstrating that loss of NLRP10 in bone-marrow-derived cells was sufficient to recapitulate the phenotype (Fig. 2a–c).

To test if the $Nlrp10^{-/-}$ mice have a defect in T-cell-driven adaptive immune processes, we compared the immunization response to the hapten trinitrophenyl (TNP) linked to either keyhole limpet haemocyanin (KLH) or Ficoll. In this model, anti-TNP antibodies are generated by activated B cells in either a T-cell-dependent (KLH) or T-cell-independent (Ficoll) manner[11,12]. Anti-TNP IgG1 antibodies were severely diminished with TNP-KLH (Fig. 2d), but there was no defect in T-cell-independent IgG3 (Fig. 2e) antibody production to TNP-Ficoll. Therefore, $Nlrp10^{-/-}$ B cells are not intrinsically impaired but T-cell activation, either secondary to a T-cell-intrinsic or T-cell-extrinsic defect, is severely impaired in $Nlrp10^{-/-}$ mice. $Nlrp10^{-/-}$ T cells can be primed and differentiated into cytokine-producing helper T-cell subsets (Supplementary Fig. 4) *in vitro*. Furthermore, adoptively transferred T-cell receptor (TCR) transgenic, $Nlrp10^{-/-}$ OT-II T cells proliferated normally in wild-type hosts after cognate antigen immunization (OVA) (Supplementary Fig. 5). Therefore, we concluded that $Nlrp10^{-/-}$ mice fail to initiate adaptive immune responses, possibly because of a T-cell-extrinsic defect in antigen presentation.

To evaluate T-cell priming *in vivo*, we adoptively transferred carboxyfluorescein succinimidyl ester (CFSE)-labelled naive wild-type TCR transgenic OT-II T cells into wild-type and $Nlrp10^{-/-}$ mice. Following immunization with cognate protein antigen, these wild-type T cells divided in wild-type, but not $Nlrp10^{-/-}$, hosts (Fig. 2f), indicating that the injected antigen was not being presented to naive T cells in the absence of NLRP10. As dendritic cells are the primary antigen-presenting cell (APC) controlling the activation fate of naive T cells following immunization, we tested whether DC maturation was defective in $Nlrp10^{-/-}$ mice[13]. $Nlrp10^{-/-}$ BMDCs *in vitro* and splenic DCs *in vivo* upregulated all requisite stimulatory molecules necessary for effective T-cell priming, including major histocompatibility complex (MHC) class II and B7 family member CD86 following LPS exposure (Supplementary Fig. 6a, d and data not shown). Similarly,

[1]Department of Laboratory Medicine, Yale University School of Medicine, New Haven, Connecticut 06520, USA. [2]Department of Immunobiology, Yale University School of Medicine, New Haven, Connecticut 06520, USA. [3]Department of Dermatology, Yale University School of Medicine, New Haven, Connecticut 06520, USA. [4]Department of Pathology, Yale University School of Medicine, New Haven, Connecticut 06520, USA. [5]Inflammation Program, Department of Internal Medicine, University of Iowa, Iowa City, Iowa 52242, USA. [6]Interdepartmental Program in Computational Biology and Bioinformatics, Yale University School of Medicine, New Haven, Connecticut 06520, USA. [7]Howard Hughes Medical Institute, Yale University School of Medicine, New Haven, Connecticut 06520, USA. [8]Veterans Affairs Medical Center, Iowa City, Iowa 52241, USA.
*These authors contributed equally to this work.
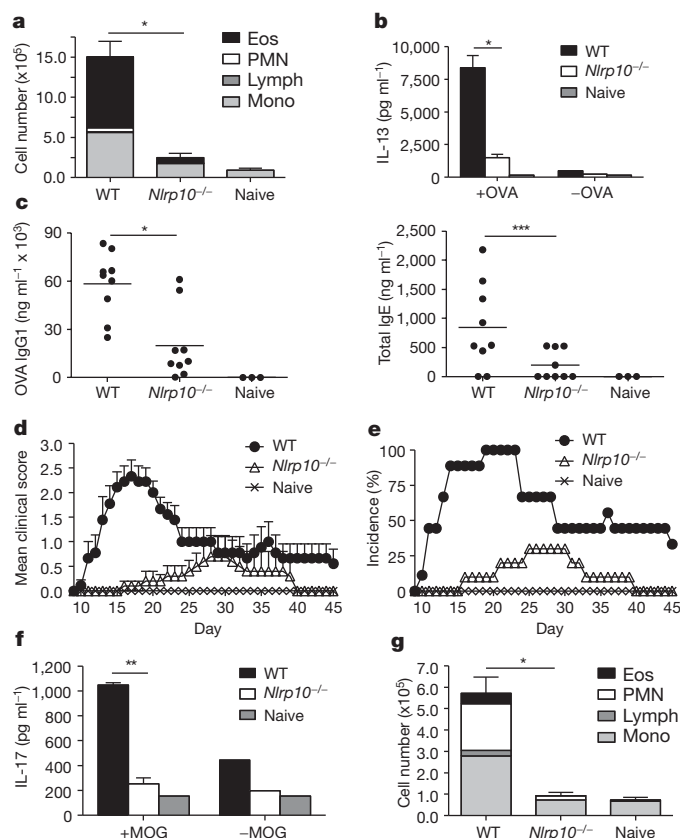
Figure 1 | Nlrp10^{−/−} mice have a global defect in adaptive immune responses. a–c, Bronchoalveolar lavage (a), mediastinal lymph node culture IL-13 (b) and serum antibodies (c) from wild-type (WT) and Nlrp10^{−/−} mice sensitized intraperitoneally with OVA/alum and challenged intranasally with OVA ($n = 3$–10 mice per group from one of five independent experiments). Eos, eosinophil; Lymph, lymphocyte; Mono, monocyte; PMN, neutrophil. d–f, Mean clinical paralysis score (d), percentage of mice with paralysis (e) and lymph node culture IL-17 concentration (f) from wild-type and Nlrp10^{−/−} mice following sensitization with MOG/CFA and pertussis toxin ($n = 8$–10 mice from one of three independent experiments). $P < 0.0001$ wild type versus Nlrp10^{−/−} by one-way ANOVA in d. g, Bronchoalveolar lavage from wild-type and Nlrp10^{−/−} mice sensitized and challenged intranasally with OVA/LPS ($n = 3$–5 mice per group). $*P < 0.0001$; $**P < 0.001$; $***P < 0.023$. All error bars show s.e.m.

Nlrp10^{−/−} DCs efficiently phagocytosed fluorescently labelled OVA *in vitro* (Supplementary Fig. 6b) and *in vivo* (Supplementary Fig. 6e). Antigen-pulsed Nlrp10^{−/−} BMDCs were also capable of activating naive CFSE-labelled wild-type OT-II T cells *in vitro* (Supplementary Fig. 6c). Therefore DC maturation following innate stimulation was

intact; yet, Nlrp10^{−/−} BMDCs loaded with protein antigen and adoptively transferred into mice harbouring CFSE-labelled naive OT-II T cells were unable to activate these T cells (Fig. 3a), indicating that the T-cell-priming defect in Nlrp10^{−/−} mice was due to a loss of DC–T-cell interactions. To test this, we used the traditional model of FITC (fluorescein isothiocyanate) skin painting to track migration of DCs from the skin to the LN[14]. FITC-painted Nlrp10^{−/−} mice contained few FITC⁺ DCs in the draining LN at 18 h, similar to mice lacking the critical LN homing chemokine receptor CCR7 (refs 14–16; Fig. 3b and Supplementary Fig. 7). However, FITC⁺ DCs were present in the ear in both wild-type and Nlrp10^{−/−} mice (data not shown), indicating that Nlrp10^{−/−} DCs were viable and capable of capturing antigen, but failed to reach the LN. Nlrp10^{−/−} mice also demonstrated a profound absence of antigen-containing DCs in the draining LN following subcutaneous injection of a fluorescently labelled antigen (0.5–5.0 µg OVA-AF647) at 18 h (Fig. 3c) or any time point evaluated out to 12 days following immunization (data not shown). This defect in antigen-containing DCs in the LN could be partially overcome in Nlrp10^{−/−} mice upon exposure to high antigen doses (50 µg OVA) (Fig. 3c), as previously observed in CCR7-deficient mice[14]. This is probably a result of passively drained antigen to the LN, which initiates weak T-cell responses[14,17]. Evaluation of mediastinal LNs after inhalation of particulate latex beads that cannot passively drain to LNs clearly indicated that Nlrp10^{−/−} DCs were unable to transport antigen to the draining LN, yet bead-containing DCs were present in the lung (Supplementary Fig. 8). Therefore Nlrp10^{−/−} mice have a profound defect in DC-dependent transport of antigen to lymph nodes. Lymphoid-tissue-resident CD8α⁺ and plasmacytoid DCs were not different between wild-type and Nlrp10^{−/−} mice (Supplementary Fig. 7 and data not shown), as would be expected, given that they enter the LN via the bloodstream. In contrast, migratory DCs which take antigen from inflamed tissue to the LN[18] and express high levels of MHC class II, but intermediate levels of CD11c, were affected by the loss of NLRP10. Specifically, within this group we found that the CD11b⁺CD207^{−}CD103^{−} DC subset, which is primarily responsible for priming helper T cells, is nearly absent in the LN of immunized Nlrp10^{−/−} mice (Supplementary Fig. 7), again similar to the defect observed in CCR7-deficient mice[14,19–21]. Consistent with the finding that antigen-containing mature DCs were present normally in the ear or lung of immunized Nlrp10^{−/−} mice (Supplementary Fig. 8), we found no DC subset deficiency in any non-lymphoid tissue from knockout mice (Supplementary Fig. 9), indicating that the development and migration of CD11b⁺ DCs to peripheral tissues is intact in the absence of NLRP10. To determine whether the defect in DC migration to the LN is cell intrinsic or extrinsic, we co-injected labelled activated wild-type and Nlrp10^{−/−} BMDCs into wild-type or Nlrp10^{−/−} host mice. Although wild-type DCs were found in the LN 18 h after subcutaneous injection, very few Nlrp10^{−/−} DCs were
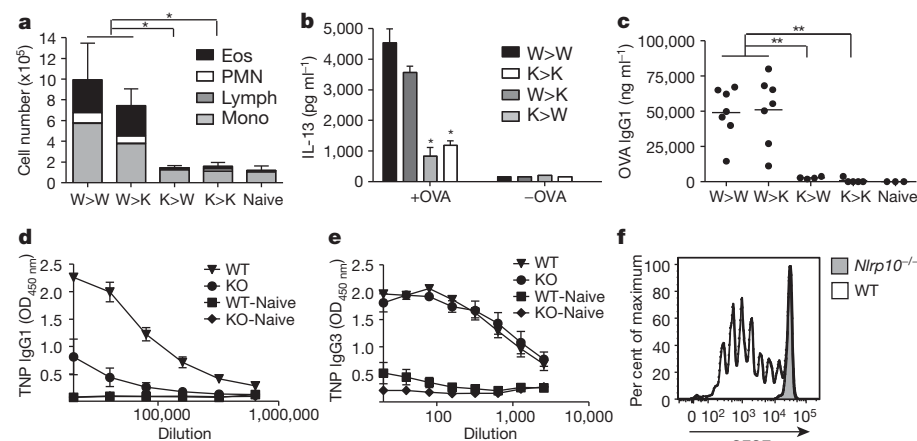
Figure 2 | Nlrp10^{−/−} mice cannot mount T-cell-dependent adaptive immune responses. a–c, Bronchoalveolar lavage (a), mediastinal lymph node culture (b) and serum antibody (c) from bone marrow chimaeras (donor>recipient; W, wild type; K, Nlrp10^{−/−}) immunized and challenged as in Fig. 1a–c ($n = 3$–7 mice per group from one of three independent experiments). d, Serum TNP-specific IgG1 in TNP-KLH-immunized wild-type or Nlrp10^{−/−} mice. $P < 0.0022$ by one-way ANOVA (KO, Nlrp10^{−/−}). e, TNP-specific IgG3 in TNP-Ficoll-immunized mice ($n = 3$–5 mice per group from one of two independent experiments, KO, Nlrp10^{−/−}). f, CFSE dilution of labelled wild-type OVA-specific OT-II T cells in the draining lymph node of wild-type or Nlrp10^{−/−} hosts 3 days after OVA/LPS immunization. One of three mice per group is shown. $*P < 0.033$, $**P < 0.0001$. All error bars show s.e.m.
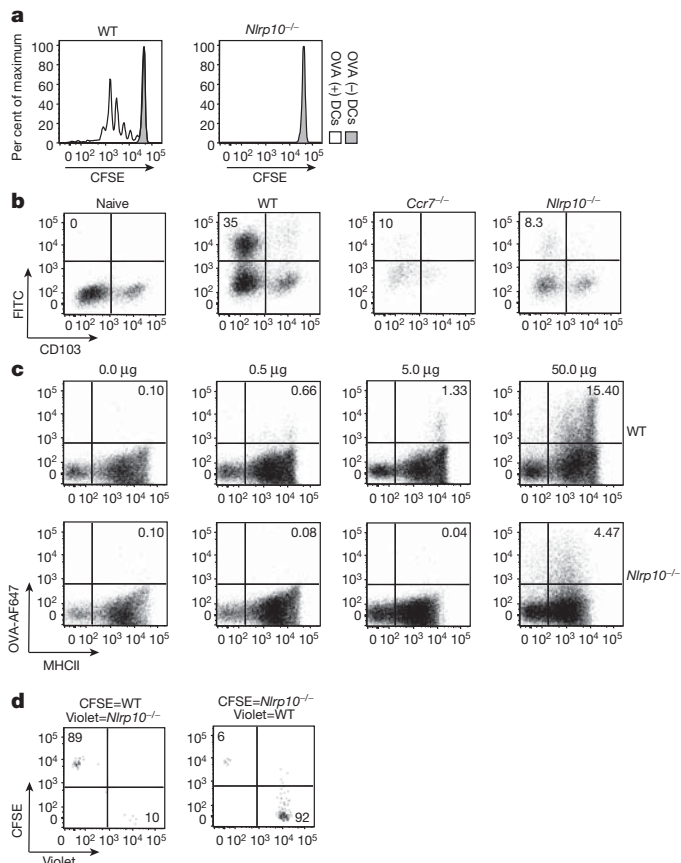
Figure 3 | *Nlrp10^{-/-}* dendritic cells do not take antigen to the draining lymph node. a, Dilution of lymph node CFSE+ OT-II T cells adoptively transferred into wild-type hosts 3 days after injection with wild-type or *Nlrp10^{-/-}* OVA-peptide-pulsed (solid line) or -unpulsed (shaded histogram) BMDCs. One of three mice per group is shown. **b**, FITC+ CD11c+MHCII^hi DCs in the draining LN of wild-type, *Ccr7^{-/-}* or *Nlrp10^{-/-}* mice painted with 1% FITC. One representative experiment out of four. **c**, CD11b+CD11c+ DCs in the LN of wild-type or *Nlrp10^{-/-}* mice injected with indicated doses of OVA-AF647 with LPS. One of three mice per group is shown. **d**, Wild-type and *Nlrp10^{-/-}* BMDCs were labelled with CFSE or CellTrace Violet and co-injected into CD45.1 mice with LPS. Inguinal lymph nodes were analysed for CD45.2+CD11c+MHCII+ BMDCs. One of two mice per group from one experiment of seven.

present (Fig. 3d), regardless of the presence or absence of NLRP10 in the host (Supplementary Fig. 10), confirming that *Nlrp10^{-/-}* DCs were incapable of reaching the LNs due to a cell-intrinsic defect. We conclude that NLRP10 is essential for DC-mediated transport of antigen to the LN from multiple peripheral sites following maturation by a wide range of innate stimuli.

Given the similarity of our findings to those described for CCR7-deficient mice, we postulated that *Nlrp10^{-/-}* DCs might have a defect in CCR7 expression. However, *Ccr7* messenger RNA (Supplementary Fig. 11a) and CCR7 surface expression (Fig. 4a) in LPS-treated *Nlrp10^{-/-}* BMDCs was equivalent to wild-type BMDCs. Consistent with CCR7 expression, *Nlrp10^{-/-}* DCs responded normally *in vitro* to a gradient of CCL19 and CCL21 as well as a CCR7-independent chemokine, CXCL12 (SDF-1), and the signalling sphingolipid S1P[14,22,23] in trans-well assays (Fig. 4b and Supplementary Fig. 11b, c), indicating that CCR7 sensing and signalling was intact and that general DC kinesis was not affected in *Nlrp10^{-/-}* mice. Despite the apparently normal homing properties of *Nlrp10^{-/-}* DCs *in vitro*, splenic DCs failed to relocalize to the T-cell zone in the spleen following LPS stimulation *in vivo* (Supplementary Fig. 12). DC relocalization requires numerous integrated steps, including emigration from the initial site of residence, the ability to home towards a chemokine
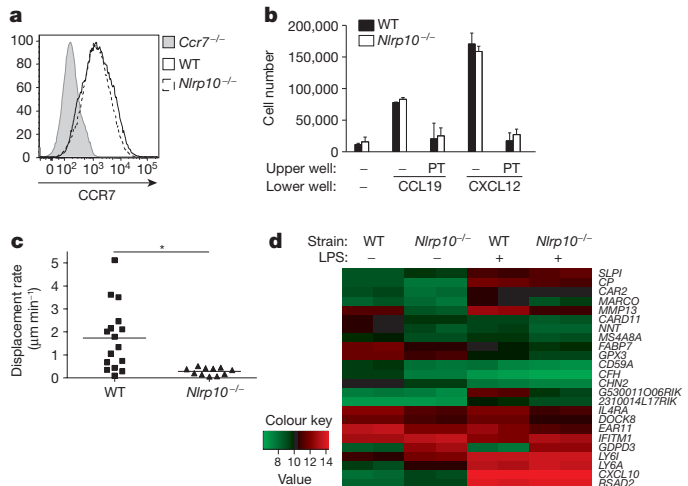
Figure 4 | *Nlrp10^{-/-}* dendritic cells cannot emigrate from inflamed tissue but remain responsive to chemokines. a, CCR7 surface expression on wild-type, *Ccr7^{-/-}* or *Nlrp10^{-/-}* BMDCs stimulated with LPS. One representative experiment out of two. **b**, Number of wild-type or *Nlrp10^{-/-}* LPS-treated BMDCs that migrated in a trans-well to CCL19 or CXCL12. Control BMDCs were treated with pertussis toxin (PT) before use. Representative of three experiments. All error bars show s.e.m. **c**, Cell-track displacement rate of BMDCs labelled with 5-(and-6)-(((4-chloromethyl)benzoyl)amino)tetramethylrhodamine (CMTMR; wild type) or CFSE (*Nlrp10^{-/-}*) co-injected into the ears of wild-type hosts and imaged 4 h later by intravital two-photon laser scanning microscopy; *P < 0.0012. **d**, Heat map of log_2-transformed gene expression values in *Nlrp10^{-/-}* and wild-type BMDCs treated with and without LPS.

gradient, transmigration through the lymphatic endothelial layer and the physical machinery to do so[15,24–26]. Yet, we found no defect in the ability of *Nlrp10^{-/-}* DCs to traverse an endothelial monolayer, to polymerize actin or general kinesis on a fibroblast cell layer (data not shown). As homing towards CCR7 ligands and S1P was intact *in vitro*, we postulated that NLRP10 regulates the emigration of DCs from inflamed tissue. To visualize DC movement *in vivo*, we used two-photon laser scanning microscopy to follow co-injected fluorescently labelled wild-type and *Nlrp10^{-/-}* DCs in wild-type hosts (Supplementary Movies 1 and 2). Tracking the movement of individual DCs within the tissue using Imaris software revealed that wild-type DCs actively moved away from the injection site and surveyed the surrounding tissue, whereas the majority of *Nlrp10^{-/-}* DCs remained near the site of injection despite their active extension of lamellipodia (Fig. 4c).

These experiments indicate that the loss of NLRP10 in DCs impairs their ability to exit inflamed tissues, suggesting a defect in a molecular pathway regulating the detachment of dendritic cells from extracellular matrix components. Yet, we did not observe altered surface expression of particular adhesion molecules including β1, β2 or β3 integrin chains, DC-SIGN nor altered *in vitro* adhesion to ICAM-1, ICAM-2, fibronectin or collagen I (data not shown). However, such surface expression or isolated *in vitro* adhesion assays will not reveal defects in chemokine receptor–integrin activation pathways. Therefore, to identify novel molecules potentially involved in NLRP10-dependent DC function, we used an unbiased gene array approach on *Nlrp10^{-/-}* BMDCs treated with or without LPS. We discovered that only 24 genes were differentially expressed (*q* value < 0.05 and absolute fold-change > 1.2) in *Nlrp10^{-/-}* DCs compared to wild-type DCs (Fig. 4d). Restricting the analysis to genes that were more than two-fold up/down regulated at baseline and after LPS stimulation revealed only three differentially expressed genes: *Il4ra*, *Mmp13* and *Gdpd3* (Supplementary Fig. 13). The first two genes identified were either not differentially expressed in *Nlrp10^{-/-}* DCs at the protein level or do not regulate DC-dependent immunization[27] (Supplementary Fig. 13a, b). We were most intrigued by the aberrant regulation of a molecule

with no known mammalian function—glycerophosphodiester phosphodiesterase domain containing 3 (GDPD3) (Supplementary Fig. 13c)—because its domain structure suggests that it has multiple transmembrane regions and structural homology to glycerophosphodiester phosphodiesterase 1 (GDE1). *Gdpd3* was more than 80-fold upregulated in *Nlrp10*$^{-/-}$ BMDCs, compared to wild-type DCs by real-time PCR (Supplementary Fig. 13c). GDPD family members catalyse the hydrolysis of glycerophosphoinositol, but in addition have functions in cell morphology, motility and G protein signalling downstream of chemokine receptors[28], indicating a potential link between NLR activity, phospholipid metabolism and the motility of mature DCs. Subsequent work characterizing GDPD3 will potentially provide important clues on how NLRP10 regulates a fundamental cellular process in DCs during inflammation. Although no other NLR or TLR reported to date affects adaptive immunity globally in this way, there is a growing body of literature to indicate that multiple NLRs and related signalling molecules are involved in controlling different aspects of DC function[29,30]. The finding that inhibition of a single NLR, NLRP10, can paralyse mature DCs could have a profound impact on the approach to treating misguided adaptive immune responses driving allergy and autoimmunity.

METHODS SUMMARY

For asthma models, mice were sensitized by either intraperitoneal injection of OVA/alum or intranasal OVA/LPS. Mice were then challenged intranasally with OVA. EAE was elicited using MOG peptide, CFA, heat-inactivated *Mycobacterium tuberculosis* and *Bordetella pertussis* toxin. For TNP immunizations, TNP-KLH or TNP-Ficoll was administered intraperitoneally and serum analysed for anti-TNP antibodies by ELISA. For intravenous LPS delivery, mice given LPS by retro-orbital injection were bled at 90 min and 6 h and serum analysed by ELISA. Spleens were analysed by flow cytometry at 6 h. For antigen tracing, Alexa Fluor 647-OVA and LPS were co-injected subcutaneously and 18 h later LNs were analysed by flow cytometry. For DC transfer labelled BMDCs were co-injected into the flank of wild-type mice, and draining LNs were analysed by flow cytometry. For *in vivo* OT-II T cell stimulation, OVA-peptide-loaded BMDCs were injected subcutaneously, and inguinal LNs collected 3 days later to evaluate T-cell proliferation. For intravital microscopy, labelled BMDCs were co-injected intradermally and imaged using an upright two-photon laser scanning microscope, and quantified using Imaris software. For gene expression analysis an Affymetrix Mouse Gene 1.0 ST Array was used.

Full Methods and any associated references are available in the online version of the paper at www.nature.com/nature.

1. Takeuchi, O. & Akira, S. Pattern recognition receptors and inflammation. *Cell* **140**, 805–820 (2010).
2. Williams, A., Flavell, R. A. & Eisenbarth, S. C. The role of NOD-like receptors in shaping adaptive immunity. *Curr. Opin. Immunol.* **22**, 34–40 (2010).
3. Medzhitov, R. & Janeway, C. A. Jr. Innate immune induction of the adaptive immune response. *Cold Spring Harb. Symp. Quant. Biol.* **64**, 429–436 (1999).
4. Imamura, R. *et al.* Anti-inflammatory activity of PYNOD and its mechanism in humans and mice. *J. Immunol.* **184**, 5874–5884 (2010).
5. Inohara, N. & Nunez, G. NODs: intracellular proteins involved in inflammation and apoptosis. *Nature Rev. Immunol.* **3**, 371–382 (2003).
6. Wang, Y. *et al.* PYNOD, a novel Apaf-1/CED4-like protein is an inhibitor of ASC and caspase-1. *Int. Immunol.* **16**, 777–786 (2004).
7. Eisenbarth, S. C., Colegio, O. R., O'Connor, W., Sutterwala, F. S. & Flavell, R. A. Crucial role for the Nalp3 inflammasome in the immunostimulatory properties of aluminium adjuvants. *Nature* **453**, 1122–1126 (2008).
8. Li, H., Willingham, S. B., Ting, J. P. & Re, F. Cutting edge: inflammasome activation by alum and alum's adjuvant effect are mediated by NLRP3. *J. Immunol.* **181**, 17–21 (2008).
9. Gris, D. *et al.* NLRP3 plays a critical role in the development of experimental autoimmune encephalomyelitis by mediating Th1 and Th17 responses. *J. Immunol.* **185**, 974–981 (2010).
10. Eisenbarth, S. C. *et al.* Lipopolysaccharide-enhanced, toll-like receptor 4-dependent T helper cell type 2 responses to inhaled antigen. *J. Exp. Med.* **196**, 1645–1651 (2002).
11. Bachmann, M. F., Hengartner, H. & Zinkernagel, R. M. T helper cell-independent neutralizing B cell response against vesicular stomatitis virus: role of antigen patterns in B cell induction? *Eur. J. Immunol.* **25**, 3445–3451 (1995).
12. Palm, N. W. & Medzhitov, R. Immunostimulatory activity of haptenated proteins. *Proc. Natl Acad. Sci. USA* **106**, 4782–4787 (2009).
13. Banchereau, J. & Steinman, R. M. Dendritic cells and the control of immunity. *Nature* **392**, 245–252 (1998).
14. Ohl, L. *et al.* CCR7 governs skin dendritic cell migration under inflammatory and steady-state conditions. *Immunity* **21**, 279–288 (2004).
15. Martin-Fontecha, A. *et al.* Regulation of dendritic cell migration to the draining lymph node: impact on T lymphocyte traffic and priming. *J. Exp. Med.* **198**, 615–621 (2003).
16. Saeki, H., Moore, A. M., Brown, M. J. & Hwang, S. T. Cutting edge: secondary lymphoid-tissue chemokine (SLC) and CC chemokine receptor 7 (CCR7) participate in the emigration pathway of mature dendritic cells from the skin to regional lymph nodes. *J. Immunol.* **162**, 2472–2475 (1999).
17. Itano, A. A. *et al.* Distinct dendritic cell populations sequentially present antigen to CD4 T cells and stimulate different aspects of cell-mediated immunity. *Immunity* **19**, 47–57 (2003).
18. Jakubzick, C. *et al.* Lymph-migrating, tissue-derived dendritic cells are minor constituents within steady-state lymph nodes. *J. Exp. Med.* **205**, 2839–2850 (2008).
19. Edelson, B. T. *et al.* Peripheral CD103$^+$ dendritic cells form a unified subset developmentally related to CD8α$^+$ conventional dendritic cells. *J. Exp. Med.* **207**, 823–836 (2010).
20. Ginhoux, F. *et al.* The origin and development of nonlymphoid tissue CD103$^+$ DCs. *J. Exp. Med.* **206**, 3115–3130 (2009).
21. Plantinga, M., Hammad, H. & Lambrecht, B. N. Origin and functional specializations of DC subsets in the lung. *Eur. J. Immunol.* **40**, 2112–2118 (2010).
22. Cyster, J. G. Chemokines, sphingosine-1-phosphate, and cell migration in secondary lymphoid organs. *Annu. Rev. Immunol.* **23**, 127–159 (2005).
23. Czeloth, N., Bernhardt, G., Hofmann, F., Genth, H. & Forster, R. Sphingosine-1-phosphate mediates migration of mature dendritic cells. *J. Immunol.* **175**, 2960–2967 (2005).
24. Dieu, M. C. *et al.* Selective recruitment of immature and mature dendritic cells by distinct chemokines expressed in different anatomic sites. *J. Exp. Med.* **188**, 373–386 (1998).
25. Gunn, M. D. *et al.* Mice lacking expression of secondary lymphoid organ chemokine have defects in lymphocyte homing and dendritic cell localization. *J. Exp. Med.* **189**, 451–460 (1999).
26. Sallusto, F. *et al.* Rapid and coordinated switch in chemokine receptor expression during dendritic cell maturation. *Eur. J. Immunol.* **28**, 2760–2769 (1998).
27. Noben-Trauth, N. *et al.* An interleukin 4 (IL-4)-independent pathway for CD4$^+$ T cell IL-4 production is revealed in IL-4 receptor-deficient mice. *Proc. Natl Acad. Sci. USA* **94**, 10838–10843 (1997).
28. Zheng, B., Berrie, C. P., Corda, D. & Farquhar, M. G. GDE1/MIR16 is a glycerophosphoinositol phosphodiesterase regulated by stimulation of G protein-coupled receptors. *Proc. Natl Acad. Sci. USA* **100**, 1745–1750 (2003).
29. Arthur, J. C. *et al.* Cutting edge: NLRP12 controls dendritic and myeloid cell migration to affect contact hypersensitivity. *J. Immunol.* **185**, 4515–4519 (2010).
30. Ippagunta, S. K. *et al.* The inflammasome adaptor ASC regulates the function of adaptive immune cells by controlling Dock2-mediated Rac activation and actin polymerization. *Nature Immunol.* **12**, 1010–1016 (2011).

Author Contributions S.C.E. and A.W. wrote the manuscript, designed, performed and interpreted experiments with technical assistance from L.X., F.S.S. generated *Nlrp10*$^{-/-}$ mice, S.J. performed *in vitro* inflammasome activation, O.R.C. and J.H.-M. assisted with trans-well assays and performed real-time PCR, L.A.Z. assisted with EAE experiments, T.S. assisted with TNP immunizations, A.R. assisted with intravenous LPS experiments, E.E. provided technical assistance with DC isolations, C.A.T. performed immunofluorescence experiments, H.M. and S.H.K. performed array analysis, D.G. and A.M.H. performed intravital microscopy and quantification. R.A.F. assisted in experimental design and interpretation. S.C.E. and R.A.F. directed the project.

METHODS

Materials. All reagents were purchased from Sigma except Imject alum (Pierce) and incomplete Freund's adjuvant (IFA) (Difco) unless indicated otherwise. Antibody pairs for ELISA were purchased from R&D Systems (IL-1β), BD Pharmingen (IL-5, IL-6, IL-17 and IFN-γ) or from eBioscience (TNF-α). OVA-specific IgG1 was measured by ELISA as previously described[10] and secondary antibodies were purchased from BD Pharmingen. TNP-specific IgG3 and IgG1 was performed as above with TNP-OVA used for coating instead of OVA and horseradish-peroxidase-conjugated secondary antibodies (Bethyl).

Mice. To generate mice specifically deficient in *Nlrp10*, exons 2 and 3 of the *Nlrp10* gene, containing the translation-initiation codon ATG, were replaced by a *neo* cassette flanked by two *loxP* sites (Supplementary Fig. 1a). The *Nlrp10*-targeting vector was electroporated into C57BL/6 embryonic stem (ES) cells (Bruce4). Homologous recombinant ES cells were identified by Southern blot analysis and were microinjected into BALB/c blastocysts. Chimaeric offspring were back-crossed to C57BL/6 mice, and germline transmission was confirmed by PCR of tail genomic DNA. Screening of *Nlrp10*$^{-/-}$ mice with the primers 5′-TAG AGTGGATACCCAGCACACACG-3′ and 5′-CATCTCGTAAGTGGAACTTC AGCG-3′ amplifies a 700-base pairs product from the wild-type allele; primers 5′-TAGAGTGGATACCCAGCACACACG-3′ and 5′-AACGAGATCAGCAGC CTCTGTTC-3′ amplify a 594-bp product from the targeted allele. RT–PCR analysis of complementary DNA isolated from *Nlrp10*$^{+/+}$ and *Nlrp10*$^{-/-}$ splenocytes confirmed the absence of *Nlrp10* mRNA in *Nlrp10*$^{-/-}$ mice. Primers used for RT–PCR analysis were as follows: *Nlrp10*, 5′-GGAGCTTGTAGACTACCTCA-3′, 5′-AAAGTCTCCACATCGACAGG-3′; *Hprt*, 5′-GTTGGATACAGGCCA GACTTTGTTG-3′, 5′-GAGGGTAGGCTGGCCTATAGGCT-3′.

The generation of mice deficient in NLRP3 have been reported previously[31]. Age and sex-matched C57BL/6 (CD45.2) mice from the National Cancer Institute were used as all wild-type controls. All naive mice were C57BL/6 unless otherwise indicated in the figure. RAG1-deficient (B6.129S7-Rag1^{tm1Mom}/J) and OT-II (B6.Cg-Tg(TcraTcrb)425Cbn/J) and CCR7-deficient mice were purchased from Jackson Labs. OT-II mice were crossed onto the *Rag1*$^{-/-}$ and CD45.1 (B6Ly5.2Cr) background from NCI. All protocols used in this study were approved by the Yale Institutional Animal Care and Use Committee.

Asthma model. For intraperitoneal sensitization, 6–8-week-old mice were injected intraperitoneally on day 0 with 50 μg of ovalbumin (Grade V; Sigma) adsorbed on 2 mg of Imject alum and again on day 10 with 25 μg of ovalbumin adsorbed on 2 mg of Imject alum. Mice were challenged intranasally with 25 μg of ovalbumin in PBS on days 21, 22 and 23 and killed for analysis on day 25. For sensitization by inhalation, 100 μg Ova with an additional 0.05 μg LPS in 50 μl PBS was given intranasally on days 0, 1 and 2 as previously described[10]. Mice were challenged intranasally with 25 μg of Ova in PBS on days 14, 15, 18 and 19 and killed on day 21 for analysis. Naive mice (wild type) were not sensitized intraperitoneally but received an intranasal OVA challenge.

Bronchoalveolar lavage analysis. Mice were primed and challenged as indicated. On the day of analysis, mice were killed and bronchoalveolar lavage was performed as described previously[32]. In brief, inflammatory cells in the airways were obtained by cannulation of the trachea and lavage of the airway lumen with 3 ml PBS. Red blood cells were lysed and total cell numbers were counted with a haemocytometer and cytospin slides were prepared by haematoxylin and eosin staining with Diff-Quick (Dade Behring).

***Ex vivo* lymphocyte restimulation.** Draining lymph nodes (inguinal or mediastinal) were removed and single-cells suspensions were generated. 5×10^6 ml^{-1} lymph node cells were cultured with 5×10^6 ml^{-1} antigen-presenting cells (see below) in the presence or absence of 200 μg ml^{-1} of OVA for 48 h. Syngeneic T-cell-depleted splenocytes were used as antigen-presenting cells and were prepared by complement lysis using antibodies to CD4 (GK1.5), CD8 (TIB105) and Thy1 (Y19), followed by treatment with mitomycin C.

Experimental autoimmune encephalomyelitis model. EAE was elicited and scored as previously described[33]. Briefly, on day 0 mice received bilateral subcutaneous flank injection of 50 μg of MOG (MEVGWYRSPFSRVVHLYRNGK) peptide in complete Freund's adjuvant (CFA) containing 500 μg of heat-inactivated *Mycobacterium tuberculosis* (Difco Labs). A dose of 200 ng of *Bordetella pertussis* toxin (PT; LIST Biological Labs) was injected intraperitoneally on days 0 and 2. Mice were monitored daily and scored as follows: 1, flaccid tail; 2, partial unilateral hindlimb paralysis or inability to right; 3, complete unilateral hindlimb paralysis; 4, complete bilateral hindlimb paralysis; and 5, moribund. After disease resolution (a majority of the paralysis resolved), mice were challenged with 50 μg MOG peptide intraperitoneally with 200 ng PT in PBS. 4 days later, spleen and inguinal LNs were collected, pooled and 5×10^6 cells were stimulated with 10 μg ml^{-1} MOG peptide and an equal number of syngeneic T-cell-depleted splenocytes (as described above). 48 h later, supernatant was collected for cytokine analysis by ELISA. Naive mice (wild type) did not receive MOG peptide.

TNP model. 300 μg TNP-KLH (29:1) and 100 μg TNP-Ficoll (90:1) (both from Biosearch Technologies) were administered intraperitoneally in PBS on day 0 and 14. Mice were killed on day 30 and anti-TNP antibodies were analysed by ELISA from serum.

Intravenous LPS model. Mice were given 25 μg of LPS by retro-orbital injection. Mice were bled at 90 min and 6 h and spleens were removed at 6 h. Spleens were treated with collagenase D (Roche) at 37 °C for 45 min, red blood cells were lysed and samples were stained and analysed by flow cytometry. Blood was allowed to clot at room temperature, serum isolated and analysed by ELISA.

Subcutaneous OVA-AF647. Indicated amounts of Alexa Fluor 647-OVA (OVA-AF647, Molecular Probes) were injected with 10 μg LPS subcutaneously in the flank bilaterally of wild-type and *Nlrp10*$^{-/-}$ mice. 18 h post injection inguinal lymph nodes were removed, digested with collagenase D for 1 h at 37 °C and stained for flow cytometry analysis.

DC transfer experiments. BMDCs were labelled with either 2 μM CFSE or 2 μM CellTrace Violet at 37 °C for 5 min. 3×10^6 labelled BMDCs were mixed in equal numbers and injected into each flank of CD45.1 C57BL/6 mice. After 1 day, draining inguinal lymph nodes were removed, digested with collagenase D for 1 h at 37 °C before antibody staining and analysis by flow cytometry. For *in vivo* OT-II T-cell stimulation, wild-type or *Nlrp10*$^{-/-}$ BMDCs were loaded for 1 h with OVA peptide (ISQAVHAAHAEINEAGR) or nothing, extensively washed and 1×10^6 were injected subcutaneously in the flank. Inguinal LNs were harvested 3 days later to evaluate T-cell proliferation.

Bone marrow chimaeras. Bone marrow was flushed from femurs, red cells were lysed and filtered through a 70-μm filter. 1×10^6 cells in 100 μl PBS were delivered by retro-orbital injection into lethally irradiated (1,000 rad) mice. For 2 weeks post engraftment mice were maintained on antibiotics and 2 weeks after transplant, chimaerism was assessed using congenic CD45 markers. All mice used in the experiments demonstrated at least 92% haematopoietic engraftment.

T-cell proliferation studies. From the spleen and LNs of OT-II transgenic mice on a RAG1-deficient background, CD4$^+$ cells were prepared by positive selection using CD4 Miltenyi beads (L3T4) as per the manufacturer's instructions. CD4-positive cells were labelled with CFSE (2 μM; Molecular Probes) for 5 min at 37 °C and then washed once in FBS and twice with PBS. For *in vivo* studies 3×10^6 cells were transferred into mice by retro-orbital injection. After 1 day, mice were challenged by subcutaneous injection of 0.25 μg OVA protein with either 100 μl CFA or 5 μg LPS in each flank and 3 days later, inguinal LNs were removed and analysed by flow cytometry. For *in vitro* studies 1×10^5 OT-II T cells were stimulated with 1×10^4 wild-type or *Nlrp10*$^{-/-}$ BMDCs loaded with 100 μg OVA or BSA in a 96-well plate for 3 days.

***In vitro* T-cell activation and skewing.** For *in vitro* T-cell skewing, polyclonal wild-type or *Nlrp10*$^{-/-}$ T cells were stimulated with plate-bound anti-CD3 (10 μg ml^{-1}) and anti-CD28 (2 μg ml^{-1}). T-cell skewing was accomplished for T$_H$1 cultures with IL-12 (3.5 ng ml^{-1}), IL-2 (0.1 ng ml^{-1}) and anti-IL-4 (10 μg ml^{-1}); for T$_H$2 cultures with IL-4 (20 ng ml^{-1}), IL-2 (0.1 ng ml^{-1}) and anti-IFN-γ (10 μg ml^{-1}); for T$_H$17 cultures with IL-6 (20 ng ml^{-1}), IL-23 (20 ng ml^{-1}), TGF-β (0.5 ng ml^{-1}) and anti-IFN-γ (10 μg ml^{-1}; XMG1.2) and anti-IL-4 (10 μg ml^{-1};11B11). After 5 days, cells were collected and restimulated with plate-bound anti-CD3 (10 μg ml^{-1}) for 8 h and supernatant was analysed by ELISA.

Flow cytometry protocols and antibodies. CD11b (M1/70), CD45.1 (A20), Valpha2 TCR (B20.1), CD4 (RM4-5), CD19 (6D5), CD3e (145-2C11), CD86 (GL1) flow cytometry antibodies were from BD. CD11c (N418), CD45.2 (104), B220 (RA3-6B2) were from Biolegend. I^{A}I^E (M5/114.15.2) was from eBioscience. Intracellular cytokine staining was done using the BD Cytofix/Cytoperm kit and according to manufacturer's protocol. IL-17A (TC11-18H10) and IFN-γ (XMG1.2) were both from BD. 5-(and-6)carboxyfluorescein diacetate, succinimidyl ester (CFSE) was from Invitrogen. CCR7 staining was performed on BMDCs after FcR blocking using a phycoerythrin-conjugated anti-CD197 (clone 4B12) antibody from BD Pharmingen at 1:100 at 37 °C for 40 min.

***In vitro* DC and macrophage stimulation.** The generation of thioglycollate-elicited peritoneal and bone-marrow-derived macrophages and bone-marrow-derived dendritic cells has been described previously[31,34]. For Supplementary Fig. 2a, cells were primed by stimulating with 50 ng ml^{-1} LPS from *Escherichia coli* serotype 0111:B4 (InvivoGen) for 16–18 h before stimulation ATP or alum. For ATP-stimulated cells, the medium was changed at 20 min. and all stimulants were replaced. All other TLR ligands were used at the concentration indicated in the figure legend. Type A CpG (InvivoGen), heat-killed *M. tuberculosis* (Difco), PolyI:C (Amersham) and Imiquimod (R837; InvivoGen). To assess antigen processing, BMDCs were incubated with 2 μg ml^{-1} Alexa Fluor 647-OVA for 1 h at 37 or 4 °C. Cells were then washed, stained with antibodies and analysed by flow cytometry.

Relative gene expression analysis. RNA from cells was isolated using TRIzol (Invitrogen) and RNA was subjected to reverse transcriptase with Superscript II (Invitrogen) with oligo(dT) primer in accordance with the manufacturer's protocol. cDNA was quantified using commercially available primer/probe sets (Applied Biosystems) by real-time PCR and analysed with the ΔC_t (change in cycle threshold) method. All results were normalized to *Hprt* quantified in parallel amplification reactions during each PCR quantification. Results are presented as levels relative to *Hprt*. The following primer/probes were used: *Ccr7* Mm1301785_m1, *Gdpd3* Mm00470322_m1, *Il4ra* Mm00439634_m1, *Mmp13* Mm00439491_m1, *Hprt* Mm00446968_m1.

Intravenous antigen injection. 5 μg of Alexa Fluor 647-OVA (molecular probes) was administered intravenously by retro-orbital injection. After 4 h spleens were harvested and treated with collagenase D and DNase I at 37 °C for 45 min, red blood cells were lysed and samples were stained and analysed by flow cytometry.

Intranasal latex bead delivery. Yellow-green fluorescent 0.5-μm latex particles (Polysciences) were diluted 1/25 in PBS and 50 μl was administered intranasally with 1 μg LPS[35]. 18 h later draining mediastinal lymph nodes were harvested and digested with collagenase D before staining and analysis by flow cytometry. In parallel, lung was minced into small pieces, incubated with a cocktail of 150 U ml^{-1} collagenase type I (Worthington Biochemical Corp) and 20 μg ml^{-1} DNase I in media supplemented with 10% FBS for 30 min at 37 °C. After passing through a 70-μm mesh, the single-cell suspension was stained and analysed by flow cytometry.

FITC painting. The ventral portion of each ear was painted with 20 μl of 1% fluorescein isothiocyanate (FITC) in carrier solution (1:1 v/v acetone:dibutyl phthalate)[14,23]. After 18 h draining lymph nodes were collected, digested with collagenase D, stained and analysed by flow cytometry. In parallel, ears were split into dorsal and ventral halves and floated dermal side down on dispase (2 mg ml^{-1}, Roche) for 30 min at 37 °C. Ears were then minced and incubated in the presence of collagenase D (5 mg ml^{-1}), DNase I (0.1 mg ml^{-1}) and hyaluronidase (2 mg ml^{-1} MP Biomedicals) for 30 min at 37 °C. After passing through a 70-μm mesh the resulting single-cell suspension was stained and analysed by flow cytometry.

Trans-well assay. BMDCs stimulated with LPS (1 μg ml^{-1}) overnight were harvested, washed twice in ice-cold PBS before suspension in RPMI supplemented with 0.1% fatty acid-free BSA (Sigma). Chemokines were suspended in RPMI supplemented with 0.1% fatty acid free BSA at 100 ng ml^{-1}. 600 μl of each was added into a 24-well non-tissue-culture-treated plate containing a 6.5 mm Transwell insert with a 5.0-μm pore size (Corning), and allowed to equilibrate for 30–45 min in tissue culture incubator before the addition of 100 μl of cells at a concentration of 1×10^7 ml to the upper chamber. After 3 h migrated cells were harvested from the lower chamber and counted using a haemocytometer. For pertussis toxin treatment cells were cultured overnight in the presence of pertussis toxin (100 ng ml^{-1}). For controls BMDCs were in media containing respective chemokines before adding to the upper chamber.

Intravenous LPS and spleen immunofluorescence staining. Wild-type and *Nlrp10*$^{-/-}$ mice were injected with 5 μg of LPS and after 4 h spleens were removed and fixed with 4% PFA solution for 4 h at 4 °C and then treated with increasing concentrations of sucrose (up to 30% in PBS) overnight. Organs were embedded in O.C.T. compound (Sakura), and 5-μm cryosections from frozen tissue blocks were prepared using a cryostat (Leica) at a working temperature of −19 °C. Frozen sections were blocked in 5% fetal bovine serum for 30 min at room temperature. Slides were incubated at 4 °C with primary antibodies to CD3 (clone17A2, BD Pharmingen) and CD11c (biotinylated, clone HL3, BD Pharmingen) followed by incubation with AlexaFluor 647-labelled chicken anti-rat IgG (Molecular Probes) and phycoerythrin-labelled streptavidin Biolegend) for 2 h at room temperature. Slides were then dried and mounted using ProLong Antifade mounting medium (Invitrogen). Images were acquired on a PerkinElmer Ultraview Spinning disk confocal microscope and images were processed using Volocity software (PerkinElmer).

Intravital microscopy. BMDCs stimulated with LPS (1 μg ml^{-1}) overnight were harvested, washed twice in ice-cold PBS before staining with either CFSE or CMTMR (Molecular Probes). After washing twice with fetal calf serum and twice with PBS, 0.5×10^5–1×10^5 cells in 10 μl of PBS and 2.5 μg LPS were injected intradermally into each ear (with or without an equal mixture of unlabelled DCs). Imaging of dendritic cell motility in ear skin of mice was performed using an upright two-photon laser scanning microscope. For image acquisition, an Olympus BX61WI fluorescence microscope with a ×20, 0.95 numerical aperture

(NA) water immersion Olympus objective and dedicated single-beam LaVision TriM laser scanning microscope (LaVision Biotec) was controlled by Imspector software. The microscope was outfitted with a Chameleon Vision II Ti:Sapphire laser (Coherent) with pulse pre-compensation. Emission wavelengths of 390–480 nm (blue, for second harmonic generation emissions), 500–550 nm (green, CFSE), and 565–665 nm (orange-red, for CMTMR) were collected with an array of three photomultiplier tubes (Hamamatsu). Mice were anaesthetized with an intraperitoneal injection of ketamine (100 mg kg^{-1}) and xylazine (10 mg kg^{-1}) before shaving and denuding ear skin with Nair. After prepping, the anaesthetized mouse was placed on a custom-designed stereotaxic restraint platform with ear bars, a nose clamp and an incisor bar to immobilize the mouse for skin imaging. A plane of deep anaesthesia was maintained using a mixture of isofluorane gas and oxygen delivered via a nosecone. Image stacks of 15 optical sections with a 400-μm field of view and 3-μm z-spacing were acquired every 30 s for 60–80 min. The two-photon laser was tuned to a wavelength of 850 nm. Volocity software (Improvision) was used to create QuickTime formatted movies of image sequences. All movies are displayed as two-dimensional maximum intensity projections of the time-resolved image stacks. The displacement rate of cells in the four-dimensional image data sets was determined using an automatic cell tracking algorithm in Imaris software (Bitplane/Perkin Elmer). All cell tracks were individually examined to confirm that they reported the behaviour of a single cell. Only viable cells with track origins at least 10 μm from an injection site were included in quantitative analysis.

Statistical analysis. We performed statistical analysis using a one-way ANOVA with a Bonferroni multiple comparison post test unless otherwise indicated. We considered $P < 0.05$ to be statistically significant. Error bars represent s.e.m. of samples within a group. In the case of all BAL data, the total BAL number was used to generate these error bars.

Affymetrix array. DNA microarray analysis was performed on two independent samples of four different populations (1) wild-type BMDCs, (2) wild-type BMDCs treated overnight with LPS (1 μg ml^{-1}), (3) *Nlrp10*$^{-/-}$ BMDCs, and (4) *Nlrp10*$^{-/-}$ BMDCs treated overnight with LPS (1 μg ml^{-1}). RNA was isolated with a Qiagen RNeasy MiniKit and was hybridized to Mouse Gene 1.0 ST Array (Affymetrix) at the Yale Keck Microarray Facility. The microarray analysis was carried out with packages in R (R Development CoreTeam, 2010). Raw microarray data in CEL file format were read in and normalized with the RMA method provided by the R oligo package. Differential gene expression was defined by two criteria: (1) an absolute fold-change ≥ 1.2 of knockout samples relative to wild-type samples and (2) a statistically significant change in expression as determined by LIMMA with a Benjamani–Hochberg false discovery rate cutoff $q < 0.05$. The microarray data discussed in this publication have been deposited in NCBI's Gene Expression Omnibus[36] and are accessible through GEO Series accession number GSE36009 (http://www.ncbi.nlm.nih.gov/geo/query/acc.cgi?acc=GSE36009).

Western blot analysis. Electrophoresis of proteins was performed with the NuPAGE system (Invitrogen) in accordance with the manufacturer's protocol. In brief, BMDCs were suspended in lysis buffer (Cell Signaling) containing a protease inhibitor cocktail (Roche). Lysates from an equal number of BMDCs were separated on a NuPAGE gel and transferred to a PVDF (poly(vinylidene difluoride)) membrane by electroblotting. To detect MMP13, rabbit polyclonal anti-MMP13 antibody (ab39012) from Abcam was used.

31. Sutterwala, F. S. *et al.* Critical role for NALP3/CIAS1/cryopyrin in innate and adaptive immunity through its regulation of caspase-1. *Immunity* **24**, 317–327 (2006).
32. Cohn, L., Homer, R. J., Niu, N. & Bottomly, K. T helper 1 cells and interferon γ regulate allergic airway inflammation and mucus production. *J. Exp. Med.* **190**, 1309–1318 (1999).
33. Laouar, Y. *et al.* TGF-β signaling in dendritic cells is a prerequisite for the control of autoimmune encephalomyelitis. *Proc. Natl Acad. Sci. USA* **105**, 10865–10870 (2008).
34. Lutz, M. B. *et al.* An advanced culture method for generating large quantities of highly pure dendritic cells from mouse bone marrow. *J. Immunol. Methods* **223**, 77–92 (1999).
35. Jakubzick, C., Helft, J., Kaplan, T. J. & Randolph, G. J. Optimization of methods to study pulmonary dendritic cell migration reveals distinct capacities of DC subsets to acquire soluble versus particulate antigen. *J. Immunol. Methods* **337**, 121–131 (2008).
36. Edgar, R., Domrachev, M. & Lash, A. E. Gene Expression Omnibus: NCBI gene expression and hybridization array data repository. *Nucleic Acids Res.* **30**, 207–210 (2002).

LETTER

Pathogen–induced human T_H17 cells produce IFN–γ or IL–10 and are regulated by IL–1β

Christina E. Zielinski[1]†, Federico Mele[1], Dominik Aschenbrenner[1], David Jarrossay[1], Francesca Ronchi[1], Marco Gattorno[2], Silvia Monticelli[1], Antonio Lanzavecchia[1,3] & Federica Sallusto[1]

IL-17-producing CD4$^+$ T helper cells (T_H17) have been extensively investigated in mouse models of autoimmunity[1]. However, the requirements for differentiation and the properties of pathogen-induced human T_H17 cells remain poorly defined. Using an approach that combines the *in vitro* priming of naive T cells with the *ex vivo* analysis of memory T cells, we describe here two types of human T_H17 cells with distinct effector function and differentiation requirements. *Candida albicans*-specific T_H17 cells produced IL-17 and IFN-γ, but no IL-10, whereas *Staphylococcus aureus*-specific T_H17 cells produced IL-17 and could produce IL-10 upon restimulation. IL-6, IL-23 and IL-1β contributed to T_H17 differentiation induced by both pathogens, but IL-1β was essential in *C. albicans*-induced T_H17 differentiation to counteract the inhibitory activity of IL-12 and to prime IL-17/IFN-γ double-producing cells. In addition, IL-1β inhibited IL-10 production in differentiating and in memory T_H17 cells, whereas blockade of IL-1β *in vivo* led to increased IL-10 production by memory T_H17 cells. We also show that, after restimulation, T_H17 cells transiently downregulated IL-17 production through a mechanism that involved IL-2-induced activation of STAT5 and decreased expression of ROR-γt. Taken together these findings demonstrate that by eliciting different cytokines *C. albicans* and *S. aureus* prime T_H17 cells that produce either IFN-γ or IL-10, and identify IL-1β and IL-2 as pro- and anti-inflammatory regulators of T_H17 cells both at priming and in the effector phase.

T_H17 cells participate in host defence against fungi and extracellular bacteria[2]. Patients with genetic defects in the T_H17 axis suffer from recurrent infections with *Candida albicans* and *Staphylococcus aureus*[3–5]. Understanding the regulation of T_H17 differentiation induced by these pathogens is therefore of both fundamental and clinical relevance.

The requirements for T_H17 differentiation in humans have been studied using polyclonal activators and recombinant cytokines. Here, we developed an antigen-specific T-cell-priming approach using whole microbes and monocytes as antigen-presenting cells. This approach takes advantage of the complexity of the microbes that provide, at the same time, a large number of antigens and a variety of stimuli for innate receptors to elicit polarizing cytokines. When carboxyfluorescein succinimidyl ester (CFSE)-labelled human naive CD4$^+$ T cells were cultured with autologous monocytes pulsed with *C. albicans* or *S. aureus*, antigen-specific proliferating T cells could be detected after 12 days in microbe-stimulated cultures, but not in cultures performed in the presence of antibodies blocking major histocompatibility complex (MHC) class II molecules (Supplementary Fig. 1a, b). In both *C. albicans*- and *S. aureus*-primed cultures a substantial fraction of proliferating cells acquired the capacity to produce IL-17 and IL-22, and expressed ROR-γt and CCR6, which are characteristics of T_H17 cells[6,7] (Fig. 1a and Supplementary Fig. 1c). Interestingly, in *C. albicans*-primed cultures most IL-17-secreting cells also produced IFN-γ and expressed ROR-γt and T-bet, whereas in

S. aureus-primed cultures most IL-17-secreting cells did not produce IFN-γ and did not express T-bet (Fig. 1b–d). Both cultures also contained T cells that produced IFN-γ only, whereas very few cells produced IL-10. These findings demonstrate that primary T-cell responses to *C. albicans* and *S. aureus* can be generated *in vitro*, leading to different types of polarized T cells: IL-17 single-producers, IL-17/IFN-γ double-producers (hereafter defined collectively as T_H17) and IFN-γ single-producers (hereafter defined as T_H1).

To investigate whether and under which conditions microbe-specific T_H17 cells produce IL-10 (ref. 8–13), we isolated T_H17 clones from *in-vitro*-primed cultures and measured their cytokine production capacity in the resting state and at different time points after restimulation (Fig. 1e, f). Resting T_H17 clones produced high amounts of IL-17 but virtually no IL-10. Surprisingly, when tested on day 5 after restimulation, *S. aureus*-specific but not *C. albicans*-specific T_H17 clones acquired IL-10 production capacity. In addition, both *S. aureus*- and *C. albicans*-specific T_H17 clones strongly downregulated IL-17 production. At later time points all clones gradually regained the original cytokine profile as the cells reverted to the resting state. These results reveal a reciprocal activation-dependent regulation of IL-17 and IL-10 production in human T_H17 cells.

The above findings show that *C. albicans* and *S. aureus* prime *in vitro* T_H17 cells with different capacities to produce IFN-γ and IL-10. To investigate whether these properties are also characteristic of *in-vivo*-primed T cells, we isolated memory T cell subsets according to the expression of chemokine receptors (Supplementary Fig. 2) and stimulated them with *C. albicans*- or *S. aureus*-pulsed autologous monocytes. In all donors tested, a robust proliferative response to *C. albicans* and *S. aureus* was detected in the CCR6$^+$CCR4$^+$ subset, which contains T_H17 as well as some T_H1 cells, whereas the response was weak or absent in the CXCR3$^+$ and CCR4$^+$ subsets, which are enriched in T_H1 and T_H2 cells, respectively (Fig. 2a). Similarly to what we observed in *in-vitro*-primed cultures, proliferating CCR6$^+$CCR4$^+$ memory T cells comprised both T_H17 and T_H1 cells, and *C. albicans*-specific T_H17 cells were mainly IL-17/IFN-γ double-producers, whereas *S. aureus*-specific T_H17 cells were IL-17 single- and IL-17/IFN-γ double-producers (Fig. 2b). Furthermore, upon restimulation with anti-CD3 and anti-CD28 or microbe-pulsed antigen-presenting cells, both *C. albicans*- and *S. aureus*-specific memory T_H17 clones downregulated IL-17 production, and *S. aureus*-specific clones, but not *C. albicans*-specific clones, upregulated IL-10 production with the same kinetics (Fig. 2c and Supplementary Fig. 3). Collectively, these findings demonstrate that the heterogeneous pattern of cytokine production and the regulated expression of IL-17 and IL-10 are characteristics shared by *in-vitro*- and *in-vivo*-primed microbe-specific T_H17 cells.

The analysis of memory T cells validated the *in vitro* priming system and prompted us to use this system to investigate the requirements for *C. albicans*- and *S. aureus*-induced T_H17 differentiation. In monocyte cultures, IL-6, TNF-α and IL-23 were elicited by both *C. albicans* and

[1]Institute for Research in Biomedicine, Via Vincenzo Vela 6, 6500 Bellinzona, Switzerland. [2]"G. Gaslini" Scientific Institute, Largo G. Gaslini 5, 16147, Genova, Italy. [3]Institute of Microbiology, ETH Zurich, Wolfgang-Pauli-Strasse 10, 8093 Zurich, Switzerland. †Present address: Department of Dermatology and Berlin-Brandenburg School for Regenerative Therapies, Charité-Universitätsmedizin Berlin, Germany.

Figure 1 | *In vitro* priming of human naive T cells with *C. albicans* or *S. aureus* induces T_H17 cells that produce either IFN-γ or IL-10. a, Naive CFSE-labelled CD4+ T cells were cultured with autologous monocytes pulsed with heat-inactivated *C. albicans* or *S. aureus*. On day 12, cells were stained with antibodies to ROR-γt and CCR6, or stimulated for 5 h with phorbol 12-myristate 13-acetate (PMA) and ionomycin (PMA+I), fixed, permeabilized, and stained with antibodies to IL-17, IL-22 and IL-10. Shown is a representative experiment and pooled data from several experiments are shown in Supplementary Fig. 1. **b, c,** IL-17 and IFN-γ production by CFSE– T cells primed by *C. albicans* or *S. aureus* as above. A representative staining is shown in **b** and pooled data are shown in **c** (mean and s.d., *n* = 3). **d,** *RORC, IL17A, TBX21* (which codes for T-bet) and *IFNG* mRNA expression assessed by quantitative RT–PCR in sorted IL-17-secreting cells. Mean and s.e.m. of triplicates are shown. Data are representative of two independent experiments. A.U., arbitrary units. **e, f,** *C. albicans*- or *S. aureus*-primed T cells were cloned by limiting dilution. T_H17 clones were selected and analysed in the resting state (day 0) and at different time points after restimulation with anti-CD3 and anti-CD28 for their capacity to produce IL-17 and IL-10 in response to PMA+I. A representative staining is shown in **e** and data from several clones (circles) and mean values (bars) are shown in **f**. Data are representative of more than five independent experiments. The amount of IL-17 and IL-10 secreted by *S. aureus*-specific T_H17 clones measured on day 5 by ELISA was 1,189 pg ml−1 (range 484–1,880) and 3,366 pg ml−1 (range 870–6,395), respectively. IL-17 production by *C. albicans*-specific T_H17 clones was 1,312 pg ml−1 (range 90–1,972). T_H1 clones isolated from the same *in-vitro*-primed cultures and restimulated under the same conditions did not upregulate IL-10 production, neither downregulated IFN-γ production.

addition of exogenous IL-12 to *S. aureus*-stimulated cultures inhibited in a dose-dependent fashion T_H17 differentiation, an effect that was significantly counteracted by IL-1β (Supplementary Fig. 5). Finally, priming with *S. aureus* in the presence of IL-1β induced T_H17 cells that produced IL-17 and IFN-γ and failed to upregulate IL-10 after restimulation (Fig. 3e, f). Taken together, these results indicate that IL-1β has multiple effects on T_H17 differentiation: it counteracts the T_H17-inhibitory activity of IL-12, induces IL-17/IFN-γ double-producing cells in an IL-12-independent manner, and inhibits IL-10 production capacity.

To establish whether IL-1β can induce IFN-γ and suppress IL-10 production in already differentiated T_H17 cells, we stimulated T_H17 clones or CCR6+CCR4+ memory T cells in the presence or absence of IL-1β and other innate cytokines. As shown in Supplementary Fig. 6a, IL-1β induced IFN-γ production in T_H17 clones to a level comparable to that induced by IL-12 (ref. 14), and suppressed IL-10 production. Furthermore, IL-1β significantly inhibited IL-10 production by CCR6+CCR4+ memory T cells, this inhibition being dominant over the enhancing effect of IL-12, IL-23 and IL-27, while it slightly enhanced IL-17 production (Fig. 3g and Supplementary Fig. 6b). In addition, IL-1β inhibited IL-10 production by CXCR3+ and CCR4+ memory T cell subsets (Fig. 3g). To assess the role of IL-1β in the regulation of IL-10 production *in vivo*, we isolated memory T cell subsets from patients with cryopyrin associated periodic syndrome (CAPS), an inflammatory disease caused by excessive production of IL-1β. IL-10 production was significantly lower in memory T cells and in T_H17 clones isolated during active disease compared to memory cells and clones isolated 7–10 days after *in vivo* administration of an IL-1RI antagonist (Fig. 3h and Supplementary Fig. 7). Taken together, these findings support the notion that IL-1β is a potent and general inhibitor of IL-10 production by memory T cells *in vitro* and *in vivo*.

A new finding emerging from this study is the transient downregulation of IL-17 production in recently activated T_H17 cells. To ask whether this is a general property of T_H17 cells and to investigate the underlying mechanisms we analysed a large number of random memory T_H17 clones (Supplementary Fig. 8). In virtually all clones, IL-17 production was downregulated on day 5 following restimulation and recovered at later time points, while IL-10 production was transiently upregulated in a fraction of the clones. In contrast, IL-22 and IFN-γ were produced in a stable fashion, irrespective of the activation state. Furthermore, the reciprocal IL-17/IL-10 regulation was observed

S. aureus, whereas IL-1β was preferentially induced by *C. albicans* and IL-12p70 was detectable only in *C. albicans*-stimulated cultures (Supplementary Fig. 4). Neutralization of IL-6 or IL-23 partially inhibited T_H17 differentiation induced by both microbes, whereas neutralization of TGF-β modestly inhibited *C. albicans*-induced and enhanced *S. aureus*-induced T_H17 differentiation (Fig. 3a). In *S. aureus*-stimulated cultures neutralization of IL-1β had only a marginal effect but showed an additive effect when combined to neutralization of IL-6 and IL-23. In contrast, in *C. albicans*-stimulated cultures, neutralization of IL-1β strongly inhibited ROR-γt induction and differentiation of IL-17/IFN-γ double-producing T_H17 cells (Fig. 3a–c). Taken together, these findings indicate that IL-6, IL-23 and IL-1β contribute to T_H17 differentiation induced by both *C. albicans* and *S. aureus*, and reveal an absolute requirement for IL-1β in *C. albicans*- but not *S. aureus*-primed cultures.

To address the IL-1β-dependency of *C. albicans*-induced T_H17 differentiation, we examined the role of IL-12, which was selectively induced by *C. albicans*. Surprisingly, in *C. albicans*-stimulated cultures the combined neutralization of IL-1β and IL-12 restored priming of IL-17-producing cells, whereas neutralization of IL-12 alone enhanced priming of IL-17/IFN-γ double-producing cells (Fig. 3d). Conversely,

Figure 2 | Cytokine production by *C. albicans*- and *S. aureus*-specific memory T$_H$17 cells. **a**, CXCR3$^+$CCR4$^-$CCR6$^-$ (CXCR3$^+$), CCR4$^+$CXCR3$^-$CCR6$^-$ (CCR4$^+$), CCR6$^+$CCR4$^+$CXCR3$^-$ (CCR6$^+$CCR4$^+$) memory CD4$^+$ T cells were isolated from immune donors, labelled with CFSE and stimulated with autologous monocytes pulsed with *C. albicans* or *S. aureus*. Shown is the CFSE profile on day 5 in one representative donor and the percentage of CFSE$^-$ proliferating cells in four donors (**$P < 0.005$, ***$P < 0.0005$). **b**, Production of IL-17 and IFN-γ by proliferating CCR6$^+$CCR4$^+$ CFSE$^-$ cells measured by intracellular staining following PMA+I stimulation (mean and s.d. of three independent experiments). **c**, *S. aureus*- and *C. albicans*-specific memory T$_H$17 clones isolated from the CCR6$^+$CCR4$^+$ subset were analysed by intracellular cytokine staining before and at different time points after restimulation with anti-CD3 and anti-CD28. Data from several clones (circles) and mean values (bars) are shown. Data are representative of five independent experiments. The amount of IL-17 and IL-10 secreted by *S. aureus*-specific memory T$_H$17 clones measured on day 5 by ELISA was 1,263 pg ml^{-1} (range 349–2,241) and 6,134 pg ml^{-1} (range 1,358–14,160), respectively. IL-17 production by *C. albicans*-specific memory T$_H$17 clones was 1,850 pg ml^{-1} (range 94–6,189).

over repeated cycles of restimulation and its extent was dependent on the strength of T-cell receptor (TCR) stimulation. The analysis of transcription factors showed that on days 2 and 5 following restimulation, T$_H$17 clones downregulated expression of *RORC* mRNAs (which encode ROR-γt), concomitant with downregulation of *IL17A* mRNA (Fig. 4a). In addition, although both resting and day 5 restimulated T$_H$17 clones phosphorylated STAT3 in response to IL-6, only restimulated clones phosphorylated STAT5 in response to IL-2, consistent with the increased expression of CD25 (Fig. 4b–d). Overexpression of ROR-γt significantly restored IL-17 production in activated T$_H$17 clones, and restimulation in the presence of a STAT5 inhibitor, or an IL-2 neutralizing antibody, rescued *RORC* mRNA expression and IL-17 production in a proportion of clones (Fig. 4e–h and Supplementary Fig. 9). These findings indicate that decreased ROR-γt expression and increased pSTAT5 levels, that may compete with pSTAT3 for binding to the *IL17A* locus[15], contribute to the transient downregulation of IL-17 production in activated T$_H$17 cells.

The coherent picture that emerges from the analysis of *in-vitro*-primed and *ex vivo* memory cells indicates that *C. albicans* and *S. aureus* elicit different types of T$_H$17 cells that produce either IFN-γ
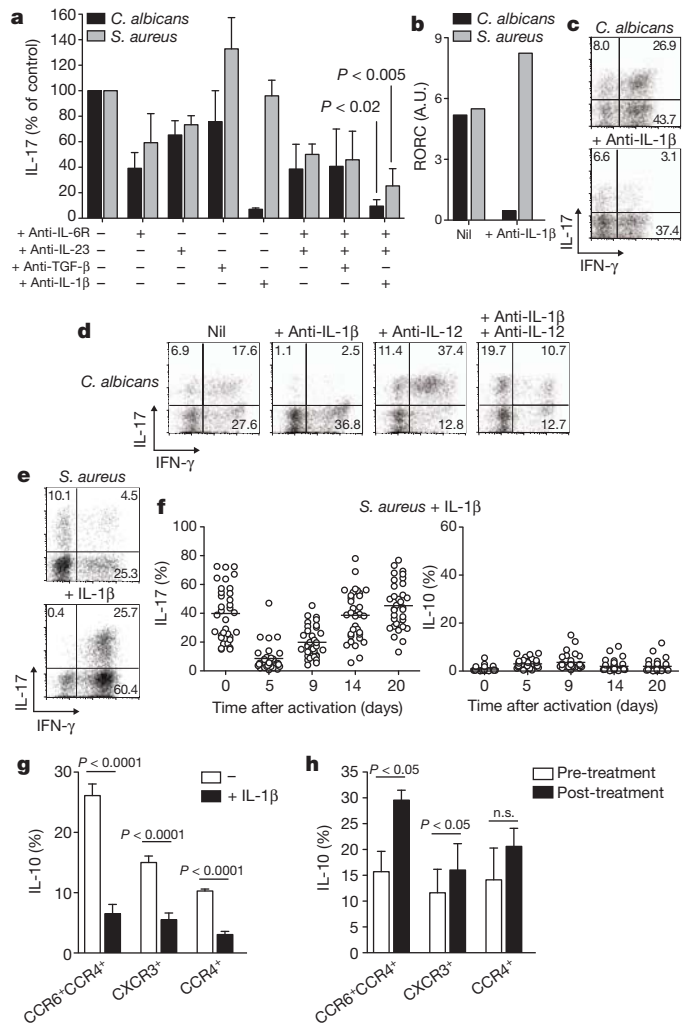
Figure 3 | Cytokine requirements for T$_H$17 differentiation induced by *C. albicans* and *S. aureus*. **a**, Naive CD4$^+$ T cells were primed by *C. albicans* or *S. aureus*-pulsed monocytes in the presence or absence of the indicated blocking antibodies. On day 12, the cells were stimulated with PMA+I and stained with antibodies to IL-17. Data are expressed as percentage of IL-17-producing cells relative to control cultures performed in the absence of neutralizing antibodies (mean and s.e.m., *n* ranging from 3 to 15). *P* values refer to control cultures. **b**, *RORC* mRNA expression in CFSE$^-$ T cells primed in the presence or absence of IL-1β-neutralizing antibodies. **c**, **d**, IL-17 and IFN-γ production by T cells primed with *C. albicans* in the absence or presence of neutralizing antibodies to IL-1β, IL-12 or both. **e**, IL-17 and IFN-γ production by T cells primed with *S. aureus* in the absence or presence of 10 ng ml^{-1} IL-1β. **f**, IL-17 and IL-10 production by resting and restimulated T$_H$17 clones isolated from cultures of T cells primed with *S. aureus* in the presence of 10 ng ml^{-1} IL-1β. Data in **b–f** are representative of at least three different experiments. **g**, Production of IL-10 by CCR6$^+$CCR4$^+$, CXCR3$^+$ and CCR4$^+$ memory CD4$^+$ T cells which were stimulated for 5 days with anti-CD3 and anti-CD28 in the presence or absence of 10 ng ml^{-1} IL-1β. Intracellular cytokine staining was performed on day 5 following PMA+I stimulation. Data are mean and s.e.m. of three independent experiments. **h**, Production of IL-10 by CCR6$^+$CCR4$^+$, CXCR3$^+$ and CCR4$^+$ memory CD4$^+$ T cells isolated from three CAPS patients at a time of active disease (pre-treatment) and 7 or 10 days after therapy with the IL-1RI antagonist anakinra (post-treatment), stimulated with anti-CD3 and anti-CD28 and tested on day 5 by intracellular cytokine staining following PMA+I stimulation. Data are mean and s.e.m.. Production of IL-17, IFN-γ and IL-4 by CCR6$^+$CCR4$^+$, CXCR3$^+$ and CCR4$^+$ memory T cells, respectively, was not significantly different in the pre- and post-treatment samples. n.s., not significant.

or IL-10. These results extend in a relevant microbial system previous observations on the role of IL-6, IL-23, IL-1β and TGF-β in induction of human T$_H$17 cells[16–21] and reveal a role for IL-1β in counteracting

the T_H17-inhibitory effect of IL-12 and in promoting the differentiation of 'inflammatory' T_H17 cells that produce IL-17 and IFN-γ but not IL-10. The role of IL-1β in *C. albicans*-induced T_H17 differentiation is also supported by the analysis of IL-1β-deficient mice which showed a severe reduction in the T_H17 response to *C. albicans* and only a modest reduction in the T_H17 response to *S. aureus* (F.R., unpublished). Thus, our findings reveal a robust mechanism of microbe-induced T-cell differentiation that is dependent on the balance between polarizing cytokines rather than their absolute amounts (Supplementary Fig. 10). Our results also show that IL-1β can inhibit IL-10 production in memory T_H17 cells, a property that extends to T_H1 and T_H2 cells. The mechanism for this inhibition remains to be established although preliminary experiments suggest that NF-κB activation is not required (D.A., unpublished results). It is therefore possible that IL-1β may act not only at priming in lymphoid organs, but also at the effector phase in target tissues, where it may increase T cell inflammatory activity in synergy or antagonism with other factors that have been shown to modulate inflammation[12,22,23].

This study also reveals a new type of regulation whereby T_H17 cells continuously stimulated by antigen downregulate production of IL-17 while still producing IL-22 and, in some cases, upregulating IL-10, which together exert tissue protective and immunosuppressive effects. Inhibition of IL-17 production in activated T_H17 cells represents a new regulatory function of IL-2 besides its role in inhibiting T_H17 differentiation[24] and in the development, survival and function of regulatory T cells[25].

In conclusion, our study illustrates the feasibility of the *in vitro* and *ex vivo* combined approach to dissect the complexity of the human T-cell response to microbes and reveals novel mechanisms for differentiation of stable subsets of T_H17 cells endowed with different inflammatory capacity as well as factors that modulate their effector function.

METHODS SUMMARY

Cell sorting. Peripheral blood mononuclear cells (PBMC) were isolated using Ficoll-Paque Plus (GE Healthcare). T cells and monocytes were isolated with CD4 and CD14 microbeads (Miltenyi Biotech), respectively. Naive T cells were sorted as $CD45RA^+CD45RO^-CCR7^+CD25^-CD8^-$. Memory $CD45RA^-CD25^-CD8^-$ T cell subsets were sorted according to the differential expression of CXCR3, CCR4 and CCR6. Viable $IL-17^+$ *in-vitro*-differentiated T cells were FACS-sorted using the cytokine secretion assay (Miltenyi Biotech) after 3-h stimulation with PMA and ionomycin.

T cell assays and cloning. CFSE-labelled naive $CD4^+$ T cells were co-cultured for 12 days with autologous irradiated monocytes (2:1 ratio) that were pre-incubated for 3 h with heat-inactivated *C. albicans* or *S. aureus*. Some experiments were performed in the presence of neutralizing antibodies or cytokines. Antigen-specific T-cell clones from *in vitro*-primed T cells or from *in vitro*-restimulated memory T cells were generated by sorting CFSE-negative cells (day 12 for T cells primed *in vitro*, day 5 for memory T cells), followed by expansion for 7 days in IL-2-containing media (50 U ml^{-1}) and cloning by limiting dilution. Random T_H17 clones were generated by direct cloning of $CCR6^+CCR4^+$ memory $CD4^+$ T cells. Resting (>day 20 after stimulation) T-cell clones were activated for 48 h with anti-CD3 (1 μg ml^{-1}, TR66) and anti-CD28 (1 μg ml^{-1} CD28.2; BD Biosciences) or *C. albicans*- or *S. aureus*-pulsed autologous monocytes and analysed at different time points.

Cytokine and transcription factor analysis. Intracellular staining for cytokines and transcription factors was performed as described in detail in Methods. Cytokine secretion by monocytes was analysed using the cytometric bead array (BD Biosciences). Cytokine and transcription factor gene expression was analysed by quantitative reverse transcription PCR (RT–PCR; all probes from Applied Biosystems).

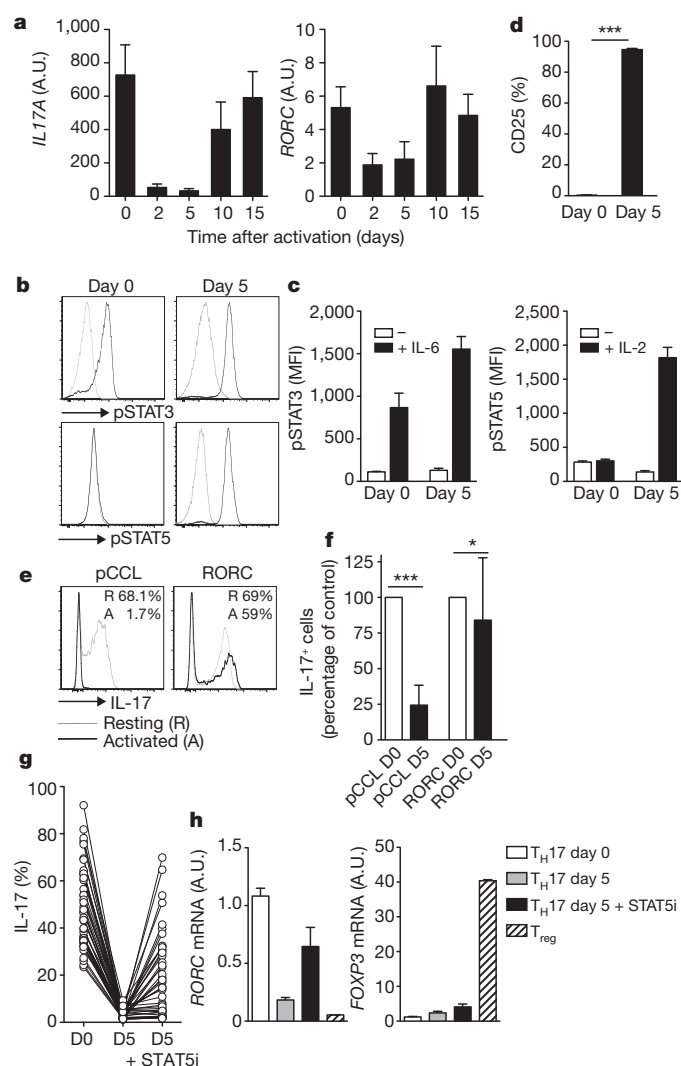**Statistics.** Student's two-tailed paired *t*-test was used for statistical comparisons; *P* values of 0.05 or less were considered as significant.

Full Methods and any associated references are available in the online version of the paper at www.nature.com/nature.

1. Korn, T., Bettelli, E., Oukka, M. & Kuchroo, V. K. IL-17 and Th17 Cells. *Annu. Rev. Immunol.* **27,** 485–517 (2009).

Figure 4 | Downregulation of ROR-γt and IL-2-mediated activation of STAT5 limit IL-17 production in activated T_H17 clones. a, T_H17 clones isolated from the $CCR6^+CCR4^+$ memory T cell subset were restimulated with anti-CD3 and anti-CD28. At the indicated time points, cells were stimulated with PMA+I for 3 h, and *IL17A* and *RORC* mRNAs were measured by quantitative RT–PCR. Data represent mean and s.e.m. of ten clones analysed. **b, c,** Resting (day 0) and day 5 restimulated T_H17 clones were exposed to IL-6 (50 ng ml^{-1}) or IL-2 (500 IU ml^{-1}) for 10 min and stained with antibodies to pSTAT3 and pSTAT5. A representative staining is shown in **b** (thin line, background staining) and mean and s.e.m. of four clones is shown in **c**. MFI, mean fluorescence intensity. **d,** Percentage of $CD25^+$ cells (mean and s.e.m.) in resting and day 5 restimulated T_H17 clones ($n = 8$, ***$P < 0.0005$). **e, f,** T_H17 clones were stably transfected with an empty lentiviral vector (pCCL) or with a vector containing the human *RORC* variant 2 (*RORC*). Percentage of $IL-17^+$ cells was measured in resting (day 0, thin line, empty bars) or in day 5 restimulated clones (thick line, black bars) 5 h after stimulation with PMA+I. Data shown are from two representative T-cell clones (**e**) and mean and s.e.m. of 12 pCCL-transfected and 28 *RORC*-transfected clones (**f**). *$P < 0.05$, ***$P < 0.0005$. **g,** T_H17 clones were restimulated with anti-CD3 and anti-CD28 in the absence or presence of 100 μM STAT5 inhibitor N'-[(4-oxo-4H-chrome-3-yl)methylene]nicotinohydrazide. IL-17 production was measured in resting (day 0) and in day 5 clones restimulated in the absence or presence of the STAT5 inhibitor (STAT5i). Data are from 44 clones in one experiment and are representative of three independent experiments. **h,** T_H17 clones that showed sensitivity to STAT5 inhibition were analysed for *RORC* ($n = 8$) and *FOXP3* ($n = 14$) mRNA levels. Peripheral blood $CD4^+CD25^+$ regulatory T cells (T_{reg}) were included as control. Data are representative of three experiments. Note that *FOXP3* mRNA was not induced in T_H17 clones.

2. Romani, L. Immunity to fungal infections. *Nature Rev. Immunol.* **11,** 275–288 (2011).

3. Milner, J. D. *et al.* Impaired T$_H$17 cell differentiation in subjects with autosomal dominant hyper-IgE syndrome. *Nature* **452,** 773–776 (2008).

4. Ma, C. S. *et al.* Deficiency of Th17 cells in hyper IgE syndrome due to mutations in *STAT3*. *J. Exp. Med.* **205,** 1551–1557 (2008).

5. Puel, A. *et al.* Chronic mucocutaneous candidiasis in humans with inborn errors of interleukin-17 immunity. *Science* **332,** 65–68 (2011).

6. Ivanov, I. I. *et al.* The orphan nuclear receptor RORγt directs the differentiation program of proinflammatory IL-17$^+$ T helper cells. *Cell* **126,** 1121–1133 (2006).

7. Acosta-Rodriguez, E. V. *et al.* Surface phenotype and antigenic specificity of human interleukin 17-producing T helper memory cells. *Nature Immunol.* **8,** 639–646 (2007).

8. Jankovic, D. *et al.* Conventional T-bet$^+$Foxp3$^-$ Th1 cells are the major source of host-protective regulatory IL-10 during intracellular protozoan infection. *J. Exp. Med.* **204,** 273–283 (2007).

9. Saraiva, M. *et al.* Interleukin-10 production by Th1 cells requires interleukin-12-induced STAT4 transcription factor and ERK MAP kinase activation by high antigen dose. *Immunity* **31,** 209–219 (2009).

10. Chung, Y. *et al.* Critical regulation of early Th17 cell differentiation by interleukin-1 signalling. *Immunity* **30,** 576–587 (2009).

11. Ghoreschi, K. *et al.* Generation of pathogenic T$_H$17 cells in the absence of TGF-β signalling. *Nature* **467,** 967–971 (2010).

12. Stumhofer, J. S. *et al.* Interleukins 27 and 6 induce STAT3-mediated T cell production of interleukin 10. *Nature Immunol.* **8,** 1363–1371 (2007).

13. McGeachy, M. J. *et al.* TGF-β and IL-6 drive the production of IL-17 and IL-10 by T cells and restrain T$_H$-17 cell-mediated pathology. *Nature Immunol.* **8,** 1390–1397 (2007).

14. Annunziato, F. *et al.* Phenotypic and functional features of human Th17 cells. *J. Exp. Med.* **204,** 1849–1861 (2007).

15. Yang, X. P. *et al.* Opposing regulation of the locus encoding IL-17 through direct, reciprocal actions of STAT3 and STAT5. *Nature Immunol.* **12,** 247–254 (2011).

16. Acosta-Rodriguez, E. V., Napolitani, G., Lanzavecchia, A. & Sallusto, F. Interleukins 1β and 6 but not transforming growth factor-β are essential for the differentiation of interleukin 17-producing human T helper cells. *Nature Immunol.* **8,** 942–949 (2007).

17. Wilson, N. J. *et al.* Development, cytokine profile and function of human interleukin 17-producing helper T cells. *Nature Immunol.* **8,** 950–957 (2007).

18. Yang, L. *et al.* IL-21 and TGF-β are required for differentiation of human T$_H$17 cells. *Nature* **454,** 350–352 (2008).

19. Manel, N., Unutmaz, D. & Littman, D. R. The differentiation of human T$_H$-17 cells requires transforming growth factor-β and induction of the nuclear receptor RORγt. *Nature Immunol.* **9,** 641–649 (2008).

20. Cosmi, L. *et al.* Human interleukin 17-producing cells originate from a CD161$^+$CD4$^+$ T cell precursor. *J. Exp. Med.* **205,** 1903–1916 (2008).

21. Volpe, E. *et al.* A critical function for transforming growth factor-β, interleukin 23 and proinflammatory cytokines in driving and modulating human T$_H$-17 responses. *Nature Immunol.* **9,** 650–657 (2008).

22. Napolitani, G., Acosta-Rodriguez, E. V., Lanzavecchia, A. & Sallusto, F. Prostaglandin E2 enhances Th17 responses via modulation of IL-17 and IFN-γ production by memory CD4$^+$ T cells. *Eur. J. Immunol.* **39,** 1301–1312 (2009).

23. Smeekens, S. P. *et al.* The *Candida* Th17 response is dependent on mannan- and β-glucan-induced prostaglandin E2. *Int. Immunol.* **22,** 889–895 (2010).

24. Laurence, A. *et al.* Interleukin-2 signaling via STAT5 constrains T helper 17 cell generation. *Immunity* **26,** 371–381 (2007).

25. Hoyer, K. K., Dooms, H., Barron, L. & Abbas, A. K. Interleukin-2 in the development and control of inflammatory disease. *Immunol. Rev.* **226,** 19–28 (2008).

METHODS

Blood samples and cell sorting. Blood from healthy donors was obtained from the Swiss Blood Donation Center of Basel and Lugano, and used in compliance with the Federal Office of Public Health (authorization no. A000197/2 to F.S). Peripheral blood was collected from three CAPS patients carrying the T50M, D303N and M406I mutation of the *NLRP3* gene[26] at a time of active disease and 7–10 days after treatment with the IL-1RI antagonist anakinra, after receiving the patient's informed consent and approval by the "G. Gaslini" Ethical board. CD14$^+$ monocytes and CD4$^+$ T cells were isolated from PBMC by positive selection using magnetic microbeads (Miltenyi Biotec). T helper cell subsets were sorted to over 97% purity as follows: CXCR3$^+$CCR4$^-$CCR6$^-$CD45RA$^-$CD25$^-$CD8$^-$ (enriched in T$_H$1 cells); CCR4$^+$CXCR3$^-$CCR6$^-$CD45RA$^-$CD25$^-$CD8$^-$ (enriched in T$_H$2 cells); CCR6$^+$CCR4$^+$CXCR3$^-$CD45RA$^-$CD25$^-$CD8$^-$ (enriched in T$_H$17 cells). The following antibodies were used for FACS-sorting and analysis: anti-CCR6–phycoerythrin (PE) (11A9), anti-CCR4–PE–cyanin 7 (Cy7) (1G1), anti-CXCR3–allophycocyanin (APC) (1C6), anti-CD45RA–PE–Cy5 (HI100; all from BD Biosciences), anti-CD8–PE–Cy5 (B9.11), anti-CD25–FITC (fluorescein isothiocyanate) (B1.49.9; both from Immunotech), and anti-ROR-γt (600380; R&D Systems, AFKJS-9; eBioscience). Naive T cells were isolated as CD45RA$^+$CD45RO$^-$CCR7$^+$CD25$^-$CD8$^-$ to a purity of over 99% after staining with anti-CD45RA, anti-CD25 and anti-CD8 as well as anti-CD45RO–FITC (UCHL1; Immunotech) and anti-CCR7 (150503; R&D Systems), followed by staining with biotinylated anti-IgG2a (1080-08; Southern Biotech) and streptavidin–Pacific blue (Molecular Probes; Invitrogen). Cells were sorted with a FACSAria (BD Biosciences). Viable IL-17$^+$ cells were FACS-sorted using the cytokine secretion assay (Miltenyi Biotec).

T-cell culture. Cells were cultured in RPMI-1640 medium supplemented with 2 mM glutamine, 1% (v/v) non-essential amino acids, 1% (v/v) sodium pyruvate, penicillin (50 U ml^{-1}), kanamycin (50 μg ml^{-1}), streptomycin (50 μg ml^{-1}; all from Invitrogen) and 5% (v/v) human serum (Swiss Blood Center). Monocytes were pre-incubated for 3 h with *C. albicans* (ratio of 1:3) or *S. aureus* (5 μg ml^{-1}) and irradiated (45 Gy) before T-cell co-culture. Microbes were killed by heating at 65 °C for 1 h according to standard methods, followed by three freeze-thaw cycles for *S. aureus*. Protein concentration was determined by the bicinchoninic acid assay (Bio-Rad) according the manufacturer's instructions. The concentration of inactivated microorganisms used in co-culture experiments was determined after titration in proliferation assays using ^{3}H-thymidine incorporation, as described previously[27]. The concentration leading to maximum proliferative responses and viability was chosen. T cells were labelled with CFSE according to standard protocols. For T-cell priming experiments, naive CFSE-labelled CD4$^+$ T cells (5×10^4) were co-cultured with autologous monocytes at a ratio of 2:1 in the absence of exogenous IL-2 for 12 days before analysis. In these primary cultures microbes did not induce apoptosis of monocytes (in one representative experiment, the percentage of annexin-V$^+$ cells in cultures of monocytes alone, monocytes and *C. albicans*, monocytes and *S. aureus* was 16.9, 18.3 and 16.5, respectively). For recall responses, CFSE-labelled purified memory T helper cell subsets were co-cultured with irradiated autologous monocytes at a ratio of 2:1 for 5 days before analysis. Some experiments were performed using glutaraldehyde-fixed *C. albicans*- or *S. aureus*-pulsed monocytes with similar results. Antigen-specific T-cell clones derived from *in-vitro*-primed T cells as well as from memory T cells were generated as previously described[28]. Briefly, CFSE-negative cell populations (day 12 for T cells primed *in vitro*, day 5 for memory T cells) were sorted, expanded for 7 days in IL-2-containing media (50 U ml^{-1}) and cloned by limiting dilution using phytohaemagglutinin (PHA, 1 μg ml^{-1}; Remel), irradiated (45 Gy) allogeneic feeder cells and IL-2. Antigen specificity of T-cell clones was confirmed by their capacity to proliferate in response to irradiated autologous monocytes pulsed with the respective microbe, as described previously[27]. T-cell clones were stimulated in the resting state (25–30 days after the first stimulation or as indicated) for 48 h with plate-bound anti-CD3 (1–5 μg ml^{-1}, clone TR66) and anti-CD28 (1 μg ml^{-1} CD28.2; BD Biosciences) or with autologous antigen-presenting cells (irradiated monocytes or Epstein–Barr virus-immortalized B cells) and microbes. In some experiments T-cell cultures were performed in the presence of neutralizing antibodies or exogenous cytokines. The following neutralizing antibodies were used (all at 10 μg ml^{-1}): anti-IL-1β (8516), anti-IL1R1 (AF269), anti-IL-6R (17506), anti-IL-23 p19 (AF1716), anti-TGF-β (1D11) (all from R&D Systems), anti-IL-12p70 (20C2, BD Biosciences), or anti-human leukocyte antigen (HLA)-DQ (SPVL-3), anti-HLA-DP (B7/21), anti-HLA-DR (L243; all from ATCC). In preliminary experiments the IL-12p70 antibody 20C2 was found to

inhibit pSTAT4 phosphorylation induced by IL-12 while not affecting pSTAT3 phosphorylation induced by IL-23 (F.M., unpublished).

Cytokine analysis. For intracellular cytokine staining, cells were restimulated for 5 h with PMA and ionomycin (PMA+I) in the presence of brefeldin A (all from Sigma-Aldrich) for the final 2.5 h of culture. Cells were fixed and permeabilized with Cytofix/Cytoperm (BD Biosciences) according to the manufacturer's instructions. Cells were stained with anti-IL-10 (JES3-19F1; BD Biosciences), anti-IL-17 (eBIO64-DEC17; eBioscience), anti-IFN-γ (B27; BD Biosciences), and anti-IL-22 (142928; R&D Systems), conjugated with different fluorochromes, and were analysed on a FACSCalibur (BD Bioscience). Flow cytometry data were analysed with FlowJo (Tree Star). IL-1β, IL-6 and TNF-α and IL-12 secretion by monocytes was measured by cytometric bead array (BD Biosciences) or Luminex (Invitrogen) according to the manufacturer's instructions.

STAT analysis. T$_H$17 clones were restimulated with anti-CD3 (5 μg ml^{-1}) and anti-CD28 (1 μg ml^{-1}). After a total incubation time of 96 h, cells were extensively washed and incubated for a further 24 h. At the end of the incubation time, cells were again extensively washed and stimulated for 10 min at 37 °C with recombinant IL-6 (50 ng ml^{-1}, R&D Systems) or recombinant IL-2 (500 U ml^{-1}, produced in our laboratory). Cells were then fixed at 37 °C for 30 min using 3.5% formaldehyde and permeabilized using 90% methanol and stained for pSTAT3 and pSTAT5 using fluorophore-conjugated antibodies (clones D3A7 an C71E5, respectively, both from Cell Signalling Technology) and analysed by FACS.

Gene expression analysis. Total RNA was extracted using TRIzol reagent (Invitrogen) according to the manufacturer's instructions. Random hexamer primers and a Moloney murine leukemia virus (MMLV) reverse transcriptase kit (Stratagene) were used for cDNA synthesis. Transcripts were quantified by RT–PCR on an ABI PRISM 7700 Sequence Detector with predesigned TaqMan Gene Expression Assays (*IL17A* Hs99999082_m1, *RORC* Hs01076112_m1, *TBX21* Hs00203436_m1, *FOXP3* Hs01085834_m1) and reagents according to the manufacturer's instructions (Applied Biosystems). For each sample, expression of target genes was normalized to 18S ribosomal RNA (Applied Biosystems) and expressed as arbitrary units (A.U.).

Plasmids and lentiviral transduction. The vectors pCLL (empty) and the pCCL.RORC2 (containing the cDNA encoding for the human RORC variant 2)[29] were provided by M. Levings. Both vectors also expressed the ΔNGFR reporter gene as a marker for transduction. Lentiviral particles were produced by transiently transfecting 293FT cells with the pCCL or pCCL.RORC2 transfer vectors together with the packaging vectors psPAX2 (Addgene plasmid 12260) and pMD2.G (Addgene plasmid 12259), as previously described[30]. Briefly, 293FT cells were transfected with a cocktail of transfer vector, psPAX and pMDG2.G at a ratio 4:3:1 in Opti-MEM, using linear polyethylenimine as transfecting agent. Viral particles were harvested at 36 and 48 h post-transfection, concentrated by centrifugation on a sucrose gradient, and titres were determined by limiting dilution on 293FT cells. Concentrated lentivirus was added to human memory T$_H$17 cell lines at a multiplicity of infection of ~60 in the presence of 500 U ml^{-1} recombinant IL-2. Three days later, the efficiency of transduction was determined by surface staining for NGFR using a biotinylated anti-CD127 antibody (BD Biosciences), and NGFR^{hi} cells were FACS-sorted and cloned. Two weeks later, 30 pCCL control clones and 96 pCCL.RORC2 clones were assessed for NGFR and IL-17 expression. The pCLL-transduced clones were 90% NGFR$^+$, of which 40% expressed IL-17, whereas 50% of the pCCL-RORC2 clones were NGFR$^+$, of which 82% expressed IL-17. Three weeks after transduction, IL-17-producing clones (12 for pCCL and 28 for pCCL.RORC2) were either left resting or were restimulated for 48 h on plate-bound anti-CD3 (5 μg ml^{-1} TR66) and anti-CD28 (1 μg ml^{-1}), and intracellular cytokine staining for IL-17 expression was performed 5 days later.

26. Gattorno, M. *et al.* Pattern of interleukin-1β secretion in response to lipopolysaccharide and ATP before and after interleukin-1 blockade in patients with *CIAS1* mutations. *Arthritis Rheum.* **56,** 3138–3148 (2007).
27. Geiger, R., Duhen, T., Lanzavecchia, A. & Sallusto, F. Human naive and memory CD4$^+$ T cell repertoires specific for naturally processed antigens analyzed using libraries of amplified T cells. *J. Exp. Med.* **206,** 1525–1534 (2009).
28. Messi, M. *et al.* Memory and flexibility of cytokine gene expression as separable properties of human T$_H$1 and T$_H$2 lymphocytes. *Nature Immunol.* **4,** 78–86 (2003).
29. Crome, S. Q., Wang, A. Y., Kang, C. Y. & Levings, M. K. The role of retinoic acid-related orphan receptor variant 2 and IL-17 in the development and function of human CD4$^+$ T cells. *Eur. J. Immunol.* **39,** 1480–1493 (2009).
30. Mayoral, R. J. & Monticelli, S. Stable overexpression of miRNAs in bone marrow-derived murine mast cells using lentiviral expression vectors. *Methods Mol. Biol.* **667,** 205–214 (2010).

IFITM3 restricts the morbidity and mortality associated with influenza

Aaron R. Everitt[1], Simon Clare[1], Thomas Pertel[2], Sinu P. John[2], Rachael S. Wash[1], Sarah E. Smith[1], Christopher R. Chin[2], Eric M. Feeley[2], Jennifer S. Sims[2], David J. Adams[1], Helen M. Wise[3], Leanne Kane[1], David Goulding[1], Paul Digard[3], Verneri Anttila[1], J. Kenneth Baillie[4,5], Tim S. Walsh[5], David A. Hume[4], Aarno Palotie[1], Yali Xue[1], Vincenza Colonna[1,6], Chris Tyler-Smith[1], Jake Dunning[7], Stephen B. Gordon[8], The GenISIS Investigators*, The MOSAIC Investigators*, Rosalind L. Smyth[9], Peter J. Openshaw[7], Gordon Dougan[1], Abraham L. Brass[2,10] & Paul Kellam[1,11]

The 2009 H1N1 influenza pandemic showed the speed with which a novel respiratory virus can spread and the ability of a generally mild infection to induce severe morbidity and mortality in a subset of the population. Recent *in vitro* studies show that the interferon-inducible transmembrane (IFITM) protein family members potently restrict the replication of multiple pathogenic viruses[1–7]. Both the magnitude and breadth of the IFITM proteins' *in vitro* effects suggest that they are critical for intrinsic resistance to such viruses, including influenza viruses. Using a knockout mouse model[8], we now test this hypothesis directly and find that IFITM3 is essential for defending the host against influenza A virus *in vivo*. Mice lacking *Ifitm3* display fulminant viral pneumonia when challenged with a normally low-pathogenicity influenza virus, mirroring the destruction inflicted by the highly pathogenic 1918 'Spanish' influenza[9,10]. Similar increased viral replication is seen *in vitro*, with protection rescued by the re-introduction of *Ifitm3*. To test the role of IFITM3 in human influenza virus infection, we assessed the *IFITM3* alleles of individuals hospitalized with seasonal or pandemic influenza H1N1/09 viruses. We find that a statistically significant number of hospitalized subjects show enrichment for a minor *IFITM3* allele (SNP rs12252-C) that alters a splice acceptor site, and functional assays show the minor CC genotype IFITM3 has reduced influenza virus restriction *in vitro*. Together these data reveal that the action of a single intrinsic immune effector, IFITM3, profoundly alters the course of influenza virus infection in mouse and humans.

IFITM3 was identified in a functional genomic screen as mediating resistance to influenza A virus, dengue virus and West Nile virus infection *in vitro*[1]. However, the role of the IFITM proteins in antiviral immunity *in vivo* is unknown. Therefore, we infected mice that are homozygous for a disruptive insertion in exon 1 of the *Ifitm3* gene that abolishes its expression[8] (*Ifitm3*^{−/−}) with a low-pathogenicity murine-adapted H3N2 influenza A virus (A/X-31). Low-pathogenicity strains of influenza do not normally cause extensive viral replication throughout the lungs, or cause the cytokine dysregulation and death typically seen after infection with highly pathogenic viral strains[9], at the doses used (Fig. 1a). However, low-pathogenicity-infected *Ifitm3*^{−/−} mice became moribund, losing >25% of their original body weight and showing severe signs of clinical illness (rapid breathing, piloerection) 6 days after infection. In comparison, wild-type littermates shed <20% of their original body weight, before fully recovering (Fig. 1a, b). There was little difference in virus replication in the lungs during the first 48 h
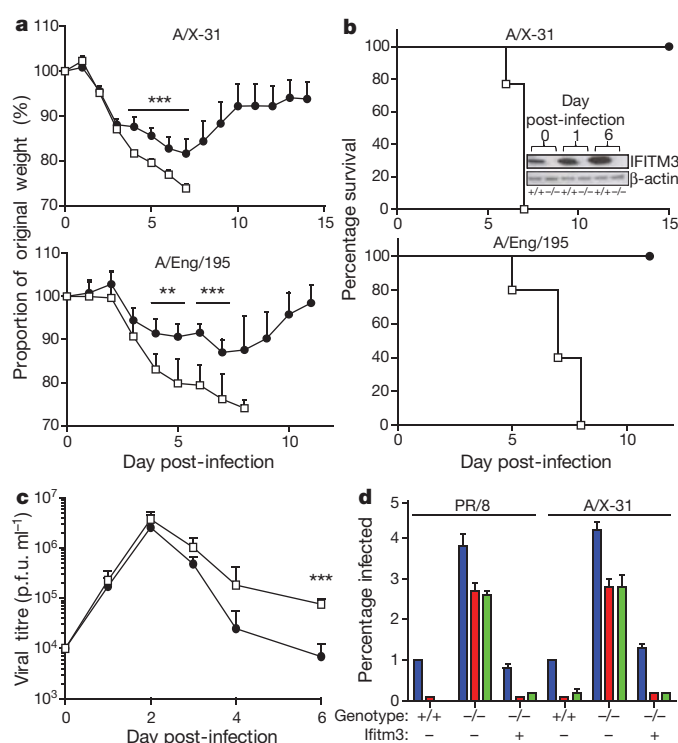
Figure 1 | Influenza A virus replicates to higher levels in *Ifitm3*^{−/−} mice. a, b, Change in body mass (**a**) and survival (**b**) of wild-type (filled circles) and *Ifitm3*^{−/−} (open squares) mice following intranasal inoculation with A/X-31 and pandemic H1N1/09 Eng/195 influenza (*n* > 5). **b,** Absence of Ifitm3 expression was verified in the *Ifitm3*^{−/−} mice at all time points, but was seen to increase in wild-type mice. **c,** A/X-31 viral load in the lungs of mice (*n* > 4) was calculated over the course of infection by plaque assay. p.f.u., plaque-forming units. *Ifitm3*^{−/−} murine embryonic fibroblasts (*n* = 3 per condition) stably expressing *Ifitm3* (+), or the empty vector (−) were left untreated (blue), or incubated with IFN-α (red) or IFN-γ (green), then challenged with either A/X-31 or PR/8 influenza. **d,** Twelve hours after infection, the cells were assessed for either haemagglutinin expression (PR/8), or nucleoprotein expression (A/X-31) IFITM3 expression was determined to be present (+) or absent (−) by western blotting (Supplementary Fig. 2). Results show means ± s.d. Statistical significance was assessed by Student's *t*-test (**P < 0.01; ***P < 0.001).

[1]Wellcome Trust Sanger Institute, Wellcome Trust Genome Campus, Hinxton CB10 1SA, UK. [2]Ragon Institute of Massachusetts General Hospital, Massachusetts Institute of Technology, and Harvard University, Charlestown, Massachusetts 02129, USA. [3]Divison of Virology, Department of Pathology, University of Cambridge, Tennis Court Road, Cambridge CB2 1QP, UK. [4]Division of Genetics and Genomics, The Roslin Institute, University of Edinburgh, Roslin EH25 9RG, UK. [5]Department of Critical Care Medicine, University of Edinburgh, Edinburgh EH16 4TJ, UK. [6]Institute of Genetics and Biophysics ''A. Buzzati-Traverso'', National Research Council (CNR), Naples, Italy. [7]Centre for Respiratory Infection, National Heart and Lung Institute, St Mary's Campus, Imperial College London, W2 1PG, UK. [8]Liverpool School of Tropical Medicine, Pembroke Place, Liverpool L3 5QA, UK. [9]Institute of Translational Medicine, University of Liverpool, Alder Hey Children's Hospital, Liverpool L12 2AP, UK. [10]Gastrointestinal Unit, Massachusetts General Hospital, Boston, Massachusetts 02117, USA. [11]UCL/MRC Centre for Medical Molecular Virology, Department of Infection, University College London, Cleveland Street, London W1T 4JF, UK.
*Lists of participants and their affiliations appear at the end of the paper.

of infection. However, virus persisted and was not cleared as quickly in $Ifitm3^{-/-}$ mice, whose lungs contained tenfold higher levels of replicating virus than the wild-type mice at 6 days post-infection (Fig. 1c). No viral RNA was detected in the heart, brain or spleen of infected wild-type or $Ifitm3^{-/-}$ mice over the course of infection, revealing that systemic viraemia was not occurring. Full-genome sequencing of virus removed from the lungs of wild-type and $Ifitm3^{-/-}$ mice showed no genetic variation. We demonstrated that IFITM3 protein expression after influenza infection was absent in $Ifitm3^{-/-}$ mice but increased substantially in wild-type controls (Fig. 1b and Supplementary Fig. 1). Infection of wild-type and $Ifitm3^{-/-}$ mice with a human isolate of pandemic influenza A H1N1 (pH1N1/09) resulted in the same severe pathogenicity phenotype in the $Ifitm3^{-/-}$ mice (Fig. 1a, b). Mouse embryonic fibroblast (MEF) lines generated from multiple matched littermates demonstrated that $Ifitm3^{-/-}$ cells are infected more readily in vitro, and lack much of the protective effects of interferon (IFN). Importantly, the stable restoration of IFITM3 conferred wild-type levels of restriction against either the X-31 strain, or the more pathogenic Puerto Rico/8/34 (PR/8) influenza strain (Fig. 1d and Supplementary Fig. 2). In addition to the role of IFITM3 in restriction of high-pathogenicity H5N1 avian influenza[7], we also show that it limits infection by recent human influenza A virus isolates and influenza B virus (Supplementary Fig. 3). Therefore, enhanced pathogenesis to diverse influenza viruses is attributable to loss of $Ifitm3$ expression and consequential changes in immune defence of the lungs.

Examination of lung pathology showed fulminant viral pneumonia with substantial damage and severe inflammation in the infected $Ifitm3^{-/-}$ mice. Lung pathology was characterized by extensive oedema and red blood cell extravasation, as well as pneumonia, haemorrhagic pleural effusion and multiple, large lesions on all lung lobes (Fig. 2a, b and Supplementary Fig. 4). We note that this pathology is similar to that produced by infection of mice and primates with 1918 H1N1 virus[9–11]. Given the higher viral load in $Ifitm3^{-/-}$ mice and increased replication of influenza A virus in $Ifitm3$-deleted cells in vitro (Fig. 1d), we examined both viral nucleic acid and protein distribution in the lung. Influenza virus infection penetrated deeper into the lung tissue in $Ifitm3^{-/-}$ compared to wild-type mice whose infection was primarily restricted to the bronchioles, with minimal alveolar infection. Influenza virus was detected throughout the entire lung in $Ifitm3^{-/-}$ sections, spreading extensively in both bronchioles and alveoli (Fig. 2c). Histopathology showed marked infiltration of cells and debris into the bronchoalveolar space of $Ifitm3^{-/-}$ mice (Fig. 2b and Supplementary Fig. 4b). The extent and mechanism of cell damage was investigated by TdT-mediated dUTP nick end labelling (TUNEL) assay, showing widespread cellular apoptosis occurring 6 days post-infection in $Ifitm3^{-/-}$ mice, whereas apoptosis in wild-type lungs was

very limited (Supplementary Fig. 4c). Together, the $Ifitm3^{-/-}$ mouse pathology is consistent with infection by high-pathogenicity strains of influenza A virus, where widespread apoptosis occurs by day 6 post-infection, whereas lungs from low-pathogenicity infections were similar to those of wild-type mice, displaying minimal damage[9,12,13].

Analysis of cell populations resident in the lung tissue on day 6 post-infection showed that $Ifitm3^{-/-}$ mice had significantly reduced proportions of $CD4^{+}$ ($P = 0.004$) and $CD8^{+}$ T cells ($P = 0.02$) and natural killer (NK) cells ($P = 0.0001$), but an elevated proportion of neutrophils ($P = 0.007$) (Fig. 3a). Despite the extensive cellular infiltration (Supplementary Figs 4b, 5a), the absolute numbers of $CD4^{+}$ T-lymphocytes in the lungs of the $Ifitm3^{-/-}$ mice were also lower and neutrophils increased compared to wild-type mice (Supplementary Fig. 6). The peripheral blood of infected $Ifitm3^{-/-}$ mice showed leukopenia (Supplementary Fig. 5c). Blood differential cell counts indicated marked depletion of lymphocytes on day 2 post-infection in the $Ifitm3^{-/-}$ mice ($P = 0.04$) (Fig. 3b), reflecting changes observed previously in high-pathogenicity (but not low-pathogenicity) influenza infections in both humans and animal models[9,12,14,15]. Heightened cytokine and chemokine levels are also hallmarks of severe influenza infection, having been observed in both human and animal models[9,16]. We observed exaggerated pro-inflammatory responses in the lungs of $Ifitm3^{-/-}$ mice with levels of TNF-α, IL-6, G-CSF and MCP-1 showing the most marked increase (Fig. 3c and Supplementary Fig. 7). This is indicative of the extent of viral spread within the lungs, as TNF-α and IL-6 are released from cells upon infection[17]. Consistent with the immunopathology data above, these changes are comparable in level to those seen with non-H5N1 high-pathogenicity influenza infections[9]. Neutrophil chemotaxis, together with elevated proinflammatory cytokine secretion, has previously been reported as one of the primary causes of acute lung injury[18].

To investigate further the extensive damage observed with low-pathogenicity influenza A virus infection in the absence of IFITM3, we infected both wild-type and $Ifitm3^{-/-}$ mice with a PR/8 influenza strain deficient for the multi-functional NS1 gene (delNS1)[19,20]. NS1 is the primary influenza virus interferon antagonist, with multiple inhibitory effects on host immune pathways[20,21]. We found that delNS1 virus was attenuated in both wild-type and $Ifitm3^{-/-}$ mice, and whereas the isogenic PR/8 strain expressing NS1 showed typical high pathogenicity in all mice tested, lower doses of PR/8 influenza (although lethal in both genotypes of mice) caused accelerated weight loss in $Ifitm3^{-/-}$ compared to wild-type mice (Supplementary Fig. 8). As delNS1 influenza A virus retains its pathogenicity in IFN-deficient mice[19], this suggests that $Ifitm3^{-/-}$ mice can mount an adequate IFN-mediated anti-viral response without extensive morbidity, and that IFITM3 blocking viral replication occurs before NS1-mediated IFN
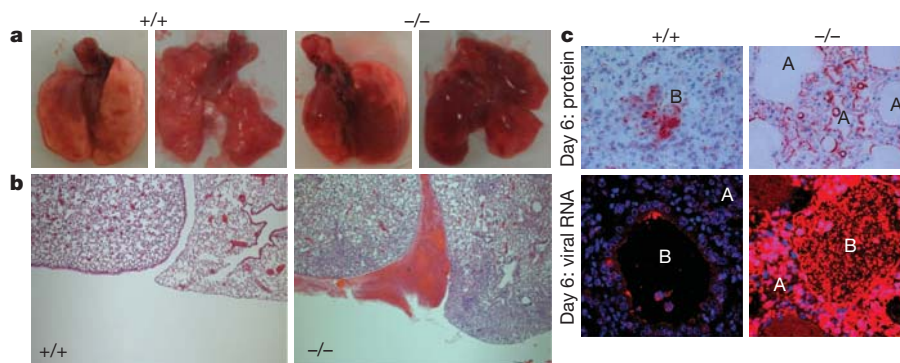
Figure 2 | Pathological examination of infected lungs. a, b, Wild-type mice showed few visible signs of external damage on lung lobes at day 6 post-infection, whereas $Ifitm3^{-/-}$ mice showed several large lesions (**a**, left, ventral view of intact lungs, right, all lobes displayed) resulting from severe oedema and hemorrhagic pleural effusion (**b**), as well as a markedly higher infiltration of cells and proteinaceous debris into the alveoli and bronchioles. **c**, Localization of virus within the lungs on day 6 indicated that virus penetrated deeper and more extensively into the lung tissue in the $Ifitm3^{-/-}$ mice, as determined by immunohistochemistry for total influenza protein and detection of virus nucleic acid (virus, red; cell nuclei, blue; A, alveolus; B, bronchiole). Original magnifications were ×5 (**b**) and ×20 (**c**).
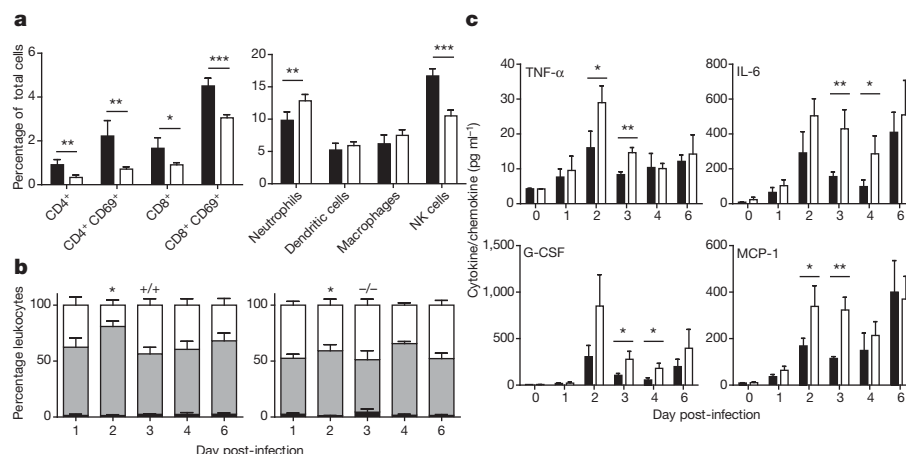
Figure 3 | Altered leukocyte and cytokine response to influenza A infection in *Ifitm3*$^{-/-}$ mice. a, Cytometric analysis of proportional resident cell populations in the lungs of mice (+/+, black; −/−, white) showed evidence of lymphopenia in *Ifitm3*$^{-/-}$ mice 6 days post-infection. **b**, Systemic lymphopenia was confirmed through differential analysis of peripheral blood cell counts, which showed a significant depletion of lymphocytes on day 2 post-infection of

Ifitm3$^{-/-}$ mice (monocytes, black; lymphocytes, grey; polymorphonuclear leukocytes, white). NK, natural killer. **c**, Levels of pro-inflammatory cytokines were also recorded as being elevated in *Ifitm3*$^{-/-}$ lungs over the course of infection (+/+, black; −/−, white). Results show means ± s.d., $n = 5$. Statistical significance was assessed by Student's *t*-test (*$P < 0.05$, **$P < 0.01$, ***$P < 0.001$).

antagonism[7]. Therefore, unchecked lung viral replication and an enhanced inflammatory response accounts for the profoundly deleterious effects of viral infection in *Ifitm3*$^{-/-}$ mice.

The human *IFITM3* gene has two exons and is predicted to encode two splice variants that differ by the presence or absence of the first amino-terminal 21 amino acids (Fig. 4a). Currently, 13 non-synonymous,

13 synonymous, one in-frame stop and one splice site acceptor-altering single nucleotide polymorphisms (SNPs) have been reported in the translated *IFITM3* sequence (Supplementary Table 1). Using tests sensitive to recent positive selection, we can find evidence for positive selection on the *IFITM3* locus in human populations acting over the last tens of thousands of years in Africa (Fig. 4b, c). We therefore
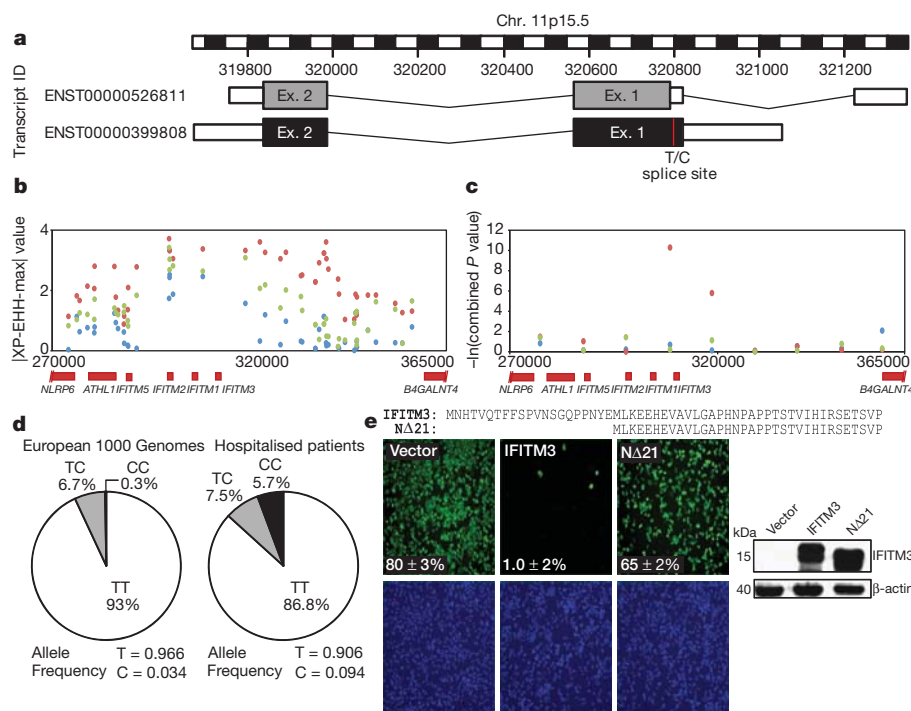
Figure 4 | Single nucleotide polymorphisms of the human *IFITM3* gene. a, Multiple single-nucleotide polymorphisms have been identified within the coding region of the human *IFITM3* gene. One such SNP, rs12252 (red), encodes a splice acceptor site altering T/C substitution mutation and may be associated with a truncated protein with an N-terminal 21 amino acid deletion. Therefore two transcripts are predicted to be expressed from the *IFITM3* gene. **b, c**, Positive selection analysis using a haplotype-based test, the cross population extended haplotype homozygosity test, maximum value (|XP-EHH-max|, **b**), where data points above 2.7 in the YRI (Africa) (red), 3.9 in the CEU (Europe) (blue) and 5.0 in the CHB+JPT (China and Japan) (green) populations are in the top 1% of values, and using a combination of three allele frequency spectrum-based test statistics (**c**), namely the composite likelihood

ratio (CLR)[23–25] on 10-kb windows along chromosome 11 encompassing the *IFITM3* locus. Evidence for positive selection is seen only in the YRI. **d**, Mutations recorded through sequencing of patients hospitalized with influenza virus during the H1N1/09 pandemic showed an overrepresentation of individuals with the C allele at SNP rs12252, relative to matched Europeans. **e**, A549 cells transduced to express either full-length (IFITM3) or truncated (NΔ21) IFITM3 (cell nuclei, blue; virus, green; ×4 magnification) show a reduction in viral restriction when the N-terminal 21 amino acids of IFITM3 are removed, relative to vector controls (Vector). Alignment of the N termini of full-length (IFITM3, top) and truncated IFITM3 (NΔ21, bottom). Values represent the mean of the percentage of infected cells ± s.d. ($n = 3$).

sequenced 1.8 kilobases of the *IFITM3* locus encompassing the exons, intron and untranslated regions from 53 individuals who required admission to hospital as a result of pandemic H1N1/09 or seasonal influenza virus infection in 2009–2010. Of these, 86.8% of patients carried majority alleles for all 28 SNPs in the coding sequence of the gene, but 13.2% possessed known variants. In particular, we discovered over-representation in cases of the synonymous SNP rs12252, wherein the majority T allele is substituted for a minority C allele, which alters the first splice acceptor site and may be associated with the *IFITM3* splice variant (ENST00000526811), which encodes an IFITM3 protein lacking the first 21 amino acids due to the use of an alternative start codon.

The allele frequencies for SNP rs12252 vary in different human populations (Supplementary Table 2). The ancestral (C) allele, reported in chimpanzees, is rare in sub-Saharan African and European populations (derived allele frequency (DAF) 0.093 and 0.026–0.036, respectively), but more frequent in other populations (Supplementary Table 2). SNP rs12252 is notable for its high level of differentiation between Europeans and East Asians, although the fixation index (F_{ST}, a measure of population differentiation) does not reach statistical significance. The genotypes associated with rs12252 in Caucasians hospitalized following influenza infection differ significantly from ethnically matched Europeans in 1000 Genomes sequence data and from genotypes imputed against the June 2011 release of the 1000 Genomes phased haplotypes from the UK, Netherlands and Germany (Wellcome Trust Case Control Consortium 1 (WTCCC1, UK): $P = 0.00006$, Netherlands: $P = 0.00001$, Germany: $P = 0.00007$; Fisher's exact test). Patients' genotypes also depart from Hardy–Weinberg equilibrium ($P = 0.003$), showing an excess of C alleles in this population (Fig. 4d). Principal components analysis of over 100,000 autosomal SNPs showed no evidence of hidden population structure differences between WTCCC controls and a subset of the hospitalised individuals from this study (Supplementary Fig. 9a, b).

To test the functional significance of the IFITM3 rs12252 polymorphism *in vitro*, we confirmed the genotypes of HapMap lymphoblastoid cell lines (LCLs) homozygous for either the majority (TT) or minority (CC) variant IFITM3 alleles (Supplementary Fig. 9c). We next challenged the LCLs with influenza A virus and found that the minority (CC) variant was more susceptible to infection, and this vulnerability correlated with lower levels of IFITM3 protein expression compared to the majority (TT) variant cells (Supplementary Fig. 10). Although we did not detect the IFITM3 splice variant protein (ENST00000526811) in the CC LCLs, we nonetheless investigated the possible significance of its presence by stably expressing the N-terminally truncated (NΔ21) and wild-type proteins to equivalent levels in human A549 lung carcinoma cell lines before infection with influenza A virus (A/WSN/1933 (WSN/33)). We found that cells expressing the NΔ21 protein failed to restrict viral replication when compared to wild-type IFITM3 (Fig. 4e), consistent with previous data showing that the amino-terminal 21 amino acids of IFITM3 are required for attenuation of vesicular stomatitis virus replication *in vitro*[4]. Similar results were obtained using other virulent viral strains (A/California/7/2009 (pH1N1), A/Uruguay/716/2007 (H3N2) and B/Brisbane/60/2008) (Supplementary Fig. 3).

We show here that IFITM3 expression acts as an essential barrier to influenza A virus infection *in vivo* and *in vitro*. The fulminant viral pneumonia that occurs in the absence of IFITM3 arises because of uncontrolled virus replication in the lungs, resulting in profound morbidity. In effect, the host's loss of a single immune effector, IFITM3, transforms a mild infection into one with remarkable severity. Similarly, the enrichment of the rs12252 C-allele in those hospitalized with influenza infections, together with the decreased IFITM3 levels and the increased infection of the CC-allele cells *in vitro*, suggests that IFITM3 also plays a pivotal role in defence against human influenza virus infections. This innate resistance factor is all the more important during encounters with a novel pandemic virus, when the host's acquired immune defences are less effective. Indeed, IFITM3-compromised individuals, and in turn populations with a higher percentage of such individuals, may be more vulnerable to the initial establishment and spread of a virus against which they lack adaptive immunity. In light of its ability to curtail the replication of a broad range of pathogenic viruses *in vitro*, these *in vivo* results suggest that IFITM3 may also shape the clinical course of additional viral infections in favour of the host, and may have done so over human evolutionary history.

METHODS SUMMARY

Mouse infection. Wild-type and *Ifitm3*$^{-/-}$ mice[8] (8–10 weeks of age) were intranasally inoculated with 10^4 p.f.u. of A/X-31 (H3N2) influenza, 200 p.f.u. of A/England/195/09 (pH1N1) influenza, or $50–10^3$ p.f.u. of A/PR/8/34 (PR/8) or the PR/8 *NS1* gene deletion mutant (delNS1)[20] (H1N1) in 50 μl of sterile PBS. Mouse weight was recorded daily as well as monitoring for signs of illness. Mice exceeding 25% total weight loss were killed in accordance with UK Home Office guidelines. Infected lungs were collected on days 1–6 post-infection and quantified for viral load by plaque assay and RT-qPCR with primers to influenza matrix 1 protein.

Pathology of infected *Ifitm3*$^{-/-}$ mice. 5-μm sections of paraffin-embedded tissue were stained with haematoxylin and eosin and microscopically examined. Apoptosis was assessed by TUNEL using the TACS XL DAB *In Situ* Apoptosis Detection Kit (R&D Systems). Viral RNA was visualized by QuantiGene viewRNA kit (Affymetrix), with a viewRNA probe set designed to the negative stranded vRNA encoding the *NP* gene of A/X-31 (Affymetrix). Lung tissue was embedded in glycol methacrylate (GMA) and viral antigens stained using M149 polyclonal antibody to influenza A, B (Takara). Single cell suspensions from the lung were characterized by flow cytometry for T-lymphocytes CD4$^+$ or CD8$^+$, T-lymphocytes (activated) CD4$^+$CD69$^+$ or CD8$^+$CD69$^+$, neutrophils CD11b^{hi}CD11c$^-$Ly6g$^+$, dendritic cells CD11c$^+$CD11b^{lo}Ly6g^{lo} MHC class II high, macrophages CD11b$^+$CD11c$^+$F4/80^{hi}, natural killer cells NKp46$^+$CD4$^-$CD8$^-$.

Sequencing and genetics of human *IFITM3*. The 1.8 kb of human *IFITM3* was amplified and sequenced to identify single nucleotide polymorphisms (SNPs). SNP rs12252 was identified and compared to allele and genotype frequencies from 1000 Genomes sequencing data from different populations including 1000 Genomes imputed. SNP rs12252 allele frequencies were determined in the publicly available genotype data sets of WTCCC1 ($n = 2,938$) and previously published data sets genotyped from the Netherlands ($n = 8,892$) and Germany ($n = 6,253$)[22].

Full Methods and any associated references are available in the online version of the paper at www.nature.com/nature.

1. Brass, A. L. *et al.* The IFITM proteins mediate cellular resistance to influenza A H1N1 virus, West Nile virus, and dengue virus. *Cell* **139,** 1243–1254 (2009).
2. Jiang, D. *et al.* Identification of five interferon-induced cellular proteins that inhibit West Nile virus and dengue virus infections. *J. Virol.* **84,** 8332–8341 (2010).
3. Yount, J. S. *et al.* Palmitoylome profiling reveals S-palmitoylation-dependent antiviral activity of IFITM3. *Nature Chem. Biol.* **6,** 610–614 (2010).
4. Weidner, J. M. *et al.* Interferon-induced cell membrane proteins, IFITM3 and tetherin, inhibit vesicular stomatitis virus infection via distinct mechanisms. *J. Virol.* **84,** 12646–12657 (2010).
5. Huang, I. C. *et al.* Distinct patterns of IFITM-mediated restriction of filoviruses, SARS coronavirus, and influenza A viruses. *PLoS Pathog.* **7,** e1001258 (2011).
6. Schoggins, J. W. *et al.* A diverse range of gene products are effectors of the type I interferon antiviral response. *Nature* **472,** 481–485 (2011).
7. Feeley, E. M. *et al.* IFITM3 inhibits influenza A virus infection by preventing cytosolic entry. *PLoS Pathog.* **7,** e1002337 (2011).
8. Lange, U. C. *et al.* Normal germ line establishment in mice carrying a deletion of the *Ifitm/Fragilis* gene family cluster. *Mol. Cell. Biol.* **28,** 4688–4696 (2008).
9. Belser, J. A. *et al.* Pathogenesis of pandemic influenza A (H1N1) and triple-reassortant swine influenza A (H1) viruses in mice. *J. Virol.* **84,** 4194–4203 (2010).
10. Tumpey, T. M. *et al.* Characterization of the reconstructed 1918 Spanish influenza pandemic virus. *Science* **310,** 77–80 (2005).
11. Kobasa, D. *et al.* Aberrant innate immune response in lethal infection of macaques with the 1918 influenza virus. *Nature* **445,** 319–323 (2007).
12. Tumpey, T. M., Lu, X. H., Morken, T., Zaki, S. R. & Katz, J. M. Depletion of lymphocytes and diminished cytokine production in mice infected with a highly virulent influenza A (H5N1) virus isolated from humans. *J. Virol.* **74,** 6105–6116 (2000).
13. Kobasa, D. *et al.* Enhanced virulence of influenza A viruses with the haemagglutinin of the 1918 pandemic virus. *Nature* **431,** 703–707 (2004).
14. Maines, T. R. *et al.* Pathogenesis of emerging avian influenza viruses in mammals and the host innate immune response. *Immunol. Rev.* **225,** 68–84 (2008).
15. Perrone, L. A., Plowden, J. K., Garcia-Sastre, A., Katz, J. M. & Tumpey, T. M. H5N1 and 1918 pandemic influenza virus infection results in early and excessive infiltration of macrophages and neutrophils in the lungs of mice. *PLoS Pathog.* **4,** e1000115 (2008).

16. Fukuyama, S. & Kawaoka, Y. The pathogenesis of influenza virus infections: the contributions of virus and host factors. *Curr. Opin. Immunol.* **23**, 481–486 (2011).
17. Julkunen, I. *et al.* Inflammatory responses in influenza A virus infection. *Vaccine* **19**, S32–S37 (2000).
18. Yum, H. K. *et al.* Involvement of phosphoinositide 3-kinases in neutrophil activation and the development of acute lung injury. *J. Immunol.* **167**, 6601–6608 (2001).
19. García-Sastre, A. *et al.* Influenza A virus lacking the NS1 gene replicates in interferon-deficient systems. *Virology* **252**, 324–330 (1998).
20. Hale, B. G., Randall, R. E., Ortin, J. & Jackson, D. The multifunctional NS1 protein of influenza A viruses. *J. Gen. Virol.* **89**, 2359–2376 (2008).
21. Billharz, R. *et al.* The NS1 protein of the 1918 pandemic influenza virus blocks host interferon and lipid metabolism pathways. *J. Virol.* **83**, 10557–10570 (2009).
22. Anttila, V. *et al.* Genome-wide association study of migraine implicates a common susceptibility variant on 8q22.1. *Nature Genet.* **42**, 869–873 (2011).
23. Tajima, F. Statistical method for testing the neutral mutation hypothesis by DNA polymorphism. *Genetics* **123**, 585–595 (1989).
24. Fay, J. C. & Wu, C.-I. Hitchhiking under positive Darwinian selection. *Genetics* **155**, 1405–1413 (2000).
25. Nielsen, R. *et al.* Genomic scans for selective sweeps using SNP data. *Genome Res.* **15**, 1566–1575 (2005).

MOSAIC Core Investigators

Benaroya Research Institute, USA D. Chaussabel[1]; **Gartnavel General Hospital, Greater Glasgow, UK** W. E. Adamson[2], W. F. Carman[2]; **Health Protection Agency, UK** C. Thompson[3], M. C. Zambon[3]; **Imperial College London, UK** P. Aylin[4], D. Ashby[4], W. S. Barclay[4], S. J. Brett[4], W. O. Cookson[4], L. N. Drumright[4], J. Dunning[4], R. A. Elderfield[4], L. Garcia-Alvarez[4], B. G. Gazzard[4], M. J. Griffiths[4], M. S. Habibi[4], T. T. Hansel[4], J. A. Herberg[4], A. H. Holmes[4], T. Hussell[4], S. L. Johnston[4], O. M. Kon[4], M. Levin[4], M. F. Moffatt[4], S. Nadel[4], P. J. Openshaw[4], J. O. Warner[4]; **Liverpool School of Tropical Medicine, UK** S. J. Aston[5], S. B. Gordon[5]; **National Institute for Medical Research, UK** A. Hay[6], J. McCauley[6], A. O'Garra[6]; **Roche, Nutley, USA** J. Banchereau[7]; **University College London, UK** A. Hayward[8], P. Kellam[8]; **University of Edinburgh, UK** J. K. Baillie[9], D. A. Hume[9], P. Simmonds[9]; **University of Liverpool, UK** P. S. McNamara[10], M. G. Semple[10], R. L. Smyth[10]; **University of Nottingham, UK** J. S. Nguyen-Van-Tam[11]; **University of Oxford, UK** L.-P. Ho[12], A. J. McMichael[12]; **Wellcome Trust Sanger Institute, UK** P. Kellam[13].

GenISIS Investigators

Critical Care Medicine, University of Edinburgh K. Everingham[14], H. Dawson[14], D. Hope[14], P. Ramsay[14], T. S. Walsh (Local Lead Investigator)[14]; **Generation Scotland, University of Edinburgh Molecular Medicine Centre** A. Campbell[15], S. Kerr[15]; **Intensive Care National Audit & Research Centre, London** D. Harrison[16], K. Rowan[16]; **Intensive Care Unit, Aberdeen Royal Infirmary** J. Addison[17], N. Donald[17], S. Galt[17], D. Noble[17], J. Taylor[17], N. Webster (Local Lead Investigator)[17]; **Intensive Care Unit, Ayr Hospital** I. Taylor (Local Lead Investigator)[18]; **Intensive Care Unit, Borders General Hospital, Melrose** J. Aldridge (Local Lead Investigator)[19], R. Dornan[19], C. Richard[19]; **Intensive Care Unit, Crosshouse Hospital, Kilmarnock** D. Gilmour[20], R. Simmons (Local Lead Investigator)[20], R. White (Local Lead Investigator)[20]; **Intensive Care Unit, Dumfries and Galloway Royal Infirmary** C. Jardine[21], D. Williams (Local Lead Investigator)[21]; **Intensive Care Unit, Glasgow Royal Infirmary** M. Booth (Local Lead Investigator)[22], T. Quasim[22]; **Intensive Care Unit, Hairmyres Hospital, Lanarkshire** V. Watson[23]; **Intensive Care Unit, Inverclyde Royal Hospital, Greenock** P. Henry[24], F. Munro[24]; **Intensive Care Unit, Monklands Hospital, Airdrie** L. Bell[25], J. Ruddy (Local Lead Investigator)[25]; **Intensive Care Unit, Ninewells Hospital, Dundee** S. Cole (Local Lead Investigator)[26], J. Southward[26]; **Intensive Care Unit, Queen Margaret Hospital, Dunfermline** P. Allcoat[27], S. Gray[27], M. McDougall (Local Lead Investigator)[27]; **Intensive Care Unit, Raigmore Hospital, Inverness** J. Matheson[28], J. Whiteside (Local Lead Investigator)[28]; **Intensive Care Unit, Royal Alexandra Infirmary, Paisley** B. Alcorn[29], K. Rooney (Local Lead Investigator)[29], R. Sundaram[29]; **Intensive Care Unit, Southern General Hospital, Glasgow** G. Imrie (Local Lead Investigator)[30]; **Intensive Care Unit, St John's Hospital, Livingston** J. Bruce[31], K. McGuigan[31], S. Moultrie (Local Lead Investigator)[31]; **Intensive Care Unit, Stirling Royal Infirmary** C. Cairns (Local Lead Investigator)[32], J. Grant[32], M. Hughes[32]; **Intensive Care Unit, Stobhill Hospital, Glasgow** C. Murdoch (Local Lead Investigator)[33]; **Intensive Care Unit, Victoria Hospital, Glasgow** A. Davidson (Local Lead Investigator)[34]; **Intensive Care Unit, Western General Hospital, Edinburgh** G. Harris[35], R. Paterson[35], C. Wallis (Local Lead Investigator)[35]; **Intensive Care Unit, Western Infirmary, Glasgow** S. Binning (Local Lead Investigator)[36], M. Pollock[36]; **Wellcome Trust Clinical Research Facility, Edinburgh** J. Antonelli[37], A. Duncan[37], J. Gibson[37], C. McCulloch[37], L. Murphy[37]; **Roslin Institute, University of Edinburgh** C. Haley[38], G. Faulkner[38], T. Freeman[38], D. A. Hume[38] & J. K. Baillie (Principal Investigator)[38].

[1]Benaroya Research Institute, 1201 9th Avenue, Seattle, Washington 98101-2795, USA. [2]West of Scotland Specialist Virology Centre, Gartnavel General Hospital, Glasgow and Clyde Health Board, 1053 Great Western Road, Glasgow G12 0YN, UK. [3]Health Protection Agency, Microbiology Services Colindale, 61 Colindale Avenue, London NW9 5EQ, UK. [4]Imperial College London, St Mary's Campus, Norfolk Place, London W2 1PG, UK. [5]Liverpool School of Tropical Medicine, Pembroke Place, Liverpool L3 5QA, UK. [6]National Institute for Medical Research (NIMR), The Ridgeway, London NW7 1AA, UK. [7]Roche, 340 Kingsland Street, Nutley, New Jersey 07110-1199, USA. [8]University College London, Gower Street, London, WC1E 6BT, UK. [9]The Roslin Institute and R(D)SVS, University of Edinburgh, Easter Bush, Midlothian EH25 9RG, UK. [10]Department of Women's and Children's Health, Institute of Translational Medicine, University of Liverpool, Alder Hey Children's Hospital, Liverpool L12 2AP, UK. [11]Epidemiology and Public Health, University of Nottingham, Clinical Sciences Building, City Hospital, Nottingham NG5 1PB, UK. [12]The Weatherall Institute of Molecular Medicine, University of Oxford, John Radcliffe Hospital, Oxford OX3 9DS, UK. [13]Wellcome Trust Sanger Institute, Wellcome Trust Genome Campus, Hinxton, Cambridge CB10 1SA, UK. [14]Department of Critical Care Medicine, The Queen's Medical Research Institute, College of Medicine and Veterinary Medicine, University of Edinburgh, 47 Little France Drive, Edinburgh EH16 4TJ, UK [15]Generation Scotland, University of Edinburgh, Molecular Medicine Centre, Western General Hospital, Crewe Road South, Edinburgh EH4 2XU, UK. [16]Intensive Care National Audit & Research Centre, Tavistock House, Tavistock Square, London WC1H 9HR, UK. [17]Intensive Care Unit, Aberdeen Royal Infirmary, Foresterhill, Aberdeen AB25 2ZN, UK. [18]Intensive Care Unit, Ayr Hospital, Dallmellington Road, Ayr KA6 6DX, UK. [19]Intensive Care Unit, Borders General Hospital, Melrose TD6 9BS, UK. [20]Intensive Care Unit, Crosshouse Hospital, Kilmarnock KA2 0BE, UK. [21]Intensive Care Unit, Dumfries and Galloway Royal Infirmary, Dumfries DG1 4AP, UK. [22]Intensive Care Unit, Glasgow Royal Infirmary, Glasgow G4 0SF, UK. [23]Intensive Care Unit, Hairmyres Hospital, Lanarkshire G75 8RG, UK. [24]Intensive Care Unit, Inverclyde Royal Hospital, Greenock PA16 0XN, UK. [25]Intensive Care Unit, Monklands Hospital, Airdrie ML6 0JS, UK. [26]Intensive Care Unit, Ninewells Hospital, Dundee DD1 9SY, UK. [27]Intensive Care Unit, Queen Margaret Hospital, Dunfermline KY12 0SU, UK. [28]Intensive Care Unit, Raigmore Hospital, Inverness IV2 3UJ, UK. [29]Intensive Care Unit, Royal Alexandra Hospital, Paisley PA2 9PN, UK. [30]Intensive Care Unit, Southern General Hospital, Glasgow G51 4TF, UK. [31]Intensive Care Unit, St John's Hospital, Livingston EH54 6PP, UK. [32]Intensive Care Unit, Stirling Royal Infirmary, Stirling FK8 2AU, UK. [33]Intensive Care Unit, Stobhill Hospital, Glasgow G21 3UW, UK. [34]Intensive Care Unit, Victoria Hospital, Glasgow G42 9TY, UK. [35]Intensive Care Unit, Western General Hospital, Crewe Road South, Edinburgh EH4 2XU, UK. [36]Intensive Care Unit, Western Infirmary, Glasgow G11 6NT, UK. [37]Wellcome Trust Clinical Research Facility, Western General Hospital, Crewe Road South, Edinburgh EH4 2XU, UK. [38]Division of Genetics and Genomics, The Roslin Institute, University of Edinburgh, Easter Bush, Midlothian EH25 9RG, UK.

METHODS

Mouse infection. Background-matched wild-type (>95% C57BL/6) and $Ifitm3^{-/-}$ mice[8] 8–10 weeks of age were maintained in accordance with UK Home Office regulations, UK Animals Scientific Procedures Act 1986 under the project licence PPL80/2099. This licence was reviewed by The Wellcome Trust Sanger Institute Ethical Review Committee. Groups of >5 isofluorane-anaesthetized mice of both genotype were intranasally inoculated with 10^4 p.f.u. of A/X-31 influenza in 50 μl of sterile PBS. In some experiments A/X-31 was substituted with 200 p.f.u. of A/England/195/09 influenza, or 50–10^3 p.f.u. of A/PR/8/34 (PR/8) or an otherwise isogenic virus with a deletion of the *NS1* gene (delNS1)[19], made as described[26]. Their weight was recorded daily and they were monitored for signs of illness. Mice exceeding 25% total weight loss were killed in accordance with UK Home Office guidelines. Littermate controls were used in all experiments.

Influenza virus quantification. Lungs from five mice per genotype were collected on days 1, 2, 3, 4 and 6 post-infection, weighed and homogenized in 5% weight/volume (w/v) of Leibovitz's L-15 medium (Invitrogen) containing antibiotic-antimycotic (Invitrogen). Samples were quantified for viral load by plaque assay in tenfold serial dilutions on Madin–Darby canine kidney (MDCK) cell monolayers overlaid with 1% Avicell medium[27]. Lungs were subjected to two freeze-thaw cycles before titration. Virus was also quantified by quantitative PCR with reverse transcription (qRT–PCR), wherein RNA was first extracted from lung, heart, brain and spleen using the RNeasy Mini Plus Kit (Qiagen). Purified RNA was normalized by mass and quantified with SYBR Green (Qiagen) using the manufacturer's instructions and 0.5 μM primers for influenza matrix 1 protein (*M1*) forward: 5′-TGA GTCTTCTAACCGAGGTC-3′, reverse: 5′-GGTCTTGTCTTTAGCCATTCC-3′ (Sigma-Aldrich) and mouse β-actin (*Actb*) forward: 5′-CTAAGGCCAACCGTG AAAAG-3′, reverse: 5′-ACCAGAGGCATACAGGGACA-3′. qPCR was performed on a StepOnePlus machine (Applied Biosystems) and analysed with StepOne software v2.1 (Applied Biosystems).

Western blotting. Lungs were homogenized in 5% w/v of Tissue Protein Extraction Reagent (Thermo Scientific) containing cOmplete Protease Inhibitor (Roche). Total protein was quantified by BCA assay (Thermo Scientific) and was normalized before loading into wells. Proteins were visualized with the following indicated primary antibodies: anti-mouse IFITM2 rabbit polyclonal was purchased from Santa Cruz Biotechnology (catalogue no. sc-66828); anti-Fragilis (Ifitm3) rabbit polyclonal antibody was from Abcam (catalogue no. ab15592). The IFITM3 and NΔ21 western blot using the A549 stable cell lines were probed with the anti-IFITM1 antibody from Prosci (catalogue no. 5807), which recognizes a conserved portion of the IFITM1, IFITM2 and IFITM3 proteins which is still present even in the absence of the first twenty one N-terminal amino acids. The LCL blots (including the A549 cell line lysate controls) were probed with either an antibody which is specific for the N terminus of IFITM3 (rabbit anti-IFITM3 (N-terminal amino acids 8–38) (Abgent, catalogue no. AP1153a)), or with anti-IFITM1 antibody from Prosci (catalogue no. 5807), as well as rabbit anti-MX1 (Proteintech, catalogue no. 13750-1-AP) and mouse anti-GAPDH (clone GAPDH-71.1) (Sigma, catalogue no. G8795). For the LCL immunoblots all antibodies were diluted in DPBS (Sigma) containing 0.1% Tween 20 (Sigma) and 5% non-fat dried milk (Carnation) and incubated overnight at 4 °C. All primary antibodies were consequently bound to the corresponding species-appropriate horseradish peroxidase-conjugated secondary antibodies (Dako). Actin antibody was purchased from either Abcam or Sigma, mouse monoclonal, catalogue no. A5316.

Pathological examination. 5-μm sections of paraffin-embedded tissue were stained with haematoxylin and eosin (Sigma-Aldrich) and were examined and scored twice, once by a pathologist under blinded conditions. The TUNEL assay for apoptosis was conducted using the TACS XL DAB *In Situ* Apoptosis Detection Kit (R&D Systems).

Immunofluorescent tissue staining: protein. Lung tissue was embedded in glycol methacrylate (GMA) to visualize the spread of viral protein, as described previously[28]. Briefly, 2-μm sections were blocked with 0.1% sodium azide and 30% hydrogen peroxide followed by a second block of RPMI 1640 (Invitrogen) containing 10% fetal calf serum (Sigma-Aldrich) and 1% bovine serum albumin (Invitrogen). Viral antigen was stained using M149 polyclonal antibody to influenza A, B (Takara) and visualized with a secondary goat anti-rabbit antibody conjugated to alkaline phosphatase (Dako). Sections were counterstained with haematoxylin (Sigma-Aldrich). Murine IFITM1 and IFITM3 protein expression in lung sections from either uninfected mice, or those 2 days post-infection with A/X-31, were immunostained with either anti-IFITM1 antibody (Abcam, catalogue no. ab106265) or anti-fragilis (anti-Ifitm3) rabbit polyclonal antisera (Abcam, catalogue no. ab15592). Sections were also stained for DNA with Hoechst 33342 (Sigma).

Immunofluorescent staining: RNA. Viral RNA was visualized in 5-μm paraffin-embedded sections using the QuantiGene viewRNA kit (Affymetrix). Briefly, sections were rehydrated and incubated with proteinase K. They were subsequently incubated with a viewRNA probe set designed against the negative stranded viral RNA encoding the *NP* gene of A/X-31 (Affymetrix). The signal was amplified before incubation with labelled probes and visualized.

Flow cytometry. Single-cell suspensions were generated by passing lungs twice through a 100-μm filter before lysing red blood cells with RBC lysis buffer (eBioscience) and assessing for cell viability via Trypan blue exclusion. Cells were characterized by flow cytometry as follows: T-lymphocytes $CD4^+$ or $CD8^+$, T-lymphocytes (activated) $CD4^+CD69^+$ or $CD8^+CD69^+$, neutrophils $CD11b^{hi}CD11c^-$ Ly6g$^+$, dendritic cells $CD11c^+CD11b^{lo}Ly6g^{lo}$ MHC class II high, macrophages $CD11b^+CD11c^+F4/80^{hi}$, natural killer cells $NKp46^+CD4^-CD8^-$. All antibodies (Supplementary Table 3) were from BD Bioscience, except CD69 and F4/80, which were from AbD Serotec. Samples were run on a FACSAria II (BD Bioscience) and visualized using FlowJo 7.2.4. Data were analysed statistically and graphed using Prism 5.0 (GraphPad Software).

Peripheral leukocyte analysis. Mice ($n = 3$ per genotype per day) were bled on days 0, 1, 2, 3, 4 and 6 by tail vein puncture. Leukocyte counts were determined by haemocytometer, whereas blood cell differential counts were calculated by counting from duplicate blood smears stained with Wright–Giemsa stain (Sigma-Aldrich). At least 100 leukocytes were counted per smear. All blood analyses were conducted in a blinded fashion. Data were analysed statistically and graphed using Prism 5.0 (GraphPad Software).

Cytokine/chemokine analysis. Lungs were collected and homogenized on days 0, 1, 2, 3, 4 and 6 post-infection from four mice of each genotype. G-CSF, GM-CSF, IFN-γ, IL-10, IL-1α, IL-1β, IL-2, IL-4, IL-5, IL-6, IL-9, IP-10, KC-like, MCP-1, MIP-1α, RANTES and TNF-α were analysed using a mouse antibody bead kit (Millipore) according to the manufacturer's instructions on a Luminex FlexMAP3D. Results were analysed and quality control checked using Masterplex QT 2010 and Masterplex Readerfit 2010 (MiraiBio). Data were analysed statistically and graphed using Prism 5.0 (GraphPad Software).

Murine embryonic fibroblast generation, transduction and infectivity assays. Adult $Ifitm3^{-/-}$ mice[8] were intercrossed and fibroblasts (MEFs) were derived from embryos at day 13.5 of gestation, as described previously[1]. MEFs were genotyped by PCR (Thermo-Start *Taq* DNA Polymerase, ABgene) on embryo tail genomic DNA using primers and the cycle profile described previously[8] to detect the presence of the wild-type allele (450 base pairs band) and the targeted/knock-out allele (650 bp band). MEFs were cultured in DMEM containing 10% FBS, 1× MEM essential amino acids, 1× 2-mercapto-ethanol (Gibco). MEFs were transduced with vesicular stomatitis virus G (VSV-G) pseudotyped retroviruses expressing either the empty vector control (pQXCIP, Clontech), or one expressing *Ifitm3*, as previous described[1]. After puromycin selection the respective cell lines were challenged with either A/X-31 virus (multiplicity of infection (m.o.i.) 0.3–0.4) or PR/8 (m.o.i. 0.4). For PR/8 infections, after 12 h the media was removed and the cells were then fixed with 4% formalin and stained with purified anti-haemagglutinin monoclonal antibody (Hybridoma HA36-4-5.2, Wistar Institute). For A/X-31 experiments, cells were processed comparably as above, but in addition were permeabilized, followed by immunostaining for NP expression (NP (clone H16-L10-4R5) mouse monoclonal (Millipore MAB8800)). Both sets of experiments were completed using an Alexa Fluor 488 goat anti-mouse secondary antibody at 1:1,000 (A11001, Invitrogen). The cells were imaged on an automated Image Express Micro microscope (Molecular Devices), and images were analysed using the MetaMorph Cell Scoring software program (Molecular Devices). Cytokines: cells were incubated with cytokines for 24 h before viral infection. Murine interferon α (PBL Interferon Source, catalogue no. 12100-1) and IFN-γ (PBL Interferon Source, catalogue no. 12500-2) were used at 500–2,500 U ml^{-1}, and 100–300 ng ml^{-1}, respectively.

A549 transduction and infectivity assays. A549 cells (ATCC catalogue no. CCL-185) were grown in complete media (DMEM (Invitrogen catalogue no. 11965) with 10% FBS (Invitrogen)). A549 stable cell lines were made by gamma-retroviral transduction using either the empty vector control virus (pQXCIP, Clontech), the full-length human *IFITM3* complementary DNA, or a truncated human *IFITM3* cDNA which is missing the first 21 amino acids (NΔ21). After puromycin selection, expression of the IFITM3 and NΔ21 proteins were confirmed by western blotting using an 18% SDS–PAGE gel and an anti-IFITM3 antibody that was raised against the conserved intracellular loop (CIL) of IFITM3 (Proteintech). A549 cell lines were challenged with one of the following strains: A/WSN/33 (a gift of P. Palese), A/California/7/2009, A/Uruguay/716/2007 and B/Brisbane/60/2008 (gift of J. Malbry) for 12 h, then fixed with 4% paraformaldehyde (PFA) and immunostained with anti-HA antibody (Wistar collection) or anti-NP antibodies (Abcam), or Millipore clone H16-L10-4R5 anti-influenza A virus antibody). Per cent infection was calculated from immunofluorescent images as described for the MEF experiments above. Alternatively, cells were transduced with lentiviral vectors to express green fluorescent protein (GFP) or IFITM3 and were stained with anti-NP antibody (Abcam) and analysed by flow cytometry following

challenge with B/Bangladesh/3333/2007 virus (NIMR, England). For the immuno-fluorescence-based viral titring experiments, virus-containing supernatant was collected from the indicated A549 cell line cultures after 12 h of infection with WSN/33 (part one). Next this supernatant was used to infect MDCK cells (ATCC) in a well by well manner (part two). Both the A549 and MDCK cells were then processed to detect viral HA expression as described above.

LCL infectivity assays. LCL TT and LCL CC cells were grown in RPMI-1640 (Sigma-Aldrich) containing 10% FCS, 2 mM L-glutamine, 1 mM sodium pyruvate, 1× MEM non-essential amino acids solution, and 20 mM HEPES (all from Invitrogen). For infectivity assays, LCL cells were either treated with recombinant human IFN-α2 (PBL Interferon Source, catalogue no. 11100) at 100 units per ml or DPBS (Sigma-Aldrich) for 16 h. The LCL cells were then counted, resuspended at a concentration of 5×10^5 cells per ml, and plated on a 96-well round-bottom plate (200 μl cell suspension per well). The cells were then challenged with WSN/33 influenza A virus (m.o.i. 0.1). After 18 h, the cells were washed twice with 250 μl MACS buffer (DPBS containing 2% FCS and 2 mM EDTA (Sigma-Aldrich)). The cells were fixed and permeabilized using the BD Cytofix/Cytoperm Fixation/Permeabilization Kit (BD Biosciences), following the manufacturer's instructions. Briefly, the cells were resuspended in 100 μl of Cytofix/Cytoperm Fixation and Permeabilization solution and incubated at 4 °C for 20 min. The cells were then washed twice with 250 μl 1× Perm/Wash buffer and resuspended in 50 ml 1× Perm/Wash buffer containing a 2 μg ml^{-1} solution of a fluorescein isothiocyanate (FITC)-conjugated mouse monoclonal antibody against influenza A virus NP (clone 431, Abcam, catalogue no. ab20921). The cells were incubated in the diluted antibody solution for 1 h at 4 °C, washed twice with 250 μl 1× Perm/Wash buffer, resuspended in 200 μl MACS buffer, and analysed by flow cytometry using a BD FACS Calibur (BD Biosciences).

Ethics and sampling. We recruited patients with confirmed seasonal influenza A or B virus or pandemic influenza A pH1N1/09 infection who required hospitalization in England and Scotland between November 2009 and February 2011. Patients with significant risk factors for severe disease and patients whose daily activity was limited by co-morbid illness were excluded. 53 patients, 29 male and 24 female, average age 37 (range 2–62) were selected. 46 (88%) had no concurrent co-morbidities. The remaining 6 had the following comorbid conditions: hypertension (3 patients), alcohol dependency and cerebrovascular disease (1 patient), bipolar disorder (1 patient) and kyphoscoliosis (1 patient). Four patients were pregnant. Where assessed, 36 patients had normal body mass (69%), one had a body mass index <18.5 and 10 had a body mass index between 25 and 39.9 and one a body mass index >40. Seasonal influenza A H3N2, influenza B and pandemic influenza A pH1N1/09 were confirmed locally by viral PCR or serological tests according to regional protocols. Consistent with the prevalent influenza viruses circulating in the UK between 2009 and 2011 (ref. 29) 44 (85%) had pH1N1/09, 2 had pH1N1/09 and influenza B co-infection, 4 had influenza B and 2 had non-subtyped influenza A virus infection. Of the adults, 24 required admission to an intensive care unit (ICU) and 1 required admission to a high dependency unit (HDU). The remainder were managed on medical wards and survived their illnesses. The GenISIS study was approved by the Scotland 'A' Research Ethics Committee (09/MRE00/77) and the MOSAIC study was approved by the NHS National Research Ethics Service, Outer West London REC (09/H0709/52, 09/MRE00/67).

Consent was obtained directly from competent patients, and from relatives/friends/welfare attorneys of incapacitated patients. Anonymized 9-ml EDTA blood samples were transported at ambient temperature. DNA was extracted using a Nucleon Kit (GenProbe) with the BACC3 protocol. DNA samples were re-suspended in 1 ml TE buffer pH 7.5 (10 mM Tris-Cl pH 7.5, 1 mM EDTA pH 8.0).

Sequencing and genetics. Human *IFITM3* sequences were amplified from DNA obtained from peripheral blood by nested PCR (GenBank accession numbers JQ610570 to JQ610621). The first round used primers forward: 5′-TGAGGGT TATGGGAGACGGGGT-3′and reverse: 5′-TGCTCACGGCAGGAGGCC-3′, followed by an additional round using primers forward: 5′-GCTTTGGGGGA ACGGTTGTG-3′and reverse: 5′- TGCTCACGGCAGGAGGCCCGA-3′. The

1.8-kb *IFITM3* band was gel-extracted and purified using the QIAquick Gel Extraction Kit (Qiagen). *IFITM3* was Sanger-sequenced on an Applied Biosystems 3730xl DNA Analyzer (GATC Biotech) using a combination of eight sequencing primers (Supplementary Table 4). Single-nucleotide polymorphisms were identified by assembly to the human *IFITM3* encoding reference sequence (accession number NC_000011.9) using Lasergene (DNAStar). Homozygotes were called based on high, single base peaks with high Phred quality scores, whereas heterozygotes were identified based on low, overlapping peaks of two bases with lower Phred quality scores relative to surrounding base calls (Supplementary Fig. 9). We identified SNP rs12252 in our sequencing and compared the allele and genotype frequencies to allele and genotype frequencies from 1000 Genomes sequencing data from different populations (Supplementary Table 3). In addition, we used the most recent release of phased 1000 Genomes data[30] to impute the region surrounding SNP rs12252 to determine allele frequencies in the publicly available genotype data set of WTCCC1 controls ($n = 2,938$) and four previously published data sets genotyped from the Netherlands ($n = 8,892$) and Germany ($n = 6,253$)[22]. In the imputation, samples genotyped with Illumina 550k, 610k and 670k platforms were imputed against the June 2011 release of 1000 Genotypes phased haplotypes using the Impute software[31], version 2.1.2. Only individuals with European ethnicities (Europe (CEU), Finland (FIN), Great Britain (GBR), Spain/Iberia (IBS), Tuscany (TSI)) were included from the 1000 Genomes reference panel. Recommended settings were used for imputing the region 200 kb in either direction from the variants of interest, along with 1 Mb buffer size. The statistical significance of the allele frequencies was determined by Fisher's exact test.

We assessed for population stratification by principal component analysis. Genotype data from the WTCCC1 1958 Birth Cohort data set were obtained from the European Genotype Archive with permission, reformatted and merged with genotype data from the GenISIS study to match 113,819 SNPs present in both cohorts. Suspected strand mismatches were removed by identifying SNPs with more than 2 genotypes and using the LD method as implemented in Plink (v1.07)[32], resulting in 105,362 matched SNPs. Quality control was applied in GenABEL version 1.6-9 to genotype data for these SNPs for the GenISIS cases and 1,499 individuals from WTCCC. Thresholds for quality control (deviation from Hardy–Weinberg equilibrium ($P < 0.05$), minor allele frequency (MAF) < 0.0005, call rate <98% in all samples) were applied iteratively to identify all markers and subjects passing all quality control criteria, followed by principal component analysis using GenABEL. We tested for positive selection using both a haplotype-based test (|XP-EHH-max|) and allele frequency spectrum-based test statistics, namely the CLR[23–25] on 10-kb windows across the entire genome as described previously[30,33]. The three statistics were combined and the combined P value was plotted corresponding to the 10-kb windows.

26. de Wit, E. *et al.* Efficient generation and growth of influenza virus A/PR/8/34 from eight cDNA fragments. *Virus Res.* **103,** 155–161 (2004).
27. Hutchinson, E. C., Curran, M. D., Read, E. K., Gog, J. R. & Digard, P. Mutational analysis of *cis*-acting RNA signals in segment 7 of influenza A virus. *J. Virol.* **82,** 11869–11879 (2008).
28. Britten, K. M., Howarth, P. H. & Roche, W. R. Immunohistochemistry on resin sections: a comparison of resin embedding techniques for small mucosal biopsies. *Biotech. Histochem.* **68,** 271–280 (1993).
29. Ellis, J. *et al.* Virological analysis of fatal influenza cases in the United Kingdom during the early wave of influenza in winter 2010/11. *Eurosurveillance* **16,** 2–7 (2011).
30. The 1000 Genomes project Consortium. A map of human genome variation from population-scale sequencing. *Nature* **467,** 1061–1073 (2010).
31. Howie, B. N., Donnelly, P. & Marchini, J. A flexible and accurate genotype imputation method for the next generation of genome-wide association studies. *PLoS Genet.* **5,** e1000529 (2009).
32. Purcell, S. *et al.* PLINK: a toolset for whole-genome association and population-based linkage analysis. *Am. J. Hum. Genet.* **81,** 559–575 (2007).
33. MacArthur, D. G. *et al.* A systematic survey of loss-of-function variants in human protein-coding genes. *Science* **335,** 823–828 (2012).

LETTER

Infection regulates pro–resolving mediators that lower antibiotic requirements

Nan Chiang[1], Gabrielle Fredman[1], Fredrik Bäckhed[2], Sungwhan F. Oh[1], Thad Vickery[1], Birgitta A. Schmidt[1] & Charles N. Serhan[1]

Underlying mechanisms for how bacterial infections contribute to active resolution of acute inflammation are unknown[1–4]. Here, we performed exudate leukocyte trafficking and mediator-metabololipidomics of murine peritoneal *Escherichia coli* infections with temporal identification of pro-inflammatory (prostaglandins and leukotrienes) and specialized pro-resolving mediators (SPMs). In self-resolving *E. coli* exudates (10^5 colony forming units, c.f.u.), the dominant SPMs identified were resolvin (Rv) D5 and protectin D1 (PD1), which at 12 h were at significantly greater levels than in exudates from higher titre *E. coli* (10^7 c.f.u.)-challenged mice. Germ-free mice had endogenous RvD1 and PD1 levels higher than in conventional mice. RvD1 and RvD5 (nanograms per mouse) each reduced bacterial titres in blood and exudates, *E. coli*-induced hypothermia and increased survival, demonstrating the first actions of RvD5. With human polymorphonuclear neutrophils and macrophages, RvD1, RvD5 and PD1 each directly enhanced phagocytosis of *E. coli*, and RvD5 counter-regulated a panel of pro-inflammatory genes, including NF-κB and TNF-α. RvD5 activated the RvD1 receptor, GPR32, to enhance phagocytosis. With self-limited *E. coli* infections, RvD1 and the antibiotic ciprofloxacin accelerated resolution, each shortening resolution intervals (R_i). Host-directed RvD1 actions enhanced ciprofloxacin's therapeutic actions. In 10^7 c.f.u. *E. coli* infections, SPMs (RvD1, RvD5, PD1) together with ciprofloxacin also heightened host antimicrobial responses. In skin infections, SPMs enhanced vancomycin clearance of *Staphylococcus aureus*. These results demonstrate that specific SPMs are temporally and differentially regulated during infections and that they are anti-phlogistic, enhance containment and lower antibiotic requirements for bacterial clearance.

The acute inflammatory response is a protective mechanism that is evolved to eliminate invading organisms. It should ideally be self-limited and lead to complete resolution, returning to homeostasis[1–4]. Evidence has emerged indicating that resolution of acute inflammation is an active process with biosynthesis of specialized pro-resolving mediators (SPMs), for example, bioactive omega-3-derived resolution phase interaction products (resolvins; recently reviewed in refs 4, 5). During natural resolution, polymorphonuclear neutrophils (PMN) required for anti-microbial defence[2] stop further infiltration, apoptose and are removed from the inflammatory site by specific macrophages[6–10]. In sterile inflammation, resolving exudates biosynthesize SPMs from essential fatty acids including lipoxins (LX) from arachidonic acid, E-series resolvins (Rv) from omega-3 eicosapentaenoic acid (EPA), D-series Rv, protectins (PD) and macrophage mediators in resolving inflammation (maresins) from docosahexaenoic acid (DHA) (reviewed in refs 4, 11). In humans, SPM production is also temporally regulated[12,13], and SPMs selectively control inflammation by stimulating resolution without immunosuppression, and are organ-protective in the eye, kidney, lung and periodontal diseases[4,14].

Self-resolving *E. coli* infections versus higher titre *E. coli* challenges: *E. coli* infections are an urgent worldwide health concern, as a recent outbreak in Germany has shown. In the United States, *E. coli* infections

account for approximately 270,000 cases per year with underreporting estimated at approximately 20-fold[15]. Here we used a well-established model of murine peritonitis, relevant to human infections[16], to identify specific SPMs that may be directly involved in resolving infections. *E. coli* inoculation at 10^5 c.f.u. per mouse intraperitoneally evoked a self-limited host response (Fig. 1a). PMN infiltration reached maximum at approximately 12 h followed by decline. Monocyte/macrophage numbers gradually increased from 2 h to 72 h; most of the exudate mononuclear cells at later time points were macrophages (~90% CD14+F4/80+ cells; Supplementary Fig. 1a), a finding consistent with anti-phlogistic actions of macrophages (for example, clearing apoptotic PMN)[6,7]. To provide quantitative analysis of resolution components with *E. coli* infection, we used resolution indices[4], because they give unbiased assessment of progress during resolution and are now in wide use (see refs 9, 17). Resolution indices were time point when PMN numbers reach maximum (T_{max}) ≈ 12 h and time point when PMN numbers reduce to 50% of maximum (T_{50}) ≈ 28 h, giving a resolution interval (R_i) of 16 h (see Methods). In sharp contrast, inoculation at 10^7 c.f.u. per mouse delayed resolution with sustained PMN infiltration (Fig. 1b). PMN numbers continued to increase until 72 h and the major mononuclear cell type at later intervals was monocytes (~90% CD14+F4/80−; Supplementary Fig. 1a), with only approximately 6% macrophages. Also with the higher inoculum of 10^7 c.f.u., bacteria counts in both blood and lavages remained elevated at 24–48 h, whereas with lower *E. coli* inoculum bacteria were cleared by 24 h (Supplementary Fig. 1b). Thus, high inoculum of 10^7 c.f.u. evoked excessive PMN accumulation and limited macrophages in exudates that reflect delayed resolution of infection. Importantly, the lower *E. coli* inoculum gave self-limited profiles (R_i = 16h), permitting differential analysis.

Infection-resolution metabololipidomics: Profiling metabololipidomics targeted on local acting lipid mediators (LM) was carried out with *E. coli* exudates using mass-spectrometry-based LM-lipidomics targeting five LM metabolomes, for example, leukotrienes, resolvins and protectins (Fig. 1c and Supplementary Fig. 1). In self-resolving peritonitis (10^5 c.f.u.), biosynthetic pathway markers for protectin D1 (PD1) and maresins (MaR1), namely 17-HDHA and 14-HDHA, were identified and elevated at the peak of PMN infiltration approximately 12 h in resolving exudates (see Supplementary Table 1 for LM identification). By comparison, mice that received higher titre of *E. coli* (10^7 c.f.u.) gave increased levels of proinflammatory LTB₄ and reduced 17-HDHA and 14-HDHA levels at 12–48 h (Fig. 1c and Supplementary Fig. 1d). Within the initial phase (4 h), RvD5 (7S,17S-dihydroxy-docosa-4Z,8E,10Z,13Z,15E,19Z-hexaenoic acid), a pivotal biosynthetic marker[18], accumulated in self-resolving exudates (120 ± 39 pg per exudate), approximately three times more than in exudates from higher titre *E. coli* infections (40 ± 11 pg RvD5 per exudate, $P < 0.05$) (Fig. 1c and Supplementary Fig. 1). At later interval 12 h, RvD5 remained elevated (326 ± 39 pg per exudate) in self-resolving exudates. It is noteworthy that PD1 levels were also significantly greater in self-resolving exudates (1,066 ± 247 pg per exudate) than in higher titre *E. coli*-challenged mice (468 ± 116 pg per exudate). In

[1]Center for Experimental Therapeutics and Reperfusion Injury, Department of Anesthesiology, Perioperative and Pain Medicine, Harvard Institutes of Medicine, Brigham and Women's Hospital and Harvard Medical School, Boston, Massachusetts 02115, USA. [2]Sahlgrenska Center for Cardiovascular and Metabolic Research/Wallenberg Laboratory, University of Gothenburg, SE-413 45 Gothenburg, Sweden.
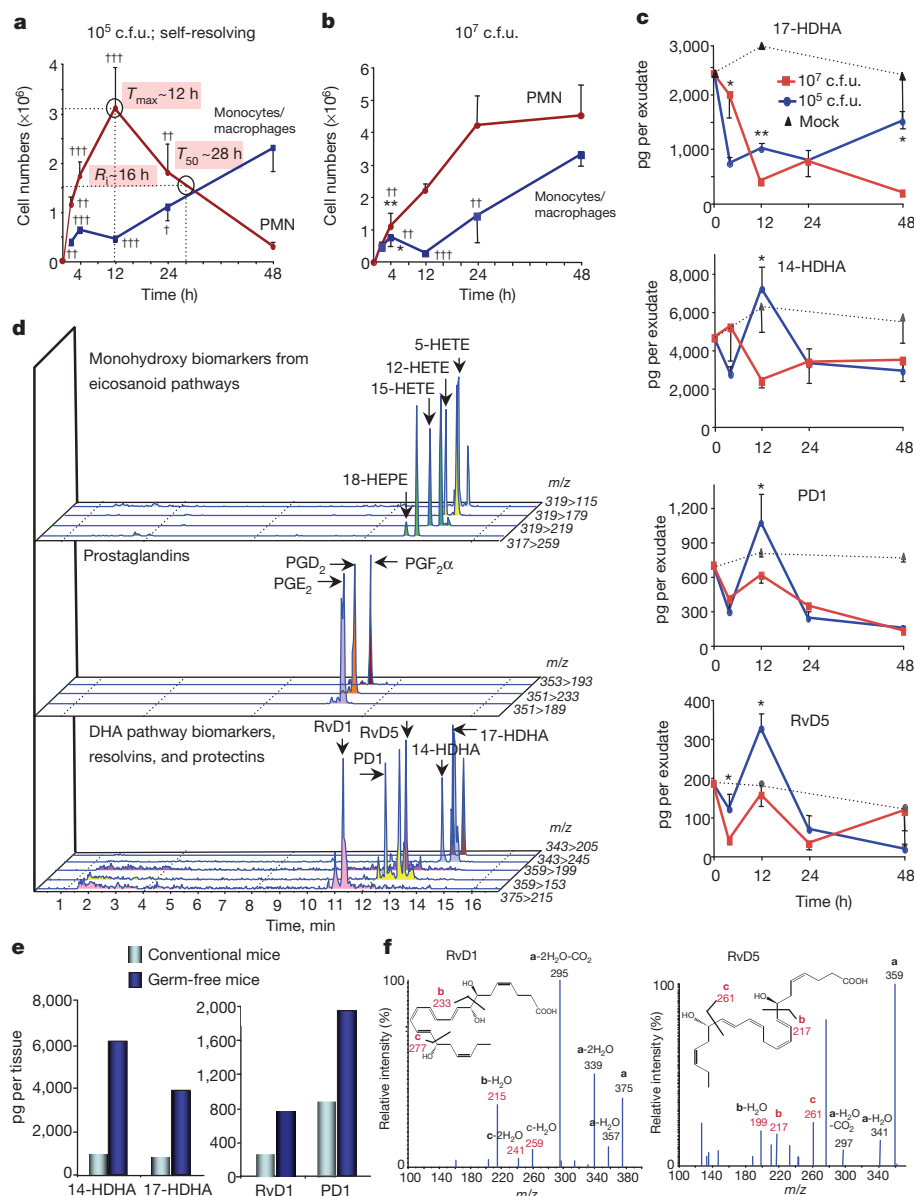
Figure 1 | Profiling of SPMs in *E. coli* infections.
a, **b**, Mice were inoculated with *E. coli* at 10^5 (**a**) or 10^7 c.f.u. (**b**) by intraperitoneal injection, and peritoneal leukocytes were counted. Results are expressed as mean ± s.e.m., $n = 4$–6. See Methods for calculation of resolution indices. *$P < 0.05$ and **$P < 0.01$ versus 24 h; †$P < 0.05$, ††$P < 0.01$ and †††$P < 0.001$ versus 48 h. **c**, Time course of SPMs and related pathway markers. Results are expressed as mean ± s.e.m. of $n = 5$ separate time courses. *$P < 0.05$, **$P < 0.01$, self-resolving (10^5 c.f.u.) versus higher titre (10^7 c.f.u.) *E. coli* exudates. **d**, Representative multiple reaction monitoring chromatograph of eicosanoid, resolvin and protectin pathway products from naive germ-free mice. Each LM was identified on the basis of published LC-MS/MS spectra[29] (see Supplementary Table 1). $Q_1 \rightarrow Q_3$ transition, M/Z, (atomic mass units); y axis, relative intensity. **e**, SPMs and pathway markers in colons of germ-free and conventional mice; representative of three mice. **f**, Representative MS/MS of RvD1 (from germ-free mice) and RvD5 (from *E. coli*-infected mice); $a = [M-H]$ (parent ion).

these exudates, RvD5 and PD1 were most abundant of the DHA metabolome. Human PMN transform 17-H(p)DHA via two distinct biosynthetic pathways to RvD5 and/or PD1 (Supplementary Fig. 2)[4,18]. These pathways were activated on infection and used endogenous essential fatty acids without supplement to biosynthesize potent novel mediators (see later). Their presence suggested specific role(s) in resolving infection.

RvD5 and PD1 both accumulated whereas RvD1 rapidly disappeared in exudates from *E. coli* infections. To monitor the metabolic flux of RvD1 during *E. coli* infections, RvD1 was administered with *E. coli* (10^5 c.f.u.) into the peritoneum (Supplementary Fig. 3a). At 12–24 h post-inoculation, only 5–10% RvD1 was recovered from peritoneal exudates. Along these lines, with human macrophages approximately 40–50% of RvD1 was lost within 0.5–2.0 h, accompanied by an increase in its further metabolite dihydro-RvD1. (Supplementary Fig. 3b). Hence, these are dynamic pathways in infectious exudates.

We calculated ratios for pro-resolving versus inflammatory mediators, that is, $RvD5/LTB_4$ and $PD1/LTB_4$. In self-resolving exudates these ratios at 12 and 24 h were greater than those in exudates from higher (10^7 c.f.u.) *E. coli* infections (Supplementary Fig. 1e), indicating that differential LM exudate profiles were present with these *E. coli* infections. To access their potential endogenous roles, we profiled these

pathways in germ-free mice[19] (Fig. 1d). In colons of naive germ-free mice, lower amounts of LTB_4 were identified and increased levels of endogenous DHA products 14-HDHA, 17-HDHA, RvD1 and PD1 (Fig. 1e, f and Supplementary Fig. 4). Hence, both endogenous and infected tissues produced D-series resolvins and PD1.

Because D-series resolvins, in particular RvD5, were one of the more abundant SPMs, we sought to determine its impact in *E. coli* infections. RvD5 given in physiologic range, that is, nanograms per mouse with *E. coli* (10^7 c.f.u.) significantly enhanced phagocyte containment of *E. coli in vivo* (160% increase) compared to mice challenged with *E. coli* alone (Fig. 2a). RvD1 shared this action, registering 42% increase. Of note, RvD1 or RvD5 markedly reduced blood and exudate bacterial counts (Fig. 2b). Infected mice developed hypothermia, giving $2.4 ± 1.2 °C$ decrements in body (surface) temperature. Both RvD1 and RvD5 prevented this (Fig. 2c and Supplementary Fig. 5a). The higher lethal dose of *E. coli* ($2.5 × 10^7$ c.f.u.) gave only 25% survival and RvD1 significantly increased survival to approximately 66% (Fig. 2d and Supplementary Fig. 5b, $P < 0.05$). Here, RvD5 significantly reduced pro-inflammatory cytokines KC and TNF-α in exudates and RvD1 decreased IL-1β (Supplementary Fig. 5c). Thus, both RvD1 and RvD5 stimulated phagocyte *E. coli* ingestion, lowered bacterial titres, protected from hypothermia and increased survival.
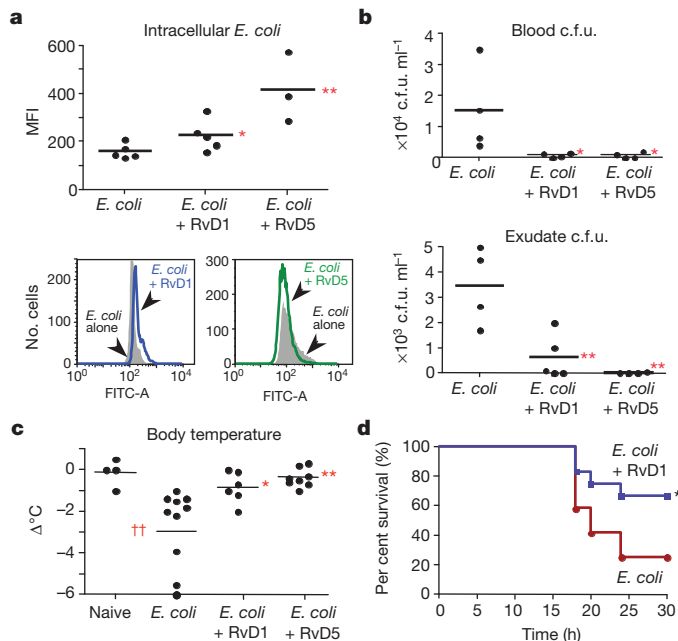
Figure 2 | RvD1 and RvD5 protect mice during infection by enhancing bacterial killing and preventing hypothermia. Mice were inoculated with *E. coli* (10^7 c.f.u.) together with RvD1 or RvD5 methyl ester (100 ng), and peritoneal exudates collected 24 h later. **a**, Intracellular *E. coli* levels. MFI, mean fluorescence intensity. Results are expressed as mean of $n = 3$–5. Bottom panel, representative histograms. **b**, Bacterial titres. Results are expressed as mean of $n = 4$–5. **c**, Changes in body temperatures expressed as mean of $\Delta°C$ (temperature at 24 h − temperature at 0 h) $n = 4$–10. *$P < 0.05$ and **$P < 0.01$ versus *E. coli* alone; ††$P < 0.01$ versus naive mice. **d**, Per cent survival of *E. coli*-inoculated mice (2.5×10^7 c.f.u.) alone or with RvD1 (100 ng per mouse). *$P < 0.05$ log rank (Mantel–Cox) test, $n = 12$ each group.

Given these *in vivo* findings, we next questioned whether SPMs have a direct impact on bacterial containment with isolated human cells. RvD1, RvD5 and PD1 each potently enhanced human macrophage phagocytosis of fluorescent *E. coli* by approximately 40–70% increases in pM to nM ranges (Fig. 3a–c). We also tested whether RvD5 activates human RvD1 receptor GPR32 expressed in a beta-arrestin reporter system[20], and found that RvD5 directly activates this receptor (Supplementary Fig. 6a). RvD5-enhanced phagocytic activity also proved dependent on GPR32. Both RvD1 and RvD5 increased macrophage phagocytosis of *E. coli*, an action further enhanced with GPR32 overexpression compared to mock-transfected cells (Supplementary Fig. 6b).

Gene array analysis with human macrophages (>90 genes) showed that *E. coli* upregulated a panel of inflammation-related genes, including NF-κB, phosphodiesterase 4B (*PDE4B*), COX-2 (also known as *PTGS2*) and *TNF-α* (also known as *TNF*). These results are consistent with Gram-negative lipopolysaccharide (LPS) stimulation of macrophages that upregulates *COX-2* (ref. 21), *PDE4B* and *TNF-α*[22]. When RvD5 (1 nM) was incubated with macrophages and *E. coli*, many of these genes were downregulated. RvD1 downregulated, for example, *PDE4B* and *COX-2* (Fig. 3d and Supplementary Table 2). Ablation of *PDE4B* protects mice from LPS-induced septic shock[23] and inhibition of COX enhances bacterial clearance of penicillin-resistant *Streptococcus pneumoniae*[24]. Therefore, RvD1 and RvD5 each counter-regulate COX and proinflammatory signalling components initiated by *E. coli* that might contribute to their actions in enhancing non-phlogistic phagocytosis (Fig. 3, Supplementary Table 2) and bacterial clearance *in vivo* (Fig. 2).

Similar findings were obtained with human PMN, where RvD1, RvD5 and PD1 each stimulated PMN anti-microbial mechanisms, increasing *E. coli* ingestion and intracellular reactive oxygen species (ROS) production for killing during *E. coli* challenge (Supplementary
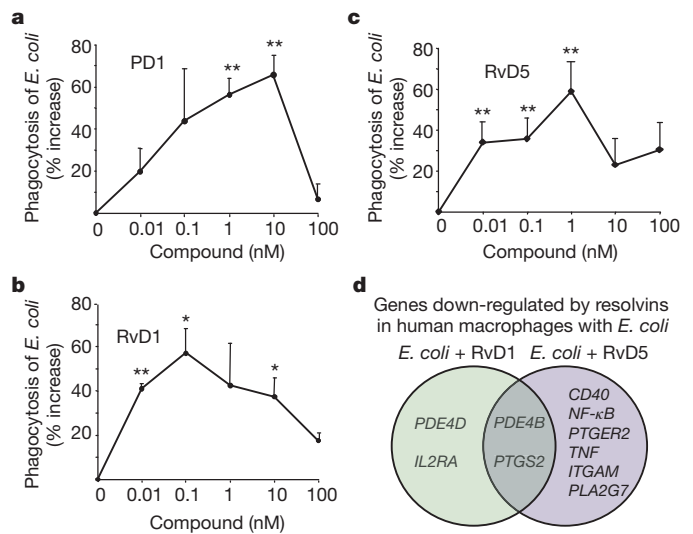
Figure 3 | SPMs enhance human macrophage phagocytosis of *E. coli*. **a**–**c**, Macrophage phagocytosis of fluorescent *E. coli* in the presence of PD1 (**a**), RvD1 (**b**) or RvD5 (**c**). Results are per cent increase above vehicle and expressed as mean ± s.e.m., $n = 3$ (PD1) or 4 (RvD1 and RvD5) with 3–4 determinations for each. *$P < 0.05$ and **$P < 0.01$ *E. coli* plus SPMs versus *E. coli* alone. **d**, Venn diagram of genes regulated by resolvins in human macrophages incubated with *E. coli*. *CD40* (*TNFRSF5*, TNF receptor superfamily member 5), *ITGAM* (coding CD11b), *PDE4D* and *PDE4B* (phosphodiesterases), *PLA2* (phospholipase A2), *PTGS2* (cyclooxygenase-2), *PTGER2* (prostaglandin E_2 receptor, EP2).

Fig. 7). These SPMs did not exhibit direct anti-bacterial activities (Supplementary Fig. 8). Together, these results characterize anti-phlogistic and host-directed antibacterial actions of RvD5, RvD1 and PD1 in that they enhance phagocytic activity of human phagocytes without evoking pro-inflammatory responses of these cells.

SPMs and antibiotics: Antibiotic-resistant bacteria are a global concern, increasing health-care costs. Ciprofloxacin, for example, is the only antibiotic recommended by the World Health Organization for management of bloody diarrhoea[25]. Unfortunately, rapid increases in bacterial resistance to ciprofloxacin reduces treatment options[25]. Hence, new strategies are needed. Given that specific SPMs enhanced bacterial containment (Figs 2, 3), we questioned whether SPM-directed host responses would improve antibiotic treatment. To this end, we determined resolution indices for ciprofloxacin and RvD1. Given along with *E. coli* (10^5 c.f.u.), RvD1 (50 ng) reduced maximal PMN (Ψ_{max}), and shortened resolution interval (R_i) from approximately 20 h to approximately 12 h (Fig. 4a). Ciprofloxacin alone at equi-doses also reduced R_i to approximately 11 h and initiated resolution at an earlier point T_{max} at about 6 h. RvD1 plus ciprofloxacin further accelerated the onset of resolution with $T_{max} \approx 4$ h, and reduced R_i to about 5 h (Fig. 4a and Supplementary Table 3).

RvD1 plus ciprofloxacin further reduced bacterial titres in blood and exudates at 4 h, compared to ciprofloxacin alone (Fig. 4b). Similar results were obtained at 12 h with exudates, whereas there were no significant differences between ciprofloxacin and ciprofloxacin plus RvD1 in blood. RvD1 actions were more pronounced at 4 h in blood. A panel of cytokines/chemokines was monitored (Supplementary Fig. 9a), and RvD1 and ciprofloxacin each gave differential actions; RvD1 significantly reduced IL-1β, IL-6 and increased IL-10 at 4 h, and IFNγ at 24 h. Ciprofloxacin alone reduced IL-12 levels at 4 h (Supplementary Fig. 9b). We also assessed LM metabololipidomic profiles: RvD1 plus ciprofloxacin significantly increased both 14-HDHA and PD1 at 4 h (Fig. 4c and Supplementary Fig. 9c, d), whereas neither alone was effective. At 12 h, RvD1 or ciprofloxacin alone increased endogenous PD1. In addition, RvD1 or ciprofloxacin alone at 4 h did not enhance macrophage containment of *E. coli*, but significantly increased
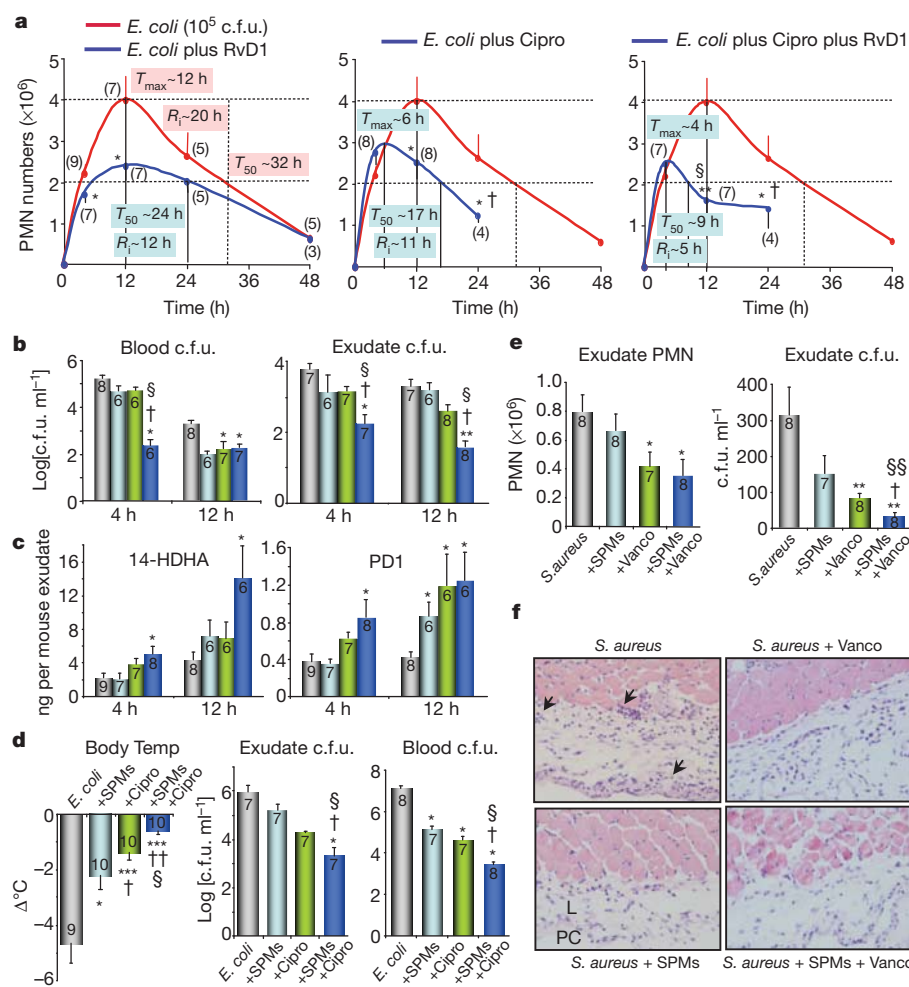
Figure 4 | SPMs and antibiotics accelerate resolution and enhance bacterial killing.
a–c, Mice were inoculated with *E. coli* (10^5 c.f.u.), RvD1 methyl ester (50 ng) and ciprofloxacin (Cipro, 50 ng). **a**, Exudate PMN numbers and resolution indices. **b**, Bacterial titres. **c**, 14-HDHA and PD1 levels determined using LC-MS/MS-based LM-lipidomics. Results are expressed as mean ± s.e.m. *$P < 0.05$ and **$P < 0.01$ versus *E. coli* alone; †$P < 0.05$ versus *E. coli* + RvD1; §$P < 0.05$ versus *E. coli* + Cipro. Grey, *E. coli* alone; blue, *E. coli* + RvD1; green, *E. coli* + Cipro; dark blue, *E. coli* + RvD1 + Cipro. **d**, Mice were inoculated with *E. coli* (10^7 c.f.u.), SPM panel (RvD1, RvD5 and PD1; 50 ng each) and Cipro (25 μg). Body temperatures and bacterial titres were determined at 24 h. Results are expressed as mean ± s.e.m. *$P < 0.05$ and ***$P < 0.001$ versus *E. coli* alone; †$P < 0.05$ and ††$P < 0.01$ versus *E. coli* + SPM; §$P < 0.05$ versus *E. coli* + Cipro. **e, f**, Murine dorsal pouches were given live *S. aureus* (10^5 c.f.u.) alone, plus SPMs (RvD1, RvD5, PD1 at 100 ng each per mouse), vancomycin (Vanco, 2.5 μg), or both SPMs and vancomycin by intra-pouch injection; pouch exudates were collected at 24 h. **e**, PMN and bacterial counts (c.f.u.). Results are expressed as mean ± s.e.m. *$P < 0.05$ and **$P < 0.01$ versus *S. aureus* alone; †$P < 0.05$ versus *S. aureus* + SPMs; §§$P < 0.01$ versus *S. aureus* + Vanco. **f**, Skin-pouch biopsies (magnifications ×40). Arrows denote PMN infiltration into pouch linings. L, linings; PC, pouch cavity. Animal numbers are denoted within brackets (**a**) or bars (**b–e**).

phagocytic activity when both were administered (Supplementary Fig. 9e). Thus, host-directed RvD1 responses plus bacteria-directed antibiotic accelerated resolution via enhanced *E. coli* killing and clearance, as well as selectively regulating both endogenous LM and cytokines.

Because the specific SPMs identified in infectious exudates were from DHA metabolome (Fig. 1), we tested RvD1, RvD5 and PD1 together (50 ng each) plus ciprofloxacin (25 μg per mouse) in higher titre *E. coli* (10^7 c.f.u.) infections. Sub-optimal doses of ciprofloxacin (25 μg, Supplementary Fig. 10a) still protected mice from hypothermia and reduced bacterial titres, actions that were enhanced by the SPM panel (Fig. 4d). In addition, treatment with both ciprofloxacin and SPMs significantly increased phagocyte ingestion of *E. coli*, whereas neither treatment alone proved effective (Supplementary Fig. 10b).

SPMs enhance actions of vancomycin in *S. aureus*-initiated infections: *Staphylococcus aureus* is an emerging cause of various skin infections and a high percentage of hospital-acquired infections are caused by antibiotic-resistant *S. aureus*[25]. To assess a second system, we determined the impact of SPMs and vancomycin in *S. aureus*-initiated infections in murine dorsal skin pouches. SPM panel (RvD1, RvD5 and PD1; 100 ng each) and/or sub-optimal doses of vancomycin (2.5 μg) were administered with *S. aureus* (10^5 c.f.u.) via intra-pouch injections. SPMs or vancomycin alone at 4 h each decreased exudate bacterial counts by approximately tenfold. Treatment with both further reduced bacterial counts by approximately 100-fold (Supplementary Fig. 11 a, b). Similar results were obtained at 24 h; SPMs and vancomycin together gave significantly lower bacterial counts compared to those from each treatment alone (Fig. 4e). In *S. aureus*-infected mice, histologic analysis demonstrated PMN infiltration and Gram stain positives within linings surrounding the pouch cavities

(Fig. 4f and Supplementary Fig. 11c) that were markedly reduced by SPMs, vancomycin and their use together (Fig. 4f).

A panel of cytokines/chemokines was also monitored. SPMs and vancomycin at 4 h significantly reduced *S. aureus*-induced IL-6 and GM-CSF in pouch exudates (Supplementary Fig. 11), whereas neither alone was effective. It is noteworthy that vancomycin reduced LTB$_4$ and increased the Rv precursor 17-HDHA (Supplementary Fig. 11). Other SPMs, including resolvin E1, protect mice from *E. coli* pneumonia and acute lung injury[26] and 15-epi-LXA$_4$, an arachidonic acid-derived SPMs, enhances resolution of *E. coli* pulmonary inflammation[27] and macrophage phagocytosis[28]. Hence, it seems that specific SPM pathways are used by the host during Gram-positive and Gram-negative bacterial infections.

Here we carried out LM-metabolomics with infectious-inflammatory exudates and identified specific pro-resolving mediators that were also present in germ-free mice. RvD1 and RvD5 each accelerated resolution of *E. coli* infections and increased survival. SPMs given together with ciprofloxacin shortened resolution intervals, stimulated phagocyte containment of *E. coli*, enhanced bacterial killing, and protected mice from hypothermia. These are the first actions identified for RvD5. With human macrophages, both RvD1 and RvD5 stimulated phagocytosis of *E. coli* in a GPR32-dependent manner. SPMs also enhanced antibiotic effectiveness in clearing Gram-positive *S. aureus* skin infections. Together, these results indicate that stimulation of targeted host resolution responses by pro-resolving mediators in conjunction with bacterial-directed antibiotics lowers the required antibiotic doses for bacterial clearance. They illustrate new opportunities to address antibiotic resistance via lowering antibiotic use by also targeting host resolution programs.

METHODS SUMMARY

Microbial-initiated inflammation *in vivo*. Peritonitis was triggered by giving mice SPMs or vehicle together with live *E. coli* (serotype O6:K2:H1; 10^5 or 10^7 c.f.u.) or saline injections (mock infection) intraperitoneally. Ciprofloxacin was given 1 h after *E. coli*. At designated points, mice were euthanized, peritoneal exudate and blood were collected. Cellular composition, intracellular *E. coli*, bacterial titres and body temperatures were determined.

Resolution indices were calculated as in ref. 4: Ψ_{max}, the maximal PMN numbers; T_{max}, the time point when PMN numbers reach maximum; R_{50}, 50% of maximal PMN; T_{50}, the time point when PMN numbers reduce to 50% of maximum; R_i (resolution interval), $T_{50} - T_{max}$, the time period when 50% PMN are lost from exudates.

Murine dorsal skin pouches. Mice were given SPMs and/or vancomycin with live *S. aureus* (serotype (b)c1; 10^5 c.f.u.) by intra-pouch injection. Pouch exudates were collected, and bacterial counts determined. Skin punch biopsies were collected for Gram and haematoxylin–eosin staining.

Mediator-metabololipidomics. Liquid chromatography-tandem mass spectrometry (LC-MS/MS)-based LM-lipidomics were carried out using either an ABI QTrap 3200 or Qtrap 5500 (AB Sciex). LM were profiled via multiple reaction monitoring (MRM) and identified using retention time and at least six diagnostic ions[29].

RvD5 synthesis. RvD5 was prepared by incubating 7(R/S)-HDHA with soybean 15-LO followed by chiral high performance liquid chromatography (HPLC) separation[29]. For methyl ester preparation, RvD5 was treated with excess ethereal diazomethane and purified using reverse-phase HPLC.

Macrophage and PMN phagocytosis. Human PMN or GM-CSF-differentiated macrophages were incubated with SPMs or vehicle for 15 min at 37 °C, followed by fluorescent-labelled *E. coli* at a 50:1 ratio (*E. coli*:macrophages) for 60 min (phagocytosis) or 120 min (gene arrays).

Statistical analysis. Statistical analyses were performed using one-way ANOVA or Student's *t* test; $P \leq 0.05$ was taken as significant. Per cent survival was analysed by log rank test (GraphPad).

Full Methods and any associated references are available in the online version of the paper at www.nature.com/nature.

1. Houck, J. C. (ed.) *Chemical Messengers of the Inflammatory Process* (Elsevier/North-Holland Biomedical Press, 1979).
2. Mantovani, A., Cassatella, M. A., Costantini, C. & Jaillon, S. Neutrophils in the activation and regulation of innate and adaptive immunity. *Nature Rev. Immunol.* **11,** 519–531 (2011).
3. Medzhitov, R. Inflammation 2010: new adventures of an old flame. *Cell* **140,** 771–776 (2010).
4. Serhan, C. N. Resolution phases of inflammation: novel endogenous anti-inflammatory and pro-resolving lipid mediators and pathways. *Annu. Rev. Immunol.* **25,** 101–137 (2007).
5. Stables, M. J. & Gilroy, D. W. Old and new generation lipid mediators in acute inflammation and resolution. *Prog. Lipid Res.* **50,** 35–51 (2011).
6. Henneke, P. & Golenbock, D. T. Phagocytosis, innate immunity, and host-pathogen specificity. *J. Exp. Med.* **199,** 1–4 (2004).
7. Rossi, A. G. *et al.* Cyclin-dependent kinase inhibitors enhance the resolution of inflammation by promoting inflammatory cell apoptosis. *Nature Med.* **12,** 1056–1064 (2006).
8. Dinarello, C. A. Anti-inflammatory agents: present and future. *Cell* **140,** 935–950 (2010).
9. Navarro-Xavier, R. A. *et al.* A new strategy for the identification of novel molecules with targeted proresolution of inflammation properties. *J. Immunol.* **184,** 1516–1525 (2010).
10. Schif-Zuck, S. *et al.* Satiated-efferocytosis generates pro-resolving CD11b^{low} macrophages: modulation by resolvins and glucocorticoids. *Eur. J. Immunol.* **41,** 366–379 (2011).
11. De Caterina, R. n−3 fatty acids in cardiovascular disease. *N. Engl. J. Med.* **364,** 2439–2450 (2011).
12. Morris, T. *et al.* Effects of low-dose aspirin on acute inflammatory responses in humans. *J. Immunol.* **183,** 2089–2096 (2009).
13. Oh, S. F., Pillai, P. S., Recchiuti, A., Yang, R. & Serhan, C. N. Pro-resolving actions and stereoselective biosynthesis of 18*S* E-series resolvins in human leukocytes and murine inflammation. *J. Clin. Invest.* **121,** 569–581 (2011).
14. Spite, M. *et al.* Resolvin D2 is a potent regulator of leukocytes and controls microbial sepsis. *Nature* **461,** 1287–1291 (2009).
15. Mead, P. S. *et al.* Food-related illness and death in the United States. *Emerg. Infect. Dis.* **5,** 607–625 (1999).
16. Klingensmith, M. E. & Soybel, D. I. in *The Physiological Basis of Modern Surgical Care* (Miller, T. A. & Rowlands B. J. eds) 478–490 (Mosby Year Book, 1998).
17. Xu, Y. N., Zhang, Z., Ma, P. & Zhang, S. H. Adenovirus-delivered angiopoietin 1 accelerates the resolution of inflammation of acute endotoxic lung injury in mice. *Anesth. Analg.* **112,** 1403–1410 (2011).
18. Serhan, C. N. *et al.* Resolvins: a family of bioactive products of omega-3 fatty acid transformation circuits initiated by aspirin treatment that counter pro-inflammation signals. *J. Exp. Med.* **196,** 1025–1037 (2002).
19. Bäckhed, F., Manchester, J. K., Semenkovich, C. F. & Gordon, J. I. Mechanisms underlying the resistance to diet-induced obesity in germ-free mice. *Proc. Natl Acad. Sci. USA* **104,** 979–984 (2007).
20. Krishnamoorthy, S. *et al.* Resolvin D1 binds human phagocytes with evidence for pro-resolving receptors. *Proc. Natl Acad. Sci. USA* **107,** 1660–1665 (2010).
21. Grkovich, A., Johnson, C. A., Buczynski, M. W. & Dennis, E. A. Lipopolysaccharide-induced cyclooxygenase-2 expression in human U937 macrophages is phosphatidic acid phosphohydrolase-1-dependent. *J. Biol. Chem.* **281,** 32978–32987 (2006).
22. Jin, S. L., Lan, L., Zoudilova, M. & Conti, M. Specific role of phosphodiesterase 4B in lipopolysaccharide-induced signaling in mouse macrophages. *J. Immunol.* **175,** 1523–1531 (2005).
23. Link, A., Selejan, S., Maack, C., Lenz, M. & Böhm, M. Phosphodiesterase 4 inhibition but not beta-adrenergic stimulation suppresses tumor necrosis factor-alpha release in peripheral blood mononuclear cells in septic shock. *Crit. Care* **12,** R159 (2008).
24. Stables, M. J. *et al.* Priming innate immune responses to infection by cyclooxygenase inhibition kills antibiotic-susceptible and -resistant bacteria. *Blood* **116,** 2950–2959 (2010).
25. World Health Organization. Antibiotics Resistance, Factsheet No. 194 http://www.who.int/mediacentre/factsheets/fs194/en/ (February 2011).
26. Seki, H. *et al.* The anti-inflammatory and proresolving mediator resolvin E1 protects mice from bacterial pneumonia and acute lung injury. *J. Immunol.* **184,** 836–843 (2010).
27. El Kebir, D. *et al.* 15-epi-lipoxin A4 inhibits myeloperoxidase signaling and enhances resolution of acute lung injury. *Am. J. Respir. Crit. Care Med.* **180,** 311–319 (2009).
28. Prescott, D. & McKay, D. M. Aspirin-triggered lipoxin enhances macrophage phagocytosis of bacteria while inhibiting inflammatory cytokine production. *Am. J. Physiol. Gastrointest. Liver Physiol.* **301,** G487–G497 (2011).
29. Yang, R., Chiang, N., Oh, S. F. & Serhan, C. N. Metabolomics-lipidomics of eicosanoids and docosanoids generated by phagocytes. *Curr. Protoc. Immunol.* **95,** 14.26.11–14.26.26 (2011).
30. Winyard, P. G. & Willoughby, D. A. (eds) *Inflammation Protocols* (Humana, 2003).

METHODS

Bacterial growth. *E. coli* (serotype O6:K2:H1) were cultured in LB broth and harvested at mid-log phase ($OD_{600\,nm} \approx 0.5$; 5×10^8 c.f.u. ml^{-1}) and washed in sterile saline before inoculation into mouse peritoneum.

Microbial-initiated peritonitis and leukocyte differentials. Mice were anaesthetized with isoflurane and experiments were carried out with male FVB mice (6 to 8 weeks; Charles River; lab diet containing essential fatty acids from supplier). Microbial-initiated peritonitis was performed in accordance with the Harvard Medical Area Standing Committee on Animals (protocol no. 02570). Briefly, mice were anaesthetized and test compounds or vehicle controls were injected into the peritoneal cavity together with live *E. coli* (10^5 or 10^7 c.f.u.). The antibiotic ciprofloxacin (Sigma) was given 1 h after *E. coli* injection. At designated points, mice were euthanized (overdose of isoflurane), blood was collected by heart puncture, and peritoneal exudate was collected by lavaging with 5 ml PBS. Cellular composition was determined by taking exudates for differential leukocyte counts determined by nuclear morphology with light microscopy using Cytofuge (Statspin) stained with Wright Giemsa stain. For flow cytometry, aliquots of exudate cells were incubated with anti-mouse CD16/32 blocking antibody (0.5 µg per 0.5×10^6 cells, 5 min) and then incubated (20 min, 4 °C) with individual antibody or combinations of FITC (fluorescein isothiocyanate)-conjugated anti-mouse CD14 (clone rmC5-3) for mononuclear cells and phycoerythrin-conjugated anti-mouse F4/80 Ab (clone BM8) for macrophages or phycoerythrin-conjugated anti-mouse Ly-6G (clone RB6-8C5) for PMN, to determine leukocyte sub-types (FACS Canto II). Antibodies were from BD Biosciences and eBioscience. Intracellular *E. coli* levels were determined using a FITC-conjugated anti-*E. coli* antibody (GTX40856; GeneTex). For bacterial counts aliquots of lavage or blood were used for serial dilution, plated onto LB agar plates, and cultured overnight at 37 °C. Body temperature was monitored using an infrared thermometer (Fluke).

Resolution indices were calculated[4]: Ψ_{max}, the maximal PMN numbers in the exudates; T_{max}, the time point when PMN numbers reach maximum; R_{50}, 50% of maximal PMN numbers; T_{50}, the time point when PMN numbers reduce to 50% of maximum; R_i (resolution interval), $T_{50} - T_{max}$, the time period when 50% PMN are lost from the exudates.

Murine dorsal skin pouches. Pouches were raised for 6 days[30]. Mice were given test SPMs and/or vancomycin with live *S. aureus* (serotype (b)c1; 10^5 c.f.u.) by intra-pouch injection. At designated points, mice were euthanized, intra-pouch exudate and blood were collected, and bacterial counts determined. Skin punch biopsies were collected for both Gram and haematoxylin–eosin staining.

Germ-free mice. Germ-free 12-week-old C57BL/6J male mice were maintained in flexible film isolators under a 12-h light cycle and fed an autoclaved chow diet (Labdiet) *ad libitum*. Mice were euthanized by cervical dislocation and colons were removed. All tissues were snap frozen in liquid nitrogen and stored at −80 °C. Animal protocols were approved by the Research Animal Ethics Committee in Gothenburg, Sweden.

Mediator-metabololipidomics. All incubations and *in vivo* samples (that is, exudates) were stopped with two volumes of cold methanol containing deuterated internal standards (d$_8$-5S-HETE, d$_4$-LTB$_4$ and d$_4$-PGE$_2$; Cayman Chemical). The internal standards were added to each sample to obtain the extraction recoveries for specific lipid mediators. Samples were taken for solid-phase extraction and LC-MS/MS-based mediator lipidomics using an HPLC-UV (Agilent 1100) coupled to an ion-trap mass spectrometer in some experiments (QTrap 3200; Applied Biosystems/Sciex); for others an ABI Qtrap 5500 equipped with a C18 column (Agilent Eclipse Plus, 4.6 mm × 50 mm × 1.8 µm) was used. The mobile phase consisted of methanol/water/acetic acid (60/40/0.01, v/v/v) and was ramped to 80/20/0.01 (v/v/v) over 5 min, to 95/5/0.01 (v/v/v) over the next 3 min and to 100/0/0.01 (v/v/v) over 6 min before returning to 60/40/0.01 (v/v/v) at a flow rate of 0.4 ml min^{-1}. Lipid mediators were profiled using multiple reaction monitoring (MRM) and identified by direct comparison with synthetic and biogenic standards using retention time and six diagnostic ions for matching criteria[29]. Linear calibration curves were determined using mixtures of lipid mediator standards: d$_8$-5S-HETE ($r^2 = 0.9939$, $n = 7$), d$_4$-LTB$_4$ ($r^2 = 0.9995$, $n = 7$), d$_4$-PGE$_2$ ($r^2 = 0.9969$, $n = 7$), RvD1 ($r^2 = 0.9954$, $n = 7$), RvD2 ($r^2 = 0.9931$, $n = 7$), RvE1 ($r^2 = 0.9941$, $n = 7$), LXA$_4$ ($r^2 = 0.9941$, $n = 7$), LXB$_4$ ($r^2 = 0.9959$, $n = 7$), PGE$_2$ ($r^2 = 0.8370$, $n = 7$), PGD$_2$ ($r^2 = 0.9893$, $n = 7$), 20-OH-LTB$_4$ ($r^2 = 0.9960$,

$n = 7$), LTB$_4$ ($r^2 = 0.9949$, $n = 7$), PD1 ($r^2 = 0.9948$, $n = 7$), 17-HDHA ($r^2 = 0.9931$, $n = 7$), 14-HDHA ($r^2 = 0.9940$, $n = 7$), 7-HDHA ($r^2 = 0.9964$, $n = 7$), 4-HDHA ($r^2 = 0.9950$, $n = 7$), 15-HETE ($r^2 = 0.9978$, $n = 7$), 12-HETE ($r^2 = 0.9975$, $n = 7$), 5-HETE ($r^2 = 0.9905$, $n = 7$) at 50, 100, 200, 400 and 800 pg. Quantification was carried out based on the peak area of the multiple reaction monitoring (MRM) transition and the linear calibration curve for each. Synthetic deuterium labelled RvD1 was prepared by N. Petasis for tracking and quantification of RvD1 in the P01(GM095467).

RvD5 synthesis and isolation. Biogenic RvD5 was prepared by incubating 7(R/S)-HDHA (Cayman Chemical) with soybean 15-LO (Sigma-Aldrich). Briefly, 7(R/S)-HDHA (50 µM) was suspended in 50 mM sodium borate buffer (pH 9.3) and 1,000 units of 15-LOX added. After 5 min, the reactions were quenched by adding the same volume of cold methanol and reduced with excess amount of sodium borohydride. Reaction mixtures were acidified and directly injected to chiral HPLC to separate 7S,17S-dihydroxy-containing product termed RvD5. Characteristic RvD5 chromophore of $\lambda_{max} = 242$ nm was used for ultra-violet monitoring[29]. For methyl ester preparation, RvD5 was treated with excess ethereal diazomethane, taken to dryness with nitrogen gas, suspended in methanol and isolated using HPLC. RvD5 reaction mixture was separated by chiral column (Chiralcel AD-RH, 150 mm × 2.1 mm × 5 µm)-equipped HPLC (Agilent HP 1100 Chemstation with DAD) with gradient eluent methanol:water:acetic acid of 95:5:0.01 to 100:0:0.01 for 10 min at the flow rate of 200 µl min^{-1}.

Macrophage phagocytosis and gene arrays. Human macrophages were obtained by differentiating peripheral blood mononuclear cells, collected from healthy volunteers, with GM-CSF (10 ng ml^{-1}) in culture medium for 7 days. Before each experiment (24 h), cells were adhered on a 24-well plate (0.1×10^6 cells per well) in culture medium deprived of GM-CSF. In parallel, *E. coli* collected at mid-log phase ($OD_{600\,nm} \approx 0.5$; $\sim 5 \times 10^8$ c.f.u. ml^{-1}) were labelled with fluorescence dye (BacLight, Molecular Probes). Macrophages were exposed to vehicle (DPBS$^{+/+}$) alone or compounds (PD1, RvD1, RvD5) for 15 min at 37 °C, followed by incubation with fluorescent-labelled *E. coli* at 50:1 ratio (*E. coli*: macrophages) for 60 min at 37 °C. Plates were gently washed, extracellular *E. coli* quenched by trypan blue, and phagocytosis determined by measuring total fluorescence (excitation 495 nm/emission 535 nm) using a fluorescent plate reader (Molecular Probes), and confirmed by flow cytometry (FACS Canto II).

For inflammatory gene arrays, human macrophages (2×10^6 cells) were adhered to 10-cm^2 Petri dishes. Next, PD1, RvD1, RvD5 (1 nM) or vehicle was added for 15 min at 37 °C, followed by addition of *E. coli* (*E. coli*:macrophages 50:1) for 120 min at 37 °C. Total RNA was isolated and inflammatory gene array carried out following manufacturer's instruction (SA Biosciences). Results were analysed using RT^2 profiler PCR array data analysis (SA Biosciences).

GPR32 receptor β-arrestin reporter system. CHO cells engineered to stably co-express human GPR32 linked to the Pro-Link peptide and β-arrestin tagged with the β-galactosidase Enzyme Acceptor (custom constructs, DiscoveRx) denoted CHO-GPR32 were routinely grown in medium with selection antibiotics, and plated in 96-well plates (at 20,000 or 10,000 cells per well) at 24 h before experiments. Receptor activation was determined by increased chemiluminescence upon conversion of hydrolysable substrate (PathHunter EFC Detection kit) catalysed by β-galactosidase using a luminometer (Molecular Probes).

PMN phagocytosis and generation of intracellular ROS. Human PMN were obtained from healthy volunteers according to Partners Human Research Committee Protocol no. 1999-P-001297. Adherent human PMN (5×10^6 cells per well in a 24-well plate) were incubated with RvD5, RvD1 or PD1 (0.1–100 nM) or vehicle for 15 min before incubation with *E. coli* (JM109; 50:1 ratio) for 60 min at 37 °C. Plates were gently washed, extracellular *E. coli* quenched by trypan blue, and phagocytosis determined by measuring total fluorescence (excitation 495 nm/emission 535 nm) using a fluorescent plate reader (Molecular Probes), and confirmed by flow cytometry (FACS Canto II). To assess intracellular ROS generation, PMN (5×10^6 cells per well in a 24-well plate) were pre-incubated with 5 µM carboxy-H2DCFDA (C400; Invitrogen) for 30 min, followed by incubation with SPMs for 15 min, and then *E. coli* (50:1 ratio) for 60 min. Probe oxidation was determined using a fluorescent plate reader.

Statistical analysis. Results are expressed as mean ± s.e.m. Statistical analyses were performed using one-way ANOVA or Student's *t* test and $P \leq 0.05$ was considered to be significant.

LETTER

Exploiting a natural conformational switch to engineer an interleukin-2 'superkine'

Aron M. Levin[1]*, Darren L. Bates[2]*, Aaron M. Ring[2]*, Carsten Krieg[3,4], Jack T. Lin[5], Leon Su[5], Ignacio Moraga[2], Miro E. Raeber[3,4], Gregory R. Bowman[6], Paul Novick[6], Vijay S. Pande[6], C. Garrison Fathman[5], Onur Boyman[3,4] & K. Christopher Garcia[1,2]

The immunostimulatory cytokine interleukin-2 (IL-2) is a growth factor for a wide range of leukocytes, including T cells and natural killer (NK) cells[1–3]. Considerable effort has been invested in using IL-2 as a therapeutic agent for a variety of immune disorders ranging from AIDS to cancer. However, adverse effects have limited its use in the clinic. On activated T cells, IL-2 signals through a quaternary 'high affinity' receptor complex consisting of IL-2, IL-2Rα (termed CD25), IL-2Rβ and IL-2Rγ[4–8]. Naive T cells express only a low density of IL-2Rβ and IL-2Rγ, and are therefore relatively insensitive to IL-2, but acquire sensitivity after CD25 expression, which captures the cytokine and presents it to IL-2Rβ and IL-2Rγ. Here, using in vitro evolution, we eliminated the functional requirement of IL-2 for CD25 expression by engineering an IL-2 'superkine' (also called super-2) with increased binding affinity for IL-2Rβ. Crystal structures of the IL-2 superkine in free and receptor-bound forms showed that the evolved mutations are principally in the core of the cytokine, and molecular dynamics simulations indicated that the evolved mutations stabilized IL-2, reducing the flexibility of a helix in the IL-2Rβ binding site, into an optimized receptor-binding conformation resembling that when bound to CD25. The evolved mutations in the IL-2 superkine recapitulated the functional role of CD25 by eliciting potent phosphorylation of STAT5 and vigorous proliferation of T cells irrespective of CD25 expression. Compared to IL-2, the IL-2 superkine induced superior expansion of cytotoxic T cells, leading to improved antitumour responses in vivo, and elicited proportionally less expansion of T regulatory cells and reduced pulmonary oedema. Collectively, we show that in vitro evolution has mimicked the functional role of CD25 in enhancing IL-2 potency and regulating target cell specificity, which has implications for immunotherapy.

To engineer a CD25-independent version of IL-2, we displayed human IL-2 on the surface of yeast as a conjugate to Aga2p, and verified proper receptor-binding properties with IL-2Rβ and IL-2Rγ ectodomain tetramers that were carboxy-terminally biotinylated and coupled to phycoerythrin-conjugated streptavidin for use as a staining and sorting reagent[9,10]. Yeast-displayed IL-2 bound to IL-2Rγ in the presence of IL-2Rβ, recapitulating the cooperative assembly of the heterodimeric receptor complex as seen with soluble IL-2 (Fig. 1a and Supplementary Fig. 1). We proceeded to carry out two generations of in vitro evolution (Fig. 1b and Supplementary Fig. 2). Our first generation in vitro evolution strategy was to create an error-prone PCR library of the entire IL-2 coding sequence (Supplementary Fig. 2), which resulted in selection of a predominant IL-2 variant containing an L85V mutation (Fig. 1c and Supplementary Fig. 3).

From inspection of the wild-type (WT) IL-2 structure, we were surprised to find that position 85 was not a direct IL-2Rβ contact residue, but rather resided on the internal face of the IL-2 C-helix, within the hydrophobic core of the cytokine (Fig. 2a). Thus, we surmised

Figure 1 | In vitro evolution of human IL-2 variants with high affinity for IL-2Rβ. **a**, IL-2 displayed on yeast recapitulates cooperative receptor-binding activity. As measured by flow cytometry, IL-2 binds weakly to IL-2Rβ (left panel), undetectably to IL-2Rγ (middle panel), and cooperatively forms the IL-2Rβ–IL-2Rγ heterodimer (right panel). **b**, Enrichment of IL-2 variants on yeast by selection with progressively lower concentrations of IL-2Rβ. Red arrows indicate an emerging population of high-affinity IL-2Rβ binders (see also Supplementary Fig. 2). **c**, Sequences and affinities for IL-2Rβ of selected mutants from the first (mutant 6-6) and second (mutants D10 and H9) generation libraries (see Supplementary Fig. 3 for an extended table). **d**, On-yeast stimulation of YT-1 cells (human NK cell line) by wild-type (WT) IL-2-yeast and high-affinity variants (IL-2 superkines) (see also Supplementary Fig. 4).

[1]Howard Hughes Medical Institute, Stanford University School of Medicine, Stanford, California 94305, USA. [2]Department of Molecular and Cellular Physiology, and Department of Structural Biology, Stanford University School of Medicine, Stanford, California 94305, USA. [3]Laboratory of Applied Immunobiology, University of Zurich, Zurich CH-8006, Switzerland. [4]Allergy Unit, Department of Dermatology, University Hospital Zurich, Zurich CH-8091, Switzerland. [5]Stanford University School of Medicine, Department of Medicine, Division of Immunology and Rheumatology, Stanford, California 94305, USA. [6]Department of Chemistry, Stanford University, Stanford, California 94305, USA.
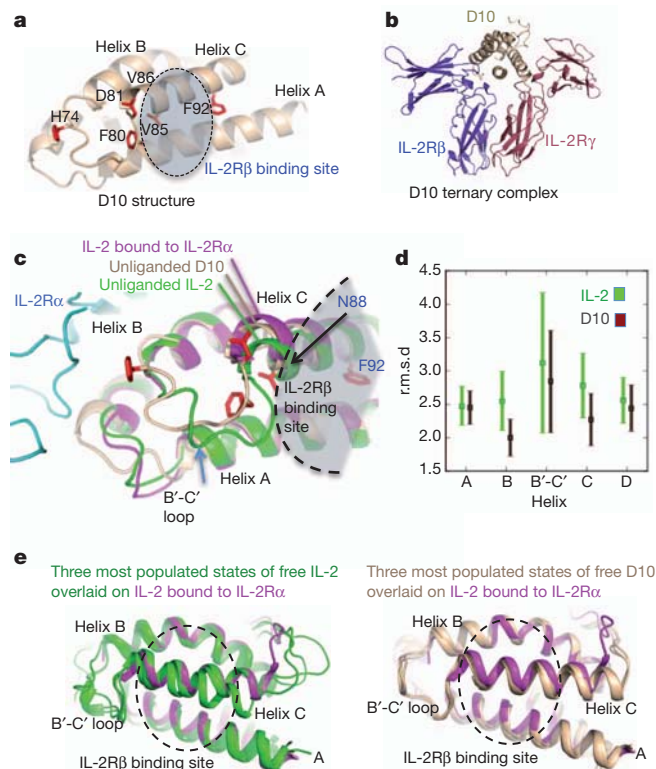*These authors contributed equally to this work.

Figure 2 | Basis of affinity enhancement for IL-2Rβ from structural and molecular dynamics characterization of the D10 IL-2 superkine. a, Crystal structure of the D10 IL-2 superkine at 3.1 Å with mutated residues in red (see also Supplementary Table 1 and Supplementary Fig. 7a). **b**, D10 in complex with human IL-2Rβ and IL-2Rγ preserves the wild-type receptor dimer geometry (see also Supplementary Fig. 7b). **c**, The unliganded D10 IL-2 superkine helix C (brown), moves towards its hydrophobic core compared to unliganded wild-type IL-2 (green, PDB ID 3INK). This helix C position is more similar to that of helix C in IL-2 bound to IL-2Rα (purple, PDB ID 1Z92) (see also Supplementary Fig. 8). **d**, A 40-ns molecular dynamics simulation shows a reduction of the average r.m.s.d. for the B and C helices, and the B-C loop in D10 versus IL-2 (see also Supplementary Fig. 8c). Error bars represent the standard error of the r.m.s.d. **e**, Helix C in IL-2 (green, left panel) drifts during the molecular dynamics simulation more than the IL-2 superkine D10 (brown, right panel) when compared to IL-2 bound to IL-2Rα (purple).

that L85V may affect the structure of helix C in a way that enhances binding to IL-2Rβ. Therefore, we carried out a second generation selection where we made a biased library that contained F/I/L/V at amino acids L80, L85, I86, I89, I92 and V93, which are contained within the hydrophobic core and linker region on helix C (Fig. 1b, c). To rapidly select the most active variants, we used the yeast-displayed cytokines themselves to stimulate STAT5 phosphorylation in the human NK cell line YT-1 by co-incubation at varying yeast:YT-1 cell ratios (Fig. 1d and Supplementary Fig. 4). Several clones stimulated substantially more STAT5 phosphorylation at lower yeast:cell ratios than yeast-displayed wild-type IL-2 (Fig. 1d and Supplementary Fig. 4). Sequencing of a selected panel of high-affinity IL-2 clones revealed a consensus set of mutations L80F/R81D/L85V/I86V/I92F (Fig. 1c and Supplementary Fig. 3).

We expressed recombinant forms of several first- and second-generation IL-2 clones to measure their binding affinities and kinetics for IL-2Rβ by surface plasmon resonance (SPR) (Fig. 1c and Supplementary Figs 3 and 5) and isothermal titration calorimetry (ITC) (Supplementary Fig. 6). By SPR, the affinity between IL-2 and IL-2Rβ was $K_d = 280$ nM. The IL-2 superkines, also called 'super-2s', clustered into low, medium and high affinity classes. The highest affinity mutants had K_ds of 1.2–1.7 nM (D10, H9). The affinity increases were

uniformly manifested in reductions in off-rates (Fig. 1c and Supplementary Figs 3 and 5).

To understand the structural consequences of the evolved mutations, we crystallized the D10 IL-2 superkine (Fig. 2a, Supplementary Fig. 7a and Supplementary Table 1). In the structure of D10 alone, five of the six mutations clustered on the B-C loop and within the C-helix core, in positions that did not contact IL-2Rβ. Notably, the B-C-helix linker region was ordered in the electron density map (Supplementary Figs 7a and 8a), compared to other IL-2 structures where this region is often disordered (Supplementary Fig. 8a). Collectively, the F80, V85 and V86 substitutions appeared to collapse into a hydrophobic cluster that stabilized the loop by pinning the C-helix into the core of the molecule. Only one of the five consensus mutations, I92F, was at a position that contacted IL-2Rβ in the receptor complex (Fig. 2a), but it was deeply inserted between the C and A helices, contributing only an additional 10 Å² of molecular surface buried by IL-2Rβ in the complex compared to Ile 92. We also determined a low-resolution (3.8 Å) structure of the D10 ternary receptor complex to assess whether the mutations have perturbed the IL-2Rβ/IL-2Rγ receptor dimer geometry compared to the wild-type IL-2 complex (Fig. 2b and Supplementary Table 1). The overall IL-2Rβ/IL-2Rγ heterodimeric architecture and mode of cytokine/IL-2Rβ contact in the D10 ternary complex were essentially identical to the previously reported IL-2 quaternary assembly (root mean squared deviation (r.m.s.d.) = 0.43 Å) (Supplementary Fig. 7b).

Previously, we found that the C-helix of IL-2 seems to undergo subtle repositioning upon binding to IL-2Rα[11] (Fig. 2c and Supplementary Fig. 8a). Inspection of three wild-type unliganded IL-2 structures revealed conformational variability in the C-helix position, consistent with higher crystallographic B-factors in this helix relative to the rest of the molecule (Supplementary Fig. 8b). We compared the structure of our D10 IL-2 superkine to that of an unliganded structure of IL-2, and IL-2 in the receptor complexes. We found that the C-helix in D10 was more similar to that seen in the two receptor-bound conformations of IL-2 than the free forms, having undergone a relatively small shift towards the helical core as a consequence of the stabilizing mutations (Fig. 2c).

We used molecular dynamics simulations of IL-2 and D10 to further interrogate the mechanism responsible for higher binding affinity to IL-2Rβ by the IL-2 superkine (Fig. 2d, e). We constructed an atomically detailed Markov state model (MSM) to probe the relative conformational flexibility of IL-2 versus D10 directly. Analysis of the MSM clearly demonstrated that D10 was more stable than IL-2, and that IL-2 visited nearly twice as many clusters as D10. For example, the most populated state of D10 had an equilibrium probability of approximately 0.20, compared to approximately 0.05 for IL-2, demonstrating that the equilibrium population of D10 was far more localized than IL-2. Helix B, the B-C loop and helix C appeared rigidified in D10 compared to IL-2 as evidenced by reduced r.m.s.d. from the starting conformations (Fig. 2d and Supplementary Movies 1, 2). F92 seemed to act as a molecular wedge between helix C and helix A, stabilizing the more C-terminal end of the helix (Fig. 2a). We also simulated both D10 and IL-2 starting in a receptor-bound-like structure and monitored the divergence in r.m.s.d. of the B-C loop and helix C from the actual receptor-bound structure. IL-2 (Fig. 2e, left, and Supplementary Fig. 8c) quickly 'wandered' from the receptor conformation and experienced drastic fluctuations compared to D10 (Fig. 2e, right, Supplementary Fig. 8c and Supplementary Movies 1 and 2). Based on these observations, we propose a mechanism whereby the reduced flexibility of helix C in the IL-2 superkine, as a result of its improved core packing with helix B, results in a superior receptor-binding poise that increases its affinity for IL-2Rβ, and consequently mimics a functional role of CD25. The structural and molecular dynamics results indicate that the evolved mutations in the IL-2 superkine cause a conformational stabilization of the cytokine that reduces the energetic penalties for binding to IL-2Rβ.

We asked if the IL-2 superkines demonstrated signalling potencies on cells in accordance with their IL-2Rβ-binding affinities, and whether their activities depended on cell surface expression of CD25. We determined the dose–response relationships of wild-type IL-2 versus the IL-2 superkines 6-6, D10 and H9 on both CD25$^-$ and CD25$^+$ human YT-1 NK cells by assaying STAT5 phosphorylation with flow cytometry (Fig. 3a–d and Supplementary Fig. 9). On CD25$^-$ YT-1 cells, the half-maximum effective concentration (EC$_{50}$) of H9 and D10 were decreased over tenfold (EC$_{50}$ = 2.5 and 1.8 ng ml^{-1}, respectively) compared to IL-2 (EC$_{50}$ = 39 ng ml^{-1}), with the 6-6 mutein yielding an EC$_{50}$ intermediate between IL-2 and H9/D10 (EC$_{50}$ = 15 ng ml^{-1}), consistent with the improved affinity of the IL-2 superkines for IL-2Rβ (Fig. 3a). On CD25$^+$ YT-1 cells, the EC$_{50}$ of IL-2 decreased over 50-fold relative to CD25$^-$ YT-1 cells, from 39 to 0.66 ng ml^{-1} (Fig. 3b). In contrast, the EC$_{50}$ of H9 and D10 improved only modestly in the presence of CD25 (EC$_{50}$ of 0.47 and 0.52 compared to 2.5 and 1.8 ng ml^{-1}, respectively) (Fig. 3b).

We sought to further probe the CD25-independence of the IL-2 superkines by taking advantage of a previously characterized mutation

in IL-2, Phe 42 to Ala (F42A), which showed reduced binding to CD25 by approximately 220-fold for H9 (K_d 6.6 nM versus 1.4 μM) and approximately 120-fold for IL-2 (K_d 6.6 nM versus 0.8 μM) (Supplementary Fig. 10)[12,13]. The F42A mutation is an alternative diagnostic probe of the relative CD25 dependence of IL-2 and the IL-2 superkine. The F42A mutation right-shifted the dose–response curve of wild-type IL-2 on CD25$^+$ cells by about 1 log, but had no effect on CD25$^-$ cells (Fig. 3c). In contrast, H9 was far less sensitive to the F42A mutation, with the dose–response curves of H9 versus H9 F42A being very similar on both CD25$^+$ and CD25$^-$ cells (Fig. 3d).

We assessed the activity of several IL-2 superkines on T cells that were either deficient in, or expressed CD25. For the former experiment, CD4$^+$ T cells were isolated from CD25-knockout mice, followed by stimulation by either wild-type IL-2 or six IL-2 superkines and assaying for STAT5 phosphorylation at a range of cytokine concentrations (Fig. 3e and Supplementary Fig. 11). CD25$^{-/-}$ CD4$^+$ T cells responded poorly to exogenous wild-type IL-2 stimulation, but the IL-2 superkines induced STAT5 phosphorylation in these cells proportional to their affinity for IL-2Rβ.

The principle functional effect of IL-2 is to promote T cell proliferation, particularly for naive T cells. Human naive CD4$^+$ T cells were isolated and left either unstimulated or stimulated with plate-bound anti-CD3 antibody with or without the different IL-2 variants (Fig. 3f and Supplementary Fig. 12). Increased proliferation effects on naive human T cells correlated with increased affinity for IL-2Rβ and STAT5 phosphorylation shown earlier, as the rank order of potency was D10 = H9 > 6-6 > wild-type IL-2 (see Supplementary Fig. 12 for the complete titration).

We next tested the IL-2 variants for their ability to induce STAT5 phosphorylation on experienced human CD4$^+$ T cells (Supplementary Fig. 13), which highly express the trimeric IL-2Rαβγ complex. Human CD4$^+$ T cells were activated in vitro by T cell receptor (TCR) stimulation and rested to generate 'experienced' human CD4$^+$ CD25$^+$ T cells. As for the CD25$^+$ YT-1 cells, we observed a much smaller difference between IL-2 and the IL-2 superkines.

We assessed the potency of the IL-2 superkine H9 on expansion of CD25^{low} versus CD25^{high} T cells, in comparison to wild-type IL-2 and IL-2–anti-IL-2 monoclonal antibody (mAb) complexes, which have been shown to exert reduced pulmonary oedema yet very potent antitumour responses in vivo[14–16]. On antigen-experienced (memory-phenotype, MP) CD8$^+$ T cells, expressing only low levels of CD25 but high levels of IL-2Rβγ, H9 induced more than three times the rate of proliferation and expansion as wild-type IL-2 (Fig. 4a and Supplementary Fig. 14a). However, on CD4$^+$ CD25^{high} T regulatory (T$_{reg}$) cells, we found that the CD25-competent wild-type IL-2 and H9 achieved comparable maximal expansion, demonstrating again that expression of CD25 mitigates the difference between the IL-2 superkine and wild-type IL-2 (Fig. 4a and Supplementary Fig. 14b). Thus, the H9 has the desired property that it shows enhanced stimulation towards CD8$^+$ T cells, but not towards T$_{reg}$ cells, compared to wild-type IL-2.

As previously reported, administration of high-dose wild-type IL-2 for 5 days induced substantial pulmonary oedema, which is known to be CD25-dependent[15] (Fig. 4b). Although significantly more stimulatory for cytotoxic CD8$^+$ T cells (Fig. 4a), the H9 IL-2 superkine caused substantially less pulmonary oedema (Fig. 4b).

Given the more favourable properties of H9 in comparison to IL-2, we assessed its ability to stimulate effector functions of cytotoxic T cells in four different tumour models in vivo, where high-dose IL-2 administration has been previously shown to result in tumour regression[15,17]. To this end, C57BL/6 mice were injected subcutaneously with B16F10 melanoma cells, followed by administration of either high-dose IL-2, IL-2–anti-IL-2 mAb complexes, or the H9 IL-2 superkine, once tumour nodules became visible and palpable. PBS-treated control mice rapidly developed large subcutaneous tumours reaching a volume of about 1,500 mm^3 on day 18 (Fig. 4c). As previously shown, high-dose IL-2 treatment was able to delay tumour growth by as much as 39% on
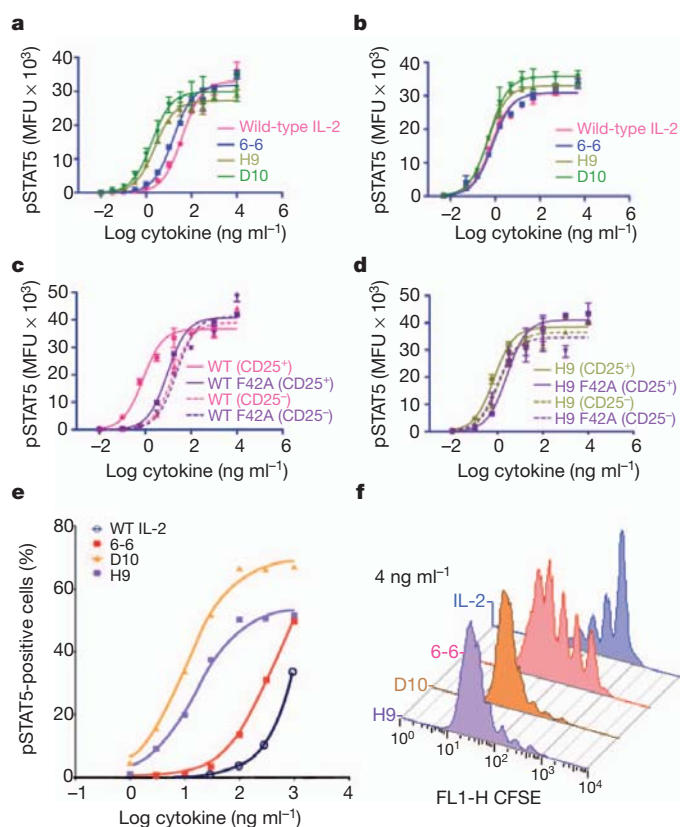
Figure 3 | Functional properties of the IL-2 superkine on human NK cells in vitro. a, b, Dose–response curves of STAT5 phosphorylation (pSTAT5) on CD25$^-$ (**a**) and CD25$^+$ (**b**) YT-1 cells with wild-type IL-2 and three IL-2 superkines. MFU, mean fluorescence units. **c,** Dose–response curves of STAT5 phosphorylation on CD25$^+$ (solid curves) and CD25$^-$ (dashed curves) YT-1 cells with wild-type IL-2 (pink curves) and IL-2-F42A mutation (purple curves). **d,** Dose–response curves of STAT5 phosphorylation on CD25$^+$ (solid curves) and CD25$^-$ (dashed curves) YT-1 cells with H9 (green curves) and H9-F42A mutation (purple curves). **e,** The IL-2 superkines have superior potency over IL-2 on T cells derived from CD25$^{-/-}$ mice as demonstrated by dose–response curves for STAT5 phosphorylation on T cells demonstrating that potency correlates with IL-2Rβ affinity (see also Supplementary Fig. 10). **f,** Proliferation of human naive CD4$^+$ T cells (CD25^{low}) reveals similar potency profiles as seen with CD25$^{-/-}$ T cells. Proliferation was measured by carboxyfluorescein succinimidyl ester (CFSE) dilution on day 5 (see also Supplementary Fig. 10). Error bars in **a–d** represent s.e.m. of mean fluorescence units for each sample at the indicated cytokine concentration.
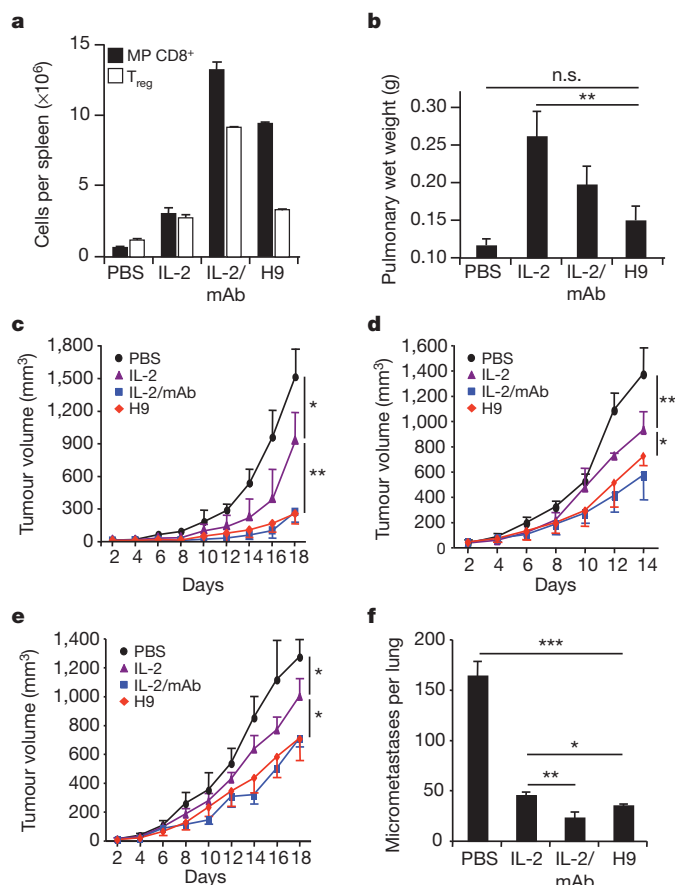
Figure 4 | Functional and antitumour activities of the IL-2 superkine *in vivo*. a, Total cell counts of host $CD3^+$ $CD8^+$ $CD44^{high}$ memory-phenotype T cells ($MP\,CD8^+$, closed bars), and host $CD3^+$ $CD4^+$ $CD25^{high}$ T cells (T_{reg}, open bars) was determined in the spleens of mice receiving either PBS, 20 μg IL-2, 1.5 μg IL-2–anti-IL-2 mAb complexes (IL-2/mAb), or 20 μg H9 (see also Supplementary Fig. 14). **b**, Pulmonary oedema (pulmonary wet weight) served to assess adverse toxic effects following IL-2 treatment, and was determined by weighing lungs before and after drying. **c–f**, C57BL/6 mice ($n = 3$–4 mice per group) were injected either subcutaneously with 10^6 B16F10 melanoma cells (c), 2.5×10^6 murine colon carcinoma 38 (d), 10^6 Lewis lung carcinoma (e), or mice received 3×10^5 B16F10 melanoma cells intravenously (f), followed by daily injections of either PBS, 20 μg IL-2, 1.5 μg IL-2/mAb complexes, or 20 μg H9 for 5 days once subcutaneous tumour nodules became visible and palpable or from day three on for intravenously-injected tumours (see also Supplementary Fig. 15). Shown is mean tumour volume in mm^3 ($\pm$ s.d.) versus time upon tumour inoculation. Error bars represent s.e.m., P values refer to comparisons of wild type with the other treatment modalities. $*P < 0.05$; $**P < 0.01$; $***P < 0.001$.

day 18 ($P < 0.05$), whereas IL-2–anti-IL-2 mAb complexes exerted very effective tumour control, reducing tumour growth by more than 80% on day 18 ($P < 0.005$) (Fig. 4c). Significantly, similar to IL-2–anti-IL-2 mAb complexes, mice receiving high-dose H9 showed a dramatic decrease of tumour load on day 18, which was reduced by more than 80% compared to PBS ($P < 0.005$) and by more than 70% compared to wild-type IL-2 ($P < 0.001$) (Fig. 4c). Similar results were obtained using three other tumour models, including murine colon carcinoma and Lewis lung carcinoma injected subcutaneously (Fig. 4d, e) and B16F10 cells administered intravenously (Fig. 4f and Supplementary Fig. 15). Collectively, these data show that the H9 IL-2 superkine is very effective against different tumours, albeit inducing reduced pulmonary oedema.

The practical implications are that this conformational nuance in IL-2 can be exploited for therapy. The IL-2 superkine robustly activates cytotoxic $CD8^+$ T cells and NK cells for potent antitumour immune

responses, yet it elicits minimal toxicity, suggesting that the IL-2 superkine could warrant reconsideration for clinical applications of IL-2.

METHODS SUMMARY

Yeast display and selection of IL-2. Error-prone and site-directed libraries of IL-2 were displayed on yeast as previously described[18] and stained with biotinylated IL-2Rβ at successively decreasing concentrations. Staining was detected with streptavidin–phycoerythrin and yeast were separated using paramagnetic anti-phycoerythrin microbeads (Miltenyi; MACS). Enrichment of positively-staining yeast was monitored by flow-cytometry.

Protein expression, purification and structural determination. Human IL-2 variants and the ectodomains of IL-2Rβ, IL-2Rγ and CD25 were expressed in Hi5 cells and purified as previously described[11]. Proteins were concentrated to 8–20 mg ml^{-1} and crystallized by vapour diffusion in sitting drops. Diffraction studies were performed at the Stanford Synchrotron Radiation Laboratory and the Advanced Light Source. Crystal structures were solved by molecular replacement with PHASER[19] and refined using PHENIX[20] and COOT[21].

Mice. C57BL/6 and Thy1.1-congenic mice on a C57BL/6 background were maintained under specific pathogen-free conditions and used at 3–6 months of age. Experiments were performed in accordance with the Swiss Federal Veterinary Office guidelines and approved by the Cantonal Veterinary Office.

***In vivo* T-cell proliferation.** Carboxyfluorescein succinimidyl ester (CFSE)-labelled $CD44^{high}$ $CD8^+$ T cells (2×10^6 to 3×10^6) from Thy1.1-congenic mice were injected intravenously to Thy1.2-congenic animals. Mice received daily intraperitoneal (i.p.) injections of PBS, 20 μg IL-2, 1.5 μg IL-2–anti-IL-2 mAb complexes, or 20 μg H9 for 5 days. On the sixth day, spleens were removed and analysed by flow cytometry.

Toxicity. Pulmonary oedema was determined by measurement of pulmonary wet weight on the sixth day after five daily i.p. injections of PBS, 20 μg IL-2, 1.5 μg IL-2–anti-IL-2 mAb complexes, or 20 μg H9 as previously described[15].

Tumour models. B16F10 melanoma cells, Lewis lung carcinoma or murine colon carcinoma 38 cells were injected into mice (3–4 mice per group), as previously reported[15,17]. Treatment consisted of five daily i.p. injections of PBS, 20 μg IL-2, 1.5 μg IL-2–anti-IL-2 mAb complexes, or 20 μg H9.

Full Methods and any associated references are available in the online version of the paper at www.nature.com/nature.

1. Rochman, Y., Spolski, R. & Leonard, W. J. New insights into the regulation of T cells by γ_c family cytokines. *Nature Rev. Immunol.* **9,** 480–490 (2009).
2. Smith, K. A. Interleukin-2: inception, impact, and implications. *Science* **240,** 1169–1176 (1988).
3. Waldmann, T. A. The biology of interleukin-2 and interleukin-15: implications for cancer therapy and vaccine design. *Nature Rev. Immunol.* **6,** 595–601 (2006).
4. Cosman, D. *et al.* Cloning, sequence and expression of human interleukin-2 receptor. *Nature* **312,** 768–771 (1984).
5. Leonard, W. J. *et al.* Molecular cloning and expression of cDNAs for the human interleukin-2 receptor. *Nature* **311,** 626–631 (1984).
6. Nikaido, T. *et al.* Molecular cloning of cDNA encoding human interleukin-2 receptor. *Nature* **311,** 631–635 (1984).
7. Hatakeyama, M. *et al.* Interleukin-2 receptor beta chain gene: generation of three receptor forms by cloned human alpha and beta chain cDNA's. *Science* **244,** 551–556 (1989).
8. Takeshita, T. *et al.* Cloning of the gamma chain of the human IL-2 receptor. *Science* **257,** 379–382 (1992).
9. Boder, E. T. & Wittrup, K. D. Yeast surface display for screening combinatorial polypeptide libraries. *Nature Biotechnol.* **15,** 553–557 (1997).
10. Chao, G. *et al.* Isolating and engineering human antibodies using yeast surface display. *Nature Protocols* **1,** 755–768 (2006).
11. Wang, X., Rickert, M. & Garcia, K. C. Structure of the quaternary complex of interleukin-2 with its α, β, and γ_c receptors. *Science* **310,** 1159–1163 (2005).
12. Mott, H. R. *et al.* The solution structure of the F42A mutant of human interleukin 2. *J. Mol. Biol.* **247,** 979–994 (1995).
13. Thanos, C. D., DeLano, W. L. & Wells, J. A. Hot-spot mimicry of a cytokine receptor by a small molecule. *Proc. Natl Acad. Sci. USA* **103,** 15422–15427 (2006).
14. Boyman, O., Kovar, M., Rubinstein, M. P., Surh, C. D. & Sprent, J. Selective stimulation of T cell subsets with antibody-cytokine immune complexes. *Science* **311,** 1924–1927 (2006).
15. Krieg, C., Létourneau, S., Pantaleo, G. & Boyman, O. Improved IL-2 immunotherapy by selective stimulation of IL-2 receptors on lymphocytes and endothelial cells. *Proc. Natl Acad. Sci. USA* **107,** 11906–11911 (2010).
16. Létourneau, S. *et al.* IL-2/anti-IL-2 antibody complexes show strong biological activity by avoiding interaction with IL-2 receptor α subunit CD25. *Proc. Natl Acad. Sci. USA* **107,** 2171–2176 (2010).

17. Rosenberg, S. A., Mule, J. J., Spiess, P. J., Reichert, C. M. & Schwarz, S. L. Regression of established pulmonary metastases and subcutaneous tumor mediated by the systemic administration of high-dose recombinant interleukin 2. *J. Exp. Med.* **161,** 1169–1188 (1985).

18. Rao, B. M., Driver, I., Lauffenburger, D. A. & Wittrup, K. D. Interleukin 2 (IL-2) variants engineered for increased IL-2 receptor α-subunit affinity exhibit increased potency arising from a cell surface ligand reservoir effect. *Mol. Pharmacol.* **66,** 864–869 (2004).

19. McCoy, A. J. *et al. Phaser* crystallographic software. *J. Appl. Crystallogr.* **40,** 658–674 (2007).

20. Adams, P. D. *et al. PHENIX*: building new software for automated crystallographic structure determination. *Acta Crystallogr. D* **58,** 1948–1954 (2002).

21. Emsley, P. & Cowtan, K. *Coot*: model-building tools for molecular graphics. *Acta Crystallogr. D* **60,** 2126–2132 (2004).

Supplementary Information is linked to the online version of the paper at www.nature.com/nature.

Author Contributions A.M.L. performed *in vitro* evolution and contributed to preparation of the manuscript. D.L.B. produced recombinant proteins, determined crystal structures, and carried out surface plasmon resonance analysis. A.M.R. carried out cellular and signalling assays, biophysical measurements and contributed to preparation of the manuscript. C.K. carried out *in vivo* experiments, analysed data and contributed to preparation of the manuscript; M.E.R. carried out *in vivo* experiments in mice. I.M. analysed cell-signalling data. G.R.B., P.N. and V.S.P. carried out and analysed molecular dynamics simulations. J.T.L., L.S. and C.G.F. performed and analysed T-cell signalling experiments. O.B. designed and supervised *in vivo* experiments, analysed data and contributed to preparation of the manuscript. K.C.G. conceived of the project, analysed data, supervised execution of the project, and prepared the manuscript.

Author Information Atomic coordinates and structure factors for the reported crystal structures have been deposited with the Protein Data Bank under accession codes 3QAZ and 3QB1. Reprints and permissions information is available at www.nature.com/reprints. The authors declare competing financial interests: details accompany the full-text HTML version of the paper at www.nature.com/nature. Readers are welcome to comment on the online version of this article at www.nature.com/nature. Correspondence and requests for materials should be addressed to K.C.G. (kcgarcia@stanford.edu) or O.B. (onur.boyman@uzh.ch).

METHODS

Yeast display of wild-type IL-2. Human IL-2 DNA was cloned into the vector pCT302 and displayed on the *Saccharomyces cerevisiae* strain EBY100 as previously described[18]. Individual colonies of IL-2 yeast were grown overnight at 30 °C in SDCAA liquid media and induced in SGCAA liquid media for 2 days at 20 °C. The yeast were stained with tetramerized biotinylated IL-2Rβ (b-IL-2Rβ), biotinylated IL-2Rγ (b-IL-2Rγ), or b-IL-2Rβ in the presence of b-IL-2Rγ. IL-2Rβ tetramers were formed by incubating 2 μM b-IL-2Rβ with 470 nM SAV-PE (streptavidin–phycoerythrin conjugate, Invitrogen) in phosphate buffered saline supplemented with 0.5% BSA and 2 mM EDTA (PBE) for 15 min on ice. Analysis was performed on an Accuri C6 flow cytometer.

Error-prone PCR IL-2 library construction and selection. Human IL-2 DNA was subjected to error-prone PCR using the GeneMorphII kit (Stratagene). The two user-determined variables in the kit were the starting concentration of DNA template and the number of cycles. We used 100 ng template and 30 cycles in an effort to maximize the number of errors. The primers used for error-prone PCR were 5′-GCACCTACTTCAAGTTCTAC-3′ for the forward primer and 5′-GCCACCAGAGGATCC-3′ for the reverse primer. The PCR product was further amplified using primers containing sequence homology to pCT302 for recombination inside the yeast: forward primer 5′-AGTGGTGGTGGTGGTTCTGG TGGTGGTGGTTCTGGTGGTGGTGGTTCTGCTAGCGCACCTACTTCAAG TTCTAC-3′ and reverse primer 5′-ACACTGTTGTTATCAGATCTCGAGCAA GTCTTCTTCGGAGATAAGCTTTTGTTCGCCACCAGAGGATCC-3′. Insert DNA was combined with linearized vector backbone and EBY100 yeast and electroporated as previously described[10]. The electroporations yielded a library of 1×10^8 transformants. Selections were performed using magnetic activated cell sorting (MACS, Miltenyi). First-round selection was performed with 1×10^9 yeast, approximately tenfold coverage of the number of transformants. Yeast were stained with 10 ml of 500 nM IL-2Rβ SAV-PE tetramers in PBE for 2 h with slow rotation at 4 °C. Cells were pelleted at 5,000g for 5 min, buffer aspirated, and washed with PBE. The pellet was resuspended in 9.6 ml PBE and 400 μl Miltenyi anti-PE microbeads, incubated for 20 min with slow rotation at 4 °C, pelleted, and washed with 14 ml PBE. The yeast were then resuspended in 5 ml PBE and magnetically separated by a Miltenyi LS column, following the manufacturer's protocols. Subsequent rounds of selection used 1×10^8 yeast cells, successively lower concentrations of monomeric IL-2Rβ for increased selection stringency, and 100 μl of Miltenyi microbeads to capture labelled yeast-displayed IL-2 variants.

Site-directed hydrophobic core IL-2 library construction and selection. The site-directed library was created by assembly PCR of 13 primers, two of which contained the following degenerate codons: Q74 = MRS, L80 = NTC, R81 = NNK, L85 = NTC, I86 = NTC, I89 = NTC, I92 = NTC, V93 = NTC. The primers used for assembly PCR were: 5′-GCACCTACTTCAAGTTCTACAA AGAAAACACAGCTACAACTGGAGCA-3′, 5′-CAAAATCATCTGTAAATC CAGAAGTAAATGCTCCAGTTGTAGCTGTG-3′, 5′-GGATTTACAGATGA TTTTGAATGGAATTAATAATTACAAGAATCCCA-3′, 5′-AACTTAGCTGT GAGCATCCTGGTGAGTTTGGGATTCTTGTAATTATT-3′, 5′-GGATGCTC ACA**GCT**AAGTTTTACATGCCCAAGAAGGCCACAGAACTG-3′, 5′-TTCTTCTAGACACTGAAGATGTTTCAGTTCTGTGGCCTTCTTG-3′, 5′-CA GTGTCTAGAAGAAGAACTCAAACCTCTGGAGGAAGTGCTAAATTTA-3′, 5′-GTGAAAGTTTTTGCT**SYK**AGCTAAATTTAGCACTTCCTCC-3′, 5′-AG CAAAAACTTTCAC**NTCNNK**CCCAGGGAC**NTCNTC**AGCAAT**NTC**AACG TA**NTCNTC**CTGGAACTAAAGGGATC-3′, 5′-CATCAGCATATTCACACA TGAATGTGTTTCAGATCCCTTTAGTTCCAG-3′, 5′-ATGTGTGAATATG CTGATGAGACAGCAACCATTGTAGAATTTCTGAACA-3′, 5′-AGATGAT GCTTTGACAAAAGGTAATCCATCTGTTCAGAAATTCTACAAT-3′, 5′-TT TTGTCAAAGCATCATCTCAACACTAACTGGATCCTCTGGTGGC-3′. The assembly PCR reaction was performed using *Pfu* DNA polymerase (Stratagene). The product DNA was further PCR-amplified using the same primers as the error-prone library. Electroporation of insert DNA and linearized vector into EBY-100 yeast yielded a library of 1.4×10^8 transformants. Selection of the site-directed library was performed as with the error-prone library, except tenfold lower concentrations of monomeric IL-2Rβ were used.

Protein expression and purification. Human IL-2 variants (amino acids 1–133), the IL-2Rβ ectodomain (amino acids 1–214), IL-2Rγ (amino acids 34–232) and CD25 (amino acids 1–217) were expressed and purified from Hi5 cells as previously described[11]. For biotinylated receptor expression, IL-2Rβ and IL-2Rγ with a C-terminal biotin acceptor peptide (BAP)-LNDIFEAQKIEWHE were co-expressed with BirA ligase with excess biotin (100 μM). CD25 was biotinylated at its free cysteine by incubation with biotin–maleimide (Sigma). For crystallization, receptor constructs were co-expressed with *N*-linked glycosylation sites IL-2Rβ residues Asn 3, 17, 45, and IL-2Rγ residues Asn 53 mutated to Gln. IL-2 proteins used for crystallization were expressed with *N*-linked glycosylation

inhibitor tunicamycin (0.2 μg ml^{-1}). Proteins were treated overnight with carboxypeptidase-A followed by size-exclusion chromatography.

Surface plasmon resonance. SPR experiments were conducted on a Biacore T100 instrument at 25 °C. All data was analysed using the Biacore T100 evaluation software version 2.0 with a 1:1 Langmuir binding model. Experiments used a Biacore SA sensor chip (GE Healthcare). Biotinylated receptors were captured at a low density ($R_{max} \approx 30$ response units) and kinetic runs were conducted at 40 μl min^{-1} to eliminate mass transport and rebinding artefacts. An unrelated biotinylated protein was immobilized as a reference surface. All measurements were made using threefold serial dilutions of IL-2 variants (GE Healthcare, 0.01% BSA). IL-2Rβ was regenerated using 10 mM sodium acetate (pH 5.5) and 1 M MgCl₂. CD25 was regenerated using 1 M NaCl. Kinetic data was determined using 120 s to 190 s of IL-2 variant association and 20 s to 600 s disassociation.

Isothermal titration calorimetry. Calorimetry experiments with the H9 and D10 IL-2 superkines with IL-2Rβ were conducted as previously described[22]. Briefly, titrations were performed on a VP-ITC calorimeter (MicroCal) at 15 °C. Prior to titration, protein and reference water was degassed for 10 min. All samples were extensively dialysed in 10 mM HEPES pH 7.4, 150 mM NaCl (HBS) before titration to minimize heat of dilution effects. Data was processed and analysed using the MicroCal Origin 5.0 software.

Crystallization and data collection. IL-2 D10 crystals were grown in sitting drops at 22 °C from 50 mM HEPES (pH 7.2), 200 mM NaCl and 30% PEG-4000. A 3.1 Å data set was collected under cryo-cooled conditions (20% glycerol) at beamline 11-1 at the Stanford Synchrotron Radiation Laboratory. IL-2 D10 ternary crystals were grown from 100 mM Bis-Tris (pH 5.5), 200 mM NH₄SO₄ and 25% PEG-3350. A cryo-cooled 3.8 Å data set was collected at beamline 8-2 at the Advanced Light Source. Diffraction data were processed using HKL2000. Data processing statistics can be found in Supplementary Table 1.

Structure determination and refinement. The IL-2 D10 and IL-2 D10 ternary crystal structures were solved by molecular replacement with the program PHASER[19] using the coordinates of IL-2 (PDB ID 1M47) and the quaternary complex (PDB ID 2B5I), respectively, and refined with PHENIX[20] and COOT[21] (Supplementary Table 1). Bulk solvent flattening was used for solvent correction in both structures. For both the IL-2 D10 free structure and the ternary complex non-crystallographic symmetry (NCS) restraints (not constraints) were used for initial stages of the refinement. Coordinate refinement strategies included rigid body, restrained individual, group atomic displacement parameters (ADP) and torsion-simulated annealing. The final rounds of refinement removed all NCS restraints for minimization and a round of individual ADP refinement.

Ramachandran analysis was performed with MolProbity[23]. Buried surface area values were calculated using the Protein Interfaces, Surfaces, and Assemblies (PISA) software[24]. IL-2 D10 consisted of eight chains with chain A displayed in the paper. The IL-2 D10 ternary complex contained 36 chains comprising 12 ternary complexes. The paper figures are from chains A, B and C. All structural figures and overlays were prepared using PyMOL[25].

Tissue culture and magnetic purification of CD25$^+$ YT-1 cells. YT-1 and CD25$^+$ YT-1 cells were cultured in RPMI 1640 medium supplemented with 10% fetal bovine serum, 2 mM L-glutamine, minimum non-essential amino acids, sodium pyruvate, 25 mM HEPES, and penicillin-streptomycin (Gibco). CD25$^+$ YT-1 cells were purified as follows: 1×10^7 cells were washed with FACS buffer (phosphate buffered saline + 2% bovine serum albumin) and stained with PE-conjugated anti-human CD25 (1:20; Biolegend) in 1 ml FACS buffer for 20 min at 4 °C. The stained cells were labelled with 200 μl paramagnetic microbeads coupled to anti-PE IgG and separated with an LS MACS separation column according to the manufacturer's instructions (Miltenyi Biotec). Eluted cells were re-suspended in complete RPMI medium at a concentration of 1×10^5 cells per ml and expanded for subsequent experiments. Enrichment of cells was monitored via flow cytometry with the FL-2 channel using an Accuri C6 flow cytometer.

YT-1 dose–response experiments and phospho-flow cytometric analysis. 2×10^5 CD25$^+$ or CD25$^-$ YT-1 cells were washed with FACS buffer and re-suspended in 200 μl FACS buffer with the indicated concentration of IL-2 variant per well in a 96-well plate. Cells were stimulated for 20 min at room temperature and then fixed by addition of formaldehyde to 1.5% and incubated for 10 min. Cells were permeabilized with 100% ice-cold methanol for 20 min on ice, followed by incubation at −80 °C overnight. Fixed, permeabilized cells were washed with excess FACS buffer and incubated with 50 μl Alexa647-conjugated anti-STAT5 pY694 (BD Biosciences) diluted 1:20 in FACS buffer for 20 min. Cells were washed twice in FACS buffer and mean cell fluorescence determined using the FL-4 channel of an Accuri C6 flow cytometer. Dose–response curves and EC₅₀ values were calculated in GraphPad Prism after subtracting the mean cell fluorescence of unstimulated cells.

For 'on-yeast' stimulation experiments, the same protocol was used with the following modifications. Induced yeast were washed twice in FACS buffer and

mixed with the 2×10^5 YT cells at the indicated ratios for 20 min in FACS buffer at room temperature. Cells were then fixed, permeabilized and stained as described above.

T cell isolation and proliferation for phospho-flow cytometric analysis. Human and mouse CD4 T cells were prepared from peripheral blood mononuclear cells (PBMC, Stanford Blood Bank) and spleens and lymph nodes of BALB/C mice, respectively, using antibody-coated CD4 T-cell isolation magnetic beads (Stem Cell Technologies and Miltenyi Biotec). For naive cell stimulation assays, cells were used immediately. For generation of *in vitro* 'experienced' T cells, wells were pre-coated with secondary antibody (Vector Labs) in bicarbonate buffer, pH 9.6 before coating plates with anti-CD3 (OKT3 for human, 2C11 for mouse, eBiosciences) at 100 ng ml^{-1}. T cells were seeded at 0.1×10^6 cells per well with soluble anti-CD28 (CD28.2 for human, 37.51 for mouse, eBiosciences). Cells were cultured for 3 days with full T-cell receptor stimulation, followed by 2 days rest in conditioned media and 2 days rest in fresh culture media. Prior to use, live cells were collected by Lympholyte-M (Cederlane) centrifugation and counted.

In vivo **studies.** C57BL/6 and Thy1.1-congenic mice on a C57BL/6 background (both from Charles River) were maintained under specific pathogen-free conditions and used at 3–6 months of age. Experiments were performed in accordance with the Swiss Federal Veterinary Office guidelines and approved by the Cantonal Veterinary Office.

Cell suspensions of spleen were prepared according to standard protocols[14] and stained for analysis by flow cytometry using phosphate-buffered saline (PBS) containing 4% fetal calf serum and 2.5 mM EDTA. Fluorochrome-conjugated monoclonal antibodies (mAbs) (from BD Biosciences unless otherwise stated) were used against: CD3 (145-2C11, eBioscience), CD4 (RM4-5, Caltag Laboratories), CD8a (53-6.7), CD25 (PC61), CD44 (IM7, eBioscience), NK1.1 (PK136), and Thy1.1 (HIS51, eBioscience). At least 100,000 viable cells were acquired on a BD FACSCanto II flow cytometer and analysed using FlowJo software (TriStar Inc.).

To prepare IL-2–anti-IL-2 mAb complexes, recombinant human IL-2 (rhIL-2) and anti-human IL-2 mAb were premixed at a 2:1 molar ratio using 15,000 international units of recombinant human IL-2, as previously described[15]. Recombinant human IL-2 and anti-human IL-2 mAb clone 5355 (MAB602) were obtained from R&D Systems.

T-cell subsets were obtained by negative T-cell enrichment (StemCell Technologies). Where indicated, purified cells were labelled with carboxyfluorescein diacetate succinimidyl ester (CFSE, Molecular Probes), as previously published[14]. 2×10^6 to 3×10^6 CD8$^+$ T cells from Thy1.1-congenic wild-type mice enriched for CD44^{high} memory-phenotype cells were injected intravenously (i.v.) to Thy1.2-congenic wild-type mice. Starting on the day of adoptive cell transfer, age- and gender-matched mice received daily intraperitoneal (i.p.) injections of either PBS, 20 μg wild-type human IL-2, 20 μg H9, or 1.5 μg human IL-2–anti-IL-2 mAb complexes for 5 consecutive days. 6 days after adoptive cell transfer, spleens were removed and analysed by flow cytometry.

Pulmonary wet weight was determined according to previously established protocols[15]. In brief, wild-type mice received daily i.p. injections of either PBS, 20 μg wild-type human IL-2, 20 μg H9, or 1.5 μg IL-2–anti-IL-2 mAb complexes for 5 consecutive days as described above. On day 6, lungs were removed and weighed before and after drying overnight at 58 °C under vacuum. Pulmonary wet weight was calculated by subtracting initial pulmonary weight from lung weight after dehydration.

To generate subcutaneous tumours, as indicated either 10^6 B16F10 melanoma (from ATCC), 10^6 Lewis lung carcinoma (provided by R. Schwendener), or 2.5×10^6 murine colon carcinoma 38 (provided by R. Schwendener) cells were injected in 100 μl DMEM into the upper dermis of the back of mice (3–4 mice per group), as previously established[15]. Treatment consisted of five daily injections of either PBS, 20 μg IL-2, 1.5 μg IL-2–anti-IL-2 mAb complexes, or 20 μg H9, and was started 1 day after tumour nodules were clearly visible and palpable at a volume of approximately 50–55 mm^3. For the generation of lung metastases, 3×10^5 B16F10 cells in 300 μl DMEM were injected into the tail vein, as previously shown[15]. Treatment was as above and was started on day 3 after tumour inoculation. On day 16 after injection, lungs were perfused, harvested and fixed in Fekete's solution (70% ethanol, 3.7% paraformaldehyde, 0.75 M glacial acetic acid), followed by dissection of lungs and counting of pulmonary micrometastases. Differences between groups were examined for statistical significance by using a one-way analysis of variance (ANOVA) with Bonferroni post-test correction.

Molecular dynamics simulations and MSM. We used MODELLER[26] with the default settings to create five starting conformations for simulations from each of three IL-2 structures (PDB ID 3INK, 1M47 and 1Z92; refs 27–29), and D10 with both the wild-type IL-2 sequence and the D10 sequence. The five conformations for a particular sequence/structure differ only where residues are missing or mutated.

Molecular dynamics simulations were run with Gromacs 4.5.2 (ref. 30) using the AMBER03 force field[31]. Each structure was placed in a dodecahedral box of about 7.1 by 7.1 by 5 nm and solvated with approximately 7,650 TIP3P water molecules. Conformations were first minimized with a steepest descent algorithm using a tolerance of 1,000 kJ mol^{-1} nm^{-1} and a step size of 0.01 nm. A 1-nm cutoff was used for Coulombic and Van der Waals interactions and a grid-based neighbour list. Conformations were then equilibrated at 300 K and 1 bar by holding protein atoms fixed and allowing the surrounding water to relax for 500 ps with a 2 fs time-step. All bonds were constrained with the LINCS algorithm[32]. Centre of mass motion was removed at every step and a grid-based neighbour list with a cutoff of 1.5 nm was updated every 10 steps. For electrostatics, we used fourth order PME[33] with a cutoff of 1.5 nm for Coulombic interactions, a Fourier spacing of 0.08 nm, and a tolerance of 1×10^{-5}. A hard cutoff of 1.2 nm was used for Van der Waals interactions with a switch starting at 1 nm. The temperature was controlled with two Nose–Hoover thermostats[34] applied to the protein and solvent respectively with a time constant of 0.5 ps. The pressure was controlled with an isotropic Berenson barostat[35] applied to the entire system with a time constant of 0.5 ps and a compressibility of 4.5×10^{-5} bar^{-1}. Long-range corrections were applied to energy and pressure. Production simulations up to 40 ns duration used the same parameters as for equilibration, with the exception that the protein atoms were no longer held fixed.

We used MSMBuilder[36] to construct an MSM with a 4-ns lag time. Based on previous work on protein folding[37], we chose to create 70 clusters (microstates) using a k-centres algorithm and the r.m.s.d. between pairs of conformations. All C$_\alpha$ and C$_\beta$ atoms were used for the r.m.s.d., thereby allowing different sequences to be used in the same clustering. Thermodynamic and kinetic properties were extracted from the MSM's eigenvalues and eigenvectors[38,39].

22. Rickert, M., Boulanger, M. J., Goriatcheva, N. & Garcia, K. C. Compensatory energetic mechanisms mediating the assembly of signaling complexes between interleukin-2 and its α, β, and γc receptors. *J. Mol. Biol.* **339,** 1115–1128 (2004).
23. Davis, I. W. *et al.* MolProbity: all-atom contacts and structure validation for proteins and nucleic acids. *Nucleic Acids Res.* **35,** W375–W383 (2007).
24. Krissinel, E. & Henrick, K. Inference of macromolecular assemblies from crystalline state. *J. Mol. Biol.* **372,** 774–797 (2007).
25. DeLano, W. L. The PyMOL Molecular Graphics System (DeLano Scientific, 2002).
26. Eswar, N. *et al. Comparative Protein Structure Modeling With MODELLER. Current Protocols in Bioinformatics.* Vol. 15 5.6.1-5.6.30 (Wiley, 2006).
27. Bazan, J. F. Unraveling the structure of IL-2. *Science* **257,** 410–413 (1992).
28. Arkin, M. R. *et al.* Binding of small molecules to an adaptive protein–protein interface. *Proc. Natl Acad. Sci. USA* **100,** 1603–1608 (2003).
29. Rickert, M., Wang, X., Boulanger, M. J., Goriatcheva, N. & Garcia, K. C. The structure of interleukin-2 complexed with its alpha receptor. *Science* **308,** 1477–1480 (2005).
30. Hess, B., Kutzner, C., van der Spoel, D. & Lindahl, E. GROMACS 4: algorithms for highly efficient, load-balanced, and scalable molecular simulation. *J. Chem. Theory Comput.* **4,** 435–447 (2008).
31. Duan, Y. *et al.* A point-charge force field for molecular mechanics simulations of proteins based on condensed-phase quantum mechanical calculations. *J. Comput. Chem.* **24,** 1999–2012 (2003).
32. Hess, B. P-LINCS: a parallel linear constraint solver for molecular simulation. *J. Chem. Theory Comput.* **4,** 116–122 (2008).
33. Essmann, U. *et al.* A smooth particle mesh Ewald method. *J. Chem. Phys.* **103,** 8577–8593 (1995).
34. Hoover, W. G. Canonical dynamics: equilibrium phase-space distributions. *Phys. Rev. A* **31,** 1695–1697 (1985).
35. Berendsen, H. J. C., Postma, P. M., van Gunsteren, W. F., DiNola, A. & Haak, J. R. Molecular dynamics with coupling to an external bath. *J. Chem. Phys.* **81,** 3684–3690 (1984).
36. Bowman, G. R., Huang, X. & Pande, V. S. Using generalized ensemble simulations and Markov state models to identify conformational states. *Methods* **49,** 197–201 (2009).
37. Bowman, G. R., Beauchamp, K. A., Boxer, G. & Pande, V. S. Progress and challenges in the automated construction of Markov state models for full protein systems. *J. Chem. Phys.* **131,** 124101 (2009).
38. Bowman, G. R., Huang, X. & Pande, V. S. Network models for molecular kinetics and their initial applications to human health. *Cell Res.* **20,** 622–630 (2010).
39. Noé, F. & Fischer, S. Transition networks for modeling the kinetics of conformational change in macromolecules. *Curr. Opin. Struct. Biol.* **18,** 154–162 (2008).

LETTER

An inverse relationship to germline transcription defines centromeric chromatin in *C. elegans*

Reto Gassmann[1]*, Andreas Rechtsteiner[2]*, Karen W. Yuen[1]†*, Andrew Muroyama[1], Thea Egelhofer[2], Laura Gaydos[2], Francie Barron[1]†, Paul Maddox[1]†, Anthony Essex[1]†, Joost Monen[1]†, Sevinc Ercan[3], Jason D. Lieb[3], Karen Oegema[1], Susan Strome[2] & Arshad Desai[1]

Centromeres are chromosomal loci that direct segregation of the genome during cell division. The histone H3 variant CENP-A (also known as CenH3) defines centromeres in monocentric organisms, which confine centromere activity to a discrete chromosomal region, and holocentric organisms, which distribute centromere activity along the chromosome length[1–3]. Because the highly repetitive DNA found at most centromeres is neither necessary nor sufficient for centromere function, stable inheritance of CENP-A nucleosomal chromatin is postulated to propagate centromere identity epigenetically[4]. Here, we show that in the holocentric nematode *Caenorhabditis elegans* pre-existing CENP-A nucleosomes are not necessary to guide recruitment of new CENP-A nucleosomes. This is indicated by lack of CENP-A transmission by sperm during fertilization and by removal and subsequent reloading of CENP-A during oogenic meiotic prophase. Genome-wide mapping of CENP-A location in embryos and quantification of CENP-A molecules in nuclei revealed that CENP-A is incorporated at low density in domains that cumulatively encompass half the genome. Embryonic CENP-A domains are established in a pattern inverse to regions that are transcribed in the germline and early embryo, and ectopic transcription of genes in a mutant germline altered the pattern of CENP-A incorporation in embryos. Furthermore, regions transcribed in the germline but not embryos fail to incorporate CENP-A throughout embryogenesis. We propose that germline transcription defines genomic regions that exclude CENP-A incorporation in progeny, and that zygotic transcription during early embryogenesis remodels and reinforces this basal pattern. These findings link centromere identity to transcription and shed light on the evolutionary plasticity of centromeres.

To characterize CENP-A localization dynamics in *C. elegans* (CeCENP-A; Supplementary Figs 1 and 2), we generated a strain in which the only source of CENP-A is a single copy green fluorescent protein (GFP)-conjugated transgene encoding GFP–CeCENP-A (Supplementary Fig. 1b). Imaging in adult hermaphrodites revealed that, in the maternal germline, CeCENP-A is removed from chromosomes as they enter the pachytene stage of meiotic prophase, and is reloaded when nuclei progress into diplotene (Fig. 1a). CeCENP-A was not detected in the nuclei of mature sperm (Supplementary Fig. 2a, b), and quantitative immunoblotting indicated that sperm have fewer than the detection limit of 300 CeCENP-A molecules (Fig. 1b and Supplementary Fig. 2c, d). To test for sperm-derived CeCENP-A in embryos, we fertilized CeCENP-A-depleted oocytes with wild-type sperm. In control embryos, CeCENP-A localized to both sperm and oocyte chromatin during chromosome condensation, pronuclear migration and mitosis

(Fig. 1c). As reported in other systems[5], this recruitment was independent of DNA replication (Supplementary Fig. 3). After fertilization of CeCENP-A-depleted oocytes with wild-type sperm, no CeCENP-A signal was detected on sperm or oocyte chromatin throughout the cell cycle (Fig. 1c). Thus, sperm chromatin does not retain CeCENP-A to propagate centromere identity through fertilization in *C. elegans*.

Pulse-chase experiments in human cells have suggested that stable inheritance of CENP-A on chromatin propagates centromere identity through cell division[6,7]. To test whether CeCENP-A is stably inherited on chromatin in embryos, we photobleached one set of GFP–CeCENP-A-labelled chromatids after separation from their sisters at anaphase onset in the one-cell embryo. GFP–CeCENP-A signals were then compared in the next round of division between cells inheriting bleached or unbleached chromatid sets. Stable inheritance of CeCENP-A on chromatin predicts that 50% of CeCENP-A is old and the other 50% is new, resulting in a bleached/unbleached ratio of 0.5. In contrast, if CeCENP-A is not stably inherited on chromatin between the two rounds of division, the bleached/unbleached ratio should be 1.0, which is close to the observed value (Fig. 1d–f and Supplementary Fig. 4). Thus, despite the short division time (only ~15 min between consecutive metaphases), CeCENP-A is nearly completely turned over on chromatin during embryonic cell divisions.

The above results indicate that pre-existing CeCENP-A nucleosomes may not be the cue that targets new CeCENP-A nucleosomes. To define the unknown guiding cue(s), we analysed the genome-wide distribution of CeCENP-A in embryos using chromatin immunoprecipitation with a CeCENP-A-specific antibody[8] followed by hybridization to a tiling microarray (ChIP-chip). As CENP-A chromatin is characterized by highly repetitive DNA in most higher eukaryotes, this offered the opportunity to define the distribution of CENP-A in an organism naturally lacking large stretches of repeats. Our ChIP-chip analysis revealed regions of CeCENP-A enrichment along the entire length of chromosomes, as predicted for holocentric chromosome architecture (Fig. 2a and Supplementary Fig. 5a–c). The genome-wide distribution of the conserved CENP-A-specific loading factor KNL-2 was indistinguishable from that of CeCENP-A, indicating that the CeCENP-A distribution reflects specific incorporation (Fig. 2a, b). A sliding-window-based domain definition algorithm revealed that CeCENP-A domains vary considerably in size (median 10–12 kilobase), cover both genic and intergenic regions, are distributed evenly throughout the genome, and do not correlate with repeat density (Fig. 2c–e and Supplementary Fig. 5d–f). Although nearly half the genome is occupied by CeCENP-A domains (Fig. 2d), quantification of CeCENP-A molecules in purified embryonic nuclei showed that there is only enough CeCENP-A to occupy at most 4% of the genome

[1]Ludwig Institute for Cancer Research and Department of Cellular & Molecular Medicine University of California San Diego, La Jolla, California 92037, USA. [2]Department of Molecular Cell and Developmental Biology, University of California Santa Cruz, Santa Cruz, California 95064, USA. [3]Department of Biology, Carolina Center for Genome Sciences and Lineberger Comprehensive Cancer Center, University of North Carolina at Chapel Hill, Chapel Hill, North Carolina 27599, USA. †Present addresses: School of Biological Sciences, the University of Hong Kong, Pokfulam, Hong Kong (K.W.Y.); Department of Craniofacial Biology, University of Colorado, Health Sciences Center, Aurora, Colorado 80045, USA (F.B.); Institute for Research in Immunology and Cancer, Department of Pathology and Cell Biology, University of Montreal, Montreal, Quebec H3C 3J7, Canada (P.M.); The Salk Institute for Biological Studies, San Diego, California 92186, USA (A.E.); Department of Neurobiology and Behavior, Cornell University, Ithaca, New York 14853, USA (J.M.).
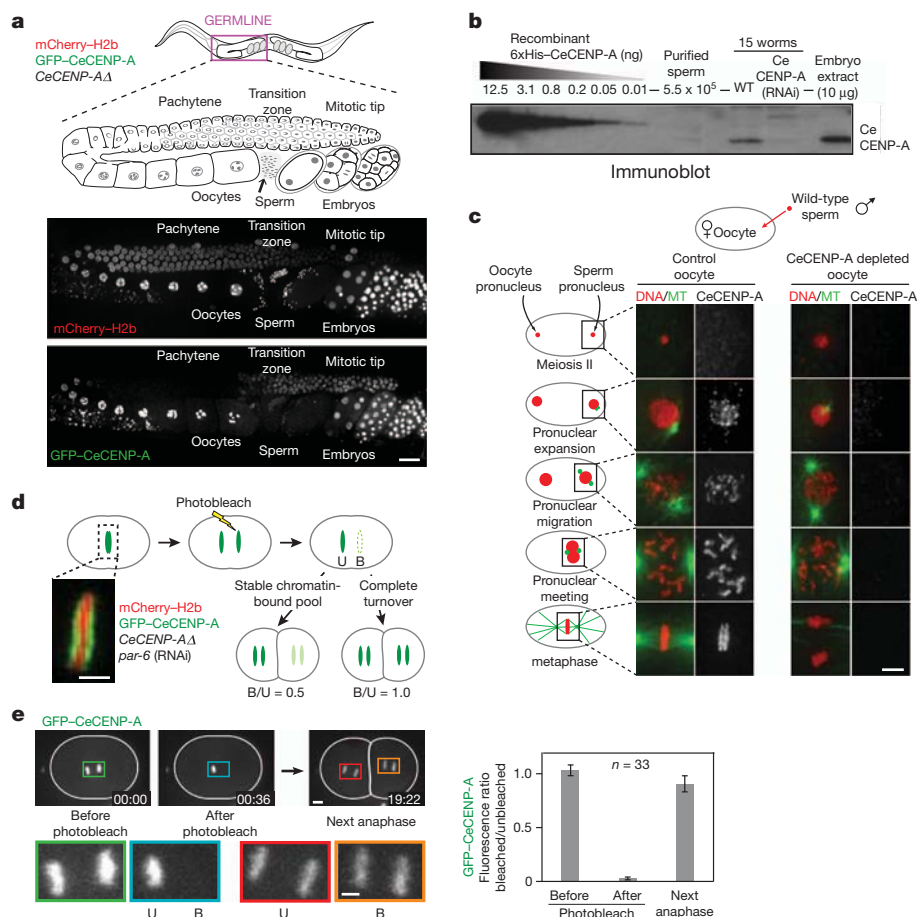*These authors contributed equally to this work.

Figure 1 | CeCENP-A dynamics in meiotic prophase, at fertilization and across embryonic divisions. a, Gonad region of an adult hermaphrodite co-expressing GFP–CeCENP-A and mCherry–histone H2b in a *CeCENP-AΔ* (also known as *hcp-3(ok1892)*; see also Supplementary Figs 1 and 2) background (see also Supplementary Figs 1 and 2). Scale bar, 20 μm. **b**, Quantitative immunoblot showing that sperm lack a significant pool of CeCENP-A (see also Supplementary Fig. 2c, d). **c**, Fertilized one-cell control or CeCENP-A-depleted embryos at different stages of the first mitotic division were immunostained for CeCENP-A and α-tubulin (MT). Wild-type (N2) males were mated to *fem-1* mutant worms to ensure all embryos were cross-progeny. Scale bar, 5 μm. **d**, Schematic of photobleaching experiment to assay CeCENP-A inheritance across early embryonic divisions. *par-6* RNA interference (RNAi) abolishes developmental asynchrony in the two-cell embryo. Unbleached (U) and bleached (B) chromatid sets are indicated. Scale bar, 2 μm. **e**, Representative images and quantification of the photobleaching experiment. Higher magnification views highlight bleached and unbleached chromatid sets. Error bars are 95% confidence intervals for the means. Scale bars, 5 μm.

(Fig. 2e and Supplementary Fig. 6a–c). Therefore, the domains enriched for CeCENP-A identified by ChIP-chip must be comprised primarily of H3 nucleosomes (Fig. 2f). Consistent with this, histone H3 ChIP-chip analysis does not show depletion in regions enriched for CeCENP-A[9] (Supplementary Fig. 6d, e). Thus, the holocentric architecture of *C. elegans* chromosomes arises from reproducible definition of domains that are permissive for low-density CeCENP-A incorporation.

The abundance of genomic regions permissive for CeCENP-A incorporation makes it unlikely that they are defined by a specific DNA sequence. Instead, a correlation emerged with transcriptional status: genes transcribed in embryos were refractory to CeCENP-A incorporation, whereas genes that are silent in embryos (but transcribed in post-embryonic tissues) were permissive for CeCENP-A incorporation (Fig. 3a). ChIP-chip analysis of RNA polymerase II (Pol II) revealed an inverse correlation with CeCENP-A that extended genome-wide (Fig. 3b, c and Supplementary Fig. 7).

The inverse correlation between transcription and CeCENP-A incorporation was puzzling, given that there is no significant RNA Pol II-dependent transcription during the first two rounds of embryonic division, and transcriptional activity remains low until the 30-cell stage[10–12]. In addition, inhibition of transcription using α-amanitin did not cause defects in chromosome segregation in early embryos (Supplementary Fig. 8). We analysed the CeCENP-A and RNA Pol II distribution in four populations of embryos that formed a developmentally timed series from very early (73% of embryos with ≤ 8 nuclei) to old (67% of embryos with > 200 nuclei) (Supplementary Fig. 9a, b). The CeCENP-A distribution remained constant across this series, despite the activation or repression of genes (Supplementary Figs 9b–d and 10a, b). Thus, CeCENP-A incorporation in embryos may not be dictated simply by active transcription.

To better assess the relationship between transcription and CeCENP-A incorporation, we analysed CeCENP-A and RNA Pol II

enrichment in different gene classes defined in previous work by their expression profiles[13]. The inverse correlation between CeCENP-A and RNA Pol II held true for four of five gene classes (Fig. 3d). However, the 'germline-only' class, which is comprised of genes transcribed in the maternal germline but not in embryos, did not show an inverse correlation. Instead, both CeCENP-A and embryonic RNA Pol II levels were low (Fig. 3e), which was confirmed by individual analysis of well-characterized genes transcribed exclusively in the germline (Fig. 3f). In addition, 'germline-only' genes failed to incorporate CeCENP-A throughout embryogenesis, despite the persistent absence of RNA Pol II (Supplementary Fig. 10a, b). Germline-only genes are enriched for histone H3 lysine 36 methylation (H3K36me), indicating that the absence of CeCENP-A and RNA Pol II signals is not a false negative[13] (Fig. 3d–f). Thus, genes transcribed in the maternal germline are refractory to CeCENP-A incorporation, even if they are transcriptionally silent in embryos. This result, together with the paucity of transcription in early embryos and the consistent CeCENP-A distribution throughout embryogenesis, indicates that transcriptional activity in the maternal germline may render genomic regions refractory to CeCENP-A incorporation. Activation of transcription during early embryogenesis probably remodels and reinforces this basal CeCENP-A pattern. In support of this, genes transcribed in early embryos, but lacking signatures of germline transcription, also show low CeCENP-A occupancy (Supplementary Fig. 10c).

If germline transcriptional activity influences CeCENP-A incorporation in the progeny, changes in germline transcription should alter the CeCENP-A distribution in embryos. An unexpected observation in embryos derived from a null mutant of *met-1*, which encodes one of two *C. elegans* H3K36 methyltransferases[14], enabled us to test this prediction. The *met-1* mutant is viable and fertile, indicating that transcription is not globally misregulated in this mutant. Consistent with this, the genome-wide distributions of H3K36me3, RNA Pol II
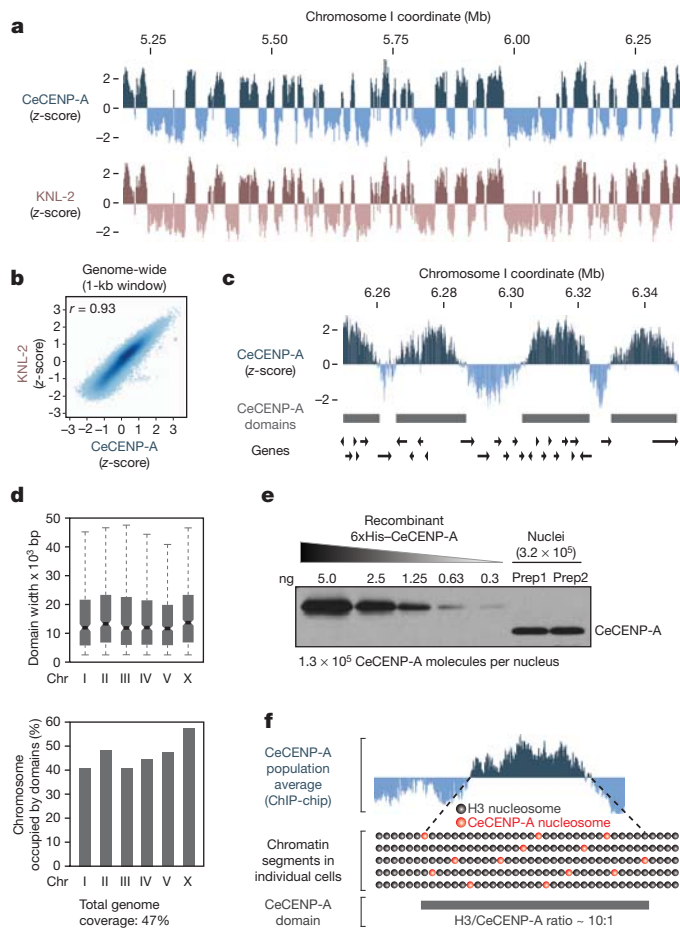
Figure 2 | Genome-wide mapping of CeCENP-A-enriched chromatin.
a, Regions enriched for CeCENP-A and its loading factor KNL-2 in a representative portion of chromosome I. For each track, the average *z*-score probe signal of two independent biological replicates is plotted. **b**, Genome-wide correlation plot of CeCENP-A and KNL-2 occupancy. The correlation coefficient (*r*) is in the upper left corner. **c**, Regions enriched for CeCENP-A with the positions of annotated genes. CeCENP-A domains were defined by a sliding window algorithm. **d**, Features of CeCENP-A domains for individual chromosomes. Boxplots: boxes indicate 25th to 75th percentile, whiskers 2.5th to 97.5th percentile. Wedges around the medians indicate 95% confidence intervals for the medians (see also Supplementary Fig. 5d–f). **e**, Two independent nuclei preparations (Prep) from early embryos (<100 nuclei) were blotted alongside a purified CeCENP-A standard (see also Supplementary Figs 2c, d and 6a–c). **f**, Hypothetical model for CeCENP-A permissive domain.

and CeCENP-A were similar in *met-1* and wild-type embryos (Fig. 4a; genome-wide correlation coefficients of 0.88, 0.9 and 0.9, respectively). However, we observed rare regions of ectopic H3K36me3 enrichment in the *met-1* mutant (Fig. 4 and Supplementary Figures 11 and 12). Out of 132 regions >5 kb in size that acquired ectopic H3K36me3 signal in *met-1* mutant embryos, 75 did not show significant RNA Pol II occupancy in embryos, suggesting that these regions are mis-transcribed in mutant germlines but not in embryos. CeCENP-A was depleted from these regions in embryos (Fig. 4a, b and Supplementary Figs 11 and 12a). To test if acquisition of H3K36me3 and loss of CeCENP-A in *met-1* mutant embryos is associated with ectopic germ-line gene transcription, we hand-dissected germlines from adult wild-type and *met-1* mutant worms and measured messenger RNA levels by quantitative PCR for nine genes in ectopic H3K36me3 regions. As controls, we used eight genes located in regions that did not show a change in H3K36me3 signal. Genes in regions with ectopic H3K36me3 signal indeed showed significantly elevated RNA levels in *met-1* mutant germlines compared to wild type (Fig. 4b and Supplementary Fig. 12b). Thus, the data obtained with the *met-1* mutant indicate
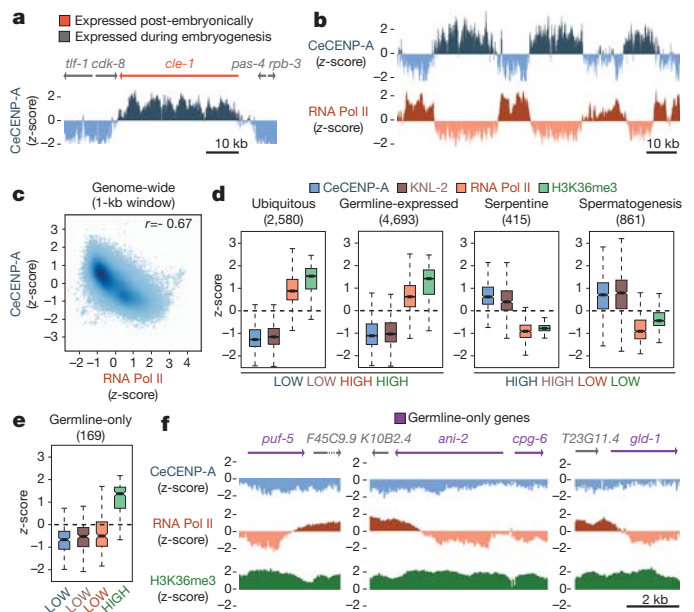
Figure 3 | Relationship between CeCENP-A and gene expression.
a, Chromosomal region containing the *cle-1* gene, which is expressed in neurons, and flanking genes that are expressed during embryogenesis.
b, Genome browser view showing inverse correlation between CeCENP-A and RNA Pol II occupancy. **c**, Genome-wide correlation plot of CeCENP-A and RNA Pol II occupancy. The correlation coefficient (*r*) is in the upper right corner. **d**, CeCENP-A, KNL-2, RNA Pol II and H3K36me3 occupancy for various gene sets defined on the basis of expression data. The number of genes in each set is shown in parentheses. Boxplots (as in Fig. 2d) show the range of *z*-scores averaged over gene bodies. **e**, CeCENP-A, KNL-2, RNA Pol II and H3K36me3 occupancy for the germline-only gene set. **f**, Genome browser views of CeCENP-A, RNA Pol II, and H3K36me3 occupancy on germline-only genes, flanked by genes expressed in embryos.

that ectopic transcription in the germline converts regions from permissive to non-permissive for CeCENP-A incorporation in the embryo progeny.

Whereas the genome-wide inverse relationship to embryonic transcription suggests the simple model that CeCENP-A deposition is random and antagonized by active transcription, such a model fails to explain restriction of *de-novo*-deposited CeCENP-A on transcriptionally silent sperm chromatin (Fig. 1d), the low CeCENP-A occupancy on the 169 'germline-only' genes throughout embryogenesis, and the results from the *met-1* mutant analysis (Supplementary Discussion). Thus, we favour the model that transcription in the germline makes regions non-permissive for CeCENP-A incorporation in the progeny (Supplementary Fig. 12c), and the onset of transcriptional activity in embryos reinforces and remodels this pattern.

In *C. elegans*, H3K36 methylation and the Argonaute CSR-1, which binds short 22G-RNAs (named for their 5′ guanosine residue and 22-nucleotide length) derived from germline transcripts, are candidate mechanisms for transmitting memory of germline transcription to early embryos[13,15]. Both H3K36 methylation (Fig. 3d–f and Supplementary Fig. 7c) and CSR-1 22G-RNA targets (Supplementary Fig. 13) are inversely correlated with CeCENP-A occupancy, and inhibition of CSR-1 and its co-factors leads to early embryonic chromosome segregation defects[15,16].

The results here demonstrate that cues unrelated to pre-existing CENP-A nucleosomes can dictate the incorporation of new CENP-A nucleosomes, challenging the view that centromeres are patterned by stable inheritance of CENP-A domains with the key mark for centromere identity being CENP-A itself. Discontinuity of chromatin-localized CENP-A in the germline, similar to the one we describe here for *C. elegans*, has recently been proposed to also occur in plants[17], suggesting that removal and reloading of CENP-A during every
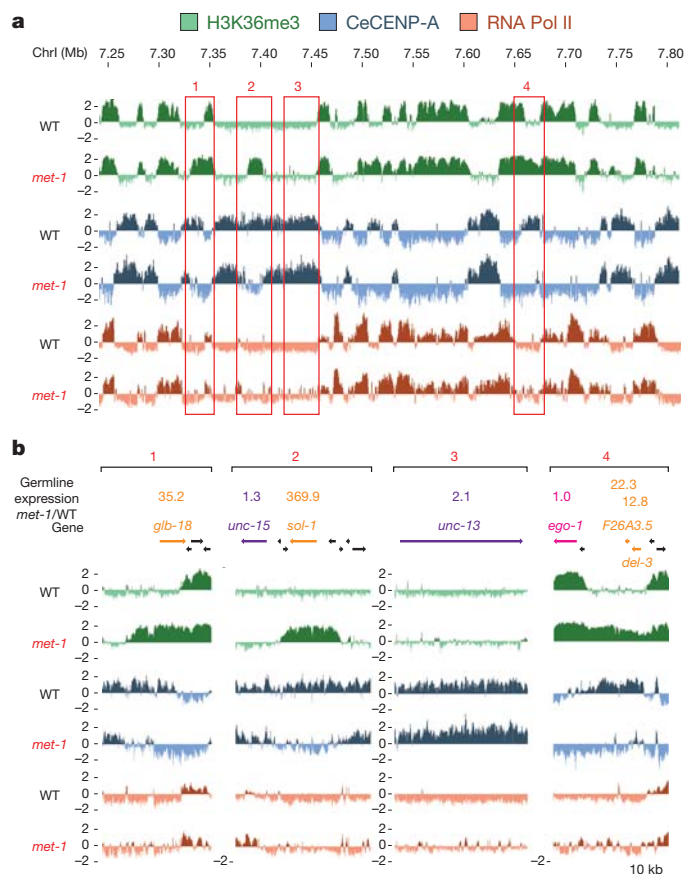
Figure 4 | Germline expression controls CeCENP-A occupancy in the progeny embryos. a, Portion of chromosome I featuring specific regions with ectopic H3K36me3 signal in the *met-1* mutant (see also Supplementary Figs 11 and 12). **b**, Screen shots of the regions boxed in (**a**). Real-time quantitative reverse transcription PCR was performed on hand-dissected wild-type and *met-1* mutant gonads. Mean *met-1*:wild-type expression ratio (four independent biological replicates each) is listed above genes (see table in Supplementary Fig. 12b for all genes analysed).

generation may be more common than is currently appreciated. In addition, the processes of neocentromerization and centromere repositioning, which occur with appreciable frequency in humans and are observed frequently during evolution[18–20], may be guided by cues that are linked to transcription.

METHODS SUMMARY

For ChIP-chip, chitinase-treated embryos were fixed with 1% formaldehyde in PBS for 10 min, suspended in ChIP buffer (50 mM HEPES-KOH pH 7.6, 140 mM NaCl, 1 mM EDTA, 0.5 mM EGTA, 0.5% NP-40, 0.1% deoxycholate, 1% sarkosyl), and sonicated with a Branson sonifier microtip. Antibody (5 μg) pre-bound to 50 μl Dynabeads (Dynal Biotech) were incubated for 4 h with embryo extract (3 mg total protein). Beads were washed and eluted, and the purified DNA amplified as described[13] before hybridization at the Roche Nimblegen Service Laboratory (2.1M probe tiling arrays with 50-bp probes; WormBase version WS170). Genome-wide scatter plots and Pearson correlations were obtained using $\log_2$ z-scores after median smoothing over 1-kb windows. GFP–CeCENP-A images were acquired with a CSU10 spinning disk confocal head (Yokogawa) and a CCD camera (iXon DV887; Andor Technology) mounted on a Nikon TE2000-E inverted microscope equipped with a solid state laser combiner (ALC) 491 nm and 561 nm lines. For quantification of CeCENP-A in nuclei, embryos were treated with chitinase and lysed by douncing in nuclei buffer (10 mM Tris-HCl pH 8, 80 mM KCl, 2 mM K-EDTA, 0.75 mM spermidine, 0.3 mM spermine, 0.1% digitonin). Nuclei were separated from debris by low-speed centrifugation steps. For germline expression analysis, total RNA from 50–100 dissected gonads was isolated using TRIzol (Invitrogen), and complementary DNA was synthesized with Superscript III reverse transcriptase (Invitrogen).

Quantitative real-time PCR was performed with iQ SYBR Green Supermix (Bio-Rad) in the iQ5 cycler (Bio-Rad) using standard protocols.

Full Methods and any associated references are available in the online version of the paper at www.nature.com/nature.

1. Malik, H. S. & Henikoff, S. Major evolutionary transitions in centromere complexity. *Cell* **138**, 1067–1082 (2009).
2. Allshire, R. C. & Karpen, G. H. Epigenetic regulation of centromeric chromatin: old dogs, new tricks? *Nature Rev. Genet.* **9**, 923–937 (2008).
3. Choo, K. *The Centromere* (Ocford Univ. Press, 1997).
4. Sullivan, K. F. A solid foundation: functional specialization of centromeric chromatin. *Curr. Opin. Genet. Dev.* **11**, 182–188 (2001).
5. Shelby, R. D., Monier, K. & Sullivan, K. F. Chromatin assembly at kinetochores is uncoupled from DNA replication. *J. Cell Biol.* **151**, 1113–1118 (2000).
6. Jansen, L. E. T., Black, B. E., Foltz, D. R. & Cleveland, D. W. Propagation of centromeric chromatin requires exit from mitosis. *J. Cell Biol.* **176**, 795–805 (2007).
7. Schuh, M., Lehner, C. F. & Heidmann, S. Incorporation of *Drosophila* CID/CENP-A and CENP-C into centromeres during early embryonic anaphase. *Curr. Biol.* **17**, 237–243 (2007).
8. Monen, J., Maddox, P. S., Hyndman, F., Oegema, K. & Desai, A. Differential role of CENP-A in the segregation of holocentric *C. elegans* chromosomes during meiosis and mitosis. *Nature Cell Biol.* **7**, 1248–1255 (2005).
9. Liu, T. *et al.* Broad chromosomal domains of histone modification patterns in *C. elegans. Genome Res.* **21**, 227–236 (2011).
10. Seydoux, G. & Dunn, M. A. Transcriptionally repressed germ cells lack a subpopulation of phosphorylated RNA polymerase II in early embryos of *Caenorhabditis elegans* and *Drosophila melanogaster. Development* **124**, 2191–2201 (1997).
11. Baugh, L. R., Hill, A. A., Slonim, D. K., Brown, E. L. & Hunter, C. P. Composition and dynamics of the *Caenorhabditis elegans* early embryonic transcriptome. *Development* **130**, 889–900 (2003).
12. Edgar, L. G., Wolf, N. & Wood, W. B. Early transcription in *Caenorhabditis elegans* embryos. *Development* **120**, 443–451 (1994).
13. Rechtsteiner, A. *et al.* The histone H3K36 methyltransferase MES-4 acts epigenetically to transmit the memory of germline gene expression to progeny. *PLoS Genet.* **6**, e1001091 (2010).
14. Andersen, E. C. & Horvitz, H. R. Two *C. elegans* histone methyltransferases repress *lin-3* EGF transcription to inhibit vulval development. *Development* **134**, 2991–2999 (2007).
15. Claycomb, J. M. *et al.* The Argonaute CSR-1 and its 22G-RNA cofactors are required for holocentric chromosome segregation. *Cell* **139**, 123–134 (2009).
16. van Wolfswinkel, J. C. *et al.* CDE-1 affects chromosome segregation through uridylation of CSR-1-bound siRNAs. *Cell* **139**, 135–148 (2009).
17. Ravi, M. *et al.* Meiosis-specific loading of the centromere-specific histone CENH3 in *Arabidopsis thaliana. PLoS Genet.* **7**, e1002121 (2011).
18. Lomiento, M., Jiang, Z., D'Addabbo, P., Eichler, E. E. & Rocchi, M. Evolutionary-new centromeres preferentially emerge within gene deserts. *Genome Biol.* **9**, R173 (2008).
19. Piras, F. M. *et al.* Uncoupling of satellite DNA and centromeric function in the genus *Equus. PLoS Genet.* **6**, e1000845 (2010).
20. Warburton, P. E. Chromosomal dynamics of human neocentromere formation. *Chromosome Res.* **12**, 617–626 (2004).

Author Contributions R.G., A.M. and T.E. performed ChIP experiments; A.R. performed analysis of all ChIP-chip datasets with advice from S.S.; K.W.Y. performed the photobleaching and α-amanitin experiments; F.B. and P.M. performed the mating inheritance experiment, analysed replication-independence and measured CeCENP-A levels in sperm; R.G. performed GFP–CeCENP-A localization analysis, quantified CeCENP-A levels in nuclei with K.W.Y., and performed qPCR on germline RNA provided by L.G.; A.E., A.M. and J.M. generated GFP–CeCENP-A strains; S.E. and J.D.L. helped initiate ChIP analysis of CeCENP-A; K.O. and A.D. made initial observations that established the project; A.D., R.G., A.R., K.W.Y. and S.S. prepared the figures and wrote the paper with advice from J.D.L. and K.O.; A.D. and S.S. supervised the project.

Author Information Reprints and permissions information is available at www.nature.com/reprints. The authors declare no competing financial interests. Readers are welcome to comment on the online version of this article at www.nature.com/nature. Correspondence and requests for materials should be addressed to A.D. (abdesai@ucsd.edu) or S.S. (sstrome@ucsc.edu).

METHODS

Antibodies. ChIP for HCP-3/CeCENP-A was performed with OD79, an affinity-purified rabbit polyclonal antibody raised against amino acids 3–183 of CeCENP-A[8]. A second antibody (SDQ0804) raised against amino acids 40–118 of CeCENP-A confirmed the ChIP-chip pattern observed with antibody OD79 (genome-wide correlation coefficient of 0.92). ChIP for KNL-2 was performed with two polyclonal rabbit antibodies (SDQ08003, SDQ08010) raised against amino acids 207–306. ChIP for RNA Pol II was performed using a monoclonal antibody against the CTD repeat YSPTSPS of RNA Pol II (8WG16; abcam ab817mod). The antibody for H3K36me3 ChIP was described previously[13]. Other antibodies used for immunoblotting and immunofluorescence were: α-tubulin (DM1α; Sigma-Aldrich), NPP-112 and SQV-8 (gifts from J. Audhya), BUB-1 (ref. 21) and KNL-2 (ref. 22).

Worm strains. For monitoring GFP–CeCENP-A and GFP–CPAR-1 localization in live adult gonads, sperm and embryos (Fig. 1 and Supplementary Figs 1 and 2), and for the photobleaching experiments of GFP–CeCENP-A in Fig. 1, worm strains expressing transgenes from a single-copy locus that includes endogenous 5′ and 3′ regions were generated using the MosSCI technique[23], as outlined in Supplementary Fig. 1b. The GFP–CeCENP-A strain OD347 fully rescued the *CeCENP-A/hcp-3* deletion allele *ok1892*, and all experiments involving GFP–CeCENP-A were performed in the *ok1892* deletion background. For imaging, the GFP–CeCENP-A (OD347) and GFP–CPAR-1 (OD588) strains were crossed with a strain expressing mCherry–histone H2b (OD56) to generate strains OD421 and OD416, respectively.

For the mating-based analysis of CeCENP-A inheritance through fertilization (Fig. 1c), wild-type (N2) males were crossed to strain BA17, which harbours a temperature-sensitive mutation that abrogates sperm production. Use of the *fem-1* strain ensured that the embryos analysed by immunofluorescence were cross-progeny. Injection of double-stranded RNA targeting *CeCENP-A* and mating with males was performed as previously described[24].

For the transcription inhibition assay (Supplementary Fig. 8), GFP–CeCENP-A-expressing hermaphrodites (OD347) were mated with *his-72p*:GFP–H3.3 and *end-3p*:mCherry–H1 co-expressing males (RW10007).

For the photobleaching analysis in Supplementary Fig. 4, a strain expressing GFP–CeCENP-A was generated by bombarding plasmid pJM12 into *unc-119(de3)* worms. In pJM12, a GFP–CeCENP-A transgene is expressed under control of the *pie-1* promoter and 3′ untranslated region (UTR). The GFP is inserted at amino acid 174 between the amino-terminal tail and histone core (Supplementary Fig. 4a). Coding sequence and introns preceding amino acid 134 were altered to preserve coding information, but make the transgene-encoded mRNA resistant to RNAi. The two introns in this part of the *CeCENP-A* locus were replaced with introns from SPhased GFP (Fire lab 2005 vector kit). Ballistic bombardment of pJM12 generated strain OD136. The transgene insertion in OD136 cannot be homozygosed—there is a low amount of embryonic lethality (12–14%) and Unc progeny. This is probably due to the transgene insertion site, as both of these phenotypes segregated with the GFP fluorescence through multiple outcrosses. A dsRNA to the re-encoded region was used to selectively deplete endogenous CeCENP-A and assess functional rescue by the transgene (Supplementary Fig. 4b). OD136 was used to generate strain OD265, where one copy of the endogenous *CeCENP-A* locus is deleted and GFP–CeCENP-A as well as mCherry–H2b are co-expressed. Photobleaching experiments in Supplementary Fig. 4d, e were performed using OD265. Strain genotypes are listed in Supplementary Table 1.

RNA interference. L4 worms were injected with dsRNA prepared as described previously[21] and incubated for 48 h at 20 °C, except for the mating experiment using the *fem-1* mutant (see above).

N2 genomic DNA was used as a template to generate PCR products for dsRNA production. The dsRNA for depletion of CeCENP-A in the inheritance experiment of Fig. 1c was described previously[8].

Oligonucleotides for production of dsRNA against the re-encoded sequence of CeCENP-A used in the rescue experiments with strain OD136 (Supplementary Fig. 4a, b): oOD1887, 5′-AATTAACCCTCACTAAAGGgccgatgacaccccaattat-3′; oOD1888, 5′-TAATACGACTCACTATAGGccgtggggagtaatcgacaag-3′. Oligonucleotides for dsRNA against GFP: oOD2423, 5′-TAATACGACTCACTATAGGgtcagtggagagggtggaaggtg-3′; oOD2424, 5′-AATTAACCCTCACTAAAGGcatgccatgtgtaatcccagcagc-3′.

For replication inhibition (Supplementary Fig. 3), dsRNAs targeting *cdc-6* and *cdt-1* were mixed to obtain equal concentrations. Oligonucleotides used for dsRNA against *cdc-6*: oOD1265, 5′-AATTAACCCTCACTAAAGGCAAATTCCTGCTGCTCCAAT-3′; oOD1266, 5′-TAATACGACTCACTATAGGCGGTCGAACCTCAAGTTCAT-3′. Oligonucleotides used for dsRNA against *cdt-1*: oOD801, 5′-AATTAACCCTCACTAAAGGCAAAAACAACGAAGCGTGTG-3′;

oOD802, 5′-TAATACGACTCACTATAGGCCTCGTTTTTCATTTTATCATTCA-3′.

Immunofluorescence and immunoblotting. Embryos were fixed and processed for immunofluorescence as described previously[21,25]. Antibodies directly labelled with fluorescent dyes (Cy2, Cy3 or Cy5; Amersham Biosciences) were used at 1 μg ml^{-1}. Images were recorded on a DeltaVision microscope at 1 × 1 binning with a ×100 numerical aperture (NA) 1.3 U-planApo objective (Olympus). Z-stacks (0.2-μm sections) were deconvolved using softWoRx (Applied Precision), and maximum intensity projections were imported into Adobe Photoshop CS4 for further processing.

Immunoblotting was performed using standard methods. For CeCENP-A immunoblots (Figs 1b and 2e), proteins were transferred for 5 h at 30 V in 25 mM Tris-HCl pH 8.3, 192 mM glycine, 20% methanol. These blotting conditions were optimized to result in quantitative transfer of CeCENP-A onto the membrane.

Live imaging and photobleaching. All live imaging was performed at 20 °C. For images of adult hermaphrodite gonads (Fig. 1a and Supplementary Fig. 2a, b) worms were anesthetized with a mixture of 1 mg ml^{-1} ethyl 3-aminobenzoate methanesulphonate and 0.1 mg ml^{-1} of tetramisole hydrochloride in M9 for 15–30 min before transferring them to an 2% agarose pad under a coverslip. Images of gonad regions were acquired with a ×40 1.3 NA PlanFluor objective by collecting an 80 × 0.5 μm Z-series of GFP and mCherry images for every Z-plane. The whole gonad views shown in Fig. 1a and Supplementary Fig. 2a were stitched together from three individual, overlapping images. Embryos (Supplementary Fig. 1c) and −1 oocytes/spermatheca (Supplementary Fig. 2b) were imaged using a ×100 1.4 NA PlanApochromat objective. Images were acquired with 1 × 1 binning on a spinning disk confocal setup mounted on a Nikon TE2000-E inverted microscope equipped with a solid-state laser combiner (ALC) (491 nm and 561 nm lines0, a Yokogawa CSU10 head and a CCD camera (iXon DV887; Andor Technology). Acquisition parameters, shutters and focus were controlled by iQ 1.10.0 software (Andor Technology). Images were processed with Fiji 1.0 and Adobe Photoshop CS4.

For the transcription inhibition assay (Supplementary Fig. 8), cross-progeny embryos from GFP–CeCENP-A expressing hermaphrodites mated with *his-72p*:GFP–H3.3 and *end-3p*:mCherry–H1 co-expressing males were dissected in L-15 blastomere culture medium[26] containing 200 μg ml^{-1} α-amanitin. GFP and mCherry Z-stacks of permeable and impermeable embryos in the same field of view were acquired at 1–4 min intervals with a ×60 1.4 NA PlanApochromat objective until embryos contained more than 50 cells.

The photobleaching experiments in Fig. 1d, e were performed with the FRAPPA unit (Andor Technology) using a ×60 1.4 NA PlanApochromat objective. Thirteen Z-sections were acquired with a spacing of 1 μm before and after bleaching in the first embryonic division and at 1-min intervals thereafter until anaphase of the second division. Maximum intensity projections were generated for each Z-stack. For each image sequence, an identical sized rectangle (R1) was drawn around each anaphase chromatid set before and after photobleaching in the first division and around anaphase chromatid sets in the second division. A larger rectangle (Rb) was drawn around each rectangle R1 and the area between the two rectangles served as a measure of background intensity. The average intensity (Avg. Int.) of the GFP signal in each R1 was measured using the formula: Avg. Int.$_{R1}$ − [(Avg Int.$_{Rb}$ × Area$_{Rb}$ − Avg. Int.$_{R1}$ × Area$_{R1}$)/(Area$_{Rb}$ − Area$_{R1}$)], and the ratio of average intensities on anaphase chromatid sets before/after bleaching and in the subsequent anaphase were calculated and averaged.

For the photobleaching experiments in Supplementary Fig. 4d, e, the microscope setup differed from the one used for the experiments in Fig. 1 as follows: the microscope was equipped with a krypton–argon 2.5 W water-cooled laser (Spectra-Physics), acquisition parameters, shutters and focus were controlled by MetaMorph software (MDS Analytical Technologies), and the 488 nm laser line for photobleaching was steered into a custom-modified epifluorescence port. GFP–CeCENP-A intensity ratios were calculated as described above, except that anaphase chromatid sets before/after bleaching in the first division were compared with metaphase plates in the second division.

Expression analysis on dissected germlines by quantitative PCR. Worms containing one or two embryos were dissected with 30-gauge needles in Egg buffer (25 mM HEPES-KOH pH 7.6, 118 mM NaCl, 48 mM KCl, 2 mM CaCl₂, 2 mM MgCl₂,) containing 1 mM levamisole and 0.5% Tween-20. Total RNA from 50–100 gonads was isolated using TRIzol (Invitrogen), and cDNA was synthesized using Superscript III reverse transcriptase (Invitrogen). Quantitative real-time PCR was performed with iQ SYBR Green Supermix (Bio-Rad) in the iQ5 cycler (Bio-Rad) using standard protocols. The average amplification efficiency (*E*) of primer pairs (Supplementary Table 2) was calculated from two standard curves (tenfold dilution series of cDNA prepared from mixed-stage N2 worms). The relative transcript abundance (RTA) of target genes in *met-1* mutant (*met-1*) versus

wild-type (WT) germlines was calculated after normalization to the reference gene *act-2* (actin homologue), using the formula: $RTA = \dfrac{E_{target}^{(C_{WT} - C_{met-1})}}{E_{reference}^{(C_{WT} - C_{met-1})}}$, where C_t denotes the threshold cycle. The assay was performed in duplicate on four biological replicates each for wild-type and *met-1* mutant germlines.

Quantification of CeCENP-A molecules in purified nuclei and sperm. 6xHis–CeCENP-A was expressed in bacteria, purified by nickel affinity chromatography under denaturing conditions followed by electroelution using the Bio-Rad Electro-Eluter. The concentration of the purified protein was measured relative to BSA on a gel. Purified sperm were a gift of S. Ward. Sperm concentration was measured by microscopy following 4′,6-diamidino-2-phenylindole (DAPI) staining.

For isolation of nuclei, early embryos (<100 cells) were harvested from synchronized adult worms and treated with chitinase as described below for embryo extract preparation. Packed embryos (1 ml) were washed with 2×50 ml chilled Egg buffer (25 mM HEPES-KOH pH 7.6, 118 mM NaCl, 48 mM KCl, 2 mM CaCl$_2$, 2 mM MgCl$_2$), hypotonically swollen for 15 min in 10 ml of 0.5× Nuclei buffer (5 mM Tris-HCl pH 8, 40 mM KCl, 1 mM K-EDTA, 0.375 mM spermidine, 0.15 mM spermine), then washed into 10 ml of 1× Nuclei buffer (10 mM Tris-HCl pH 8, 80 mM KCl, 2 mM K-EDTA, 0.75 mM spermidine, 0.3 mM spermine) supplemented with 0.1% digitonin (Sigma-Aldrich) and protease inhibitors, and immediately dounced with about 50 strokes in a 15-ml Wheaton Dounce homogenizer using pestle B. Large debris was pelleted at 100g for 3 min and re-dounced once as above. Supernatants containing the nuclei were combined and spun at 2,000g for 15 min. The nuclei pellet was suspended in 1× Nuclei buffer supplemented with 0.1% digitonin and protease inhibitors and layered onto a 30% (w/v in Nuclei buffer + 0.1% digitonin) sucrose cushion. Nuclei were recovered in the pellet after spinning at 2,000g for 15 min.

Embryo isolation, fixation and extract preparation. N2 adult worms were grown from synchronized L1 larvae in S-basal medium. Batches of 500 ml in 2.8-l Fernbach flasks shaking at 230 r.p.m. were incubated at 17 °C (early embryos) or 19 °C (late embryos) for approximately 65 h. The exact time of harvest was determined by checking embryo production under a microscope (for early embryos, this was five embryos per worm or less). Gravid adults were separated from debris by sucrose floating, and embryos were recovered by dissolving adults with a bleach/NaOH solution. 10 μl and 2 μl of packed embryos were set aside for expression profiling and staging by fluorescence microscopy after DAPI staining, respectively. The remainder was suspended in 2 volumes of Egg buffer (25 mM HEPES-KOH pH 7.6, 118 mM NaCl, 48 mM KCl, 2 mM CaCl$_2$, 2 mM MgCl$_2$) and incubated with 0.15 units ml^{-1} chitinase (Sigma-Aldrich) until visible disintegration of the eggshell. Embryos were washed with 2×50 ml chilled phosphate-buffered saline (PBS) and suspended in 40 ml PBS. Fixation was performed for 10 min on ice after adding 4 ml of cross-linking solution (11% formaldehyde, 50 mM HEPES-KOH pH 8, 0.1 M NaCl, 1 mM Na-EDTA, 0.5 mM Na-EGTA), and excess formaldehyde was quenched with 120 mM glycine. Fixed embryos were washed with 3×50 ml PBS and suspended in five pellet volumes of ChIP buffer (50 mM HEPES-KOH pH 7.6, 140 mM NaCl, 1 mM EDTA, 0.5% NP-40, 0.5% Triton X-100, protease inhibitors). Sonication was performed using a Branson sonifier microtip in cycles of 10 s duration (0.9 s on, 0.1 s off) with the power setting at 25% (2 cycles), 30% (2 cycles), 35% (10 cycles), 40% (2 cycles), and 45% (2 cycles), and a pause of 1 min between cycles. Crude extracts were spun for 20 min at 10,000g, the supernatant was removed and glycerol added to 10%. Protein concentration was determined by the Bradford method and aliquots of 3 mg protein were flash-frozen in liquid nitrogen.

Chromatin immunoprecipitation (ChIP). Extract corresponding to 3 mg protein was diluted to 900 μl with ChIP buffer. After addition of sarcosyl to 1%, Na-deoxycholate to 0.1%, and PMSF to 1 mM, the extract was spun for 10 min at maximum speed in a tabletop centrifuge and the supernatant was used for ChIP. 50 μl was removed for preparation of input DNA. To the rest, 50 μl of Dynabead Sheep anti-Rabbit or anti-Mouse IgG suspension (Dynal Biotech), pre-bound to 5 μg of target antibody, were added, and the mixture was incubated at 4 °C for 4 h or overnight (<16 h). Beads were recovered with a Dynal Magnetic Particle Concentrator (Invitrogen) and washed 2×5 min with buffer FA (50 mM HEPES-KOH pH 7.6, 150 mM NaCl, 1 mM EDTA, 1% Triton X-100, 0.1% Na-deoxycholate), 10 min with FA-1000 (50 mM HEPES-KOH pH 7.6, 1 M NaCl, 1 mM EDTA, 1% Triton X-100, 0.1% Na-deoxycholate), 10 min with FA-500 (50 mM HEPES-KOH pH 7.6, 500 mM NaCl, 1 mM EDTA, 1% Triton X-100, 0.1% Na-deoxycholate) in a new tube, 10 min with TEL buffer (10 mM Tris-HCl pH 8.0, 0.25 M LiCl, 1 mM EDTA, 1% NP-40, 1% Na-deoxycholate), and once briefly with TE (10 mM Tris pH 8, 1 mM EDTA). Antibody-bound chromatin was recovered in 50 μl Elution buffer (10 mM Tris-Cl pH 8.0, 1 mM EDTA, 250 mM NaCl, 1% SDS) by shaking at 67 °C for 15 min. Input and ChIP chromatin samples were subsequently processed in parallel. Cross-links were reversed over night at 65 °C in Elution buffer, proteins were digested with 0.45 mg

ml^{-1} proteinase K for 2 h at 37 °C, and nucleic acids were recovered by phenol/chloroform extraction and precipitation with ethanol. RNA was digested with 0.3 mg ml^{-1} RNase A in TE at 37 °C for 2 h, and DNA purified with a column (PCR Purification Kit, Qiagen).

The ChIP procedure for the *met-1* mutant analysis (Fig. 4 and Supplementary Figs 11 and 12) differs slightly from the above and was described in detail previously[13].

Ligation-mediated PCR. DNA ends were blunted with 5 units ml^{-1} T4 DNA polymerase (New England Biolabs) at 12 °C for 20 min and the DNA recovered by phenol/chloroform extraction and ethanol precipitation. Annealed oligomer adaptors (oligo1: 5′-GCGGTGACCCGGGAGATCTGAATTC-3′; oligo2: 5′-GAATTCAGATC-3′) were ligated to blunt DNA ends at 2 μM with 4,000 units ml^{-1} T4 DNA ligase (New England Biolabs) overnight at 16 °C, and DNA was precipitated with ethanol. DNA fragments were amplified for 22 cycles (55 °C, 2 min; 72 °C, 5 min; 95 °C, 2 min; 95 °C, 1 min; 60 °C, 1 min; 72 °C, 2 min; start cycle again at step 4) using 1 μM oligo 1 and a *Taq* DNA polymerase (100 units ml^{-1})/*Pfu* DNA polymerase (0.5 units ml^{-1}) mix. Amplified DNA was purified with a column (PCR Purification Kit, Qiagen).

Microarray hybridizations, data analysis and display. Amplified ChIP DNA was labelled and hybridized by the Roche Nimblegen Service Laboratory. 2.1M probe tiling arrays, with 50-bp probes, designed against WormBase version WS170 (ce4) were used for all experiments. ChIP samples were labelled with Cy5 and their input reference with Cy3. One ChIP was dye-swapped, which resulted in the same pattern (not shown). For each probe, the intensity from the sample channel was divided by the reference channel and transformed to log$_2$. The enrichment scores for each replicate were calculated by standardizing the log ratios to mean zero and standard deviation one (z-score). Genome-wide scatter plots and Pearson correlations between all ChIP targets and replicates were obtained using all probe z-scores after median smoothing over 1-kb windows.

The average z-score of two replicates was used for all analyses, except in Supplementary Figs 9, 10 and 13c, where individual data sets from extracts with distinct age distributions of embryos are compared. Accession numbers for data sets used in this study are listed in Supplementary Table 3. Scatter plots and boxplots for genes were generated by averaging z-scores of probes located completely within the transcript start site (TSS) and end site (TES). TSS and TES coordinates were obtained from WormBase (WS170).

Gene body profile plots (Supplementary Fig. 7b) were generated by aligning genes of length greater than 2 kb at their TSS and TES. The genomic regions 1.5 kb upstream to 1 kb downstream from TSS and 1 kb upstream to 1 kb downstream from TES were divided into 50-bp bins, and probes were assigned to the nearest bin. Gene group profiles were generated by averaging probe z-scores within each bin across genes in the group.

Definition of CeCENP-A-enriched domains. CeCENP-A signal was averaged over 2-kb windows, every 50 bp. A random distribution for the window averages was obtained by randomly sampling and assigning CeCENP-A values for each chromosome. The resulting random CeCENP-A tracks were also averaged over 2-kb windows. A cutoff was selected so that the number of random window averages above the cutoff was less than 3% of the number of non-randomized windows above the cutoff, effectively providing a 3% false positive rate with respect to the random window averages. Overlapping windows above the cutoff were combined into domains. Domains with gaps smaller than 2 kb were merged, and domains smaller than 2.5 kb were excluded.

Definition of gene classes based on expression profiling data sets. Gene classes were defined on the basis of expression data, as described previously[13]. In brief, 'Ubiquitous' or housekeeping have transcripts present in muscle, gut, neuron and adult germline SAGE (serial analysis of gene expression) data sets[27,28]; 'Germline-expressed' genes have transcripts present in the dissected adult hermaphrodite germ line SAGE data set[27]; 'Serpentine' receptor genes are expressed in mature neurons and silent in embryos[29]; 'Spermatogenesis' genes are classified as expressed during sperm production on the basis of comparative microarray analysis[30]; 'Germline-only' genes are expressed exclusively in the maternal germ line, as their transcripts are enriched in the germline[30], maternally loaded into embryos[11], and absent from muscle, gut and neuron SAGE data sets[27,28]; transcripts of 'Embryo-expressed' genes are not maternally provided and increase in level during embryogenesis[11].

Criteria for identifying genes with maximal changes in RNA Pol II levels. Genes with maximal changes in RNA Pol II levels between the two averaged early embryo (EE) and late embryo (LE) extracts (Supplementary Fig. 10a, b), were identified by applying a moderated *t*-test[31] and requiring a false discovery rate smaller than 5% (ref. 32). In addition, RNA Pol II levels for those genes were required to show at least a twofold change in RNA Pol II ChIP-chip hybridization signal between the averaged EE and LE extracts.

Transcriptional profiling of embryos. RNA was isolated from 10 μl of packed embryos using TRIzol (Invitrogen) and the RNeasy kit (Qiagen). RNA (20 μg) was

hybridized to a single-colour 4-plex Nimblegen expression array with 72,000 probes (three 60-mer oligo probes per gene). Quantile normalization[33] and the robust multichip average (RMA) algorithm[34] were used to normalize and summarize the multiple probe values per gene to obtain one expression value per gene and sample. The expression values per gene were averaged across samples as indicated in the figure legends.

21. Oegema, K., Desai, A., Rybina, S., Kirkham, M. & Hyman, A. A. Functional analysis of kinetochore assembly in *Caenorhabditis elegans*. *J. Cell Biol.* **153,** 1209–1226 (2001).
22. Maddox, P. S., Hyndman, F., Monen, J., Oegema, K. & Desai, A. Functional genomics identifies a Myb domain-containing protein family required for assembly of CENP-A chromatin. *J. Cell Biol.* **176,** 757–763 (2007).
23. Frøkjær-Jensen, C. *et al.* Single-copy insertion of transgenes in *Caenorhabditis elegans*. *Nature Genet.* **40,** 1375–1383 (2008).
24. Dammermann, A. *et al.* Centriole assembly requires both centriolar and pericentriolar material proteins. *Dev. Cell* **7,** 815–829 (2004).
25. Cheeseman, I. M. *et al.* A conserved protein network controls assembly of the outer kinetochore and its ability to sustain tension. *Genes Dev.* **18,** 2255–2268 (2004).
26. Edgar, L. G. Blastomere culture and analysis. *Methods Cell Biol.* **48,** 303–321 (1995).
27. Wang, X. *et al.* Identification of genes expressed in the hermaphrodite germ line of *C. elegans* using SAGE. *BMC Genomics* **10,** 213 (2009).
28. Meissner, B. *et al.* An integrated strategy to study muscle development and myofilament structure in *Caenorhabditis elegans*. *PLoS Genet.* **5,** e1000537 (2009).
29. Kolasinska-Zwierz, P. *et al.* Differential chromatin marking of introns and expressed exons by H3K36me3. *Nature Genet.* **41,** 376–381 (2009).
30. Reinke, V., Gil, I. S., Ward, S. & Kazmer, K. Genome-wide germline-enriched and sex-biased expression profiles in *Caenorhabditis elegans*. *Development* **131,** 311–323 (2004).
31. Smyth, G. K. Linear models and empirical Bayes methods for assessing differential expression in microarray experiments. *Stat. Appl. Genet. Mol. Biol.* **3,** Article3 (2004).
32. Storey, J. D. & Tibshirani, R. Statistical significance for genomewide studies. *Proc. Natl Acad. Sci. USA* **100,** 9440–9445 (2003).
33. Bolstad, B. M., Irizarry, R. A., Astrand, M. & Speed, T. P. A comparison of normalization methods for high density oligonucleotide array data based on variance and bias. *Bioinformatics* **19,** 185–193 (2003).
34. Irizarry, R. A. *et al.* Summaries of Affymetrix GeneChip probe level data. *Nucleic Acids Res.* **31,** e15 (2003).

The anti–Shine–Dalgarno sequence drives translational pausing and codon choice in bacteria

Gene-Wei Li[1], Eugene Oh[1] & Jonathan S. Weissman[1]

Protein synthesis by ribosomes takes place on a linear substrate but at non-uniform speeds. Transient pausing of ribosomes can affect a variety of co-translational processes, including protein targeting and folding[1]. These pauses are influenced by the sequence of the messenger RNA[2]. Thus, redundancy in the genetic code allows the same protein to be translated at different rates. However, our knowledge of both the position and the mechanism of translational pausing _in vivo_ is highly limited. Here we present a genome-wide analysis of translational pausing in bacteria by ribosome profiling—deep sequencing of ribosome-protected mRNA fragments[3–5]. This approach enables the high-resolution measurement of ribosome density profiles along most transcripts at unperturbed, endogenous expression levels. Unexpectedly, we found that codons decoded by rare transfer RNAs do not lead to slow translation under nutrient-rich conditions. Instead, Shine–Dalgarno-(SD)[6]-like features within coding sequences cause pervasive translational pausing. Using an orthogonal ribosome[7,8] possessing an altered anti-SD sequence, we show that pausing is due to hybridization between the mRNA and 16S ribosomal RNA of the translating ribosome. In protein-coding sequences, internal SD sequences are disfavoured, which leads to biased usage, avoiding codons and codon pairs that resemble canonical SD sites. Our results indicate that internal SD-like sequences are a major determinant of translation rates and a global driving force for the coding of bacterial genomes.

Our current understanding of sequence-dependent translation rates _in vivo_ derives largely from pioneering work begun in the 1980s[9–13]. These studies, which measured protein synthesis times using pulse labelling, established that different mRNAs could be translated with different elongation rates. In particular, messages decoded by less abundant tRNAs were translated slowly, although this effect was exaggerated by the overexpression of mRNA, which can lead to the depletion of available tRNAs[10]. Even with fixed tRNA usage, different synonymously coded mRNAs were translated at different rates[13]. This result, together with the observation of biased occurrence of adjacent codon pairs[14], suggested that tRNA abundance is not the only determinant of elongation rates. Further investigations addressing what determines the rate of translation _in vivo_, however, have been hampered by the limited temporal and positional resolution of existing techniques.

To provide a high-resolution view of local translation rates, we used the recently developed ribosome profiling strategy[3–5] to map ribosome occupancy along each mRNA (Supplementary Fig. 1). We focused on two distantly related bacterial species, the Gram-negative bacterium _Escherichia coli_ and the Gram-positive bacterium _Bacillus subtilis_. To preserve the state of translation, cells were flash-frozen in liquid nitrogen after the rapid filtration of exponential-phase cultures. Ribosome-protected footprints were generated through nuclease treatment of cell extract in the presence of inhibitors of translation elongation (see Methods). These steps ensured that most ribosomes were polysome-associated after lysis and stayed assembled as 70S particles during digestion (Supplementary Fig. 2). After deep sequencing, 2,257 genes in _E. coli_ and 1,580 genes in _B. subtilis_ had an average coverage of at least ten sequencing reads per codon. The observed variability of

ribosome footprint profiles across individual genes was highly reproducible ($r = 0.99$ between biological replicates; Supplementary Fig. 3).

Several observations argued that ribosome transit time is proportional to the occupancy at each position. First, we observed negligible internal initiation and early termination associated with ribosome pause sites (Supplementary Fig. 4). Second, ribosomes remained intact during footprinting, which enabled the large majority of ribosome-protected fragments to be captured (Supplementary Fig. 2). Third, the variability introduced during the conversion of RNA fragments into a sequenceable DNA library contributed minimally to our measures of variability in ribosome occupancy (Supplementary Fig. 5).

With our genome-wide view of local translation rates, we confirmed established examples of peptide-mediated stalling at transcripts _secM_[15] and _tnaC_[16] in _E. coli_ and _mifM_[17] in _B. subtilis_ (Fig. 1a and Supplementary Fig. 6). Strikingly, in addition to these known stalling sites, the observed ribosome occupancy was highly variable across coding regions, as illustrated for _secA_ in Fig. 1a. We found that ribosome density often surpasses by more than tenfold the mean density, and the vast majority of these translational pauses are uncharacterized.

We first sought to determine whether the identity of the codon being decoded could account for the differences in local translation rates, by examining the average ribosome occupancy for each of the 61 codons in the ribosomal A-site. Surprisingly, there was little correlation between the average occupancy of a codon and existing measurements of the abundance of corresponding tRNAs[18] (Fig. 1b, c and Supplementary Fig. 7). Most notably, the six serine codons had the highest ribosome occupancy for _E. coli_ cultured in Luria broth (Fig. 1b). Because serine is the first amino acid to be catabolized by _E. coli_ when sugar is absent[19,20], we reasoned that the increased ribosome occupancy might be due to limited serine supply. Indeed, serine-associated pauses were greatly decreased in glucose-supplemented MOPS medium (Fig. 1c). The increase in serine codon occupancy when glucose becomes limiting confirmed our ability to capture translation rates at each codon. However, the identity of the A-site codon, which had less than a twofold effect on ribosome occupancy (Fig. 1c), could not account for the large variability in ribosome density along messages.

What, then, are the sequence features that cause slow translation? Without a priori knowledge about where such features would be located relative to the ribosomal A-site, we calculated the cross-correlation function between intragenic ribosome occupancy profiles and the presence of a given trinucleotide sequence on the mRNA independently of reading frames. Strong correlation was observed for six trinucleotide sequences (Fig. 1d) that resembled features found in Shine–Dalgarno (SD)[6] sequences. The highest correlation occurred when the SD-like feature was 8–11 nucleotides upstream of the position occupied by the ribosomal A-site. This spacing coincides with the optimal spacing for ribosome binding at start codons[21]. However, unlike canonical SD sites, which enable initiation of translation, the observed pauses were associated with SD-like features within the body of coding regions. The accumulation of ribosomes at internal SD-like sequences was observed across two divergent phyla of bacteria (Fig. 2a), suggesting that the phenomenon occurs generally in bacteria.

[1]Department of Cellular and Molecular Pharmacology, Howard Hughes Medical Institute, University of California, San Francisco, California 94158, USA.
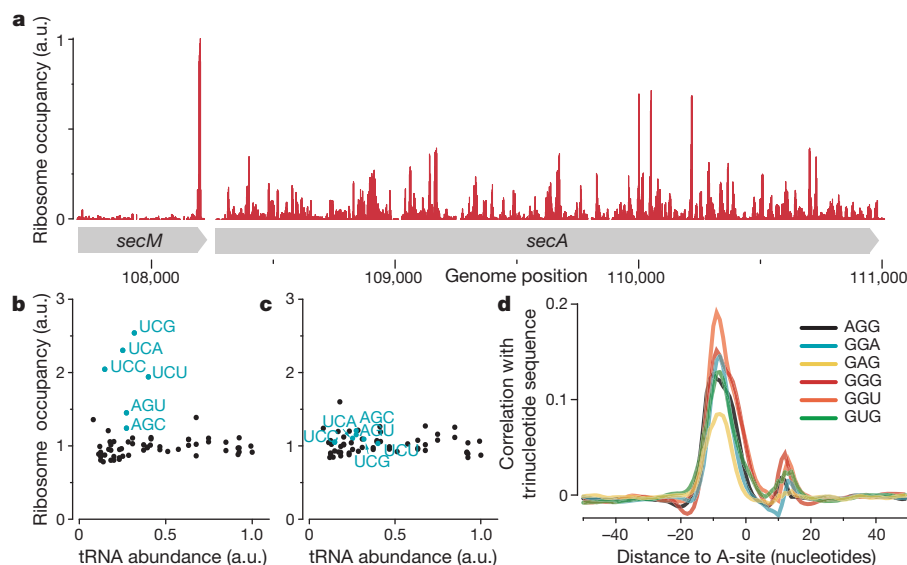
Figure 1 | Analysis of translational pausing using ribosome profiling in bacteria. a, Validation of the ribosome stalling site in the *secM* mRNA. **b, c,** Average ribosome occupancy of each codon relative to their respective tRNA abundances for *E. coli*. **b,** For growth in Luria broth, elevated occupancy at serine codons (blue) probably reflects preferential depletion of this amino acid. **c,** In glucose-rich medium, the ribosome occupancy is independent of tRNA abundance. **d,** Plot of cross-correlation function between ribosome occupancy profiles and the presence of the indicated trinucleotide sequences for *E. coli*.

The same correlation was not observed for the budding yeast *Saccharomyces cerevisiae*, whose ribosomes, like those of other eukaryotes, do not contain an anti-SD (aSD) site.

As predicted by a model in which the interaction between mRNA and the aSD site of the 16S rRNA drives pausing, the predicted hybridization free energy of a hexanucleotide to the aSD sequence

Figure 2 | Relationship between ribosome pausing and internal Shine–Dalgarno sequences. a, Plot of correlation between ribosome occupancy and SD-like features for *E. coli, B. subtilis* and *S. cerevisiae*. **b,** Plot of the average ribosome occupancy of hexanucleotide sequences relative to their affinity for the anti-Shine–Dalgarno sequence. **c,** Reprogrammed pausing by recoding the *ompF* mRNA. Ribosome occupancy (red) increases when the A-site is 8–11 nucleotides downstream (arrow) of SD-like features (green). Synonymous mutations replacing the SD-like sequence (GGUGGUG) in wild-type *ompF* (top) with a sequence (GGCGGCG) with lower affinity for the aSD site (bottom) caused a corresponding decrease in ribosome pausing.
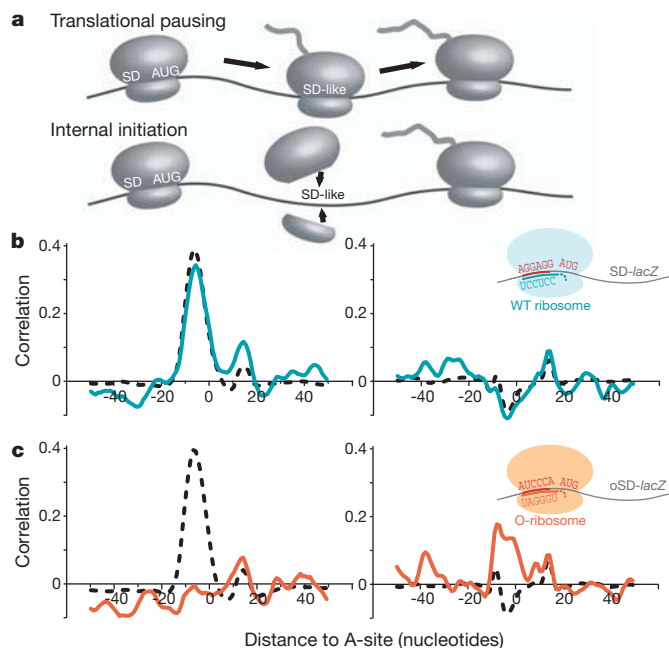
was a strong indicator of its average downstream ribosome occupancy (Fig. 2b). Furthermore, there was a clear correspondence on individual transcripts between SD-like sequences and pauses. For example, Fig. 2c shows that in *ompF*, individual SD-like features are associated with elevated ribosome occupancy 8–11 nucleotides downstream. Moreover, a synonymous mutation (GGUGGU to GGCGGC) that decreased the affinity for the aSD site led to reduced ribosome occupancy specifically at the mutated sequence, suggesting a causal relationship between the SD-like feature and the excess ribosome density.

We next sought to evaluate directly whether the excess footprint density seen at internal SD-like sequences was due to pausing of elongating ribosomes rather than attempted internal initiation, driven by SD–aSD interactions (Fig. 3a). To distinguish between these possibilities, we used a previously described orthogonal ribosome (O-ribosome) system in which a mutant form of the 16S rRNA with an altered aSD site is expressed together with wild-type 16S rRNA[8]. O-ribosomes containing the mutant 16S RNA will only translate a target mRNA that has the corresponding orthogonal SD (O-SD) sequence before its start codon. Conversely, a message whose translation is driven by the O-SD sequence will only be translated by O-ribosomes, and not by wild-type ribosomes. This system thus allows one to determine the source of regions of excess ribosome footprints, because elongating O-ribosomes would pause at internal O-SD sequences, whereas attempted internal initiation would still occur at SD sequences as a result of the cellular pool of wild-type ribosomes.

We compared the ribosome occupancy profiles of a *lacZ* message that was translated by either O-ribosomes or wild-type ribosomes. The occupancy profile of the *lacZ* message exclusively translated by O-ribosomes was correlated with O-SD-like features, and not with SD-like features (Fig. 3c). This is in marked contrast with the same *lacZ* sequence translated by wild-type ribosomes (Fig. 3b). As an internal control in O-ribosome-expressing cells, all other genes, which were translated by wild-type ribosomes, still maintained SD-correlated ribosome occupancy profiles (Fig. 3c). These observations established that elongating ribosomes pause during protein synthesis and that hybridization between the aSD site in the elongating ribosome and internal SD-like sequences gives rise to these pauses.

Global analysis of pause sites revealed that internal SD-like sequences are the dominant feature controlling translational pausing: about 70% of the strong pauses (that is, those that have ribosome

Figure 3 | Pausing of elongating ribosomes due to SD–aSD interaction.
a, Two models could account for the excess ribosome density at internal SD-like sequences. **b**, Ribosome occupancy of *lacZ* mRNA translated by wild-type ribosome. Like other genes translated by the wild-type ribosome, the ribosome occupancy pattern along *lacZ* is correlated with the presence of SD-like sequences (left), not with the O-SD sequence (right). Cyan, *lacZ*; black; all other genes. **c**, Ribosome occupancy of *lacZ* mRNA translated by orthogonal ribosome (O-ribosome). Unlike other genes in the same cells, the specialized O-SD *lacZ* has ribosome pausing at internal O-SD-like sequences (right), not at SD-like sites (left). Orange, *lacZ*; black; all other genes.

occupancies more than tenfold over the mean) are associated with SD sites (Supplementary Fig. 8). Although the interaction between internal SD sequences in a message and elongating ribosomes has been documented in specialized cases, including promoting frame-shifting *in vivo*[22,23] and ribosome stalling in single-molecule experiments *in vitro*[24], there was little indication that internal SD-like sequences are the major determinant of elongation rate during translation.

Because translational pausing limits the amount of free ribosomes available for initiating protein synthesis, widespread internal SD-like sequences could decrease bacterial growth rates. Accordingly, we found that strong SD-like sequences are generally avoided in the coding region of *E. coli* genes: hexamer sequences that strongly bind aSD sites are universally rare, whereas low-affinity hexamers have variable rates of occurrence (Fig. 4a). Consistent with translational

pausing being the driving force for this bias, depletion of SD-like sequences was observed only in protein-coding genes, and not in genes encoding rRNA or tRNA (Supplementary Fig. 9). The selection against SD-like features in turn impacts both synonymous codon choice and codon-pair choice. At the codon level, SD-like codons GAG, AGG and GGG are all minor codons in *E. coli* and *B. subtilis*. The evolutionary origin of codon selection is often attributed to differences in tRNA abundance[2,25] because its level is correlated with codon usage[18]. Instead, we propose that SD-like codons are disfavoured as a result of their interactions with rRNA, and that tRNA expression levels followed codon adaptation.

At the codon-pair level, we can now account for the selection against two consecutive codons that resemble SD sequences. This is illustrated for Gly-Gly pairs, which are coded by GGNGGN sequences (Fig. 4b). The most abundant Gly-Gly coding sequence, GGCGGC, has the lowest affinity for the aSD sequence, whereas Gly-Gly coding sequences that strongly resemble SD sites, including GGAGGU, which perfectly complements the aSD site, rarely appear. This under-representation holds even after correcting for the usage of individual codons (Fig. 4b, colour coding); for example, GGAGGU is considerably less common than GGUGGA. Other amino-acid pairs that can be coded with strong SD sites also showed the same bias (Supplementary Fig. 10). The preference in codon pairs stems from the sequence identity and not codon identity, because the same trend is seen in hexamers that are not aligned to codon pairs (Supplementary Fig. 11). Although not every bias in codon-pair usage can be explained here, the disadvantage associated with SD-induced translational pausing offers a clear mechanistic view of why certain codon pairs are avoided.

Despite the selection against internal SD-like sequences, they remain a major driving force for translational pausing. In addition, we found similar pausing patterns between conserved genes in *E. coli* and *B. subtilis* (Fig. 4c). For an mRNA encoding a specific protein, it may not be possible to fully eliminate sequences with affinity for the aSD site without changing the peptide sequence. For example, in the case of Gly-Gly, even the GGCGGC pair has substantial affinity for the aSD site. The optimization for translation rate therefore cannot be achieved only at the level of mRNA coding: it is also constrained by the requirement to make a functional peptide sequence.

The observation that the ability of elongating ribosomes to interact with SD-like sequences is highly conserved suggests that this mechanism of pausing is exploited for functional purposes. Indeed, a highly conserved internal SD site exists in the gene encoding peptide chain release factor 2 (RF2)[26]. This sequence has an important function in promoting a translational frameshift to enable its expression. In addition, pausing at internal SD-like sites could modulate the co-translational folding of the nascent peptide chain (Supplementary Fig. 12). Finally, given the coupling between transcription and translation in bacteria[27,28], pausing
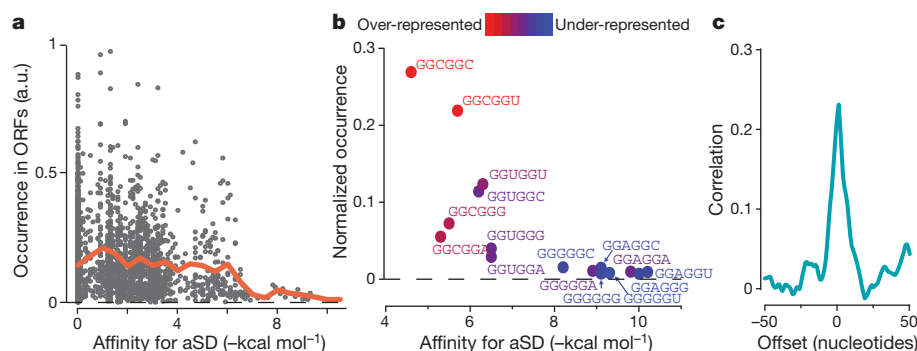

Figure 4 | Selection against SD-like sequences and the constraint on protein coding. **a**, Rate of occurrence of hexanucleotide sequences in *E. coli* messages relative to their predicted affinity for the aSD site. The orange line shows the average occurrence within a bin size of 0.5 kcal mol⁻¹. **b**, Occurrence of codon-pairs for Gly-Gly residues relative to their predicted affinity for the aSD site.

The colour coding represents the enrichment in occurrence of codon pairs after correcting for the usage of single codons. **c**, Cross-correlation function of ribosome occupancy profiles between conserved genes in *E. coli* and *B. subtilis*. Zero offset means that the two sequences are aligned at each amino-acid residue.

at SD sites could be exploited for transcriptional regulation. We observed internal SD sites and pausing near the stop codon of transcription attenuation leader peptides[29], including *trpL* and *thrL* (Supplementary Fig. 13). In contrast to ribosome stalling at regulatory codons during starvation, slow translation near the stop codon could protect alternative structural mRNA elements to prevent the formation of anti-termination stem-loops, thereby ensuring proper transcription termination[30]. Our approach and the genome-wide data lay the groundwork for further gene-specific functional studies of translational pausing.

From a more practical perspective, ribosome pausing at internal SD sites presents both a challenge and an opportunity for heterologous protein expression in bacteria. Overexpression of eukaryotic proteins with strong internal SD sites would sequester ribosomes and compromise protein yield. Internal SD sequences could be reduced by recoding the gene, which has not been considered in conventional strategies of simple codon optimization or overexpression of rare tRNAs. Conversely, recoding can introduce internal SD sites if pausing is required for co-translational processing. Positioning of internal SD sites therefore adds another dimension to the optimization of heterologous protein expression.

METHODS SUMMARY

E. coli MG1655 and *B. subtilis* 168 were used as wild-type strains. *E. coli* BJW9 has synonymous substitutions at G141 and G142 in the *ompF* gene. The orthogonal ribosome experiment was performed in *E. coli* BW25113 with two plasmids: pSC101-G9, expressing orthogonal 16S rRNA, and pJW1422, expressing O-SD-*lacZ* mRNA. pSC101-G9 was a gift from J. Chin[8]. pJW1422 has *lacZ* driven from a *tacII* promoter and an O-ribosome binding site 5′-AUCCCA-3′. Luria broth was used for *B. subtilis* culture. Cell cultures were harvested at a D_{600} of 0.3–0.4. Flash-freezing and ribosome footprinting was described previously[5]. 5′-Guanylyl imidodiphosphate (3 mM) was added to the lysate before thawing and during footprinting to prevent translation after lysis. Conversion of mRNA footprints to a complementary DNA library was described previously[4,5]. Deep sequencing was performed on an Illumina HiSeq 2000 system, and the results were aligned to reference genomes using Bowtie v. 0.12.0. The cross-correlation function is defined as

$$C_i = \frac{\langle x_{j+i} y_j \rangle - \mu_X \mu_Y}{\sigma_X \sigma_Y}$$

for the series $X = x_1, x_2, …, x_N$ and $Y = y_1, y_2, …, y_N$, where μ_X and σ_X are the average and the standard deviation of series X, respectively.

Full Methods and any associated references are available in the online version of the paper at www.nature.com/nature.

Received 21 November 2011; accepted 16 February 2012.
Published online 28 March 2012.

1. Kramer, G., Boehringer, D., Ban, N. & Bukau, B. The ribosome as a platform for co-translational processing, folding and targeting of newly synthesized proteins. *Nature Struct. Mol. Biol.* **16,** 589–597 (2009).
2. Plotkin, J. B. & Kudla, G. Synonymous but not the same: the causes and consequences of codon bias. *Nature Rev. Genet.* **12,** 32–42 (2011).
3. Ingolia, N. T., Ghaemmaghami, S., Newman, J. R. & Weissman, J. S. Genome-wide analysis *in vivo* of translation with nucleotide resolution using ribosome profiling. *Science* **324,** 218–223 (2009).
4. Ingolia, N. T., Lareau, L. F. & Weissman, J. S. Ribosome profiling of mouse embryonic stem cells reveals the complexity and dynamics of mammalian proteomes. *Cell* **147,** 789–802 (2011).
5. Oh, E. *et al.* Selective ribosome profiling reveals the cotranslational chaperone action of trigger factor *in vivo*. *Cell* **147,** 1295–1308 (2011).
6. Shine, J. & Dalgarno, L. The 3′-terminal sequence of *Escherichia coli* 16S ribosomal RNA: complementarity to nonsense triplets and ribosome binding sites. *Proc. Natl Acad. Sci. USA* **71,** 1342–1346 (1974).
7. Hui, A. & de Boer, H. A. Specialized ribosome system: preferential translation of a single mRNA species by a subpopulation of mutated ribosomes in *Escherichia coli*. *Proc. Natl Acad. Sci. USA* **84,** 4762–4766 (1987).
8. Rackham, O. & Chin, J. W. A network of orthogonal ribosome•mRNA pairs. *Nature Chem. Biol.* **1,** 159–166 (2005).
9. Varenne, S., Buc, J., Lloubes, R. & Lazdunski, C. Translation is a non-uniform process. Effect of tRNA availability on the rate of elongation of nascent polypeptide chains. *J. Mol. Biol.* **180,** 549–576 (1984).
10. Pedersen, S. *Escherichia coli* ribosomes translate *in vivo* with variable rate. *EMBO J.* **3,** 2895–2898 (1984).
11. Sorensen, M. A., Kurland, C. G. & Pedersen, S. Codon usage determines translation rate in *Escherichia coli*. *J. Mol. Biol.* **207,** 365–377 (1989).
12. Andersson, S. G. & Kurland, C. G. Codon preferences in free-living microorganisms. *Microbiol. Rev.* **54,** 198–210 (1990).
13. Sorensen, M. A. & Pedersen, S. Absolute *in vivo* translation rates of individual codons in *Escherichia coli*. The two glutamic acid codons GAA and GAG are translated with a threefold difference in rate. *J. Mol. Biol.* **222,** 265–280 (1991).
14. Gutman, G. A. & Hatfield, G. W. Nonrandom utilization of codon pairs in *Escherichia coli*. *Proc. Natl Acad. Sci. USA* **86,** 3699–3703 (1989).
15. Nakatogawa, H. & Ito, K. The ribosomal exit tunnel functions as a discriminating gate. *Cell* **108,** 629–636 (2002).
16. Gong, F. & Yanofsky, C. Instruction of translating ribosome by nascent peptide. *Science* **297,** 1864–1867 (2002).
17. Chiba, S. *et al.* Recruitment of a species-specific translational arrest module to monitor different cellular processes. *Proc. Natl Acad. Sci. USA* **108,** 6073–6078 (2011).
18. Dong, H., Nilsson, L. & Kurland, C. G. Co-variation of tRNA abundance and codon usage in *Escherichia coli* at different growth rates. *J. Mol. Biol.* **260,** 649–663 (1996).
19. Pruss, B. M., Nelms, J. M., Park, C. & Wolfe, A. J. Mutations in NADH:ubiquinone oxidoreductase of *Escherichia coli* affect growth on mixed amino acids. *J. Bacteriol.* **176,** 2143–2150 (1994).
20. Sezonov, G., Joseleau-Petit, D. & D'Ari, R. *Escherichia coli* physiology in Luria–Bertani broth. *J. Bacteriol.* **189,** 8746–8749 (2007).
21. Chen, H., Bjerknes, M., Kumar, R. & Jay, E. Determination of the optimal aligned spacing between the Shine–Dalgarno sequence and the translation initiation codon of *Escherichia coli* mRNAs. *Nucleic Acids Res.* **22,** 4953–4957 (1994).
22. Weiss, R. B., Dunn, D. M., Dahlberg, A. E., Atkins, J. F. & Gesteland, R. F. Reading frame switch caused by base-pair formation between the 3′ end of 16S rRNA and the mRNA during elongation of protein synthesis in *Escherichia coli*. *EMBO J.* **7,** 1503–1507 (1988).
23. Larsen, B., Wills, N. M., Gesteland, R. F. & Atkins, J. F. rRNA–mRNA base pairing stimulates a programmed −1 ribosomal frameshift. *J. Bacteriol.* **176,** 6842–6851 (1994).
24. Wen, J. D. *et al.* Following translation by single ribosomes one codon at a time. *Nature* **452,** 598–603 (2008).
25. Ikemura, T. Correlation between the abundance of *Escherichia coli* transfer RNAs and the occurrence of the respective codons in its protein genes: a proposal for a synonymous codon choice that is optimal for the *E.coli* translational system. *J. Mol. Biol.* **151,** 389–409 (1981).
26. Baranov, P. V., Gesteland, R. F. & Atkins, J. F. Release factor 2 frameshifting sites in different bacteria. *EMBO Rep.* **3,** 373–377 (2002).
27. Burmann, B. M. *et al.* A NusE:NusG complex links transcription and translation. *Science* **328,** 501–504 (2010).
28. Proshkin, S., Rahmouni, A. R., Mironov, A. & Nudler, E. Cooperation between translating ribosomes and RNA polymerase in transcription elongation. *Science* **328,** 504–508 (2010).
29. Kolter, R. & Yanofsky, C. Attenuation in amino acid biosynthetic operons. *Annu. Rev. Genet.* **16,** 113–134 (1982).
30. Elf, J. & Ehrenberg, M. What makes ribosome-mediated transcriptional attenuation sensitive to amino acid limitation? *PLOS Comput. Biol.* **1,** e2 (2005).

METHODS

Strains, plasmids and growth conditions. *E. coli* K-12 MG1655 and *B. subtilis* 168 were used as wild-type strains. *E. coli* BJW9 with recoded *ompF* (GGT to GGC synonymous substitutions at G141 and G142) at the endogenous locus was constructed by lambda-Red recombination[31] in MG1655. The orthogonal ribosome experiment was performed in *E. coli* BW25113, which is a K-12-derived strain with a *lacZ* deletion[31].

Plasmid pSC101-G9 (gift from J. Chin), expresses orthogonal 16S rRNA from an intact *rrnB* operon except that the 3′ end of *rrsB*, which codes for the 16S rRNA, was changed from 5′-CCTCCTTA-3′ to 5′-TGGGATTA-3′ (ref. 8). Plasmid pJW1422 harbours the *lacZ* gene with a *tacII* promoter. The ribosome-binding site of the *lacZ* mRNA is replaced with 5′-AUCCCA-3′, thus allowing initiation of translation by orthogonal ribosomes.

Unless otherwise noted, *E. coli* strains were grown in MOPS medium supplemented with 0.2% glucose, 20 amino acids, vitamins, bases and micronutrients as described[32] (Teknova). *B. subtilis* was grown in Luria broth (BD Difco). For the strain containing pSC101-G9 and pJW1442, the medium was supplemented with 25 μg ml^{-1} kanamycin and 15 μg ml^{-1} tetracycline. For experiments with *E. coli*, an overnight liquid culture was diluted 1:400 into fresh medium. For experiments with *B. subtilis*, an overnight culture on a Luria broth plate was washed and diluted to a D_{600} of 0.00125 in Luria broth. Cell cultures were grown at 37 °C until D_{600} reached 0.3–0.4.

Ribosome profiling. The protocol for bacterial ribosome profiling with flash freezing was described in ref. 5. Cell culture (200 ml) was rapidly filtered by passing through a prewarmed nitrocellulose filter with a 200-nm pore size. Cell pellet was flash-frozen in liquid nitrogen and combined with 650 μl of frozen lysis buffer (10 mM MgCl$_2$, 100 mM NH$_4$Cl, 20 mM Tris-HCl pH 8.0, 0.1% Nonidet P40, 0.4% Triton X-100, 100 U ml^{-1} DNase I (Roche), 1 mM chloramphenicol, 3 mM 5′-guanylyl imidodiphosphate (GMPPNP)). Addition of GMPPNP together with chloramphenicol inhibits translation after lysis. Cells were pulverized in 10-ml canisters prechilled in liquid nitrogen. Lysate containing 0.5 mg of RNA was digested for 1 h with 750 U of micrococcal nuclease (Roche) at 25 °C. The ribosome-protected fragments were isolated using a sucrose gradient and phenol extraction. The footprints were ligated to a 5′-adenylated and 3′-end-blocked DNA oligonucleotide (/5rApp/CTGTAGGCACCATCAAT/3ddc; Integrated DNA Technologies)[4,5]. Unless otherwise noted, the ligation was performed with truncated T4 RNA ligase 2 (New England Biolabs) as described previously[4,5]. To remove lot-to-lot difference in the activity from the commercial source, we have recently switched to recombinantly expressed truncated T4 RNA ligase 2 K227Q produced in our laboratory. We used this ligase to generate a library for the high-coverage data set for *E. coli*. The 3′-ligated RNA fragments were converted to sequenceable DNA library by using reverse transcription, circularization and PCR amplification as described previously[4,5].

Sequencing was performed on an Illumina HiSeq 2000 system. Sequence alignment with Bowtie v. 0.12.0 mapped the footprint data to the reference genomes NC_000913.fna (*E. coli*) or NC_000964.fna (*B. subtilis*) obtained from the NCBI Reference Sequence Bank. The data from BJW9 were aligned to a reference modified from NC_000913.fna. The footprint reads varied between 25 and 42 nucleotides in length, mostly as a result of the specificity of micrococcal nuclease. In contrast to eukaryotic systems, in which the 5′ end of the footprint is sufficient to carry the positional information[3,4], here we distribute the positional information into several nucleotides in the centre of the footprint[5]. For each footprint read, the centre residues that were at least 12 nucleotides from either end were given the same score, which was weighted by the length of the fragment.

To assign the A-site position to the centre of ribosome footprints, we made use of the ribosome density at two independent sets of well-defined pause sites. The first set consisted of pausing at stop codons[5], where the ribosomal A-site was aligned to stop codons before binding of release factors. The second set consisted of peptide-mediated ribosome stalling sites, where the A-site codons had been identified. These two alignments were consistent with each other. In addition, the pausing at serine codons at the A-site during starvation confirmed the position assignment of ribosome footprints.

mRNA sequencing. Total RNA was phenol extracted from the same lysate that was used for ribosome footprinting[5]. Ribosomal RNA and small RNA were removed from the total RNA with MICROBExpress and MEGAclear (Ambion), respectively. mRNA was randomly fragmented as described[4]. The fragmented mRNA sample was converted to a complementary DNA library with the same strategy as for ribosome footprints, and was described previously[5].

Data analysis. Data analysis was performed with scripts written for Python 2.6.6. Global pausing analyses were based on 2,257 genes (*E. coli*) and 1,580 genes (*B. subtilis*) with an average coverage of at least ten sequencing reads per codon in the ribosome profiling data set. In addition, analyses on 997 genes in *E. coli* and 1,189 genes in *B. subtilis* with a coverage of between one and ten sequencing reads per codon showed qualitatively consistent results. For *E. coli*, *tufA* and *tufB* genes

were not included in the analysis because of their sequence homology with each other. Genes with known frame-shifting sites (*prfB* and *dnaX*) were not included in codon-specific analyses. On gene-specific analyses, the coverage was at least 30 sequencing reads per codon in each case.

To focus on the kinetics of translation elongation, the analysis was performed on the basis of ribosome occupancy profiles within protein-coding genes, excluding the first ten codons and the last ten codons. To calculate the average ribosome occupancy associated with each codon at the A-site, the ribosome occupancy profile of each gene was normalized by the mean occupancy of the gene, and the normalized occupancy for each codon was averaged across all genes. Similarly, the average ribosome occupancy for each hexanucleotide at the SD position was calculated by averaging normalized occupancy at between 7 and 12 nucleotides downstream of the hexanucleotide sequence. For each codon, the corresponding tRNA abundance plotted in Fig. 1 and Supplementary Fig. 7 was the sum of the expression levels of the cognate tRNA species measured in refs 18, 33.

To identify dominating sequence features either upstream or downstream of the pausing sites, we slid the ribosome occupancy profile ($X = x_1, x_2, …, x_N$) along the coding sequence and, at every offset position i, calculated the correlation with the presence of a given sequence ($Y = y_1, y_2, …, y_N$). In mathematical terms it is given by the normalized cross-correlation function (C_i):

$$C_i = \frac{\langle x_{j+i}y_j \rangle - \mu_X \mu_Y}{\sigma_X \sigma_Y}$$

where μ_X and μ_Y are the average of the series X and Y, respectively. σ_X and σ_Y are the standard deviations of the series X and Y, respectively. $\langle x_{j+i}y_j \rangle$ is the expectation value of $x_{j+i}y_j$ for all possible values of j. We used Python to calculate $\sum x_{j+i}y_j$ using the 'correlate' function in the 'same' mode in the numpy package. The expectation value is obtained by dividing the summation by $N - |i|$. For each gene with more than ten sequencing reads per codon and more than 160 base pairs long, we calculated the normalized cross-correlation function. The average over these cross-correlation functions is presented in this paper.

Hybridization free-energy prediction. The hybridization free energy between mRNA and the aSD site was predicted with the RNAsubopt program in the Vienna RNA package[34]. The energy was predicted for 37 °C with a contribution from dangling ends. For each hexanucleotide sequence, the lowest possible hybridization free energy was assigned as its affinity for the aSD site. We used the eight-nucleotide sequence 5′-CACCUCCU-3′ as the aSD sequence. To calculate the cross-correlation function between ribosome occupancy profile and SD-like features (Fig. 2a), we built the aSD affinity profile for each mRNA by scanning the transcript in overlapping units of ten nucleotides and calculating the affinity of aSD to the middle eight nucleotides. The affinity was assigned to the eighth position in the ten-nucleotide window, which corresponds to U in the canonical SD sequence. The distance from the P-site to U in the canonical SD sequence is often defined as the aligned spacing[21]. Because we align ribosome footprints to the A-site, the distance reported here is three nucleotides longer than the aligned spacing.

Analysis of O-ribosome translated messages. Because a *lacZ* message whose translation is driven by O-SD is exclusively translated by O-ribosomes[8], the translational pausing model outlined in Fig. 3a predicts that for the O-SD driven *lacZ* there will be both the appearance of new ribosome density peaks at internal sites that resemble the O-SD sequence and the disappearance of peaks at the SD-like sequences found when translation is driven by the wild-type SD sequence. This prediction is confirmed by our data in Fig. 3c: the ribosome occupancy profile of *lacZ* with O-SD-driven translation no longer shows a correlation with SD-like sequences, and instead is correlated with O-SD-like sequences. Moreover, because the endogenous messages are still translated solely by wild-type ribosomes even when the O-ribosome is present, the ribosome peaks in the endogenous messages are found at SD-like sequences, not at sequences that resemble the O-SD site, regardless of whether O-ribosomes are present. This is again confirmed by the data shown in Fig. 3c.

Conservation analysis. Conservation analysis of pausing patterns in *E. coli* and *B. subtilis* was performed in a set of 31 proteins from the curated alignment database AMPHORA[35]. The nucleotide sequences and the ribosome density profiles were trimmed and concatenated on the basis of the protein alignment. The cross-correlation function between *E. coli* and *B. subtilis* ribosome occupancy was calculated for each gene, and then averaged over 31 genes to give the conservation of pausing patterns.

Occurrence of hexamers and codon pairs. The occurrence of hexamers and codon pairs was counted from annotated protein-coding genes available from the NCBI Reference Sequence Bank. Normalized occurrence ($p_{i,j}$) was calculated by dividing the occurrence of a given codon pair (i and j) by the total occurrence of the corresponding amino-acid pair. The correction for the usage of single codons

was calculated by dividing the normalized occurrence of the codon pair ($p_{i,j}$) by the frequency of the two individual codons (q_i and q_j); that is, enrichment $= p_{i,j}/q_iq_j$. The frequency of individual codons was normalized to the occurrence of the corresponding amino acid.

Protein structure analysis. Protein secondary structure was predicted by the PSIPRED method[36], with the filtered reference database UniRef90 (ref. 37). Secondary structures were predicted for 271 proteins. Cross-correlation function between the structural assignment with either ribosome occupancy or SD-like features was calculated at the nucleotide level.

31. Datsenko, K. A. & Wanner, B. L. One-step inactivation of chromosomal genes in *Escherichia coli* K-12 using PCR products. *Proc. Natl Acad. Sci. USA* **97,** 6640–6645 (2000).

32. Neidhardt, F. C., Bloch, P. L. & Smith, D. F. Culture medium for enterobacteria. *J. Bacteriol.* **119,** 736–747 (1974).

33. Kanaya, S., Yamada, Y., Kudo, Y. & Ikemura, T. Studies of codon usage and tRNA genes of 18 unicellular organisms and quantification of *Bacillus subtilis* tRNAs: gene expression level and species-specific diversity of codon usage based on multivariate analysis. *Gene* **238,** 143–155 (1999).

34. Gruber, A. R., Lorenz, R., Bernhart, S. H., Neubock, R. & Hofacker, l. L. The Vienna RNA websuite. *Nucleic Acids Res.* **36** (suppl. 2), W70–W74 (2008).

35. Wu, M. & Eisen, J. A. A simple, fast, and accurate method of phylogenomic inference. *Genome Biol.* **9,** R151 (2008).

36. Jones, D. T. Protein secondary structure prediction based on position-specific scoring matrices. *J. Mol. Biol.* **292,** 195–202 (1999).

37. Li, W., Jaroszewski, L. & Godzik, A. Clustering of highly homologous sequences to reduce the size of large protein databases. *Bioinformatics* **17,** 282–283 (2001).

LETTER

Live–cell delamination counterbalances epithelial growth to limit tissue overcrowding

Eliana Marinari[1]*, Aida Mehonic[2]*, Scott Curran[1], Jonathan Gale[3], Thomas Duke[2] & Buzz Baum[1]

The development and maintenance of an epithelium requires finely balanced rates of growth and cell death. However, the mechanical and biochemical mechanisms that ensure proper feedback control of tissue growth[1–4], which when deregulated contribute to tumorigenesis, are poorly understood. Here we use the fly notum as a model system[5] to identify a novel process of crowding-induced cell delamination that balances growth to ensure the development of well-ordered cell packing. In crowded regions of the tissue, a proportion of cells undergo a serial loss of cell–cell junctions and a progressive loss of apical area, before being squeezed out by their neighbours. This path of delamination is recapitulated by a simple computational model of epithelial mechanics, in which stochastic cell loss relieves overcrowding as the system tends towards equilibrium. We show that this process of delamination is mechanistically distinct from apoptosis-mediated cell extrusion[6–8] and precedes the first signs of cell death. Overall, this analysis reveals a simple mechanism that buffers epithelia against variations in growth. Because live-cell delamination constitutes a mechanistic link between epithelial hyperplasia and cell invasion, this is likely to have important implications for our understanding of the early stages of cancer development.

To better understand the role of epithelial cell dynamics and mechanics in the development of a well-ordered tissue, we studied the refinement of the fly notum[5,9] from 12 h after pupariation (AP), as the tissue undergoes a final process of topological reorganization before terminal differentiation. The refinement of cell packing in this tissue occurs largely without concomitant changes in overall tissue form or size[5,9]. Using the constitutive expression of E-cadherin–GFP to follow apical junctional dynamics (Supplementary Movie 1), we observed a significant level of regionalized epithelial cell delamination in the tissue. In the midline region, where cells have an anisotropic geometry at 12 h AP, 32.5 ± 13.6% of cells underwent basal delamination, compared with 0.5 ± 0.3% of cells in the surrounding tissue (means ± s.d., $n = 4$ pupae) (Fig. 1c). The pattern of delamination varied between animals, was not symmetric across the midline, and involved a variable proportion of cells leaving the tissue both before and after cell division (Fig. 1b). This rules out a deterministic role for cell lineage, position or developmental time in delamination, implying that it is a stochastic process. Before the onset of delamination, cells within the midline of the tissue were 2.7-fold longer than they were wide when measured along the anterior–posterior axis of the animal, despite their having similar apical areas ($48.5 ± 14.2 \mu m^2$ in the midline and $51.3 ± 12.7 \mu m^2$ outside the midline). By 26 h AP, however, midline cells were isotropic in form and could no longer be distinguished from those in the rest of the tissue (Fig. 1a). Regionalized delamination therefore accompanies the topological rearrangement as the tissue tends towards a uniform cell organization. This suggests a possible role for delamination in the refinement of this tissue before terminal differentiation.

Although it is not currently known how epithelial growth is regulated during development or homeostasis, mechanical stresses generated as
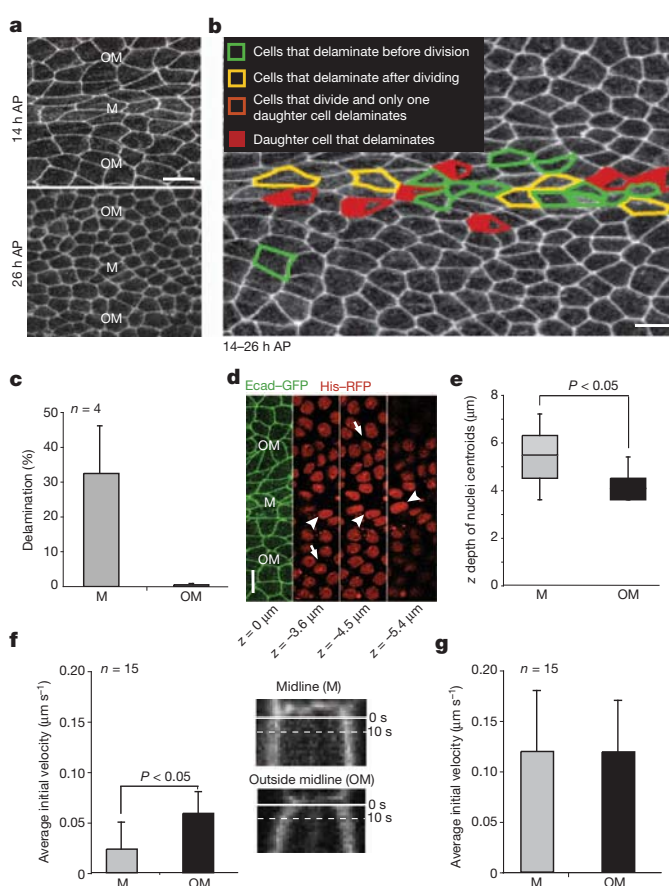

Figure 1 | Stochastic cell delamination from crowded regions of a tissue during normal development. a, E-cadherin–GFP notum at 14 h and 26 h AP. **b**, Cells delaminating between 14 h and 26 h AP were coloured according to their behaviour (see key). **c**, The percentage of cells delaminating in the midline (M) and outside the midline (OM), calculated as the ratio between the number of cells that delaminated in 11 h and the total initial number of cells from four animals. **d**, Tissue expressing E-cadherin–GFP and His–RFP (to mark nuclei) along different planes in z. Midline nuclei are indicated by arrowheads and those outside the midline by arrows. **e**, Box plot showing the z-depth of nuclei centroids in M and OM. The median is represented by horizontal lines; the 75th and 25th centiles are at the top and bottom of the boxes, respectively. **f**, Quantification and kymograph analysis of average initial velocity of vertex displacement after laser cutting for early pupae (14–16 h AP). Images show the junction before the cut at 0 s and the kymograph after the cut. Dotted lines indicate 10 s after cutting. The average initial velocity does not correlate with junction length (Supplementary Fig. 2b–d). **g**, Quantification of the average initial velocity of vertex displacement of single junctions after laser ablation for late pupae (24–26 h AP). In **f** and **g**, n represents 15 cuts for 5 animals. All error bars indicate s.d. Scale bars, 10 μm.

[1]Medical Research Council Laboratory of Molecular Cell Biology, University College London, Gower Street, London WC1E 6BT, UK. [2]London Centre for Nanotechnology and Department of Physics and Astronomy, University College London, Gower Street, London WC1E 6BT, UK. [3]UCL Ear Institute, University College London, 332 Gray's Inn Road, London WC1X 8EE, UK.
*These authors contributed equally to this work.

a consequence of cell proliferation have been proposed to have a function[1,4]. Several lines of evidence suggest that cells across the developing notum are subject to regional differences in forces that could, through mechanical feedback, lead to local differences in cell behaviour. First, at 14 h AP, nuclei in the midline region are found at variable depths along the z axis (Fig. 1d, e), whereas nuclei outside the midline lie in the same confocal plane (Fig. 1d, e). At the same time, cell–cell junctions within the midline region seem convoluted, whereas those outside the midline seem taut (Supplementary Fig. 1a). Furthermore, when junctions are cut with a diffraction limited laser, there is a threefold difference in the initial velocity of the junctional recoil in these two regions. Thus, the vertices of severed junctions outside the midline open with an initial velocity of $0.06 \pm 0.02\ \mu m\ s^{-1}$, whereas vertices in the midline remain relatively unmoved ($0.02 \pm 0.03\ \mu m\ s^{-1}$; Fig. 1f and Supplementary Fig. 2a). In contrast, by 26 h AP, when nuclear and junctional morphology seem homogeneous across the tissue (Supplementary Fig. 1b), rates of vertex displacement are similar within the midline ($0.12 \pm 0.06\ \mu m\ s^{-1}$) and outside it ($0.12 \pm 0.05\ \mu m\ s^{-1}$; Fig. 1g and Supplementary Fig. 2a). These differences in tissue mechanics were confirmed by using different patterns of laser-induced dissection (Supplementary Figs 3 and 4). Because local delamination rates correlate with local differences in mechanics across the tissue, delamination could relieve local overcrowding to help generate the regular cell packing and uniform tissue mechanics seen at the end of development.

To test this hypothesis, we used RNA-mediated interference (RNAi) to determine whether rates of cell delamination are sensitive to changes in cell crowding. We began by silencing components of the phosphatidylinositol-3-OH kinase (PI(3)K) and Hippo pathways (Fig. 2a, b and Supplementary Fig. 5). These treatments increased cell growth without significantly increasing tissue area, resulting in an increase in epithelial height and a corresponding increase in the rate of tissue-wide cell delamination (Fig. 2a–d and Supplementary Movie 2). Rates of epithelial cell delamination were highest in the midline and in crowded epithelial folds that formed as the result of tissue buckling (Fig. 2g). Conversely, rates of midline cell delamination were significantly decreased when growth and crowding were inhibited (Fig. 2a–d, f and Supplementary Movies 3 and 4). Moreover, in tissue expressing high levels of Tsc1 and Tsc2 the decrease in growth was accompanied by a corresponding increase in junctional tension across the tissue, measured by vertex displacement after cutting (Fig. 2e), as expected if crowding affects tissue mechanics. This marked decrease in the rate of delamination seen in tissues with decreased growth was not a simple consequence of the accompanying decrease in cell division, because delamination continued unabated when cell division was directly inhibited through the depletion of Cdc25/String (Supplementary Fig. 6 and Supplementary Movie 5). Furthermore, differences in the rate of delamination could not be explained by growth-induced changes in developmental timing, because similar results were seen when we normalized on the basis of the timing of P1 cell divisions (Supplementary Fig. 7). These data suggest that local tissue mechanics influence the tendency of cells to delaminate.

To gain insight into the potential role of mechanics in driving cell delamination within a crowded epithelium, we developed a computational model of the notum (details in Supplementary Information) in which the topological organization of cells changed over time as the result of junctional rearrangements while overall tissue area remained fixed (Figs 3a and 4a). First, we used the model to test the likely effects of tissue growth on dynamic cell organization, through the introduction of a variable crowding parameter γ, equal to the ratio of the area that cells would naturally prefer to occupy relative to the fixed tissue area (details in Supplementary Information). In simulations, delamination was directly correlated with crowding, such that high γ favoured delamination by forcing cells to compete for limited space (Fig. 3b). We then examined the effects of cell geometry on delamination by running simulations in which cells either had an isotropic shape or an
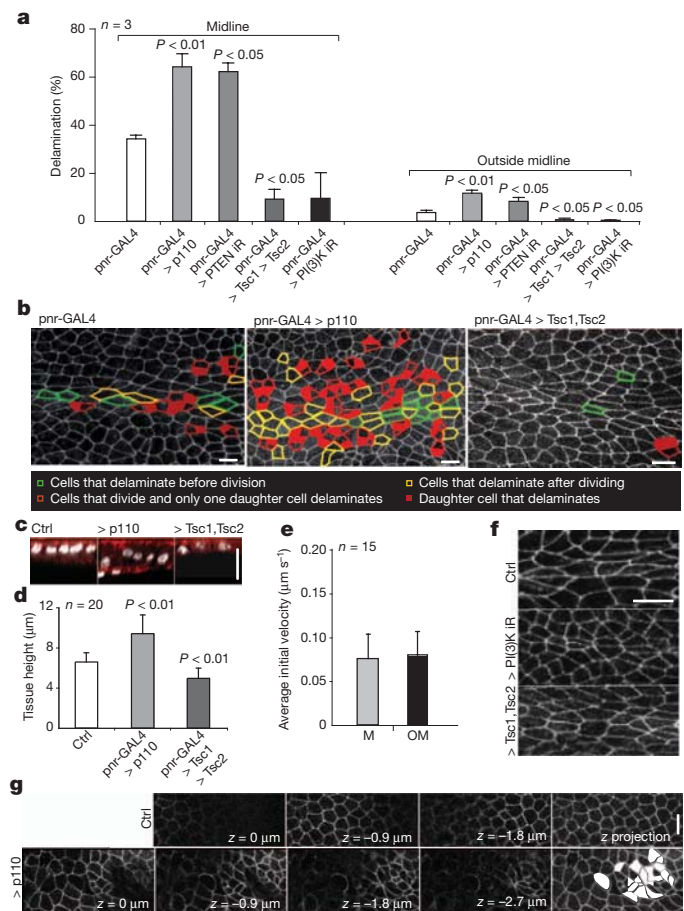

Figure 2 | Delamination counter-balances tissue growth. a, Average rates of delamination ($n = 3$ pupae) for cells in the midline and outside midline in control animals, in tissues where growth was increased (p110 PI(3)K, PTEN RNAi) and in nota with decreased growth (p110 PI(3)K RNAi, Tsc1 and Tsc2). b, Cells delaminating were coloured according to their behaviour (see inset). c, xz axis of tissues stained with 4′,6-diamidino-2-phenylindole and labelled phalloidin. d, Average tissue height ($n = 20$ different regions from 4 different pupae). e, Quantification of average initial velocity of vertex displacement after laser dissection of single junctions in early pupae for tissues expressing Tsc1 and Tsc2, with n representing 15 cuts from 5 pupae. f, Midline geometry for nota at 14 h AP. g, xy image planes for different z-slices. Delamination is most prevalent in tissue folds after p110 PI(3)K overexpression (coloured white in the z projection). All error bars indicate s.d. P values were calculated relative to the control. Scale bars, 10 μm.

average initial aspect ratio of 2.7:1, to model cells of the notum midline. This showed that cellular anisotropy promoted delamination (Fig. 3c), which in turn homogenized cell packing (Figs 1a and 3c). Significantly, by combining the two factors, crowding and geometry, we were able to accurately replicate the behaviours of cells within the midline (with anisotropic geometry and increased crowding) and outside the midline (isotropic geometry and no growth-induced crowding) using a single set of fixed parameters (Fig. 3d).

A closer examination of simulations revealed the typical path of cell delamination. Spontaneous fluctuations in the length of individual cell–cell junctions cause a subset of cells to suffer a stochastic serial loss of junctions through neighbour exchange events[10,11] (Fig. 3e). The concomitant progressive loss in apical area results in the removal of these cells from the simulated tissue. In view of this computational analysis, when we examined the precise path of cell delamination in the developing fly notum we identified two mechanistically distinct paths of delamination. First, we identified a population of cells that leave the tissue over an extended and variable period of time as they undergo a consecutive series of neighbour exchange events[10,11], accompanied by a
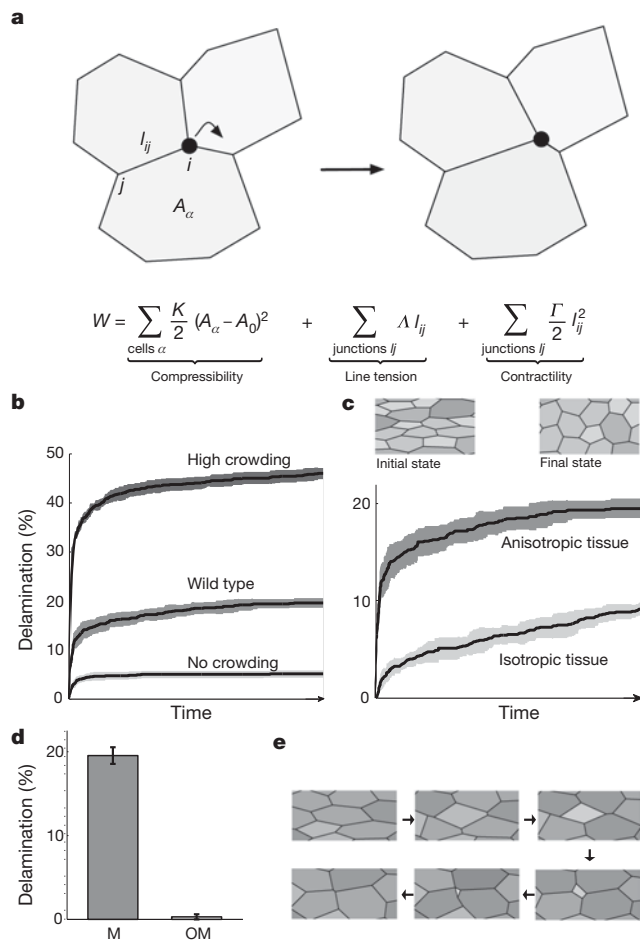
Figure 3 | Topological rearrangements drive a stochastic process of delamination in overcrowded tissues. a, Schematic diagram of the model of mechanical forces that act in the plane of the epithelium: junctional line tension (Λ), contractility of cortical acto-myosin (Γ) and limited cell compressibility (K) based on a target area (A_0). The tissue evolves by small stochastic displacements of the vertices, biased towards changes that decrease the work function, W. **b**, Cumulative proportion of cells delaminating from wild-type tissue ($\gamma = 2$) and a tissue with high ($\gamma = 4$) or low ($\gamma = 1$) crowding as a function of time, all three with anisotropic geometry. **c**, Still images showing initial and final cell configurations for the midline simulation (anisotropic); values of parameters correspond to moderate crowding ($\gamma = 2$ in both cases). **d**, Final proportions of cells delaminating in simulations of wild-type tissue within and outside the midline. The midline has anisotropic geometry and $\gamma = 2$; tissue outside the midline has isotropic geometry and $\gamma = 1$. **e**, An example showing the serial loss of junctions and the progressive loss of apical area that precedes cell extrusion. In **b**, **c** and **d** mean values and standard errors of the data are averaged over six simulations. Grey shades represent standard errors of the data.

progressive loss of junctions and apical area (Fig. 4a, b). We term this type of delamination a D1 process. Once these cells had fewer than five neighbours and less than ~25% of their initial area, they were forced out of the tissue within a short and reproducible timescale (about 10 min). This final push was associated with the recruitment of a contractile myosin II ring that formed within neighbouring cells (Fig. 4g). When the actomyosin cable was cut, both cell delamination and delamination-induced cell death were prevented (Supplementary Fig. 8). In addition, we identified a second pathway, which we term a D2 process, by which cells delaminated from the epithelium over a period of about 50 min, as the result of a progressive loss of apical area, without a concomitant change in neighbour relationships (Fig. 4c). This D2 process resembled apoptotic cell extrusion as described previously[6] in that it was associated with the formation of rosette-like intermediates and the loss of junctional E-cadherin (Fig. 4g and
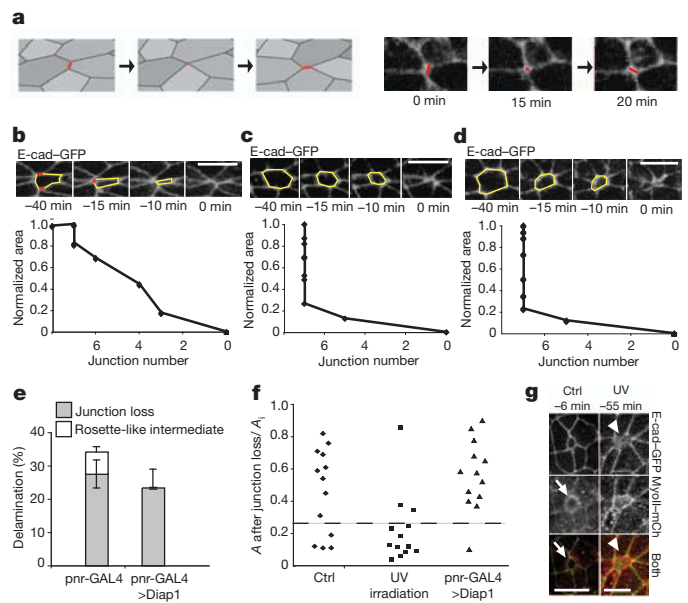
Figure 4 | Crowding-induced delamination is a cause not a consequence of cell death and is distinct from apoptosis-mediated extrusion. a, Changing neighbours by means of a T1 transition in the model and *in vivo*. **b**, A typical midline wild-type cell delaminating (yellow perimeter) and a plot to show the relative timing of the loss of apical area and neighbours as it leaves the tissue. Junctions disappearing between frames are indicated in red. **c**, A cell (yellow perimeter) delaminating from the midline in the wild-type tissue by means of rosette formation. **d**, A delaminating cell (yellow perimeter) after ultraviolet (UV) irradiation. **e**, Percentage midline delamination ($n = 3$ pupae) for control pupae and after DIAP1 overexpression. Error bars indicate s.d. **f**, Plots showing the area (A) of delaminating cells ($n = 25$) after they have lost two junctions (or one junction in the case of five-sided cells) as a fraction of their initial area (A_i). Cells above the dotted line delaminate by losing junctions; cells below the dotted line delaminate through the formation of rosette-like intermediates. **g**, Control and ultraviolet-irradiated tissues marked with E-cadherin–GFP and MyoII–Cherry (mCh). The cytoplasmic myosin II ring is indicated with arrows. In the ultraviolet-irradiated tissue the arrowheads indicate E-cadherin loss and junctional myosin II accumulation. Numbers refer to the time in minutes before delamination. Scale bars, 10 µm.

Supplementary Fig. 9). Moreover, this D2 process was actively induced by ultraviolet irradiation (Fig. 4d, f, g). To test whether D1 and/or D2 processes were triggered by dying cells in the wild-type notum, we then monitored cell behaviour in nota that overexpressed an inhibitor of apoptosis, DIAP1 (ref. 12). This led to a small but reproducible decrease in the overall rate of delamination as the result of a selective inhibition of D2-type delamination events (Fig. 4e, f and Supplementary Movie 6). Therefore, although a subset of cells are extruded from the notum as a direct consequence of cell death[13] by means of a D2-type process, the vast majority of cells leave crowded regions of the tissue while alive, by means of a series of stochastic neighbour exchange events (D1). These live delaminated cells then die in a process akin to anoikis, their nuclei becoming visibly condensed and pyknotic (Supplementary Fig. 10a) before they are cleared from underneath the epithelium by circulating macrophages (Supplementary Fig. 10b). We confirmed that death is a consequence not the cause of D1-type delamination events[14] by showing that midline cell delamination continued unabated in nota expressing RNAi targeting JNK, p53 or Flower (Supplementary Fig. 11) and after p35 expression (data not shown). Finally, we verified that only a subset of cells delaminated from the midline during the entire course of normal development, as expected for a stochastic process (Supplementary Fig. 12).

Taken together, these data identify a previously unknown two-step process of live-cell delamination, which contributes to the refinement of epithelial cell packing at the end of development. We show that this process of crowding-induced delamination can be recapitulated by

using a simple mechanical model of a epithelium in which cells compete for space that includes, first, stochastic junctional fluctuations that are capable of triggering neighbour exchange events, and, second, a final push that can remove cells with small apices from the tissue. Because many epithelia are both crowded and topologically active, we expect crowding-induced delamination to be a common process that buffers tissue growth to aid normal tissue homeostasis in a wide variety of systems. This study also reveals a potential mechanistic link between tissue hyperplasia and delamination, which may have important consequences for our understanding of cancer because it suggests that the spread of a primary epithelial tumour will be limited not by a switch from an epithelial to a mesenchymal state but simply by the tendency of delaminating cells to die[14].

METHODS SUMMARY

For this study, fluorescently marked *pnr-Gal4* pupae expressing different transgenes or RNAi constructs were imaged between 14 h and 26 h AP. Three or more animals were used for each experiment and, when data were quantified, significance was established with an unpaired *t*-test. For ultraviolet irradiation, pupae were dissected at 15 h AP and the exposed notum was irradiated with a Stratalinker 1800 crosslinker at $100 \, mJ \, cm^{-2}$, before live imaging. For laser ablation of single junctions at 14 h and 24 h AP, the tissue was imaged with 488-nm light from an Ar–Kr laser every 2 s and ablated with 730-nm multiphoton excitation from a Chameleon-XR Ti–Sapphire laser (AIM, Zeiss).

Full Methods and any associated references are available in the online version of the paper at www.nature.com/nature.

1. Hufnagel, L., Teleman, A. A., Rouault, H., Cohen, S. M. & Shraiman, B. I. On the mechanism of wing size determination in fly development. *Proc. Natl Acad. Sci. USA* **104**, 3835–3840 (2007).
2. Kafer, J., Hayashi, T., Maree, A. F., Carthew, R. W. & Graner, F. Cell adhesion and cortex contractility determine cell patterning in the *Drosophila* retina. *Proc. Natl Acad. Sci. USA* **104**, 18549–18554 (2007).
3. Farhadifar, R., Roper, J. C., Aigouy, B., Eaton, S. & Julicher, F. The influence of cell mechanics, cell–cell interactions, and proliferation on epithelial packing. *Curr. Biol.* **17**, 2095–2104 (2007).
4. Aegerter-Wilmsen, T. *et al.* Exploring the effects of mechanical feedback on epithelial topology. *Development* **137**, 499–506 (2010).
5. Cohen, M., Georgiou, M., Stevenson, N. L., Miodownik, M. & Baum, B. Dynamic filopodia transmit intermittent Delta–Notch signaling to drive pattern refinement during lateral inhibition. *Dev. Cell* **19**, 78–89 (2010).
6. Rosenblatt, J., Raff, M. C. & Cramer, L. P. An epithelial cell destined for apoptosis signals its neighbors to extrude it by an actin- and myosin-dependent mechanism. *Curr. Biol.* **11**, 1847–1857 (2001).
7. Toyama, Y., Peralta, X. G., Wells, A. R., Kiehart, D. P. & Edwards, G. S. Apoptotic force and tissue dynamics during *Drosophila* embryogenesis. *Science* **321**, 1683–1686 (2008).
8. Manjon, C., Sanchez-Herrero, E. & Suzanne, M. Sharp boundaries of Dpp signalling trigger local cell death required for *Drosophila* leg morphogenesis. *Nature Cell Biol.* **9**, 57–63 (2007).
9. Zeitlinger, J. & Bohmann, D. Thorax closure in *Drosophila*: involvement of Fos and the JNK pathway. *Development* **126**, 3947–3956 (1999).
10. Fristrom, D. The cellular basis of epithelial morphogenesis. A review. *Tissue Cell* **20**, 645–690 (1988).
11. Irvine, K. D. & Wieschaus, E. Cell intercalation during *Drosophila* germband extension and its regulation by pair-rule segmentation genes. *Development* **120**, 827–841 (1994).
12. Brand, A. H., Manoukian, A. S. & Perrimon, N. Ectopic expression in *Drosophila*. *Methods Cell Biol.* **44**, 635–654 (1994).
13. Koto, A., Kuranaga, E. & Miura, M. Apoptosis ensures spacing pattern formation of *Drosophila* sensory organs. *Curr. Biol.* **21**, 278–287 (2011).
14. Emoto, Y. Cellular aggregation facilitates anoikis in MDCK cells. *J. Physiol. Sci.* **58**, 371–380 (2008).

Supplementary Information is linked to the online version of the paper at www.nature.com/nature.

Author Contributions E.M. conducted the experiments detailed in the paper, aided by S.C. The laser ablation work was done with technical assistance from J.G. A.M. performed the theoretical analysis. T.D. oversaw the theoretical analysis. B.B. oversaw the experimental work.

METHODS

Fly stocks and genetics. The following stocks were used: *pnr-GAL4* (Bloomington:3039), *E-cadherin–GFP* (*ubi-DE-cad-GFP*)[15], *E-cadherin–GFP His-RFP* (III) (*ubi-DE-cad-GFP/CyO;His-RFP/TM6B*), *Act-5c-GAL4* (Bloomington: 25374), p110 overexpression (*w;UAS-myc-Dp110*)[16], DIAP1 overexpression (III) (*if/CyO;UAS-DIAP1*), Tsc1 and Tsc2 overexpression (III) (*hsFLP;;UAS-Tsc1,Tsc2*), *Resille::GFP*[17]. *E-cadherin–GFP* was crossed with the *pnr-GAL4* line (*ubi-DE-cad-GFP;pnr-GAL4/TM6B*) to drive gene or IR expression. For IR expression, males from each *UAS-IR* fly line were crossed with *Ecad–GFP; pnr-GAL4* virgin females. Crosses between *UAS-hairpin RNAi* males and *Ecadherin–GFP*; *pnr-GAL4* females were raised at 22 °C and shifted to 29 °C during larval stages. RNAi lines were used to silence the expression of the following genes: *cdc25* (ID17760), *fwe* (ID104993), *bsk* (ID34138), *pI3k* (ID38985), *pten* (ID35731), *r5 s* (ID27792), *warts* (ID9928). All RNAi lines came from the Vienna *Drosophila* RNAi Center (VDRC) library[18].

Live imaging and dissections. Live imaging[19] was performed by cutting a window in the pupal case attached to a slide with double-sided tape, and placing a coverslip carrying a drop of injection oil over the notum, supported by coverslips at either end. Nota were imaged from 14 h AP for 12 h during development. For stained tissues, nota from 16 h AP pupae were dissected in PBS for direct fixation in 4% formaldehyde for 20 min before being permeabilized with PBS containing 0.1% Triton X-100 (PBT). The nota were then stained for 2 h at 25 °C with 4′,6-diamidino-2-phenylindole (Sigma) for nuclei and Alexa-568 phalloidin (Invitrogen) for actin. The acquisition was performed with a Leica SP2 laser scanning confocal microscope with 40×/1.3 numerical aperture oil objective for both fixed and live-imaging experiments; three or more animals were used for each experiment and, when data were quantified, significance was established with an unpaired *t*-test in Excel.

Ultraviolet irradiation. Pupae were dissected at 15 h AP and the exposed notum was irradiated with a Stratalinker 1800 crosslinker at 100 mJ cm^{-2}, before live imaging.

Laser ablation. Single junctions were ablated in pupae at 14–16 h (early pupae) and 24–26 h (late pupae), using 730-nm multiphoton excitation from a Chameleon-XR Ti-Sapphire laser, under software control (AIM, Zeiss). A 3 × 3-pixel (pixel size 0.17 µm) region of the junction was irradiated at slow scan speed (pixel dwell time 2.56 µs) at 25% laser power, under software control. The power required to ablate junctions was determined empirically each time and was used in each experiment (AIM, Zeiss). Ablations were triggered during time-lapse imaging (every 2 s), using 488-nm light from an Ar–Kr laser coupled to a Zeiss 510NLO upright confocal microscope and a 40×/1.3 numerical aperture oil objective.

Image processing and analysis. The images presented were processed with ImageJ (http://rsb.info.nih.gov/ij/) and Adobe Photoshop CS (Adobe Systems, Inc.). Unless otherwise noted, images of the tissue represent maximum intensity *z*-projections, and sections were 0.9 µm apart. For laser ablation, the displacement of vertices was measured after a cut with the ImageJ Kymograph plugin. Statistics were calculated in each case on the basis of 15 junctions in 5 different pupae.

15. Oda, H. & Tsukita, S. Real-time imaging of cell–cell adherens junctions reveals that *Drosophila* mesoderm invagination begins with two phases of apical constriction of cells. *J. Cell Sci.* **114,** 493–501 (2001).

16. Leevers, S. J., Weinkove, D., MacDougall, L. K., Hafen, E. & Waterfield, M. D. The *Drosophila* phosphoinositide 3-kinase Dp110 promotes cell growth. *EMBO J.* **15,** 6584–6594 (1996).

17. Morin, X., Daneman, R., Zavortink, M. & Chia, W. A protein trap strategy to detect GFP-tagged proteins expressed from their endogenous loci in *Drosophila. Proc. Natl Acad. Sci. USA* **98,** 15050–15055 (2001).

18. Dietzl, G. *et al.* A genome-wide transgenic RNAi library for conditional gene inactivation in *Drosophila. Nature* **448,** 151–156 (2007).

19. Georgiou, M., Marinari, E., Burden, J. & Baum, B. Cdc42, Par6, and aPKC regulate Arp2/3-mediated endocytosis to control local adherens junction stability. *Curr. Biol.* **18,** 1631–1638 (2008).

LETTER

Crowding induces live cell extrusion to maintain homeostatic cell numbers in epithelia

George T. Eisenhoffer[1]*, Patrick D. Loftus[1]*, Masaaki Yoshigi[2], Hideo Otsuna[3], Chi–Bin Chien[3], Paul A. Morcos[4] & Jody Rosenblatt[1]

For an epithelium to provide a protective barrier, it must maintain homeostatic cell numbers by matching the number of dividing cells with the number of dying cells. Although compensatory cell division can be triggered by dying cells[1–3], it is unknown how cell death might relieve overcrowding due to proliferation. When we trigger apoptosis in epithelia, dying cells are extruded to preserve a functional barrier[4]. Extrusion occurs by cells destined to die signalling to surrounding epithelial cells to contract an actomyosin ring that squeezes the dying cell out[4–6]. However, it is not clear what drives cell death during normal homeostasis. Here we show in human, canine and zebrafish cells that overcrowding due to proliferation and migration induces extrusion of live cells to control epithelial cell numbers. Extrusion of live cells occurs at sites where the highest crowding occurs _in vivo_ and can be induced by experimentally overcrowding monolayers _in vitro_. Like apoptotic cell extrusion, live cell extrusion resulting from overcrowding also requires sphingosine 1-phosphate signalling and Rho-kinase-dependent myosin contraction, but is distinguished by signalling through stretch-activated channels. Moreover, disruption of a stretch-activated channel, Piezo1, in zebrafish prevents extrusion and leads to the formation of epithelial cell masses. Our findings reveal that during homeostatic turnover, growth and division of epithelial cells on a confined substratum cause overcrowding that leads to their extrusion and consequent death owing to the loss of survival factors. These results suggest that live cell extrusion could be a tumour-suppressive mechanism that prevents the accumulation of excess epithelial cells.

To examine how cells are eliminated during homeostasis, we immunostained human colon tissues, developing zebrafish epidermises, and cultured Madin–Darby canine kidney (MDCK) epithelial cells for active caspase-3 to identify apoptotic cells, and actin and DNA to highlight cell borders and extrusion[4,6]. Surprisingly, we found that predominantly caspase-negative cells extrude from the surfaces of colon epithelia (80%, $n = 46$ extruding cells), from zebrafish epidermis (88%, $n = 160$ extruding cells in three experiments), and from overgrown monolayers in culture (67%, $n = 300$ extruding cells in three experiments; Fig. 1a, b, d, e, g, h). By contrast, extrusions resulting from inducing apoptosis in zebrafish with G418 or cultured monolayers with ultraviolet-C were almost exclusively caspase-3 positive[6]. These findings suggest that during homeostasis and development, live rather than dead cells are eliminated by extrusion. Similar live cell extrusions have been observed during mammary gland involution[7]. Because these non-apoptotic _in vivo_ extrusions looked identical to apoptotic extrusion, we hypothesized that the extrusion pathway operates in two diverging manners: one to maintain homeostatic cell numbers in epithelia and the other to remove apoptotic/damaged cells.

When quantifying extrusion in both adult human colon and developing zebrafish epidermis, we noticed that extrusions occurred predominantly at the fin edges and colon surfaces, where cell densities were highest (1.7- and 1.8-fold higher than fin centre or crypt side

(Supplementary Fig. 1a, b), respectively, indicated by yellow cells in Fig. 1c, f). Extrusion zones were also more curved _in vivo_; yet, because they occurred most frequently in regions with higher cell density (1.8-fold) compared to proliferative regions in flat cell culture monolayers (Fig. 1i and Supplementary Fig. 1c), we decided to experimentally test if overcrowding strain could induce cells to extrude.

To simulate overcrowding observed _in vivo_, we grew MDCK cells to confluence on a silicone membrane stretched to 28% of its original length and then released it from stretch (Fig. 2a). Within 30 min after release, the number of cells per $100 \, \mu m^2$ increased 1.3-fold, from 112 ± 5 to 144 ± 4 (Fig. 2b–f). ZO-1 and β-catenin staining confirmed that tight and adherens junctions were still intact and that the average cell diameter had decreased by 30 min after crowding (Fig. 2g–i and Supplementary Fig. 2). Moreover, crowded monolayers maintained adhesion to Cy-5-labelled fibronectin-coated membranes (Fig. 2j). By 6 h after crowding, the number of cells per field equilibrated to pre-release levels (110 ± 10 cells per $100 \, \mu m^2$, see Fig. 2e, f), indicating that MDCK epithelia eliminate cells to achieve homeostatic cell numbers.
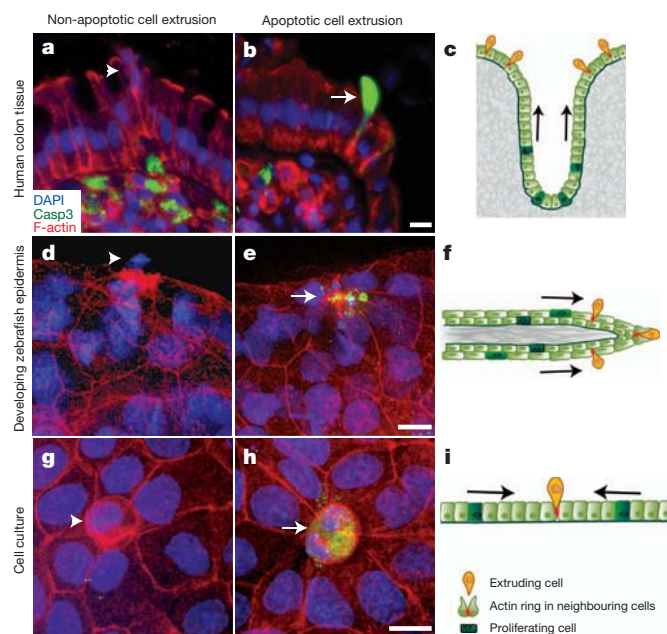

Figure 1 | Both apoptotic and non-apoptotic epithelial cells extrude at locations of high crowding during homeostasis and development.
a, **b**, **d**, **e**, **g**, **h**, Non-apoptotic (caspase-negative, arrowheads) and apoptotic (caspase-positive, arrows) extrusions at the surface of human colon epithelia (**a**, **b**), zebrafish epidermis (**d**, **e**), and confluent MDCK monolayers (**g**, **h**). **c**, **f**, **i**, Extrusions typically occur at sites of high crowding (indicated by yellow cells). Arrows indicate direction of force from mitoses and migration. Scale bars, 10 μm.

[1]Department of Oncological Sciences, Huntsman Cancer Institute, University of Utah, 2000 Circle of Hope Drive, Salt Lake City, Utah 84112, USA. [2]Department of Pediatrics, University of Utah, 295 Chipeta Way RM 2S010, Salt Lake City, Utah 84108, USA. [3]Department of Neurobiology and Anatomy, University of Utah, 401 MREB, 20N 1900E, Salt Lake City, Utah 84132, USA. [4]Gene Tools, LLC, 1001 Summerton Way, Philmath, Oregon 97370, USA.
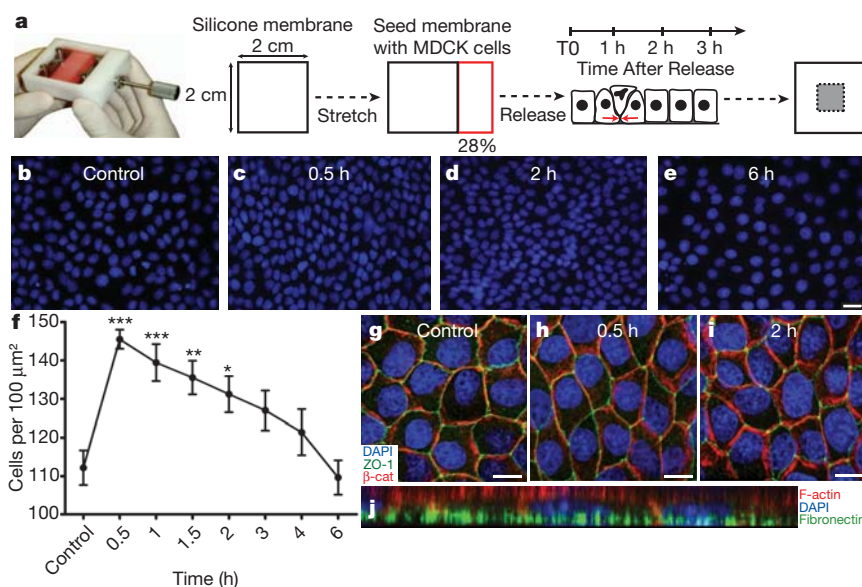*These authors contributed equally to this work.

Figure 2 | Characterization of experimental overcrowding. a, Experimental design for overcrowding monolayers grown on stretched matrix. Only cells in the grey area (right) were analysed to ensure a homogeneous strain field. **b–f,** Images of the nuclei of control unstretched monolayers and monolayers 0.5–6 h after overcrowding (**b–e**) were quantified in **f. f,** Mean number of nuclei per field are plotted, error bars represent s.e.m. **g–i,** Monolayers at 0.5 and 2 h after release show that adherens and tight junctions maintain integrity after overcrowding, as compared to control. β-cat, β-catenin. **j,** Monolayer stained for actin and DNA at 2 h after release on Cy5-labelled fibronectin shows that contacts to substratum are maintained. Scale bars, 10 μm. ***$P < 0.0005$, **$P < 0.005$, *$P < 0.05$.
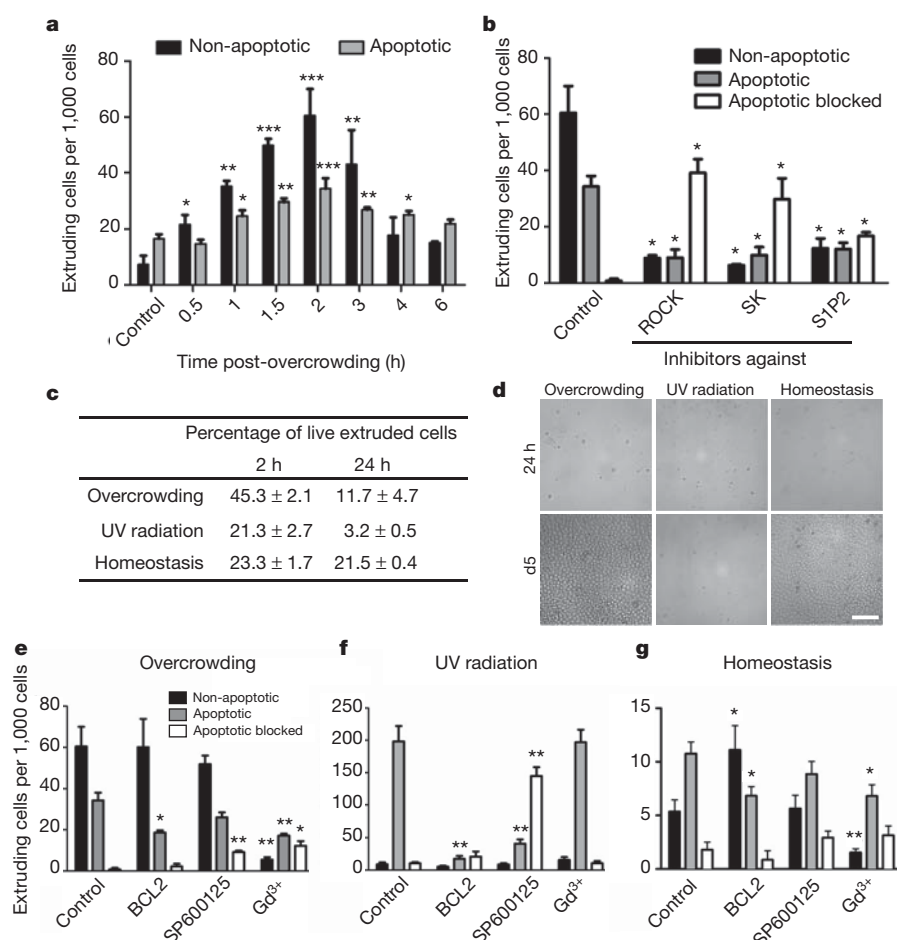
Figure 3 | Overcrowding MDCK monolayers promotes extrusion of non-apoptotic cells. a, Quantification of live and apoptotic extruding cells 2 h after overcrowding. **b,** Live cell extrusion requires ROCK, sphingosine kinase (SK) and S1P$_2$. **c,** Cell viability 2 or 24 h after extrusion. UV, ultraviolet. **d,** Growth of extruded cells collected at 2 h post-crowding after 24 h and 5 days (d5). **e–g,** Gd^{3+} inhibits both overcrowding-induced extrusion (**e**) and homeostatic extrusion (**g**) whereas BCL2 overexpression and JNK inhibition only affect ultraviolet-C-induced apoptotic extrusion (**f**). $n \leq 7$ independent experiments, mean ± s.e.m. Scale bars, 100 μm. ***$P < 0.0005$, **$P < 0.005$, *$P < 0.05$.

Immunostaining for actin and active caspase-3 showed that overcrowding induced predominantly non-apoptotic extrusion, as seen during homeostasis (Fig. 3a). Filming crowded MDCK monolayers expressing Lifeact–green fluorescent protein (GFP)[8] to highlight F-actin, or the active caspase-3 indicator NucView, confirmed that live cells are extruded by contracting actin rings (Supplementary Movie 1 and Supplementary Fig. 4). The numbers of live extruding cells eventually decreased by 6 h after overcrowding, concordantly with the decrease in cell densities. The percentage of non-apoptotic extrusion also correlated to the percentage of crowding (Supplementary Fig. 3).

To determine whether live cell extrusion required the same factors that control apoptotic cell extrusion, we blocked signals required for extrusion during experimental overcrowding. We previously identified sphingosine-1-phosphate (S1P) as the signal apoptotic cells produce to activate the S1P receptor 2 (S1P$_2$), which triggers Rho-mediated contraction to squeeze the dying cells out[5]. Inhibiting Rho kinase (ROCK) or S1P signalling markedly decreased the percentages of both non-apoptotic and apoptotic cell extrusions (Fig. 3b). Although it was not possible to score non-apoptotic cells blocked from extrusion, as they look like any other cells within the monolayer, the significant decreases in the percentages of non-apoptotic cell extrusion indicated that live cell extrusion, like apoptotic cell extrusion, requires S1P signalling through ROCK-mediated actomyosin contraction.

To assess the fate of overcrowding-induced extruded cells, we analysed their viability using flow cytometry and their ability to survive and proliferate by plating them on new substrata. After collecting extruded cells from the medium 2 h after crowding, $45.3 \pm 2.1\%$ were alive, whereas only $21.3 \pm 2.7\%$ were alive after ultraviolet-induced apoptotic extrusion (Fig. 3c and Supplementary Fig. 5a). Overcrowding and homeostatically extruded cells were able to proliferate into confluent monolayers, whereas those collected from apoptosis-induced extrusion were not (Fig. 3d). If, however, cells extruded from homeostatic or post-crowded monolayers were collected after 24 h, most cells died instead of proliferating after re-plating (Supplementary Fig. 5b), suggesting that extruded cells typically die unless a new substratum is provided. Presumably, during *in vivo* homeostasis most extruded cells die from anoikis, apoptosis due to loss of survival signals from engagement with the underlying matrix[9–11].

We next investigated which signals trigger live cell extrusion during homeostasis or overcrowding. We previously found that overexpression of BCL2 inhibits both apoptosis and extrusion in response to apoptotic stimuli[12] (Fig. 3f); however, BCL2 overexpression did not block live cell extrusion during homeostasis or after overcrowding (Figs 3e, g). To investigate signals that might regulate live cell extrusion after overcrowding, we tested two candidates that are activated by cell stress: the carboxy-terminal JUN kinase (JNK; also known as MAPK8)[13] and stretch-activated channels[14,15]. JNK inhibitor blocked apoptotic extrusion in response to ultraviolet-C but not live cell extrusion after overcrowding or homeostatic cell turnover (Figs 3e–g). In contrast, we found that inhibiting stretch-activated ion channels with gadolinium (Gd^{3+})[16,17] significantly reduced the percentage of both apoptotic and non-apoptotic extrusion events after overcrowding or during epithelial homeostasis, yet had no effect on apoptotic cell extrusion in response to ultraviolet light (Figs 3e–g). When cell extrusion is blocked by Gd^{3+}, the number of cells per 100 μm^2 remains high at 2 h after crowding (167 ± 12) compared to control crowded cells (112 ± 5), demonstrating that extrusion relieves overcrowded cell densities. Thus, whereas BCL2 and JNK control apoptosis-induced extrusion, stretch-activated signalling controls live cell extrusion during homeostasis that is induced by overcrowding, presumably upstream of S1P signalling (Fig. 4l).

If stretch-activated signalling controls extrusion-mediated homeostatic cell turnover, blocking this pathway *in vivo* should lead to accumulation of excess epithelial cells. By immunostaining and filming the epidermis of developing zebrafish with *Tg(cldnb:lynGFP)*[18], we found that cells proliferate at 37 h post-fertilization (hpf) and migrate
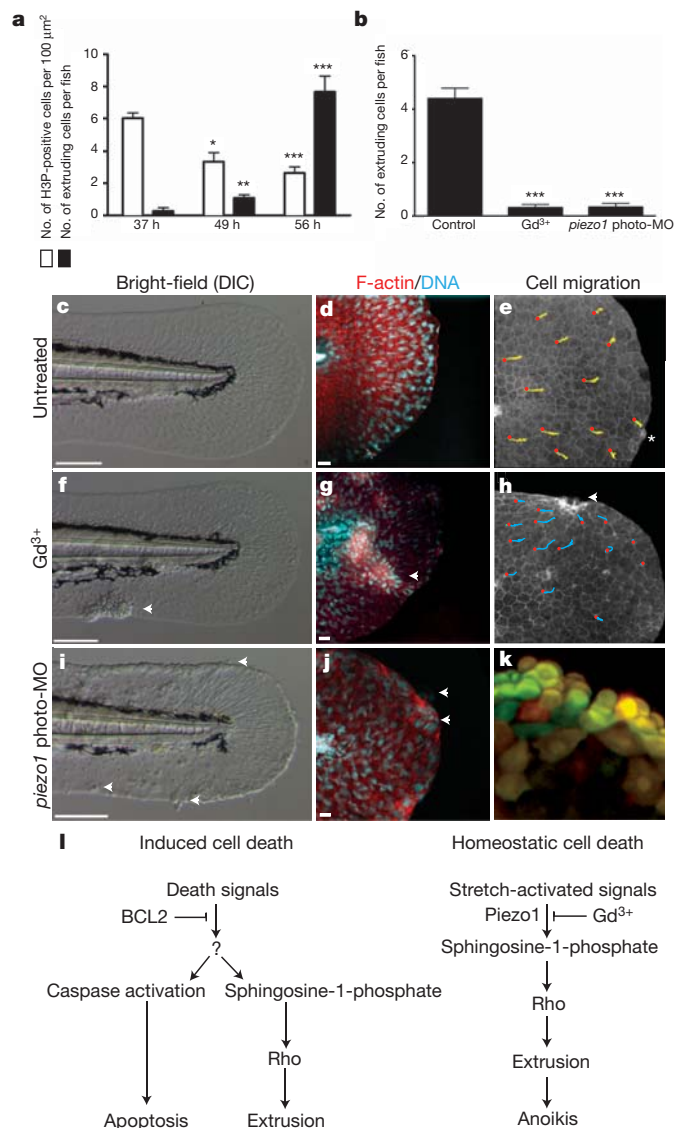

Figure 4 | Disrupting the stretch-activated channel Piezo1 *in vivo* blocks live cell extrusion and causes epithelial mass formation. a, Proliferation and extrusion rates during zebrafish tail fin development. H3P, phospho-histone 3. **b**, Gd^{3+} treatment and *piezo1* photo-morpholino (photo-MO) block extrusion ($n = 15$–17 embryos from three independent experiments, mean $\pm$ s.e.m.). **c, d, f, g, i, j**, Bright-field and confocal projections of untreated (**c, d**), Gd^{3+}-treated (**f, g**), and *piezo1* photo-morpholino knockdown (**i, j**) in 60 hpf developing zebrafish. DIC, differential interference contrast. **e, h**, Tracks from red circle mark the movement of individual epithelial cells in control and Gd^{3+}-treated *Tg(cldnb:lynGFP)* developing zebrafish. **k**, Epidermal cell mass from a *piezo1* photo-morpholino knockdown in Kaede zebrafish, where yellow cells are photo-converted. **l**, Model of induced cell death versus homeostatic cell death. Arrowheads denote cell accumulations and asterisk an extrusion. Scale bars in **c, f, i**, 100 μm; in **d, g, j**, 10 μm. ***$P < 0.0005$, **$P < 0.005$, *$P < 0.05$.

to the fin edges between 48–59 hpf, where they extrude at 56–60 hpf (Fig. 4a, c–e, Supplementary Fig. 6 and Supplementary Movie 2). Treating 32-hpf zebrafish with Gd^{3+} blocked homeostatic cell extrusion and resulted in epidermal cell mass formation at the fin edges, the number of which was dependent on Gd^{3+} concentration (Fig. 4b, f–h, Supplementary Fig. 7 and Supplementary Movie 3). Live imaging of Gd^{3+}-treated *Tg(cldnb:lynGFP)* zebrafish revealed that the cell masses formed at zones of convergence, where cells failed to extrude (Fig. 4h and Supplementary Movie 4).

By knocking down candidate stretch-activated channels in zebrafish with morpholino oligonucleotides, we found that live cell extrusion

requires the channel Piezo1 (ref. 14). To prevent developmental defects from early knockdown (Supplementary Fig. 8a, b), we used a photo-cleavable morpholino (photo-morpholino) to knockdown Piezo1 at 30 hpf (Supplementary Fig. 8c, d)[19]. By 60 hpf, Piezo1 morphants, like Gd^{3+}-treated fish, could not extrude cells and developed epidermal masses at the fin edges and other sites of tissue strain (Figs 4b, i–k and Supplementary Figs 9 and 10), indicating that Piezo1 regulates extrusion to maintain homeostatic epithelial cell numbers in vivo.

As extrusion seems to control cell numbers during homeostasis, we predict that alterations in extrusion could lead to various epithelial pathologies. Aberrant signalling or tensions that block extrusion could lead to formation of cell masses, as those produced in zebrafish when stretch-activated channels are disrupted. Furthermore, these cell masses may set the stage for tumorigenesis by allowing retention of oncogenic or defective cells. In support of this, we found increased cell densities and no clearly identified extrusions in colon polyp sections compared to control sections (Supplementary Fig. 11). Conversely, hyper-contraction of bronchial epithelia following bronchoconstriction in asthmatics could lead to excessive extrusion and characteristic epithelial denuding. The resulting poor barrier could lead to the increased inflammation and infection seen in asthmatics[20–22]. Whereas mathematical models have suggested that mechanical forces could control tissue homeostasis[23], our results show that cell division and migration within epithelia cause overcrowding strain, which induces live cells to extrude and later die. Thus, homeostatic live cell extrusion provides the previously missing link between proliferation and epithelial cell death (Fig. 1c, f, i).

METHODS SUMMARY

All cell cultures, cell staining, ultraviolet irradiation and imaging were done using MDCK cells, as previously described[6]. Cells were treated with 10 μM SKI-II (Calbiochem), 10 μM JTE-013 (Tocris Bioscience), 10 μM SP600125, 10 μM Gd^{3+}, (both Sigma-Aldrich), or 1% DMSO as a control. Flow cytometry was done using a Beckman-Dickinson FACScan after treating cells with 1 μg per 250 μl of propidium iodide (Sigma-Aldrich). The Huntsman Cancer Institute Tissue Resource and Applications Core provided human colon sections. Developing wild-type AB zebrafish were treated with 10 mM Gd^{3+} at 28.5 °C from 32 hpf until 60 hpf, and immunostained as described previously[6], or filmed with a Nikon spinning disc confocal microscope using Andor software. The antisense morpholino oligonucleotides and photo-morpholino oligonucleotides were acquired from Gene Tools, LLC. For the photo-morpholino experiments, the translation blocking antisense morpholino was mixed at a 1:1 molar ratio with a 25 bp sense photo-morpholino and injected into 1–2-cell-stage wild-type AB or $Et(Gal4-VP16)^{zc1044a};Tg(UAS-E1b:Kaede)^{s1999t}$ zebrafish embryos. At 28–32 hpf, embryos were exposed to 350 nm light for 20 s to release the caging sense morpholino, then fixed and immunostained at 60 hpf.

Full Methods and any associated references are available in the online version of the paper at www.nature.com/nature.

1. Fan, Y. & Bergmann, A. Apoptosis-induced compensatory proliferation. The Cell is dead. Long live the Cell! *Trends Cell Biol.* **18,** 467–473 (2008).
2. Fan, Y. & Bergmann, A. Distinct mechanisms of apoptosis-induced compensatory proliferation in proliferating and differentiating tissues in the *Drosophila* eye. *Dev. Cell* **14,** 399–410 (2008).
3. Ryoo, H. D., Gorenc, T. & Steller, H. Apoptotic cells can induce compensatory cell proliferation through the JNK and the Wingless signaling pathways. *Dev. Cell* **7,** 491–501 (2004).
4. Rosenblatt, J., Raff, M. C. & Cramer, L. P. An epithelial cell destined for apoptosis signals its neighbors to extrude it by an actin- and myosin-dependent mechanism. *Curr. Biol.* **11,** 1847–1857 (2001).
5. Gu, Y., Forostyan, T., Sabbadini, R. & Rosenblatt, J. Epithelial cell extrusion requires the sphingosine-1-phosphate receptor 2 pathway. *J. Cell Biol.* **193,** 667–676 (2011).
6. Slattum, G., McGee, K. M. & Rosenblatt, J. P115 RhoGEF and microtubules decide the direction apoptotic cells extrude from an epithelium. *J. Cell Biol.* **186,** 693–702 (2009).
7. Monks, J., Smith-Steinhart, C., Kruk, E. R., Fadok, V. A. & Henson, P. M. Epithelial cells remove apoptotic epithelial cells during post-lactation involution of the mouse mammary gland. *Biol. Reprod.* **78,** 586–594 (2008).
8. Riedl, J. et al. Lifeact: a versatile marker to visualize F-actin. *Nature Methods* **5,** 605–607 (2008).
9. Frisch, S. M. & Francis, H. Disruption of epithelial cell-matrix interactions induces apoptosis. *J. Cell Biol.* **124,** 619–626 (1994).
10. Gilmore, A. P. Anoikis. *Cell Death Differ.* **12** (suppl. 2), 1473–1477 (2005).
11. Reddig, P. J. & Juliano, R. L. Clinging to life: cell to matrix adhesion and cell survival. *Cancer Metastasis Rev.* **24,** 425–439 (2005).
12. Andrade, D. & Rosenblatt, J. Apoptotic regulation of epithelial cellular extrusion. *Apoptosis* **16,** 491–501 (2011).
13. Tournier, C. et al. Requirement of JNK for stress-induced activation of the cytochrome c-mediated death pathway. *Science* **288,** 870–874 (2000).
14. Coste, B. et al. Piezo1 and Piezo2 are essential components of distinct mechanically activated cation channels. *Science* **330,** 55–60 (2010).
15. Olsen, S. M., Stover, J. D. & Nagatomi, J. Examining the role of mechanosensitive ion channels in pressure mechanotransduction in rat bladder urothelial cells. *Ann. Biomed. Eng.* **39,** 688–697 (2011).
16. Bhattacharya, M. R. et al. Radial stretch reveals distinct populations of mechanosensitive mammalian somatosensory neurons. *Proc. Natl Acad. Sci. USA* **105,** 20015–20020 (2008).
17. Yang, X. C. & Sachs, F. Block of stretch-activated ion channels in *Xenopus* oocytes by gadolinium and calcium ions. *Science* **243,** 1068–1071 (1989).
18. Haas, P. & Gilmour, D. Chemokine signaling mediates self-organizing tissue migration in the zebrafish lateral line. *Dev. Cell* **10,** 673–680 (2006).
19. Tallafuss, A. et al. Turning gene function ON and OFF using sense- and antisense-photo-morpholinos in zebrafish. *Development.* (in the press).
20. Holgate, S. T. The airway epithelium is central to the pathogenesis of asthma. *Allergol. Int.* **57,** 1–10 (2008).
21. Knight, D. A. & Holgate, S. T. The airway epithelium: structural and functional properties in health and disease. *Respirology* **8,** 432–446 (2003).
22. Swindle, E. J., Collins, J. E. & Davies, D. E. Breakdown in epithelial barrier function in patients with asthma: identification of novel therapeutic approaches. *J. Allergy Clin. Immunol.* **124,** 23–34,–quiz 35–36 (2009).
23. Shraiman, B. I. Mechanical feedback as a possible regulator of tissue growth. *Proc. Natl Acad. Sci. USA* **102,** 3318–3323 (2005).

METHODS

Cell culture and overcrowding assays. MDCK II cells were grown as described[6]. A custom-designed Teflon chamber was fabricated to culture cells on flexible silicone membranes in stretched states (2×2 cm, 0.5 mm thickness)[24,25]. Prior to cell seeding, 2×2 cm silicone membranes were stretched and coated with $5 \mu g\,ml^{-1}$ fibronectin (BD Biosciences) at $4\,^\circ C$ for 24 h. To stretch membranes with our device, one edge of the silicone membrane was clamped in place, while the other side was clamped to a movable shaft, which moves through a Teflon chamber with a sealing gasket. The movable shaft was pulled out to lengths representing 11%, 22% and 28% strain. 750,000 cells ml^{-1} were plated onto the 2×2 cm silicone matrices in a stretched state in the device or in a culture dish (for non-stretched controls) and grown to confluence, then released from their stretched states, thereby crowding cells in monolayer. Epithelial monolayers were fixed and stained or filmed using a Nikon 90i wide-field fluorescence microscope. BCL2-overexpressing cell lines are described previously[12].

Drug and ultraviolet assays. Confluent MDCK monolayers on silicone membranes were pre-treated with SP600125 JNK inhibitor at 10, 50 and $100 \mu M$ or 10, 50 and $100 \mu M$ gadolinium III chloride (Gd^{3+}) for 30 min at $37\,^\circ C$. Apoptosis was induced by exposing monolayers to $1,200 \mu J\,cm^{-2}$ ultraviolet (254 nm) irradiation in a UV series II (Spectroline). Cells were fixed and stained from 1–6 h post-ultraviolet treatment depending on the experiment. The minimal drug concentrations ($10 \mu M$) established in the ultraviolet-induced extrusion assay were used in the overcrowding and homeostatic assays. For testing extrusion following overcrowding, chambers were pretreated with $10 \mu M$ JTE-013 (Tocris Bioscience), $10 \mu M$ SKI II (Calbiochem) or $10 \mu M$ Y-27632 (Tocris) for 30 min before overcrowding until 2 h after crowding.

Cell immunostaining. Fixation and staining of MDCK cells for actin, DNA, active caspase-3, ZO-1 and β-catenin was carried out as previously described[6]. Fibronectin was labelled with an Amersham Cy5 Ab Labelling Kit (GE Healthcare).

Live cell imaging. Standard MDCK cells or Lifact–GFP-expressing[8] MDCK cells were grown to confluent monolayers and imaged on a Nikon 90i wide field fluorescent microscope with the stage kept at $37\,^\circ C$. For the NucView experiments, cells were incubated with the activated caspase-3 indicator NucView at 1:200 for 30 min before imaging.

Colon sections. Human colon tissue samples were fixed, imbedded in paraffin, and cut into 10 μm sections by the Huntsman Cancer Institute Tissue Resource and Applications Core. The sections were deparaffinised and rehydrated by incubating in citrus clearing solvent (CCS; Richard Allen Scientific), 100%, 95%, 80%, 70% ethanol, and PBS. Antigens were retrieved by heating the slides in 10 mM sodium citrate at $95\,^\circ C$ for 20 min, then rinsed three times with PBS, blocked with 5% BSA/0.5% Tween-20 in PBS for 24 h, and incubated overnight with active caspase-3 antibody, rinsed five times with PBS, incubated in Alexa-488 anti-rabbit antibody, $1 \mu g\,ml^{-1}$ Hoechst, and Alexa-568 anti-actin antibody for 2 h, rinsed three times in PBS, and mounted in Prolong Gold (Invitrogen).

Microscopy. Images were captured on a CTR6000 microscope (Leica) with a $\times 63$ oil lens using a Micromax charge-coupled device camera (Roper Scientific) or on a Nikon Eclipse TE300 inverted microscope converted for spinning disc confocal microscopy (Andor Technologies) using a $\times 20$ or $\times 60$ plan fluor 0.95 oil lens with an electron-multiplied cooled CCD camera $1,000 \times 1,000$, 8×8 mm^2 driven by the IQ software (Andor Technologies). Image J was used to stack 8–10 consecutive 1 μm confocal sections into Z series, which were then colour-combined and reconstructed into a three-dimensional image using Metamorph (GE Healthcare). IP Lab 4.0.8 s and Image J software were used to analyse percentages of apoptosis and extrusion. For quantification of extrusion in tissue culture, extruding cells were manually scored as non-apoptotic extruding, apoptotic extruding, or blocked apoptotic extrusions based on the presence of an actin ring and caspase-3 staining in 10,000 monolayer cells.

Statistical analyses. Statistical analysis was done on at least four independent experiments for the overcrowding control and time analysis. Three separate assays were used for drug treatments and for FACS analysis. The error bars in all figures are s.e.m. All P values were determined from a two-sided unpaired Student's t-test using GraphPad Prism software.

FACS and proliferation analysis. Confluent homoeostatic, ultraviolet, and overcrowding monolayers were rinsed three times with PBS to remove any previous cells in suspension. The media was replaced and collected at each denoted analysis time. Media was collected and centrifuged at $1,458g$ in a Damon/IEC Division Clinical Centrifuge for 1 min. The cells were resuspended in 250 μl of PBS containing $4 \mu g\,ml^{-1}$ propidium iodide and analysed by FACS. Samples were analysed on a Beckman Dickinson FACScan and 50–1,000 cells were analysed for propidium iodide fluorescence at each condition. For proliferation analysis, pelleted cells were instead re-plated in a 96-well dish and representative pictures

were taken at 24 h and 5 days after re-plating. Results are from three independent experiments.

Zebrafish care and maintenance. Adult zebrafish were maintained under standard laboratory conditions, with a regular light/dark cycle of 14 h light and 10 h of darkness. Embryos were collected and raised in E3 embryo medium at $28.5\,^\circ C$ and staged as previously described[26]. The Institutional Animal Care and Use Committee (IACUC) at the University of Utah (Animal Welfare Assurance no. 10-07017) have approved all procedures performed in this protocol using the zebrafish *Danio rerio*.

Zebrafish drug treatments. Zebrafish embryos were dechorionated at 24 hpf. At 32 hpf approximately 50–100 embryos were transferred to dishes containing E3 embryo medium with or without (control) 10 mM Gd^{3+} and allowed to develop at $28.5\,^\circ C$ until 60 hpf, when the animals were either imaged live or fixed for immunostaining.

Zebrafish immunostaining. Developing zebrafish larvae were fixed in 4% formaldehyde for 1–2 h at room temperature ($20\,^\circ C$) or overnight at $4\,^\circ C$. Fixed specimens were then permeablized by rinses with PBSTx (0.5%) and incubated in blocking buffer (1% DMSO, $2 mg\,ml^{-1}$ BSA, 0.5% Triton X-100 and 10% goat serum in PBS) for 2 h. Specimens were then incubated overnight in primary antibodies for phospho-histone H3 (H3P; Abcam, 1:500) or activated caspase-3 (BD Pharmigen, 1:700). Samples were subsequently washed six times with PBSTx and then incubated in blocking buffer for 2 h before incubation with the appropriate secondary antibodies or Alexa-phalloidin (488/568/647) (Invitrogen). After incubation with secondary antibodies or Alexa-phalloidin, the specimens were rinsed five times with PBSTx, incubated with DAPI (1:1,000) for 15 min, rinsed once more and then mounted in Prolong Gold. Depending on the situation, either whole specimens or only tail fragments (from the yolk extension back) were mounted for imaging. For quantification of H3P-positive cells, the region from the cloaca back to the edge of the tail fin was quantified.

Zebrafish imaging. Developing zebrafish were immunostained as described previously[6] and imaged with either the wide-field fluorescent microscope or a spinning disc confocal microscope, described above. For live imaging, wild-type or Gd^{3+}-treated developing *Tg(cldnb:lynGFP)* zebrafish, a gift from T. Piotrowski, were anaesthetized with 0.02% tricaine in E3, mounted in 1% low melt agarose and imaged on a spinning disc confocal microscope using a $\times 20$ objective, capturing a z-series every 2 min for 3–6 h. Manual tracking of individual cells was performed using Metamorph.

Morpholino antisense oligonucleotide knockdown of Piezo1. All of the morpholino oligonucleotides and photo-morpholino oligonucleotides used in this study were acquired from Gene Tools, LLC. Developing zebrafish embryos were injected with 2–4 ng of a standard translation blocking antisense morpholino oligonucleotide directed against the 5′ untranslated region (UTR) of *piezo1* (accesssion XM_691263) at the 1–2-cell stage and then allowed to develop at $28.5\,^\circ C$. For the photo-cleavable morpholino experiments, the translation blocking antisense morpholino (TBMO) was mixed at a 1:1 molar ratio with a sense-photo morpholino, with a 4 bp mismatch around the photo-linker (see Supplementary Fig. 8c for schematic of strategy) and then injected into 1–2-cell-stage wild-type AB or $Et(Gal4\text{-}VP16)^{zc1044a};Tg(UAS\text{-}E1b:Kaede)^{s1999t}$ embryos. At 28–32 hpf, the developing embryos were then exposed to 350 nm light for 20 s using a $\times 10$ objective on a Nikon 90i wide-field fluorescent microscope to activate the morpholino. Some injected embryos were not converted as a control for 'leakiness' of the sense photo-morpholino. Likewise, some wild-type or Kaede-expressing embryos that were not injected were exposed to 350 nm light to ensure photo-conversion did not cause any adverse effects. Morpholinos: FAM38A 5′ UTR antisense morpholino oligonucleotide: GAGCGACACTTCCACTCACATT CCT; FAM38A 5′ UTR sense photo-morpholino oligonucleotide: AGGAAT GTGAaxttAGTGTCGCTC.

Western blot analyses of Piezo1. *piezo1* TBMO injected animals ($n = 15$–20) were collected at 28 hpf and homogenized in lysis buffer, boiled at $85\,^\circ C$ for 5 min, spun down and the supernatant collected. A Bradford assay was performed to assess protein concentration. 10–15 μg of protein was run out on a 3–8% Tris-Acetate gel at 150 V for 1 h. Detection was performed with an anti-Piezo1 antibody (Proteintech catalogue no. 15939-1-AP) using standard ECL (enhanced chemi-luminescence) methods. HC11, a mammary epithelial cell line, was used as a control for protein levels in mammalian tissues. Piezo1 protein levels are presented relative to the α-tubulin loading control. Quantification of the scanned blot was performed using Image J.

Kaede expression in the zebrafish embryonic epidermis. To generate the $Et(Gal4\text{-}VP16;myl7:GFP)^{zc1044a}$ enhancer-trap line, a plasmid along with *tol2* mRNA was injected into 1-cell-stage developing zebrafish embryos. The potential founders were then crossed to $Tg(UAS\text{-}E1b:Kaede)^{s1999t}$ (ref. 27) and subsequently identified by Kaede expression. The identified F1 transgenic embryos were then

imaged at 2 and 5 days post-fertilization for identification and characterization of epithelial-specific expression patterns.

24. Yoshigi, M., Clark, E. B. & Yost, H. J. Quantification of stretch-induced cytoskeletal remodeling in vascular endothelial cells by image processing. *Cytometry A* **55A,** 109–118 (2003).

25. Yoshigi, M., Hoffman, L. M., Jensen, C. C., Yost, H. J. & Beckerle, M. C. Mechanical force mobilizes zyxin from focal adhesions to actin filaments and regulates cytoskeletal reinforcement. *J. Cell Biol.* **171,** 209–215 (2005).

26. Kimmel, C. B., Ballard, W. W., Kimmel, S. R., Ullmann, B. & Schilling, T. F. Stages of embryonic development of the zebrafish. *Dev. Dyn.* **203,** 253–310 (1995).

27. Davison, J. M. *et al.* Transactivation from Gal4-VP16 transgenic insertions for tissue-specific cell labelling and ablation in zebrafish. *Dev. Biol.* **304,** 811–824 (2007).

CORRECTIONS & AMENDMENTS

Corrigendum: DNA–binding factors shape the mouse methylome at distal regulatory regions

Michael B. Stadler, Rabih Murr, Lukas Burger, Robert Ivanek, Florian Lienert, Anne Schöler, Erik van Nimwegen, Christiane Wirbelauer, Edward J. Oakeley, Dimos Gaidatzis, Vijay K. Tiwari & Dirk Schübeler

In the original version of this Article Erik van Nimwegen (Biozentrum of the University of Basel and Swiss Institute of Bioinformatics, Klingelbergstrasse 50-70, CH 4056 Basel, Switzerland) was inadvertently omitted from the author list. In the 'Author contribution' section the sentence beginning "Bioinformatic and statistical analyses..." should read "Bioinformatic and statistical analyses were conceived and conducted by M.B.S., L.B., R.I. and E.v.N." In addition, in the Supplementary Information section 'Unsupervised Segmentation of CpG Methylome', the HMM emission means were given as percentages instead of fractions, contained a typo in the third variance parameter, and should read as follows: "Emission probabilities of HMM states were modelled as Gaussian distributions with means 0.8, 0.28, 0.03 and variances 0.01, 0.005, 0.0026...". The PDF and HTML versions of this paper have been corrected, and the Supplementary Information has been replaced.

CAREERS

TECHNOLOGY

A lab app for that

Having a mobile device can save researchers a huge amount of time. It can also mean that they never switch off.

BY KENDALL POWELL

Phuong Pham's smartphone has given her more than just easy access to contacts, the Internet and social media. It has, she says, shaved months off her research projects. An epidemiologist at the Harvard Humanitarian Initiative in Cambridge, Massachusetts, Pham no longer has to lug reams of paper containing sensitive data into and out of conflict-ridden areas, and her data entry has been transformed. "We used to collect 1,000 10-page interviews, then manually enter them into a computer, doing double data-entry to avoid errors," she says. Now, she and her team collect the data directly on their phones and simply upload them to a secure server every night.

Like millions of other users, Pham uses her smartphone to improve her daily efficiency by checking her calendar, task lists and e-mail on the go. But researchers can also now use smartphones and tablets to keep tabs on the scientific literature, track their experiments remotely and stay in contact with laboratory members. More than just mini-computers,

they have become digital notebooks that can be used at the bench and in the field. With several applications, or apps, particularly suited to researchers, gadget gurus say that mobile devices are much more likely to foster productivity than procrastination (see table).

NO MORE FILING CABINETS

Scientists deal with numerous manuscripts, and mobile devices allow them to read papers wherever they might be. Jaime Carvajal, a developmental biologist at the Andalusian Centre for Developmental Biology in Seville, Spain, says that he will sit in an airport lounge, in the cafeteria or in the living room and pick up his iPad just "as you would grab a journal to read".

Brenton Graveley, a molecular biologist at the University of Connecticut Health Center in Farmington, stores and organizes his PDFs using the app 'Papers', which also has a built-in PubMed search function and bibliography features, and is searchable by keyword, author name and journal title. The app allows him to read articles on his iPad and use the touchscreen to highlight text or make notes in the margins, then e-mail that annotated version to colleagues. Like many other apps, Papers can be synchronized among devices, so Graveley always has access to the most current version of his library. He says that it is easier to upload old literature into Papers than to look for it in his filing cabinet. And having his whole library searchable and at his fingertips meant that he could get rid of reams of paper. "I recycled thousands of hard copies of papers I had collected since I was a graduate student," he says. "It felt liberating."

Some researchers use the app 'GoodReader' for reading, marking up and e-mailing huge documents, such as doctoral theses, on their mobile devices. Many also use the free 'PubSearch' app for searching the PubMed database on the go and 'BioGene', which is also free, to search for the ID number and other information about a particular gene. But apps can do more than just organize information; they can help researchers to decide which information is likely to be worth their time. For example, the American Chemical Society in Washington DC has created the app ACS Mobile to send subscribers the most up-to-date research published in its 39 journals. "It's a very convenient way to keep up with the literature because you use bits of spare time to read the abstracts," says Eugenio Vázquez, an organic chemist at the University of Santiago de Compostela ▶

M. WOOD/BO VIRKELYST JENSEN/ADDSOUL DESIGN STUDIO

Postdoc Miguel García Toscano uses his iPhone app to look up DNA amplification reactions.

▶ in Spain. Vázquez says that he would rather spend his transit time perusing papers than playing games. Similar apps from other journals are replacing e-mail alerts and the need to check individual websites.

Some scientists use their mobile devices to track the 'buzz' in their field through Twitter feeds, following big-name colleagues, breaking news and conference proceedings. "I'm finding it to be invaluable because I get more good information about research going on, links to articles and data sets than from any other source," says Dawn Wright, chief scientist at Esri, a software company in Redlands, California. "I don't have to wait for a major scientific meeting or go to someone's website to learn about what my colleagues are doing."

Apps can also help to navigate the buzz at big science conferences. Wright raves about the American Geophysical Union's app, which is designed each year for the union's annual meeting. The app lets conference attendees search the meeting abstracts and sessions, and 'friend' other attendees to message them directly. It also includes maps of the convention centre and information about local hotels and restaurants. "I hate having to carry these big folders and books around to all the sessions," says Wright, who used the app at last year's conference to coordinate dinner with friends and alert colleagues to interesting poster presentations.

LAB TOOLS

When it comes to doing bench work, various apps can help to save time. Carvajal uses 'OD-260' to convert optical units into nucleic-acid concentrations; 'LabTimer' to keep track of incubating test tubes; and 'Notes' to jot down experimental protocols. His phone gives him all the calculators, timers and notebooks he needs both when he is at his bench and roving between lab spaces.

Several reagent companies offer free time-saving apps. New England Biolabs, Qiagen, Promega and Bio-Rad have all created apps that provide useful formulae, conversions and recipes for common molecular-biology reactions to replace the paper pamphlets and catalogues that inevitably go missing from lab benches.

When doing calculations, 'Mathematical Formulas' and 'Solutions' can come in handy for looking up bits of information that were learned in school and promptly forgotten, such as the quadratic equation. Miguel García Toscano, a senior postdoc at the Andalusian Centre for Genomics and Oncological Research in Granada, Spain, carries his iPhone at all times, using it to look up DNA amplification reactions and take pictures of catalogue numbers he needs to remember.

Some pieces of research are best viewed on the bigger screen of a tablet. Carvajal uses his iPad to look up mouse gene-expression patterns in the Jackson Laboratory's Mouse Genome Informatics database (informatics.jax.org). The screen allows him to instantly visualize almost all the known data on a mouse gene, including images of the gene's expression in various tissues or stages of development in a whole animal or embryo. "It's an absolutely fantastic tool I could not do without," he says.

With a bit of practice, the devices can help researchers to take and access huge volumes of notes. "I don't take my laptop to conferences any more," says Carvajal. "Just my iPad and iPhone and I've got everything I need." He uses the 'Bamboo Paper' app and digital pen stylus to take notes and sketch diagrams while listening to talks. Graveley does the same with the 'Notability' app, which also records audio and time-stamps the recording whenever he makes a note or sketch.

Although computer programs have made digital note-taking a reality in the lab (see *Nature* **481**, 430–431; 2012), the apps on mobile devices are cheaper, although not as sophisticated. Toscano makes two copies of everything — he transcribes entries in his lab notebook into Word and Excel on his computer, then converts

USEFUL APPS FOR SCIENTISTS

App	Description	Compatibility	Price
Reference			
Micromedex Drug Information	Database of drug information and interactions and evidence-based medicine	Android, iPhone, iPod touch, iPad	Free
Mathematical Formulas	Database of basic and commonly used formulae	iPhone, iPod touch, iPad	£0.69/$0.99
Solutions	Calculates volume, weight and molarity of chemical solutions	iPhone, iPod touch, iPad	£0.69/$0.99
Lab tools			
MedCalc	Formulas to determine, for instance, body mass index, heart rate and iron deficiency	iPhone, iPod touch, iPad	£0.69
OD-260	Calculates nucleic-acid concentration	iPhone, iPod touch, iPad	Free
LabTimer	Count-up or -down alarmed timer	iPhone, iPod touch, iPad	Free
Organizers			
Papers	PDF organizer with PubMed search and bibliography features	iPhone, iPod touch, iPad	£10.49/$14.99
GoodReader	PDF organizer that lets users read, mark up and e-mail documents	iPhone, iPod touch, iPad	£2.99/$4.99
Wunderlist	Task organizer that allows information to be shared among colleagues	Android, iPhone, iPad	Free
Documents To Go	Converts Microsoft Office and PDF files to phone-friendly versions	Android, iPhone, iPod touch, iPad	Free on Android; £6.99/$9.99 on Apple devices
Things	Task manager that syncs with desktop version	iPhone, iPod touch, iPad	£6.99/$9.99
Alerts			
ACS Mobile	Publication alerts from the American Chemical Society	Android, iPhone, iPod touch, iPad	Free
Notebooks			
Bamboo Paper	Make notes and sketches	iPad	Free
Notability	Make notes and record audio	iPad	£0.69/$0.99
Evernote	Make notes, capture photos, create to-do lists, record voice reminders	Android, iPhone, iPod touch, iPad	Free
Trello	Collaboration tool that allows users to see who is working on what part of a project through shared bulletin boards	iPhone, iPod touch, iPad	Free

the files to phone-friendly versions using 'Documents to Go' so that he can carry all his data with him and can check them when he meets with his supervisor. "Loading everything digitally is a time-consuming task, but it's helpful when writing a manuscript, and later on I appreciate it," he says.

But will the portability and capabilities of these gadgets ever replace traditional paper lab notebooks? Toscano is not convinced; electronic devices don't mix well with chemical solvents, and paper notebooks never run out of batteries. And when virtual notebooks are shared between multiple users, sloppy mistakes can accumulate and the work becomes prone to sabotage.

But Vázquez is testing those fallibilities using an online program called 'Evernote'. Most lab notebook programs, he says, are designed for industry use — to guard and time-stamp sensitive proprietary or patient information — and are "crazy expensive". But with a low-cost Evernote subscription, Vázquez can store any kind of file and data, up to 1 gigabyte a month, in an organized and searchable fashion on a server that automatically syncs 'notes' between his devices. Some of these services are available in the freely available program 'Dropbox', although Evernote has six times more storage and more organizing options. "My plan is to get a couple more accounts and to start testing shared notebooks with a couple of my students, which should make it far easier to follow their progress," Vázquez says.

Of course paper notebooks tend to stay in the lab and do not beep distractingly. The portability of mobile devices can mean that scientists never completely disconnect from their work. "That's the hardest thing about this technology," says Graveley. "You can be available 24–7." He frequently turns the sound off on his phone so that he is not reacting to every call, text message or e-mail alert that comes in. But resisting the temptation to play games or check e-mail constantly is no different from avoiding the vices on a desktop computer, Toscano says.

When the iPad first came out in 2010, Graveley offered to buy one for each of his trainees, but they all refused, sceptical back then of its value. "The utility of these mobile devices is based on the apps that other people develop, so you don't know what they're going to be capable of next," he says. Now, with an explosion of apps written by scientists for scientists and many available at no cost or for nominal sums, it is hard to imagine smartphones and tablets not eclipsing the laptop, notes Carvajal, who says he would like to see them in the hands of "every single graduate student and postdoc". ■

Kendall Powell *is a freelance writer based in Lafayette, Colorado.*

TURNING POINT
Lisa Kaltenegger

Astrophysicist Lisa Kaltenegger is one of six recipients of Germany's 2012 Heinz Maier-Leibnitz Prize for early-career researchers. She divides her time between the Max Planck Institute for Astronomy in Heidelberg, Germany, and the Harvard–Smithsonian Center for Astrophysics in Cambridge, Massachusetts.

What is the most important thing that you've done to shape your career?
Move to a new country. Through travel and unfamiliar experiences, I learned how to think differently and explore alternative approaches to science — important for any young person. I pursued master's degrees in both astrophysics and engineering, from the University of Graz in Austria and the Graz University of Technology, respectively. But I did the research for both in other countries. With Erasmus mobility funding from the European Union, I travelled for six months to the Institute of Astrophysics of the Canary Islands, Spain; we were trying to detect extrasolar planets using ground-based telescopes. I also studied biomedical engineering at Johns Hopkins University in Baltimore, Maryland, where the Graz University of Technology had an exchange programme.

So you considered going into medicine. Why did you choose astrophysics?
Both fields interested me because I wanted to have an impact on society — I wanted either to work towards a cancer cure or to seek another Earth. I had offers to do both. But I got a job opportunity at the European Space Agency (ESA), which was designing a mission to look for other planets, and I could see myself doing this fascinating job for a long time. It wasn't necessarily a logical decision, because astronomy can be a risky career path. But I had engineering as a fall-back option.

What was the highlight of your time at ESA?
Helping to design and optimize a mission to search for habitable planets. I had very little experience, but the team encouraged creative thinking and ideas. I had to model what the atmosphere of a habitable planet would look like to work out how to find one — insights that later helped me to get a PhD in astrophysics from the University of Graz.

You didn't publish much of your PhD work. Was it difficult to get a postdoc?
I wasn't allowed to publish most of my work because the technology to look for planets was proprietary, and I couldn't very well publish data without details on how they were obtained. I wasn't aware of this limitation when I started. But I was one of the few people working on exoplanet characterization who had a background in engineering, so I knew how to make trade-offs between instrument design and detection capabilities that wouldn't hamper the science and would keep costs down. Doing presentations at meetings and workshops connected me with Wesley Traub, an astrophysicist then at the Harvard–Smithsonian Center, who invited me to apply for a postdoc.

How did you end up with positions at both Harvard and the Max Planck Institute?
After finishing my postdoc at Harvard, I got an offer from Max Planck to establish my own lab, but Harvard wanted me to stay. Luckily, I had funding — a German Research Foundation Emmy Noether award, which helps early-career scientists to build a team and achieve independence. Because I had this funding, I suggested that I split my time between the two institutes — spending nine months of the year in Heidelberg and three months at Harvard. Exoplanet characterization is not something that many people do in Germany, so there is an extra incentive to maintain international collaborations.

You've won multiple awards. Will any have an impact on your career?
The young-researcher awards mean the most because they give early-career scientists credence and notoriety. In hierarchical systems, such as in Europe, they help to level the field a bit. The validation comes from being nominated by a peer who thinks your work is exciting. Whether you get the prize is often a gamble, but the positive reinforcement from peer recognition keeps you going. ■

INTERVIEW BY VIRGINIA GEWIN

the files to phone-friendly versions using 'Documents to Go' so that he can carry all his data with him and can check them when he meets with his supervisor. "Loading everything digitally is a time-consuming task, but it's helpful when writing a manuscript, and later on I appreciate it," he says.

But will the portability and capabilities of these gadgets ever replace traditional paper lab notebooks? Toscano is not convinced; electronic devices don't mix well with chemical solvents, and paper notebooks never run out of batteries. And when virtual notebooks are shared between multiple users, sloppy mistakes can accumulate and the work becomes prone to sabotage.

But Vázquez is testing those fallibilities using an online program called 'Evernote'. Most lab notebook programs, he says, are designed for industry use — to guard and time-stamp sensitive proprietary or patient information — and are "crazy expensive". But with a low-cost Evernote subscription, Vázquez can store any kind of file and data, up to 1 gigabyte a month, in an organized and searchable fashion on a server that automatically syncs 'notes' between his devices. Some of these services are available in the freely available program 'Dropbox', although Evernote has six times more storage and more organizing options. "My plan is to get a couple more accounts and to start testing shared notebooks with a couple of my students, which should make it far easier to follow their progress," Vázquez says.

Of course paper notebooks tend to stay in the lab and do not beep distractingly. The portability of mobile devices can mean that scientists never completely disconnect from their work. "That's the hardest thing about this technology," says Graveley. "You can be available 24–7." He frequently turns the sound off on his phone so that he is not reacting to every call, text message or e-mail alert that comes in. But resisting the temptation to play games or check e-mail constantly is no different from avoiding the vices on a desktop computer, Toscano says.

When the iPad first came out in 2010, Graveley offered to buy one for each of his trainees, but they all refused, sceptical back then of its value. "The utility of these mobile devices is based on the apps that other people develop, so you don't know what they're going to be capable of next," he says. Now, with an explosion of apps written by scientists for scientists and many available at no cost or for nominal sums, it is hard to imagine smartphones and tablets not eclipsing the laptop, notes Carvajal, who says he would like to see them in the hands of "every single graduate student and postdoc". ■

Kendall Powell *is a freelance writer based in Lafayette, Colorado.*

TURNING POINT
Lisa Kaltenegger

Astrophysicist Lisa Kaltenegger is one of six recipients of Germany's 2012 Heinz Maier-Leibnitz Prize for early-career researchers. She divides her time between the Max Planck Institute for Astronomy in Heidelberg, Germany, and the Harvard–Smithsonian Center for Astrophysics in Cambridge, Massachusetts.

What is the most important thing that you've done to shape your career?
Move to a new country. Through travel and unfamiliar experiences, I learned how to think differently and explore alternative approaches to science — important for any young person. I pursued master's degrees in both astrophysics and engineering, from the University of Graz in Austria and the Graz University of Technology, respectively. But I did the research for both in other countries. With Erasmus mobility funding from the European Union, I travelled for six months to the Institute of Astrophysics of the Canary Islands, Spain; we were trying to detect extrasolar planets using ground-based telescopes. I also studied biomedical engineering at Johns Hopkins University in Baltimore, Maryland, where the Graz University of Technology had an exchange programme.

So you considered going into medicine. Why did you choose astrophysics?
Both fields interested me because I wanted to have an impact on society — I wanted either to work towards a cancer cure or to seek another Earth. I had offers to do both. But I got a job opportunity at the European Space Agency (ESA), which was designing a mission to look for other planets, and I could see myself doing this fascinating job for a long time. It wasn't necessarily a logical decision, because astronomy can be a risky career path. But I had engineering as a fall-back option.

What was the highlight of your time at ESA?
Helping to design and optimize a mission to search for habitable planets. I had very little experience, but the team encouraged creative thinking and ideas. I had to model what the atmosphere of a habitable planet would look like to work out how to find one — insights that later helped me to get a PhD in astrophysics from the University of Graz.

You didn't publish much of your PhD work. Was it difficult to get a postdoc?
I wasn't allowed to publish most of my work because the technology to look for planets was proprietary, and I couldn't very well publish data without details on how they were obtained. I wasn't aware of this limitation when I started. But I was one of the few people working on exoplanet characterization who had a background in engineering, so I knew how to make trade-offs between instrument design and detection capabilities that wouldn't hamper the science and would keep costs down. Doing presentations at meetings and workshops connected me with Wesley Traub, an astrophysicist then at the Harvard–Smithsonian Center, who invited me to apply for a postdoc.

How did you end up with positions at both Harvard and the Max Planck Institute?
After finishing my postdoc at Harvard, I got an offer from Max Planck to establish my own lab, but Harvard wanted me to stay. Luckily, I had funding — a German Research Foundation Emmy Noether award, which helps early-career scientists to build a team and achieve independence. Because I had this funding, I suggested that I split my time between the two institutes — spending nine months of the year in Heidelberg and three months at Harvard. Exoplanet characterization is not something that many people do in Germany, so there is an extra incentive to maintain international collaborations.

You've won multiple awards. Will any have an impact on your career?
The young-researcher awards mean the most because they give early-career scientists credence and notoriety. In hierarchical systems, such as in Europe, they help to level the field a bit. The validation comes from being nominated by a peer who thinks your work is exciting. Whether you get the prize is often a gamble, but the positive reinforcement from peer recognition keeps you going. ■

INTERVIEW BY VIRGINIA GEWIN

PERCHANCE TO BLEAM

Sleep no more …

BY RONALD D. FERGUSON

Three days since the radio burst and Martin hadn't slept. Normally, Martin worked nights monitoring data from the radio telescope. When alone, he broke the monotony of the scrolling star signatures by snacking; but since insomnia had struck, he had become increasingly restless. By the second sleepless day, he had night-walked among the antennas and wished the friendly stars would soothe him. But when he went home the next morning, his eyes still refused to close.

Homespun remedies were ineffective. Martin gagged at the thought of another glass of warm milk. Encapsulated tryptophan made him listless, not sleepy. Likewise, the exercise theory gave him sore muscles but not sleep. Despite his efforts, Martin never got drowsy.

Over a weekend brunch, he shared his sleep problems with Julia. Last year, they had unsuccessfully worked on a romance, but that relationship had degenerated into a close friendship.

Julia sympathized. After three glasses of wine, she reached across the table and touched his hand.

"I remember what puts you to sleep."

The experience was memorable, certainly better than warm milk, but Martin finished invigorated rather than enervated.

When darkness finally punctuated the rhythm of Julia's breathing, Martin wrestled his thoughts and waited for sleep. Hours later, sleep hadn't come. He illuminated his watch: 8:47 p.m., time to get up. He caressed Julia's shoulder, eased himself from the bed and got dressed.

In the hall, he scribbled a thank-you-call-tomorrow note and stuck it to the mirror. Outside, the cool night air refreshed him, and he walked the streets until dawn.

"How do you feel, Martin?"

"Not bad, Dr Hendley. Irritable. Mildly depressed."

"No aches or pains?"

"My health is fine. I saw my doctor before I came to you. He couldn't do much for me, except pronounce I was in good health."

"I'm surprised. No pharmaceuticals?"

"I tried a sleep clinic two days ago, but it didn't work. They thought I was sleeping with my eyes open, but I wasn't. Drugs rendered me unconscious twice, but never to REM sleep."

"How long now?"

"Eight days. I haven't slept in eight days."

"That's the fifth massive burst in the past two weeks. Did you read the transmission? Martin? Hey, Martin, are you awake?"

Of course he was awake. He was always awake, working double shifts to fill his time — what the heck!

As he watched the computer screen, invisible nanos assembled into robot roaches and marched intricate formations backlit by the LCDs. First, they spelled 'Hello', then they lined up and presented their antennae for inspection. The antics entranced him. Martin pointed to the screen and giggled.

Strong hands pulled at his arms and helped him to stand. Martin appreciated their effort, but he resisted, straining towards the screen because the roaches had more to tell him.

"What's wrong with him?" A distant voice, maybe it was God, asked. "Is he on drugs?"

"The guy hasn't slept in weeks, not since we attended the SETI conference. You know, the night of the first big transmission burst?"

"Okay. Call EMS. Get him to the hospital."

"Why must people sleep, Dr Hendley?" Martin swallowed two aspirins.

"I'm more interested in why you can't sleep. Fifteen days now."

"Doesn't worry me anymore."

"Maybe not worrying is another hallucination, Martin. Stay focused."

"But why should I sleep? Give me one good reason. With that, I'm sure I could sleep."

"Okay." Dr Hendley sighed. "Prolonged sleep deprivation harms your health."

"That's not my question."

"I understand, but the rest is only an opinion. Sleep allows our bodies to recover, but more, sleep allows the mind to assimilate its experiences. I believe dreams are the mind's attempt to reconcile the day's experiences with what it already knows."

"So dreams install a software upgrade, and waking is the required system reboot. We sleep to dream."

"Nice analogy. I hadn't thought of that. I'm not big with computers."

Martin rocked his chair. The rhythm soothed him. "What if it's too much?" he whispered.

"What if what's too much?"

"The day's experiences. What if the information is so massive, so at odds with what the mind already knows, that each installation attempt results in failure?"

"When that happens with my computer, the tech says I need a hardware upgrade. But to answer your question, Martin, I don't know. Do you think that's what happened to you?"

"Maybe mental hardware is different." Martin closed his eyes. "Maybe eventually, the mind upgrades itself. Too late for me. I'm exhausted. Death almost looks good."

"Courage, Martin. I've called sleep specialists in New York and Los Angeles. They are fascinated by your … Martin? Are you okay?"

The waking hallucination of dream-filled sleep became a sleeping dream displaying distorted reality. Roaches waved antennae at him. Data flashed across his screen. Recursive memory filled, but for this iteration, reallocated storage before it could overflow. Reboot. Reload the dream to finish the installation.

The bleam opened in multidimensional high definition with vivid colours and surround sound. Was the overture a celestial choir or a galactic orchestra? The unfiltered vibrations assaulted Martin with rumbling lows and tingling highs that soared past human experience. He absorbed sounds beyond the limits of his ears. His mind juggled colours below the infrared and above the ultraviolet. The dream issued smell, taste and feel. The view expanded to a four-dimensional kaleidoscope of scenes and senses.

Finally awake to the mystery of the bleam, Martin smiled in his sleep. What an introduction, what a spectacular greeting from the radio-telescope data.

… And a big hello right back at you. ∎

Ronald D. Ferguson *lives with his wife and five feral cats in the Texas Hill Country.*

nature OUTLOOK

MALARIA

26 April 2012 / Vol 484 / Issue No. 7395

Cover art: Nik Spencer

*H*omo versus *Plasmodium*. It's a war that has raged for millennia and that still claims hundreds of thousands of lives each year. The struggle against this mosquito-borne parasite has shaped the genomes of people in endemic regions. Past attempts to eradicate malaria have failed. What will it take to finally beat it into submission?

It is predominantly the richer countries with temperate climates that have eliminated malaria so far. The disease is still endemic in hotter, poorer countries; in some parts of western Africa, the burden is so high that elimination would require more than a 99% reduction in transmission rate (page S14). At least in Africa, where 90% of malaria-related deaths occur, the standard artemisinin-combination therapy (ACT) is still an effective cure. Parts of Southeast Asia are not so lucky. There is evidence that resistance to ACT is emerging there but, despite huge international drug development efforts, there are no new treatments to replace it (S16).

A vaccine for malaria has been a big research goal for more than a hundred years. *Plasmodium* is a master of disguise, and researchers have to try a diverse range of tactics to target the parasite — in both its human and mosquito hosts (S24). Indeed, understanding human immunity to malaria and identifying parasite antigens are two of the top research priorities identified by our panel of experts (S22). And any successful strategy to eradicate malaria will have to include controlling mosquitoes — such ideal vectors (S26).

But by far the greatest challenge is not in the lab; it is on the ground in endemic countries. It concerns access to care, encompassing education about malaria, availability of ACTs, infrastructure, presence of healthcare workers and government support. And in a country like Uganda, as our reporter Amy Maxmen found when she visited — these are in short supply (S19).

We acknowledge the financial support of Medicines for Malaria Venture (MMV), Sigma-Tau and Vestergaard Frandsen New York in producing this Outlook. As always, *Nature* has full responsibility for all editorial content.

Michelle Grayson
Senior Editor, Nature Outlook.

CONTENTS

THE NUMBERS GAME

Nature Outlook *maps the challenges in tackling the malaria epidemic. By Priya Shetty.*
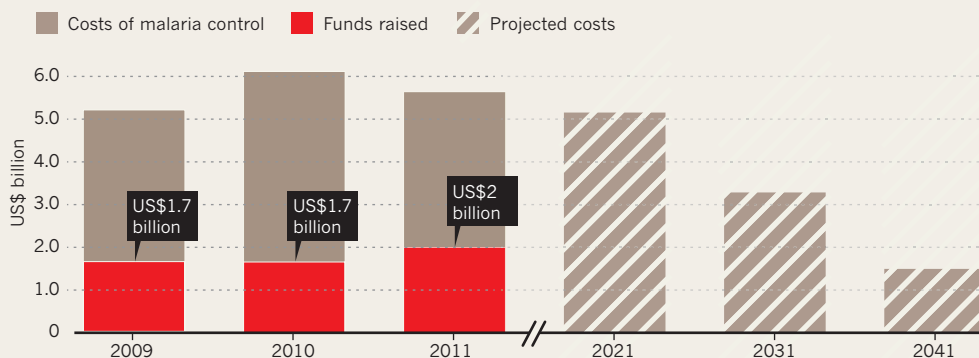
MAPPING MALARIA

Malaria is still one of the 'big three' diseases, along with HIV and tuberculosis, affecting the developing world. While it has been eliminated in many regions, it remains a scourge of poorer countries, especially those in sub-Saharan Africa, where *Plasmodium falciparum* is the leading cause of malaria. Elsewhere in the world, malaria is caused by a mix of *P. falciparum* and *P. vivax*, as well as a few less common sub-species.

Malaria-free
Eliminating malaria
Endemic

Required reduction in transmission to eliminate malaria

90–99%
>99%

DEATHS BY REGION (WHO)

90% Africa
6% Southeast Asia
2% Eastern Mediterranean
1% The Americas
1% Western Pacific

60 Every 60 seconds a child dies of malaria

90%
90% of malaria deaths are in Africa

MALARIA DEATH DISPARITY

The Lancet numbers differ because the authors used verbal autopsy, in which they interview the relatives of a person who has recently died to determine a cause of death. Interviews can identify people who died of malaria but went undiagnosed or treated.

1.24M deaths worldwide, 714,000 under the age of 5

655,000 deaths worldwide, 563,300 under the age of 5

Lancet

WHO

= 50,000 people
Deaths
Deaths under 5yrs

COTE D'IVOIRE
WHO: 1,023
Lancet: 31,664

BENIN
WHO: 964
Lancet: 14,415

UGANDA
WHO: 8,431
Lancet: 41,648

THE MONETARY GAP

The good news is that if current efforts to control malaria are strengthened, the costs of the epidemic (including prevention through bed nets and insecticides, treatment with antimalarials, diagnosis, and R&D) are set to fall over the next few decades. However funding has not matched these ambitions.

Costs of malaria control
Funds raised
Projected costs

US$ billion

6.0
5.0
4.0
3.0
2.0
1.0
0

US$1.7 billion
US$1.7 billion
US$2 billion

2009 2010 2011 2021 2031 2041
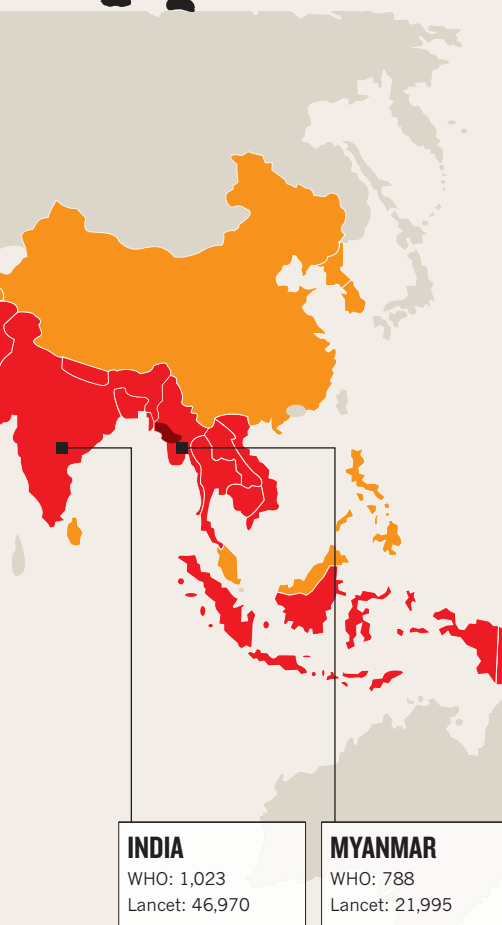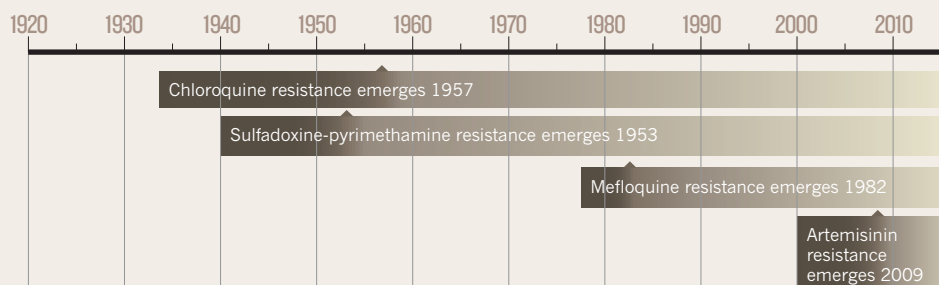
VULNERABLE GROUPS

Children: Most malaria deaths happen in children under 5 years old because their immune systems are not developed enough to fend off the parasite's attack.

Pregnant women: A pregnant woman is 4-times more likely to get malaria, and twice as likely to die from it, than another adult. This is because her immune system is partially suppressed during pregnancy. Malaria in pregnancy has dangerous consequences for the baby too.

People living with HIV: HIV infection weakens the immune system, making people more vulnerable to malaria. Malaria infection causes HIV viral loads to shoot up, which could increase its transmission. The diseases are linked in other ways too – the *DARC* gene that protects against vivax malaria might increase susceptibility to HIV.

TIMELINE OF RESISTANCE

Malaria has defeated many drugs in the past, often less than a decade after they were introduced.

1920   1930   1940   1950   1960   1970   1980   1990   2000   2010

Chloroquine resistance emerges 1957

Sulfadoxine-pyrimethamine resistance emerges 1953

Mefloquine resistance emerges 1982

Artemisinin resistance emerges 2009

INDIA
WHO: 1,023
Lancet: 46,970

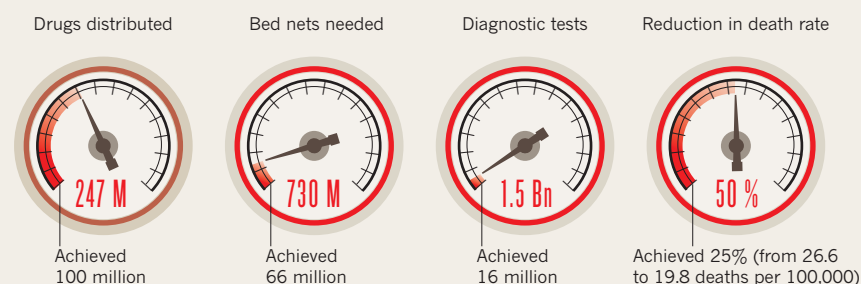**MYANMAR**
WHO: 788
Lancet: 21,995

DANGER ZONE: DRUG RESISTANCE THAILAND, CAMBODIA

Artemisinin-combination therapies (ACTs) were the great hope of malaria control, as the parasite has steadily become resistant to older drugs. Just a couple of years after ACTs were introduced to this part of Southeast Asia in 2005, drug resistance emerged. Why this area is such a hotspot for drug resistance is not entirely clear, there seems to be many factors: counterfeit medicines are rife, drugs are available too easily over the counter, and the drugs are sold on their own rather than in combination (which makes it easier for the parasite to develop resistance).

LOFTY AMBITIONS

In 2007, Bill Gates's rallying call for eradication took some malaria experts by surprise. New drugs and insecticide-treated bed nets were helping control the spread of the infection, yet the world was some way off beating the parasite for good. Opinion is divided, especially as many of the goals set by the WHO so far haven't been achieved.

TARGET BY 2010:

Drugs distributed	Bed nets needed	Diagnostic tests	Reduction in death rate
247 M	730 M	1.5 Bn	50 %
Achieved 100 million	Achieved 66 million	Achieved 16 million	Achieved 25% (from 26.6 to 19.8 deaths per 100,000)

TARGET BY 2015:

Number of deaths	Reduction in cases
ZERO	75 %

Can these targets be achieved?
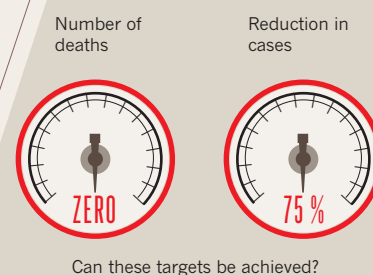
Cambodia is cracking down on counterfeit malaria drugs and has outlawed artemisinin monotherapies.

DRUG DEVELOPMENT

Holding out for reinforcements

Signs of emerging drug resistance are turning the hunt for new malaria treatments into a race against the clock.

BY MICHAEL EISENSTEIN

The first signs of trouble were subtle. Several patients living near the Thai-Cambodia border had received first-line malaria treatment of artemisinin-combination therapy (ACT), but failed to clear the *Plasmodium* parasites from their blood. Their doctors were flummoxed. "There were these sentinel sites reporting reduced efficacy of ACTs," recalls Arjen Dondorp, deputy director of the Mahidol-Oxford Tropical Research Unit in Bangkok. Dondorp and his colleagues suspected drug resistance. "But it was always uncertain, and could potentially be ascribed to the drugs not being taken properly or underdosed." In 2006, they started to investigate the likelihood of ACT resistance more thoroughly.

The stakes are high. The emergence of drug resistance has already rendered once-effective malaria treatments — chloroquine and sulfadoxine-pyrimethamine — less reliable. Today, ACTs are the weapon of choice against malaria, and the possibility of losing them has the research community scrambling to

understand the situation and to develop new drugs as reinforcements or even replacements.

CRACKS IN THE ARMOUR

Artemisinin is a molecule extracted from the sweet wormwood plant *Artemisia annua*. In its natural form, it is degraded in a matter of hours within the body. Treatment requires a week-long course — a demanding regimen that can fail if patients do not complete it.

Clinical researchers overcame the limitations of natural artemisinin by developing more robust derivatives, such as artesunate or artemether, and coupling them with partner drugs such as mefloquine or lumefantrine. The World Health Organization (WHO) recommends five such combinations for distribution to endemic malaria regions. They have, in general, proven successful, ridding most patients of the immature blood-stage parasites after only 3 days.

Resistance has only recently become the biggest concern with ACT. For years, the primary issue was uncertainty with supply. Production depended on *A. annua* agriculture, and drug

prices were prone to dramatic fluctuations. "The average price for 1 kilogram of high-quality artemisinin spiked to US$1,000 in 2005 due to a shortage, but dropped to around US$195 in 2007 due to overproduction," says Tue Nguyen, vice president for research and preclinical development at OneWorld Health, a non-profit organization in South San Francisco, California. "The current price is around US$450/kg and increasing." Nguyen's organization is leading efforts to counter this volatility, partnering with Amyris — a synthetic-biology company in Emeryville, California — and French pharmaceutical giant Sanofi to produce bulk quantities of artemisinic acid, an artemisinin precursor, using genetically-engineered yeast. In 2012, Nguyen anticipates making 9,000 kg of artemisinin — enough for millions of doses — at an initial price of US$400/kg; in 2013 they expect to quadruple production. Stabilizing supply of artemisinin should help reduce some of the volatility in the cost of ACTs and smooth the availability of drugs.

Nevertheless, a stable supply will be of little comfort to patients in Southeast Asia facing potential treatment failure. Several independent investigations by Dondorp and Harald Noedl of the Medical University of Vienna have confirmed the emergence of ACT resistance in the region[1], and the problem appears to be spreading. "There was a dramatic slowing of parasite clearance," says Dondorp. "ACTs are starting to fail in western Cambodia, but what may be even worse is that this phenotype has also arrived in western Thailand, at the Thai–Myanmar border." In some communities, a standard ACT course no longer stops malaria in up to half of the patient population. This resistance is specific to artemisinin, but it could eventually lead to resistance to partner drugs too.

Southeast Asia has incubated treatment-resistant malaria in the past (see The numbers Game, page S14). With both chloroquine and sulfadoxine-pyrimethamine, resistance spread to the Indian subcontinent and eventually Africa. With ACT, "So far, we have not seen any signs of resistance outside of Southeast Asia," says Pascal Ringwald, coordinator of the Drug Resistance and Containment Unit within the WHO's Global Malaria Programme, which is closely monitoring reports of potential malaria resistance.

Unfortunately, the basis of this resistance remains unclear. "We have screened 185 different *P. falciparum* isolates — mostly from Southeast Asia — and they are all extremely sensitive to the artemisinins *in vitro*," says Xinzhuan Su, chief of the Malaria Functional Genomics section at the National Institute of Allergy and Infectious Diseases in Bethesda, Maryland. Nevertheless, many of these strains

show resistance to artemisinin in malaria patients. A study published in April 2012 identified a segment of the *P. falciparum* genome that appears to contribute to reduced parasite clearance in patients from Cambodia and Thailand, although further analysis will be needed to identify the relevant genetic variants[2].

David Fidock, a microbiologist at Columbia University, New York, suspects that the resistance seen in *Plasmodium* is only a transient survival mechanism, and that genetic mutations that confer robust artemisinin resistance without weakening the parasite's fitness are yet to emerge. "My personal sense is that it's very difficult for the parasite to gain stable resistance to artemisinin," says Fidock. "Lab studies indicate that the initial gain of drug tolerance is readily lost by the parasite after the removal of drug pressure." Furthermore, many scientists think that artemisinin works in a nonspecific manner: as *Plasmodium* feeds on haemoglobin, iron is released that activates artemisinin, causing extensive chemical damage to the parasite (see 'One parasite — many hiding places')."There's probably not a specific target on the parasite that the drug is attacking that could mutate to prevent inhibition," says Fidock.

Even without a clear cause, the problem is undeniable, and the WHO has produced the Global Plan for Artemisinin Resistance Containment (GPARC), now being implemented across Southeast Asia. GPARC pairs surveillance with improved clinical practice: catching malaria early and ensuring complete elimination of *Plasmodium*. "We're focusing on the success of diagnostics and treatment," says Ringwald, "and using very effective first-line drugs, mosquito control, lots of advocacy and research into new operational strategies to kill off reservoirs of the parasite."

New drugs would also help. One of the most promising is a compound known as OZ439, which differs structurally from the artemisinin drugs, but retains the endoperoxide chemical group that is crucial to their success. OZ439 outperforms artemisinin in an important regard. "It has a half-life that has never been seen for an artemisinin derivative," says biochemist Sergio Wittlin of the Swiss Tropical and Public Health Institute (Swiss TPH), who helped discover the compound. "Natural products have half-lives in the range of 1 hour, but this has a half-life of 20 hours in orally dosed rats, which also held true in a phase I trial." The drug is currently in phase II trials, and hopes are high that OZ439's prolonged existence in the bloodstream, paired with its novel structure, will make it effective where ACTs are failing.

NOT SO NEGLECTED

The past decade has seen a surge in investment in antimalarial drug discovery. According to a report by the Bill & Melinda Gates Foundation's Global Funding of Innovation for Neglected Diseases (G-FINDER) programme, 2010

ONE PARASITE — MANY HIDING PLACES

Plasmodium falciparum and *P. vivax*, the parasite species primarily responsible for malaria in humans, have complicated lifecycles. Both parasites have multiple developmental stages, each with its preferred target cell type in humans or mosquitoes, making it a challenge to eliminate infection — especially for the hibernation-prone *P. vivax*. However, scientists are fighting back, by expanding the arsenal of antimalarial drugs (in white boxes).
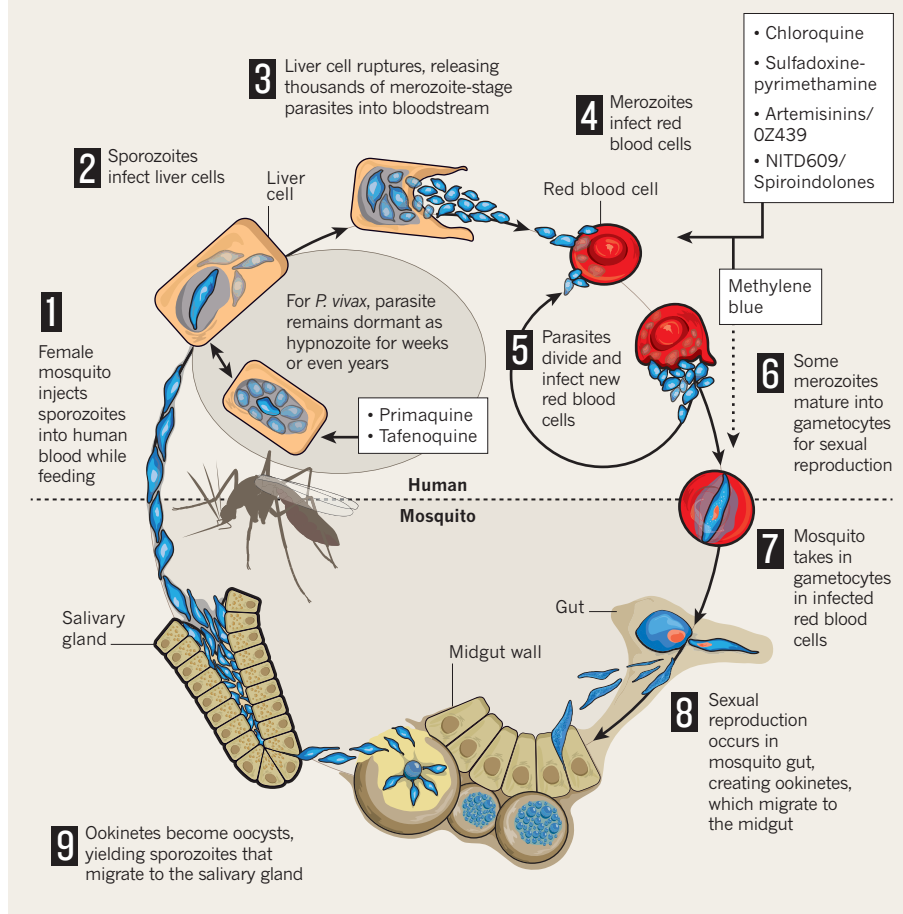
global spending on malaria research and development (R&D) totalled US$547.2 million, with drug research accounting for the largest component (42%). Nearly a quarter of this R&D investment came from the private sector, an important contribution to what was previously considered a neglected tropical disease.

Alongside the Gates Foundation as a driver of this funding boom is the Medicines for Malaria Venture (MMV). With pharmaceutical and biotechnology partners, MMV coordinates distribution of public-sector and philanthropic funds to ensure that money can be rapidly allocated to scientists making progress in malaria drug development at any institution, anywhere in the world. "MMV is so knowledgeable and focused and professional in its efforts — it's like a virtual drug discovery organization," says Nick Cammack, who heads medicinal development for GlaxoSmithKline (GSK) in Tres Cantos, Spain. The Tres Cantos campus is devoted to tropical-disease research and a nexus for public–private sector collaboration. "We fund research on a 50:50 basis, with GSK and MMV each contributing

half, and we have joint objectives to find new molecules for clinical development," he says.

As well as investment and expertise, drug companies engaged in the drive for antimalarial research are also contributing libraries of chemicals — resources once kept under lock and key. Wittlin's Swiss TPH colleague Matthias Rottmann is part of a multi-institutional collaboration with the Novartis Institute for Tropical Diseases that has worked with one such library. "It was almost 2 million products, basically all the chemicals Novartis has," says Rottmann. In 2010, GSK surprised many observers by making public the chemical structures and screening data of more than 13,000 molecules with apparent antimalarial activity, identified from its library of roughly 2 million compounds[3]. MMV has since worked with GSK, Novartis and St Jude Children's Research Hospital in Memphis, Tennessee, to compile a 'greatest hits' collection called the Malaria Box, a freely available sampler of 400 chemicals with demonstrated activity against *P. falciparum*. According to MMV's chief scientific officer Tim Wells, this curated collection

is proving popular. "It became available in the last week of December 2011, and it has already 'sold out' its first batch," he says.

Compounds that show promise in these screens are only starting points. "I saw one article that described our findings as '13,000 new malaria drugs', which is an exaggeration to say the least," says GSK's Cammack. Each promising lead will need significant optimization work, he adds. Accordingly, although scientists are free to use the Malaria Box as they like, Wells anticipates that most will seek further assistance through MMV or private sector partners to shepherd promising molecules into clinical testing.

MMV is assisting in early stage development of dozens of potential drug candidates. Among the most promising is the synthetic molecule NITD609, one of several spiroindolones isolated in 2010 from a Novartis library[4]. "They were fairly potent in cellular assays right away, and they were attractive with regard to how long they stay in the bloodstream and their chemical tractability," says cell biologist Elizabeth Winzeler at The Scripps Research Institute in La Jolla, California, and a corresponding author on the study. NITD609 is now poised for a phase II trial in Thailand. "It has a very good safety profile, and looks very promising," says

Rottmann, who has also worked on NITD609. Unfortunately, patient recruitment has stalled owing to events such as catastrophic flooding — problems that have also dogged trials of OZ439. "Now the malaria season is past its peak, researchers at the trial sites will have to wait until next season to finish the phase II trial," said Wittlin, in January 2012. The onset of the rains in June should enable these trials to get back on track.

SEEKING THE ULTIMATE WEAPON

Although the early data for both OZ439 and NITD609 are encouraging, their efficacy has been demonstrated only against blood-stage parasites. Yet *Plasmodium* has a complex, multi-stage lifecycle — especially *P. vivax*, which remains an especially tricky target (see 'Danger below the radar'). Any therapeutic strategy intended to eradicate malaria must wipe out gametocytes — the stage of the parasite lifecycle that moves from humans to mosquitoes. The ultimate goal for researchers is to design treatments that render a person inhospitable to parasitic infection after one dose: a strategy termed 'single-encounter radical cure and prophylaxis'. Efforts are underway to pinpoint vulnerabilities in non-blood-stage parasites, and although no new drugs have unambiguously passed this test, Fidock's team has obtained surprising data on a very old drug — methylene blue[5]. "This was the first synthetic compound ever used in humans — in 1891 — and it has very potent activity against both early and late-stage gametocytes, including the ability to block transmission to mosquitoes," says Fidock. Methylene blue fell into disuse because of its disconcerting tendency to turn urine green and the whites of the eyes blue, but these might be acceptable side effects should the compound prove valuable for parasite eradication.

The motivation and resources are clearly present for antimalarial drug discovery and development, but time is a looming problem. "When you talk about next-generation drugs, launch dates are projected for 2018 or 2019," says MMV's Wells, "but people are worried about what's going to happen next year." For the time being, surveillance and containment strategies are the best hope. "It all comes back to whether emerging ACT resistance might soon leave us with essentially no effective treatments for a period of some years," says Fidock, "and that's an unresolved question right now." ∎

DANGER BELOW THE RADAR
Targeting the 'other' Plasmodium *species*

When people talk about malaria, they're generally talking about *Plasmodium falciparum*, the predominant species in Africa and the cause of hundreds of thousands of deaths each year. *Plasmodium vivax*, more of a problem in Asia and South America, tends to get overlooked, largely because of its reputation for being less lethal.

Epidemiologist J. Kevin Baird, of the Eijkman-Oxford Clinical Research Unit in Jakarta, Indonesia, sees this as a serious mistake. "You can still read in current medical textbooks that *P. vivax* very rarely kills," says Baird. "But that's just not so, and there's very good evidence that it kills patients in the same variety of ways as *P. falciparum*." He cites recent unpublished data from his team indicating that *P. vivax* was the sole parasite found in 28% of malaria deaths in one Indonesian hospital.

Plasmodium vivax's mild reputation is only part of the problem — it's also hard to study. It infects only blood-cell precursors known as reticulocytes, which are difficult to obtain and vanish quickly in culture. "*Vivax* can only be cultured on a short-term basis," says Matthias Rottmann, a biochemist at the Swiss Tropical and Public Health Institute. "A reticulocyte ages very fast: after a few days it's not a reticulocyte any more — it's an erythrocyte." This means drug studies must be performed at sites where *P. vivax* is readily available, and makes genetic manipulation of the parasite virtually impossible.

Furthermore, it has a nasty tendency to hide. *P. vivax* enters a dormant stage — a hypnozoite — in the liver, lingering for months before re-awakening. "We know nothing about hypnozoite metabolism," says Elizabeth Winzeler, a cell biologist at The Scripps Research Institute in La Jolla, California. "We don't know what targets would be useful, and we have no way of validating them."

Antimalarial drugs that kill blood parasites leave hypnozoites unscathed. A drug called primaquine eliminates *P. vivax* hypnozoites, but can be profoundly toxic for people with a mutated form of the *G6PD* gene. In a cruel irony, such mutations are widespread in malarial regions — and detecting them requires clinical resources that can be scarce in the developing world. "Even here in Jakarta, I would have a hard time finding somebody who could do a *G6PD* test," says Baird. A related drug, tafenoquine, now in phase II trials, allows a sharply reduced dosing regimen, lowering the risk of harm for G6PD-deficient patients. Nevertheless, toxicity may still prove an issue, in which case effective use would require improved G6PD diagnostics or better-designed dosing strategies.

Lack of access to good experimental models is another limiting factor. Winzeler's team developed an assay to screen compounds against liver cells infected with a rodent-specific strain of malarial parasite[6]. This yielded at least one lead, although it has not yet been tested against human hypnozoites. Otherwise, the best models available are rhesus macaques — far from ideal, as monkey models are logistically complicated, expensive and ill-suited to large-scale drug discovery.

Fortunately, this once-neglected problem is getting a lot more attention. "The Gates Foundation put quite a lot of money in two years ago, and there are five or six programmes looking at how to improve cell culture," says Tim Wells, chief scientific officer at Medicines for Malaria Venture. But Baird believes that priority should go to bolstering research efforts in regions where the crisis is most acute. "As difficult and expensive as it might be," he says, "we have to invest in research sites near where malaria patients live."

—ME

Michael Eisenstein *is a freelance science journalist based in Philadelphia, Pennsylvania.*

1. Dondorp, A.M. *et al. N. Engl. J. Med.* **365**, 1073–1075 (2011).
2. Cheeseman, I. H. *et al. Science* **336**, 79–82 (2012).
3. Gamo, F.-J. *et al. Nature* **465**, 305–310 (2010).
4. Rottmann, M. *et al. Science* **329**, 1175–1180 (2010).
5. Adjalley, S.H. *et al. Proc. Natl. Acad. Sci. USA* **108**, E1214–1223 (2011).
6. Meister, S. *et al. Science* **334**, 1372–1377 (2011).

A child's grave lies near a hut in Tororo — an all too familiar sight in Uganda.

PUBLIC HEALTH

Death at the doorstep

Even a cure is not preventing deaths from malaria in Uganda. Poor education and limited access to healthcare are among the reasons why.

BY AMY MAXMEN

Mary Nyaburu recalls how, several years ago, one of her nine children convulsed in her arms while she waited at the district hospital in Tororo, a rural area in eastern Uganda. The other women waiting at the hospital urged her to go at once and see a traditional healer who could exorcise the evil spirits in possession of her one-year-old baby. Worried, Nyaburu fled the clinic and found a healer who sold her a concoction as useless in the fight against malaria as the anti-inflammatory paracetamol she had tried earlier that week. The following day, her child could no longer swallow water. Death followed soon after.

Many mothers in Tororo have similarly heart wrenching stories. In small villages across Uganda, a child-size grave lies within a few metres of many of the huts. Young children are particularly vulnerable to malaria. And in Uganda, where 1 in 7 children die before their fifth birthday, this mosquito-delivered disease is the biggest killer. Although some villagers interpret seizures — one symptom of severe malaria — as a supernatural phenomenon, most mothers nevertheless recognize the progression of joint pain, fevers, vomiting and dehydration that comes with the onset of the disease.

That malaria has an inexpensive cure makes these deaths even more devastating, says Grant Dorsey, an infectious disease researcher at the University of California, San Francisco, who works in Tororo for a couple of months each year. "In our clinical trials we've monitored well over 5,000 patients with malaria and they all respond to the therapy within a day or two. So my own feeling is that — at least in Africa where malaria is caused by *Plasmodium falciparum* — no one dies if treated quickly. The obstacle really just becomes about access to care."

Rates of malaria incidence and mortality are falling around the world, thanks in part to the widespread distribution of artemisinin-based combination therapies (ACTs), along with insecticide-treated bed nets. Although such measures have come to Uganda, this country of 33 million people is yet to witness much success in reducing the ravages of malaria. In fact, a study published in 2011 claims that the incidence of malaria in Uganda has, if anything, risen since 2005 (ref. 1). In neighbouring Rwanda, by comparison, malaria incidence dropped by 60% between 2005 and 2010 (ref. 2). Uganda's tragic failure to abate malaria has numerous political, geographic, economic and social factors — and illustrates the reality that it takes more than scientific breakthroughs and cheap drugs to solve this persistent menace.

BLOOD-THIRSTY SWARMS

Uganda is a victim of its own lush lands. The moist soil, wetlands and great lakes for which the country is celebrated also provide a year-round refuge for the mosquitoes that transmit the malaria parasite. The World Health Organization (WHO) estimates that, in 2010, the country had more than 11 million cases of malaria — the most in Africa — and ranked it fifth in the number of deaths from the disease across the continent. What's more, Uganda has the world's highest recorded rate of malaria transmission: reaching 1,586 infective bites per person in 2001 in the swampy Apac district near the Nile River. On average, Tororo's rate is less than half this level, but still higher than rates recorded within Rwanda (81 bites per person per year), Kenya (120) and Sierra Leone (541). Children in Tororo can expect to catch malaria several times each year. Compounding this problem is a feeble healthcare infrastructure that cannot manage malaria's toll on the poor. And Uganda is very poor: 81% of its population live in rural areas, where 96% of households lack electricity and 91% do not have access to flushing toilets.

If Tororo wasn't so plagued by *Plamodium*-infected mosquitoes, bed nets might do more for villagers, says Abel Kakuru, a doctor who collaborates with Dorsey in

Tororo. When their study site was in the capital city of Kampala, Kakuru says he saw about one case of malaria every two weeks. "And then we moved to Tororo and although the cohort was half the size, we began to see at least five cases in our study cohort every day," he says. "The burden here is so heavy that we need multiple interventions, like indoor residual spraying." But this control measure is too costly to roll out across the entire country — especially in poor places like Tororo.

A steady stream of women clutching infants and small children flows through the gates of Tororo district hospital. Some ride in on the back of bicycles or motorcycle taxis called boda-bodas. Those who can't afford the US$3 ride arrive on foot. Patients will often wait for most of the day to see a doctor, meaning that mothers who accompany sick children also miss a day's work.

Waiting in the hospital is Florence Aketch, a mother with a shy 4-year old boy on her lap. Every few weeks, Aketch travels the 7km to the hospital with either her son, who gets ill with malaria monthly, or his twin sister, who becomes feverish slightly less often. Both twins sleep under a mosquito net, but it doesn't seem to matter. She reckons that her children get bitten while they eat dinner just after dusk. Even if they dine inside the house, mosquito-proof sealing or window screens would be of little use: in Aketch's village, straw thatch covers clay or cement huts about the size of a one-car garage. If there's a door, it is a flimsy piece of wood.

IN SHORT SUPPLY
Public hospitals in Uganda offer ACTs free of charge. The private sector dropped the price of drugs to about US$1.30 for a 3-day course, thanks to the Affordable Medicines Facility for malaria (AMFm), a programme run by one of the largest malaria-control funders, The Global Fund to Fight AIDS, Tuberculosis and Malaria. The AMFm subsidies have helped slash the cost of malaria treatment in Uganda and five other African countries. However, cost is incidental when the drugs aren't available. So-called 'stock-outs' have been the rule rather than the exception during the past five years, especially at small public clinics, says David Okumu, a doctor and an administrator at the Ugandan Ministry of Health who coordinates health services in Tororo.

Stock-outs began abruptly in 2005 when The Global Fund froze grants totalling US$201 million over allegations that some members of Uganda's Ministry of Health had misused the money. Although the funds were partially restored within a few months, and despite the fact that The Global Fund and the Ugandan government made arrangements to continue to supply vital drugs, many lives were lost. The supply chain for medicines like ACT "came to a halt", says James Tibenderana, the African technical director of the Malaria Consortium, a non-profit organization that partners

with international and local groups to control malaria in Africa and Asia. The African branch of the consortium is based in Kampala. "We essentially had no ACTs in the country in 2006 and 2007, and we were delayed with deploying insecticide-treated nets. We still have not recovered."

The suspension of international funding can trigger tumultuous cascades in countries with frail infrastructure. When funds froze in 2005, for example, Uganda was gearing up to switch from cheaper, less effective antimalarials to ACTs. At the highest levels of the Ministry of Health, this switch meant that administrators had to draft lots of different documents — contracts with drug suppliers, reports to aid organizations, procurement plans and bidding documents — all to be discussed and signed. At the other end of the chain, vendors in cramped makeshift drug stores on dirt roads needed to be taught about the usage, price and storage of the new antimalarials. Each step requires manpower and money. And when logistics don't flow — as when the staff at large pharmacies have neither the time nor the training to predict demand and

Even in the dry season, Uganda's lush lands provide plentiful ground for mosquitoes to breed.

place appropriate orders — stock-outs occur. And because the drugs expire in a matter of months, they cannot be stockpiled. There are stories of ACTs going to waste in the relatively malaria-free southwestern regions of Uganda, while children in northern places like Tororo die for lack of medicines.

Funding bottlenecks, inefficient procurement processes, transportation problems and inadequate stock keeping share the blame for the delay in introduction of ACTs for routine use — which did not happen in Uganda until 2008 (an advancement which regressed in 2009 with more nationwide stock-outs). Likewise, the latest first-line treatment for severe malaria recommended by the WHO is yet to reach the country. Before the Ugandan government can endorse this new intravenous therapy, which consists of the artemisinin derivative artesunate, it must ensure

a steady supply chain and train hospital staff nationwide. In the meantime, doctors continue to treat severe malaria with intravenous quinine — a harsh substance that causes tinnitus, vomiting and vertigo, as well as increasing the risk of cardiac arrest.

When *Nature Outlook* visited public and privately owned pharmacies in Tororo and Kampala in January 2012, ACTs were available. And according to an administrator at Tororo district hospital, they had been for a while. But Moses Kamya, head of the Department of Medicine at Makerere University College of Health Sciences in Kampala, predicts that stock-outs will happen again. As prices continue to drop, sales will rise and could exceed capacity. A big reason for this supply instability is that in Uganda, as in many African countries, privately owned pharmacies dispense ACTs to anyone who can pay for them, even without a prescription. One taxi driver in Kampala told *Nature Outlook* he swallows ACTs as a prophylaxis whenever he feels slightly sick.

"Globally, we are in a precarious situation for ACTs," says Sonali Korde, an advisor at the US President's Malaria Initiative based in Washington, DC. If countries mismanage their supplies or sell too many to people without the disease, she warns, stock-outs will happen and people will perish.

ABANDONED INFIRMARIES
Boosting the number and quality of staff in public healthcare would undoubtedly improve Uganda's situation. A shortage of doctors plagues much of sub-Saharan Africa. Uganda, like its neighbours Rwanda, Kenya, Ethiopia, the Democratic Republic of Congo (DRC) and Tanzania, has at most 1 doctor per 10,000 people, compared to 8 per 10,000 people in South Africa, 27 in both the US and UK, and 64 in Cuba. As a result, long waits for overwhelmed doctors often deter people from seeking medical help until it's too late. And village health workers, who deliver health education and occasionally malaria medicines, are unpaid volunteers in Uganda — as a result, Kamya says, these positions are often vacant.

Some say the issue boils down to money. The son of peasants in western Uganda, Kakuru dreamed of being a doctor from a young age. He says he never tires of watching sick children recover. But he worries that the US$300 per month salary paid to public sector doctors will not be enough for him to provide a better quality of life for his young daughter than he himself experienced. "When we talk about a pay raise, the government just tells us that we have to love our nation," Kakuru says. Many of his colleagues from medical school have left the country or joined non-governmental organizations (NGOs) that offer US$1,200 per month or more. "My friends have even taken NGO jobs in dangerous places like South Sudan if it means earning a better living," he says.

It is staff retention, not recruitment, that is Uganda's problem. "There are enough health

Villagers travel to Tororo public hospital on foot, bicycle or boda-boda (left) where mothers and children wait in long queues to see a doctor.

workers trained in this country, but few stay in the public sector," says Seraphine Adibaku, the malaria programme manager at the Ministry of Health. "You find healthcare facilities that are closed or struggling with very few staff," he says. "The President has said that health is a priority area, but usually when it comes to sharing the annual budget, you find it falls short of what well-meaning leaders want to achieve."

SEEKING SUSTAINABLE ANSWERS

Aid from international organizations is vital to malaria control. The Global Fund, which assembles donations from 54 governments, the Bill & Melinda Gates Foundation and other donors, has disbursed nearly US$162 million to Uganda to fight malaria since 2003. In addition, the US President's Malaria Initiative has given US$144 million since 2006. Aid has helped buy and distribute insecticide-treated bed nets and ACTs, educate villagers about malaria, train health workers, and spray homes in northern districts with insecticide.

However, the projects don't include supplementing the salaries of doctors as an incentive for them to remain in the public sector. In other African countries, including Rwanda, The Global Fund provides salary 'top-ups' for doctors who meet performance criteria determined by its Ministry of Health. Yet the Ugandan government has not asked for this type of support, and The Global Fund has not provided it.

Grants from international research institutions can enhance health infrastructure, although only indirectly. Fourteen years ago, Kamya collaborated with Phil Rosenthal, from the University of California, San Francisco, on a study funded by the WHO and the US National Institutes of Health (NIH); their efforts led to the formation of a non-profit organization called the Infectious Diseases Research Collaboration (IDRC). The IDRC now employs about 200 people, who help run clinical trials, studies and surveys in Uganda. Kamya says that patients who enrol in the trials receive quality care as well as health education, and the hospitals that host the research teams also benefit. "In Tororo, our doctors work as surgeons when they can, and we let the hospital use our generator when the lights go out during operations," he says.

"Some people say that $6 billion is a lot of money, but I don't think it's an outrageous thing to ask for."

Unfortunately, like the programmes operated by international organizations, grants for research projects must eventually end, often abandoning their local staff and patients. Still, past collaborations have created a cadre of trained investigators: a local resource that did not exist in Uganda when Kamya authored his first scientific paper in 1995. Kamya and other investigators now lead their own studies and train students year round. Nurturing local talent is important from more than simply a resource point of view. "We regularly share data with the Ministry of Health," he says, "and hearing about the country's needs from a Ugandan is different than hearing about it from an American."

GLOBAL PROBLEM; LOCAL SOLUTIONS

The global death toll from malaria is anywhere from 655,000 to 1.2 million (ref. 3). The reasons people die from this preventable and curable disease vary from region to region. Mountainous terrain in northeast India complicates the distribution of ACTs, whereas conflict in Burma, South Sudan and DRC has destroyed clinics where people might have gone for help.

What is common to all the countries with a high incidence of malaria is that their people are poor and have inadequate access to education, drugs, diagnostic tests and doctors. Infrastructure improvements will be essential for malaria elimination, says Rob Newman, director of the Global Malaria Programme at the WHO — so if international aid lapses, health workers and hospitals will still be there. These systems aren't impossible to build, Newman says, but they do take long-term investments in human resources, logistics, regulation and surveillance.

According to the 2011 WHO World Malaria Report, malaria elimination will cost nearly US$4 billion more than the US$2 billion pledged (see 'The numbers game', page S14'). However, there are no new sources of funding on the horizon, so meeting this target before 2015 seems unlikely. "Some people say that $6 billion is a lot of money, but I don't think it's an outrageous thing to ask for," Newman says. "Ask someone if they think a person should die because they can't afford a $5 bed net, a 50-cent diagnostic test and a $1 drug." Although sophisticated in their simplicity, these things mean nothing without practical ways to get them into the hands of mothers in distress. ∎

Amy Maxmen *is a freelance science journalist in New York.*

1. Okiro, E. A. *et al. BMC Medicine* **9**, 37 (2011).
2. US President's Malaria Initiative, Malaria Operational Plan, Rwanda Fiscal Year 2011.
3. Murray, C. J. *et al. Lancet* **379**, 413–431(2012).

The missing pieces

Nine experts give their opinion on the 'known unknowns' in malaria research.

BRENDAN S. CRABB & JAMES G. BEESON
Unravel natural immunity

Burnet Institute, Melbourne, Australia.

Parasite development goes through several distinct stages in both the human host and mosquito (see 'One parasite — many hiding places', page S17). After repeated infections with *Plasmodium falciparum* or *P. vivax*, the two main causes of malaria, people do eventually develop effective immunity that prevents symptomatic and severe illness and controls the blood-stage infection. This observation has long provided a strong rationale for malaria vaccine development, yet we know remarkably little of how malaria immunity works in naturally exposed individuals. Our limited knowledge of both the key molecular targets and the specific immunological mechanisms has severely constrained vaccine development. What we do know is that protective immune responses predominantly act against the blood stages of *Plasmodium* parasites and have multiple targets and effector mechanisms. Although immune responses also develop against liver-stage parasites and transmissible forms of the parasite (gametocytes), even less is known about their nature and relevance.

Malaria research needs to establish the relative significance of the many known or predicted antigens. It should focus on

A malaria parasite in the liver stage of its complex lifecycle.

defining the mechanisms that clear or prevent infection, and should be complemented by studies into how malaria immunity is acquired and maintained as well as how the parasite evades the immune response. To help achieve these goals, government and private funding agencies must build research capacity in malaria-endemic countries, which will help promote greater linkages between immunology research, population studies and clinical trials. Understanding the basis of human immunity will be key to developing long-lasting malaria vaccines, and will also enable us to identify populations at highest risk and to monitor those populations in malaria elimination programmes over time.

ROGERIO AMINO & ROBERT MÉNARD
Identify the critical antigens

Unité de Biologie et Génétique du Paludisme, Institut Pasteur, Paris.

The symptoms of malaria arise only after *Plasmodium* has left the hepatocytes (liver cells) and infected red blood cells — or erythrocytes. Therefore, an important goal is to develop an efficient vaccine against the pre-erythrocytic (PE) stages of the parasite — the sporozoites injected into the skin by the mosquito and the parasite forms that develop inside hepatocytes. Live PE parasites attenuated by irradiation or gene inactivation are known to provide solid protection against infection; however, their use as vaccines for humans in endemic areas faces major technical and logistical limitations (see 'The take-home lesson', page S24). The subunit vaccines now in clinical trials, which are based on sporozoite antigens, have shown limited efficacy. Clearly, other vaccine candidates must be identified. The biggest research need is to identify the right antigens among the thousands expressed by PE parasite stages.

Studies of the attenuated parasite vaccine in rodents indicate the crucial protective role of a certain type of immune cell, CD8+

T cells, which detect and destroy hepatocytes infected by the malaria parasite. A functional assay that exploits this ability of CD8+ T cells would help identify such antigens. Recent technical developments, such as transcriptomics and proteomics to identify PE antigens, expression cloning procedures to catalogue the many antigens found, and new imaging technologies, make possible systematic screens to find antigens capable of eliciting protective immunity.

ANDY WATERS
Focus on the ookinete

Institute of Infection, Immunity and Inflammation, University of Glasgow, United Kingdom.

Female *Anopheles* mosquitoes transmit the malaria parasite. In the mosquito gut, male and female gametocytes fuse to create a zygote, which develops into an ookinete. The ookinete crosses the mosquito midgut wall and implants, where it continues to develop. A successful ookinete has overcome tremendous odds to survive, and it exists in a hostile environment, surrounded by human blood cells that are being enzymatically digested. It is here in the mosquito gut that the *Plasmodium* parasite suffers the greatest proportional loss of numbers of any stage of its lifecycle, making it an interesting target for blocking transmission.

In 1911, Ronald Ross (who won a Nobel prize for his work linking malaria transmission to the *Anopheles* mosquito) recognized that, in many endemic settings, malaria dies out if transmission rates drop below a certain level. Although transmission is dropping in Africa, mainly thanks to insecticide-treated bed nets, we need additional measures to accelerate that trend. An increased understanding of ookinete biology would help this effort, including the identification of virulence factors critical to its survival, and the discovery of elements that could stimulate an innate immune response in the mosquito. Logically, targeting the weakest link in the Plasmodium lifecycle will be the best way to develop new vaccines, drugs

SEATTLE BIOMED
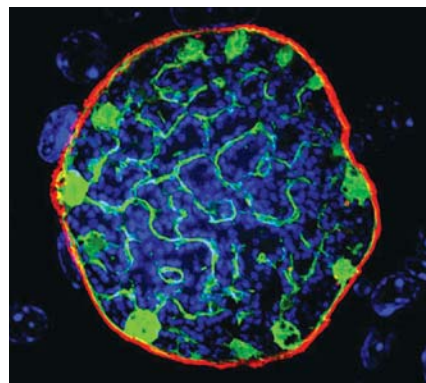
or vector-control methods that will further reduce the passage of the parasite through the mosquito and hasten its extinction.

ELIZABETH A. WINZELER
Don't ignore vivax

University of California, San Diego, School of Medicine, La Jolla.

Malaria caused by *P. vivax* is more widespread than that caused by *P. falciparum* — it endangers up to 40% of the world's population. Indeed, of the two parasites, most scientists agree that the malaria caused by *P. vivax* will be the more difficult to control and eliminate: infections are trickier to detect; the parasite can hide as a hypnozoite (a dormant form) in the liver and cause relapses years after initial infection; and there are fewer tools available to study *P. vivax*.

The only licensed drug that is able to eliminate *P. vivax* hypnozoites is primaquine. This drug needs to be given at low doses over 2 weeks because of its potentially lethal toxicity to individuals who are deficient in the metabolic enzyme glucose-6-phosphate dehydrogenase. Parasite resistance to primaquine is suspected but, within an endemic region, there is currently no accepted method to distinguish relapses caused by drug failure from those caused by reinfection. Furthermore, *ex-vivo* assays cannot accurately assess resistance because primaquine becomes active only after the liver metabolizes it.

Although it is widely agreed that we need a new drug to replace primaquine, there are no established anti-hypnozoite targets, nor are there accepted screening methods that do not involve non-human primates. These are crucial gaps for researchers to address.

MATS WAHLGREN
Tackle severe malaria

Department of Microbiology, Tumour and Cell Biology Karolinska Institutet, Stockholm.

Improvements in supportive care, including adjunct drugs, could lower the fatality rate for the 10 million or so individuals who develop severe malaria each year.

The critical factor in malaria pathogenesis is the obstruction of blood-flow that results when parasitized red blood cells block the human microvasculature and cause inflammation. Indeed, in patients with cerebral malaria, the level of vascular obstruction correlates directly with the depth of coma. For severe *P. falciparum* malaria cases, death rates remain high in spite of the availability of anti-parasitic drugs (artesunate — derived from artemisinin), intravenous fluids and state-of-the-art intensive care. No adjunctive treatment has been shown to be of benefit in severe malaria and there are few clinical data regarding the optimal supportive care of patients in the early stages of their hospitalization.

In patients with severe malaria, the majority of deaths occur within the first 48 hours of hospitalization. It is therefore crucial for the physician to be able to 'unstick' the infected cells and restore blood-flow without delay. Research that helps us understand the molecular details of this process is vital because it will allow for the development of novel anti-adhesive and anti-inflammatory strategies. Questions such as 'how does the parasitized red blood cell bind in the human microvasculature' and 'how do these cells block the capillaries and cause inflammation' need to be answered.

DAVID A. FIDOCK
Define resistance

Departments of Microbiology & Immunology and of Medicine, Columbia University Medical Center, New York.

Recent evidence for the emergence of *P. falciparum* parasite resistance to derivatives of the antimalarial artemisinin suggests that in a few short years we may be faced with the loss of this vital drug (see 'Holding out for reinforcements', page S16). Despite intense efforts to discover and develop new antimalarial agents, no suitable alternative is ready to replace artemisinin. How can the research community best help, at a time of shrinking science budgets? Understanding the biological features of artemisinin tolerance or resistance is key to defining molecular markers to monitor its spread, and to developing therapeutic strategies that effectively treat drug-resistant strains. This will require an exceptional level of sharing of reagents, technologies and knowledge, as the genetic and molecular basis of decreased parasite susceptibility to this drug is likely to be particularly complex.

More research is also required to define how artemisinins work, how this translates into parasite death, and what metabolic pathways enable parasites to withstand drug action. Such investigations will involve the application of next-generation sequencing, genetic association studies to define candidate loci, faster methods of genetic manipulation of *P. falciparum*, and metabolomics. Research into mechanisms of resistance also needs to extend to the partner drugs used in artemisinin-based combination therapies and to the new chemical entities that are entering clinical trials.

The recent reductions in malaria deaths are very encouraging, but these gains are fragile. We cannot allow malaria to resurge.

SOLOMON NWAKA
Harness local knowledge

African Network for Drugs and Diagnostics Innovation (ANDI); and Special Programme for Research and Training in Tropical Diseases, World Health Organization, Geneva.

About 80% of the populations of Africa, Asia and Latin America rely on local traditional medicines to meet their primary healthcare needs. In some instances, these local solutions have spurred innovation that has transcended national borders to save millions of lives around the world. Take artemisinin, for example. Now the mainstay of malaria control, this drug was derived from centuries-old traditional Chinese medicine. But there is a significant knowledge gap on how best to tap into local knowledge. Research and guidelines are needed to: inform and develop sample collection methods; generate and evaluate data on the efficacy, safety and quality of traditional medicines; and to help us understand how these approaches work.

Several discoveries based on traditional African medicines are also in our hands, but these are in desperate need of translation into usable products. This is true not only for treatment and control of malaria, but for a variety of other diseases.

Our work with the African Network for Drugs and Diagnostics Innovation (ANDI) and by other groups suggest that what is needed are coordinated mechanisms and investment to support the translation of local knowledge into affordable, safe and accessible products. Sustainable solutions can be realized only if appropriate regulatory and policy frameworks are established to guide research, development, production and use of such medicines. ∎

Mosquitoes bred for vaccine research are reared in cardboard cups.

VACCINES

The take–home lesson

The nearly century–long search for a malaria vaccine might end in the bottom of a cup.

BY SARAH DEWEERDT

Takeout containers — cardboard cups of the sort used to bring home soup from the deli — are the surprisingly low-tech housing in which Seattle BioMed rears 20,000 to 30,000 malaria-carrying mosquitoes each week. At the nonprofit research institute in Washington, dozens of containers line the shelves of its humid walk-in incubator, mosquitoes clinging upside-down to mesh inserts.

There are similar set ups in labs around the world: mosquitoes biding time, before being encouraged to gorge on human volunteers, or have their parasite-laden salivary glands dissected by a deft lab technician. Although the first partially effective malaria vaccine might be only a few years away from clinical use, the search for a truly effective vaccine is far from over.

The problem is the complexity of malaria parasites — single-celled organisms belonging to the genus *Plasmodium*. The parasite has more than 5,000 genes — 50 times more than some viruses, for example — and has a multiphase lifecycle that means it shows a different side to the immune system at different stages of its development. "It's difficult to see which of the tsunami of immune responses that are provoked by the parasite are associated with protection," says Robert Sauerwein, head of the Centre for

Clinical Malaria Studies at Radboud University in Nijmegen, the Netherlands. Without knowing which immune response a vaccine needs to stimulate, researchers can only guess.

Immunology is not the only uncertainty: producing vaccines practically and in large volumes is another hurdle. Malaria researchers "know how to make a protective malaria vaccine, but don't know how to manufacture it," says Stefan Kappe, malaria programme director at Seattle BioMed. "And the vaccines we know how to manufacture don't protect that well."

BITS AND PIECES

A number of malaria vaccine candidates have entered clinical trials. The furthest along, known as RTS,S, is about 50% effective against the disease. It's a subunit vaccine which presents to the immune system the circumsporozoite protein (CSP), a molecule that studs the surface of the sporozoite stage of *Plasmodium falciparum*. It's the sporozoite that passes from the mosquito to the human host (see 'One parasite — many hiding places', page S17). Investigators in seven African countries have enrolled more than 15,000 infants in a phase III clinical trial of RTS,S. In late 2011, they reported the first set of results from 6,000 of these infants. Those who received RTS,S had 56% fewer malaria episodes and 47% fewer cases of severe malaria over the course of a year

compared to controls[1]. "This is the first vaccine that has proved substantial efficacy," says Didier Leboulleux, the Ferney, France-based director of the Clinical Unit at the PATH Malaria Vaccine Initiative (MVI), a nonprofit that is developing RTS,S in partnership with pharmaceutical giant GlaxoSmithKline.

If initial results hold up, RTS,S could be rolled out for clinical use in 2015. But, Leboulleux acknowledges, "It's clearly a first-generation vaccine." Most investigators agree that eradication of malaria will require a vaccine that can prevent the disease 80–90% of the time.

One approach to developing a more effective vaccine is to try different vaccination strategies using CSP. "We're trying to milk that antigen for as much as we can with things like prime–boost approaches," says Ashley Birkett, director of research and development at PATH MVI. Path's prime-boost strategy delivers the same antigen in two different ways in order to improve the immune response.

Another possibility might be to add more antigens to the vaccine. For example, researchers have tested vaccines based on merozoite surface protein 1 (MSP1) and apical membrane antigen 1 (AMA1), each of which is expressed by the parasite during the blood stage of its lifecycle. These antigens have shown poor effectiveness on their own, but adding them to RTS,S might

improve the chances of generating a protective immune response, reckons Christopher Plowe, professor of medicine at the University of Maryland in Baltimore.

Other researchers are not as confident. "It will be very hard to reach that 80–90 percent efficacy with a subunit vaccine," says Sauerwein. He argues that a whole-organism vaccine, which presents the immune system with hundreds of parasite antigens, is a better bet. "Everybody makes his or her own cocktail of immune responses, eventually leading to protection," he adds.

There is precedent for a whole-organism approach. In the 1970s, researchers showed that people bitten by irradiated malaria-carrying mosquitoes gained protection from the disease. The radiation-weakened sporozoites couldn't cause malaria, yet were up to 90% effective at inducing immunity.

But it took up to 1,000 mosquito bites to generate this protection — hardly a practical approach for a mass-vaccination campaign. "Nobody thought it would be possible to make a whole-sporozoite vaccine," says Stephen Hoffman, chief scientific officer of the Rockville, Maryland-based biotech firm Sanaria.

Hoffman, formerly director of the malaria programme at the US Naval Medical Research Center, founded Sanaria in 2003 to try to counteract that pessimism within the malaria community. The company developed a method that involves freezing sporozoites painstakingly dissected by hand from the salivary glands of mosquitoes. But standard intradermal or subcutaneous injection of irradiated sporozoites has failed to protect humans against malaria[2]. Intravenous injection might work better. Monkeys inoculated intravenously generated high levels of CD8$^+$ T cells in their livers specific to the malaria parasite — a key component of immunity to the disease, Hoffman says. Sanaria, in collaboration with the Vaccine Research Center, part of the US National Institutes of Health, has entered the vaccine into clinical trials, with results expected in late 2012.

IN THE GENES

"Whoa," says Seattle Biomed's Kappe, sucking in his breath, "giving intravenous vaccinations to children in Africa is difficult to envision." Seattle BioMed has a different strategy for a whole-organism vaccine. Instead of using radiation to weaken the parasites, Kappe favours a genetic engineering approach: knocking out selected genes so that sporozoites can infect liver cells and trigger the immune system, but are unable to progress to the blood stage of their lifecycle and cause disease[3].

Kappe and others say that genetic engineering will weaken the parasites in a more predictable, uniform way to enable vaccination — eventually using a needle and syringe — at a much lower dose than irradiation. Kappe describes an unpublished study, where five of six volunteers bitten by mosquitoes infected with sporozoites lacking the *p36* and *p52* genes developed robust

THE ALTRUISTIC APPROACH
Transmission–blocking vaccines

Most efforts at developing a malaria vaccine target the parasite in the liver or blood of the human host. But what if you could give a person a vaccine that would affect parasites inside a mosquito? "It's odd, yes. I know," says Rhoel Dinglasan, a professor of molecular microbiology and immunology at Johns Hopkins University in Baltimore, Maryland.

And yet, despite the oddness of the idea, there's growing interest in 'transmission-blocking vaccines' as this approach is called. Such a vaccine would be like altruism in a syringe: it wouldn't prevent vaccine recipients from contracting malaria, but it would prevent any mosquito that bites them from passing the parasite to someone else.

Researchers have tried vaccines based on a variety of proteins — P25, P28, P230, to list a few — that are produced by the parasite inside the mosquito. But it has often been difficult to manufacture these proteins in sufficient quantities and, in a few cases, the vaccines have caused serious side effects[4].

Dinglasan is taking a different approach. The vaccine he is working on is based on a mosquito antigen — a molecule called AnAPN1, found on the surface of cells lining the mosquito's gut that serves as a kind of docking station for malaria parasites[5]. The theory is that a person injected with an AnAPN1 vaccine will make antibodies to the molecule, which a mosquito then imbibes along with the parasites in its blood meal. Once in the mosquito gut, the antibodies block AnAPN1 and prevent the malaria parasites from latching on and entering the cells.

The vaccine is at least a year or two away from being tested in humans. So far, Dinglasan's team has had encouraging results in rabbits. Interestingly, as well as inhibiting *Plasmodium falciparum*, the anti-AnAPN1 antibodies can block *P. vivax*, a species of malaria parasite that is common outside Africa. Very little vaccine research targets *P. vivax*, so the possibility of a double-strike is especially tantalizing. "This is something that evolution has given us as a gift," Dinglasan says, "and we're lucky enough to have found it."

SD
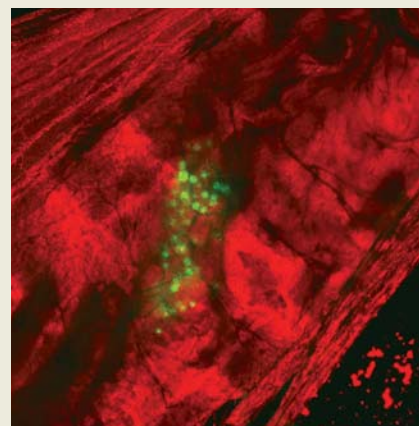
Target: the parasite (green) in the mosquito gut.

immune responses. But the sixth got malaria from the vaccine — unacceptable odds when it comes to safety.

Kappe plans to test lower doses of this genetically weakened parasite, and is developing another strain of sporozoite with other genes missing. He hopes that additional safety mechanisms could be engineered in, such as a suicide gene that would cause the parasite to self-destruct if it did reach the blood stage.

Sauerwein is also preparing genetically engineered parasites and, in parallel, is investigating an even more radical approach: immunizing with live *Plasmodium* parasites that aren't weakened at all. Ten people exposed to malaria-carrying mosquito bites and dosed with the antimalaria drug chloroquine to protect them from getting sick, all developed immunity to the disease; some remained protected for as long as 28 months (ref. 3).

Sauerwein's radical approach "gives the best protective immunity of any malaria intervention ever" — even better than those experiments with irradiated parasites that were the benchmark for the field for decades, says Hoffman, who is collaborating with Sauerwein on related work. He suggests Sanaria's method for manufacturing sporozoites could make this type of controlled infection a feasible approach to vaccination, at least for military personnel and travellers to malaria-endemic regions.

Sauerwein and Hoffman are not alone in trying multiple approaches — many researchers in this field are cooking several leads for a malaria vaccine at the same time. Kappe, for example, muses on the possibility that, rather than make it all the way to an approved vaccine, his engineered parasites will simply reveal promising antigens to include in a next-generation subunit vaccine. For now, nothing is off the menu. ∎

Sarah DeWeerdt *is a freelance science writer in Seattle, Washington.*

1. The RTS,S Clinical Trials Partnership. *N. Engl. J. Med.* **365**, 1863–1875 (2011).
2. Epstein, J. E. *et al. Science* **334**, 475 (2011).
3. Roestenberg, M. *et al. Lancet* **377**, 1770–1776 (2011).
4. Wu, Y. *et al. PLoS ONE* **3**, e2636 (2008).
5. Dinglasan, R. R. & Jacobs-Lorena, M. *Trends Parasitol.* **24**, 364–370 (2008).

VECTOR CONTROL

The last bite

Preventing mosquitoes from transmitting the malaria parasite is a crucial piece of the eradication puzzle.

BY LAUREN GRAVITZ

Mosquitoes are the ideal vector — they provide a safe haven for a parasite to reproduce, then inject it directly into the human bloodstream. What's more, mosquitoes are a moving target. The females of nearly 70 species of *Anopheles* transmit malaria, biting indoors and out. They have evolved resistance to once highly effective pesticides[1], and some species might have even changed their behaviour to bite earlier in the evening when people are less likely to be shielded by bed nets.

To achieve a definitive end to malaria transmission, mosquito populations must be controlled. Some countries with low transmission rates, such as Tunisia and the United Arab Emirates, got rid of malaria using vector control, aggressive treatment and stiff monitoring, but in parts of Africa transmission rates are so high that even reducing bite frequency by 99% would still result in around 10 infectious bites per person per year. In these circumstances, elimination means extraordinary levels of control. "You're talking 99.99% control, which is different from any other pathogen on the planet," says Gerry Killeen, a mosquito biologist and malaria expert who splits his time between the Liverpool School of Tropical Medicine in the United Kingdom and the Ifakara Health Institute in Tanzania. "It makes flu look difficult to transmit."

The last big international push to eradicate malaria, spearheaded by the World Health Organization (WHO), ran from 1955 to 1969 and involved spraying insecticides — primarily the newly developed DDT — on the inside walls of houses[2]. But coverage was inconsistent, high in some countries while low or non-existent in others, and some mosquito populations, such as those that lived in tropical forests, went untouched. This effort managed to eliminate the disease in North America, Europe and parts of Asia, and tamped it down in other regions. Yet by the early 1970s malaria was resurgent on several continents, often reaching epidemic proportions.

The WHO campaign was a massive disappointment — and eradication became known as 'the E word' in some circles. It wasn't until after the successful roll out of insecticide-treated bed nets in the 1990s that governments across the world thought it worth trying again. At first glance, the effort appears to be working: the WHO estimates that it has saved more than a million lives since 2000. But more is needed in order to extinguish the last hotspots of malaria transmission.

HISTORY REPEATING

Many researchers in the field believe that eradicating malaria is possible, but it would require a global strategy that employs a variety of insect-control techniques. "We've seen a vast resurgence of interest and investment in malaria, which is attributable to the advent of the treated net," says Jo Lines, an entomological epidemiologist at the London School of Hygiene and Tropical medicine. As with the 1955 campaign, "The whole business again rests on the effectiveness of the massive scale-up of a single technology."

And once again there are signs of weakness. Lines and others point to insecticide-resistant mosquitoes as a particularly disturbing trend. Pyrethroid insecticides are, by far, the most commonly used pesticide in endemic regions: they're cheap, long-lasting, effective at both repelling and killing mosquitoes, and safe enough that a baby can suck on a pyrethroid-treated bed net without harm. That optimal profile, however, also means that the family of chemicals has been massively overused and is in danger of becoming ineffective.

Similar concerns apply to chemicals besides the pyrethroids. All of the insecticides currently in use for malaria control have come from agriculture; decades of use against bollworms and beetles have had the unintended side effect of exposing mosquitoes to the same chemicals. Now that the mosquitoes are encountering them in people's homes, resistance is spreading. "The frequency with which we hear new reports of insecticide resistance is increasing," says Tom McLean, chief operating officer of the Innovative Vector Control Consortium (IVCC), a UK-based non-profit that partners with companies to pursue novel insecticides. It seems that almost wherever an entomologist looks, he adds, "they find insecticide resistance."

The global health community is working on solutions. In the short term, for example, one aim is to repurpose agricultural pesticides: fast-degrading chemicals for crop use are being reformulated to create longer-lasting insecticides for indoor spraying. Yet these are only stop-gap measures. Many malariologists contend that, in order to maintain progress, they need a larger toolbox.

SPRAY AWAY

Vector control should combine a diverse mix of insecticides for indoor spraying and treating bed nets, a range of repellents — both new and old — and novel ways to decrease population sizes of the worst-offending mosquito species[3]. Researchers are pursuing all strategies.

McLean is optimistic about the outcome of IVCC's projects. "The rate at which we're finding new chemicals suitable for development suggests we'll reach our endpoint by around 2020: a whole new set of insecticides with which we can implement mosaics of vector control," he says.

Matthew Thomas, an entomologist at Pennsylvania State University in University Park, has been working on a different type of insecticide. Rather than synthetic pesticides, he's developing one based on a fungus, with the aim of making it resistance-proof. The fungus, *Beauveria bassiana*,

⟳ NATURE.COM
Efforts to control the mosquito continue:
go.nature.com/zu1djn

TO KILL A MOSQUITO
Various technologies to control malarial mosquitoes are available or are in development

Strategy	Advantages	Disadvantages	Current research aims
Indoor residual spraying	• Deters mosquitoes from entering buildings • Kills mosquitoes that land on walls	• Lasts only 6–12 months • Growing issues of resistance • Needs trained workers • Useless outdoors	• Develop inexpensive and long-lasting insecticides • Develop novel insecticides that act on resistant mosquitoes
Insecticide-treated bed nets	• Deters mosquitoes • Kills mosquitoes that land • Relatively inexpensive	• Last up to 3 years • Growing issues of resistance • Need to be under them indoors	• Investigate long-term • Develop alternative, safe pesticides
Odour-baited insecticide traps	• Reduce outdoor biting	• Can be expensive • Not as useful in rural settings	• Determine most effective structure • Perform cost–benefit analyses
Pesticide applied to water where mosquitoes breed	• Targets species that breed in large, stagnant bodies of water • Hits a different stage of lifecycle, prolonging time to resistance	• Useless against breeding sites in puddles or streams • Must monitor breeding sites • Very expensive and energy intensive	• Develop baited stations and install near breeding pools
Fungus that hobbles and eventually kills mosquitoes	• Works in a different way from current insecticides, so can target resistant mosquitoes	• Not yet field-tested • Only effective in enclosed spaces	• Determine if slow-acting formulations better than fast-acting
Bacterial infection of mosquito to prevent parasite transmission	• Potential long-term control of mosquito populations • Potential to slow transmission of infection	• Requires species-specific *Wolbachia* strains, introduced separately • *Anopheles* proven difficult to infect	• Develop ways to infect the common species • Prove transmission of bacteria through mosquito generations
Genetically engineered mosquitoes	• Long-term control of mosquito populations • Slows transmission of disease	• Sheer number of different species • Widespread fear of genetically modified organisms (GMOs)	• Find most effective mutations • Assess whether GMO would integrate into native populations

starts to work upon contact — the spores attach to a mosquito, penetrate its exoskeleton and burrow inside where they grow, multiply, and produce toxins to fend off an immune attack. The mosquitoes can't fly, eat or smell properly. "It's like a head cold," Thomas says. "Ultimately the insect dies, and how quickly that happens, whether 5 days or 2 weeks, depends on the isolate [fungal strain] we choose."

A faster-acting isolate kills a mosquito before she's old enough to transmit the malaria parasite, which takes 2 weeks to mature. However, the risk is that only the most vulnerable mosquitoes will die whereas more resilient ones will manage to breed and spread resistance. A slower-acting isolate could act as a late-life insecticide: hampering a mosquito's ability to feed and to transmit the parasite yet allowing her to lay some eggs before she dies, thus limiting selective pressure. "We should rethink how we use insecticides," says Thomas. "Not that killing quickly is a bad thing, but it increases speed to resistance." He adds that using the fungal pathogen in combination with other pesticides could further deter resistance by reducing reliance on a single technology.

STEALTH ATTACK
Perhaps the more ambitious of the long-term projects are the ones that aim to change the mosquitoes themselves. Researchers are investigating an assortment of techniques: male sterilization, genetic engineering, even the introduction of bacteria that reduce a mosquito's ability to transmit the malaria parasite. It's an uphill battle — because dozens of different species transmit malaria, scientists will need to separately engineer, breed and distribute each kind of modified mosquito.

The uphill battle, at least for genetic modification, has an army of industry and academic researchers on the case. "There are people doing genomics, bioinformatics, population genetics, protein engineering, computational protein design, germline transformation of mosquitoes, modelling, and working with potential field sites," says Mark Benedict, a molecular biologist and visiting fellow at the University of Perugia in Italy. Benedict is part of an international team that is starting with some conservative modifications — sexually sterile males — and working up to more ambitious plans, such as males that have mostly male offspring. He is developing a strategy to move some of the more promising mosquito strains out of the lab to see if the experimental insects can integrate themselves into natural populations. "The lab experiments are moving very well, very fast. If we had the most powerful, most effective strains in the field in 10 years, I'd be quite happy," he says. But genetically engineered insects have another hurdle to get over: the widespread fear of genetically modified organisms.

Some scientists are trying to circumnavigate that fear by working another angle. Bacteria from the *Wolbachia* genus can infect mosquitoes and decrease parasite transmission. Moreover, the bacteria are transmitted from one generation of mosquitoes to the next, making the infection self-sustaining. *Wolbachia* has been successfully introduced into one mosquito species that transmits another problem disease: dengue. Small trials of the infected vectors in Australia look promising, and show that the bacteria-laden insects quickly integrate into native populations. Within 14 weeks of the release of 250,000 *Wolbachia*-infected mosquitoes, 90% of the populations in the test areas were positive for the bacterium[4].

Such an approach could work for malaria, too. The trick is finding the appropriate *Wolbachia* species — something that has proved very difficult. But entomologist Zhiyong Xi, at Michigan State University in East Lansing, might have found one. He says so far he's managed to introduce the bacterium into one species that's prominent in India and the Middle East and has begun promising efforts with three African species. Xi says he is just beginning talks with India's National Institute of Malaria Research about testing the relevant mosquitoes.

Of course, by the time modified mosquitoes are ready for release, any number of advances could be available, including an anxiously awaited vaccine (see 'The take-home lesson', page S24). Environmental change will also affect the malaria burden. Land development has removed the forests that shelter large mosquito populations. More modern-style houses, with tin roofs instead of mud — ideally with screens on the windows and doors — to prevent mosquitoes from entering in the first place.

The future of mosquito control must ultimately consist of a mixture of current technologies combined with both concentrated science and social development (see 'To kill a mosquito'). Insecticide-treated nets and indoor spraying have helped enormously, "but there's a limit to what they can do," says Killeen. In Tanzania, thanks to these measures, "malaria has crashed down to levels that are normal in other areas. Even at those levels, it's still a major public health problem." ∎

Lauren Gravitz *is a freelance science journalist in Los Angeles, California.*

1. Greenwood, B. *et al. J Clin Invest.* **118**, 1266 (2008).
2. Nájera, J. A., González-Silva, M. & Alonso, P. L. *PLoS Med.* **8**, e1000412 (2011).
3. Ferguson, H. M. *et al. PLoS Med.* **7**, e1000303 (2010)
4. Hoffman, A. A. *et al. Nature* **476**, 454–457 (2011).